

UNIVERSITY OF BIRMINGHAM

SYNTHESIS OF NEW CARBOXYPHOSPHONATE METAL-ORGANIC FRAMEWORKS (MOFS) AND THEIR POTENTIAL AS ELECTROCATALYSTS FOR CO_2 REDUCTION

By

Oriyomi Ogunbanjo

A thesis submitted to the University of Birmingham for the degree of Doctor of Philosophy

School of Chemistry
College of Engineering and Physical Sciences
The University of Birmingham
October 2024

UNIVERSITY OF
BIRMINGHAM

University of Birmingham Research Archive

e-theses repository

This unpublished thesis/dissertation is copyright of the author and/or third parties. The intellectual property rights of the author or third parties in respect of this work are as defined by The Copyright Designs and Patents Act 1988 or as modified by any successor legislation.

Any use made of information contained in this thesis/dissertation must be in accordance with that legislation and must be properly acknowledged. Further distribution or reproduction in any format is prohibited without the permission of the copyright holder.

Abstract

The increasing concentration of CO_2 in the atmosphere is alarming for modern society and the reduction of CO_2 into valuable products would be an ideal solution. Metal–organic frameworks (MOFs), constructed from organic linkers interconnected with metal nodes, with high porosity and large surface area, are an emerging class of electrocatalysts for reduction of CO_2. The research presented in this thesis aimed at developing new carboxyphosphonate metal-organic frameworks (MOFs) and exploring their potentials as electrocatalyst for the CO_2 reduction reaction. This study started with the synthesis of the carboxyphosphonate MOF, BIRM-1, exploring its ion exchange capability with nickel metal, producing a new ion exchange material named Ni^{2+}-BIRM-1. Findings revealed that nickel (II) cations were successfully incorporated into BIRM-1 after 24 hours of ion exchange experiment, maintaining its crystallinity as confirmed by powder XRD and SEM. The extent of nickel cation exchange was evaluated via SEM-EDX analysis, with the result showing that the calculated molar ratio of Ni:P:Zn in Ni^{2+}-BIRM-1 matched the expected molar ratio, indicating 100% ion exchange efficiency. Single crystal XRD also revealed that Ni^{2+}-BIRM-1 retained BIRM-1's crystallographic characteristics, with no ammonium cations in the pores, confirming full ion exchange and structure preservation. However, cyclic voltammetry indicated that Ni^{2+}-BIRM-1 was not electrochemically active for CO_2 reduction. New carboxyphosphonate materials were synthesised using 3-phosphonopropionic acid ligand and characterised using single crystal XRD, resulting in five new structures: BIRM-11(Zn), BIRM-12(Cu), BIRM-13(Cu), BIRM-14(Cu), and BIRM-15(Co) which are either layered compounds or 2D MOFs. The pH played a critical role in deprotonating the carboxylphosphonate ligand and achieving metal-ligand coordination. In BIRM-11(Zn), BIRM-14(Cu), and BIRM-15(Co), complete deprotonation was achieved, and their structures appeared as 2D frameworks with covalent bonds while in BIRM-12(Cu) and BIRM-13(Cu) structure,

incomplete deprotonation led to hydrogen-bonded layered structures. Efforts to convert BIRM-13 (Cu) into 3D structures using 4,4-bipyridine resulted in the 2D MOF, BIRM-14. Preliminary electrochemical studies using cyclic voltammetry technique showed that BIRM-12 (Cu), BIRM-13 (Cu), and BIRM-15 (Co) were active for hydrogen evolution, while BIRM-14 was promising for CO_2 reduction. A previously synthesized 2D nickel carboxyethylphosphonate also demonstrated significant potential as an electrocatalyst for the reduction of CO_2 to syngas, giving an onset potential of -0.51 V *vs* RHE and a current-mass activity of 9.5 mA/mg. Long-term electrolysis at -0.8 V (vs. RHE) produced a CO and H_2 mixture in a 30:70 ratio. DFT calculations indicated a 0.52 eV difference in limiting potentials for HER and CO_2RR, favouring HER, highlighting the thermodynamic driving forces behind the predominant production of H_2 over CO. The flexibility of 3-phosphonopropionic acid ligand makes the synthesis of 3-dimensional porous framework structures difficult, so a more rigid ligand, namely, 4-phosphonobenzoic acid was further explored for new MOF synthesis. A total of five novel framework materials (BIRM-17, BIRM-18, BIRM-19, BIRM-20 & BIRM-21) were synthesised and characterised via single crystal XRD. BIRM-17 is a 2D layered structure; optimising the synthesis temperature and time produced the 3D porous frameworks BIRM-18 and 19. Topological analysis shows that BIRM-18 and BIRM-19 exhibits a (4;2)-connected GIS-type topological structure seen in zeolites, with voids and channels ideal for gas adsorption and ion exchange. BIRM-20 and 21 crystalised as 2D layered nickel and cobalt-containing phosphonate MOFs.

Acknowledgements

I would like to thank my supervisors – Professors Paul Anderson and Paramaconi Rodriguez for their invaluable supervision, support, and tutelage during the course of my PhD degree.

My gratitude extends to the Petroleum technology development fund (PTDF) for the funding opportunity to undertake my studies at the University of University of Birmingham.

I would also like to thank Dr Louise Male for all the help and training with single crystal diffraction, both the data collection and analysis.

I also thank Dr. Bashiru, Dr. Muideen Gbadamosi, Dr. Ysusuf for their encouragement. I would like to thank my friends, lab mates, colleagues and research team – Musa, Joe, Josh, Abbey, Luke, Jake, Beatrice, Lizzi, Nashwa, Dan, Alex for a cherished time spent together in the lab, and in social settings.

My appreciation also goes out to my family and friends for their encouragement and support all through my studies.

Dedication

First, giving honour to God, the Giver and Sustainer of life:

"I will bless the Lord at all times; His praise shall continually be in my mouth".

Psalm 34:1(NKJV)

This thesis is dedicated to my grandma (Mrs. Rosalia Adeeko) and my mother (Mrs. Florence Oduntan) whose sacrifice made me what I am today. Unfortunately, they are not alive to eat the fruit of their labour. May their soul continue to rest in perfect peace (Amen).

Table of Abbreviations

ATR	Attenuated total reflectance
BET	Brunauer-Emmett-Teller
BIRM-1	MOF with formula $(NH_4)_2[Zn_2(O_3P(CH_2)_2COO)_2] \cdot 5H_2O$
BIRM-11	Layered framework with formula $Zn_3(O_3PCH_2CH_2COO)_2$
BIRM-12	Layered framework with formula $Cu(O_3PC_2H_4COOH)\ (H_2O)_2$
BIRM-13	Layered framework with formula $Cu(O_3PC_2H_4COOH)$
BIRM-14	Layered framework with formula $Cu_3(O_3PC_2H_4COO)\ (C_5H_4N)_2$
BIRM-15	Layered framework with formula $Co_3(O_3PCH_2CH_2COO)_2.(H_2O)_3].3H_2O$
BIRM-16	Coordination network with formula $Co(C_5H_4N)_2(CHOO)$
BIRM-16(Ni)	Coordination network with formula $Ni(C_5H_4N)_2(CHOO)$
BIRM-17	Layered framework with formula $Zn_2\ (O_3PC_2H_4CO_2)_3$ (DMF)(DMA)
BIRM-18	MOF with formula $Zn_2[(O_3PC_6H_4COO)_2]$.(DMF)2(DMA)4(H_2O)
BIRM-19	MOF with formula $Zn_2[(O_3PC_6H_4COO)_2]$.2(DMA)
BIRM-20	Layered framework with formula $Ni(O_3PC_6H_4COOH)\ (C_5H_4N)_2\ (H_2O)_3$
BIRM-21	Layered framework with formula $Co(O_3PC_6H_4COOH).\ H_2O$
BTC	1,3,5-benzenetricarboxylic acid
CE	Counter electrode
CNT	carbon nanotube
CO_2RR	CO_2 electrochemical reduction reaction
CPE	controlled potential electrolysis
CV	Cyclic voltammetry
DEF	N,N-diethylformamide
DMA	Dimethylamide
DMF	N,N-Dimethylformamide
DTG	Differential thermal gravimetric
ECSA	Electrochemically active surface area
EDL	Electrical double layer
EDX	Energy dispersive X-ray
EPD	Electrophoretic deposition

EXAF	Extended X-ray Absorption Fine Structure
FE	Faradaic efficiency
FTIR	Fourier transform infrared
FTO	Fluorine-doped tin oxide
GCE	Glassy carbon electrode
GDE	gas diffusion electrode
HAADF	High angle annular dark field
HER	Hydrogen evolution reaction
HRTEM	High resolution transmission electron microscopy
IL	Ionic liquid
MOFs	Metal–organic frameworks
MWCNTs	multi-walled carbon nanotubes
Ni^{2+}-BIRM-1	Nickel ion exchanged BIRM-1
$(NBu_4)PF_6$	Tetrabutylammonium hexafluorophosphate
OCP	Open circuit potential
OLEMS	Online electrochemical mass spectrometry
POMs	Polyoxometalates
PXRD	Powder X-ray diffraction
RE	Reference electrode
RHE	Reversible hydrogen electrode
SAM	Self-assembled monolayer
SBU	Secondary building unit
SCXRD	Single Crystal X-ray diffraction
SEM	Scanning electron microscopy
SURMOF	Surface anchored Metal–organic framework
TBATFB	Tetrabutylammonium tetrafluoroborate
TCNQ	Tetracyanoquinodimethane
TCPP	Tetrakis (4-carboxyphenyl) porphyrin
TEM	Transmission electron microscopy
TGA	Thermogravimetric analysis
TOF	Time of flight
WE	Working electrode

XAS	X-ray absorption spectroscopy
XRD	X-ray diffraction
ZIF	Zirconium imidazolate framework

Chapter One: Introduction

1.1. Carbon dioxide emissions 1

1.2. Electrochemical reduction of CO_2 4

1.3. Metal–Organic Frameworks 8

1.3.1. Carboxylate-based MOFs 11

1.3.2. Phosphonate-based MOFs 133

1.3.3. Carboxyphosphonate-based MOFs 22

1.3.4. BIRM-1 28

1.4. MOF Synthesis 31

1.5. MOFs as electrocatalyst for CO_2 reduction 37

1.5.1. Addressing conductivity challenges in MOFs 38

1.5.2. Addressing chemical stability challenge in MOFs 43

1.6. Harnessing the performance of various methods of MOF electrocatalyst preparation 50

1.6.1. Drop casting 51

1.6.2. Direct solvothermal synthesis 52

1.6.3. Liquid phase epitaxy (LPE) 54

1.6.4. Electrochemical synthesis 56

1.7. Recent progress in utilizing MOFs for electrocatalyst for CO_2 reduction 59

1.7.1. Pristine MOFs as electrocatalysts for CO_2 reduction 59

1.7.2. MOF composites as electrocatalysts for CO_2 reduction 67

1.7.3. MOF-derived materials as electrocatalysts for CO_2 reduction 72

1.8. Thesis aims 76

Chapter Two: Experimental Techniques

2.1. Synthesis techniques 77

2.1.1. Hydrothermal synthesis 77

2.1.2. Solvothermal synthesis 77

2.1.3. Slow crystallization 78

2.2. Fundamentals of crystallography and diffraction[273-275] 78

2.2.1. Crystalline structure 78

2.2.2. Lattice planes and directions 82

2.3. X-ray diffraction technique 83

2.3.1. Powder X-ray diffraction 85

2.3.2. Powder diffraction data analysis 88

2.3.2.1. Indexing 88

2.3.2.2. Rietveld refinement 90

2.3.3. Single crystal X-ray Diffraction[276, 278-280] 91

2.4. Scanning electron microscopy[278, 282] 93

2.5. Transmission electron microscopy[107] 95

2.6. Thermogravimetric analysis[284, 285] 96

2.7. Fourier transform infrared spectroscopy (FTIR)[284, 286] 97

2.8. Raman spectroscopy[289] 98

2.9. X-ray fluorescence spectroscopy[290] 99

2.10. Gas adsorption[107, 291, 292] 100

2.11. Electrochemical methods 102

2.11.1. Electrochemical mass transport[293-296] 102

2.11.1.1. Diffusion……102

2.11.1.2. Voltammetry at microelectrode……104

2.11.1.3. Microelectrode arrays……106

2.11.1.4. Porous electrode……108

2.11.2. Cyclic Voltammetry[297-300] ……109

2.11.3. Chronoamperometry[298-301] ……112

2.11.4. Three electrode cell configurations[284, 297, 299, 302] ……114

2.11.5. Online electrochemical mass spectrometry[304-306] ……116

Chapter Three: Ion exchange studies of BIRM-1 with Nickel ion

3.1. Introduction ……118

3.2. Experimental ……120

3.2.1. Materials ……120

3.2.2. Synthesis of BIRM-1 ……120

3.2.3. Ion exchange with nickel (II) ions ……120

3.3. Characterization ……121

3.3.1. Laboratory powder XRD ……121

3.3.2. Single crystal XRD structure of Ni^{2+}-BIRM-1 ……123

3.3.3. FTIR studies of Ni^{2+}-BIRM-1 ……125

3.3.4. Morphological studies of Ni^{2+}-BIRM-1 ……127

3.3.5. Thermal stability studies of Ni^{2+}-BIRM-1 ……129

3.3.6. Porosimetry measurement ……132

3.4. Electrochemical characterization toward CO_2 reduction ……133

3.5. Conclusion ……136

Chapter Four: Synthesis, crystal structures and CO_2 reduction potential of some 2D-layered metal carboxyphosphonates

4.1. Introduction 138

4.2. Experimental 139

4.2.1. Solvothermal synthesis of Zn framework 139

4.2.2. Crystal structure of BIRM-11 [$Zn_3(O_3PCH_2CH_2COO)_2$] 140

4.2.3. FTIR studies of BIRM-11 142

4.2.4. Morphology of BIRM-11 143

4.2.5. Thermal stability of BIRM-11 144

4.3. Room temperature synthesis of Cu framework 145

4.3.1. Crystal structure of BIRM-12 [$Cu(O_3PC_2H_4COOH)\ (H_2O)_2$] 146

4.3.2. FTIR studies of BIRM-12 149

4.3.3. Morphology of BIRM-12 150

4.3.4. Thermal stability of BIRM-12 151

4.3.5. Electrochemical characterisation of BIRM-12 152

4.4. Hydrothermal synthesis of Cu framework 154

4.4.1. Crystal structure of BIRM-13 [$Cu(O_3PC_2H_4COOH)$] 155

4.4.2. Optimisation of the synthesis conditions 158

4.4.2.1. Adjusting the pH 158

4.4.2.2. Varying the temperature 159

4.4.2.3. Varying the mole ratio and use of solvent mixtures 160

4.4.3. FTIR studies of BIRM-13 160

4.4.4. Morphological studies of BIRM-13 162

4.4.5. Thermal stability of BIRM-13 162

4.4.6. Electrochemical characterization of BIRM-13 163
4.4.7. Use of auxiliary ligand 165
4.4.8. Crystal structure of BIRM-14 [$Cu_3(O_3PC_2H_4COO)(C_5H_4N)_2$] 166
4.4.8.1. FTIR studies of BIRM-14 169
4.4.8.2. Morphological studies of BIRM-14 170
4.4.8.3. Thermal stability of BIRM-14 171
4.4.8.4. Electrochemical characterisation of BIRM-14 171
4.5. MOF synthesis with cobalt metal 173
4.5.1. Crystal structure of BIRM-15 [$Co_3(O_3PCH_2CH_2COO)_2(H_2O)_3$].$3H_2O$ 175
4.5.2. FTIR studies of BIRM-15 178
4.5.3. Morphology of BIRM-15 180
4.5.4. Thermal stability of BIRM-15 180
4.5.5. Electrochemical characterization of BIRM-15 181
4.5.6. Synthesis attempts with auxiliary ligand 183
4.5.7. Structure of BIRM-16 [$Co(C_5H_4N)_2(CHOO)$] 184
4.5.7.1. FTIR studies of BIRM-16 186
4.5.7.2. Morphology of BIRM-16 188
4.5.7.3. Thermal stability studies of BIRM-16 188
4.6. BIRM-16(Ni), an isoreticular version of BIRM-16 189
4.6.1. Morphology studies of BIRM-16 (Ni) 191
4.6.2. Thermal stability of BIRM-16(Ni) 192
4.7. Optimizing the reaction conditions for BIRM-16 and BIRM-16(Ni) 193
4.8. Conclusion 194

Chapter Four: Synthesis, characterization, and crystal structure of novel metal-organic frameworks containing a rigid aromatic carboxyphosphonate linker

5.1. Introduction 197

5.2. Experimental 198

5.2.1. Solvothermal Synthesis 198

5.3. Synthesis of BIRM-17 [Zn_2 $(O_3PC_6H_4CO_2)_3$ (DMF)(DMA)] 199

5.4. Porous Framework: BIRM-18 [$Zn_2[(O_3PC_6H_4COO)_2]$. $4(H_2O)$ (DMF) 2(DMA)] 201

5.4.1. Crystal structure of BIRM-18 202

5.4.2. FTIR studies of BIRM-18 206

5.4.3. Morphological studies of BIRM-18 208

5.4.4. Thermal stability studies of BIRM-18 209

5.5. Synthesis Optimization 211

5.6. Second Porous Framework: BIRM-19 [$Zn_2[(O_3PC_6H_4COO)_2]$.2(DMA)] 213

5.6.1. Crystal structure of BIRM-19 213

5.6.2. FTIR studies of BIRM-19 217

5.6.3. Morphological studies of BIRM-19 219

5.6.4. Thermal stability studies of BIRM-19 219

5.7. MOF synthesis attempt with Ni metal 221

5.8. Layered Structure of BIRM-20 [$Ni(O_3PC_6H_4COOH)$ $(C_5H_4N)_2$ $(H_2O)_3$] 223

5.8.1. FTIR studies of BIRM-20 226

5.8.2. Morphological studies of BIRM-20 228

5.8.3. Thermal stability studies of BIRM-20 229

5.9. MOF synthesis attempt with Co metal 231

5.9.1. Layered structure of BIRM-21 [$Co(O_3PC_6H_4COOH)$. H_2O] 231

5.9.2. FTIR studies of BIRM-21 234

5.9.3. Thermal stability studies of BIRM-21 236

5.10. Conclusion 237

Chapter six: Probing the activity and selectivity of nickel carboxylphosphonate 2D-MOF for the electrochemical conversion of CO_2 to syngas.

6.1. Introduction 239

6.2. Experimental section 242

6.2.1. Material synthesis 242

6.2.2. Physical characterization 242

6.2.3. Electrochemical characterisation 243

6.2.4. Product characterisation 244

6.2.5. Computational details 244

6.3. Results and discussion 246

6.3.1. Characterization of $Ni_2(HO_3PC_2H_4COO)_2(4,4'\text{-bipy})_2(H_2O)$ 246

6.3.2. Electrochemical characterization of the catalyst and assessment of its catalytic activity for the CO_2RR 250

6.3.3. Mechanistic insights 257

6.4. Conclusion 259

Chapter Seven: Conclusion and future work

7.0. Conclusions and future work 260

8.0. References 265

9.0. Appendix 286

CHAPTER ONE

Introduction

1.1. Carbon dioxide emissions

Greenhouse gases (often abbreviated as GHG) are gases which absorb and emit thermal infrared radiation at the range of wavelength emitted by our planet.[1] Carbon dioxide is earth's most important greenhouse gas: a gas that absorbs and radiates heat.[2] Unlike oxygen or nitrogen (which make up most of our atmosphere), greenhouse gases absorb heat radiating from the earth's surface and re-release it in all directions—including back toward earth's surface.[2] We are all aware that the levels of atmospheric carbon dioxide are increasing, and it is well established that human activities, such as the burning of fossil fuels and deforestation, are primarily cause of this phenomenon (Figure 1.1).[3] The atmospheric CO_2 had been kept almost constant at about 280 ppm before the industrial revolution (Figure 1.2).[4] After the industrial revolution, it became higher than 290 ppm for about 100 years. During subsequent 100 years from the 1870s to 1970s, the industrial development of the world led to its constant increase at about 0.28 ppm every year.[4] After 1970, carbon dioxide continued to accumulate in the atmosphere at a very high rate and its atmospheric concentration exceeded 400 ppm by 2023. Atmospheric carbon dioxide level has been projected to reach 450 ppm by 2050 if drastic efforts are not taken to arrest the current trend of CO_2 emission. Consequently, this elevated concentration of atmospheric CO_2 has been associated with the rise in global average temperature, leading to the escalation of extreme weather events, with attendant adverse effect on our ecosystem.[5] The global average temperature has already increased by 1°C when compared

to the pre-industrial levels (1850-1900), and at the current pace of emissions, global warming is likely to reach 1.5°C by 2040 (Figure 1.3).[6]

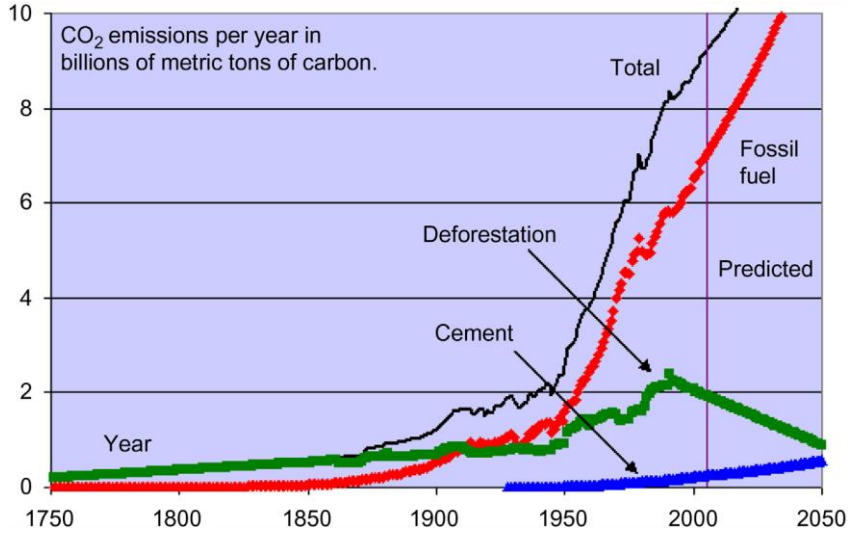


Figure 1.1. Global CO_2 emissions by major sources, 1750-2050. Reproduced from Scibioh and Viswanathan.[5] Copywrite 2018, Elsevier.

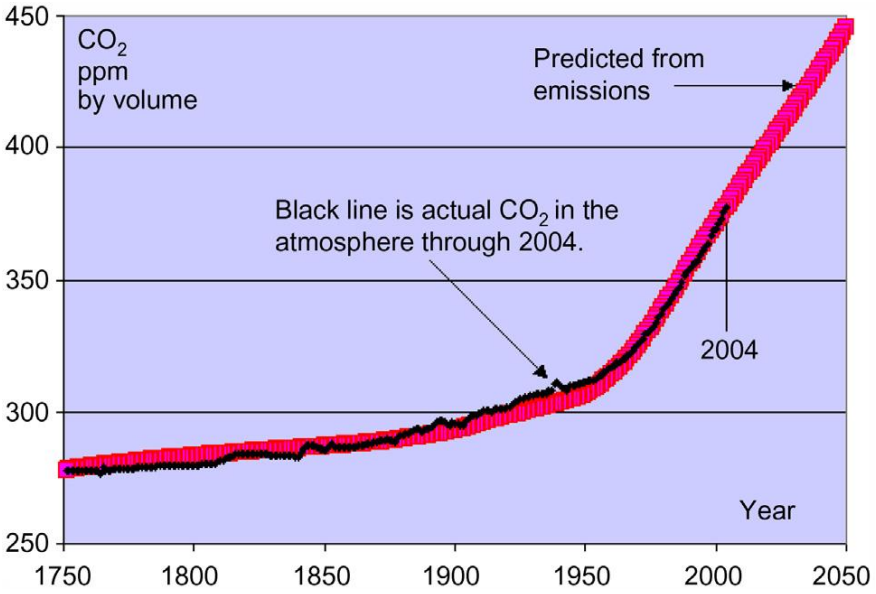


Figure 1.2. Global carbon dioxide levels since the beginning of Industrial revolution. Reproduced from Scibioh and Viswanathan.[5] Copywrite 2018, Elsevier.

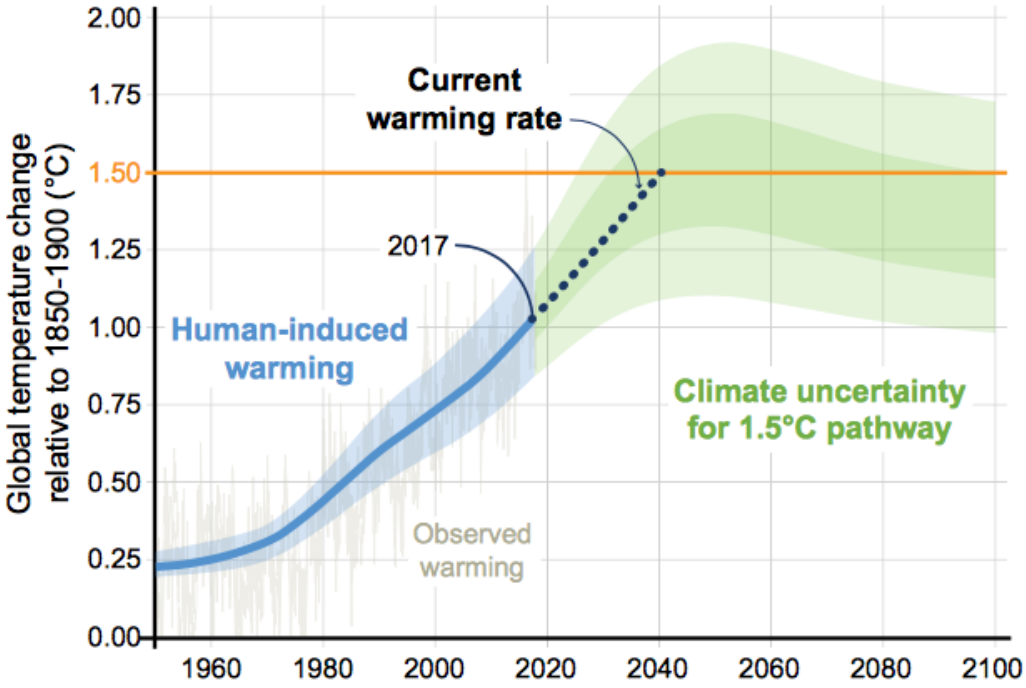


Figure 1.3. Graph showing global average temperature reaching approximately 1°C above pre-industrial level in 2017. The green section of the diagram represents the range of uncertainty in how much global temperature would continue to rise before levelling off, assuming that reductions in carbon dioxide emissions were to begin immediately and reach zero by 2055. Reproduced from IPCC Special Report on Global Warming of 1.5°C. Copyright 2018, International Panel on Climate Change.

The growing concern worldwide about the impact of increasing CO_2 emissions and climate change due to global warming has spurred both national and international political actions. In 2008, the UK government passed the climate change act, which set a goal to reduce net UK CO_2 emissions to less than 80% of the 1990 baseline by 2050 and established an independent committee on climate change.[7] Additionally, the United Nations Paris agreement, endorsed by a majority of countries globally in 2016, aimed to address the climate change crisis on a global scale by striving to limit the rise in global temperatures to 1.5°C above pre-industrial levels within the framework of sustainable development and economic progress.[8] Subsequently, at the UN climate summit held in September

2019, the Secretary-General of the UN called on member countries to commit to limiting the temperature increase to 1.5°C, and 65 countries vowed to achieve net zero greenhouse gas emissions by 2050.[9] In order to address the current dependency on fossil fuels for energy generation, lower greenhouse gas emissions to reach the goal of net zero CO_2 emissions and increase the likelihood of meeting the target of limiting the temperature rise to 1.5 °C, it is important to prioritize sustainable and efficient carbon-neutral methods for producing, storing, and transporting energy. Ideally, these methods should rely on naturally abundant resources that avoid the adverse environmental impacts linked to the combustion of fossil fuels.

1.2. Electrochemical reduction of CO_2

The electrochemical reduction of CO_2 (ERC) is a promising CO_2 utilization technology that can convert CO_2 into a wide variety of fuels and chemicals via electrochemical reactions (Figure 1.4). Unlike other chemical processes, electrochemical CO_2 reduction can be performed at ambient temperature using green renewable energy sources and water as a source of the protons, making the overall operation a carbon neutral process.[10] As shown in Figure 1.4, the anodic reaction produces O_2 by oxidizing water and generates electrons that flow through the external circuit to the cathode, while protons pass through an aqueous electrolyte to the cathode. At the cathode, electrons combine with protons to produce H_2 or reduce CO_2 to form various products. The proportion of electrons used for producing H_2 or reducing CO_2 depends on the activation barriers for each reaction.

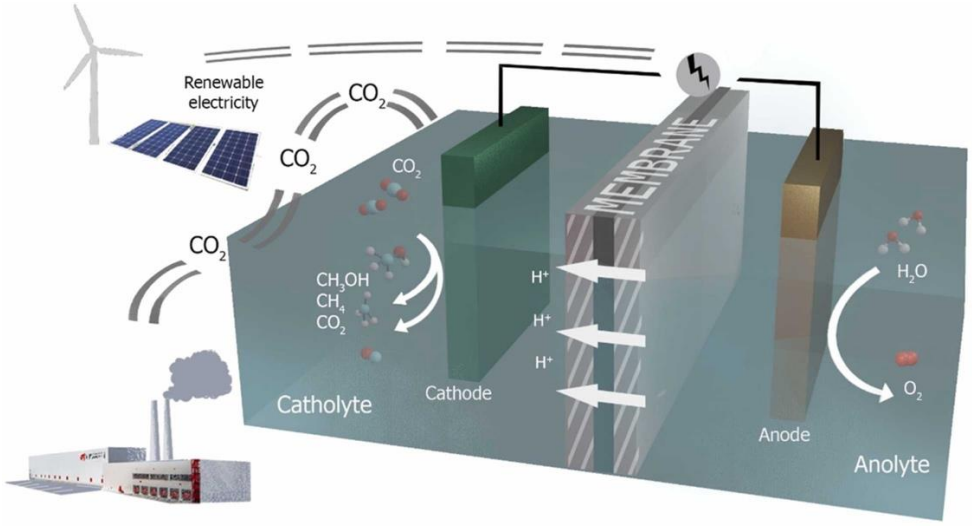


Figure 1.4. Schematic of a typical electrochemical reduction of CO_2. Reproduced from Wiranarongkorn et al.[11]. Copyright 2023, Elsevier.

However, so far, the electrochemical reduction of CO_2 still suffers from high overpotential (large energy requirement) and poor product selectivity, making yet unfeasible from the industrial point of view, the practical application of electrochemical CO_2 reduction. The high overpotentials and poor product selectivity are the result of non-ideal adsorption energies of key reaction intermediates.[12] The low faradaic efficiencies are due to the competition with the hydrogen evolution reaction (HER (1)), which takes place in the same potential window as CO_2 reduction.[13]

$$2H^+ + 2e \rightarrow H_2 \qquad E^0 = 0 \text{ V vs SHE} \qquad 1.1$$

For electrochemical reduction of CO_2 to be performed in an efficient manner, highly active and durable electrocatalysts, as well as electrodes and electrolytes that have high conductivity and allow for sufficient mass transport of the reactants and products to/from the catalyst layers are required. The electrochemical CO_2RR can be viewed as a multiple proton–electron reaction leading to various products. The first step to activate CO_2 for subsequent reduction is to apply high potential (-1.90 V *vs* SHE), prompting a single-electron reduction of CO_2 (linear stable molecule) to $CO_2^{\cdot-}$ ion (bent

radical anion), which become coordinated to catalyst surface.[14] Upon receiving additional electron, $CO_2^{\cdot-}$ become reduced to either CO or HCOOH depending on the coordination mode of $CO_2^{\cdot-}$ to the catalyst surface. In general, it has been observed that catalysts that bind CO_2 through oxygen form HCOOH as a major product, while the binding via carbon results in CO formation.[15] As seen in Figure 1.5, a key difference in the mechanism for CO *vs*. formate production is the bond formed between CO_2 and the catalyst. Secondly, the two proposed reaction mechanism are pH dependent. While CO production path is affected by proton concentration, the formate reaction pathway is independent of pH.[16]

$$CO_2 + e \rightarrow CO_2^{\cdot-} \qquad E^0 = -1.90\ \text{V vs SHE} \qquad 1.2$$

$$CO_2 + 2e + 2H^+ \rightarrow CO + H_2O \qquad E^0 = -0.10\ \text{V } vs\ \text{SHE} \qquad 1.3$$

$$CO_2 + 2e + 2H^+ \rightarrow HCOOH \qquad E^0 = -0.20\ \text{V } vs\ \text{SHE} \qquad 1.4$$

The nature and the strength of CO coordination to the catalyst will determine whether the reaction will terminate at 2e electron reduction product or proceed further. Catalyst with weakly adsorbed CO will only desorbed CO or formate as reaction product while CO that is strongly adsorbed unto the catalyst surface can be further reduced to form hydrocarbons and alcohols according to the following reactions[15] :

$$CO_2 + 4e + 4H^+ \rightarrow HCHO + H_2O \qquad E^0 = -0.071\ \text{V } vs\ \text{SHE} \qquad 1.5$$

$$CO_2 + 6e + 6H^+ \rightarrow CH_3OH + H_2O \qquad E^0 = 0.03\ \text{V } vs\ \text{SHE} \qquad 1.6$$

$$CO_2 + 8e + 8H^+ \rightarrow CH_4 + 2H_2O \qquad E^0 = 0.17\ \text{V } vs\ \text{SHE} \qquad 1.7$$

$$2CO_2 + 12e + 12H^+ \rightarrow C_2H_4 + 4H_2O \quad E^0 = 0.085\ \text{V } vs\ \text{SHE} \qquad 1.8$$

From Figure 1.5, two reaction mechanisms are proposed for CO reduction. For instant the coordinated *CO is protonated to form *CHO intermediate which is further reduced to methane (CH_4) and secondly, *CO could undergo C–C coupling with another *CO to form C_2H_4 and C_2H_5OH.[17] The reduction of CO_2 into these multi-carbon products is highly desired and is of interest as a potential component of a carbon energy cycle [18]. Copper is the only notable heterogeneous catalyst capable of facilitating these value-added reactions at reasonable rate, however, the process requires remarkable energy, coupled with poor product selectivity which is still an impediment to its practical application.[16, 19]

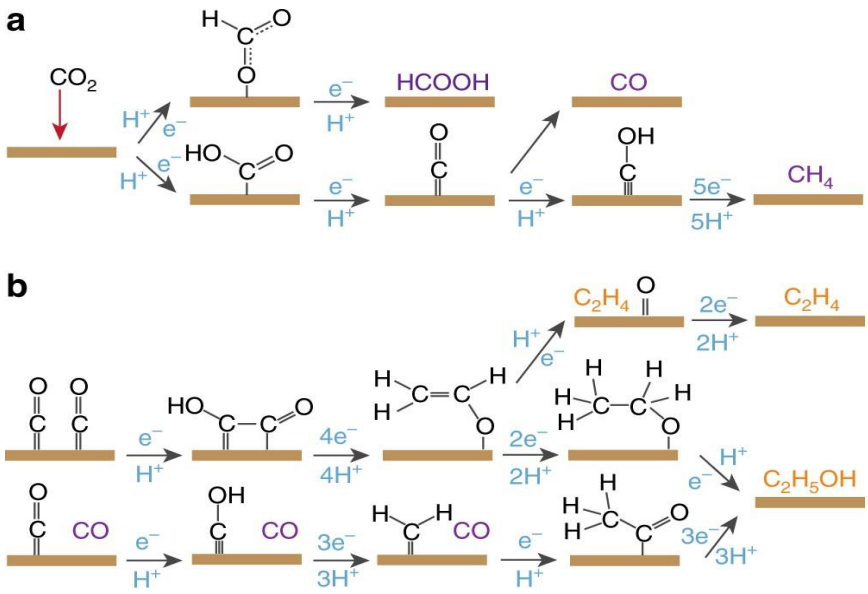


Figure 1.5. Scheme of the CO_2 reduction pathway toward different reaction products. Reproduced from Ren *et al.*[16]. Copyright 2018, Nature.

The conversion of CO_2 is generally limited by the high chemical stability of the C=O bond (bond enthalpy +805 kJ/mol), thus requiring a high energy to break the bond. Additionally, since CO_2 are thermodynamically stable having low electron affinity, there is still need to scale a considerable high kinetic hurdle to achieve effective CO_2 conversion devoid of competitive hydrogen evolution. Therefore, the overall research effort on electrocatalytic CO_2 reduction is to find suitable cathode

materials that will favour the selective CO_2 reduction into a specific product at high efficiency, low overpotentials and with long-term stability.[20]

1.3. Metal–Organic Frameworks

In recent years, metal-organic frameworks (MOFs), a relatively novel category of porous materials, have captured significant attention from both industrial and academic researchers. This has led to their emergence as one of the most dynamic and prolific areas within the field of chemistry and materials science.[21] MOFs are a specific class of materials constructed by joining metal-containing units, termed secondary building units (SBUs), with organic linkers using strong bonds to create open crystalline frameworks with permanent porosity (Figure 1.6).[22] The flexibility of the combination of these inorganic and organic units has produced more than 20,000 of MOF structures.[23] The idea of the metal-organic framework can be dated back to the invention of coordination chemistry by a Swiss chemist, Alfred Werner in 1893, in which he proposed the arrangement of a coordination complex to include a central metal bounded by organic or inorganic ligands.[24] After several decades of research efforts, the synthesis of first porous coordination framework was attributed to Hoskins *et al*.[25] where they synthesise a series of 3D rod-linked frameworks with large cavities and windows (exemplified by $\{Cu^{I}[C(C_6H_4CN)_4]\}_n^{n+}$ and shown in Figure 1.7). They also predicted that employing a broad range of general synthetic methods could result in the creation of numerous new and beneficial materials.[26] This claim has been supported by scientists globally, who have successfully synthesized a broad array of stable crystalline porous materials for various potential uses.[27-30]

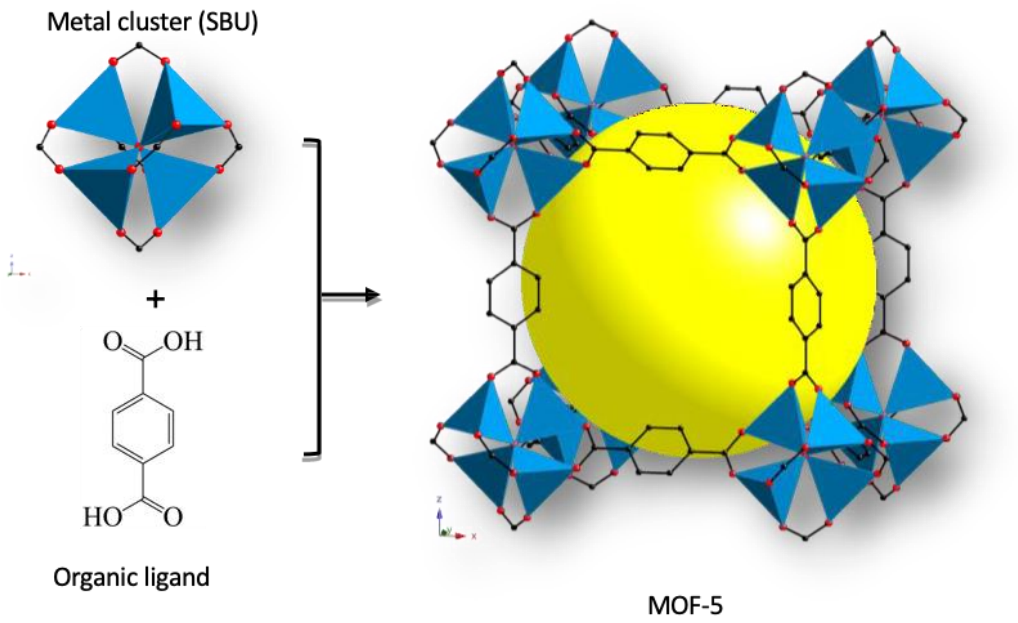


Figure 1.6. MOF framework constructed from organic ligand (linker) and metal cluster (node).

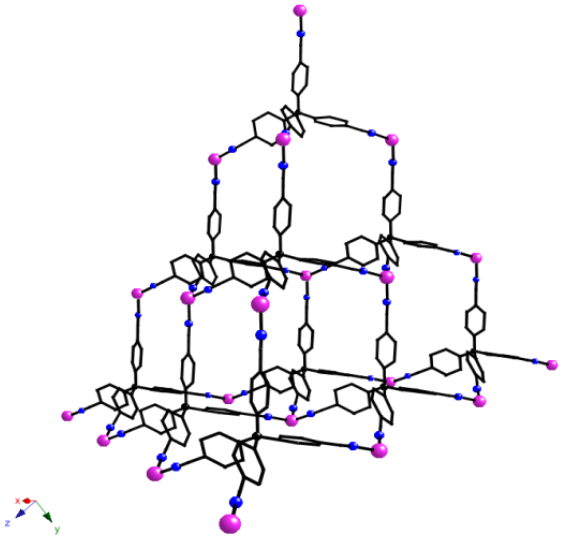


Figure 1.7. The framework structure of $\{Cu^{I}[C(C_6H_4CN)_4]\}_n^{n+}$ illustrating a diamond-like network composed of rod-linked (C-C_6H_4-CN-Cu) units; hydrogen atoms and internal solvent have been omitted for clarity; colour scheme: Cu – purple, N – blue, C – black.

The term MOF was introduced in 1995 by Yaghi's group whose first work was published as a metal-organic framework in Nature.[31] Between 1995 and 1999, significant advancements were made in the field of coordination polymers. In 1995, Yaghi *et al.*[31] synthesized a layered Co microporous MOF with reversible sorption properties. Two years later, Kitagawa *et al.*[32] reported three 3D porous MOFs with room temperature gas adsorption capabilities. In 1999, Li *et al*.[33] introduced the 3D material MOF-5 with a unique pore topology, pioneering the concept of isoreticular synthesis and influencing the design of new crystalline materials. Subsequent publications by Yaghi's group in 2002 (Figure 1.8) popularized the concept of isoreticular chemistry and the term MOF.[34]

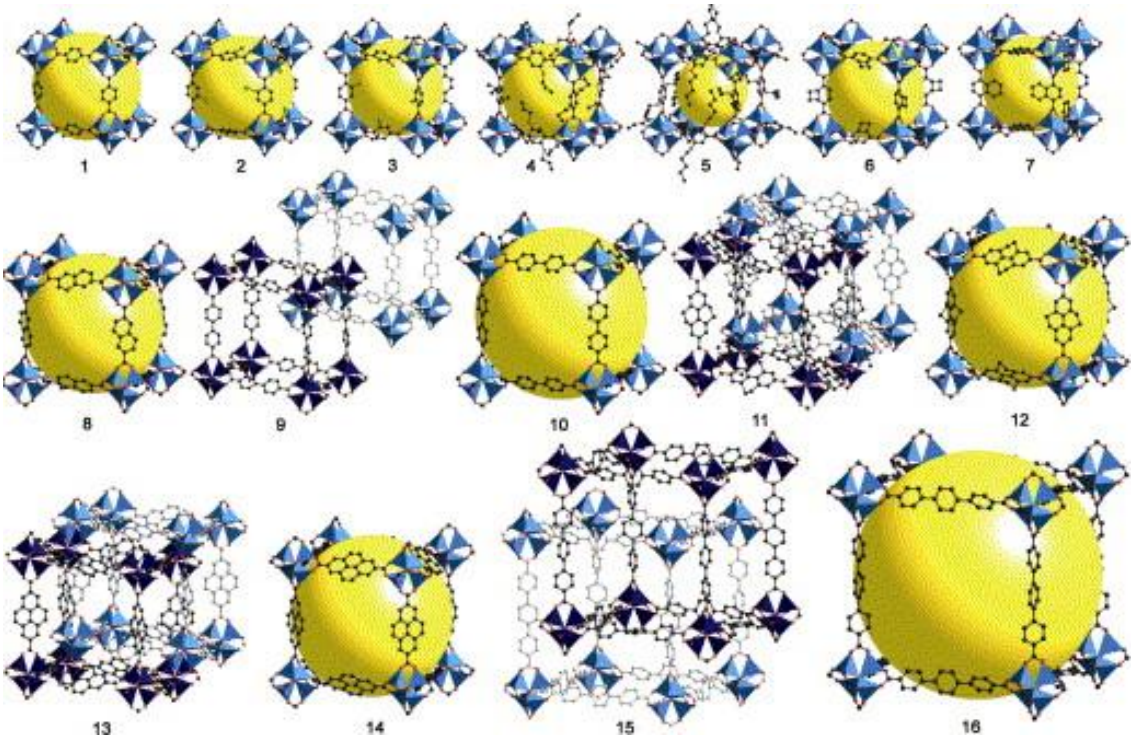


Figure 1.8. Framework structures of IRMOF family synthesized with different dicarboxylic acid Ligands as published by Eddaoudi *et al.*[35] The increase in the internal void space is represented by yellow spheres, with some of the framework allowing the formation of catenated phases (IRMOF-9, -11, -13 and -15). Reproduced from Rowsell and Yaghi[34]. Copyright 2014, Elsevier.

1.3.1. Carboxylate-based MOFs

Carboxylate coordinating groups are the most explored linkers for MOF synthesis since carboxylic acids can be easily deprotonated and can bind metals in a variety of ways, making them the ideal ligand for the synthesis of robust metal organic framework. In the early stages of MOF development, many structures employed neutrally charged nitrogen-based linkers, as seen in the research led by Hoskins and Robson[25], but encountered issues related to low thermal stability. Moreover, carboxylates' negative charge balances the positive charge of metal ions, unlike numerous nitrogen-based linkers. This results in a neutral framework without the need for balancing counter-ions in the internal pores, which could be undesirable depending on the application. Figure 1.9 show some examples of carboxylate-based linker molecules. It is important to note that carboxylate ligand with rigid carbon chains such as aromatic, alkene, or alkyne group are mostly preferred for the synthesis of MOF due to the high chance of producing framework with permanent porosity compared to flexible aliphatic chains which may result in frameworks that are unlikely to offer permanent porosity. Nevertheless, despite this consideration, many MOF materials continued to be synthesized using flexible linkers, as permanent porosity is not always a critical requirement for certain applications.

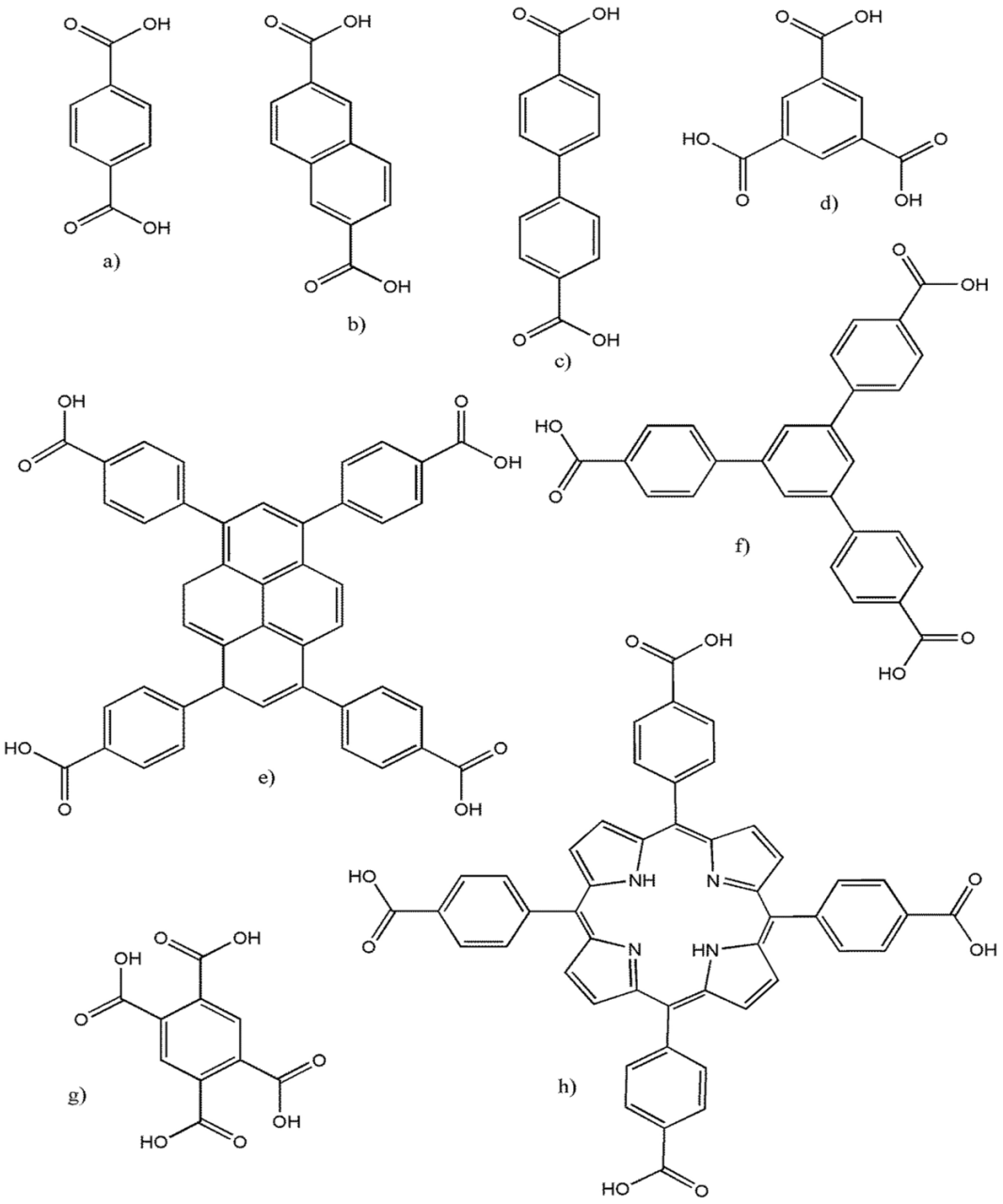


Figure 1.9. Chemical structure of commonly used carboxylic acid linkers for the synthesis of MOFs.

Meanwhile, since the discovery of permanently porous carboxylate metal-organic frameworks (MOFs) such as zinc terephthalate MOF-5[33], copper trimesate HKUST-1[36] and trivalent and tetravalent metal terephthalates such as MILL-47[37], MIL-53[38], MIL-88[39] and MIL-101[40] (Figure 1.10), there has been an exponential increase in the number of the known porous carboxylate MOFs. Attention has been extended to tricarboxylate and tetracarboxylate linkers, the use of

functionalized linkers, and reactions with larger linker with similar geometry and the same functional groups. This latter approach has in some cases demonstrated examples of isoreticular synthesis[41] where frameworks with the same topology, but different dimensions can be prepared. The synthesis of this ever-expanding family of porous materials, with its diverse structural chemistry and properties, is currently being attended to by the search for application in gas storage, separation, drug delivery, catalysis and material properties such magnetism, ferroelectricity etc.[42]

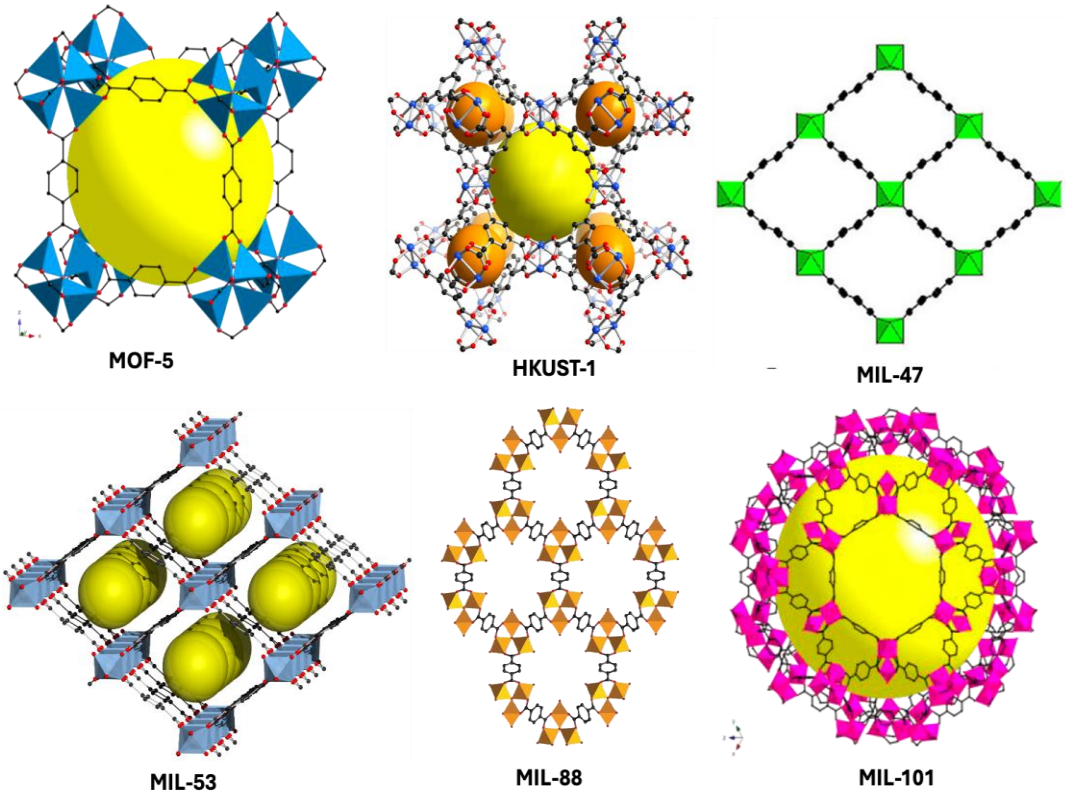


Figure 1.10. Some examples of MOFs with permanent porosity.

1.3.2. Phosphonate-based MOFs

Phosphonate-based linkers are less commonly utilized in making MOFs compared to carboxylates for various reasons. They are not as readily available commercially and tend to be more expensive due to their complex synthesis process. Moreover, their coordination chemistry is somewhat less

predictable than carboxylates, as phosphonates have three oxygen atoms capable of forming coordination bonds instead of two like carboxylates.[43] While this introduces unpredictability, it also offers the potential for creating new frameworks with coordinating geometries that are not achievable using carboxylates. Similar to carboxylates, phosphonates can form strong coordination bonds, providing good thermal stability crucial for many applications.[44] However, the drawback of phosphonate-based linkers is their tendency to crystallize rapidly into layered phases.[43] Although this rapid crystallization can hinder the synthesis of porous MOFs, it also complicates the growth of single crystals and subsequent structural determinations.[43]

The history of chemistry of metal phosphonate can be dated back to the pioneering works of Alberti[45], and Clearfield and Constantino.[46] The first known set of metal phosphonates was prepared by Alberti *et al*.[47] in 1978 by direct reaction of phosphonic acids with zirconium as shown in general equation below,

$$\mathrm{Zr^{IV}} + 2\mathrm{RPO_3H_2} \rightarrow \mathrm{Zr(O_3PR)_2} + 2\mathrm{H^+} \qquad 1.9$$

Where R is an alkyl or aryl group. It was not until 1993 that the structure of the phenylphosphonates $\mathrm{Zr(O_3PR)_2}$ namely; $Zr(HOCH_2PO_3)_2{\cdot}H_2O$, $Zr(C_6H_5PO_3)_2$ and $Zr(C_2H_5OPO_3)_2$ were solved by Poojary *et al*.[48] based on the sample prepared in Alberti's laboratory. Subsequent to Alberti's discovery, similar diphosphonate-based and monophosphonate-based compounds were developed, resulting in pillared-layered structures or analogous layered, respectively.[49, 50] Although zirconium and other tetravalent metals made up the earliest metal phosphonate compounds, other structures based on divalent metal ions appeared in the late 1970s and 1980s. These studies predominantly featured metal phosphonate compounds with densely packed layered structures that lacked porosity. Efforts were made to alter the chemical environment within the interlayer either through direct modifications or post-synthesis treatments. This includes incorporating functionalities like

catalysis[51], serving as hosts for intercalation compounds[52], facilitating protonic conduction[53], and introducing pillaring moieties to increase interlayer space.[54, 55]

Le Bideau and co-workers reported the first 3D framework metal phosphonate, β-$Cu(O_3PCH_3)$, featuring a 1D channel system in 1994 (Figure 1.11).[56] The framework channels consist of 24-membered rings (referred to as 12-MR in zeolite terminology), with methyl groups covalently bonded to phosphorus atoms extending into the channels. Because the estimated effective pore size of this materials is around 3 Å and is too narrow for small adsorbates like nitrogen to penetrate, it does not meet the criterial for the definition of MOF. Following that, Maeda and co-workers described the synthesis of polymorphs α- and β-$Al_2(CH_3PO_3)_3$ with zeolite-like frameworks.[57] [58] These frameworks include trivalent aluminium cations arranged in both tetrahedral and octahedral geometries, connected by phosphonate groups. This arrangement resulted in hexagonal channels lined with methyl groups, providing approximately 5 Å of free diameter channels for both compounds. After these reports, syntheses of novel open-framework metal phosphonates were accelerated.[59] Not only methylphosphonic acid but also methylenediphosphonic acid was successfully used in preparation of 3D open frameworks.

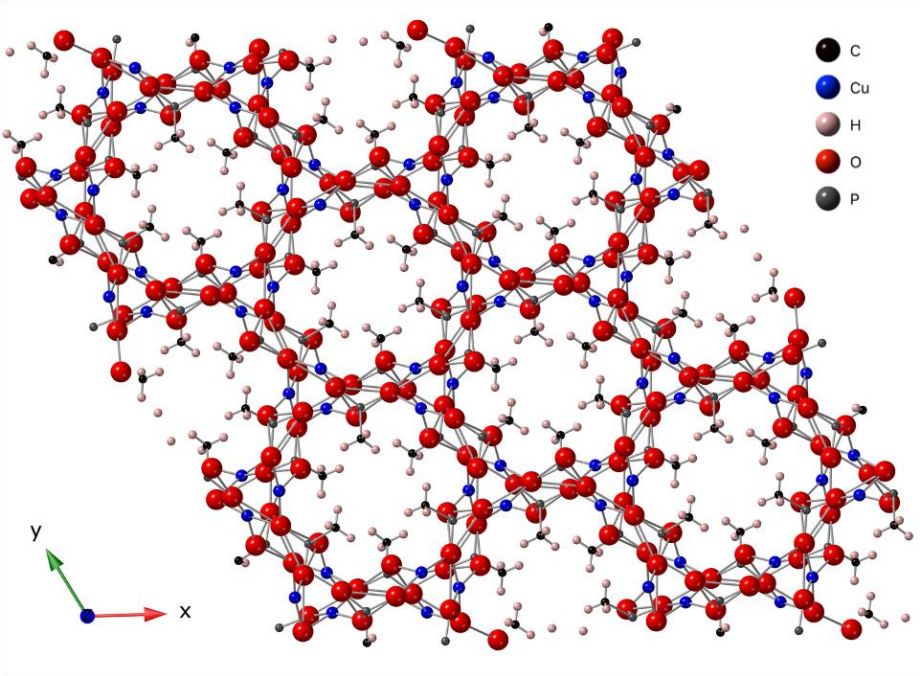


Figure 1.11. Framework structure of $Cu(O_3PCH_3)$.

In 1997, Lohse *et al*.[60] utilized methylenediphosphonic acid as a ligand to synthesise a 3D porous phosphonate material. The structure, illustrated in Figure 1.12, is a porous neutral framework with water molecules situated inside the pores. Cobalt (II) ions adopted both octahedral and tetrahedral configurations. The structure of this framework can be visualized as layers of CoO_6 trimers interconnected by CoO_4 tetrahedra and extensively decorated with $P–CH_2–P$ units. A noteworthy feature of this material is that the incorporation of a carbon chain enabled chain extension, leading to the enlargement of pores. Subsequently, isostructural materials were developed based on zinc[61] and nickel.[62]

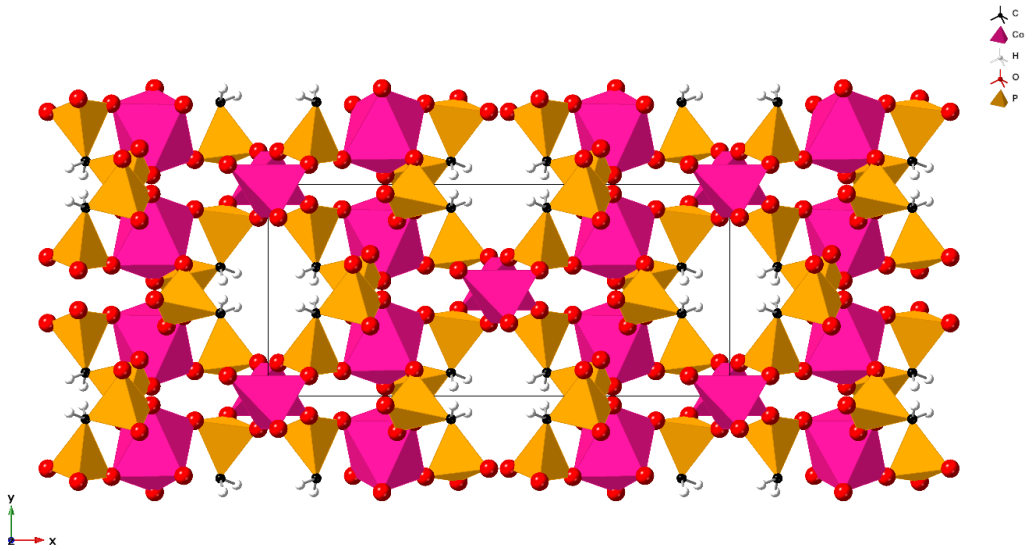


Figure 1.12. Framework structure of $Co_2(O_3PCH_2PO_3)\cdot H_2O$, illustrating the construction of the structure; internal solvent have been omitted for clarity.

Following the synthesis of this framework, efforts were made to increase the chain length of alkylbisphosphonic acid $[H_2PO_3(CH_2)_nPO_3H_2]$ to enlarge the pore size of the metal phosphonate framework.[63-65] However, this effort produced dense pillared–layered structures composed of 2-dimensional inorganic sheets of metal oxide and CPO_3 tetrahedra which would then be linked together by the carbon chains. The stacking arrangement between layers varies based on conformation of the numbered organic chains and metal coordination states. Some selected examples are given in Figure 1.13.

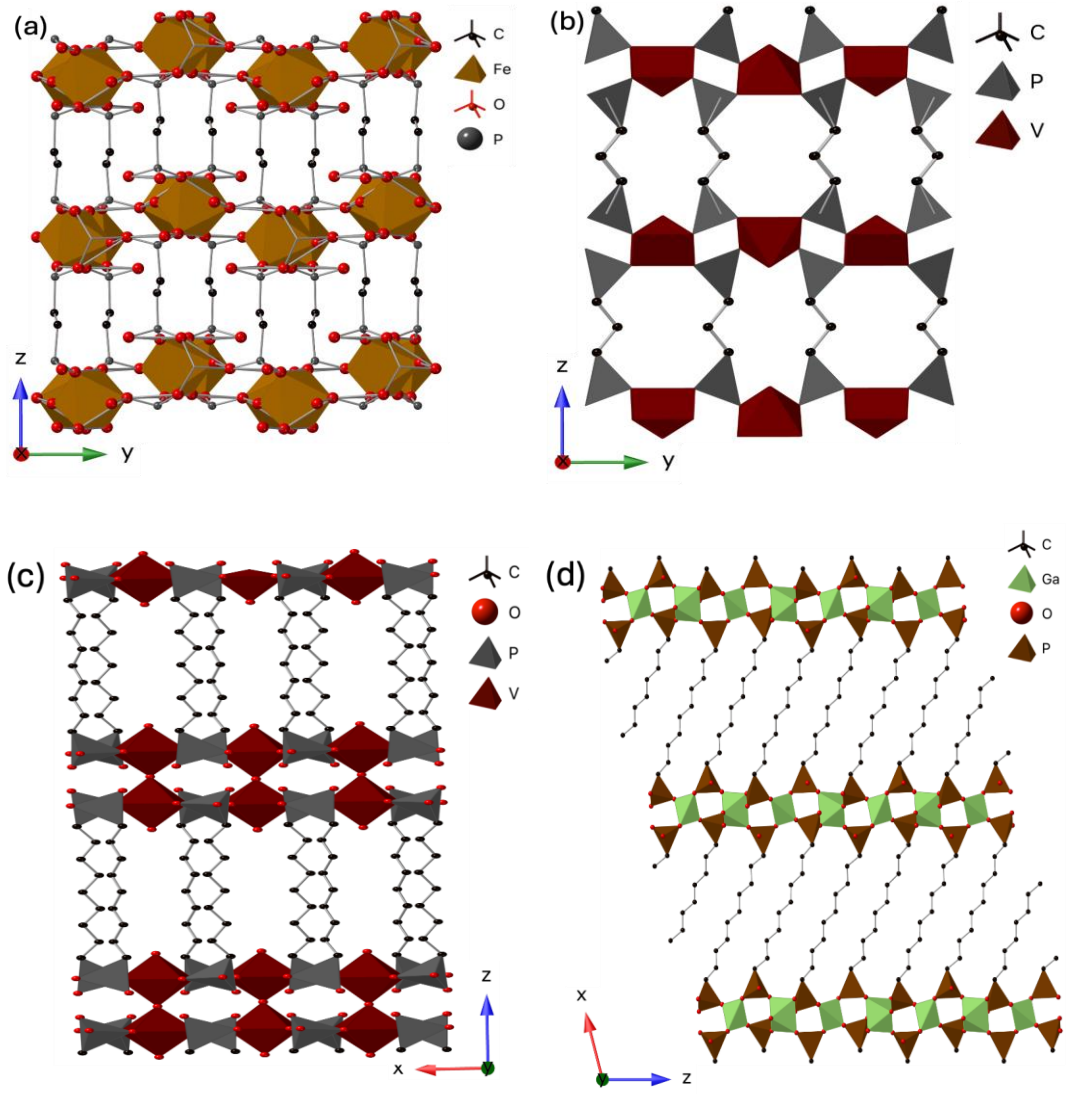


Figure 1.13. Framework structures of some alkyldiphosphonates with different chain lengths: (a) $Fe(HO_3P(CH_2)_2PO_3)\cdot(H_2O)$[63], built with FeO_6 octahedra and CPO_3 tetrahedra, linked with $(CH_2)_2$; (b) $V_2O_2(H_2O)[O_3P(CH_2)_3PO_3]\cdot 2H_2O$[64], built with VO_6 octahedra and CPO_3 tetrahedra, linked with $(CH_2)_3$; (c) $V_2O_2(H_2O)[O_3P(CH_2)_5PO_3]\cdot 3H_2O$[64], built with VO_6 octahedra and CPO_3 tetrahedra, linked with $(CH_2)_5$; (d) $Ga[HO_3P(CH_2)_{10}PO_3]$[65], built with GaO_6 octahedra and CPO_3 octahedra, linked with $(CH_2)_{10}$.

Effort to tune the dimensionality of these metal phosphonate to 3D open frameworks yielded several 3D pillared layered structures with varying alkyl chain length. As a result of this difficulties, some groups started exploring the possibility of adding extra functionality to the linker or

crystallizing frameworks with a co-linker. The idea was that the added functionality and coordinating groups could interfere with the formation of the typical layered structures and potentially promote the crystallization of open frameworks. Piperazinylphosphonic acid and its derivatives, is an interesting ligand for MOF synthesis as it contains two phosphonic acids, both capable of three states of protonation, as well as two amino nitrogen atoms capable of two protonation states.[66] For example, the use of N,N'-piperazinebis(methylenephosphonic acid) as a linker resulted in major advancements in the field, leading to the synthesis of series of porous framework.[66, 67] This ligand and some of its derivatives are shown in Figure 1.14. The combination of N,N'-piperazinebis(methylenephosphonic acid) with some divalent and trivalent metals resulted in dense 3D frameworks with 1D channels. Notable examples include the STA-12[68] (St Andrews microporous material number 12) STA-16[69] and MIL-91[70] (MIL = Material Institut Lavoisier).

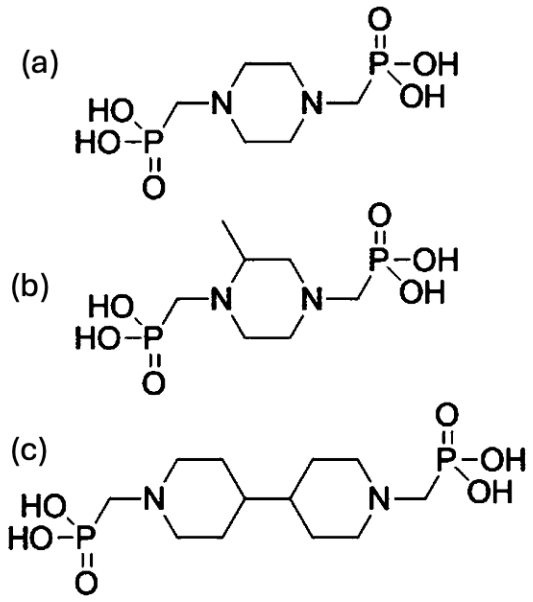


Figure 1.14 (a) *N,N*'-piperazinebis(methylenephosphonic acid) (b) *N,N*'-2 methylpiperazinebis (methylenephosphonic acid) (c) *N,N*'-4,4' bipiperidinebis(methylenephosphonic acid).

STA-12 possesses pores with a diameter of approximately 10 Å which are filled with extra framework water molecules (Figure 1.15a). The structure comprises inorganic chains of octahedrally coordinated metal cations, MO_5N (M = Ni^{2+}, Mn^{2+}, Fe^{2+}, and Co^{2+}). In each MO_5N octahedron, a metal cation is coordinated with four oxygen atoms from two distinct phosphonate tetrahedra, one oxygen atom from water, and a nitrogen atom from the piperazine ring of the phosphonic acid. This material was the first 3-dimensional large-pore metal phosphonate synthesized.[68] In the case of STA-16, the structure is isoreticular to STA-12 but incorporates a larger phosphonic acid, N,N'-4,4'-bipiperidinebis(methylenephosphonic acid), giving a framework with much greater pore size diameter (18.5 Å) (Figure 1.15b). These two compounds are interesting due to their exceptionally large pore size, as well as their ability to retain porous structures after dehydration, with potential application in gas absorption.[71]

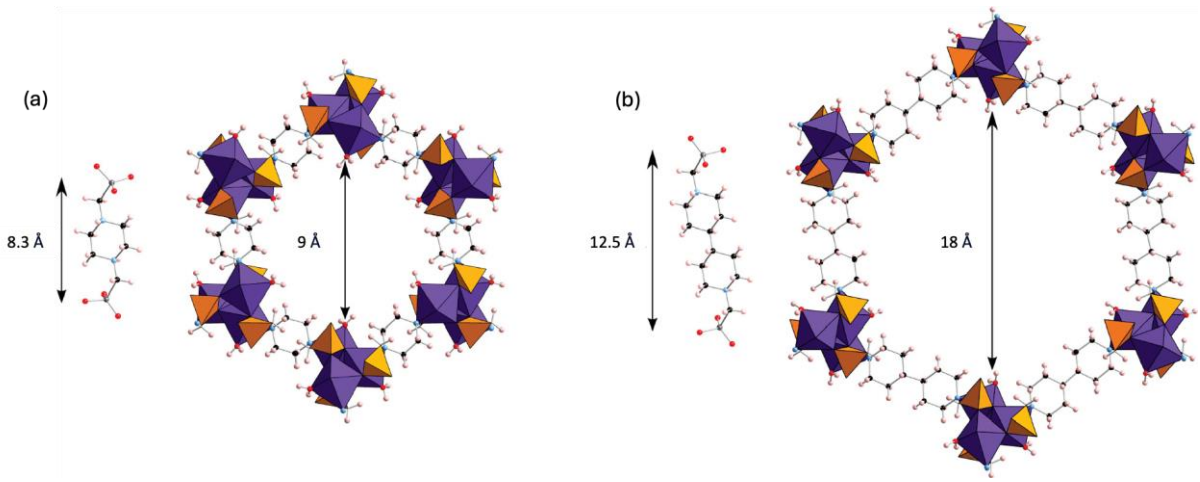


Figure 1.15. Framework structures of (a) STA-12(Ni) and (b) STA-16 (Co), illustrating the isoreticular structures; hydrogen atoms and internal solvent molecules have been omitted for clarity. Reproduced from Mysore *et al.* [72]. Copyright 2020, MPDI.

Recently, the use of stiff linkers having non-linear geometries, like Ni-tetrakis(4-phosphonophenyl)porphyrin has proven successful in creating MOFs with enduring porosity.[73] This linker was combined with tetravalent (Hf and Zr)[74] and divalent metals (Ni, Mn, Cd and Co)[75, 76] to create completely porous materials known as CAU-30, CAU-36 and CAU-29, respectively. Particularly noteworthy is CAU-30, which is among the most porous metal phosphonates reported to date, boasting specific surface areas of 910 or 970 m^2 g^{-1} for the zirconium or hafnium forms, respectively. Moreover, CAU-30 demonstrates exceptional stability against temperature and pH variations. It remains stable up to 420 °C in air and within a pH range of 0-12 in HCl/NaOH environments. The framework of CAU-30 is depicted in Figure 1.16.

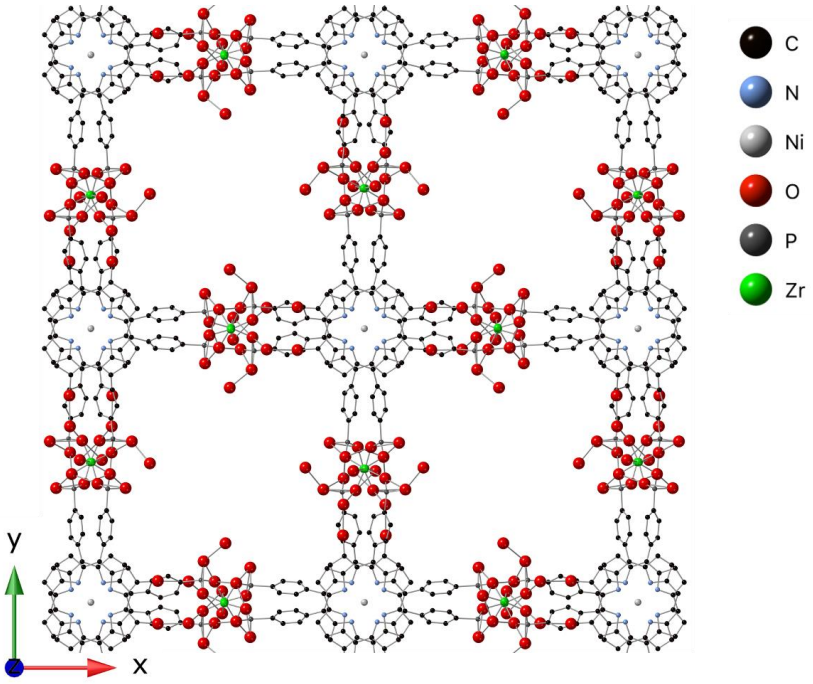


Figure 1.16. Crystal structure of CAU-30(Zr). Water molecules have been omitted for clarity.

1.3.3. Carboxyphosphonate-based MOFs

The possibility of synthesising open framework metal phosphonate materials has also been extended to the use of carboxyphosphonic acid linkers. Since it has been very challenging to grow single crystal with phosphonate linkers, coupled with the tendency of producing layered structure, the use of bifunctional ligand like carboxyphosphonic acid ligand can draw on the benefit embedded in this ligand.[77] That is, the new functional group on the phosphonate ligand could perturb the layered structure in metal phosphonates with the possibility of increasing its dimensionality to 3D open framework.[77] The first known attempt at synthesising metal phosphonate materials with carboxyphosphonic acid ligand can be dated back to the early 1990s.[78] This initial efforts focused primarily on the use of short carboxyalkylphosphonates in which majority of the material produce crystalises either as layered or dense pillared frameworks.[78] After this initial attempt, the use of carboxyphosphonic acid ligand became popular for MOF synthesis[79-86], with the evidence of successful synthesis of open frameworks found in the literature.[87-90]

Stucky and co-workers documented a fascinating open-framework of Zn-carboxyphosphonate, $Zn_3(O_3PCH_2COO)_2(O_3PCH_2COOH)$ $(NH_3CH_2CH_2NH_3)\cdot(BTC)$.[87] This structure featured a complex, interrupted tetrahedral zeolite-like configuration (Figure 1.17), which stood out from structures created with other aliphatic diphosphonates or carboxyphosphonates.[91-94] The framework boasted spacious 24-ring channels lined by the carboxylate end of the ligand, $H_2O_3PCH_2COOH$. These channels were filled with free benzenetricarboxylate (BTC) molecules used during synthesis. Interestingly, the structure-directing agents were not positioned at the center of the 24-ring channels but within the wall separating these channels. Although this material tempted us to expect

various applications utilizing the large pore and dangling functional groups, successful removal of the occluded benzenetricarboxylate moieties is not reported up to now.

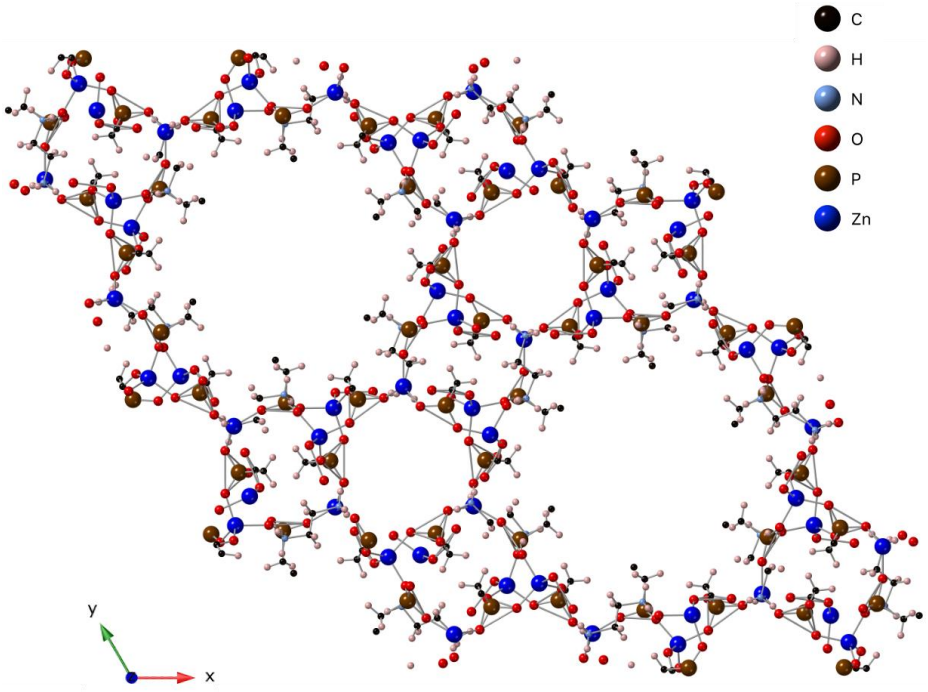


Figure 1.17. Open-framework of Zn carboxymethylphosphonate, possessing large 24-membered channels and smaller 8- and 12-membered rings.

Following the work of Stucky *et al.,* Férey and co-workers documented the first open-framework Praseodymium-carboxyphosphonates, $Pr_4(H_2O)_7[O_2CC_5H_{10}NCH_2PO_3]_4{\cdot}(H_2O)_5$ MIL-84(Pr) (Figure1.18).[88] This lanthanide compound exhibited a three-dimensional open-framework structure and demonstrated notable thermal stability. The structure featured a one-dimensional inorganic subnetwork constructed from chains of edges- sharing rare-earth polyhedra, interconnected via the organic acids to form an open-framework structure with small water-filled pores. X-Ray thermodiffractometry confirmed that MIL-84(Pr) remained stable up to 523 K and displayed reversible hydration-dehydration behaviour.

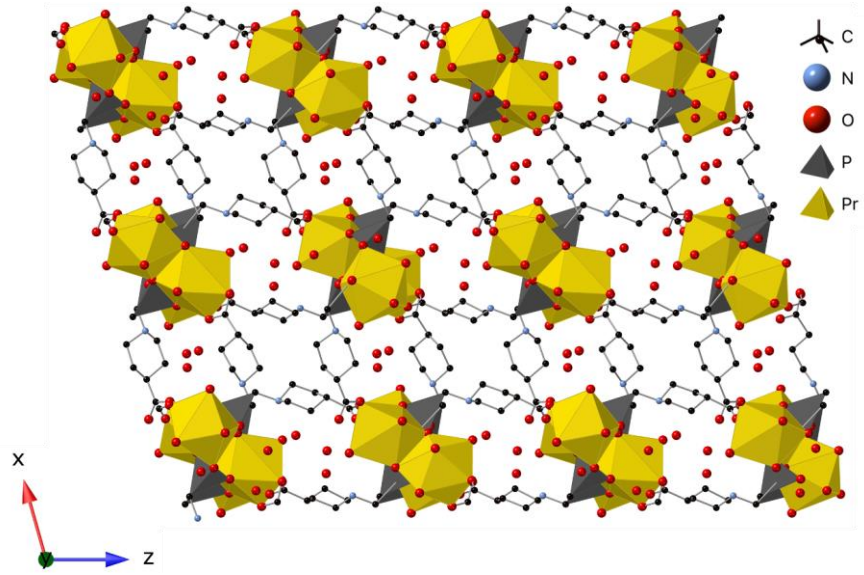


Figure 1.18. Framework structure of MIL-84(Pr). Hydrogen atoms have been omitted for clarity.

Hix *et al*. documented several metal carboxyphosphonate frameworks in which one of the published structures, $Zn_3(O_3PCH_2CO_2)_2.3H_2O$, has a framework with large channels measuring 10 × 6.8 Å (Figure 1.19a).[95] Subsequently, structures with the same ligand involving Cu, Mn, and Pb were reported by another research groups; however, most of these frameworks displayed dense structures without significant pores (Figure 1.19b–d).[80, 96, 97] The flexibility of aliphatic carboxyphosphonic acid ligand make it extremely difficult to construct open framework, therefore the use of aryl carboxyphosphonic acid became a popular choice leading to a significant number of framework materials.[89, 98-100] Chen *et al*.[89] reported six frameworks using 4-phosphonobenzoic acid linker, with three possessing zeolitic open frameworks (Figure 1.20). These frameworks were synthesized under mixed-solvothermal conditions using amine-based templating agents.

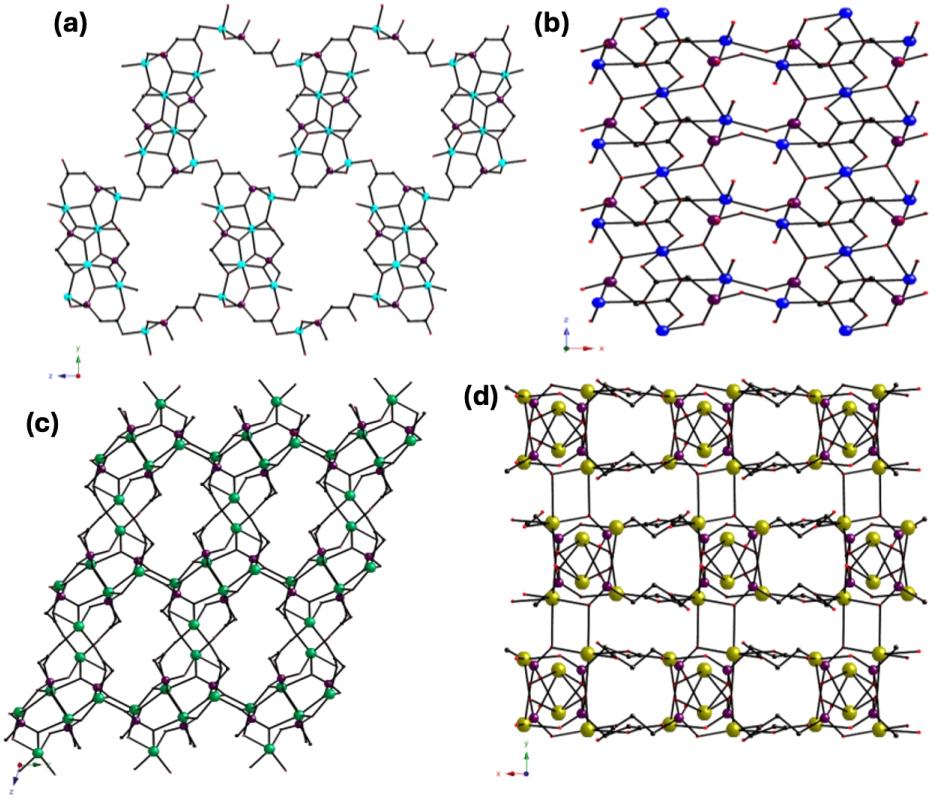


Figure 1.19. Framework structures of (a) $Zn_3(O_3PCH_2CO_2)_2 \cdot 3H_2O$[95], (b) $Cu_{1.5}(O_3PCH_2CO_2) \cdot H_2O$[64], (c) $Mn_3(O_3PCH_2CO_2)_2$[80], (d) $Pb_3(O_3PCH_2CO_2)_2$[81], illustrating the channels present; hydrogen atoms and internal solvent have been omitted for clarity; colour scheme: Zn – cyan, Cu – blue, Mn – green, Pb – gold, P – purple, O – red and C – black.

As seen in Figure 1.20a and b, the double-crankshaft inorganic chains of $Zn_2(pbc)_2 \cdot 2Hdma \cdot DMF \cdot H_2O$ and $Zn_2(pbc)_2 \cdot H_2teta \cdot H_2O$ were formed by corner-sharing of ZnO_4 and CPO_3 tetrahedra connected by organic moieties, resulting in gismondine-like zeolite topologies. The structure of $Zn(pbc) \cdot H_3O$ in Figure 1.20c showcased cages typically found in zeolites.[101] For all the structures, their templating agents are retained within the channels of the framework. The TGA information shows that it is quite challenging to activate these frameworks as these templating agents remain present until the framework collapses, making their potential application for gas adsorption not visible.[89]

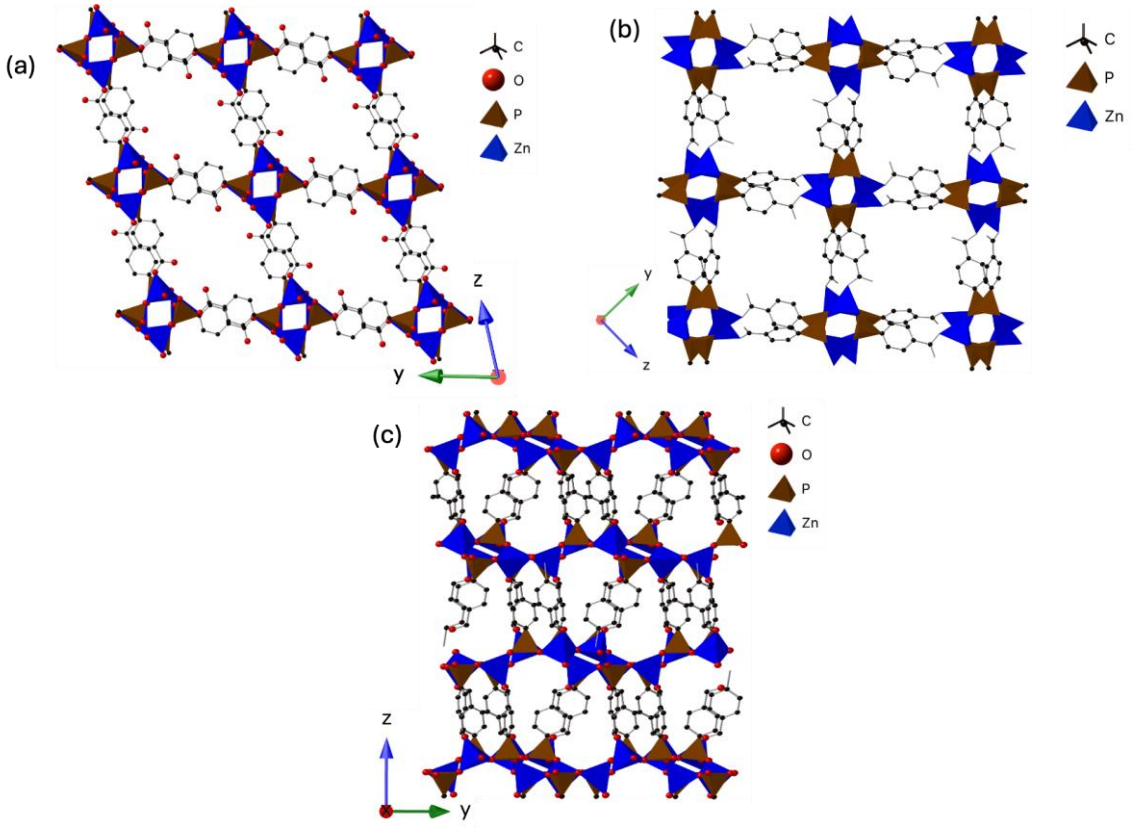


Figure 1.20. Open framework structures of (a) $Zn_2(pbc)_2{\cdot}2Hdma{\cdot}dmf{\cdot}H_2O$, (b) $Zn_2(pbc)_2{\cdot}H_2teta{\cdot}H_2O$, (c) $Zn(pbc){\cdot}H_3O$, showing the zeolite-type topologies; hydrogen atoms and internal solvent have been omitted for clarity.

With the same ligand used by Chen *et al*., Le and co-workers constructed two isostructural pillared layered frameworks via hydrothermal synthesis, using 4,4'-bipyridine and dabco (1,4-diazabicyclo[2.2.2]octane) as auxiliary ligands.[100] These compound are given as $Zn(H_2O)_6[Zn_8(pbc)_6(4,4'\text{-bipy})]$ and $(Hdabco)_2[Zn_8(pbc)_6]{\cdot}6H_2O$ and their crystal structures is shown in Figure 1.21. The inorganic layers of these two compounds consist of ZnO_4, ZnO_3N, and CPO_3 tetrahedra with 12-membered rings, interconnected by 4-phosphonobenzoic acid and 4,4'-bipyridine/dabco through coordination with zinc atoms. The anionic framework's charge was balanced by hexaaqua zinc atoms situated within the cages formed by the inorganic window and organic pillars. This research is notable for its cavity structures with 12-membered windows and for

showcasing a method to regulate pore size distribution by using a second organic ligand to template the structure. However, further research appears to be necessary on Metal-Organic Frameworks (MOFs) utilizing the basic 4-phosphonobenzoic acid linker, as the framework materials currently published are either dense or do not appear to exhibit substantial accessible internal surface area.

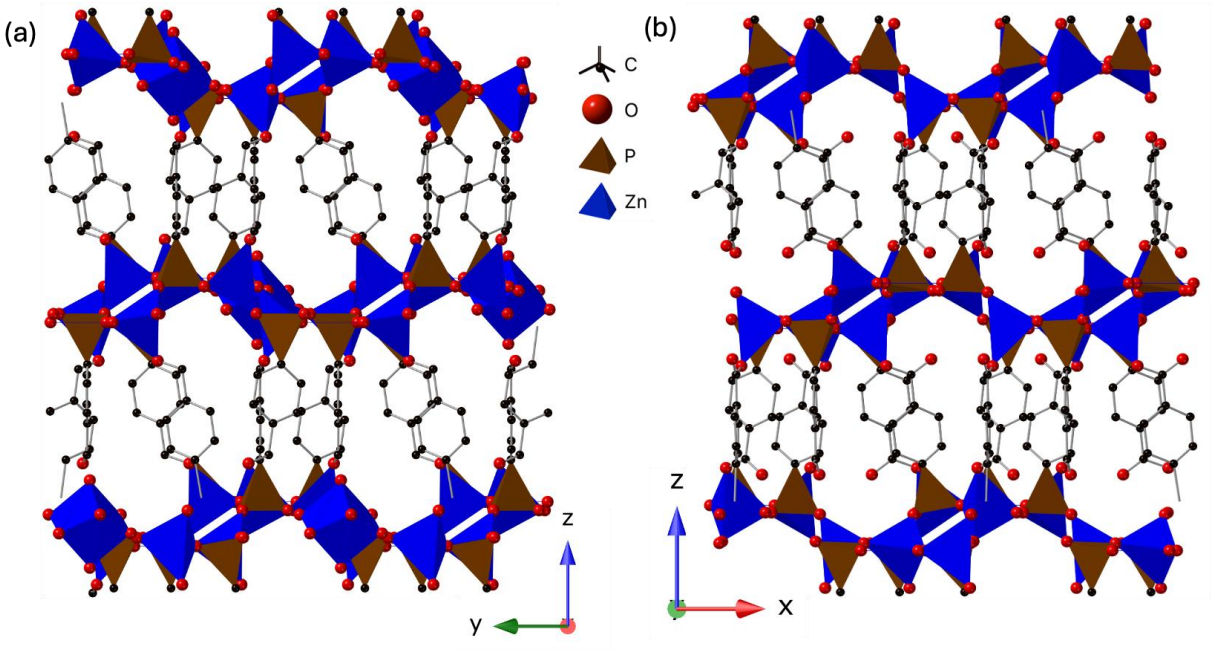


Figure 1.21. Framework structures of (a) $Zn(H_2O)_6[Zn_8(pbc)_6(4,4'\text{-bipy})]$, (b) $(Hdabco)_2[Zn_8(pbc)_6]\cdot 6H_2O$; hydrogen atoms and internal solvent have been omitted for clarity.

In conclusion, the field of carboxyphosphonate frameworks remains relatively underexplored, particularly when compared to phosphonate and carboxylate frameworks. Progress seems to have been stagnated in recent years, with only a few new structures being reported since 2015.[90, 102-104] This is surprising, considering the potential for unique structures that can emerge from the various coordination modes of phosphonate groups and the capability of carboxylate groups to mitigate some of the limitations associated with phosphonates.

1.3.4. BIRM-1

BIRM-1, a zinc-based carboxyethylphosphonate metal-organic framework (MOF), was first synthesised at the University of Birmingham by Chao Zhao.[90, 105] This material is produced through a one-pot hydrothermal synthesis method involving the reaction of zinc nitrate, 3-phosphonopropionic acid, urea, and tetraethylammonium bromide. The synthesis reaction occurs at 87 °C and typically lasts for 24 hours. During this reaction, urea decomposes in-situ to form ammonium carbonate, which deprotonates the linker molecule, facilitating slow crystal growth. The structure of BIRM-1, as depicted in Figure 1.22a, is composed of CPO_3 and ZnO_4 tetrahedra that combine via corner sharing to form double chains arranged in a helical fashion along the z-axis (Figure 1.22b). These double chains have small pores with an approximate diameter of 4 Å and the connection between these double helical chains is facilitated by the fully deprotonated carboxyethylphosphonate linker. This linking results in the formation of a larger pore, approximately 7.6 Å in diameter, situated between the four helices and are filled with ammonium cation formed from the decomposition of urea. The structural formula and basic crystallographic details of BIRM-1 are given in Table 1.1.

Table 1.1 Basic crystallographic data for BIRM-1.[90]

Sample	BIRM-1
Formula	$(NH_4)_2[Zn_2(O_3P(CH_2)_2COO)_2]\cdot 5H_2O$
Space group	$I4_1/acd$
a (Å)	22.3019(2)
b (Å)	22.3019(2)
c (Å)	17.7384(1)
Volume ($Å^3$)	8822.6(11)

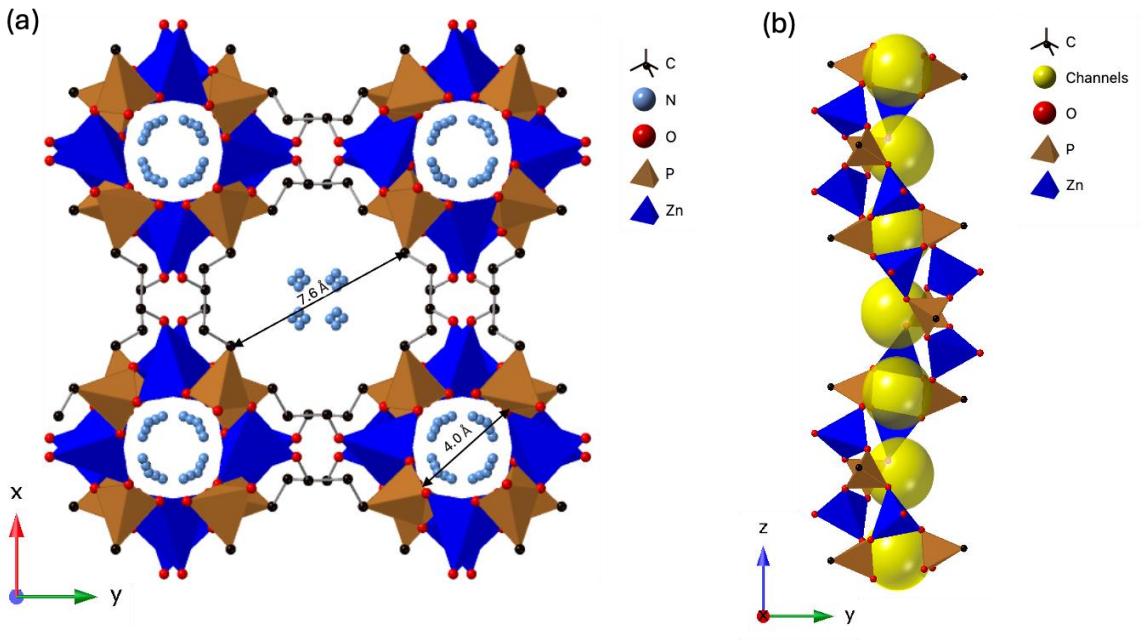


Figure 1.22. (a) Framework structure of BIRM-1 viewed along *z*-axis and (b) the structure of the helical double chains as viewed along the x-axis. Oxygen atoms from solvent water have been removed for clarity. Location of hydrogen atoms from ammonium cations could not be determined in Zhao's work.

Furthermore, Zhao identified two distinctive properties in BIRM-1 which are ion exchanging properties, and the ability to undergo reversible dehydration and retain its porosity upon rehydration. Zhao found that the ammonium cation in BIRM-1 channels can undergo ion-exchange with a range of cations including alkali, alkaline earth and even some transition metals. [90, 105] Some of these ion-exchanged variants are isostructural to BIRM-1 with a proportion of ammonium cations exchanged for the new cations. One example of this is the potassium exchanged form of BIRM-1 (K^+-BIRM-1), shown in Figure 1.23, which exchanges to roughly 80%.[90] The ion-exchange capability of BIRM-1 is a notable feature that sets it apart. Among the vast array of Metal-Organic Frameworks (MOFs), only a small subset demonstrates the ability to effectively undergo ion-exchange with extra

framework ions. This property of ion-exchange not only introduces new potential applications but also offers the opportunity to enhance the properties of BIRM-1 for various uses. More importantly, the exchange of transition metals could create open metal sites capable of more strongly adsorbing gases or even serving as catalytic sites.

Zhao also conducted hydrogen uptake experiments with BIRM-1. Findings shows that BIRM-1 has minimal hydrogen uptake capacity and also became amorphous after dehydration, potentially causing pore collapse. Despite unsuccessful dehydration attempts using different methods, BIRM-1 can undergo solvent exchange without structural damage. The material shows reversible dehydration behaviour, with crystallinity returning when exposed to humid air, suggesting non-uniform deformation rather than complete breakdown of the framework. [90]

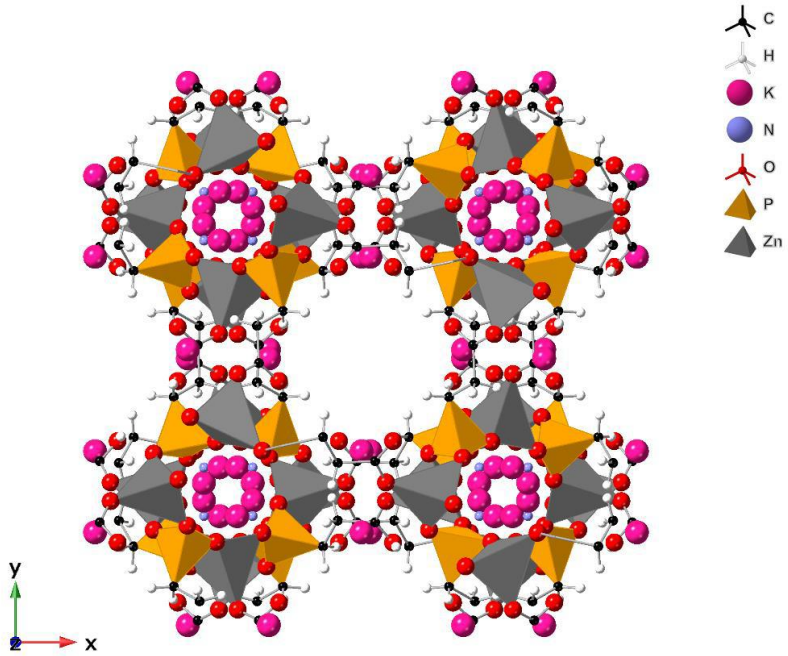


Figure 1.23. Crystal structure of K^+-BIRM-1 looking along the z-axis. Oxygen atoms from solvent water have been removed for clarity. Location of hydrogen atoms from residual ammonium cations could not be determined in Zhao's work.

1.4. MOF Synthesis

The synthesis of Metal-Organic Frameworks (MOFs) is commonly conducted using a solvothermal method, wherein a solvent mixture containing metal salts and organic linkers is heated.[106] The reaction temperature, typically ranging from 60°C to 150°C, is adjusted based on the rate of crystal growth and the types of solvents used. In the narrow sense, the definition of solvothermal synthesis is heterogeneous reactions in nonaqueous solvents above their boiling point and 1 atm and typically, an autoclave reaction vessel is used to grow crystalline solid materials. However, when an aqueous solvent is use as the reaction medium for growing MOF crystal, the synthesis is called hydrothermal synthesis.

Aside from the use of an autoclave reaction vessel for the hydro-(solvo)-thermal synthesis, MOF synthesis have also been carried out in glass vials.[107] The solutions containing an organic linker and metal salt can be used to prepare a reaction mixture and then added to the vial. After mixing and dissolving all starting materials, the vial is tightly capped by hand and heated in oven to grow MOF crystal. The disadvantage of this method is that the glass vial may not withstand higher temperature compared to autoclave reaction vessel.

Some more modern and complex MOF materials have had room-temperature synthesis methods developed for them.[107-109] MOFs powders can be formed immediately just after mixing the solution containing metal salt and linker even at an ambient temperature. MOF synthesis without heating is advantageous for the cost-effective scaled-up reactions and the use of thermally unstable starting materials. IRMOF-0 [Zn_4O(acetylenedicarboxylate)$_3$] is a typical example, where heating is not suitable due to the low thermal stability of the organic linker.[109] In this case, starting materials of zinc acetate and acetylenedicarboxylic acid are dissolved in DMF separately. These solutions were

mixed to obtain a clear solution, and trimethylamine (TEA) was added to the stirring solution. The reaction mixture was stirred overnight at room temperature to yield microcrystalline powders.

Some of the early work on MOF synthesis have employed simple crystallization method such as evaporative crystallisation or diffusion crystallisation techniques.[110] These techniques have been proven successful in obtaining large single crystals for structure solution from diffraction. In evaporative crystallisation, MOF precursors dissolved in solvent is allowed to stand in an open air under stirring for the solvent to evaporate, causing increase in the concentration of the reactant. Growth of MOF crystal will begin to occur when the concentration of the reactant exceeds the critical nucleation concentration.[111] Some prominent MOFs such as MOF-5, MOF-74, MOF-177, HKUST-1 and ZIF-8, have been obtained using this simple evaporative crystallization method.[109, 112] Two diffusion approaches are often used to synthesize MOFs; a vapor diffusion method and a liquid–liquid diffusion method. As for vapor diffusion method, the reaction mixture of the organic linker and the metal salt is slowly exposed to amine vapor, such that the slow deprotonation of the organic linker can allow slow crystallization of the reactants. More specifically, two different sizes of glass vials are typically used, where the smaller vial is placed into the larger vial (Figure 1.24a). The small inner vial contains the solvent mixture of linker and metal salt, while large outer one contains diluted amine solution. In the case of liquid–liquid diffusion, crystal growth is achieved at the interface of two solvent mixtures (Figure 1.24b). To create this distinct interface for crystal growth, a half-filled crystallization tube with the first solution is gently added to the second solution. Some typical examples of MOFs synthesised using this approach are MOF-2 and ZIF-8[113, 114]

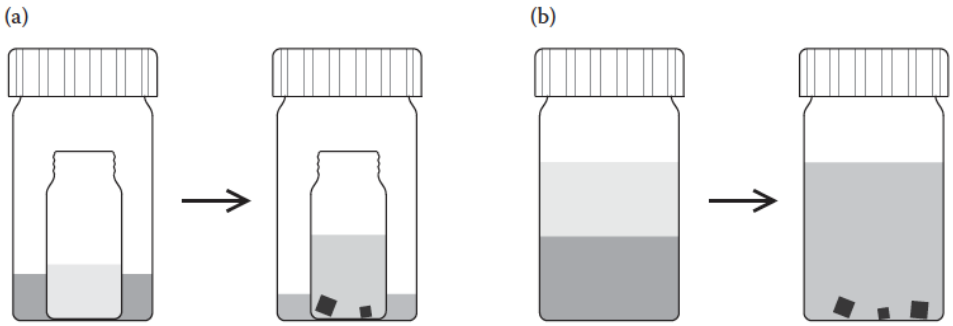


Figure 1.24. Schematic of (a) vapor diffusion and (b) liquid–liquid diffusion-assisted crystallization methods. Reproduced from Glover and Bin.[107] Copyright 2018, CRC Press.

Alternative synthetic procedures that can enable short-time synthesis and/or large-scale production of MOFs are being developed over the years. They include microwave-assisted solvothermal synthesis, sonochemical synthesis, mechanochemical synthesis, electrochemical synthesis etc.

Typically, conventional solvothermal method requires a day or longer periods to prepare MOFs, which could prevent large-scale MOF production per time, but this challenge can be overcome using microwave-assisted synthesis. A microwave with frequency range of 300 MHz to 300 GHz is applied to MOF precursor solution and this microwave irradiation induces polar molecules to rotate and generate thermal energy that drives the chemical reactions (Figure 1.25). As long as the reaction mixture absorbs microwave energy, it is possible to heat the reaction mixture higher than 100 ^{o}C. Due to the direct heating of the reactants, the nucleation rate is accelerated, leading to drastically shorter MOF formation time (1 h) compared to a conventional solvothermal method. Microwave-assisted heating was found to be the method of choice to rapidly synthesize HKUST-1 crystals in the range of 10-20 µm in high yields (90%) within 1 h.[115] Other MOFs such as Fe-MIL-53[116], Fe-MIL-101-NH2[117], IRMOF-3[118], and ZIF-8[119] were also synthesized using microwave-assisted synthesis method.

A significant drawback to this method is that these syntheses are not always easy to replicate on different microwave synthesis instruments by different manufacturers.

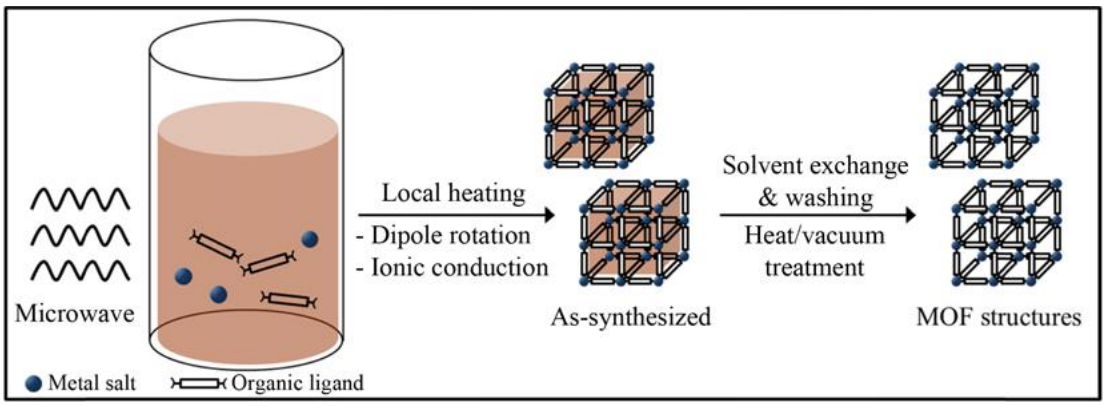


Figure 1.25. Schematic showing microwave-assisted synthesis of MOF. Reproduced from Lee *et al.*[120] Copyright 2013, Springer.

Sonochemical synthesis is another method for fast crystal growth of MOFs, where high-energy ultrasound with frequency range of 20–40 kHz is used to drive the reaction of MOF precursors. When ultrasound is made to transmit via a MOF precursor solution, it leads to the generation of high and low-pressure regions inside the solution, resulting in subsequent compression and expansion. This phenomenon results in the formation and collapse of bubbles in the solution, known as acoustic cavitation, generating a very high local temperatures (~ 5,000 K) and pressures (~ 1,000 bar) and subsequently induce homogeneous nucleation and crystal growth (Figure 1.26). High quality MOFs such as MOF-5[121], HKUST-1[122], ZIF-8[123], Mg-MOF-74[124] etc., has been reported using sonochemical method.

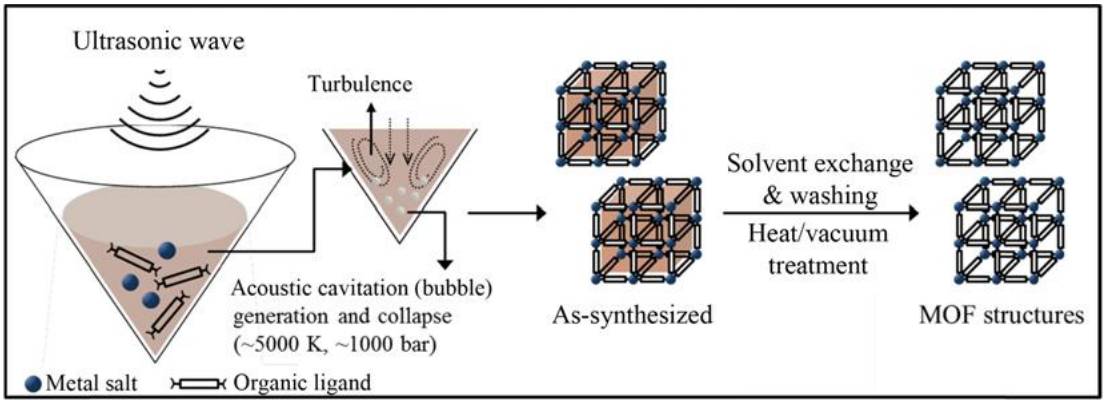


Figure 1.26. Schematic showing sonochemical synthesis of MOF. Reproduced from Lee *et al.*[120] Copyright 2013, Springer.

Mechanochemical synthesis have also found it use in MOF synthesis.[125-128] A typical mechanochemical synthesis involves grinding/milling the mixture of solid precursors in a ball miller under solvent-free conditions. In this method, MOF synthesis is achieved via mechanical breakage of intramolecular bonds followed by a chemical transformation of the MOF precursors (Figure 1.27). Thus, this method gives an opportunity to use insoluble metal sources, which sometimes are difficult to dissolve in the solvents used in conventional syntheses of MOFs. Initially, mechanochemical reactions were performed by using mortar and pestle. Nowadays, automatic ball mills/grinders are predominantly used. These special instruments provide high grinding energy which facilitates mechanochemical reactions.

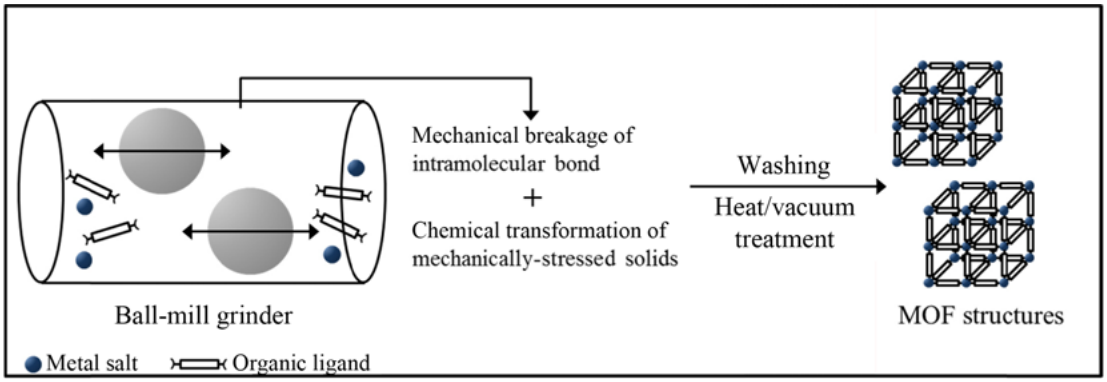


Figure 1.27. Schematic showing mechanochemical synthesis of MOF. Reproduced from Lee *et al.*[120] Copyright 2013, Springer.

Lastly, some MOFs have been synthesised in an electrochemical cell, where a high voltage (typically 4–15 V, current density of 0.5–50 mA/cm^2) is applied between two electrodes immersed in a reaction mixture.[120, 129] The electrochemical synthesis of MOFs uses metal ions continuously supplied through anodic dissolution as a metal source instead of metal salts, which react with the dissolved linker molecules and a conducting salt in the reaction medium (Figure 1.28). This method of MOFs synthesis was first reported in 2005 by researchers at BASF for HKUST-1[120] and this technique has been extended to synthesis of several other MOFs like ZIF-8, Al-MIL-100, Al-MIL-53, and Al-MIL-53-NH_2.[130]

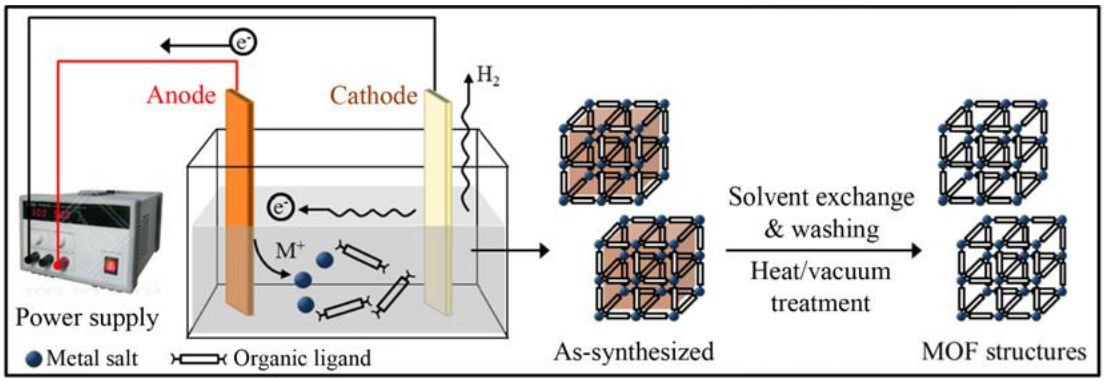


Figure 1.28. General scheme for the electrochemical MOF synthesis. Reproduced from Lee *et al.*[120] Copyright 2013, Springer.

1.5. MOFs as electrocatalyst for CO_2 reduction

The growing interest in the application of MOFs as homogeneous and heterogeneous electrocatalysts in CO_2 reduction reaction has been attributed to their intriguing catalytic properties.[131-133] The exceptionally high surface area of MOFs provides plentiful catalytic active sites for a surface-related reactions such as adsorption/desorption, insertion/de-insertion, surface redox reactions, and heterogeneous catalysis.[134] The large pore volume commonly exhibited by MOFs facilitates mass transport of selected substrates to the active sites and as well providing a platform for loading guest species.[134] Catalytically active sites and an understanding of where they originated from, are essential in MOF catalytic applications (Figure 1.29). For pristine MOFs, catalytically active sites often originate from coordinatively unsaturated metal sites which act as Lewis acid sites, and the dangling acid/base site from the organic linkers.[135]

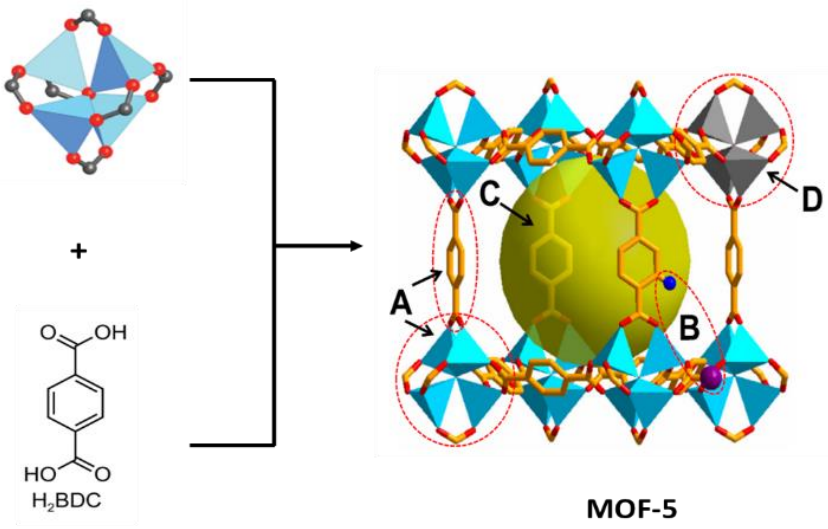


Figure 1.29. Metal-organic framework catalyst structure where: i) A is connecting site for metal clusters and linkers in pristine MOFs ii) B is a site for grafting metal/non-metal in MOFs by modification iii) C is a site for encapsulated in MOF composites iv) D is the sites generated in MOF derivatives upon thermal/chemical conversion. Reproduced from Li *et al.* [135] Copyright 2019, Elsevier.

Secondly, the porous nature of MOFs makes it practically possible to post synthetically modify it with various catalytically active species, such as molecular catalysts, metal-based nanoparticles (NPs), enzymes, *etc*., which can stimulate structural-defect within the MOFs for efficient catalysis. Thirdly, the catalytically active sites of MOFs can be exposed to chemical/thermal treatment to obtain porous materials, including metal-based compounds, porous carbons, and their composites. These MOF derivatives are promising candidates for catalytic application because of their exceptionally large surface area, excellent stability, tunable structures/composites and highly dispersed active sites. An interesting attribute of MOF-derived materials is their ability to retain, to a certain degree, the morphological architecture of the pristine MOF, which upon doping with heteroatoms, can improve the conductivity and the degree of graphitization, resulting in better performance in electrocatalytic applications.[135-137] Based on these merits, the electrocatalytic application of MOF-based nanocomposites have become the subject of intense discussion in recent years.[138-142] Despite the encouraging performance of MOF as electrocatalyst in CO_2RR, the challenges of electrical conductivity and chemical stability in highly basic or acidic aqueous environments need to be addressed.[143] In addition, many doubts are raised regarding the normalization and comparison of results between different MOF materials and scientific reports due to the lack of a standard methods to determine the true electrochemical surface area and the active sites.

1.5.1. Addressing conductivity challenges in MOFs

Based on the literature reports so far, conductivity range in the MOFs can vary from 10^{-10} to 10^{3} S cm^{-1} [144, 145] which is still far below electrical conductivity requirement for industrial application in electrochemical system. The poor electrical conductivity of MOFs has been linked to *(i)* the

insulating character of the organic ligand, attributable to the lack of free charge carriers and *(ii)* poor overlap between π orbitals of organic ligand and the *d* orbitals of the metal ions, which present barrier for charge transfer.[10] Conductivity has become an important milestone to measure the suitability of MOFs in electrochemical application.[146] Since electrical conductivity (σ) in MOFs are dictated by the amount of charge density (n) and mobility (μ) of electrons (e) and hole (h), it is highly essential to maximize both charge density and mobility of charge carriers (Equation (1.10)) to achieve high conductivity.

$$\sigma = e\,(\mu_e n_e + \mu_h n_h) \qquad (1.10)$$

The general requirement for constructing MOF with high conductivity is to select building blocks with loosely bound charge carriers, otherwise regarded as materials with high charge density. The metal ions, organic ligands or guest molecule in a MOF could serve as sources of charge carriers. Facile charge migration is required for efficient MOF electrocatalysts; otherwise, the reaction would only occur at the catalytic centers in direct proximity to the electrode. Therefore, pathway for the charge mobility within a MOF material can be describe by two important techniques namely; redox hopping and band transport (figure 1.30).[147]

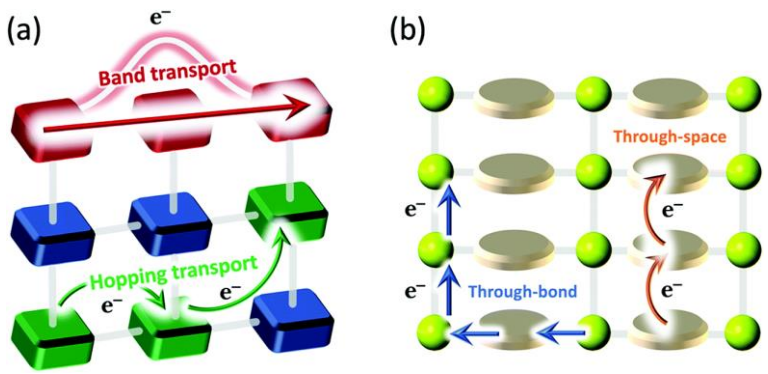


Figure 1.30. Schematics of two charge-transport (a) mechanisms and (b) pathways in metal–organic frameworks.

In redox hopping, the charge carrier (such as redox centers) is usually localized at specific sites within the framework which often result in the charge hopping between neighbouring sites MOFs. However, in order to maintain electroneutrality during charge hoping, counter ion usually diffused through the MOF structure, thereby limiting the charge transport (figure 1.30).[147] Therefore, charge transport via redox hopping are evaluated based on diffusion phenomenon where the measurable diffusion coefficient D_e ($cm^2\ s^{-1}$) for electron-hopping mechanism in MOF is related to total redox-active linker concentration C_P^0, the electron-exchange rate constant k_e (s^{-1}) and average hopping distance d via the following equation;[148]

$$D_e = \frac{k_e}{6} C_P^0 d^2 \qquad (1.11)$$

Hence to optimize charge transport via redox hopping, MOF must be designed in such a way that its pore size is sufficiently large enough to allow smooth diffusion of counter ion thereby enhancing MOF conductivity. One strategy to improve charge transport is via post-synthetic incorporation of guest redox molecules into the frameworks.[149, 150] These guest molecules form charge transport pathways through guest to guest or guest to framework interactions. Iodine, redox-active molecules and some macromolecules or clusters are popular guest molecules that can be incorporated into the pores of MOFs to improve their conductivities.[150] For example Kobayashi *et al.* reported a significant increase in conductivity of $Cu[Ni(pdt)_2]$ from 10^{-8} to $10^{-4}\ S\ cm^{-1}$ after I_2 vapor treatment.[151] The authors attributed the increase in conductivity to the partial oxidation of the $Cu[Ni(pdt)_2]$ framework induced by I_2 doping. Talin *et al.* also reported that conductivity of $Cu_3(BTC)_2$ thin film MOF improve drastically from ca. $10^{-8}\ S\ cm^{-1}$ to $0.07\ S\ cm^{-1}$ when the MOF is infiltrated with Tetracyanoquinodimethane (TCNQ) which is redox-active molecule(figure 1.31).[152] Based on spectroscopic data and first principle modelling report, the authors reveal that conductivity arise from TCNQ guest molecules bridging the binuclear copper paddlewheels in the

framework, leading to strong electronic coupling between the dimeric Cu subunits. Unfortunately, the disadvantage of this strategy is the blockage of pore channels resulting in the reduction of the surface area which are key properties for electrocatalysis.[150] Therefore, care must be taken to choose MOF and guest molecule to minimize these effects. Another early example of this strategy was reported by Kung *et al.*, where their findings shows a great improvement in conductivity of NU-1000 from 9.1×10^{-12} S cm^{-1} to 2.7×10^{-7} S cm^{-1} after loading nickel bis(dicarbollide) into the micropores of the MOF.[153] In a more recent findings by Xin *et al., the* electrocatalytic activity of MOF-545-Co for the CO_2RR was greatly enhanced after the incorporation of cobaltocene which is acting as potential donor and carrier to enhance the electron density within the MOF structure.[154] While the pristine MOF-545-Co FE_{CO} was 55% at −0.8 V *vs.* RHE, the presence of guest molecule is reported to improve the FE_{CO} up to 97% at −0.7 V *vs* RHE. This was attributed to the increased conductivity which play a crucial role in enhancing the electrocatalytic activity of MOF.

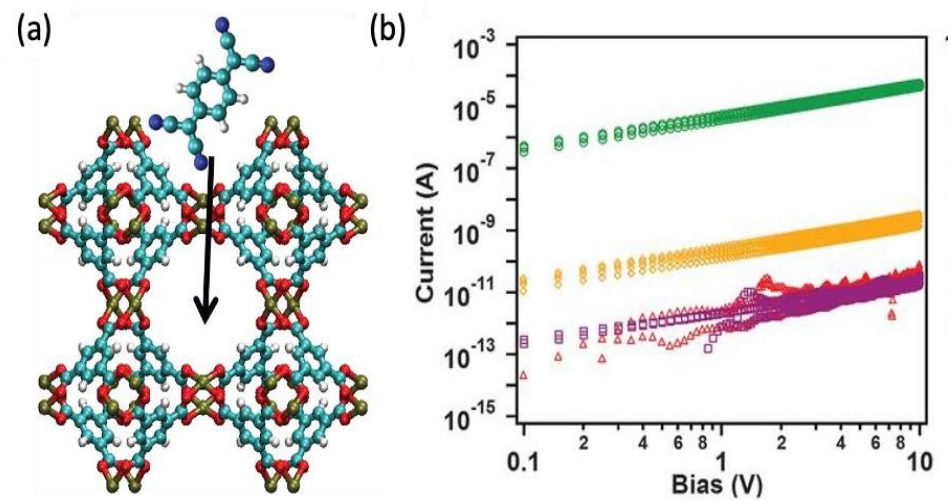


Figure 1.31. (a) Fabrication of electrically conductive TCNQ@$Cu_3(BTC)_2$ via post-synthetic incorporation (b) I-V curve showing the electrical conductivity of pristine $Cu_3(BTC)_2$ (red), and after infiltrated with TCNQ (green), F4-TCNQ (gold) and H4-TCNQ (purple). Reproduced with permission from Talin *et al.*[152] Copyright The American Association for the Advancement of Science, 2014.

The second and more efficient techniques used in obtaining high charge transport and enhance conductivity in MOF is through band transport.[146] This is achieved by increasing the extent of delocalization between the framework components by introducing mixed valent states of the node/linker, donor-acceptor type interactions, π-π stacking or π-conjugation into the framework which could lead to improved charge propagation.[155] Carefully selecting atoms with diffuse frontier orbitals, such as softer transition metal ions (Fe, Mn, Co, Ni and Cu) and linkers containing nitrogen or sulfur can result in construction of highly delocalized MOFs.[156] Sun *et al.*, demonstrated that when a linker 2,5- dihydroxybenzene-1,4-dicarboxylic acid is replaced with 2,5-disulfhydrylbenzene-1,4-dicarboxylic acid in the construction of Mn-MOF, an infinite 1D metal–sulfur chains is created within the framework, prompting charge delocalization and resulting in a dramatic increase in conductivity.[157] The presence of extended π- π-stacking or π-conjugation in MOF destined for electrocatalysis have been proven to create pathway for the efficient delocalization of charge carriers within the framework.[158] The strategy of extended π- π-stacking was implemented by some researchers to design MOFs with functionalized TTF (tetrathiafulvalene) derivatives, with the π-π stacking of TTF moieties resulting in the formation of highly conductive charge transport columns within the framework, leading to improved conductivity.[159-161] In a similar strategy, incorporation of in-plane π-conjugation into MOF framework has been discovered to induce charge delocalization in the 2D MOF.[162-164] Of particular interest is the work of Zhu *et al*. in 2015 where they reported that 2D MOF Cu-BHT (BHT = benzenehexathiol) displays great charge delocalization due to extended 2D π-conjugation, prompting conductivity as high as 1580 S cm^{-1} at room temperature.(figure 1.32)[144] Overall, findings has shown that both π-conjugation and π–π stacking strategies have resulted in the largest increase in conductivity.[145, 165]

The reports on conductive MOF for electrocatalysis has been encouraging thus far. However, opportunities still abound in developing conductive MOFs with optimal electrocatalytic performance by carefully selecting ligand, metal center and guest molecule that will promote redox hopping and band transport within the MOFs. It is important to notice that the vast majority of the reports, if not all, have provided information on the conductivity of pristine or post synthetic modified MOF catalyst, however, information on the conductivity of the catalyst after the electrochemical experiments is missing. Such information is key on the understanding of the changes of MOF under operation conditions, its stability and changes on the product selectivity.

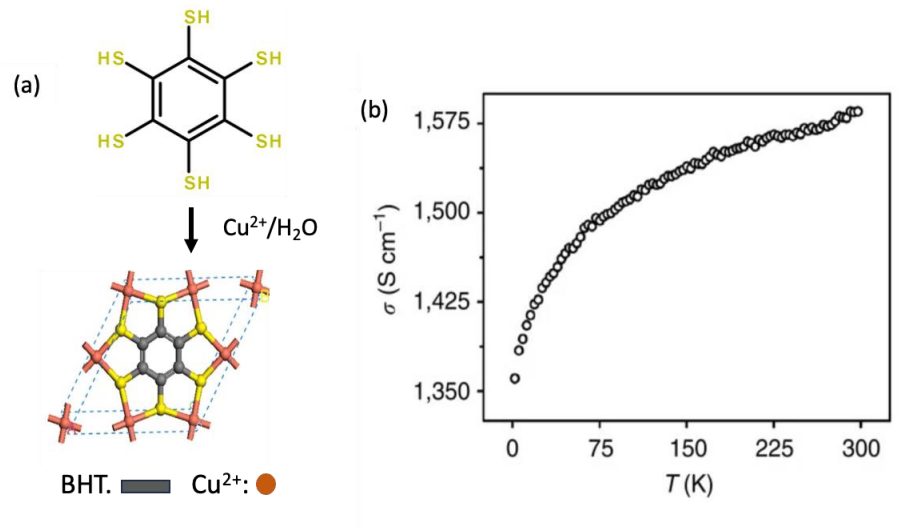


Figure 1.32. (a) electrically conductive Cu-BHT 2D MOFs designed by π-conjugation (b) Electrical conductivity measurement of Cu-BHT film as a function of temperature ranging from 2 to 300 K. Reproduced with permission from Zhu *et al*. [144] Copyright Nature communication, 2015.

1.5.2. Addressing chemical stability challenge in MOFs

Stability of MOFs during electrochemical operations is another crucial factor for utilizing MOFs in electrocatalytic applications. During electrocatalysis, the voltage applied induces diffusion of ion/molecules unto the MOFs surface to establish electrical double layer (EDL) (Figure 1.33A). This

MOF charged surface creates a concentration gradient of ions (H^+ in this case), causing the local pH in EDL to drift to acidic/basic ends resulting in complete or partial destruction of the MOF structure (Figure 1.33B and C).[166] Therefore, one of the main challenges to overcome in the CO_2RR on MOF is to deliver materials that are stable in neutral and strongly alkaline media. Additionally, start/stop cycles mimic using potential cycling (Figure 1.33D) induced repeatedly within the MOFs cation/anion chemical gradients which can promote destructive redox reactions at metal nodes and organic linkers (Figure 1.33E) capable of transforming MOFs into metal oxides, hydroxide, as well as oxyhydroxide during catalysis.[167-169]

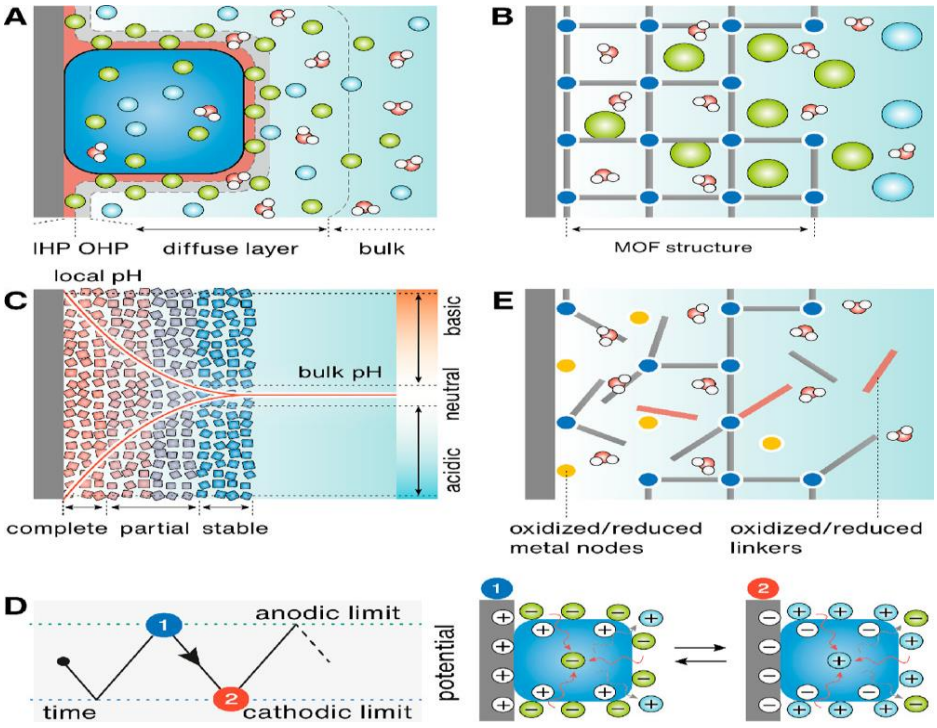


Figure 1.33. (A) Established EDL structure on the surface of MOF particle. (B) Diffusion of ions/molecules into the framework of MOF in the established EDL. (C) Cross-sectional illustration of MOF-coated electrode in neutral electrolyte. (D) EDL formation and ion diffusion on the surface or inside the pores of MOFs (right) due to the dynamic potential sweeping (left). (E) Structural destruction of MOFs due to the redox reaction of metal nodes and/or organic linkers. Reproduced from Zheng *et al.*[170] Copyright American Chemical Society, 2021.

While it might be challenging to address both the chemical and electrochemical stability of MOF without some form of trade off, research has evolved over the years on how to improve MOF stability in electrocatalytic applications.[171, 172] There are questions which are still subject of discussion regarding the role of MOFs during electrocatalysis: are MOFs the real catalysts? or are the MOFs merely the precursors to produce active phases during the electrochemical treatment? It is therefore important to understand the reactivity of MOF in chemical and electrochemical environment, and confirm, either in situ or post-mortem, their chemical and structural integrity in order to design and construct stable MOF for electrocatalytic application**.** The chemical environment of MOF during electrochemical reaction comprises of water, counter ions, reactants and products from electrocatalysis, as well a flow of electrons due to the applied potential. Generally, water has the tendency of interacting with metal−linker coordination sites, prompting the decomposition of the framework, producing hydrated/hydroxide metal species in (basic electrolytes) and/or protonated linkers (in acidic electrolytes) that further diffuse to the electrolyte.[173] Aside from hydrolysis of MOFs, the effect of counter ion have also be documented to be destructive. For example, phosphate buffered (PB) solution contain PO_4^{3-} anion (hard Lewis base) which can strongly interact with high valency metal ions. An example of this effect has been found when using UiO-66 framework, which disintegrates within a few minutes in PB solution as a result of strong interaction of PO_4^{3-} anion with Zr^{4+} node of UiO-66 framework.[174] Similarly, Mirsaidov's group demonstrated the lack of stability of ZIF-8 in Co^{2+}-containing solution resulting in the formation of $ZnCo(OH)_x$ in solution.[175] The possibility of the products from electrocatalysis have not been given the utmost attention as the possible cause of instability of MOFs. For example, it has been shown that nanobubbles can be generated at the active sites during gas evolution reactions which can pose both mechanical and chemical challenges to structural integrity of MOFs.[176, 177] Other products, such as

formate/ CH_3OH from CO_2 reduction reaction (CO_2RR) and NH_4^+ from nitrogen reduction reaction (NRR), may pose a similar threat.[170]

Due to the poor stability, some MOFs could become erratic upon exposure to moisture which can attack the metal center within the framework, causing decomposition and phase transformation of the MOFs. Some report have anticipated that the bond strength between the metal cation and the organic ligands is one of the main criteria that influence the stability of MOFs.[178-181] Therefore, the chemical stability of a MOF can be intrinsically improved by judicious selection of metal nodes and design of linkers.[182] *De novo* synthesis of MOF by linking carboxylate-based ligands (hard bases) with high-valent metal ions (hard acids) have been explored in search of MOF with improved stability. Based on the HSAB principle, high-valent metals with high charge density (hard acids), such as Zr^{4+}, Cr^{3+}, Al^{3+}, Fe^{3+}, *etc.*, tend to form strong coordination bond with O donor ligands (hard bases) (Figure 1.34) thereby presenting MOF with good chemical stability.[40, 183-185] Interestingly, the strong coordination bonds and the low pK_a of carboxylate linkers endow the high-valent metal ion-containing MOFs with a decent level of acidic stability.

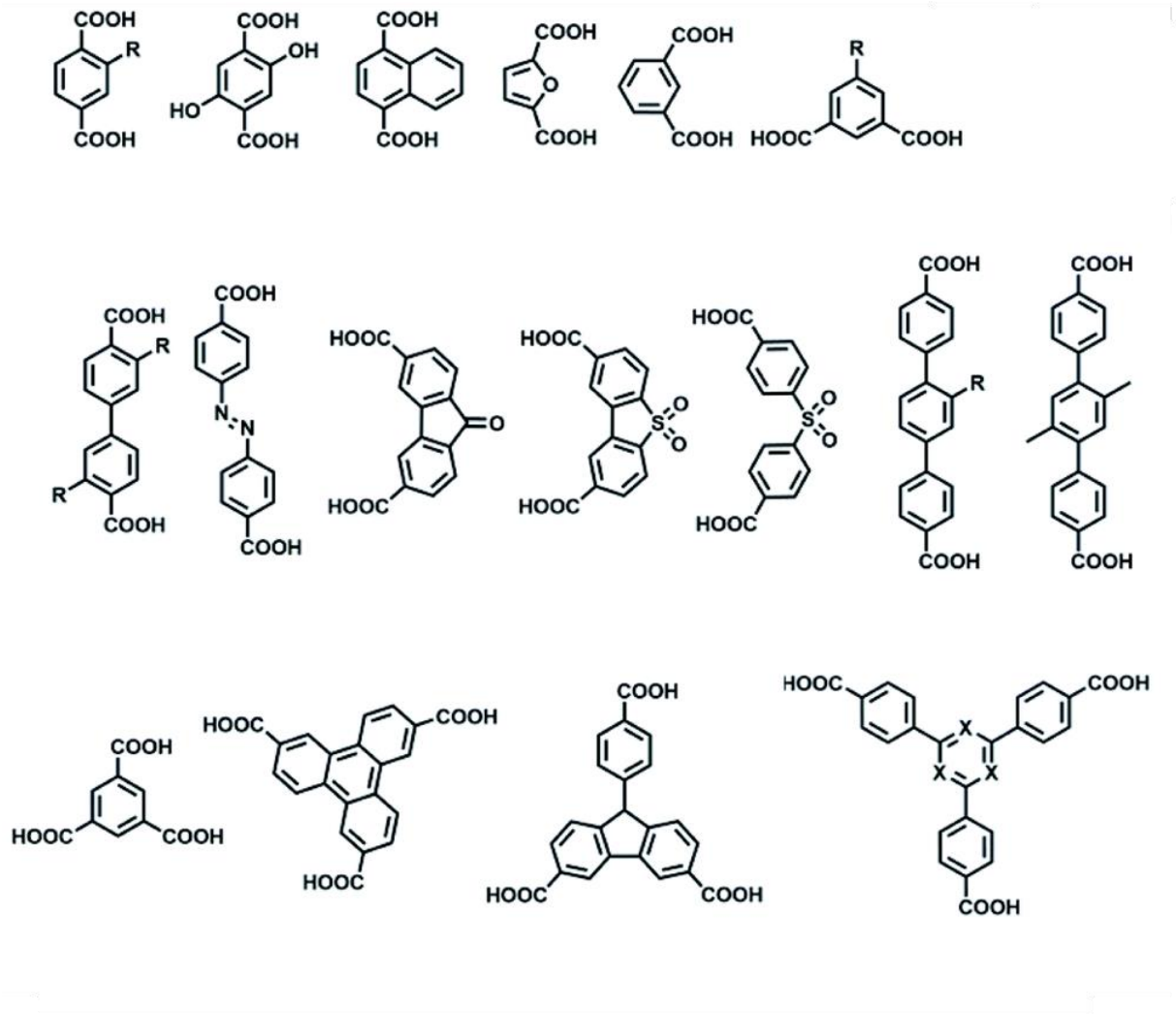


Figure 1.34. Some representatives of low pK_a O donor ligands referred to in the text. Reproduced from Ding *et al.* [171] Copyright RSC, 2019.

On the other hand, low-valent metal ions, including Zn^{2+}, Co^{2+}, Ni^{2+}, Fe^{2+}, and Ag^{+}, which are considered as soft acids can form a strong coordination bond with suitable N-containing linkers (soft bases) (Figure 1.35) producing a highly stable MOFs.[186-188] The high pK_a of azoles and strong coordination bonds usually bestowed these MOFs with remarkable stability in basic solutions. Generally speaking, MOFs built from high-valent metal ions and carboxylate ligands tend to be stable in acids and decompose in basic solutions while MOFs constructed using low-valent metals and azolate linkers tend to be stable under alkaline conditions while being readily hydrolysed by

acids.[189] The introduction of hydrophobic/rigid ligand, and phosphonate/carboxyphosphonate ligand into MOF synthesis have also been suggested as another way to improve MOF stability.[190, 191] Surface hydrophobicity prevents the adsorption of water into pores and/or the condensation of water around the metal clusters, which enhances the MOF stability in the presence of water. Phosphonate/carboxyphosphonate MOFs have been shown to exhibit robust structural tolerance in cruel chemical environment[43], the feature which have been attributed to the stronger metal-ligand bond formed when the three O from phosphonic acid coordinated to metal ion compared to the corresponding carboxylate MOFs.

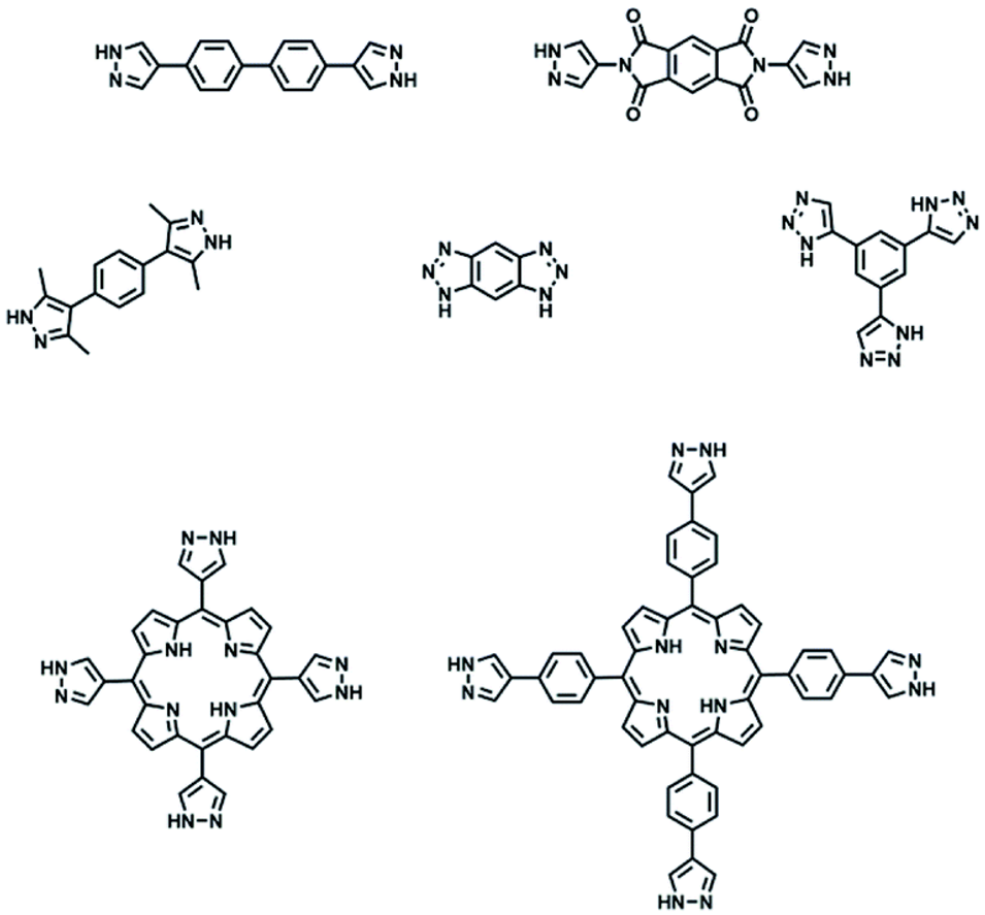


Figure 1.35. Some representatives of high pK_a N donor ligands referred to in the text. Reproduced from Ding *et al.* [171] Copyright RSC, 2019.

The challenge of electrochemical stability can be approach by optimizing the various electrocatalyst parameters. For example non-aqueous electrolytes such as tetrabutylammonium hexafluorophosphate ($TBAPF_6$) in acetonitrile or DMF, have been used as substitute in studying the catalytic activity of MOFs that are unstable in aqueous electrolytes.[192] The implementation of organic solvents as electrolyte can also be linked to its ability to increase the solubility of CO_2 which can as a result, reduce mass transport limitations.[193] In addition, the low proton concentration inhibits the competing process of the hydrogen evolution reaction which is predominant in aqueous electrolyte. Nevertheless, aqueous electrolytes remain the choice electrolyte as water is a green and abundant solvent that can be used in large scale processes.[194] Therefore, the use of catalytically active MOFs stable in the presence of bicarbonate ions is necessary for future applications. MOFs constructed with nitrogen-containing linkers such as ZIFs have been found to be highly stable in water in a wide pH range and this family of MOFs have consistently shown promising activity towards CO_2RR in aqueous electrolytes.[186, 195, 196] On a final note, MOFs under electrochemical conditions must meet two additional stability requirements: *i)* maintaining physical attachment to the electrode surface, and *ii)* remaining structurally intact under reducing and/or oxidizing conditions during electron flow through the framework.[189] The likelihood of meeting the first stability challenge – the potential for delamination or generally loss of MOF from an electrode surface – depends to a large degree on how the electrode is prepared. The second stability issue of resisting degradation under electron flow while in the presence of substrate is a much more MOF-specific challenge. MOFs constructed from ligands which are able to give reversible electrochemical responses are considered to be stable under electrochemical conditions. However, significant number of reports have not performed an adequate and exhaustive characterization of the MOF after electrochemical experiments. It should be expected and a common practice to evaluate the

structural and composition integrity of the MOF catalyst after electrochemical experiments including atomic scale HRSTEM, EDX and if possible, in-situ XAS experiments to confirm the oxidation state and coordination of the metal centres. Numerous electrochemically-stable MOFs have been successfully built from ligands based on a naphthalene diimide core[197, 198 199], a moiety that seems to be stable when reduced. For more in-depth discussion, readers are directed to a recent review by Liu and Yin.[200] Future studies focusing on the structural evolutions of MOFs under CO_2RR conditions is fundamental to establish structure–activity correlations and to understand the different effects that contribute to the stability of MOF-based catalysts.

1.6. Harnessing the performance of various methods of MOF electrocatalyst preparation

Electrochemical evaluation of MOFs requires interfacing of the MOF with an electrode. Finding an effective method of preparing MOF-modified electrode play an important role in the attachment of the MOF catalyst to the electrode and by extension determine the MOF electrochemical response-specifically regarding the rate of electron transfer between the electrode and the first MOF layer as well as how much of the bulk MOF is electrochemically accessible.[189] The type of MOF/- electrode attachment can also have a large impact on the strength of mechanical adhesion, with poor adhesion resulting in delamination.[189, 201] Two approaches have generally been adopted in preparing MOF-modified electrode for CO_2RR and other applications. The first approach entails immobilising the MOF on a conductive substrate via physical interactions or through the formation of chemical bonds between the substrate and the MOF. The second method involves synthesising MOFs directly on the electrodes. MOFs for electrochemical studies are generally prepared by four methods: drop-casting, direct solvothermal growth on a bare electrode surface, self-assembled monolayer

deposition on the electrode surface and electrochemical methods. Each of these methods have different characteristics on mechanical stability, preparation time, and ease of electron transfer between the MOF and conductive electrode substrate. Despite the diversity of synthetic approaches used for preparing MOF-modified electrodes, some of them, like direct growth on conductive substrate is yet to be fully explored for preparing MOF electrode for CO_2RR unlike in other electrochemical reactions such as OER and ORR.[202]

1.6.1. Drop casting

Drop casting is one of the facile methods for immobilizing MOFs on conductive electrode for electrochemical studies. In this case, catalyst ink is usually prepared by dispersing (typically by sonication) MOF powder into solvent or solvent mixture. The electrode is either left to dry in an open air or oven dry at 60^{o}C, leaving behind a thin film of the MOF dispersed on the electrode for electrochemical analysis (Figure 1.36a). Additives such as carbon black and graphite can be added to catalyst ink to increase the MOF electrical conductivity[203-205], while polymeric binder such as Nafion can be added to improve catalyst immobilization on the electrode.[206] However, it is also possible for the electrochemical system to be contaminated by these additives, thereby increasing resistance and possibly blocking some MOF's active sites, leading to a decrease of the desired catalytic activity or even change in selectivity.[207] . Common working electrode substrates, where the drop casting takes place, include GC (glassy carbon), carbon paper, and FTO (fluorine-doped tin oxide).[195, 208, 209 206, 210, 211] However, despite the simplicity of this method of preparing MOF electrodes, controlling the resulting MOF films' thickness and morphology is quite challenging.[189] As a result of their poor stability, MOF films prepared by drop casting can only be used as electrodes for fundamental studies and it is not meant to be used in electrolyzers. Alternatively, MOF-based

gas diffusion electrode (GDEs) prepared by airbrushing catalyst ink on porous carbon paper have been proposed to overcome the above challenges(Figure 1.36b).[212, 213] In GDEs, since CO_2 gas are fed directly on one side of the electrode, the possible hindrance caused by the low solubility of CO_2 in the electrolyte are reduced. The work of Albo *et al.* [214] and Sikdar *et al*.[212] have used MOF-based GDEs in CO_2RR with some promising results in terms of high selectivity of the CO_2RR towards hydrocarbon formation.

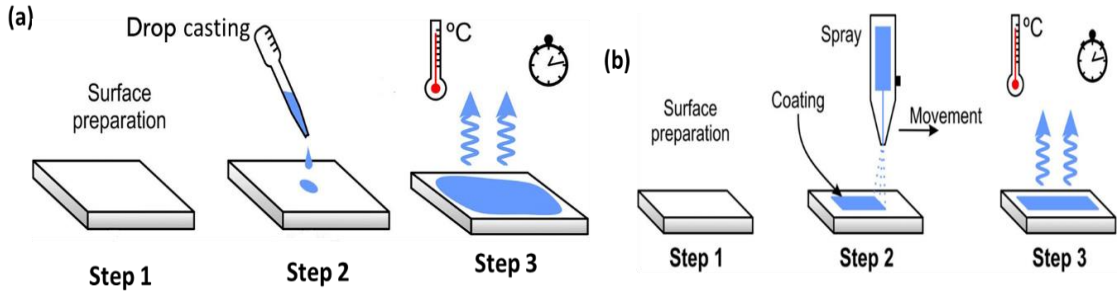


Figure 1.36. MOF-based electrode construction by (a) drop casting (b) spray coating methods.

1.6.2. Direct solvothermal synthesis

In this method, direct growth of MOFs on conductive substrates is achieved by placing the electrode in a the solvothermal reactor with the standard MOF precursors and heated up for the reaction to take place (Figure 1.37).[189, 215] The direct solvothermal synthesis method has a significant advantage over the drop casting which is that the resulting MOF is directly attached to the electrode surface without the need of additional additives that might interfere with electrochemical performance. During synthesis, the rugosity of the surface of the electrode itself provides nucleation sites for MOF crystallization. To achieve effective MOF binding, electrode is usually pre-treated in a dilute linker, creating a monolayer of the linker, which provide the binding site for the first secondary building

unit (SBU) layer and subsequently initiate further growth.[216] Similarly to the drop casting method, glassy carbon, FTO glass, and metal foams are commonly used as electrode substrates.

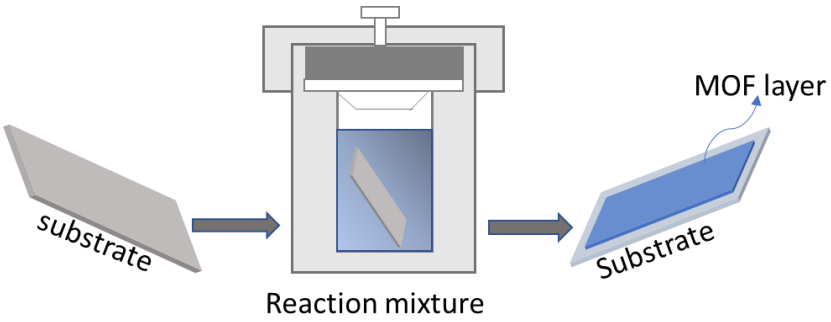


Figure 1.37. MOF-based electrode construction by direct solvothermal growth.

When the MOF is grown on carbon electrode, the carbon is usually pre-treated to created functional group such as carboxylic groups that facilitate nucleation and subsequent MOF growth. As for FTO and ITO substrates, the metal oxides of the electrode provide centres for the nucleation of MOF precursors, facilitating MOF growth on the FTO and ITO, resulting in a uniform MOF thin-film of nanocrystals.[217] On the other hand, the main drawback in these substrates, apart from the cost, is its reduced conductivity when compared with carbon electrodes.[10] Some research groups have focused part of their investigations on determining the effect of the preparation of the electrode on the catalytic activity. For instance, *Duan et al*. compared the electrochemical performance of NiFe–2,6-naphtalenedicarboxylate MOF catalyst prepared by solvothermal synthesis on Ni foam and that of the bulk MOF deposited over a GC electrode for water splitting. The authors found that for both anodic and cathodic reactions, the overpotentials at a current density of 10 mA cm^{-2} for MOF grown solvothermally over Ni foam are lower (240 mV and 134 mV) compared to the overpotentials of other MOF electrode preparation methods, indicating that MOF that are solvothermally grown on electrode exhibit better performance (Figure 1.38).[205] The significantly enhanced performance of

NiFe-MOF catalyst for water splitting has been attributable to its optimal structural characteristics for electrocatalysis, including highly exposed molecular metal active sites owing to controllable MOF thickness, improved electrical conductivity through 2D nanostructures, and a combination of hierarchical porosity. The direct growth of NiFe-MOF on nickel foam eliminates the need for insulating chemical binders, which can reduce the contact area between electrolytes and catalytic active sites and deteriorate the overall conductivity of electrode.

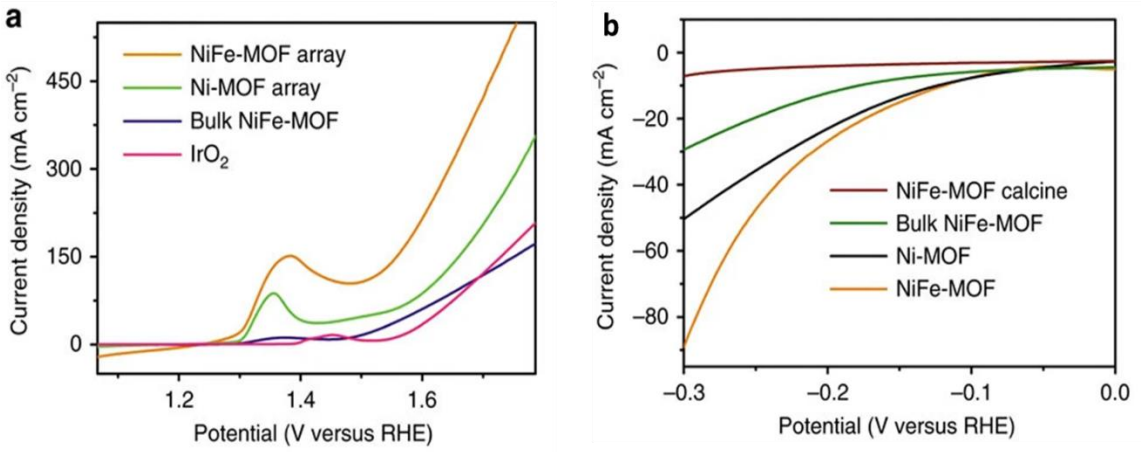


Figure 1.38. (a) LSV in 0.1 M KOH of NiFe-MOF, nickel-based metal-organic framework (Ni-MOF), bulk NiFe-MOF and IrO_2 for (a) OER (b) HER. LSV were measured at 10 mVs^{-1}. Reproduced from Duan e*t al.*[205] Copyright 2017, Nature.

1.6.3. Liquid phase epitaxy (LPE)

The liquid phase epitaxy method for the preparation of MOF electrodes was first proposed by Shekhah *et al.*[218] The first step of the method involve the pre-coating of substrate with self-assembled monolayers (SAM) of organic molecules bearing carboxylate or pyridine moieties, which later will serve as nucleation site.[219] Then the substrate is immersed sequentially into different solutions of MOF precursors in a layer-by-layer fashion, producing a highly orientated and

homogeneous MOF thin films directly over the support (Figure 1.39).[215] This strategy is also known as SURMOFs (surface-bound metal–organic frameworks) in the literature.

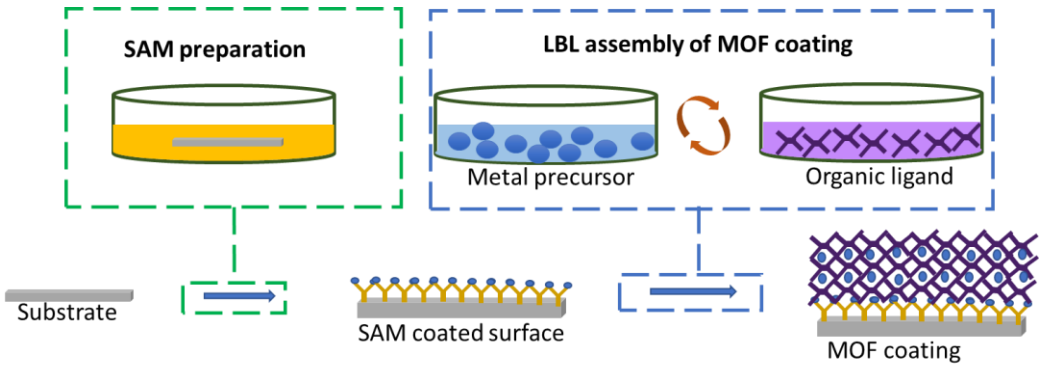


Figure 1.39. MOF-based electrode construction by liquid phase epitaxy (LPE).

Although this techniques has useful advantages like control of orientation, tuneable thickness, and strong adhesion to the substrate's surface[220, 221], the resulting SAM could also constitute an insulating layer between the electrode surface and the MOF, resulting in an increase of the electrical resistance, thus hindering the electrochemical performance of the MOF-modified electrode.[222] Since its inception in over a decade ago, there has been extensive research work on SURMOFs and related epitaxial growth methods[223, 224], however, few SURMOFs prepared by LPE have been tested as electrocatalysts.[221] This, however, is a synthesis method that could be further explored since the strong bond between the MOF and the substrate must be advantageous for long-term electrolysis. It is also possible to leverage on the highly oriented nature of SURMOF to tune its morphology and thickness in order to promote mass and charge transport through the MOF which could possibly enhance its catalytic performance.

1.6.4. Electrochemical synthesis

Two approaches have been identified for preparing MOF thin films on substrates for electrochemical application: direct and indirect electrosynthesis. With the direct electrosynthesis, the process can be anodic or cathodic. On the other hand, electrophoretic deposition is one of the popular indirect electrosynthesis method used in depositing MOF thin film on conductive substrate. The characteristics of these methods are summarized in Table 1.2. The first MOF synthesised by anodic dissolution was HKUST-1. In this method, a potential of 12–19 V was applied for 150 min to a Cu anode which oxidized to Cu^{2+} ions into a BTC linker containing solution. The chemical reaction between the Cu ions and the BTC linker resulted in the formation of HKUST-1 layer on the electrode surface.[225] Since its first deployment on HKUST-1 synthesis, many other MOFs have been produced using electrochemical synthesis.[226-230] Dinca *et al*. in 2011 reported the first MOF synthesised by cathodic deposition producing $Zn_4O(BDC)_3$ (MOF-5).[231] The synthesis was carried out by immersing FTO electrode in MOF-5 precursors and $(NBu_4)PF_6$ as conducting electrolyte (Figure 1.40). As constant cathodic potential of −1.6 V was applied for 15 min at a current density of −6.6 mA cm^{-2}, the probase (P) become reduced to an base equivalent (B) which increase the local pH near the electrode surface.[232] This change in pH induce deprotonation of ligand (H_2BDC), which further coordinate with metal ions and eventually trigger precipitation of MOF-5 crystals.

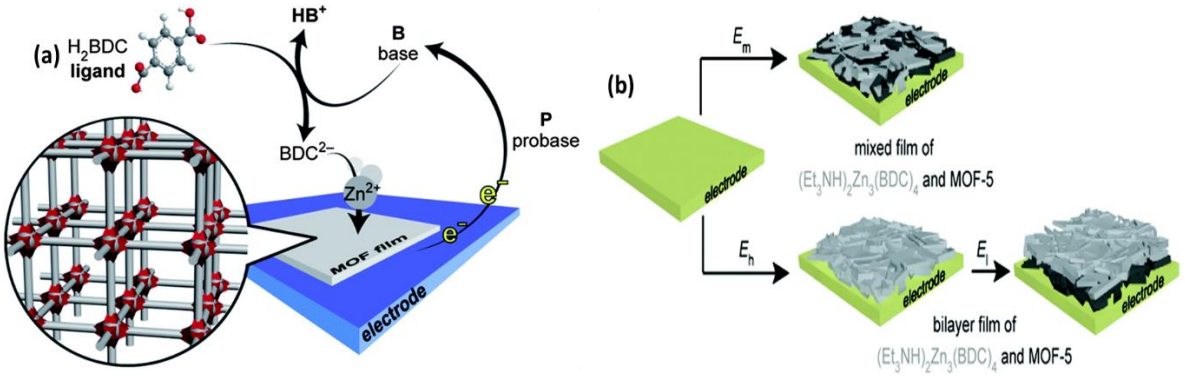


Figure 1.40. (a) General scheme for the cathodically induced electrochemical deposition of MOFs, involving the reduction of probase (P), the generation of base equivalents (B), the deprotonation of ligands (H_2BDC), and MOF crystallization from BDC^{2-} and metal ions (Zn^{2+}). (b) Schematic illustration of the formation of a biphasic mixed film**.** Reproduced from Li and Dinca.[232] Copyright 2013, RSC.

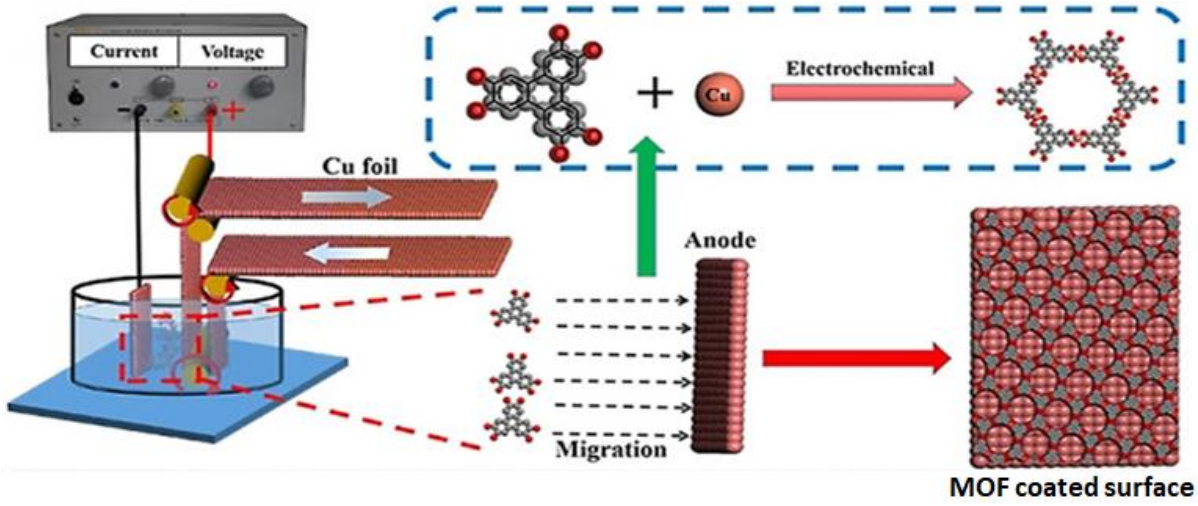


Figure 1.41. MOF-based electrode construction by electrophoretic deposition. Reproduced from Dutt *et al.*[233] Copyright 2023, MPDI.

Table 1.2. Summary of electrochemical synthesis methods

Direct Electrosynthesis		Indirect Electrosynthesis
Anodic electrosynthesis	**Cathodic electrosynthesis**	**Electrophoretic deposition**
• Metal ions electrogenerated by oxidation. • Organic ligand is present in the electrolyte. • Thin films are formed on the surface of the electrode.	• Anode and cathode electrodes are immersed into the electrolyte contain MOF precursors. • MOFs are formed directly on the cathode electrode surface by an electrochemical reaction.[225] • The electrodes merely act as source of electron and surface for nucleation and MOF growth	• Two similar electrodes acting as the anode and the cathode are immersed in a cell containing MOF suspension and supporting electrolyte. • After applying potential for some time, the MOF diffuse into the electrolyte and become deposited onto the oppositely biased electrode surface depending on the partial charges on the MOF (Figure 1.41).[234]
• MOF properties are independent of the metal precursor since no metal salts are used. [235] • Different metal oxidation states can be generated at different potentials which lead to a better control over the MOF properties.[225] • MOFs are generated at high potential (12–19 V) and longer time.	• MOFs are generated at lower potential (1.5–10 V) and within few minutes at room temperature. • Two different electrodes act as anode and cathode	• Higher applied potential and longer time (typically 50–100 V during 1–3 h) are required to produce MOF films. • Longer deposition time is advantageous as it allows control of MOF electrode properties. e.g MOF films thickness and particle-particle connectivity at FTO surfaces .[234]

It has been proposed that electrochemical synthesis has the potential to produce more CO_2RR efficient MOF-modified electrode. For example, Kang *et al.*[236] synthesised MFM-300 on indium foil electrodes by immersing it in a solution containing the organic linker and supporting electrolyte and the MOF-modified electrode system was found to be catalytically active for the CO_2RR, exhibiting a current density of 46.1 mA cm^{-2} at applied potential of -2.15V vs Ag/Ag^+, demonstrating an incredible faradaic efficiency of 99.1% for the formation of formic acid. Similarly, Hod *et al.* [222] deployed electrophoretic deposition method to obtain Fe-porphyrin MOF thin film on FTO electrode which show unprecedented catalytic activities towards CO_2RR, generating mixture of CO and H_2 at 100% faradaic efficiency. However, despite these promising results, not many MOF catalysts for the CO_2RR prepared by electrochemical synthesis have been reported, and this is a promising path that seems to remain largely unexplored.

1.7. Recent progress in utilizing MOFs for electrocatalyst for CO_2 reduction

1.7.1. Pristine MOFs as electrocatalysts for CO_2 reduction

To our knowledge, Hinogami *et al.*[237] pioneered the use of pristine MOFs in catalysing CO_2 reduction. The authors reported the used of Cu rubeanate framework containing coordinatively unsaturated metal sites as catalyst for the CO_2RR to formic acid at 98% selectivity and 30% faradaic efficiency (Figure 1.42). Kumar *et al*.[208] reported the electrochemical conversion of CO_2 to oxalic acid ($H_2C_2O_4$) at 90% selectivity, 51% faradaic efficiency on $Cu_3(BTC)_2$ (1,3,5-benzenetricarboxylic acid [BTC]) thin film catalyst deposited on glassy carbon electrode (Figure 1.43). In Figure 1.43a, cyclic voltammograms shows distinct reversible oxidation and reduction of Cu (II) to Cu(I) at 0.14 and 0.02 V *vs* SCE, respectively. A reduction peak at 0.5 V *vs* SCE and a sharp oxidation peak at 0.102 V *vs* SCE

indicate the presence of the Cu (0) to Cu(I) redox couple. $Cu_3(BTC)_2$ exhibited a cyclic voltametric response indicative of copper being in the Cu^{2+} ionic state, whereas Cu electrodes in 0.1 M KCl solution did not exhibit such a peak behaviour (Figure 1.43a inset). Figure 1.43b shows the redox activities of GCE and $Cu_3(BTC)_2$ coated GCE in electrolyte without CO_2 bubbling (1 and 3) and in CO_2-saturated 0.01 M TBATFB/DMF (2 and 4), indicating that direct reduction potential of CO_2 starts at potential more positive in $Cu_3(BTC)_2$ coated GC electrode (– 1.12 V *vs* Ag/Ag^+) than bare GC electrode (– 1.75 V *vs* Ag/Ag^+), and also showing that cathodic evolution current density is increased from 2.27 $mAcm^{-2}$ to 19.22 $mAcm^{-2}$. These two pioneering studies have proven the importance of nature and density of active site (metal center) and the electronic environment (ligand) in deciding the product selectivity and efficiency.

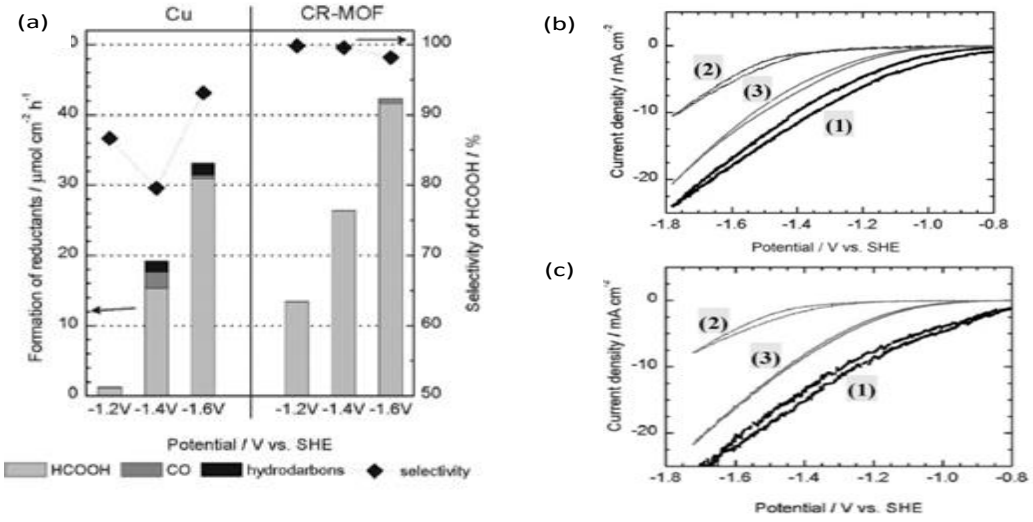


Figure 1.42. (a) Product distributions of the CO_2RR on CR-MOF electrodes an its comparison to the product distribution of the CO_2RR on Cu electrodes(b) CV curve of CR-MOF (1), bare CP (2), and Cu metal electrode (3) in CO_2-saturated and (c) in N_2-saturated 0.5 M $KHCO_3$ electrolyte. Reproduced from Hinogami *et al.*[237] Copyright 2012, EC.

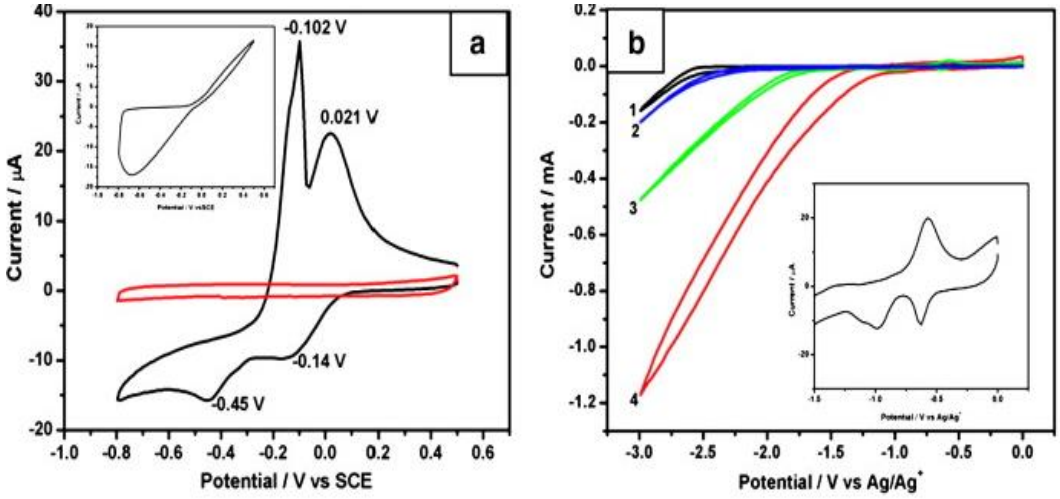


Figure 1.43. (a) CV readings of $Cu_3(BTC)$ + GCE (b) CV scan showing redox activities of 1) GCE, 2) GCE in presence of CO_2, 3) $Cu_3(BTC)_2$ + GCE and 4) $Cu_3(BTC)_2$ + GCE in CO_2-saturated 0.01 M TBATFB/DMF. Reproduced from Kumar *et al.*[208] Copyright 2012, Electrochemistry communication.

In-situ growth of MOFs into a thin layer has been recently explored to control MOF thickness which can enhance mass and charge transfer, thereby promoting higher catalytic activity towards CO_2 reduction. Kornienko *et al.*[238] demonstrated this idea by synthesizing a thin-film of cobalt–porphyrin MOF ($Al_2(OH)_2$TCPP-Co) via atomic layer deposition (ALD) on a transparent conducting fluorine-doped tin oxide (FTO) support. An analysis of this MOF's voltammogram trace showed that it displayed an enhanced current density under CO_2-saturated solutions relative to argon-saturated solutions and an irreversible catalyst peak, producing CO and H_2, with selectivity for CO reaching up to 76% at −0.7 V *vs* RHE (Figure 1.44a and c). The stability of the MOF catalyst was tested over an extended period of 7 hr at −0.7 V *vs* RHE in CO_2-saturated aqueous bicarbonate buffer, reaching a stable current density after several minutes, generating 16 mL of CO with estimated turnover number of 1400 (Figure 1.44d). According to the author, the thin-layer configuration of $Al_2(OH)_2$TCPP-Co MOF

was observed to enhance the reduction of CO_2 to CO. In another findings by Wu *et al*. [209], layering of copper porphyrin MOF (Cu_2(CuTCPP) into nanosheet was reported to enhance the catalytic conversion of CO_2 into formate (FE=68.4% at the −1.55 V) and acetate (Figure 1.45). Furthermore, spectroscopic studies showed that Cu_2(CuTCPP) was converted into copper clusters (CuO, Cu_2O and Cu_4O_3) which in turn catalysed CO_2 to formate and acetate.

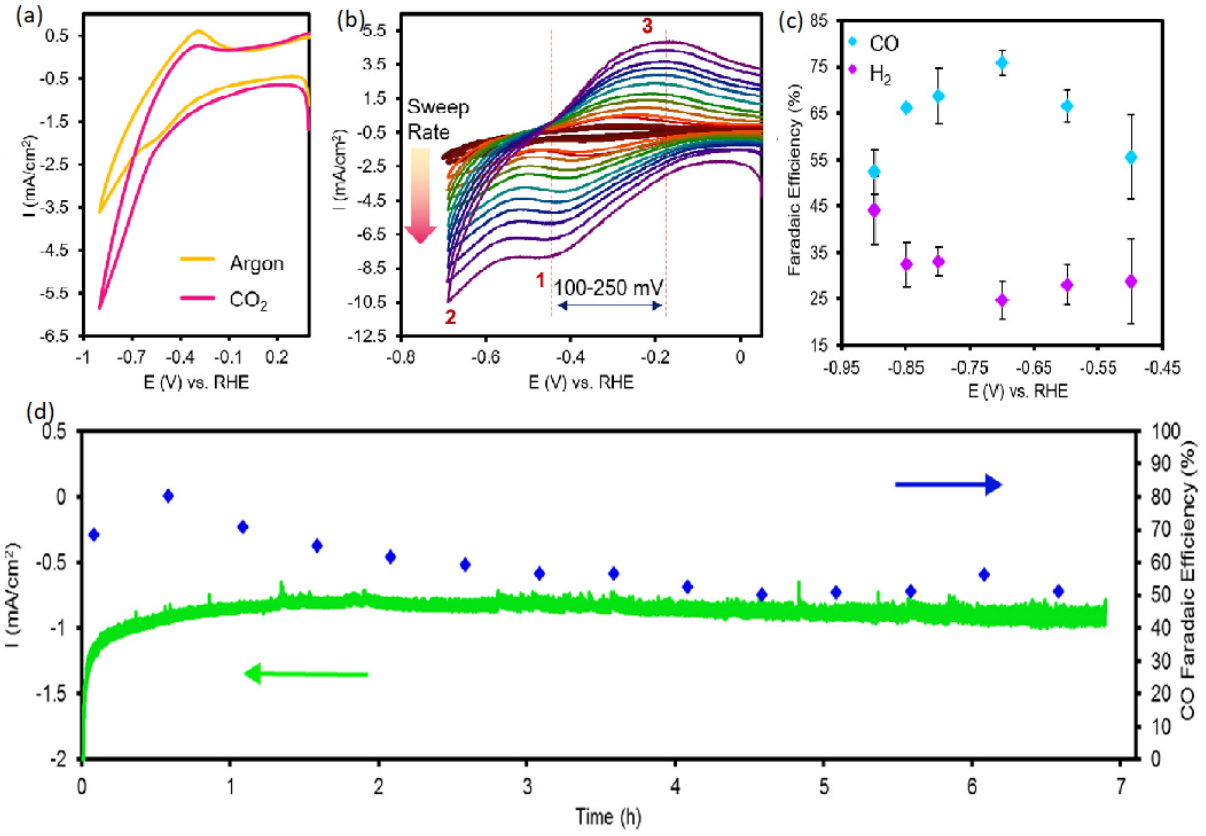


Figure 1.44. (a) CV scan of the MOF catalyst showing a current increase in a CO_2 environment relative to an argon-saturated environment. (b) Varying scan rate with corresponding redox potentials (c) Plot of the faradaic efficiency at the potential range of −0.5–0.9 V *vs*. RHE; (d) MOF stability test with corresponding FE measurement. Reproduced from Kornienko *et al.*[238]. Copyright 2015, ACS.

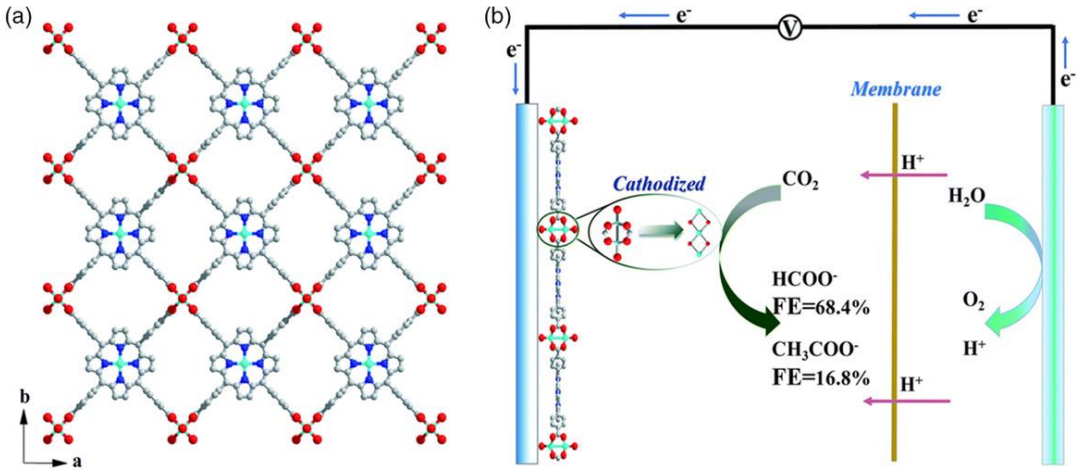


Figure 1.45. a) Crystal structure of Cu_2(CuTCPP) MOF nanosheets; b) schematic of electrochemical system showing electrocatalytic reduction of CO_2 on Cu_2(CuTCPP) nanosheets. Reproduced from Wu *et al.* [209]. Copyright 2019, RSC.

The choice of electrolyte has also proven to enhance performance and product selectivity of catalytic MOFs toward CO_2RR. For instant, Kang *et al.*[239] observed that using ionic liquids (ILs) as the electrolyte was able to influence the selective conversion of CO_2 to CH_4 using Zn-MOF catalyst. Findings shows that imidazolium based ILs can interact with CO_2 by physical absortption[240], thereby serving as both robust electrolytes and CO_2 activation promoters.[241] The cyclic voltammetry profile shows that the CO_2 reduction activities of Zn-MOF in CO_2-saturated saturated IL 1-butyl-3-methylimidazolium tetrafluoroborate (BmimBF$_4$) gives a current density of 3 mAcm^{-2} at reduction peak of about −2.2 V *vs.* Ag/Ag$^+$ while current density of the N_2-saturated system was negligible (Figure 1.46a). After 2h of electrolysis, CH_4 was the dominant product (FE= 80% at −2.2 V *vs.* Ag/Ag$^+$), showing no decrease in current density with time, suggesting that the Zn-MOF electrode and the IL were stable (Figure 1.46b and c).

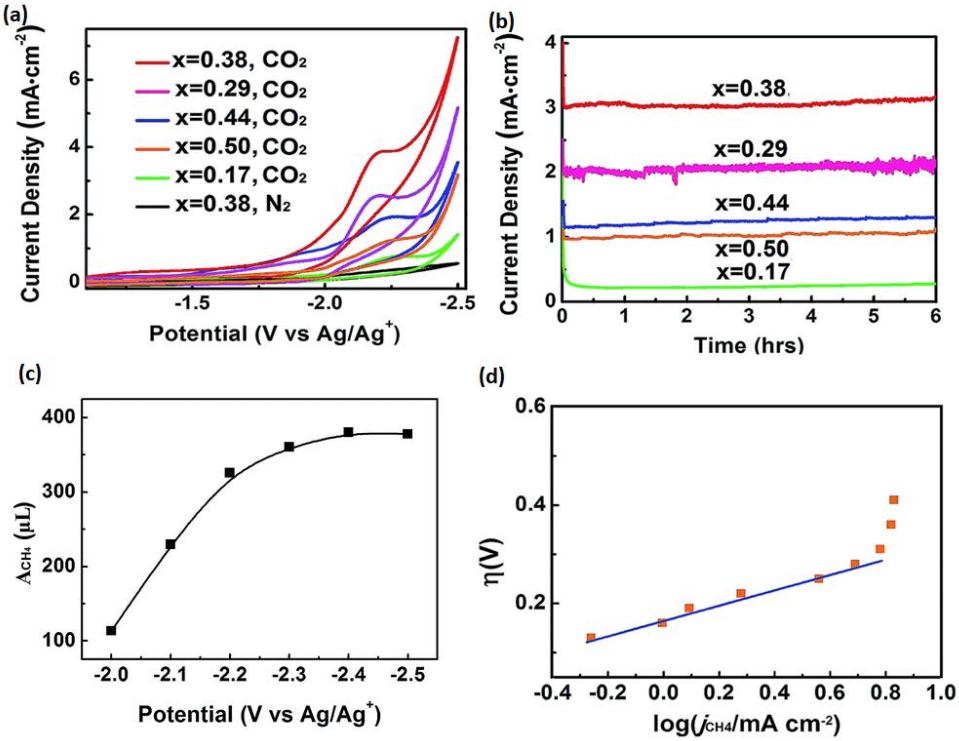


Figure 1.46. (a) CV scans in CO_2-saturated and (b) Stability test of different Zn-MOF/CP cathodes (c) Amount of CH_4 (A_{CH4}, volume at standard temperature and pressure) generated in 2 h under different potentials. (d) Tafel plot for CH_4 of the Zn-MOF/CP cathode using Zn-MOF synthesized at x = 0.38. Reproduced from Kang *et al.*[239] Copyright 2017, Wiley.

Downsizing the dimensionality of MOFs into 2D nanosheets destined for catalytic application can; increase their surface area thereby exposing more metal active sites and improve electrical conductivity by decreasing the electron transfer distance from the ultrathin nanosheets to the current collector of the electrodes.[242] The use of 2D MOF as electrocatalyst for CO_2RR was demonstrated by Yang *et al.*[243] where they attributed the significant catalytic activity and product affinity of their Cu-MOF nanosheets to the cathodized restructuring of the framework. Similarly, Zhang *et al.*[244] showed that using 2D porphyrin-based MOF (TCPP(Co)/Zr-BTB) to catalyse CO_2RR result in the production of CO with satisfactory results.

Table 1.3 Summary of MOF-based materials as Electrocatalytic for CO_2 reduction

Electrocatalyst	Synthetic method	Electrode potential	FE (%)	Peak j_{total} (mA cm^{-2})	Current normalization	Main Product	Electrolyte	Reference
Pristine MOFs as electrocatalysts								
CR-MOF	Solution self-assembly	-0.78	98	~7.1	GSA	HCOOH	0.5 M $KHCO_3$	237
HKUST-1	Room temperature synthesis	-2.5 *vs* Ag/Ag^+	51	19	N/A	oxalic acid	0.01 M TBATFB in DMF	208
$Al_2(OH)_2TCPP$-Co	Microwave	−0.7 V *vs*. RHE	76	~1	N/A	CO	0.5 M $KHCO_3$	238
Fe_MOF-525	Electrophoretic deposition	-1.3 *vs* NHE	50	4	GSA	CO	1 M $TBATF_6$ in DMF	222
Cu_2(CuTCPP)	Vigorous stirring at temperature of 85 °C	−1.55 V *vs* Ag/Ag^+	68.4	1.0	GSA	Acetate	CH_3CN with 1 M H_2O and 0.5 M $EMIMBF_4$	209
Cu_2(CuTCPP)	Vigorous stirring at temperature of 85 °C	−1.40 V to −1.65 V	38.8% to 85.2%	3.5	GSA	Formate	CH_3CN with 1 M H_2O and 0.5 M $EMIMBF_4$	209
HKUST-1	Electrophoretic deposition	-2.2 *vs* Ag/Ag^+	80	3	ECSA	CH_4	$BmimBF_4$	239
HKUST-1	Solvent-free synthesis by oven heating	-0.9 *vs* Ag/Ag^+	15.9	10	GSA	CH_3OH and C_2H_5OH	0.5 m $KHCO_3$	245
ZIF–8	Room temperature synthesis under vigorous stirring	-1.14 *vs*. SCE	65	~3	N/A	CO	0.5 M NaCl	246
MOF composites as electrocatalysts								
Ligand doped ZIF-8	Room temperature synthesis	-1.2 V *vs.* RHE	90	10.1	N/A	CO	0.1 M $KHCO_3$	247
Cu^{II}/ade-MOFs	Room temperature synthesis	−1.4 V *vs.* RHE	45	8.5	ECSA	C_2H_4	0.1 M $KHCO_3$	*243*
Cu^{II}/ade-MOFs	Room temperature synthesis	−1.4 V *vs.* RHE	50	15	ECSA	CH_4	0.1 M $KHCO_3$	*243*
2D *c*-MOF	Solvothermal synthesis	−0.7 V vs. RHE	88	8	N/A	CO	0.1 M $KHCO_3$	*21*
Re-SURMOF/FTO	Liquid-phase epitaxy	−1.6 V *vs*. NHE	93 ± 5	>2	N/A	CO	0.1 M TBAH in CH_3CN+5% CF_3CH_2OH	221

M-PMOF	Hydrothermal	−0.8 V *vs*. RHE	98.7	38.9	GSA	CO	0.5 M $KHCO_3$	[248]
FeTCPP- UiO-66	Thermal treatment	0.45	100	1.3	ECSA	CO	0.1 M $KHCO_3$	[249]
Cu_2O@Cu-MOF	Hydrothermal	-1.71	63.2	-14	ECSA	CH_4	0.1 M $KHCO_3$	[250]
Cu-SIM NU-1000	Heat treatment	-0.82	28	-1.2	GSA	$HCOO^-$	0.1 M $NaClO_4$	[251]
Ag_2O/layered ZIF Composite	Refluxed at high temperature	−1.2 V *vs*. RHE	80.5	26	ECSA	CO	0.25 M K_2SO_4	[252]
TCPP(Co)/Zr-BTB	Thermal treatment	-0.769 *vs*. RHE	85.1	6	GSA	CO	0.5 M $KHCO_3$	[244]
PCN-222(Fe)	Thermal treatment	1.2	91	-0.6	GSA	CO	0.5 M $KHCO_3$	[203]
HKUST-1 mediate Cu	Thermal treatment	−1.07 V *vs*. RHE	45	262	GSA	C_2H_4	1 M KOH	[253]
MOF-derived materials as electrocatalysts								
OD Cu/C-1000(Cu-based HKUST-1)	Carbonization	−0.1 V *vs*. RHE	45.2-71.2	~8.9	GSA	CH_3OH and C_2H_5OH	0.1 M $KHCO_3$	[254]
ZIF/MWCNT	Pyrolysis	–0.86 V *vs*. RHE	100	7.7	ECSA	CO	0.1 M $NaHCO_3$	[255]
ZIF-8 to Ni SAs/N-C	Pyrolysis	−1.0 V *vs*. RHE	71.9	10.48	GSA	CO	0.5 M $KHCO_3$	[256]
Co/Zn ZIFs derived Co-N_2	Pyrolysis	−0.8 V *vs*. RHE	94.7	18.1	N/A	CO	0.5 M $KHCO_3$	[257]
C-AFC©ZIF-8	Pyrolysis	−0.43 V *vs*. RHE	93	2.8	N/A	CO	0.1 M $KHCO_3$	[258]
Ni SAs/NCNTs	Pyrolysis	-1.0 V *vs*. RHE	95	57.1	GSA	CO	0.5 M $KHCO_3$	[259]
ZIF-8 derived NC	Pyrolysis	−0.5 V *vs* RHE	95.4	1	N/A	CO	0.5 M $KHCO_3$	[260]
ZIF-8 derived NC	Pyrolysis	-0.93 *vs.* RHE	78	1.1	N/A	CO	0.1 M $KHCO_3$	[261]
ZIF-8 derived Fe-N-C	Pyrolysis	−0.6 V *vs.* RHE	91	17.8	N/A	CO	0.5 M $KHCO_3$	[262]
ZIF-8 derived Fe-N	Pyrolysis	-0.4 *vs*. RHE	90	6.8	GSA	CO	0.5 M $NaHCO_3$	[263]

1.7.2. MOF composites as electrocatalysts for CO_2 reduction

Another strategy to obtained catalytic active MOFs is by incorporating catalytic/electrically conducting molecules which can be achieved either via *in-situ* synthesis or post synthetic modification.[264] Since *in-situ* synthesis strategy is very difficult to achieve due to kinetic challenges and steric hindrance, post synthetic modification has been more explored to incorporate molecules such as metal ions, metal nanoparticles or organic linker-based functional groups into the framework.[143] Findings reveal that doping of MOF ligand could improve their electron-donating ability thus affecting their electrocatalytic activity towards the CO_2RR.[265] For example, Dou *et al.*[247] proposed that the ZIF-8 doped with 1,10-phenanthroline molecule enhance the charge transfer ability of ZIF-8, thereby promoting the catalytic conversion of CO_2 into CO (FE_{CO}=90.47% and j_{CO} = 10 mA cm^{-2} at the −1.1V *vs* RHE) compared to pristine ZIF-8 (FE_{CO} = 50 %) (Figure 1.47). Yang *et al.*[243] reported that when Cu–adenine MOF was doped with acetic acid, the electrocatalytic activities towards CO_2RR increased and the selectivity towards the formation of ethylene and methane improved (Figure 1.48).

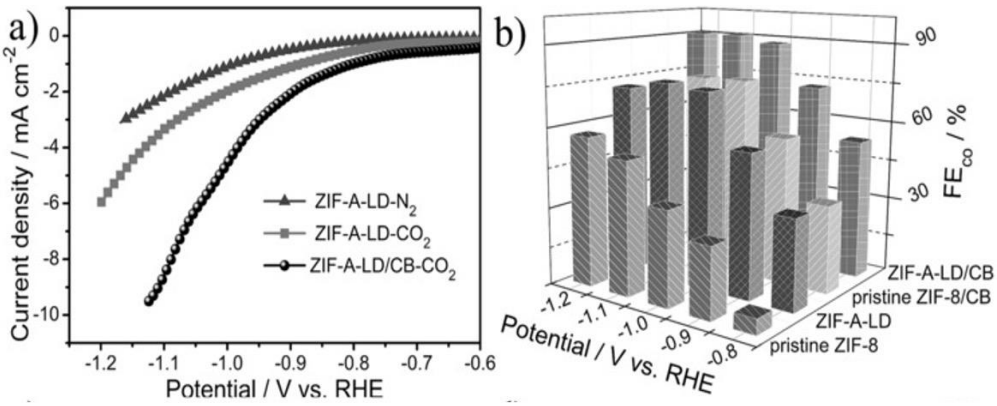


Figure 1.47. (a) LSV curves of ZIF-A-LD in N_2- and CO_2-saturated 0.1 M $KHCO_3$ solution in comparison with ZIF-A-LD/CB b) FE_{CO}. Reproduced from Dou *et al.*[247] Copyright 2019, Wiley.

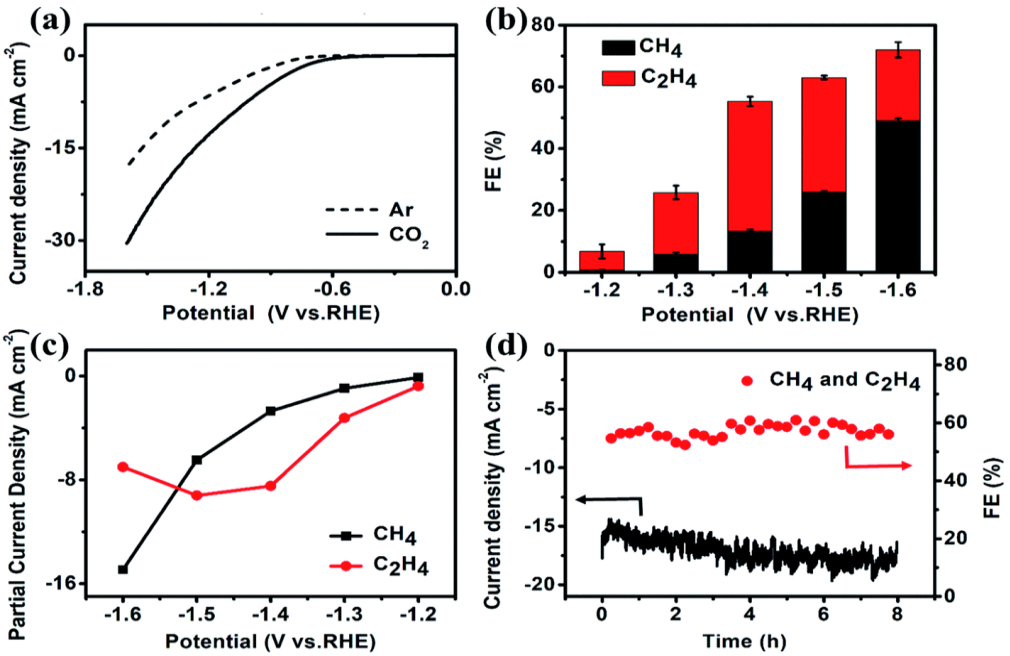


Figure 1.48. (a) LSV curves, (b) the FE of CH_4 and C_2H_4, (c) partial current density of CH_4 and C_2H_4, and (d) FE and current density test at −1.4 V *vs.* RHE for the s-Cu–ade MOF. Reproduced from Yang *et al.*[243] Copyright 2019, RSC.

Functionalizing the metal component of MOFs (active sites) with catalytic metals/NPs can create more coordinatively unsaturated sites (CUSs) within MOFs thereby boosting its catalytic activities for CO_2RR.[264] Feng *et al.*[21] demonstrated this strategy by using a MOF constructed from zinc-bis(dihydroxy) complex as node and copper-phthalocyanine as ligand to drive CO_2 reduction reaction producing syngas. *In-situ* XAS was able to confirm that ZnO_4 being the active sites was responsible for CO_2RR while CuN_4 act as support base to promote proton and electron transport. In this system, the authors claim that the CuN_4 might be responsible to draw electrons and H_2O to produce protons which become transformed into molecular H_2. On the other hand, the adsorbed CO_2 on ZnO_4 complexes is reduced to *COOH by coupling with these protons/electrons from the CuN_4 sites and electrode/electrolyte, releasing CO as the final product (Figure 1.49). The possibility of having dual metallic sites in a catalyst is

highly desirable, considering the overall effect it will have on electrocatalytic performance towards CO_2RR. However, this strategy has not been widely explored and therefore presents great opportunities for further research.

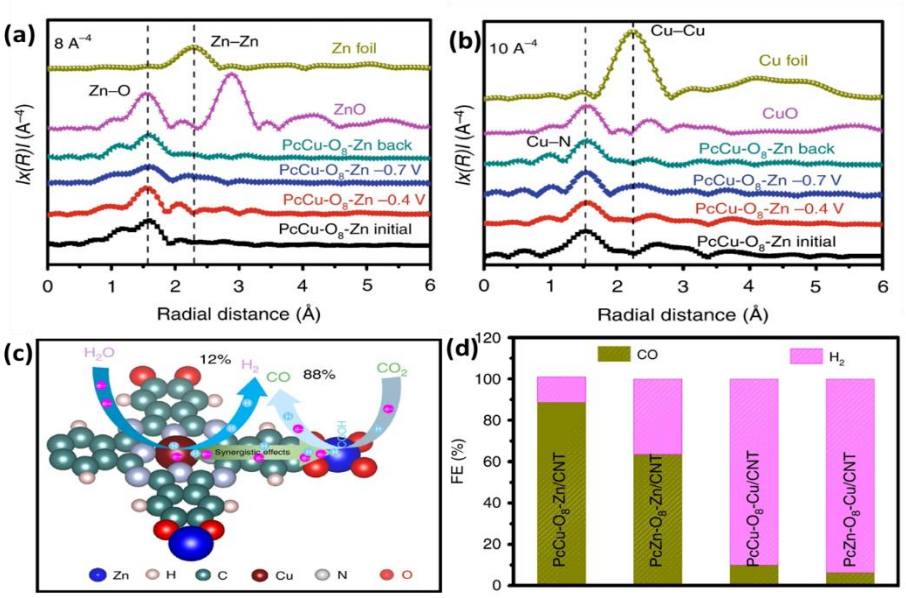


Figure 1.49. (a)Zn *K*-edge Fourier transform EXAFS spectra of Zn foil, ZnO and PcCu-O_8-Zn samples. (b) Cu *K*-edge Fourier transform EXAFS spectra of Cu foil, CuO and PcCu-O_8-Zn samples (c) Schematic HER and CO_2RR reaction process of PcCu-O_8-Zn (d) Faradaic efficiency of CO and H_2 for PcCu-O_8-Zn/CNT, PcCu-O_8-Cu/CNT, PcZn-O_8-Zn/CNT and PcZn-O_8-Cu/CNT at −0.7 V vs. RHE. Reproduced from Feng *et al.*[21] Copyright 2020, Nature.

It has been suggested that incorporating conductive materials (e.g. carbon black or graphene oxides) or catalytic species into MOF via guest–host interaction is a plausible way to improve the catalytic performance in MOFs.[264] Ye *et al.*[221] adopted this strategy to enhance the catalytic performance of HKUST-1 MOF by grafting in its framework a catalytically active carboxylate-based complex-ReL$(CO)_3$Cl (L=2,2'bipyridine-5,5'-dicarboxylic acid) (Figure 1.50). The author reported that thin film of this catalyst on FTO achieved selectivity towards CO formation of up 93 ± 5%, in comparison to just Re-linkers as catalysts. According to the authors, the higher %

FE_{CO} of this Re-SURMOF was attributed to the highly oriented structure of Re-SURMOF on the electrode surface. Wang *et al.*[248] proposed the implementation of polyoxometalates MOFs (PMOFs) catalyst prepared from the reductive polyoxometalates (POMs) and metalloporphyrin (M-TCPP). Among the metal polyoxometalates MOF tested, the activity of Co-PMOF exhibit superior performance (99% FE_{CO} at 38.9 mA cm^{-2}) over metal polyoxometalate MOFs. The performance of this Co-PMOF was attributed to synergistic cooperation between Co-porphyrin and POMs (Figure 1.51).

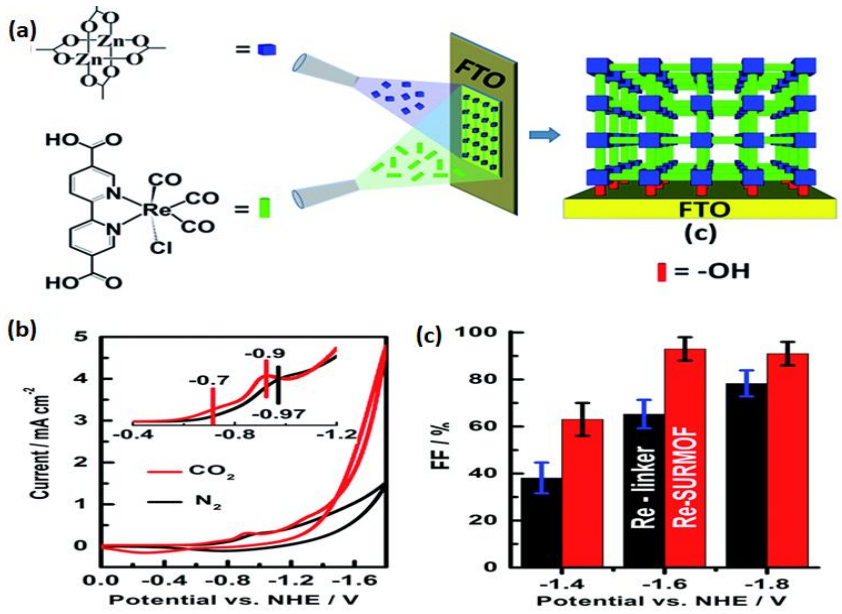


Figure 1.50. (a) Schematic description of the preparation of Re-SURMOF on fluorine-doped titanium oxide (FTO) electrode (b) CV scan and (c) FE of Re-SURMOF and Re-linker at different applied potentials. Reproduced from Ye *et al.* [221] Copyright 2016, RSC.

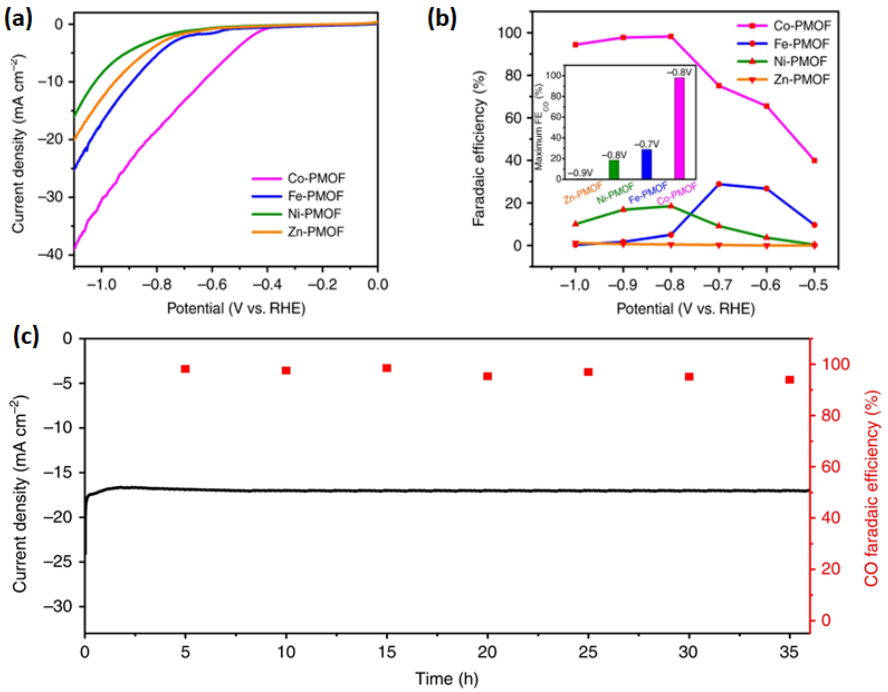


Figure 1.51. Schematic of electrocatalytic activities of M-PMOFs showing (a) LSV readings (b) $FE_{(CO)}$ (c) Durability test of Co-PMOF at −0.8 V *vs*. RHE potential in 0.5 M $KHCO_3$ electrolyte. Reproduced from Wang *et al.*[248]. Copyright 2018, Nature.

Tan *et al.*[250] reported the CO_2RR over encapsulated Cu_2O into Cu-MOF with 1,1,3,5-tricaboxylic acid (H_3BTC) as ligand. Such catalyst showed improved performance when compared to pristine Cu_2O and Cu-MOF. Relevant to this study is the good selectivity towards the formation of CH_4 (FE=63.2% at -1.71 V *vs* RHE) (Figure 1.52). Similarly, Kung *et al.*[251] reported the CO_2RR performance of a composite thin films MOF prepared by incorporating Cu-NPs into Zr-based MOF (Nu-1000). The authors reported the conversion of CO_2 to formate with % FE of 31% and current density of -1.2 mA cm^{-2} at 0.82V *vs* RHE. The Cu-NPs which are uniformly dispersed within the framework was suspected to be the active site responsible for improved catalytic performance of the MOF.

Besides all the reported alternatives and values, it is very important to notice lack of standards in the normalization process of electrochemical activities. While comparisons in catalytic activity are made across different works and materials, those comparisons, in occasion

"benchmarking" using geometrical areas, surface areas measured from BET curves or electrochemical surface areas from capacitive curves are not only unreliable but also misleading.

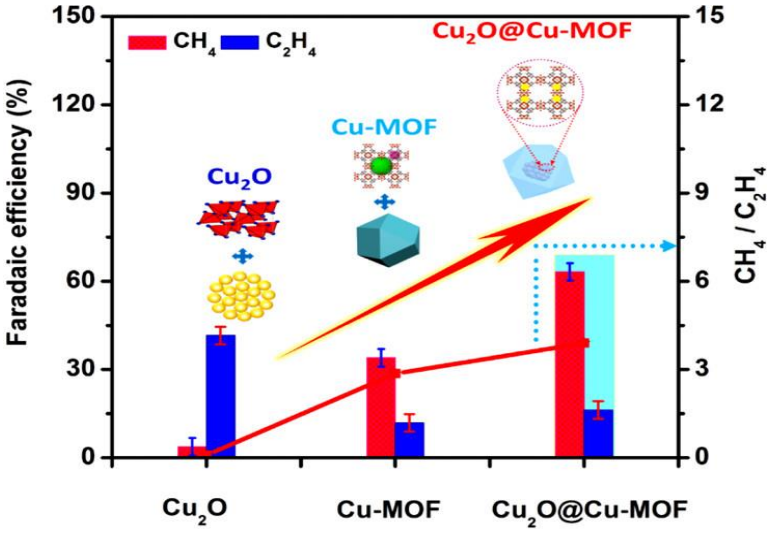


Figure 1.52. Scheme showing the performance of Cu_2O@Cu-MOF in driving the production of hydrocarbon in comparison to Cu-MOF and Cu_2O catalyst. Reproduced from Tan *et al.*[250]. Copyright 2019, ACS.

1.7.3. MOF-derived materials as electrocatalysts for CO_2 reduction

Despite the popularity of research on the use of pristine MOFs as electrocatalyst for CO_2RR, lack of electrical conductivity and structural stability are still major issues in most MOFs.[10] In fact, some of those factors have induce discussions among the electrochemical community on the use of MOF as electrocatalyst. While significant amount of reports on MOFs electrocatalysts claim to exhibit long term stability, very few to none of these works, have performed an appropriate post reaction analysis of the catalyst to justify these claims.[266] Very few works, have shown that upon exposure of the MOF or MOF-composites to electrochemical conditions, the integrity of the MOF gets compromised resulting in the "segregation" of the metal centre and the formation

of active metal cluster supported on organic matrix. With this in mind, some groups have proposed the use of MOF as sacrificial template to generate more stable carbon supported catalysts for efficient CO_2RR. The pristine MOF, upon calcination/pyrolyze at various temperatures, can generate carbon-derived metal catalysts with inherited porosity and surface area. These MOF derived material which comprises of metal cluster, NPs, metal-free catalysts or single-metal atom coordinated N-doped graphitic carbon materials, are claimed to possess improved physicochemical and electrocatalytic properties including large surface area, better electronic conductivity (in comparison with MOFs), evenly dispersed single-atom active sites, clusters or NPs.[267] One example of this strategy is given by Zhao *et al.* [254] who pyrolyzed HKUST-1 to produce oxide-derived Cu/carbon (OD Cu/C) catalyst. During the CO_2RR, the OD Cu/C showed formation of alcohols at potentials as low as -0.1 V vs RHE. The improvement in selectivity and activity of oxide-derived Cu/carbon was linked to the mutual interaction between the matrix of porous carbon and the highly dispersed copper. Nitrogen doped carbon material (N-Cs) obtained from pyrolysis of MOFs have been described as electrocatalyst materials with good electrical conductivity and sufficient mesoporous surface for effective transport.[143] The work of Guo *et al.* [255] demonstrated effectiveness of using hybrid material obtained from pyrolysis of zeolitic imidazolate frameworks (ZIFs) and multi-walled carbon nanotubes (MWCNTs) to catalyses the CO_2RR, producing CO at almost 100% efficiency, overpotential of 740 mV and a current density of 7.7 mA cm^{-2} (Figure 1.53). Upon adding Fe into the composite, higher FE_{CO} of 97% was observed at low overpotentials. The excellent CO_2RR activities of this material were linked to synergistic cooperation between the inherent active

sites in the hybrid material and the carbon nanotube (CNT) support which promote electron and mass transport.

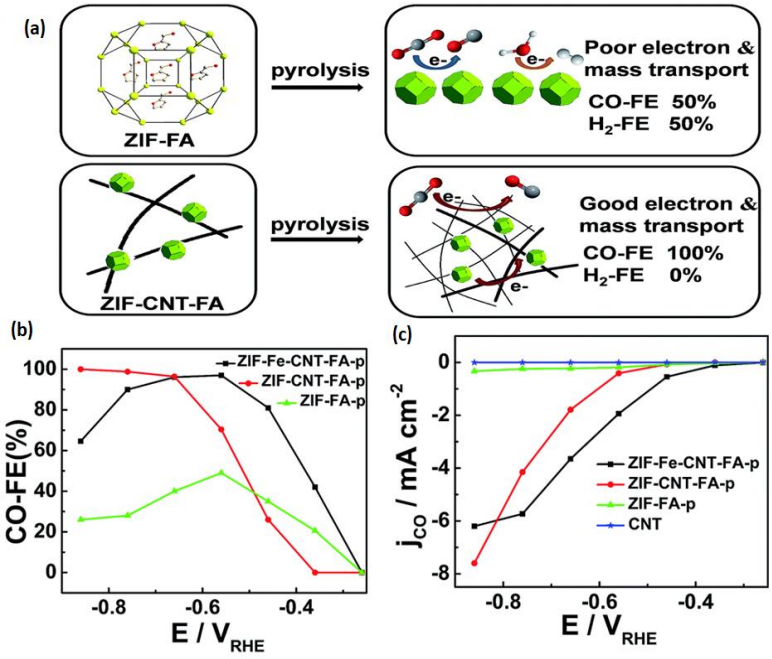


Figure 1.53. (a) schematic showing the pyrolysis of ZIFs on multi-walled carbon nanotubes (MWCNT) which aid interparticle conductivity and enhance the mass transport in CO_2RR. (b) $FE_{(CO)}$ and (d) Partial CO current for different catalysts at different applied potentials. Reproduced with permission from Guo *et al.* [255]. Copyright 2017, RSC.

The concept of single atom catalysts (SACs), first proposed by Zhang *et al.*[268] in 2011, has proven to be a good strategy to prepare MOF-derived SACs, with great electrocatalytic potential for CO_2RR. Regulating the metal sites to the atomic level endows SACs with the greatest atomic utilization, unique electronic structure, and strong metal–support interaction.[259, 269] Zhao *et al*.[256] in their work, obtained a Ni-single atoms dispersed in nitrogen-doped porous carbon (Ni-SAs/N-C) from ZIF-8 as precursor. On evaluating its catalytic potential, Ni-SAs/N-C successfully catalysed CO_2 to CO at 71.9% faradaic efficiency, current density of 10.48 mA cm^{-2}, overpotential of 0.89 V and high TOF of 5273 h^{-1}, performing better than Ni foam and Ni NPs (Figure

1.54). The clearly improved CO_2 reduction performance of Ni SAs/N-C may be attributed to the increased number of surface-active sites, lower adsorption energy of CO over single Ni sites, and improved electronic conductivity.[270] In a similar report, Wang *et al.* [257] used ZIF-8 as sacrificial template to obtained cobalt single metal catalyst anchored on nitrogen-doped carbon (Co-SAs/N_x-C) which performed excellently well catalysing CO_2 to CO, achieving FE of 94%, high current density of 18.1 mA cm^{-2} and TOF of 18200 hr^{-1}. In comparison to the work of Zhao *et al.,* it was reported that regulating the coordination number of single atom catalyst obtained from ZIF-8 can enhanced its CO_2RR activities. Some important works from Ye *et al.* [258], Zhang *et al.*[260], Lu *et al.* [259], R. Wang *et al.* [261], Yan *et al.*[262], Huan *et al.* [263] have also demonstrated the use of pyrolysis approach to obtain metal-N-C catalyst materials which have proven to show promising performance toward CO_2 reduction in terms of selectivity and activity.

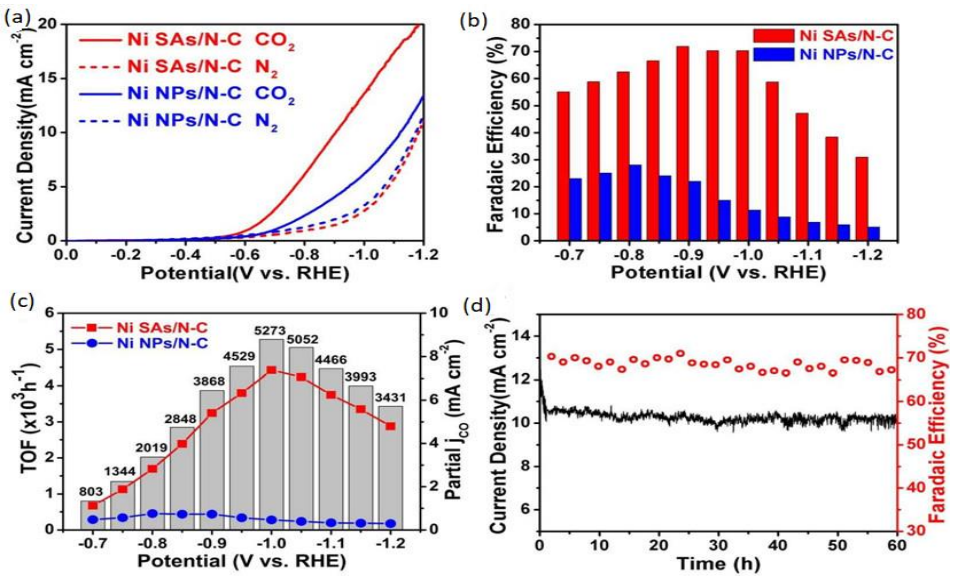


Figure 1.54. (a) LSV curves in the N_2-saturated (dotted line) or CO_2-saturated (solid line) 0.5 M $KHCO_3$ electrolyte at a scan rate of 10 mV s^{-1}. (b) FEs of CO and (c) partial CO current density plots and TOFs of Ni SAs/N-C and Ni NPs/N-C at different applied potentials. (d) Stability of Ni SAs/N-C at a potential of −1.0 V *vs* RHE for Ni SAs/N-C during 60 h. Reproduced from Zhao *et al.*[256]. Copyright 2017, ACS.

1.8. Thesis aims

The first aim of this research work is to design and synthesise novel and porous carboxyphosphonate metal organic frameworks based on different metals and different linkers. We started this research by first studied the ion exchanging properties of BIRM-1 with nickel cations to established it ion exchanging capacity for this metal and to further explore it potential application in electrocatalysis. The synthesis protocol of BIRM-1 was then modified to explore the possibility of synthesising new MOFs or MOFs that are isostructural to BIRM-1. The study was later shifted towards using a new and more rigid carboxyphosphonate linker and different metals to synthesise new carboxyphosphonate Metal-Organic Frameworks (MOFs) with the aim of developing MOFs that exhibits enduring porosity. The second aim of the study focused on the electrochemical studies of these new MOF materials with the view to establishing their potentials for CO_2 reduction. Cyclic voltametric technique was used to screen these new MOF materials, and the analysis of products of electrochemical reaction were then carried out with on-line electrochemical mass spectrometry (OLEMS) with the goal of identify the products of CO_2RR.

CHAPTER TWO

Experimental Techniques

2.1. Synthesis techniques

2.1.1. Hydrothermal synthesis

This method of synthesis can be used to crystallize MOFs under high temperature and vapour pressures. Typically, metal precursors and organic linkers are dissolved in water and placed in a closed reaction vessel for the formation and self-assembly of MOFs crystals.[271] Template agents, crystal modulators and some bases can be added to promote ligand deprotonation, slow down the crystallization process and the control coordination mode of the MOF structure. This synthesis method was employed in preparing some of the carboxylphosphonate MOFs obtained in this research work. In these experiments, MOF precursors including metal salt, linker etc., were weighed out accurately in the desired mole ratios using an analytical balance. The resulting mixtures were then dissolved in water and transferred into the autoclaves which were then sealed and placed into ovens for heating. After a defined period of time, the autoclaves were removed from the ovens and allowed to cool. Once cool the product was recovered *via* vacuum filtration and washed. Further optimization of the pH value, reaction time and temperature were carried out to achieve the desired phase purity of the material.

2.1.2. Solvothermal synthesis

This method of MOF preparation is similar to hydrothermal synthesis, except that organic reagents such as DMF, N,N-dimethylformamide (DMF), N,N-diethylformamide (DEF)

methanol etc can be used as reaction medium in place of water. In this work, some of the carboxylphosphonate MOFs were synthesised in either DMF or a mixture of DMF/water/ethanol.

2.1.3. Slow crystallization

This is the commonly used conventional method for MOF synthesis where slow evaporation of solvents of a reaction solution occurs at room temperature without any external energy supply.[272] The slow crystallization method was used to prepare one of the MOFs in this research work. In this experiment, precursor solutions of metal salt and linker were prepared and adjusted to appropriate pH and then left in open air for a period of time. The solvent slowly evaporates, leaving behind crystals suitable for structural characterisation.

2.2. Fundamentals of crystallography and diffraction[273-275]

Crystallography and diffraction are two powerful techniques in understanding the structure of solid-state materials. While crystallography is the science that examines the arrangement of atoms in crystalline solids, diffraction techniques utilize X-rays, neutrons or electrons as probing tools to study this atomic arrangement.

2.2.1. Crystalline structure

In crystallography, crystal structures are described as a unique arrangement of atoms, molecules or ions in a regular and repeated pattern and when these arrangements are extended to infinity in all directions, it is called long range order. A crystal structure comprises of a motif, which is a set of atoms arranged in a particular way, and a lattice. A lattice is a regular, periodic arrangement of points in a crystal, and these lattices can be represented by

set of translation vectors in two and three dimensions as shown in figures 2.1a and b, respectively.

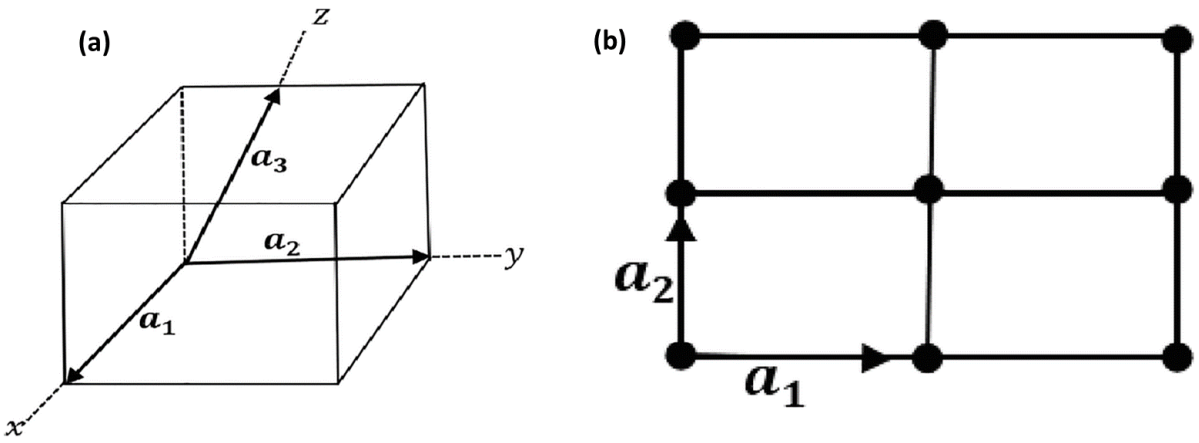


Figure 2.1. Diagram showing the three dimensional (a) and two-dimensional representations (b) of a lattice with translational vectors. Reproduced from Ameh.[275] Copyright 2019, Springer.

The smallest representative unit of a lattice that gives complete information on the atomic arrangement and reveal the symmetry of a crystal structure is called the unit cell. This implies that if the distribution of atoms in one unit cell is known, the whole crystal can be built by simply propagating this unit cell along one, two or three directions independently. In three dimensions, the shape and size of the unit cell can be described by the length of three axes (a, b, c) and the angles between the axes (Figure 2.2).

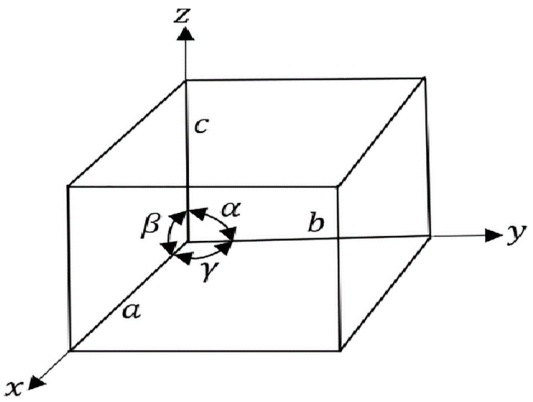


Figure 2.2. Diagram of a unit cell showing the length of the axes and the angle between each axis. Reproduced from Ameh.[275] Copyright 2019, Springer.

Based on difference in the length of unit cell dimensions and angles between them, lattices can be classified into seven crystal systems (Table 2.1). However, on the basis of four types of lattice centring, namely, primitive centring (P), body centring (I), base centring (C) and face centring (F), Bravais further classified these seven crystal systems into 14 Bravais lattices (Figure 2.3). When the eight types of symmetry elements are factored in, crystals can be classified into 32-point groups. Furthermore, if the classification is extended by including space groups (translational and point group symmetries), glide reflection axes and screw axes, there will be 230 classifications in terms of space group as illustrated in Figure 2.4. This implies that all crystals belong to one of 230 space groups.

Table 2.1 Summary of seven crystal systems and their essential symmetry features.

S/N	Crystal System	Unit cell characteristic	Symmetry
1	Cubic	$a = b = c$, $\alpha = \beta = \gamma \neq 90^0$	4 x 3-fold rotation axes
2	Tetragonal	$a = b \neq c$, $\alpha = \beta = \gamma = 90^0$	1 x 4-fold rotation axes or a 4-fold rotation inversion axes
3	Orthorhombic	$a \neq b \neq c$, $\alpha = \beta = \gamma = 90^0$	3 x 2-fold rotation axes, or 2 planes intersecting in a 2-fold axis
4	Hexagonal	$a = b \neq c$ $\alpha = \beta = 90^0$, $\gamma = 120^0$	1 x 6-fold rotation axes
5	Trigonal	$a = b = c$ $\alpha = \beta = \gamma \neq 90^0$	1 x 3-fold rotation axes
6	Monoclinic	$a \neq b \neq c$ $\alpha = \beta = 90^0 \neq \gamma$	1 x 2-fold rotation axes or one plane
7	Triclinic	$a \neq b \neq c$ $\alpha \neq \beta \neq \gamma$	No plane and no axes

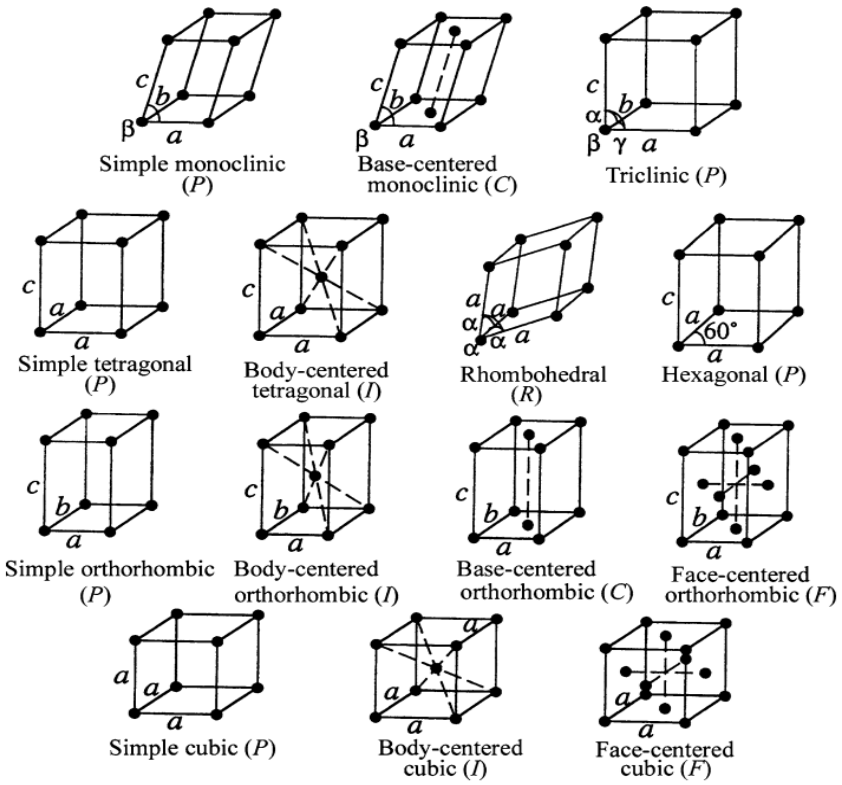


Figure 2.3. The 14 types of Bravais lattice. Reproduced from Ameh.[275] Copyright 2011, Springer.

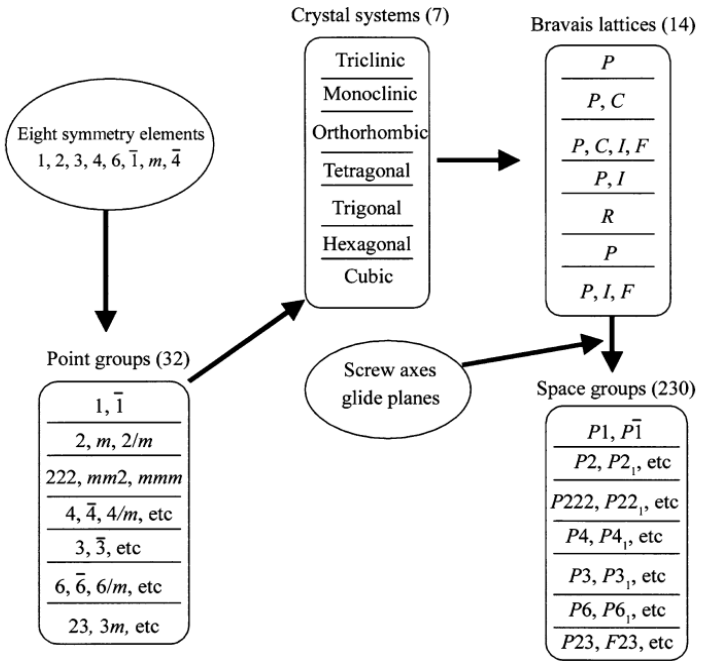


Figure 2.4. Symmetry elements in crystals and their relationships for classification. Reproduced from Ameh.[275] Copyright 2011, Springer.

2.2.2. Lattice planes and directions

Lattice planes are defined as a set of planes that intersect all lattice points. In crystallography, the lattice plane of a crystal is described by three integer indices h, k, and l which are called crystallographic or Miller indices. *These* three integers or Miller indices are enclosed in *a* curvilinear bracket as (hkl*), and* each index denotes the value of the reciprocal of a fraction of the unit cell vectors, a, b and c, respectively. Provided the atomic d-spacing along each plane is the same, crystallographic planes are equivalent to each other by symmetry. For example, cubic crystal system whose front and back faces intercept the x-axis and are parallel to y- and z-axes, yields (100) Miller indices while a cubic crystal whose left and right faces the intercept the y-axis but are parallel to both the x- and z-axes have (010) Miller indices. Similarly, the Miller indices of (001) is assigned to a cubic crystal whose top and bottom face intercept the z-axis and are parallel to x- and y-axis. The equivalent planes are called family or form of indices and represented as follows: 100 = (100), (010), (001), (110), (101), (011) etc. Some examples of lattice planes are represented in Figure 2.5. The distance between lattice planes is given as d_{hkl}, sometimes called d-spacing or simply d. For instance, the d_{hkl} for tetragonal and orthorhombic systems can be derived from equations 2.1 and 2.2.

Tetragonal: $$\frac{1}{d_{hkl}^2} = \frac{h^2+k^2}{a^2} + \frac{l^2}{c^2} \qquad 2.1$$

Orthorhombic: $$\frac{1}{d_{hkl}^2} = \frac{h^2}{a^2} + \frac{k^2}{b^2} + \frac{l^2}{c^2} \qquad 2.2$$

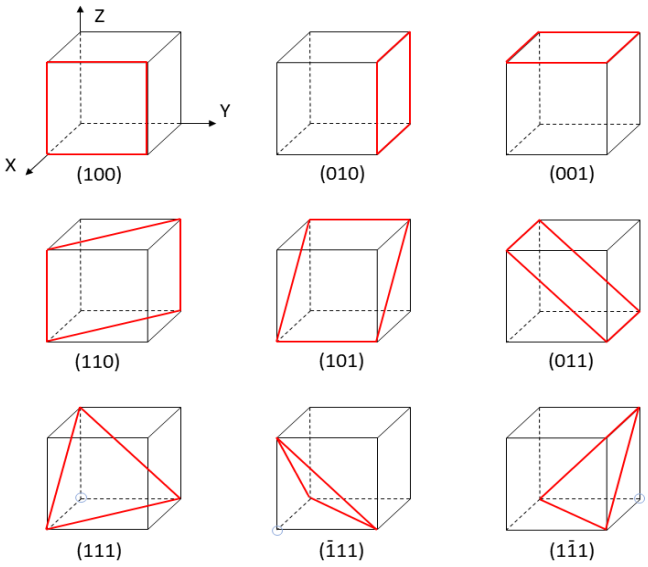


Figure 2.5. Some of the most commonly used Miller indices for lattice planes in a cubic system.

2.3. X-ray diffraction technique

X-ray production is a critical aspect of studying the diffraction of crystalline materials to understand their atomic arrangement. X-rays for crystal diffraction are generated in an X-ray tube which comprises of a copper anode and tungsten cathode. When the tungsten filament cathode is electrically heated, electrons are generated and are accelerated toward the copper anode by a high electrostatic potential (30 to 60 kV). These high energy electrons impinge the copper metal, causing the ejection of inner electrons, thereby creating vacancies in lower orbitals which are filled by electrons from outer orbitals. This electronic transition results in the emission of X-ray energy which comprises of a combination of K_α and K_β radiation depending on the type of electronic transition (Figure 2.6). Among the three X-rays produced, $K_{\alpha 1}$ radiation has highest intensity and is ideal for X-ray diffraction. Therefore, a monochromator can be used to filter off $K_{\alpha 2}$ and K_β.

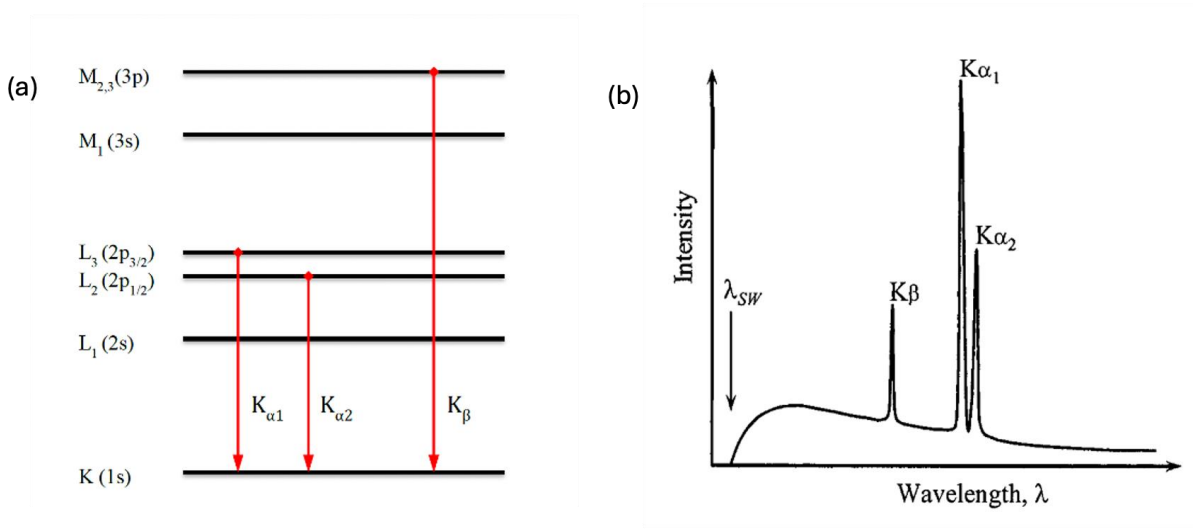


Figure 2.6. (a) Energy transition diagram for Cu atom and (b)the corresponding x-ray emission spectrum. Figure b was reproduced from Pecharsky and Zavalij.[276] Copyright 2003, Springer.

Since the plane spacings of crystals (d_{hkl}) are similar to the wavelength of X-rays, they can therefore provide an ideal diffraction grating. The exposure of the atomic planes of a crystal to beam of X-rays at an angle, causes the scattering of X-rays in all directions. These emitted signals can result in either constructive or destructive interference. However, constructive interference give rise to a beam of incident radiation reflected at a specific angle and this effect is called diffraction. The mathematical relationship between the diffraction angle and the spacing between the atom planes are given by Bragg's law and is elucidated in Figure 2.7. By applying the concept of trigonometry, Bragg equation can then be derived (Equation 2.3).

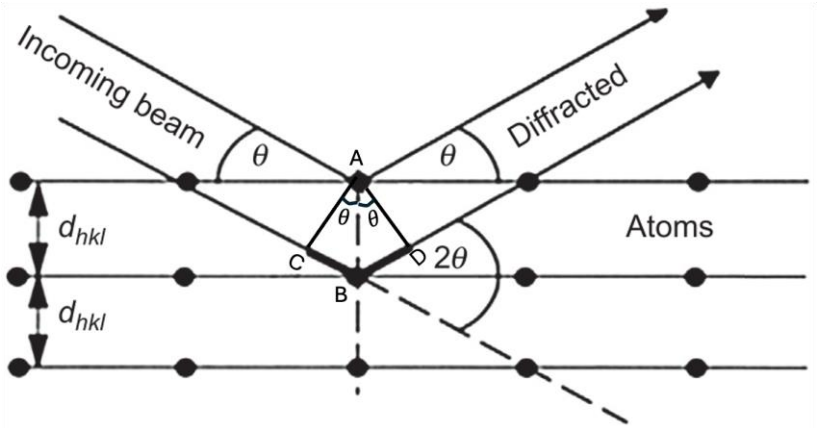


Figure 2.7. Diagram showing X-ray diffraction in accordance with Bragg's law

$$\mathrm{CD} + \mathrm{BD} = (\mathrm{d_{hkl}}\sin\theta) + (\mathrm{d_{hkl}}\sin\theta) = 2\mathrm{d_{hkl}}\sin\theta \qquad 2.3$$

d_{hkl} is the interplanar distance between the planes while θ is the incident angle.

According to the Bragg's law constructive interference occurs only if the total path difference is equal to a multiple of the wavelength (*n*λ). Therefore equation 2.3 can be further simplified as:

$$\mathrm{n}\lambda = 2\mathrm{d_{hkl}}\sin\theta \qquad 2.4$$

2.3.1. Powder X-ray diffraction

Powder X-ray diffraction (PXRD) is a rapid analytical technique used for characterisation of crystalline materials. This analytical technique is particularly suitable for routine phase identification of a polycrystalline material which contain many small crystallites. A powder sample contains many randomly oriented crystals which are packed together. When these crystallites are impinged with a beam of X-rays at different angles, all possible diffraction peaks from the powder will be detected as defined by Bragg's Law, providing information on the micro-structural features of the material. An instrument dedicated to performing such powder measurements is called a powder diffractometer. A typical powder X-ray diffractometer comprise an X-ray source, sample holder and the detector whose operational

arrangement is most often represented either in Debye-Scherrer (θ/θ) or Bragg-Brentano (θ/2θ) geometry (Figure 2.8).

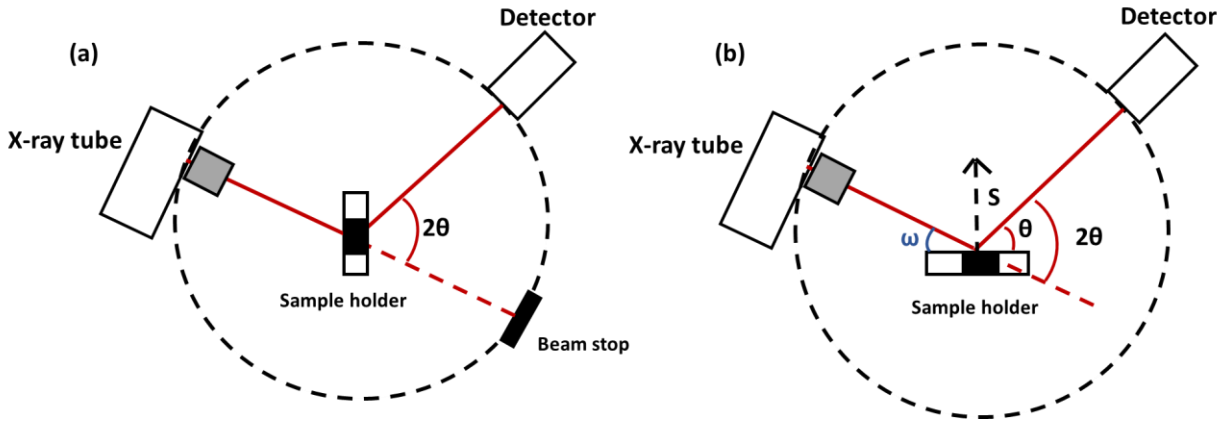


Figure 2.8. Simplified representation showing (a) a Debye-Scherrer θ/θ geometry diffractometer (b) a Bragg-Brentano θ/2θ geometry diffractometer.

In a Debye-Scherrer (θ/θ) diffractometer, the sample is held stationary, usually in the horizontal position, whilst the source and detector are both moved by θ degrees (Figure 2.8a). Meanwhile in a typical X-ray diffractometer with Bragg-Brentano geometry configuration (Figure 2.8b), the position of X-ray source is fixed while the flat-plate sample holder at the centre of the goniometer (ω-axis) and the detector (2θ-axis) moved in a circular path by θ and 2θ degrees, respectively.

During measurements, the 2θ-axis rotates two times as much as the ω-axis, and therefore it is often called a two-theta scan. The result of the measurement is plotted as measured intensity vs Bragg angle 2-theta (Figure 2.9). An important aspect of the diffraction pattern is the Bragg reflected peak, featuring peak position, peak shape and peak intensity, which elucidates the structural information in the crystalline sample. For instance, peak position gives information about the unit cell dimensions. Since unit cell dimensions can be correlated to interatomic distances, anything that changes interatomic distances will be reflected by a change in peak position. Factors such as change in lattice parameters, microstrain, stress,

crystal size, temperature, instrumental factor such as zero-point errors can cause a shift in the peak position.

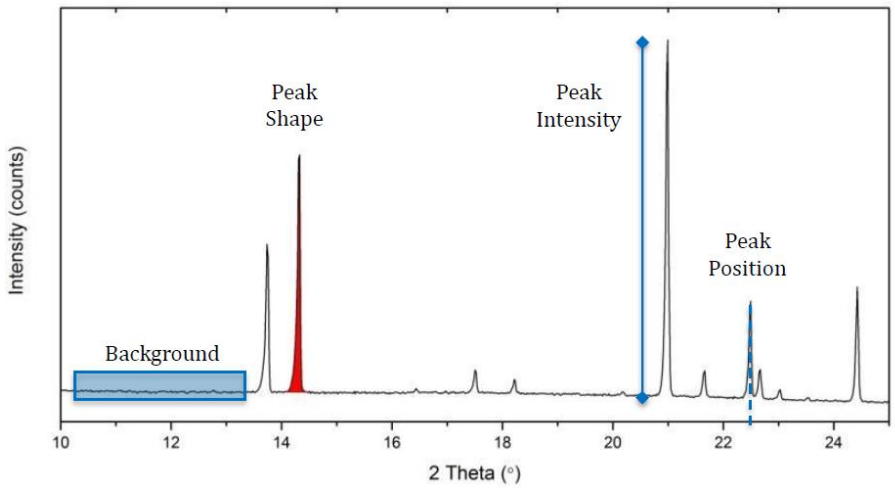


Figure 2.9. Plot showing X-ray diffraction pattern.

As for peak shape, which describe broadening in a diffraction peak, gives information about the crystallite size which is of interest in materials characterization. The relationship between crystallite size and peak broadening is described by the Scherrer equation.

$$\beta = \frac{K\lambda}{L\cos\theta} \qquad 2.5$$

where β is the Bragg peak broadening, in radians, K is the constant of proportionality, λ is the X-ray wavelength, θ is the diffraction angle of the reflection, and L is the average crystallite diameter. Other factors that contribute to the broadening of the observed peak are summarized as follows.

$$\beta_{obs} = \beta_{instr} + \beta_{sample} = \beta_{instr} + \beta_{size} + \beta_{strain} \qquad 2.6$$

The intensity of an XRD peak is related to the number of atoms in the crystal that are capable of scattering X-rays. Therefore, a higher peak intensity indicates a higher number of atoms in the crystal which could indicate higher degree of crystallinity. Factors such as the efficiency

of the detector, scattering power of the X-ray source and data collection time can affect absolute intensity of the X-ray diffraction pattern. For a monophasic crystal, the relative intensities of different Bragg peaks are mainly dependent on the type and position of the atoms located inside the unit cell while for crystals with mixed phase, the overall intensity is largely dependent on the relative concentration of each phase.

2.3.2. Powder diffraction data analysis

2.3.2.1. Indexing

When a new crystalline material is made and the powder XRD data is collected, the first step to deducing the structure is to index the powder pattern in order to calculate the unit cell parameters. However, it often difficult to find true unit cell from powder data because it only presents one-dimensional projection of the three- dimensional reciprocal lattice recorded as a function of a single independent variable, the Bragg angle. Thus, in a powder diffraction experiment, only the lengths of the reciprocal lattice vectors are measurable while their directions are unknown. Therefore, indexing of powder data is done by assigning the triplets of Miller indices to every observed Bragg peak based on the selected unit cell as described by the equation 2.7.

$$d^*_{hkl} = ha^* + kb^* + lc^* \qquad 2.7$$

Taking the reciprocal of the equation above and squaring the result gives equation 2.8 below, Bragg's law can be used to obtain d_{hkl} allowing the use of Equation 2.8 to calculate the unit cell.

$$\frac{1}{d^2_{hkl}} = \frac{h^2}{a^2} + \frac{k^2}{b^2} + \frac{l^2}{c^2} \qquad 2.8$$

Crystals with high symmetry usually have lattice cells with 90° angles and fewer Bragg peaks and can be easily indexed by applying the above equation. However, manual indexing becomes more complicated with lower symmetry crystals, therefore auto-indexing using computer algorithms can be employed. The software used for indexing of this work was GSAS-II, the indexing algorithms written into this software are based on methodology developed by Coehlo.[277]

The intensity I_{hkl} of each hkl reflection is determined by the identity and positions of the atoms inside the unit cell via the structure factor, F_{hkl}:

$$F_{hkl} = \sum_{j} t_j f_j \exp\left[2\pi i\left(hx_j + ky_j + lz_j\right)\right] \qquad 2.9$$

$$I_{hkl} \alpha \left|F_{hkl}\right|^2 \qquad 2.10$$

Here, x_j, y_j, and z_j are fractional atomic coordinates of atom j, and f_j describes the scattering factor of atom j as a function of sin θ/λ. The t_j term accounts for the fact that atoms vibrate around their average positions in real samples, which decreases I_{hkl} intensities. For a powder diffraction experiment, several factors usually appear in the $I_{hkl} \alpha \left|F_{hkl}\right|^2$ proportionality constant: an overall scale factor (K), factors describing the diffractometer geometry in the Lorentz polarization factor (LP), and the multiplicity of the Bragg reflection (m) which counts the number of symmetry equivalent reflections for each hkl.

In this work, powder X-ray diffraction (PXRD) patterns were collected with a Bruker D8 advanced X-ray diffractometer in Bragg-Brentano θ/2θ geometry (40 kV, 30 mA) with Cu Ka radiation (λ=1.5406 Å) operated in the 2θ range from 5 ° to 70 ° with a scan speed of 1 s/step and a step size of 0.05 °. Secondly the PXRD was used to confirm that a given synthesis yielded

the target phase by comparing the PXRD pattern of the synthesised material to a simulated pattern for a known single crystal structure through a process called Rietveld refinement.

2.3.2.2. Rietveld Refinement

Rietveld refinement is a "whole-pattern-fitting" strategy usually conducted to fit the calculated diffraction pattern to the observed data by adjusting each of the variables that describe the diffraction pattern. It is a least-squares minimisation process whereby the difference between the observed intensities $y_{obs,i}$ and the calculated intensities $y_{calc,i}$ are reduced as much as possible by adjusting parameters such as the lattice cell parameters, atomic positions and occupancies. These parameters are carefully refined in a logical sequence to achieve agreement between all the data points from the observed and the calculated diffraction patterns. This minimisation is given by Equation 2.11

$$s_y = \sum_{i=1}^{N} w_i\left(y_{obs,i} - y_{calc,i}\right)^2 \qquad 2.11$$

where:

S_y is the residual that needed to be minimized,

w_i is weighting factor which is equal to $1/y_{obs,i}$,

$y_{obs,i}$ is the observed intensity at the *i*th step, and

$y_{cal,i}$ is the calculated intensity at the *i*th step.

N is the number of data points.

The quality of the refinement is mostly described by several statistical measures, including the profile reliability factor (R_p) and the weighted profile factor (R_{wp}), which are expressed as percentages (equation 2.12 and 2.13). The minimum achievable value with the refinement experimental parameters in Rietveld analysis is also of interest and can be written as R_{exp}.

$$R_p = \frac{\sum_{i=1}^{N} |y_{obs,i} - y_{calc,i}|}{\sum_{i=1}^{N} y_{obs,i}} \times 100\% \qquad 2.12$$

$$R_{wp} = \sqrt{\frac{\sum_{i=1}^{N} w_i |y_{obs,i} - y_{calc,i}|^2}{\sum_{i=1}^{N} w_i |y_{obs,i}|^2}} \times 100\% \qquad 2.13$$

$$R_{exp} = \sqrt{\frac{N - P - C}{\sum_{i=1}^{N} w_i |y_{obs,i}|^2}} \times 100\% \qquad 2.14$$

w_i is the weighting factor assigned to the point i,

N is the number of the points measured from the diffraction pattern,

P is the number of the refinement parameters, and

C is the number of the constraints used in the refinement.

Combining the R_{wp} and R_{exp} factors together will get the factor for the goodness of the fit (χ^2, equation 2.15). When the model is poor, the χ^2 starts out large and decreases as the model alters to achieve better agreement with the data during the refinement process.

$$\chi^2 = \left(\frac{R_{wp}}{R_{exp}}\right)^2 \qquad 2.15$$

2.3.3. Single crystal X-ray Diffraction[276, 278-280]

Single-crystal X-ray diffraction is a non-destructive analytical technique which provides detailed information about the internal lattice of crystalline substances, including unit cell dimensions, bond-lengths, bond-angles, and details of site-ordering. Single crystal X-ray diffraction has the same working principle as powder XRD but have a different goniometer arrangement. Single-crystal diffractometers use either 3- or 4-circle goniometers. These

circles refer to the four angles (2θ, χ, ϕ, and Ω) that define the relationship between the crystal lattice, the incident ray and detector (Figure 2.10).

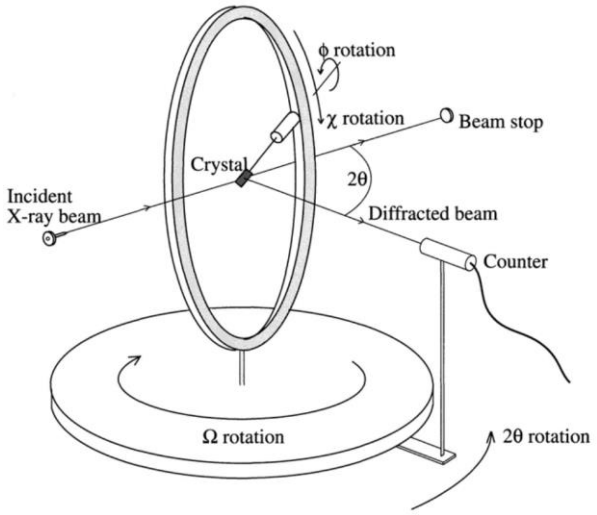


Figure 2.10. Schematic of 4-circle diffractometer; the angles between the incident ray, the detector, and the sample. Reproduced from Putnis.[281] Copyright 1992, Cambridge University Press.

The single crystal diffractometer used in this work was an Agilent Supernova. This diffractometer was set up with the kappa geometry and a CCD detector. This instrument has both a copper and a molybdenum source which can be used depending on the crystalline material. The instrument was also fitted with an Oxford Cryosystems cryostream, and data collection was performed at 100 K. In the experiment, suitable and well diffracting single crystals of MOF were carefully selected under microscope and glued to a thin glass fibre. Samples were mounted on thin glass fibres which were attached to brass pins and mounted onto the goniometer head. Adjustment of the X, Y and Z orthogonal directions allows centring of the crystal within the X-ray beam. For structures reported in this work, data were collected with single crystal diffractometer from the school of chemistry, University of Birmingham and National Crystallographic Service based at the University of Southampton.

After data collection was completed, data reduction was then performed, and all data were corrected for Lorentz and polarisation effects. In this process, the data were integrated to correct intensities for each hkl value, which were assigned to each spot in the diffraction pattern. After data reduction, the crystal structures were solved with help of Olex2 software.[273] The initial structure solution was obtained with SHELXT while structure refinement of this initial structure model was carried out with SHELXL using the least squares method. Both SHELXT and SHELXL programs are implemented within the Olex2 software. Structures were then refined anisotropically as far as data quality allowed. Hydrogen atoms were added to appropriate atoms as fixed riding models with thermal parameters linked to the parent atom. All structures reported in this work were solved either by Dr Louise Male from the School of Chemistry, University of Birmingham or the National Crystallographic Service based at the University of Southampton.

2.4. Scanning electron microscopy[278, 282]

Scanning electron microscopy (SEM) is a widely used technique for imaging the microstructure of a material to reveal information about its morphology. SEM comprises the following major component namely, electron source, electromagnetic lenses for focusing electrons, electron detectors, sample chamber and computer for image output (Figure 2.11). In SEM, the surface of the material is scanned with a focused beam of high energy electrons generated from tungsten filament, the energy of which is usually higher than 10 keV depending on the sample evaluation strategy. The surface-electron interaction causes the electrons to scatter both inelastically (secondary electrons, SE) and elastically (back scattered electrons, BSE). The electron–sample interactions are detected by an electron detector and

are converted to electric signal, giving image output with a large depth of field, high resolution and magnification.

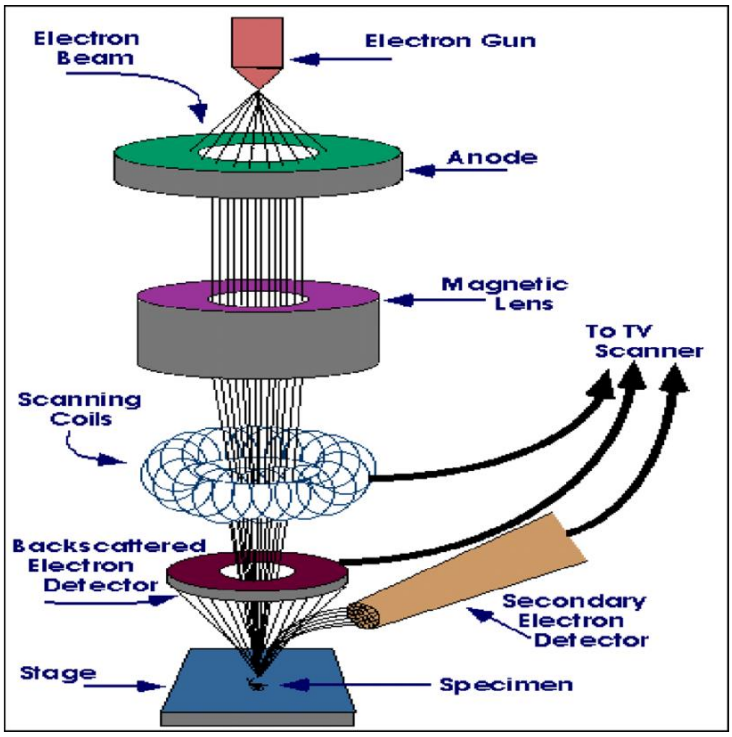


Figure 2.11. Schematic diagram showing various component of SEM. Reproduced from Singh.[283] Copyright 2014, Nirbhay Kumar Singh.

In some cases, SEM can be coupled with energy-dispersive X-ray spectroscopy (EDX), making it possible to carry out elemental analysis of the sample. To carry out elemental analysis with SEM-EDX, the incident electron beam generated from SEM drives deeper into the sample, causing ejection of core electrons, thereby creating electron holes. Electrons from the outer orbitals or higher energy levels then relax to fill these holes, releasing X-ray radiation which is detected by the spectrometer (Figure 2.12). The energy of the ejected photon can then be related to the characteristic element present in the sample, thereby enabling the elemental composition to be analysed.

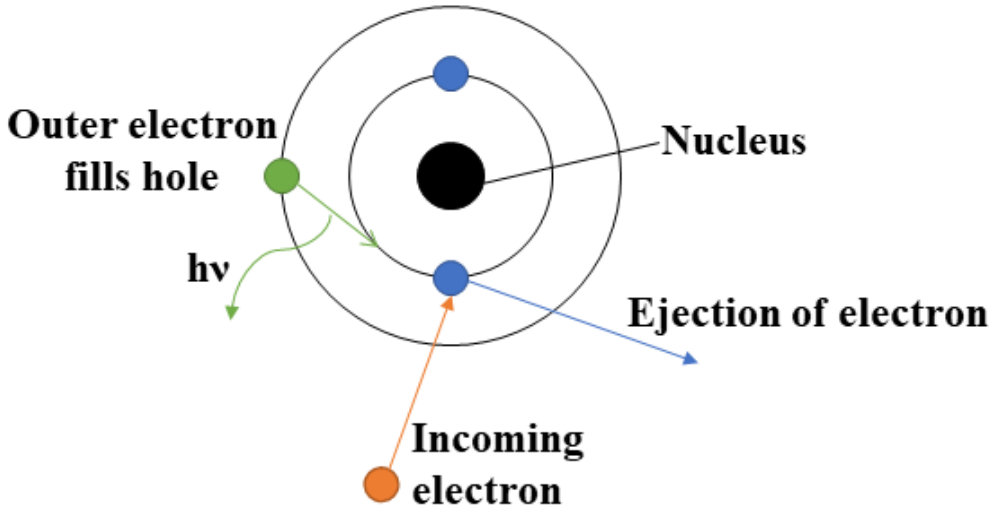


Figure 2.12 Diagram showing the working principle of SEM-EDX.

For this work, a benchtop Hitachi TM4000 Plus SEM equipped with an AztecOne EDX detector was used to study the morphology and to carry out elemental composition analysis of our MOF materials. Each sample was applied to an adhesive carbon film on the sample holder and coated with carbon before examination.

2.5. Transmission electron microscopy[107]

Transmission Electron Microscopy (TEM) utilizes a high electron beam, typically with an accelerating voltage of 100–300 kV, for imaging purposes. Unlike Scanning Electron Microscopy (SEM), TEM detects electrons that are transmitted through the sample. The resulting image is either displayed on a fluorescent screen or recorded using a CCD detector or photographic film. The images projected onto the screen in TEM provide only two-dimensional information, resulting in a generally small depth of field. One of the key advantages of TEM over SEM is its superior resolution (magnification). TEM can achieve sub-nanometer level resolution, allowing for the collection of atomic or molecular level images, in contrast to the morphological observations possible with SEM. However, Metal-Organic

Framework (MOF) materials are typically highly sensitive to the TEM electron beam. To minimize electron beam damage, the beam density should be reduced by using low-dose imaging conditions, such as a cumulative exposed dose of 200 electrons/nm².

Transmission electron microscopy analyses for this work were carried out in a FEI Titan X-FEG operated at 300 kV. The microscope was equipped with a spherical aberration corrector for the electron probe which was previously aligned using a gold standard sample assuring a spatial resolution of 0.8 Å. The column was also fitted with an Oxford EDS analyzer and Gatan Tridiem Energy Filter (GIF) for chemical analysis. Samples were prepared by crushing the crystals using mortar and pestle and dispersing them in ethanol. A few drops of the suspension were then placed onto lacey carbon copper microgrids. Due to the severe e-beam instability of MOFs low dose conditions (below 500 $e^-/Å^2$) were used.

2.6. Thermogravimetric analysis[284, 285]

Thermogravimetric analysis (TGA) is a material characterisation technique performed to study the stability and decomposition of materials including MOFs. In this process, a small amount of sample is heated in a crucible under a controlled atmosphere such as N_2, O_2, H_2, Ar, air or vacuum and the quantitative measurement of mass change in relation to both thermal degradation and material transitions is then carried out to determine the thermal stability and decomposition products of a material. The TGA instrument used in this work was a Perkin Elmer instruments STA 6000 thermo gravimetric analyser. In this the samples were subjected to a maximum heating temperature of 900 ^{0}C at a rate of 10 K/min under a flowing atmosphere of nitrogen. In this work, TGA was used to analyse the mass changes occurring on the degradation of the MOF structure.

2.7. Fourier transform infrared spectroscopy (FTIR)[284, 286]

Fourier transform infrared spectroscopy (FTIR) is a widely used spectroscopic techniques to reveal the presence of organic functional group within a material or molecule. In the FTIR process, when infrared radiation generated from the visible and microwave regions of the electromagnetic spectrum falls on a material, certain electromagnetic radiation is absorbed, causing bond vibration and alteration in the dipole moment of the molecule. This absorbed energy, if equal to the energy gap between vibrational states, can cause excitation of molecules from the ground vibrational state into a higher vibrational state. The transition between vibrational energy states produces a wide range of infrared spectrum. However, the most frequently observed transitions are those between a vibrational ground state and the first excited state which corresponds to the mid-infrared portion (wavenumber = 400 cm^{-1} to 4000 cm^{-1}) of the electromagnetic spectrum. The detector measures the amount of the intensity of transmitted radiation as a function wavelength which is then analysed by computer using Fourier transforms to obtain the infrared spectrum (Figure 2.13).

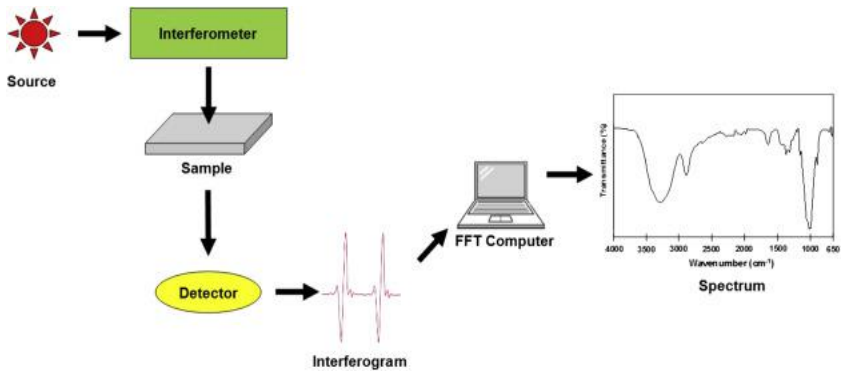


Figure 2.13 Basic components of a Fourier transform infrared spectrometer. Reproduced from Vamsi *et al.*[287] Copyright 2021, Elsevier.

The FTIR used for this work was Bruker Alpha II FTIR spectrometer with an attenuated total reflectance (ATR) attachment which used a diamond crystal. This type of experimental set-up makes it possible to measure the FTIR of a solid sample. In this procedure, the infrared beam is internally reflected by the diamond crystal, generating an evanescent wave which penetrates the sample, producing the infrared spectrum of the solid sample (Figure 2.14).

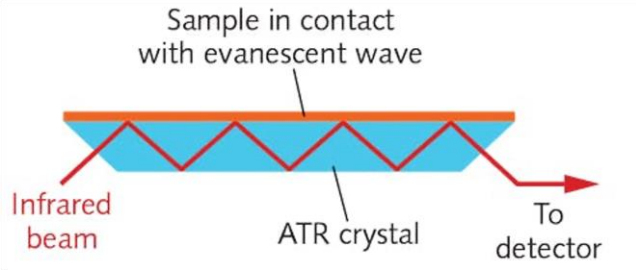


Figure 2.14. Graphical representation of attenuated total reflectance in FTIR. Reproduced from Dhillon *et al.* [288]. Copyright 2016, Laser Focus World.

2.8. Raman Spectroscopy[289]

Raman spectroscopy is complementary to IR spectroscopy in that they both probe the vibrations of molecules, but from different perspectives. Whereas FTIR spectroscopy detects the absorption of IR light by exciting vibrations, Raman is a light scattering technique, whereby a molecule scatters incident light from a high intensity laser light source. Typically, a sample is illuminated with a laser beam. Electromagnetic radiation from the illuminated spot is collected with a lens and sent through a monochromator. The elastic scattered radiation otherwise known as Rayleigh scattering, is filtered out using different types of filters. The inelastic scattered radiations (Raman scattering) are then dispersed onto a detector, giving the information about the vibrational modes in the system. The Raman microscope used for this work is Bruker Senterra II.

2.9. X-ray Fluorescence spectroscopy[290]

X-ray fluorescence (XRF) is a popular technique for both qualitative and quantitative elemental analysis. In XRF analysis, a primary X-ray beam interacts with a specimen, causing excitation of an inner shell electron (Figure 2.15). As this electron relaxes, a higher-energy electron fills the resulting vacancy, releasing excess energy in the form of fluorescent X-rays. The fluorescence spectrum displays characteristic peaks corresponding to the concentration of elements in the sample, offering a simple method to determine elemental composition. Two systems can analyze fluorescence: WDXRF (wavelength dispersive), which separates X-rays based on their wavelengths, and EDXRF (energy dispersive), which directly measures the energies of the emitted X-rays from the sample. In this work, measurements were carried out on a Bruker S8 high end wavelength dispersive X-ray fluorescence (WDXRF) spectrometer. Spectra plus software was used for the data analysis.

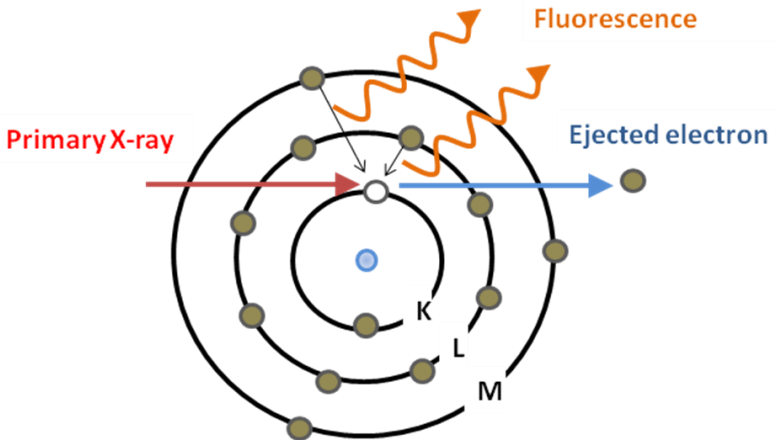


Figure 2.15. Generation of XRF by photoelectric effect.

2.10. Gas adsorption[107, 291, 292]

Gas sorption is an analytical technique utilized for studying porous materials, enabling the calculation of surface area, pore size, and pore shape. In a gas sorption experiment, a material is exposed to a gas, commonly nitrogen, which accumulates on the material's surface (the adsorbent), forming a layer of molecules or atoms known as adsorbates. This adsorption process occurs due to weak van der Waals forces between the adsorbates and the adsorbent, a phenomenon termed physisorption. During a nitrogen adsorption isotherm experiment, the volume of nitrogen adsorbed by a solid is measured as the pressure increases while maintaining a constant temperature of -196 °C (the boiling point of nitrogen). An isotherm is generated by plotting the volume of nitrogen adsorbed against the relative pressure ratio, P/P_0, where P_0 represents the saturation vapor pressure of nitrogen at -196 °C. The shape of the isotherm provides insight into the type of porosity present in the sample.

The profile of the isotherm is sensitive to the adsorbent material and analysis gas; therefore, the IUPAC recommended classifying the profile of isotherms into six types based on the analysis of a variety of gas/vapor adsorption isotherm (Figure 2.16). Type I and Type IV isotherms are most frequently observed in porous Metal-Organic Frameworks (MOFs). Generally, materials with micropores exhibit a steep uptake in the low pressure region due to the strong adsorbent–adsorbate interaction (Type I, also known as Langmuir-type adsorption isotherm), while significant gas uptake in this region is not observed when the interaction is weak (Types III and V). When materials have mesopores, higher pressure is required to fill the pore with guest molecules (Types IV and V). The stepwise isotherm (Type

VI) is not common for MOF materials, but this can be seen when guest molecules exhibit layer-by-layer adsorption.

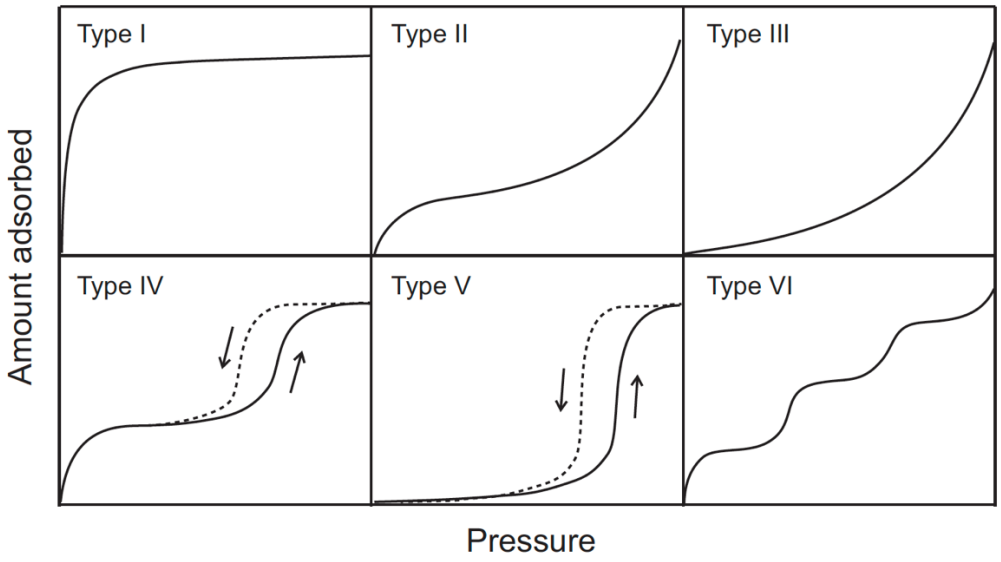


Figure 2.16. Types of physisorption isotherms as defined by IUPAC. Reproduced from Glover and Mu.[107] Copyright 2018, CRC Press.

The Brunauer-Emmett-Teller (BET) method is the most widely used procedure for the determination of the surface area of common porous materials, including MOFs. The BET equation is as follows:

$$\frac{P}{V(P_o - P)} = \frac{1}{V_m C} + \frac{(C-1)}{V_m C} \cdot \frac{P}{P_o} \qquad 2.16$$

Where V is the amount of gas adsorbed at pressure P, Vm is the amount of gas in a monolayer and C is a constant. The BET plot is a plot of P/V(P0-P) against P/P0 that shows a linear relationship. This linear relationship only occurs in the P/P0 range of 0.05 to 0.30., where processes such as capillary condensation and saturation are not taking place. C and V_m can be calculated from the BET plot and the surface area is calculated using:

$$\text{BET surface area} = V_m . L . a_m \qquad 2.17$$

Where L is the Avogadro's constant and a_m is the molecular cross-section are of the adsorbate.

2.11. Electrochemical Methods

2.11.1. Electrochemical mass transport[293-296]

Of the three modes of mass transport mechanisms of the electroactive species to and from the electrode, diffusion is most generally of interest to electrochemists. Electrochemical experiments are typically carried out in the presence of a large excess of inert electrolyte. This compresses the potential drop at the electrode-solution interface to within a very short distance of the electrode surface. Consequently, the potential gradient within the bulk solution is close to zero, rendering mass transport via migration insignificant. Additionally, mass transport driven by natural convection, resulting from temperature or density gradients, can be disregarded if experimental timescales are kept short.

2.11.1.1. Diffusion

Diffusion of electrochemical species are generally governed by Fick's laws of diffusion. Fick's laws are differential equations describing the flux of a substance (J) and its concentration (c) as functions of time (t) and position (x).

Fick's first law states that the flux of a substance ($J_{O(x,\,t)}$) is proportional to the concentration gradient, $\frac{\partial c_o}{\partial x}$:

$$-J_{O(x,\ t)} = D_O \frac{\partial c_{O(x,\ t)}}{\partial x} \qquad 2.18$$

Where D_O is diffusion coefficient and is given as $\nabla x^2/2\nabla t$, and allowing ∇x and Δt to approach zero, making it possible to obtain equation 2.18 above.

Fick's second law described the change in concentration (c) due to diffusion as a function of time (t):

$$\frac{\partial c_{O(x,\ t)}}{\partial t} = D_O \left(\frac{\partial^2 c_{O(x,\ t)}}{\partial x^2} \right) \qquad 2.19$$

In a typical electrochemical system, changes in the concentration of the electroactive species during electrolysis can be infinitesimal, making the variations in diffusion coefficient to be negligible. However, at high concentrations of the electroactive component, significant changes in solution properties like viscosity can occur, requiring more complex treatments. If the relevant boundary conditions are set for the diffusion of electrochemical species, the general formulation of Fick's second law for any geometry can be simplify as:

$$\frac{\partial c_O}{\partial t} = D_O \nabla^2 c_O \qquad 2.20$$

Where ∇^2 is the Laplacian operator which represent operators for different electrode geometries. There are different electrode geometries employed in electrochemical system, but the most common one is the electrode with spherical geometry. The diffusion equation employed for spherical electrode is given as:

$$\frac{\partial c_{O(r,\ t)}}{\partial t} = D_O \left(\frac{\partial^2 c_{O(r,\ t)}}{\partial r^2} + \frac{2}{r} \frac{\partial c_{O(r,\ t)}}{\partial r} \right) \qquad 2.21$$

Where r is the radius of the spherical electrode.

Suppose the electroactive species O is strictly transported by diffusion to an electrode, it redox equation can be given as:

$$O + ne \leftrightarrows R \qquad 2.22$$

If no other electrode reactions occur, then the current is related to the concentration of electroactive species O at the electrode surface (x = 0), J_o (0, t), by the equation:

$$-\mathrm{J_{O(0,\ t)}} = \frac{\mathrm{i}}{\mathrm{nFA}} = \mathrm{D_O}\left[\frac{\partial \mathrm{c_{O(x,\ t)}}}{\partial \mathrm{x}}\right]_{\mathrm{x=0}} \qquad 2.23$$

If several electroactive species exist in the solution, the current is related to the sum of their fluxes at the electrode surface and is given by the equation:

$$\frac{\mathrm{i}}{\mathrm{nFA}} = -\sum_{\mathrm{k=1}}^{\mathrm{q}} \mathrm{n_k\, J_{k(0,\ t)}} = \sum_{\mathrm{k=1}}^{\mathrm{q}} \mathrm{n_k D_k}\left[\frac{\partial \mathrm{c_{k(x,\ t)}}}{\partial \mathrm{x}}\right]_{\mathrm{x=0}} \qquad 2.24$$

Where n is the number of electrons, F is Faraday constant and A is electrode surface area.

2.11.1.2. Voltammetry at microelectrode

Microelectrode is an electrode which has its characteristic dimension on the scale of micrometres. The use of microelectrodes in electrochemical system has become popular over the years. The reason for this increased popularity has been due to the faster rate of mass transport, facilitating the measurement of faster kinetics both heterogeneously and homogeneously. Unlike macroelectrodes, microelectrodes diffusion current does not decay to zero but rather to the steady-state current. The most common geometries for microelectrodes are discs, bands and hemispheres. For spherical or hemispherical macroelectrode, the flux of reactant (J) at the electrode surface is given as:

$$\mathrm{J/mol\,cm^{-2}\,s^{-1}} = \mathrm{Dc^*}\left\{\frac{1}{\sqrt{\mathrm{D\pi t}}} + \frac{1}{\mathrm{r_e}}\right\} \qquad 2.25$$

Where r_e is the electrode radius.

Depending on the dimension of r_e, equation 2.25 above can be simplify into two. The first equation is called short-time limit equation:

$$J = \frac{c^* \sqrt{D}}{\sqrt{\pi t}} \qquad 2.26a$$

This equation holds when the $\sqrt{D\pi t} \ll r_e$ and it is useful for the analysis of reactant flux in spherical electrode with larger radii. The second equation is called long-time limit equation:

$$J = D\frac{c^*}{r_e} \qquad 2.26b$$

This equation holds when the $\sqrt{D\pi t} \gg r_e$ and it is useful for the analysis of reactant flux in spherical electrode with small radii. It can therefore be deduced that for a spherical or hemispherical microelectrode, a steady-state current will always dominate for electrode with small radii (r_e).

For a microdisc electrode (Figure 2.17a), the electrode is not uniformly accessible by the electroactive species and as such, flux is not constant over the electrode surface as described by modified Fick's second law.

$$\frac{\partial c}{\partial t} = D\frac{\partial^2 c}{\partial r^2} + \frac{D}{r}\frac{\partial c}{\partial r} + D\frac{\partial^2 c}{\partial z^2} \qquad 2.27$$

where z is the perpendicular distance from the electrode surface and r is a radial coordinate from the centre of the disc.

With relevant set of boundary conditions and for a n-electron electrode process, a transient response is observed leading to a steady-state current given as:

$$I = 4nFc^*Dr_e \qquad 2.28$$

The full current-time transient for either short or long times, has been calculated as;

$$I = 4nFc^*Dr_e f(\tau)$$

Where the dimensionless time, $\tau = 4Dt/r_e^2$. For short times, when $\tau < 1$, the flux equation is modified as shown equation 2.29. Thus, diffusion to the electrode surface become planar (linear).

$$f(\tau) = \left(\frac{\pi}{4\tau}\right)^{1/2} + \frac{\pi}{4} + 0.094\tau^{1/2} + \cdots, \qquad 2.29$$

Whilst at long times, $\tau > 1$, the flux become modified as equation 2.30 below. At long time, diffusion layer spread beyond the edge of the disc and the shape of the diffusion layer approaches hemispherical, as shown in Figure 2.17b

$$f(\tau) = 1 + 0.71835\tau^{-1/2} + 0.005626\tau^{-3/2} - 0.00646\tau^{-5/2} + \cdots \qquad 2.30$$

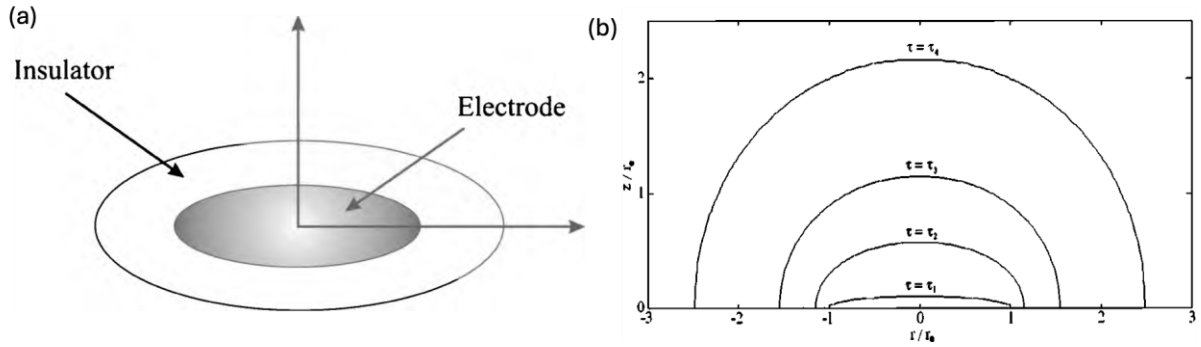


Figure 2.17. A microdisc electrode and the cylindrical coordinates (r and Z) used to describe it (b) Contour plots showing depletion of the electroactive species at a disc electrode. Reproduced from Compton and Bank.[294] Copyright 2018, World Scientific Publishing Europe Ltd.

2.11.1.3. Microelectrode arrays

Microelectrode arrays provide an attractive alternative to macroelectrodes because they can produce a voltammetric response of similar magnitude to their macro counterparts, but with a considerably less background/capacitive current. Hence, microelectrode arrays are increasingly used in electroanalytical applications, and much research is dedicated to

designing new types of arrays containing increasingly smaller micro/nanoelectrodes in both regular and random distributions. However, the fabrication of random array microdisc or RAM are very simple and cheap compared to regular array microdisc which are fabricated lithographically. In a typical random array microdisc, approximately 3000 randomly dispersed carbon microfibres of a few microns diameter are randomly embedded in epoxy resin. The voltammetry observed at microelectrode arrays can be qualitatively divided into four categories (Figure 2.18) depending on the relative values of (i) individual electrode size, (ii) electrode separation and (iii) diffusion layer thickness.

Case 1: The diffusion layer is small compared to both the size of each electrode and the inter-electrode distance. Linear diffusion operates and the depletion zones of adjacent electrodes do not overlap: the electrodes are "diffusionally independent". The current response at such an array is equivalent to a macroelectrode with the same area as the combined areas of the microelectrodes in the array.

Case 2: The diffusion layer is large compared to the electrode size, but smaller than the electrode separation. The electrodes remain diffusionally independent, but diffusion is now convergent in nature and the array behaves like a micro-electrode with the current response multiplied by the number of electrodes in the array. This is the optimum case for maximising the signal-to-noise ratio.

Case 3: The diffusion layer is large compared to the electrode and comparable to the electrode separation. The diffusion zones at adjacent electrodes begin to overlap, meaning individual electrodes are no longer diffusionally independent, leading to intermediate behaviour.

Case 4: The diffusion layer is much larger than both the electrode size and separation. The diffusion zones of all electrodes are completely overlapping so that the diffusion is linear

across the entire array and so the behaviour is once more equivalent to that of a macroelectrode.

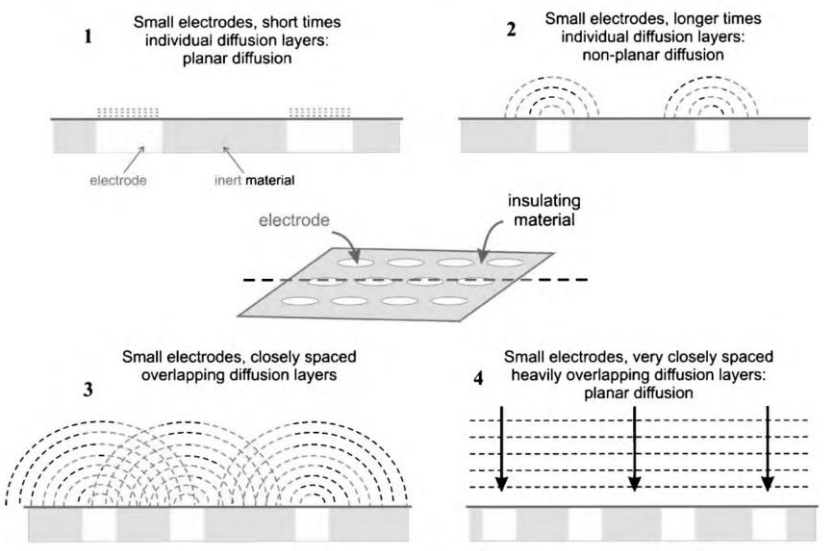


Figure 2.18. Schematic diagram of the four categories of diffusion profile to which an array of microelectrodes may belong. Reproduced from Compton and Bank.[294] Copyright 2018, World Scientific Publishing Europe Ltd.

2.11.1.4. Porous electrode

The voltammetric behaviour of a porous electrode can also be simulated to obtain information about diffusion through the porous electrode. Different type of porous coating on an electrode surface can be formed by immobilising a layer of nanoparticles or nanotubes onto a planar electrode. Alternatively, polymer films can be cased onto the electrode, sometimes with a not dissimilar effect. Figure 2.19 shows a nanotube modified electrode in schematic form. The surface can be thought of as a porous layer in which pockets of the electroactive species are trapped in between multiple layers of nanotubes. The array of layers of nanoparticles immobilise on an electrode can be modelled using semi-infinite and thin layer diffusion model (Figure 2.19a). Findings shows that the surface area of the porous material (area of the thin layer electrode) was far greater than the geometric area of the

underlying supporting electrode, indicating that the thin layer model produces a smaller peak-to-peak separation than the semi-infinite model (Figure 2.19b).

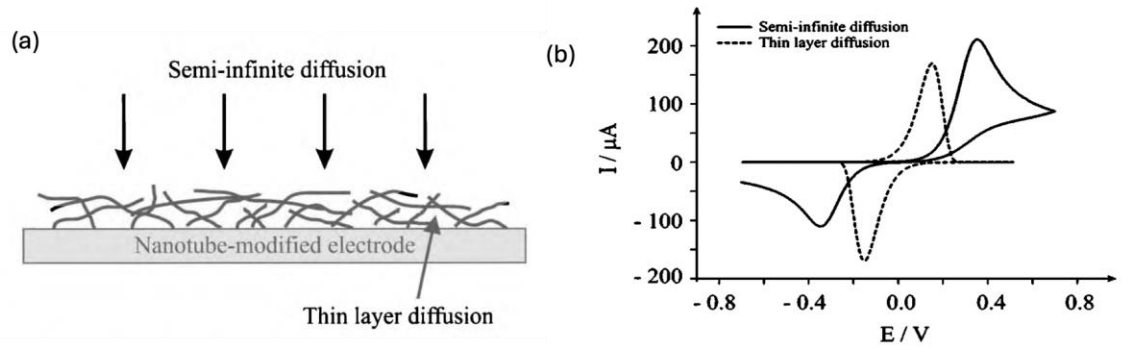


Figure 2.19. (a) schematic of the two types of diffusion that contribute to current at a carbon nanotube modified electrode (b) Comparison of linear sweep voltammetry using semi-infinite and thin layer planar diffusion models. Reproduced from Compton and Bank.[294] Copyright 2018, World Scientific Publishing Europe Ltd.

It can therefore be deduced that modifying an electrode with porous layer can influence mass transport. If the contribution to the voltammetry from material within the porous layer dominates, then it is possible to think that the reduction in peak- to-peak voltage separation is as a result of the electrocatalytic effect of the material forming the porous coating rather than linking it to mass transport phenomena, as revealed in Figure 2.19b where the same electrochemical rate constant is used for both current-voltage curves.

2.11.2. Cyclic Voltammetry[297-300]

Cyclic voltammetry is the most commonly employed electrochemical method for studying molecular electrocatalysts. Its wide application in electrocatalysis has been due to its versatility, non-destructive nature and its ability to provide rich information about the electroactivity of a material within the shortest possible time. This technique is useful for preliminary screening of a prospective catalyst as it is quick and effective at providing useful

data about the redox process and allows identification of potentials required for various electrochemical transformations. In cyclic voltammetry, current response is measured as potential sweep is applied from an initial potential (E_i) to a chosen potential (E_s) which is relevant to the species being investigated. The initial potential (E_i) is usually somewhere in a region of no faradaic current, otherwise known as a double layer region and where the composition of the analyte solution is not affected. As the potential scan wave reaches E_s, the potential sweep direction is reversed and returned to E_i, showing the presence of any observable redox reactions with corresponding current response. The forward potential sweep gives oxidative peak current while the reverse potential sweep gives reductive peak current or reductive overpotential depending on scan direction and the nature of the species under examination. A schematic of the potential waveform used in a typical CV is given in Figure 2.20.

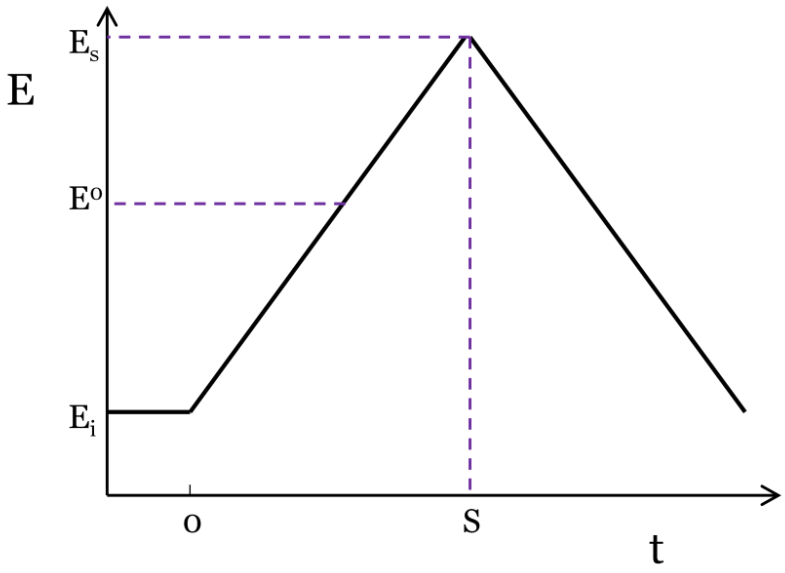


Figure 2.20. Potential scheme as a function of time for cyclic voltammetry.

A plot of current response against the applied potential otherwise known as a cyclic voltammogram (CV), is obtained, from where the information on electrochemical oxidation and reduction can be deduced, an example of which is given in Figure 2.21.

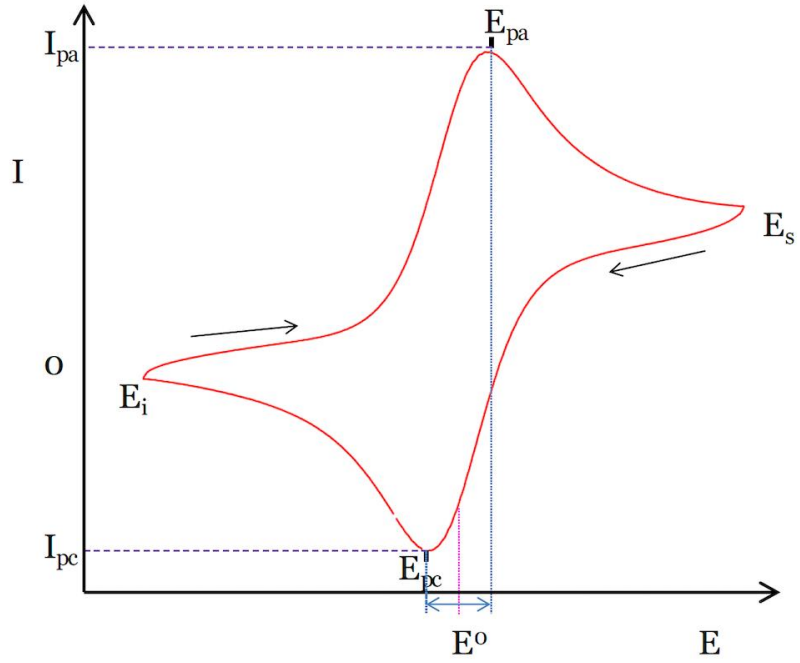


Figure 2.21. A typical reversible cyclic voltammogram. Arrows indicate the direction of the potential sweep.

As demonstrated in the schematic CV above, the initial potential sweep (E_i) is carefully selected at a point where no current flows. However, as the potential is scanned in the positive direction and toward the standard potential (E^o), an anodic current is produced which increases with potential, indicating mass transport of electroactive material via diffusion to the electrode surface where oxidation reaction takes place. This current increase continues until a maximum current is reached (E_{pa}, I_{pa}) after which current response begins to drop as the potential is scanned further positive. This implies that before the peak current (I_{pa}), a large influx of analyte flooded the electrode surface and became oxidized and as such the system witnessed a rapid current response. However, at peak current, the mass transport of analyte

become limited by diffusion and the decay in current response witnessed thereafter is as a result of decrease in the concentration of the analyte reaching the electrode surface, followed by corresponding growth in the depletion layers. The rise in anodic current observed prior to the diffusion limited stage can be explained by the Nernst equation, shown below.

$$E = E^{o\prime} + \frac{RT}{nF} \ln\left(\frac{C_o}{C_r}\right) \qquad 2.9$$

where C_o and C_r are the concentration of oxidised and reduced redox species, E is the applied potential, $E^{o\prime}$ is the formal potential while R, T, n and F are the ideal gas constant, temperature, number of electrons transferred per molecule and faradaic constant, respectively.

At the switching potential, the scan direction is reversed, and the opposite processes occur with the product of the forward scan being reduced back to the starting material and the cathodic current flow following the same principles as described for the anodic current. For a completely reversible process the ratio of the oxidative and reductive peak currents, Ipa/-Ipc equals unity.

2.11.3. Chronoamperometry[298-301]

Chronoamperometry is a well-established amperometric technique and it involves applying a pulse potential to a working electrode in an unstirred solution and the current response is measured as a function of time to give current transients or chronoamperograms. Just like cyclic voltammetry, chronoamperometry also involves starting at a potential E_i where no reaction is anticipated and minimal current flows, moving to a set potential E_s, where the electron transfer of interest (oxidation or reduction) is observed. During the application of E_s, the local concentration of the analyte drops to zero as it reacts to form a new species, thereby

creating a depletion or diffusion layer and as such, a concentration gradient is generated that enables the transfer of analyte through diffusion from bulk solution (higher concentration) to the electrode surface. The diffusion layer increases with time as the electroactive analyte is depleted resulting in lower current response. The chronoamperometry processes are shown in Figure 2.22 below.

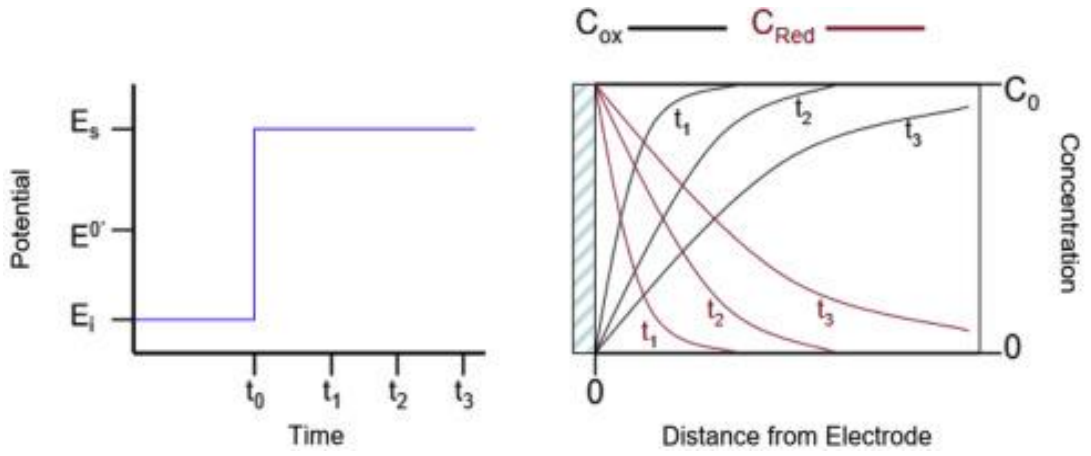


Figure 2.22. Schematic diagram of chronoamperometry process. Reproduced from Rezaei *et al.*[298] Copyright 2019. Elsevier.

Generally, there are two possible forms of potential sweep that can be carried out in a chronoamperometry experiment namely (i) single potential step in which a forward potential is applied, and the current response is recorded, and (ii) double potential step in which a forward potential is applied, after which the potential is returned to the initial value while monitoring the current response during a specified period of time. For a single potential step chronoamperometry experiment, Cottrell's equation can be used to describe the instantaneous flow at each point in time.

$$I = \frac{nFACD^{1/2}}{(\pi t)^{1/2}} \qquad 2.10$$

where *n* is the number of the electrons transferred in a redox system and *F* is the faraday constant. Also, *A*, C and D represent the electrode surface area in cm^{-2}, concentration in

mol cm^{-1} and diffusion constant of the electroactive species in cm s^{-1}, respectively. In this research work, single potential step chronoamperometry experiment were performed to evaluate the catalyst stability and the current output during the electrochemical CO_2 reduction reaction. This technique was also used in conjunction with online electrochemical mass spectrometry for product identification and quantification.

2.11.4. Three Electrode Cell Configurations[284, 297, 299, 302]

Figure 2.23 below depicted a typical electrochemical cell set-up, and the three electrodes represent a counter electrode (CE), reference electrode (RE) and working electrode (WE) respectively. During electrochemical reaction, current usually flows between the counter and working electrodes, with the reference electrode being accurately used to measure the applied potential in relation to a stable reference reaction.

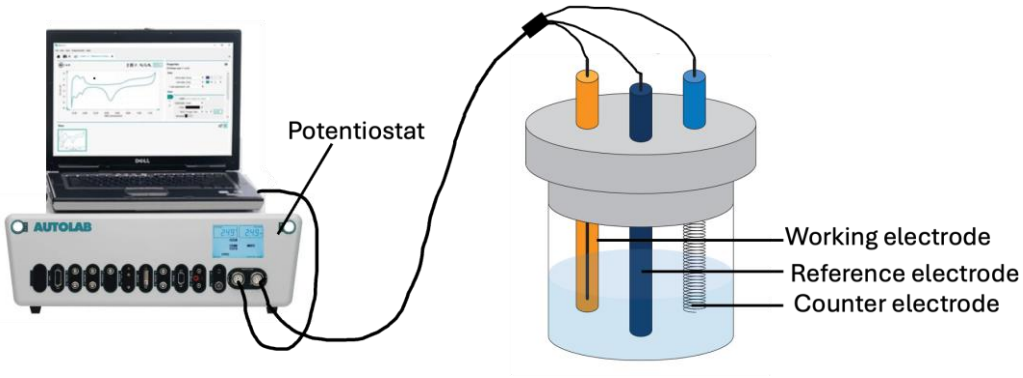


Figure 2.23. Schematic diagram of a three-electrode electrochemical cell system.

The working electrode (WE) is an important aspect of an electrochemical cell as it is an electrode that carries out the electrochemical event of interest. An important feature of an ideal working electrode material is that it should be inert in the potential range of interest. It is crucial to ensure that the working electrode has a well-defined surface area and is extremely well cleaned, as this can affect the potentials associated with electron transfer,

adsorption and desorption reactions. The surface of a working electrode can be cleaned by polishing it on a polishing pad containing different particle size of diamond suspension or water-alumina slurry, after which it is sonicated in ultrapure water to remove particles from the electrode surface. Further cleaning can be performed by performing several CV scans in simple electrolyte and across a wide potential window to remove any adsorbed impurities left over from the polishing procedure. The working electrode used in this work was a glassy carbon electrode and it was cleaned following the above procedure.

The reference Electrode (RE) is an electrode that provides a reference point for the potential of another electrode to be measured in the electrochemical cell. It is important to use a stable and relevant reference electrode depending on the type and pH environment of the electrolyte. For example, in aqueous electrolyte, AgCl/Ag and Hg/HgO electrodes are ideal for basic pH environments while a Hg/Hg_2Cl_2 electrode is stable in acidic environments. In a nonaqueous electrolyte, the ideal reference electrodes commonly used are those based on the Ag^+/Ag couple and can be constructed by dipping a silver wire in a solution containing silver salt, e.g $AgNO_3$. In this work, an Hg/HgO (1.0 M KOH) reference electrode, was used. All applied potentials collected were subsequently calibrated to the reversible hydrogen electrode (RHE) according to the equation: $E_{RHE} = E_{Hg/HgO} + 0.098 + 0.0591 \times pH$.[303]

The counter electrode (CE) is included in an electrochemical system to complete the electrical circuit and to avoid current flow the into reference electrode. This implies that current is flowing (as electron) between the WE and CE as potential is applied to the working electrode to drive redox reactions. Since it is possible for the reaction occurring at the counter electrode to inhibit those occurring at the working electrode, a counter electrode with surface area larger than the working electrode is used to minimise this interference. Additionally, the counter electrode can be isolated from the rest of the system by enclosing it within a partially

permeable fritted compartment. This will ensure that possible by-products generated from the counter electrode do not contaminate the working electrode. Examples of commonly used counter electrodes are platinum wire or disk and carbon-based counter electrodes. Platinum counter electrodes was used throughout the electrochemical experiments in this research work since it can easily be cleaned by flame annealing.

2.11.5. Online electrochemical mass spectrometry[304-306]

Online electrochemical mass spectrometry (OLEMS) otherwise known as differential electrochemical mass spectrometry has been described as a useful technique to identify gaseous or volatile products of electrochemical reactions. This technique involves performing a potential sweep and the ion current corresponding to the gaseous product of interest is recorded in parallel to the faradaic electrode current to give a mass signal-potential profile, otherwise called mass spectrometric voltammograms (MSCV). The OLEMS instrumental set-up used in this work generally comprises of an injection chamber, differential pump chamber, quadruple mass spectrometer (MS) and detector (Figure 2.24). The product of an electrode reaction can be injected into the mass spectrometer via a porous Teflon membrane which allows dissolved gaseous and other volatile species to pass to the MS via a differentially pumped vacuum system. Two turbomolecular pumps, one positioned close to injection chamber and other placed at proximity to the ionization chamber, provides the differential pressure that drive the gaseous species to the ionization chamber. At the MS ionization chamber, the gaseous species are converted to ions by bombardment with fast moving electrons. The ions get separated based on mass-to-charge ratio as they travel through the quadrupole towards the detector. A typical SEM or Faradaic detector with multiple detection channels can then be used for simultaneous detection of various products. The data of each

gaseous product generated are then processed and presented as a plot of ion current vs time or partial pressure vs time.

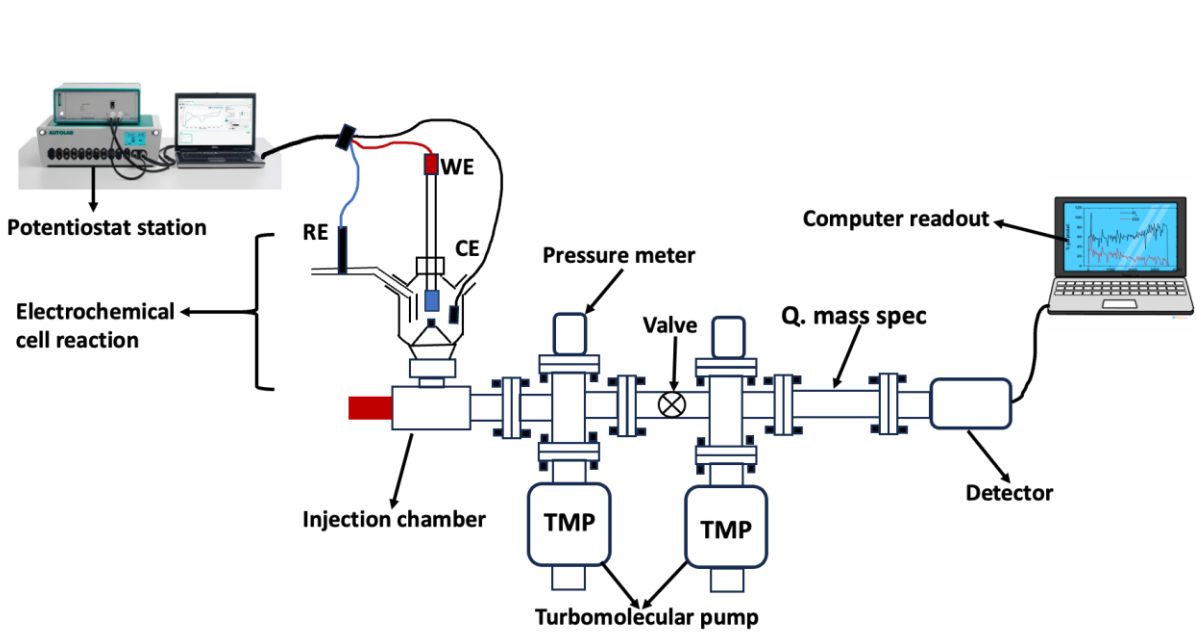


Figure 2.24 Schematic diagram of online electrochemical mass spectrometer (OLEMS).

CHAPTER THREE

Ion exchange studies of BIRM-1 with Nickel ion

3.1. Introduction

Owing to the intriguing structural diversity[307] and potential applications in gas sorption[308, 309] catalysis[310], drug delivery[311], luminescent materials[312], and as porous conductors[313], metal organic frameworks (MOFs) have witnessed explosive growth in the field of solid-state functional materials.[314] One of the desirable properties in porous MOF material that is crucial to environmental and energy application is the ability to undergo post-synthetic modification by ion exchange.[90] This crucial property can both potentially facilitate the removal or trapping of harmful ions,[315, 316] and help in fine-tuning the properties for various applications. However, despite the discovery of hundreds of different metal-organic frameworks and extensive study of their properties and possible applications, only a very small number of MOFs are known to undergo ion exchange.[317-319]

The discovery of BIRM-1, opened up the several possibilities for this three-dimensional and ion exchangeable porous zinc carboxyethyl phosphonate MOF[90]. The structural framework of BIRM-1 is negatively charged, and this charge is balanced by weakly bound ammonium cations inside the channels of BIRM-1 (Figure 3.1). It was therefore postulated that if BIRM-1 is placed in an ionic solution, there is every likelihood that cations from the solution could diffuse into the structure and interchange with an equivalent quantity of ammonium cations. Zhao *et al.* demonstrated the exchange of Li^+, K^+, Na^+, Co^{2+}, Mn^{2+} and Mg^{2+} with NH_4^+ in the pores of BIRM-1 with the structure of Li^+-BIRM-1 and K^+-BIRM-1 fully solved without a change in the

crystal structure of BIRM-1 after ion exchange reaction. However, findings reveal that the crystal system of BIRM-1 changed from tetragonal to a lower symmetry of orthorhombic after ion exchange with Co^{2+}, Mn^{2+} and Mg^{2+} ions [320].

In this chapter, the ion exchange properties with nickel (II) cations were investigated in detail with a view to producing a functional porous MOF material. It is evident from the powder XRD pattern that the nickel-exchanged product (Ni^{2+}-BIRM-1) exhibited a similar structure to BIRM-1(NH_4^+), which suggests that the structure remained intact and similar to the parent material, which should help with structural characterization.

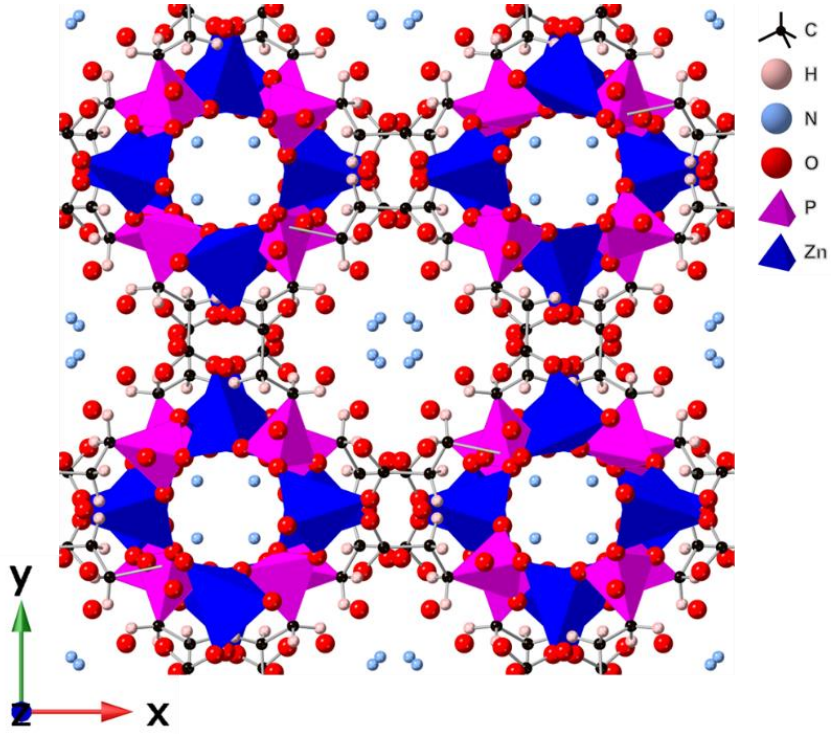


Figure 3.1. Crystal structure of BIRM-1 looking along the z-axis. Oxygen atoms from solvent water have been removed for clarity.

3.2. Experimental

3.2.1. Materials

All the chemicals used for this experiment were obtained from Sigma Aldrich and were of reagent quality and used without further purification. Chemicals used for these experiments were: $Zn(NO_3)_2.6H_2O$ (98%), 3-phosphonopropionic acid (94%), tetraethylammonium bromide (98 %), urea (99.5 %), nickel (II) acetate (99.99 %).

3.2.2. Synthesis of BIRM-1

Hydrothermal synthesis of BIRM-1 was carried out as given by Chao Zhao.[90] In this method, 1.6695 g zinc nitrate hexahydrate was dissolved in 11.25 mL of deionized H_2O. To this solution, 1.5098 g 3-phosphonopropionic acid, 1.5342 g tetraethylammonium bromide and 3.0631 g urea were added to give a clear solution after stirring for 30 minutes. Then the resulting mixture was placed in a Parr Teflon-lined stainless-steel autoclave, which had a capacity of 23 mL. The reaction mixture was heated under autogeneous pressure at 87°C for a period of 24 hours, after which it was removed and allowed to cool in air. The product was then washed with water and recovered by filtration.

3.2.3. Ion exchange with nickel (II) ions

Ion exchange experiments was carried out on BIRM-1 using nickel salts. In this experiment, 1 × 10^{-3} moles of BIRM-1 crystal were mixed with 0.1M nickel (II) acetate solution. After stirring for 10 minutes, 0.1 M HCl solution was added dropwise into the solvent to adjust the pH to about 5.5. The resulting solution was then placed in a round-bottom flask and slowly stirred for 24 hours at ambient temperature. The product was separated, washed several times with deionized water to remove excess salt and then air dried. Green needle-like crystals were

obtained and a preliminary check under the microscope showed that the material consisted of shining prism-like shape crystals (Figure 3.2). The sample was submitted to the School of Chemistry's single crystal diffraction service for structural characterisation.



Figure 3.2. Ni^{2+}-BIRM-1 crystals.

3.3. Characterization

3.3.1. Laboratory powder XRD

The powder XRD pattern of the nickel-exchanged product (Figure 3.3) was similar to BIRM-1 after 24 hours of ion exchange. However, the relative intensities of certain peaks had changed significantly as a result of the ion exchange reaction. Indexing of the powder XRD pattern of the Ni-BIRM-1 was carried out with the GSAS 2 computer program giving the crystal system as tetragonal, with the unit cell parameters given as a = 22.243(3) Å, c = 18.020(0) Å, *I*41/*acd* (see chapter 9 Figure A3.1 for full index details). Upon further refinement of these unit cell parameters by Le Bail fitting in GSAS 2, the final unit cell output was given as a = 22.165(7) Å, c = 17.978(6) Å. There was a slight difference between this structure and the unit cell of BIRM-1 (Table 3.1). This difference can be seen in the slight modification in the relative intensity of some of the peaks in Ni-BIRM-1. The slight change in relative peak intensities indicates a

change in cell contents, which is consistent with ion exchange as this behaviour is commonly noticed in ion exchange of some inorganic materials such as zeolites.[321, 322]

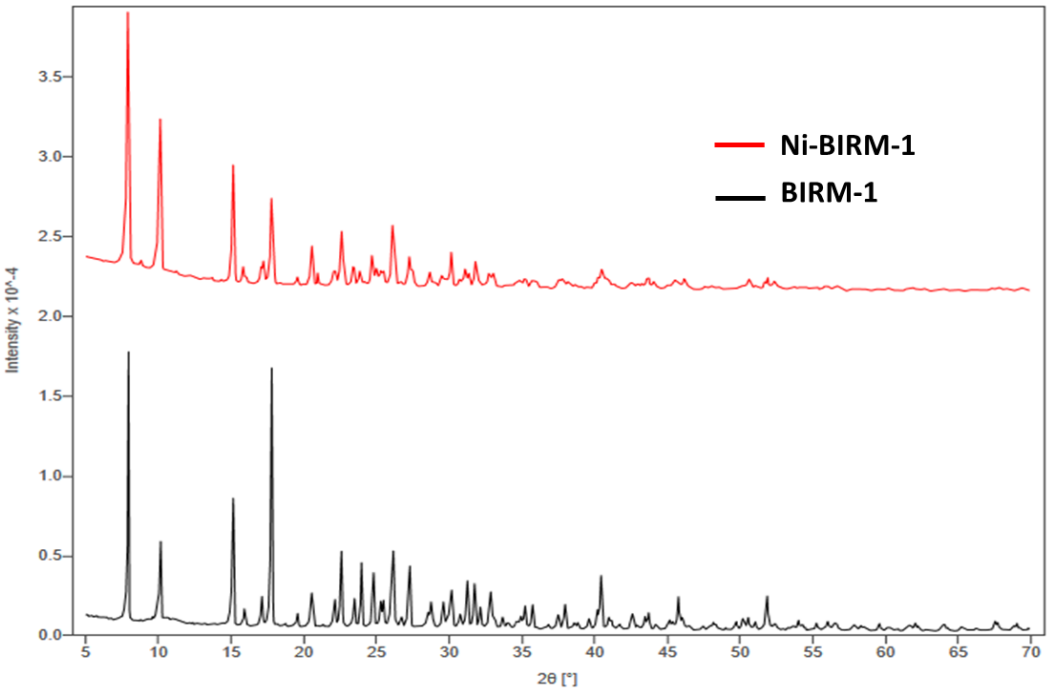


Figure. 3.3. Powder XRD patterns of Ni^{2+}-BIRM-1 (red) and BIRM-1 (black).

Table 3.1 Lattice parameters of BIRM-1 and Ni^{2+}-BIRM-1.

	BIRM-1	**Ni^{2+}-BIRM-1**
Crystal System	Tetragonal	Tetragonal
Space Group	*I*41/*acd*	*I*41/*acd*
***a*/Å**	22.302(2)	22.165(7)
***c*/Å**	17.738(1)	17.978(6)
Volume/Å^3	8822.6(1)	8847.951

3.3.2. Single crystal XRD structure of Ni^{2+}-BIRM-1

A suitable and well diffracting crystal was picked for analysis and high-resolution single crystal XRD data were collected. The structure of Ni^{2+}-BIRM-1 was solved with the assistance of Dr. Louise Male, the XRD facility manager in the School of Chemistry at the University of Birmingham. The result from the single crystal XRD analysis shows that the framework of BIRM-1 was preserved after the ion exchange experiment (Table 3.2, see Chapter 9 Table A3.1-3.7 for more structure details). Ni^{2+}-BIRM-1 also crystallizes in tetragonal space group of *I*41/*acd.* The asymmetric unit of this crystal comprises two Zn (II) cation, two $(O_3PC_2H_4CO_2)^{3-}$ anion, five water oxygen atoms and some disordered nickel atoms (Figure 3.4).

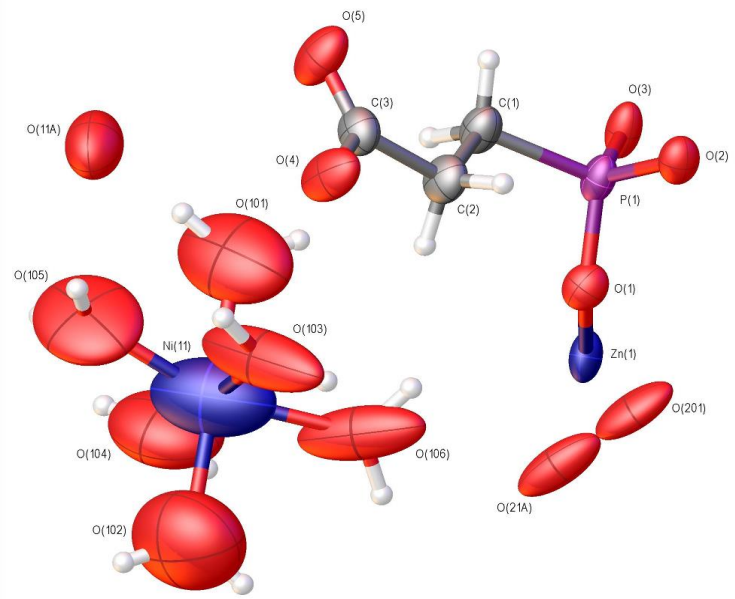


Figure 3.4. The asymmetric unit of Ni^{2+}-BIRM-1 with ellipsoids drawn at the 50 % probability level.

The Zn atom in Ni^{2+}-BIRM-1 is tetrahedrally coordinated by four oxygen atoms, one of which is from a carboxylate group of the $(O_3PC_2H_4CO_2)^{3-}$ ligand (O4) and the other three from three different CPO_3 groups (O1-O3) (Figure 3.5a). The corner-shared connection between the ZnO_4 and CPO_3 tetrahedra give rise to double-crankshaft (dc) circular rings of inorganic clusters

which are further cross-linked by the organic moieties of the ligands, giving rise to a 3-dimensional structure with two different channels along z-axis (Figure 3.5b and c). The nickel cations were successfully exchanged into the structure and located in the large channels, while the small channels are filled with water oxygen atoms. The nickel cations in the large channel were found to be distributed over different positions. The absence of ammonium ion nitrogen in the framework channels indicates that 100% ion exchange was achieved. The structure contains one $Ni(OH_2)_6$ complex per two Zinc atoms, disordered over a symmetry element, making refinement of the occupancy parameters extremely difficult. The same cavity contains a free water molecule, O(11A), also disordered over a symmetry element (Figure 3.5). Another cavity contains another free water molecule, O(201)/O(21A), one per two zinc atoms, disordered over two positions at a refined occupancy ratio of 0.26(2): 0.24(2). It was not possible to successfully refine hydrogen atoms on the free water molecules. All hydrogen atoms were fixed as riding models with the isotropic thermal parameters (U_{iso}) based on the U_{eq} of the parent atom.

Table 3.2 Crystallographic data for Ni^{2+}- BIRM-1.

Sample	Ni^{2+}-BIRM-1
Formula	$Ni(OH_2)_6[Zn_2(O_3PCH_2CH_2COO)_2]\cdot 2H_2O$
Formula Weight	637.66
Space group	*I*41/*acd*
a (Å)	22.1734(4)
c (Å)	17.8103(5)
Volume	8756.6(4)
Goodness-of-fit on F2	1.070
wR2	0.2750
Largest diff. peak/hole / e $Å^{-3}$	1.82/-1.81

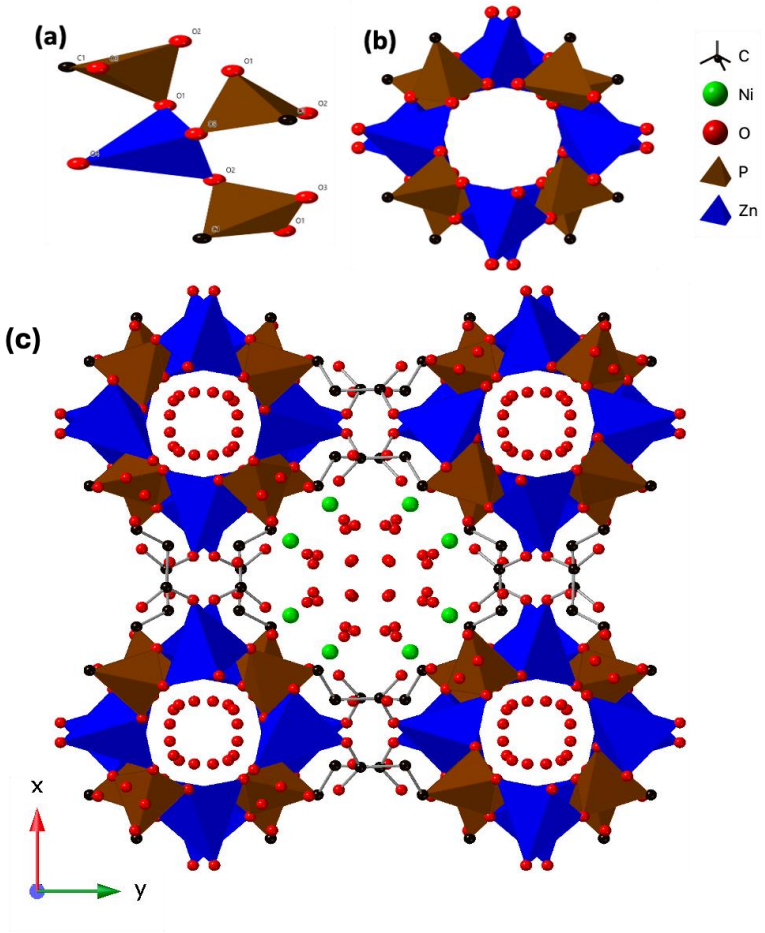


Figure 3.5. (a) Coordination network of ZnO_4 and CPO_3 tetrahedrons (b) double-crankshaft (dc) circular ring of the inorganic clusters and **(c)** Polyhedral view of Ni^{2+}-BIRM-1 along *z*-axis showing the atomic positions of exchanged nickel atoms, and water oxygen atoms. Hydrogen atoms have been omitted for clarity.

3.3.3. FTIR studies of Ni^{2+}-BIRM-1

The FTIR spectrum of Ni^{2+}-BIRM-1 was recorded to obtain some additional crystallochemical information (Figure 3.6, Table 3.3). The FT-IR spectra of some BIRM-1 and ion exchange products from the previous work of Zhao[90] were used as a guide to assign various functional groups in Ni^{2+}-BIRM-1. An important characteristic of the IR spectrum of BIRM-1 was the doublet at 3200 cm^{-1} and 3040 cm^{-1} from stretching vibrations of O–H from coordinated water molecules and N–H stretching from ammonium molecules. However, the broad band

occurring at around 3040 cm^{-1} completely disappeared after ion exchange, which could be related to the absence of N–H vibrations engendered by the complete removal of the exchangeable ammonium cations by ion exchange (Figure 3.6b). The rest of the IR data shows a qualitatively similar spectrum. The symmetric and asymmetric stretching vibrations of the carboxyl group are evident as strong bands at 1591 cm^{-1} and 1420 cm^{-1}, respectively. The P–C stretching bands were observed as sharp peaks at 1305 cm^{-1}, while the P–O stretching modes of the phosphonate group are seen as several sharp peaks in the range 1150–950 cm^{-1}. After exchange of nickel ions into the porous structure of BIRM-1, FTIR data indicated that the structure of BIRM-1 was maintained after the ion exchange.

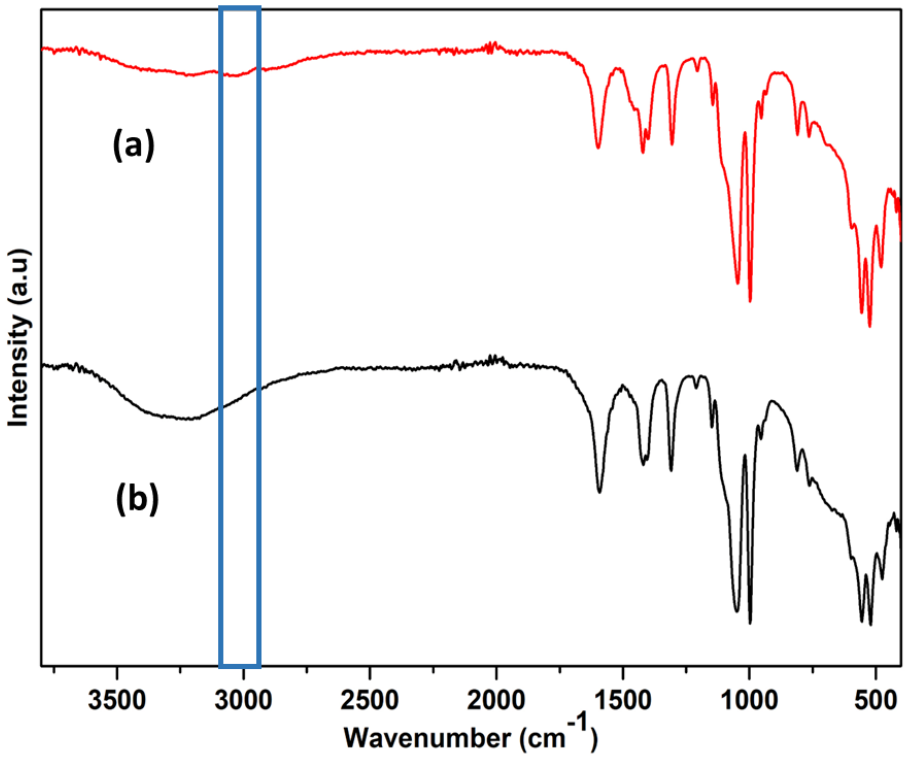


Figure 3.6. FTIR spectra for (a) BIRM-1 and (b) Ni^{2+}-BIRM-1; the blue area illustrates the peak disappearing after the ion exchange.

Table 3.3 Observed FTIR shifts and assignments for Ni^{2+}-BIRM-1 in comparison to BIRM-1.

BIRM-1		Ni^{2+}-BIRM-1	
Wavenumber (cm^{-1})	**Peak Assignment**	**Wavenumber (cm^{-1})**	**Peak Assignment**
3200	O−H (H_2O)	3200	O−H (H_2O)
3040	N−H (NH_4^+)	3040	Peak disappeared
1591	Carboxylate C−O (sym)	1591	Carboxylate C−O (sym)
1420	Carboxylate C−O (asym)	1420	Carboxylate C−O (asym)
1305	P−C (stretching)	1305	P−C (stretching)
1150–950	P−O stretching	1150–950	P−O stretching
<900	Zn−O	<900	Zn−O

3.3.4. Morphological studies of Ni^{2+}-BIRM-1

The SEM image shown in Figure 3.7 is used to describe the crystal morphology of Ni^{2+}-BIRM-1 in comparison to mother material BIRM-1. The rectangular prism-like crystal shape of BIRM-1 can be observed to be preserved in Ni^{2+}-BIRM-1 as depicted in the SEM image. The quantity of nickel ions in the Ni^{2+}-BIRM-1 was measured with EDX. Since the depth of profiling in EDX is about 1 µm compared to the unit cell dimension of Ni^{2+}-BIRM-1 is around 20 Å × 20 Å × 18 Å, nickel ion exchanged in the BIRM-1 framework can be easily detected in the structure.

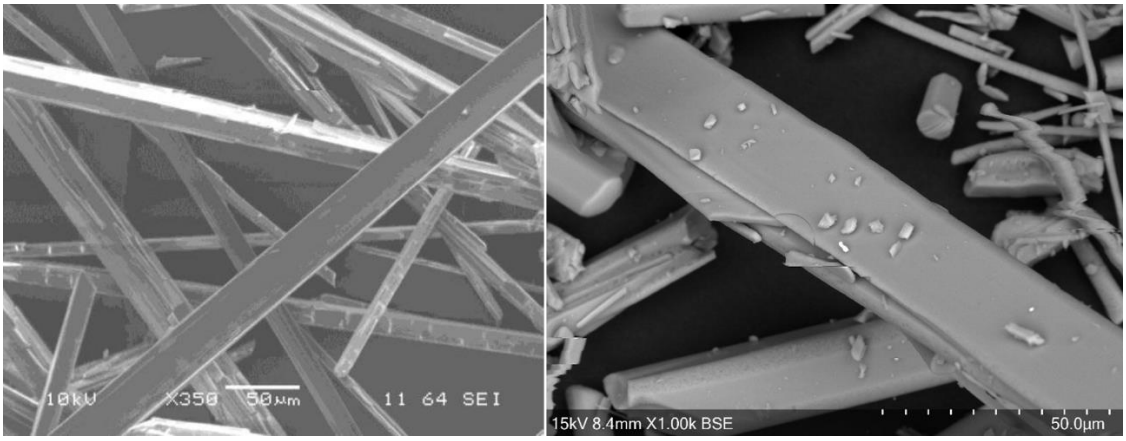


Figure 3.7 SEM images for Ni^{2+}-BIRM-1.

The results of spot and area analyses (Table 3.4) conducted on a smooth surface of different exchanged crystals, further confirmed that ion exchange had been successful. The average molar ratios of Zn: P: Ni observed were 1.12: 1: 0.52. The molar ratio of Zn to P is very close to the theoretical value 1: 1, and the average molar ratio of Ni to Zn/P is about 0.52: 1 (1.12). Therefore, the degree of ion exchange is estimated to be roughly 100%

Table 3.4 Energy dispersive X-ray spectroscopy results for Ni^{+}-BIRM-1 crystals.

	Zn	P	Ni
Weight %	18.80	8.78	13.88
	20.62	11.19	13.33
	20.33	8.65	19.84
	26.84	8.81	6.86
	22.78	14.23	16.51
	19.74	5.65	21.46
	22.65	7.42	6.52
	22.89	9.22	7.08
	20.53	6.82	9.05
	20.53	6.82	9.05
	19.63	7.04	9.75
	24.06	10.04	11.66
	23.40	10.27	17.28
	20.10	7.75	15.92
	16.07	12.49	16.07
Mean	19.19	7.49	19.25
Standard Deviation	4.55	2.74	10.5
Molar Ratio (normalized to P)	1.12	1	0.52
Expected Molar Ratio	1	1	0.5

3.3.5. Thermal stability studies of Ni^{2+}-BIRM-1

Thermogravimetric behaviour of Ni^{2+}-BIRM-1 is presented in Figure 3.8. The weight loss of 14.30 % at around 100°C, which is equivalent to 5 molecules of water (Calcd.14.1 %), can be attributed to the evaporation of the uncoordinated water and part of the water coordinated to nickel. The framework witnessed continuous weight loss till around 425°C, with a

significant weight loss of 21.13 % occurring at around 505°C, signalling the loss of the remaining coordinated water molecules, combustion of the organic ligand and collapse of the framework. It can therefore be inferred that Ni^{2+}-BIRM-1 is stable up to 425°C which is above the stability of BIRM-1 (302 °C). This increase in structural strength is probably obtained after ion exchange, as nickel could interact with the BIRM-1 framework and hold the structure stable to a higher temperature. In principle, a stable dehydrated phase could be obtained by dehydrating Ni^{2+}-BIRM-1 around this temperature. This could confer a functional property on Ni-BIRM-1 by creating more porous space within the structure and as well provide access to additional open binding sites, which would be necessary to facilitate gas storage and other potential applications.

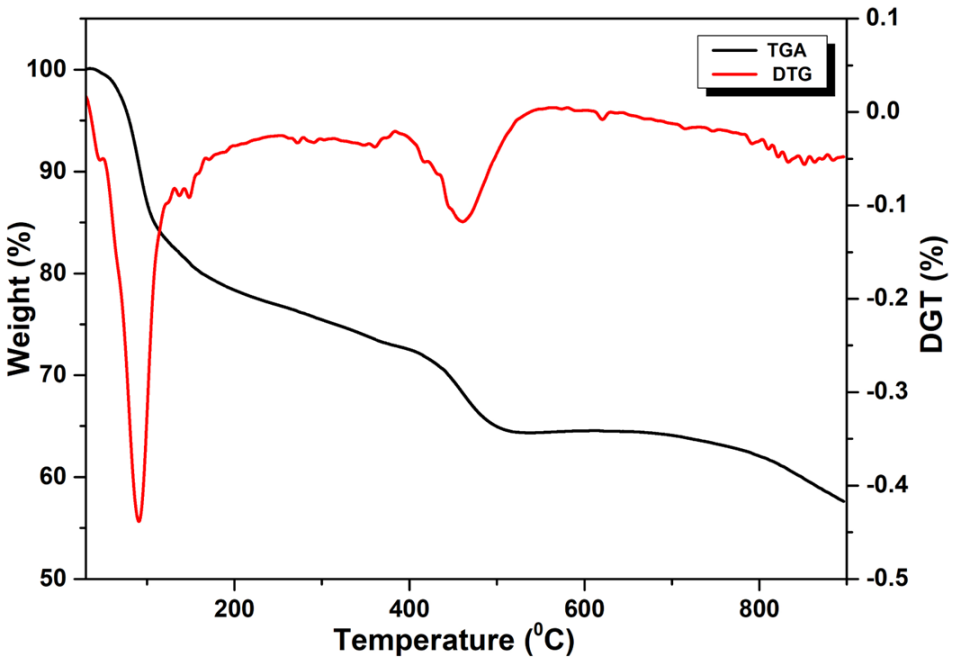


Figure 3.8 TGA (black trace) and DTG (red trace) of Ni-BIRM-1.

After heating, the material left in the crucible was identified by powder XRD as a mixture of $Zn_2P_2O_7$[323] with a small amount of Ni_2P[324] (Table 3.5). The CIF files of these compounds were then obtained from ICSD database and used as starting models for quantitative phase analysis.

Quantitative phase analysis (Figure 3.9) was carried out through Rietveld refinement of the structures in GSAS2.[325] The background was refined using a Chebyshev polynomial with 9 variables. Subsequently, unit cell, thermal and instrumental parameters were refined individually until minimum acceptable weighted profile factor (R_{wp}) and goodness of fit (χ^2) were obtained. More information on Rietveld refinement including unit cell parameters, occupancies and atomic positions is shown in the Chapter 9, table A3.8 to A3.10. The result obtained suggested that the molar ratio of Zn:P:Ni is about 1:0.96:0.48 which is broadly consistent with the EDX results. The possible explanation for the small discrepancy is that, during the heating process, an amorphous or poorly crystalline nickel compound may form, which would not contribute to diffraction peaks, and therefore not determined by the Rietveld quantification formula.

Table 3.5 Quantitative phase analysis results.

Phases	Weight percentage (%)
$Zn_2P_2O_7$	90.40
Ni_2P	9.60

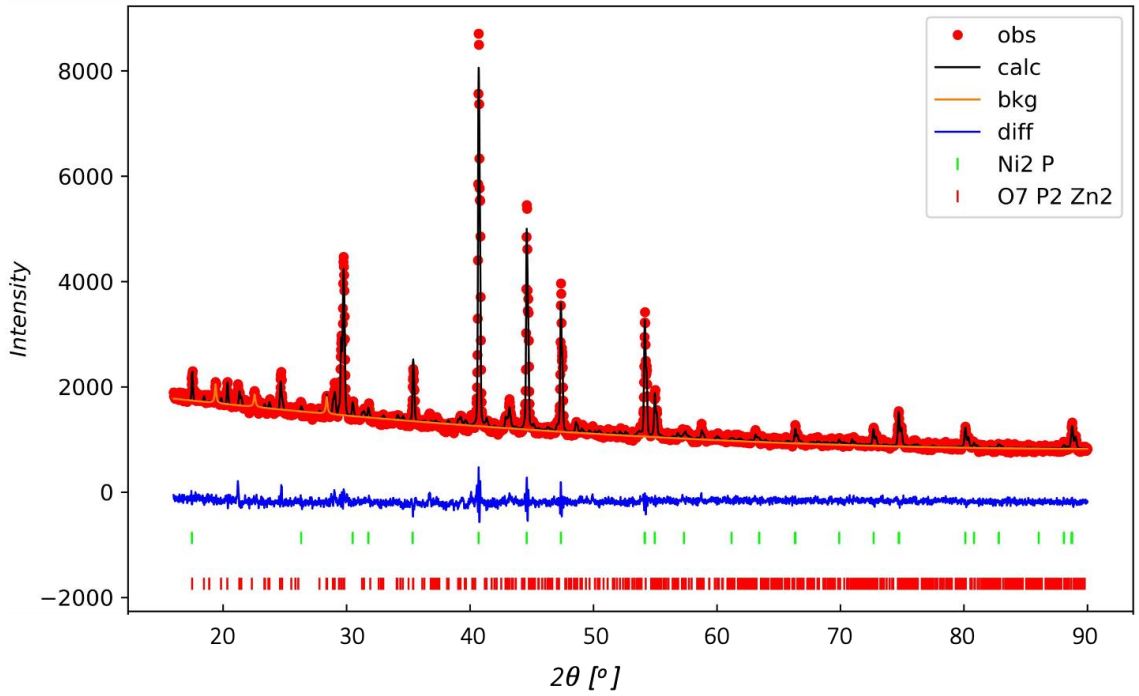


Figure 3.9. Final observed (red dot), calculated (solid line, black), difference (blue) and reflection positions [green top lines indicate peaks from Ni_2P, and red lower lines indicate peaks from $Zn_2P_2O_7$] for the final Rietveld refinements against powder XRD data for nickel ion-exchanged BIRM-1 TGA products, R_{wp} = 3.94 %, GoF = 1.40 %.

3.3.6. Porosimetry measurement

One of the shortcomings of BIRM-1 and some of its ion exchanged products is the loss of its long-range ordering when attempting to evacuate the water molecules present in the channels. For Ni^{2+}-BIRM-1, crystallographic information has revealed that all the ammonium ions present in the pores and channels of BIRM-1 were fully exchanged with nickel ions, leaving only uncoordinated water in the structure and can be potentially dehydrated without the structure collapsing. Based on this evidence, nitrogen adsorption-desorption isotherms (Figure 3.10) were recorded to access the porosity and surface area of this material. The result indicated that the isotherm takes the shape of a reversible type III isotherm which is typical for macroporous material[326]. It can also be observed that the isotherms follow the same path ascribed to unrestricted multilayer adsorption. The surface area of Ni^{2+}-BIRM-1 based on the

Brunauer–Emmett–Teller (BET) analysis was estimated to be 75 m^2/g which suggested that the material showed little or no porosity.

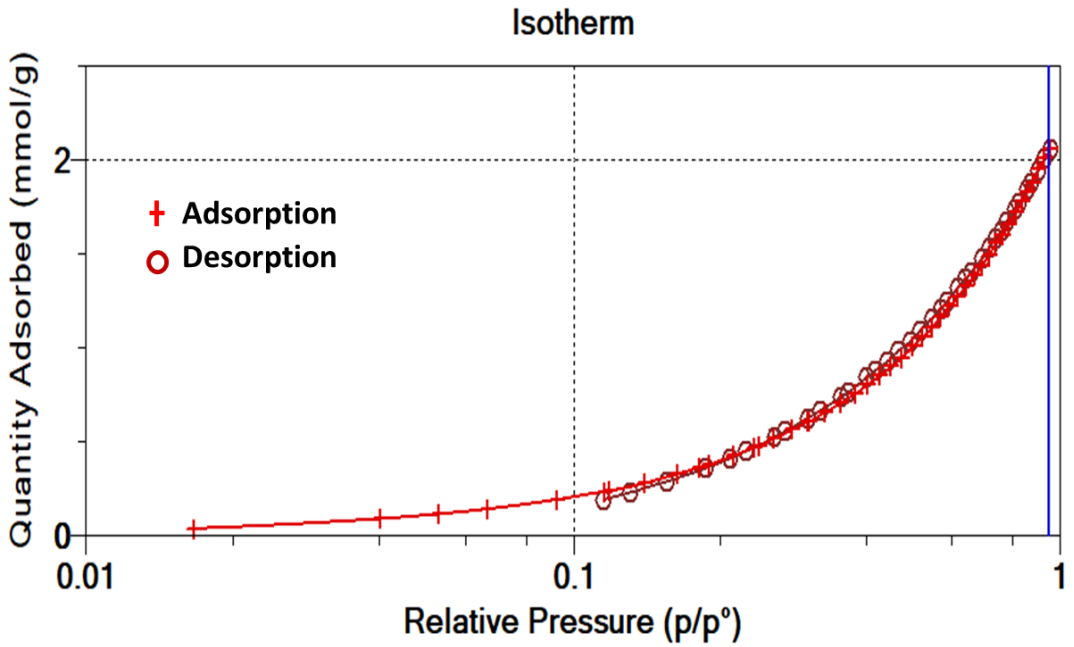


Figure 3.10. N_2 adsorption isotherms by the BET analysis of the Ni^{2+}-BIRM-1.

3.4. Electrochemical characterization toward CO_2 reduction

Since nickel ions present in the Ni^{2+}-BIRM-1 framework can potentially act as active sites for catalysis, its electrochemical activities toward CO_2 reduction reaction were explored. To examine its electrocatalytic performance, cyclic voltammetry of the Ni^{2+}-BIRM-1 catalyst supported on a glass carbon electrode (GCE) was performed in 0.1 M carbonate buffer (pH 9.2) electrolyte. The catalyst ink was prepared by dispersing 30 mg of the catalyst in 950 µL of ultrapure water containing 50 µL of Nafion solution (5 % in ethanol) and ultrasonically treated for 10 min, then drop-cast on glassy carbon substrate and dried in a fan oven at 60 °C. A three-electrode cell configuration comprising a GCE with the drop-cast catalyst as a working electrode, a high-surface area gold flag as a counter electrode and Hg/HgO (1.0 M KOH) as reference electrode, was used. Cyclic voltammetry (CV) experiments were performed using a

PGSTAT302N system (Metrohm Autolab B. V.,Utrecht, Netherlands). Before measurement, the electrolyte was degassed by bubbling with argon for at least 30 min for removal of oxygen, and then purged continuously with CO_2. All CV measurements were conducted from 1.4 to -1.2 V (*vs* Hg/HgO) at a scan rate of 50 mV s^{-1} in 0.1 M carbonate buffer (pH ~9.2) electrolyte produced from $NaHCO_3$ (Acros Organics, >98%) and Na_2CO_3 (Sigma, ≥99%). The catalytic activity of the electrocatalyst were normalized to current per milligram mass of the nickel active sites in the electrocatalyst. All potentials collected were subsequently calibrated to the reversible hydrogen electrode (RHE) according to the equation: $E_{RHE} = E_{Hg/HgO} + 0.098 + 0.0591 \times pH$.

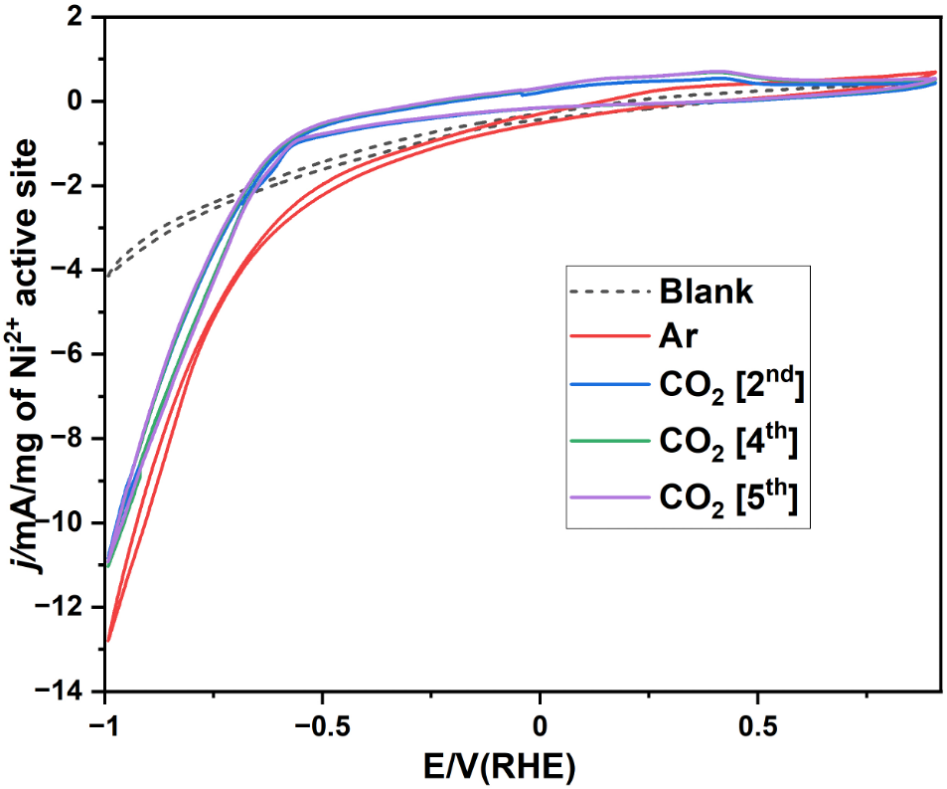


Figure 3.11. CV scan of Ni^{2+}-BIRM-1 recorded at 50 mVs^{-1} in CO_2-saturated 0.1M carbonate buffer (pH ~9.2) electrolyte at different potential ranges.

As observed in Figure 3.11, the voltametric profile of Ni^{2+}-BIRM-1 catalyst in the absence of CO_2 showed no visible cathodic current peak during forward sweep. Conversely, when the solution was saturated with CO_2, a current wave was observed in the cathodic scan at *ca.* 0.4 V (*vs*. RHE) during forward sweep and this peak can be attributed to oxidation of $Ni^{(0)}$ atom to $Ni^{(II)}$. This was followed by rapid increase in current between -0.4 V to -1.0 V which is associated with the competitive CO_2 reduction reaction and hydrogen evolution reaction. It can be observed from the cyclic voltammetry profile that there is little or negligible CO_2RR activities taking place. There are myriad reasons that could be responsible for lack of CO_2 reduction activities. It may be that nickel is completely buried inside the BIRM-1 framework, making it difficult to receive electrical signal. Another possibility is that nickel might have gone into the electrolyte in exchange for sodium or the amount of nickel in Ni^{2+}-BIRM-1 material immobilized on GCE is not sufficient to give a redox signal.

It is envisaged that if the Ni^{2+}-BIRM-1 can be pyrolysed, the nickel active site may be exposed with the possibility of obtaining a nickel single atom catalyst which can be active toward CO_2 reduction. However, upon pyrolysis at 900^0C for 2hrs under N_2 at a rate of $5^oC/min^{-1}$ and examination of its electrocatalytic performance, the cyclic voltametric profile of the material did not show any significant CO_2 reduction activity (Figure 3.12). It is therefore concluded that Ni^{2+}-BIRM-1 is not electrically active toward CO_2 reduction reaction.

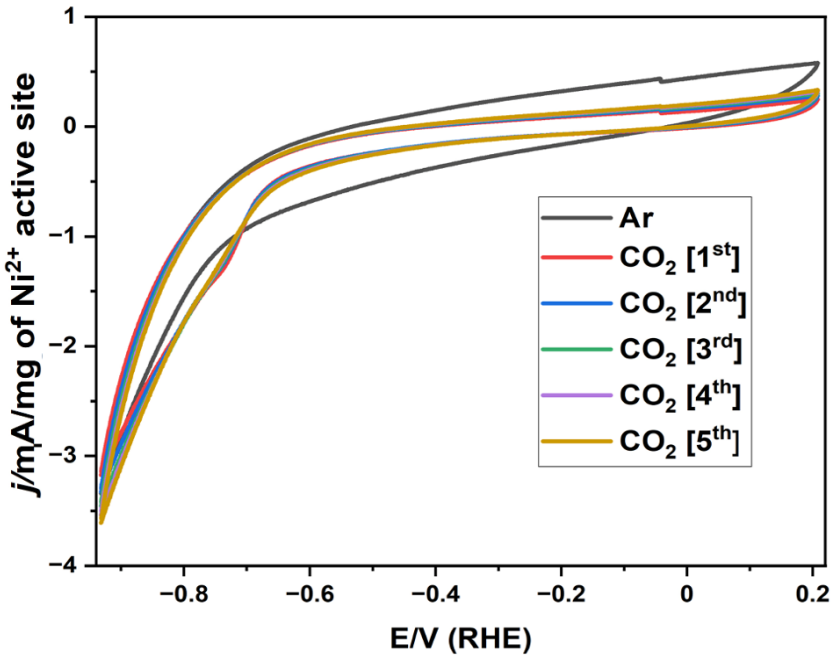


Figure 3.12. CV scan of pyrolysed Ni^{2+}-BIRM-1 recorded at 50 mVs^{-1} in Ar/CO_2-saturated 0.1 M $NaHCO_3$/$NaCO_3$ buffer solution.

3.5. Conclusion

In this chapter, nickel (II) cations have been shown to incorporate into BIRM-1 via ion exchange experiments. Preliminary characterization with powder XRD and SEM indicates that the crystallinity of BIRM-1 was preserved after 24 hours of ion exchange. Additionally, the extent of nickel exchange was probed by calculating the molar ratio from the result of the elemental composition of Ni^{2+}-BIRM-1 obtained from SEM-EDX. The result shown that the calculated molar ratio agreed with the expected molar ratio, indicating that the ion exchange was roughly 100 %. Also, upon solution of the crystal structure, it was revealed that the crystallographic properties of Ni^{2+}-BIRM-1 tallied with those of BIRM-1, with no ammonium cations present in the pores and channels of Ni^{2+}-BIRM-1, indicating structure preservation and full ion exchange. However, the porosimetry measurement showed that the BET surface area of Ni^{2+}-BIRM-1 was estimated to be 75 m^2/g suggesting that the material showed little

or no porosity. The electrochemical activity of Ni^{2+}-BIRM-1 toward CO_2 reduction was also explored. The cyclic voltametric results showed that Ni^{2+}-BIRM-1 catalyst is not electrochemically active towards CO_2 reduction reaction. The future direction in this work is to explore other experimental methods to dehydrate the water present in the framework of Ni^{2+}-BIRM-1 in order to achieve a structure with permanent porosity which is the key feature for most MOF applications.

CHAPTER FOUR

Synthesis, crystal structures and CO_2 reduction potential of some 2D-layered metal carboxyphosphonates

4.1. Introduction

In chapter 3 the ion exchange potential of BIRM-1 was exploited to incorporate nickel metal which can be potential electrocatalysts for CO_2 reduction. The incorporation of Ni^{2+} cations showed that the framework of BIRM-1 retained its structure after the ion exchange. However, the exploration of Ni^{2+}-BIRM-1 as an electrocatalyst showed that the catalyst is electrochemically active towards the hydrogen evolution reaction while showing little or no activity toward the CO_2 reduction reaction.

Previously, efforts have been made to achieve permanent porosity in BIRM-1 and as well attempted synthesis of MOFs that are isostructural to BIRM-1. While previous attempts adopted almost the same protocol used for the synthesis of BIRM-1, we initiated exploratory synthesis by first modifying the BIRM-1 synthesis protocol and thereafter attempted a new synthesis strategy with the goal of obtaining new functional 3D carboxylphosphonate framework materials. The carboxylphosphonate ligand used in this synthesis is again 3-phosphonopropionic acid (Figure 4.1).

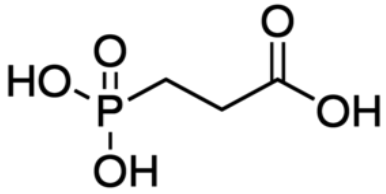


Figure 4.1. Chemical structure of 3-phosphonopropionic acid, the linker used in this work.

4.2. Experimental

4.2.1. Solvothermal synthesis of Zn framework

Since BIRM-1 has not yet been shown to possess permanent porosity as several efforts to evacuate the material resulted in the collapse of the framework, it was decided to explore different synthesis strategies with the possibility of obtaining MOFs with permanent porosity. We started by modifying the reaction conditions of BIRM-1. Water was first replaced with DMF as reaction solvent as it can serve a dual function and subsequently, solvent mixtures were attempted. Apart from being a reaction medium, DMF can protonate to dimethylammonium ions at high temperature and become coordinated to the structure with the possibility of directing the dimensionality of the structure.[272 327] As a result, a series of experiments (Table 4.1) was set up to examine a broad range of variables and their effect on the synthesis outcome in order to identify any conditions that may lead to novel materials. After several trials, methods I – III gave a crystalline powder. Methods IV – VIII produced a mixture of crystals and crystalline powder, and a single crystal was picked from the mixture of phases for structure characterisation. However, the crystals were weakly diffracting and as such, full characterisation could not be carried out. As for methods IX-XII, a mixture of phases was also obtained, however, a well diffracting crystal, suitable for structure characterisation was obtained with method XII. The sample was submitted to the School of Chemistry's single crystal diffraction facility for structural characterisation. This material will now be named BIRM-11.

Table 4.1 List of experimental conditions used in search of novel materials.

Method	$Zn(NO_3)_2 \cdot 6H_2O$	3-phosphonopropionic acid	Solvent/Solvent mixture	Heating
I	0.2 mmol	0.1 mmol	DMF (10 mL)	80°C/24 h
II	0.2 mmol	0.1 mmol	DMF (10 mL)	80°C/48 h
III	0.2 mmol	0.1 mmol	DMF (10 mL)	80°C/72 h
IV	0.2 mmol	0.1 mmol	DMF (10 mL)	80°C/96 h
V	0.2 mmol	0.1 mmol	DMF (7mL)/H_2O (3 mL)	80°C/24 h
VI	0.2 mmol	0.1 mmol	DMF (7 mL)/H_2O (3 mL)	80°C/48 h
VII	0.2 mmol	0.1 mmol	DMF (7 mL)/H_2O (3 mL)	80°C/72 h
VIII	0.2 mmol	0.1 mmol	DMF (7 mL)/H_2O (3 mL)	80°C/96 h
IX	0.2 mmol	0.1 mmol	DMF (5 mL)/H_2O (3 mL)/EOH (2 mL)	80°C/24 h
X	0.2 mmol	0.1 mmol	DMF (5 mL)/H_2O (3 mL)/EOH (2 mL)	80°C/48 h
XI	0.2 mmol	0.1 mmol	DMF (5 mL)/H_2O (3 mL)/EOH (2 mL)	80°C/72 h
XII	0.2 mmol	0.1 mmol	DMF (5 mL)/H_2O (3 mL)/EOH (2 mL)	80°C/96 h

4.2.2. Crystal structure of BIRM-11 $[Zn_3(O_3PCH_2CH_2COO)_2]$

BIRM-11 crystalized in the monoclinic space group $P2_1/c$ (Table 4.2). More extensive crystallographic information is given in Chapter 9 Table A4.1. The asymmetric unit comprises of three Zn (II) cations and two $(O_3PCH_2CH_2COO)^{3-}$ anions (Figure 4.2). All the three Zn (II) cations are coordinated to the phosphonic oxygen at O2 and O3, with Zn1 exhibiting octahedral geometry and the remaining two Zn (II) cations (Zn2) featuring tetrahedral geometry (Figure 4.3a). One of the Zn2 is bridged by two phosphonate oxygens at O2 and O3. The Zn-O bond distances range from 1.933(4) to 2.260(4) (see Chapter 9 Table A4.4). The $[ZnO_6]/[ZnO_4]$ polyhedral and $[CPO_3]$ tetrahedral were alternately connected to form a 1-dimensional chain in which two adjacent chains are bridged by phosphonate ligands to form a 2D pillared layered framework in the xz plane (Figure 4.3b). Complete deprotonation of the carboxylphosphonate ligand was achieved in BIRM-11, with the all phosphonic and carboxylic oxygen covalently bonded to the Zn metal, making the crystal structure of BIRM-11 to be described as a 2D metal organic framework (MOF). It is envisaged that by tuning other

synthetic parameters such as temperature, molar ratio etc., higher dimensionality (3D) compounds may be achieved. However, several modification and optimization of the synthesis condition did not yield suitable crystal for structure characterization.

Table 4.2 Crystallographic data for BIRM-11.

Sample	BIRM-11
Formula	$Zn_3(O_3PCH_2CH_2COO)_2$
Formula weight	498.17
Space group	$P2_1/c$
a (Å)	8.0779(8)
b (Å)	9.1238(7)
c (Å)	8.8421(9)
Volume($Å^3$)	631.92(11)
Goodness-of-fit on F2	0.913
wR2	0.1110
Largest diff. peak/hole / e $Å^{-3}$	1.07/-0.61

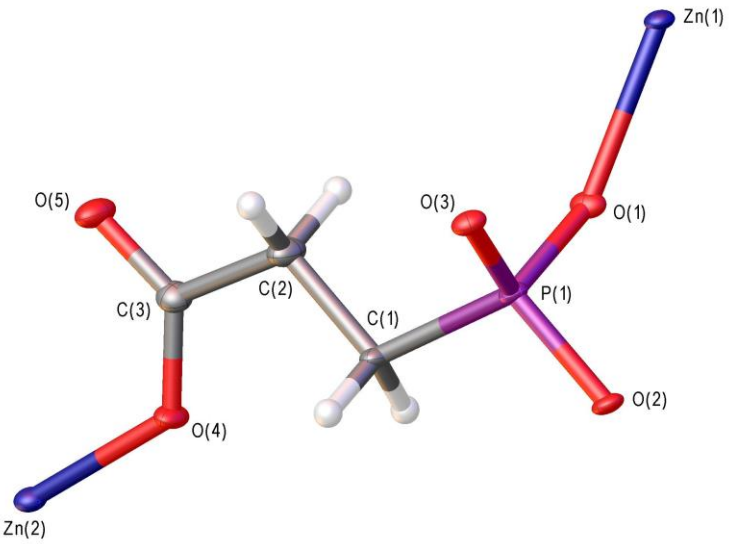


Figure 4.2. Asymmetric unit of BIRM-11. The thermal ellipsoids are drawn at the 50% probability level.

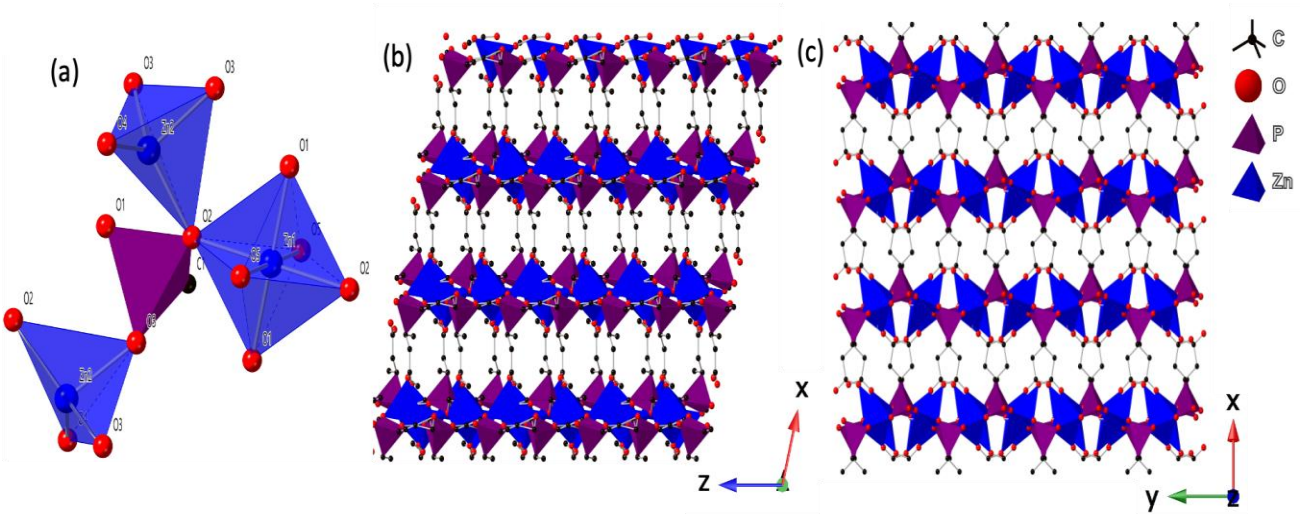


Figure 4.3. Coordination network of the inorganic building block (a), Layer structure of BIRM-11 viewed in xz-plane (b) and xy-plane (c).

4.2.3. FTIR studies of BIRM-11

The FTIR spectrum of BIRM-11 was recorded to obtain some additional crystallochemical information (Figure 4.4, Table 4.3). The FTIR spectra of some metal phosphonates from the previous work of Hix et al.,[95, 328] and Zhao et al.,[90] were used as a guide to assign various functional groups in BIRM-11 and other subsequent materials. A weak band at 3441 cm^{-1} indicates O-H stretching vibration from water molecules; however, this is likely to be water absorbed in the sample as there are no water molecules present in the solved structure. Also, the stretching vibrations observed at the 1592–1539 cm^{-1} are attributed to the carbonyl functional groups while the P=O and P−C stretching derived from the phosphonate functional group has been linked to the spectral bands at 1392 and 1330 cm^{-1}, respectively.[95, 329] The several sharp observed peaks in the region of 1073–470 cm^{-1} are present due to the ν(P–O) and ν(Zn–O) bond stretching vibration modes.[329] It can therefore be concluded that all the characteristic bands of functional groups present in the solved structure are revealed by FTIR result.

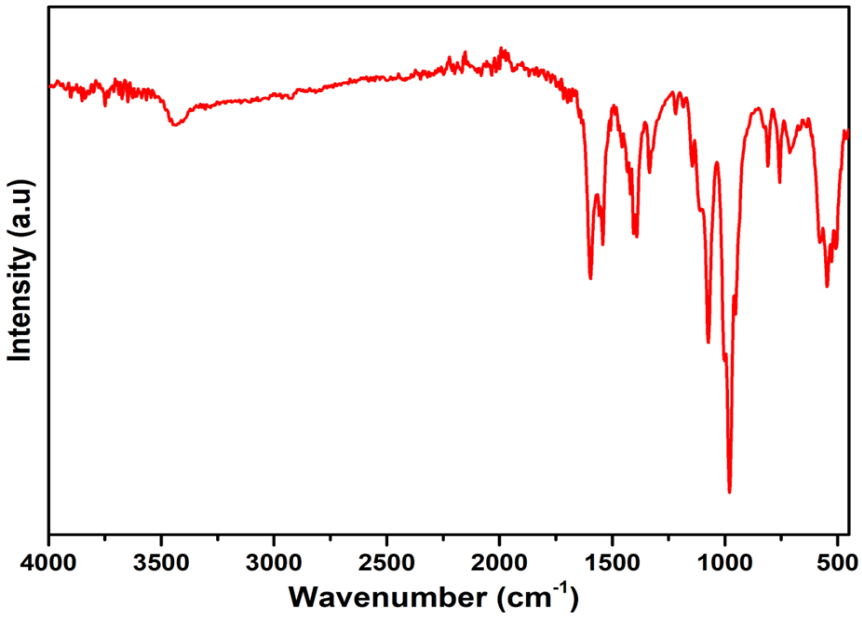


Figure 4.4. FTIR spectrum for BIRM-11.

Table 4.3 Observed FTIR shifts and assignments for BIRM-11.

Wavenumber (cm^{-1})	Peak Assignment
3441	Absorbed H_2O (O–H)
1592	Carboxylate C=O
1539	Carboxylate C–O
1392	Phosphonate P=O
1330	Phosphonate P–C
1073	Phosphonate P–O
980	Phosphonate P–O
<980	Zn-O

4.2.4. Morphology of BIRM-11

Figure 4.5 is an SEM image of BIRM-11 at 1000× magnification. The image shows that BIRM-11 can be identified as plate-shaped crystals, with each plate stacking over each other. EDX analysis found an average Zn:P ratio of 1.5:1 which is in agreement with the Zn:P ratio found in the solved structure (1.5:1).

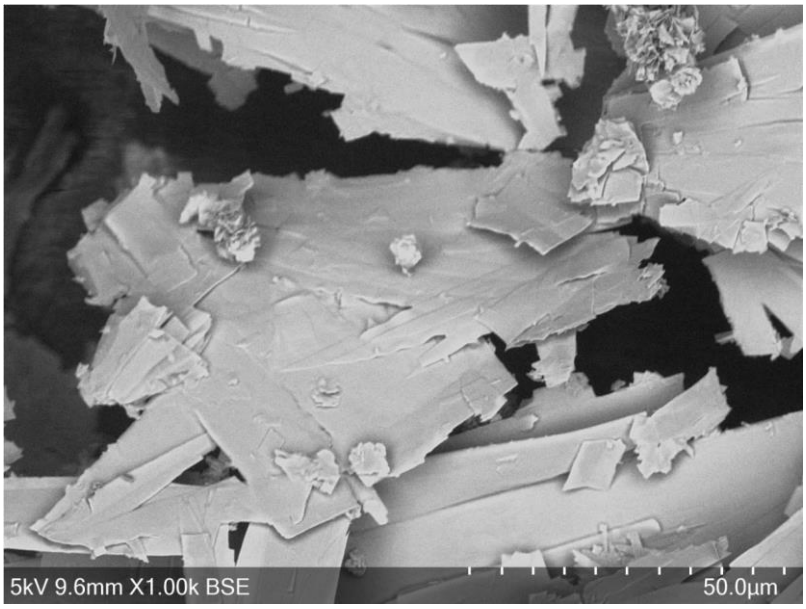


Figure 4.5. SEM image for BIRM-11 crystals.

4.2.5. Thermal stability of BIRM-11

Thermal stability of BIRM-11 was examined by thermogravimetry (TGA) and differential thermogravimetric analysis (DTG) (Figure 4.6). As soon as the heating began, physisorbed water in the system began to desorb, and at the range of 50 °C to 100 °C, a total weight loss of about 7.5% was observed. The DTG curve confirms this result and shows an endothermic event with a sharp peak at temperature of 94 °C. Above this temperature, the product showed a nearly continuous weight loss without a clear step, with a 5 % weight loss obtained at 480 °C. At a temperature range of 480–580 °C, BIRM-11 underwent another weight loss of 7.7% which can be attributed to the decomposition of the framework. As seen from the DTG curve, there is a corresponding broad endothermic peak at a maximum temperature of 500 °C. The DTG curve shows no notable change above this temperature range, which agrees with no significant weight loss in the TGA curve at higher temperatures.

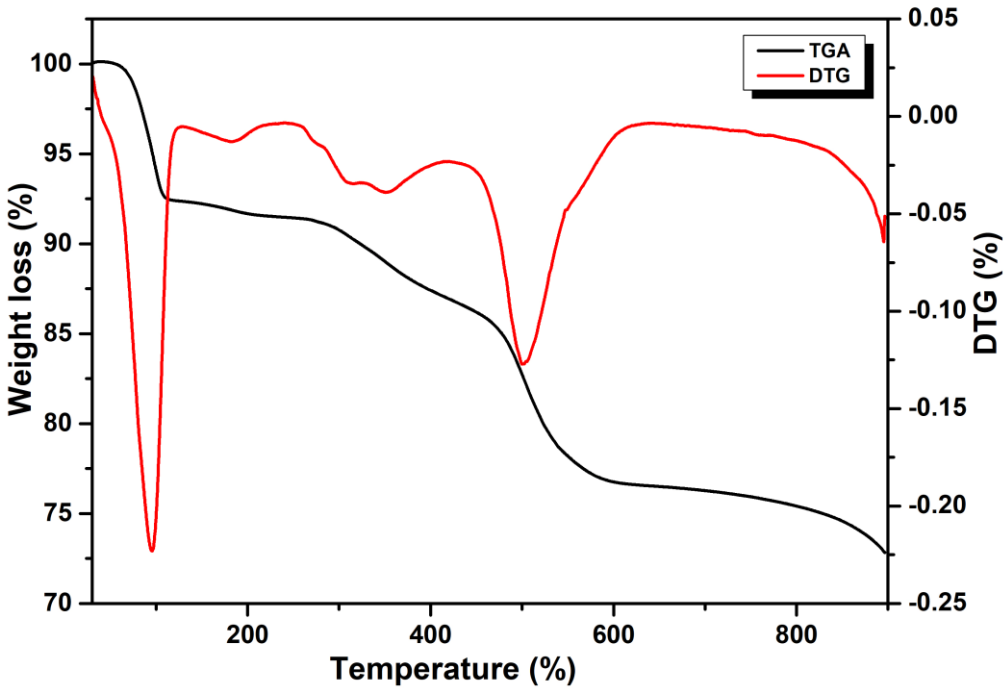


Figure 4.6. TGA (black trace) and DTG (red trace) of BIRM-11.

4.3. Room temperature synthesis of Cu framework

As zinc is not known to be active as an electrocatalysts for CO_2 reduction, an initial attempt at synthesising a novel copper-based framework using 3-phosphonopropinoic acid was conducted using a room temperature approach, otherwise known as the classic evaporative crystallisation method.[272, 330] This method involves preparing a precursor solution of metal salt and linker, adjusting the solution to appropriate pH and then leaving it in the open air for the solvent to evaporate, leaving the product behind. We started this synthesis with copper as node, 3-phosphonopropinoic acid as linker, NaOH as pH adjuster and water as solvent. All reagents used for this work were sourced from Sigma-Aldrich. The synthesis started by dissolving the quantities of reagents in Table 4.4 in 5mL of distilled water, adjusted to pH 3 with 2M NaOH. The solution was left in a beaker at room temperature for 4 days after which blue block crystals were obtained (Figure 4.7). The sample was submitted to the School of

Chemistry's single crystal diffraction facility for structural characterisation. This material will now be named BIRM-12.

Table 4.4 Quantities of reagents used in the initial synthesis attempt of a Cu framework material.

	$Cu(CO_2CH_3)_2.H_2O$	3-phosphonopropionic acid
Mass (g)	0.02	0.02
Molar ratio	1	1.2



Figure 4.7. Optical photography of BIRM-12 crystals.

4.3.1. Crystal structure of BIRM-12 [$Cu(O_3PC_2H_4COOH)(H_2O)_2$]

From the single crystal XRD analysis, BIRM-12 is found to crystalize in orthorhombic space group Pbca (Table 4.5, Chapter 9 Table A4.6). Each asymmetric unit comprises of one crystallographically independent Cu (II) cation, one $(O_3PCH_2CH_2COOH)^{2-}$ anion and two lattice water molecules (Figure 4.8). The Cu (II) cation exhibits a square planar geometry with the four planar vertices occupied by three phosphonate oxygen atoms (O1, O2 and O3) from three separate $(O_3PCH_2CH_2COOH)^{2-}$ anions and one oxygen atom (O6) from one of the lattice waters (Figure 4.9). The remaining apical position in the basal plane was occupied by second lattice water oxygen. The Cu-O bond distances ranged from 1.9410(17) to 2.2896(17) (Chapter 9

Table A4.9) which are similar to those reported previously for Cu(II) carboxyphosphonates.[331] The [CuO_5] square pyramidal basal planes were interconnected via [CPO_3] tetrahedra, forming a 1-dimensional chain along the y-axis and z-axis. These inorganic layers are hydrogen bonded via the carboxylic oxygen of the carboxylphosphonate ligand, giving rise to a layered structure in the xy and xz planes (Figure 4.10). As can be observed in Figure 4.11, no significant additional diffraction peaks other than those present in the simulated pattern were present in the powder pattern, indicating that BIRM-12 constitutes the only phase present in the BIRM-12 crystal sample.

Table 4.5 Crystallographic data for BIRM-12.

Sample	BIRM-12
Formula	$Cu(O_3PC_2H_4COOH)\ (H_2O)_2$
Formula weight	251.61
Space group	Pbca
a (Å)	20.9797(17)
b (Å)	8.0859(7)
c (Å)	9.1604(8)
Volume($Å^3$)	1554.0(2)
Goodness-of-fit on F2	1.046
wR2	0.0784
Largest diff. peak/hole / e $Å^{-3}$	0.59/-0.45

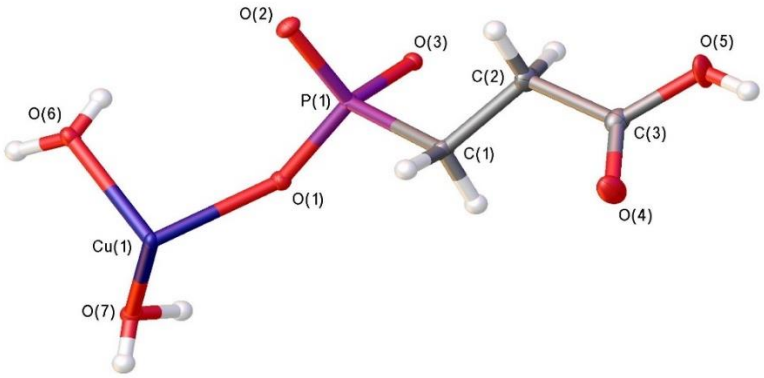


Figure 4.8. Asymmetric unit of BIRM-12. The thermal ellipsoids are drawn at the 50% probability level.

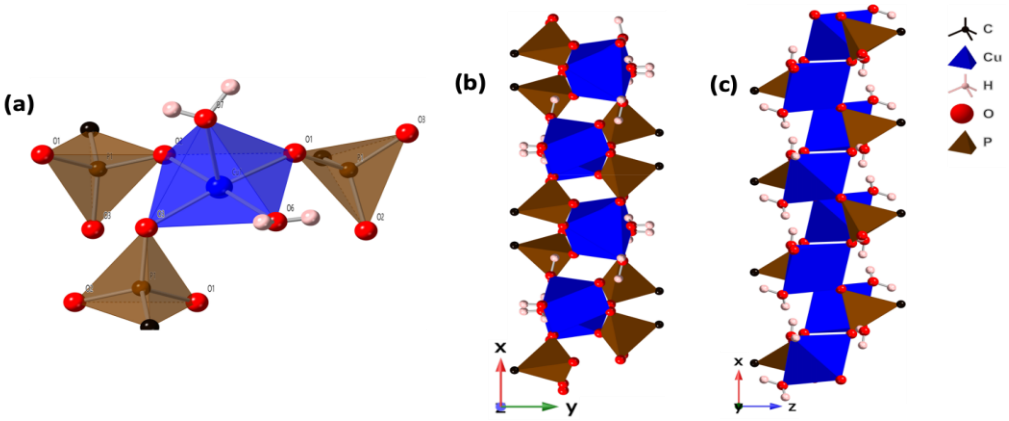


Figure 4.9. (a) Coordination network and one-dimensional chain of the inorganic building block of BIRM-12 viewed in (b) xy-plane and (c) xz-plane.

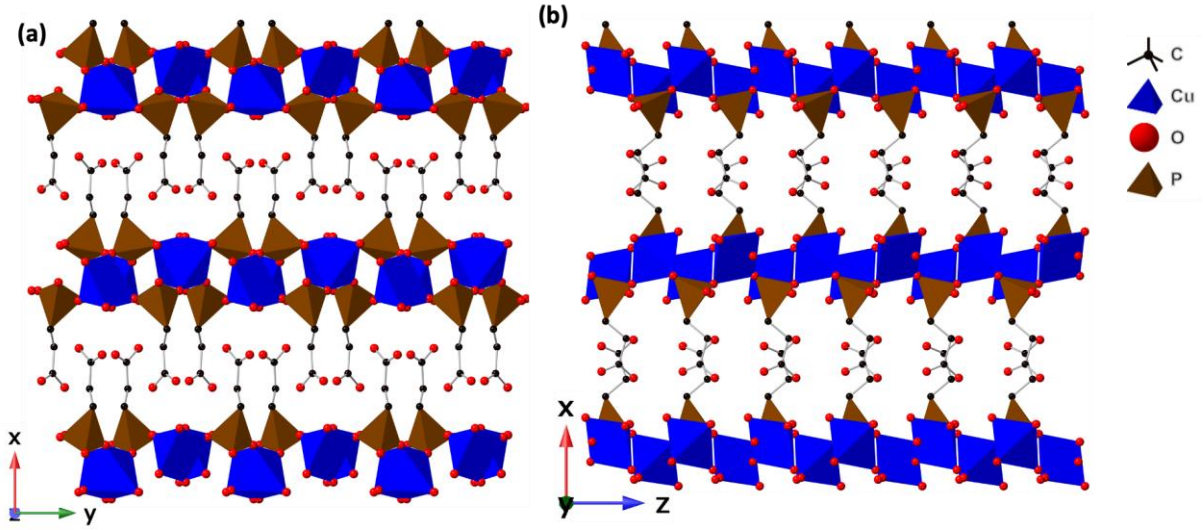


Figure 4.10. Layered structure of BIRM-12 viewed in (b) xy-plane and (c) xz-plane.

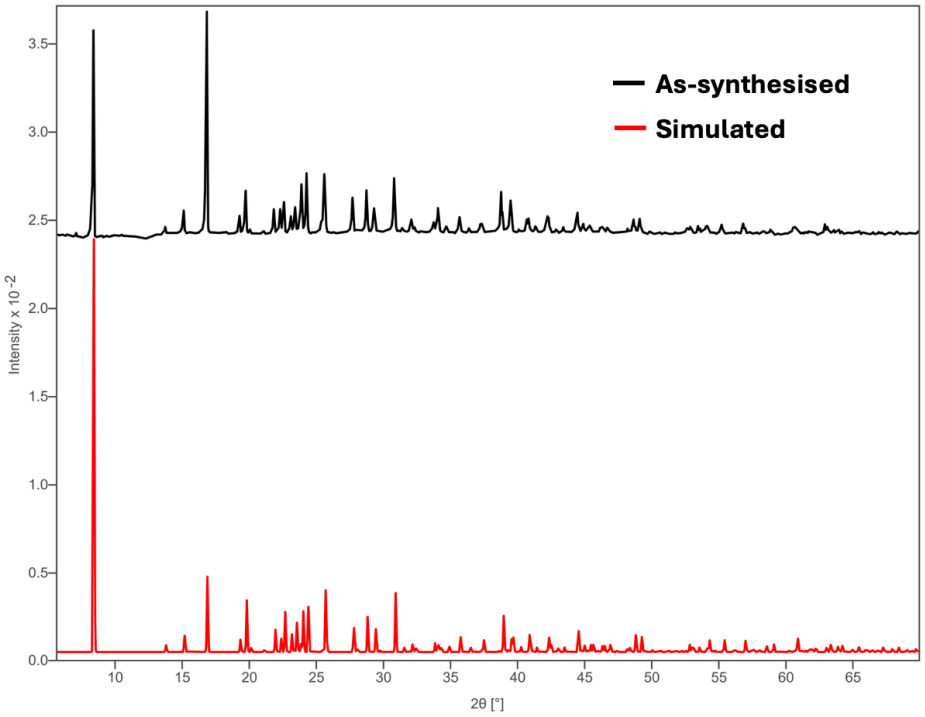


Figure 4.11 As-synthesised (black) and simulated (red) XRD pattern BIRM-12.

4.3.2. FTIR studies of BIRM-12

The FTIR spectrum of BIRM-12 is shown in figure 4.12 and Table 4.6. As expected, all peaks in this figure strongly supported the presence of all the functional group present in BIRM-12. A broad and weak peak found around 3037 cm^{-1} and sharp peak at 1684 cm^{-1} are due to stretching vibrations of O–H and bending vibration of H-O-H from the coordinated water molecules.[328] Visible at 1413 cm^{-1} and 1250 cm^{-1} are the absorption bands for the P=O and P-C stretching vibrations, while a number of sharp peaks observed in the range of 1047–955 cm^{-1} are the P–O stretching modes of phosphonate group[328]. The peaks in the region less than 990 cm^{-1} are consistent with the presence of Cu-O bonds.

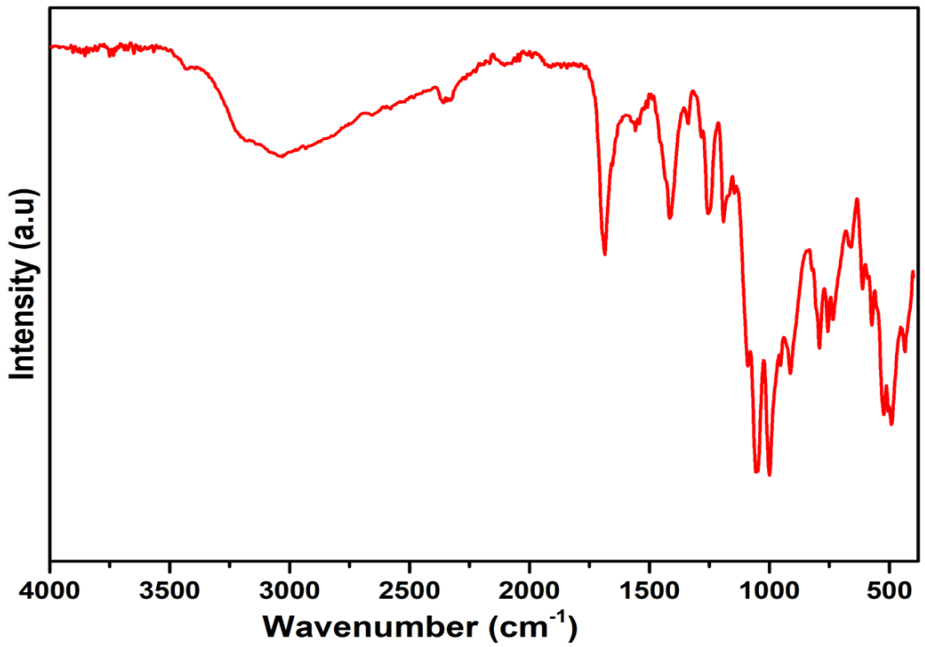


Figure 4.12. FTIR spectrum for BIRM-12.

Table 4.6. Observed FTIR shifts and assignments for BIRM-12.

Wavenumber (cm^{-1})	Peak Assignment
3326-2675	carboxylic acid O–H
1684	Water H-O-H (bending vibration)
1553	Carboxylate C-O
1413	Phosphonate P=O
1250	Phosphonate P-C
1047	Phosphonate P–O
993	Phosphonate P–O
<990	Cu-O

4.3.3. Morphology of BIRM-12

SEM images of BIRM-12 crystals (figure 4.13) were taken to determine their morphology. It can be observed from the SEM image shown that the crystals did not show any visible regular morphology. However, there are some agglomerated particles and white patches on the

surface of the BIRM-12 crystal, suggesting the presence of impurities which could be excess organic material or some other amorphous phase. EDX analysis was also performed on the sample, finding shows a phosphorus to copper ratio of 1:1.1, which is in reasonable agreement with the structure solved through single crystal diffraction (1:1).

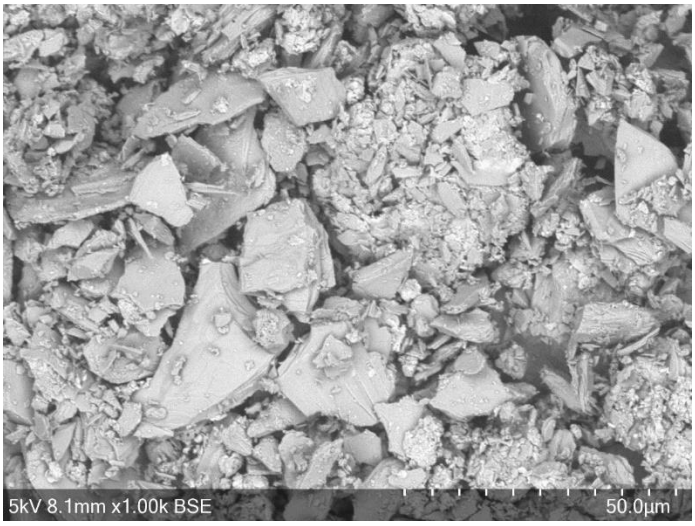


Figure 4.13. SEM image for BIRM-12 crystals.

4.3.4. Thermal stability of BIRM-12

Figure 4.14 shows the TGA and DTG curves for BIRM-12. The appearance of more than one peak in the DTG curve indicates that at least two stages are involved in the thermal degradation of the BIRM-12. The first weight loss (10.7%), between 100 °C and 264 °C, as shown by the TGA curve, corresponds to the desorption of lattice water from the BIRM-12 structure (Calcd. 14.3 %). The DTA curve confirms this result and shows an endothermic event with a broad peak at temperature of 136 °C. However, the second predominant stage is between 264 °C – 335 °C during which 29.9% of weight loss was observed and this correspond to a sharp endothermic DTG peak with a maximum temperature of 293 °C. This weight loss can be attributed to the combustion of the organic ligand and collapse of the framework structure. At higher temperature, the material continues to exhibit continuous weight loss

until the transformation was complete at about 900°C, resulting in a total weight loss of 68.6 % as evidence in the TGA and DTG curves.

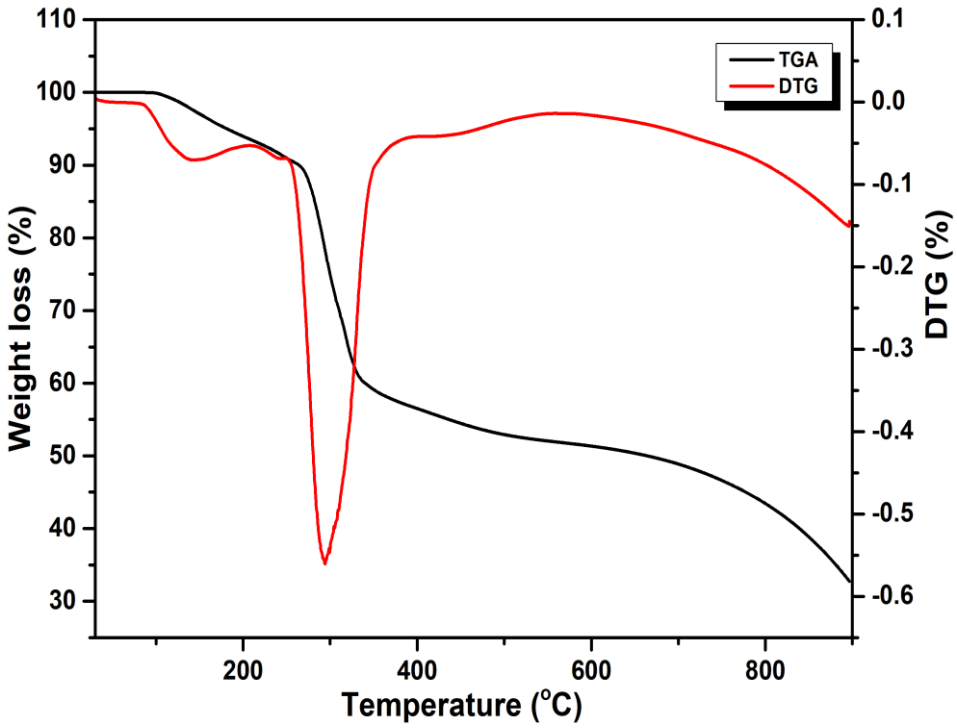


Figure 4.14. TGA (black trace) and DTG (red trace) of BIRM-12.

4.3.5. Electrochemical characterisation of BIRM-12

Copper-based MOFs have been demonstrated to show remarkable electrocatalytic activities toward CO_2 reduction, with potential for higher hydrocarbon production.[332, 333] The presence of copper in BIRM-12 as a potential catalyst active site, raises the possibility that it may be a potential electrocatalyst. Therefore, electrochemical characterisation of BIRM-12 was carried out in order to assess its potential application in CO_2 reduction. To examine the electrocatalytic performance, cyclic voltammetry of the BIRM-12 catalyst supported on a glassy carbon electrode (GCE) was performed in 0.1 M carbonate buffer (pH ~9.2) electrolyte. The catalyst ink was prepared by dispersing 30 mg of the catalyst in 950 µL of ultrapure water containing 50 µL of Nafion solution (5 % in ethanol) and ultrasonically treated for 10 min, then

drop-cast on a glassy carbon substrate and dried in a fan oven at 60 °C. A three-electrode cell configuration comprising a GCE with the drop-cast catalyst as a working electrode, gold sheet as a counter electrode and Hg/HgO (1.0 M KOH) as reference electrode, was used. Cyclic voltammetry (CV) experiments were performed using a PGSTAT302N system (Metrohm Autolab B. V.,Utrecht, Netherlands). Before measurement, the electrolyte was degassed by bubbling with argon for at least 30 min for removal of oxygen, and then purged continuously with CO_2. All CV measurements were conducted from -1.6 to 0.2 V (*vs* Hg/HgO) at a scan rate of 50 mV s^{-1} in 0.1 M carbonate buffer (pH ~9.2) electrolyte produced from $NaHCO_3$ (Acros Organics, >98%) and Na_2CO_3 (Sigma, ≥99%). The potential was opened as far as -1.0 V (RHE) to explore the reduction activities of the catalyst in respect to CO_2 reduction reaction. All potentials collected were subsequently calibrated to the reversible hydrogen electrode (RHE) according to the equation: $E_{RHE} = E_{Hg/HgO} + 0.098 + 0.0591 \times pH$. The result of the CV experiment is presented in figure 4.15 below and were normalized as current per mass (mg) loading of the copper active sites in the electrocatalyst.

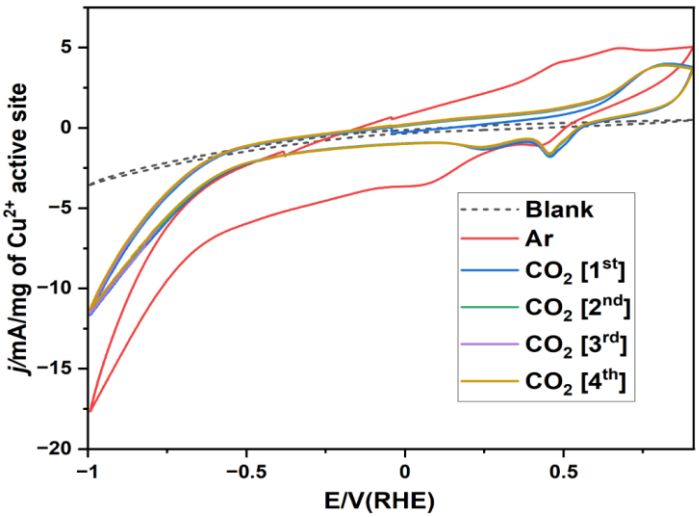


Figure 4.15. Cyclic voltammograms of blank GCE (dotted line) and catalyst in Ar-saturated. (red line) and CO_2-saturated (other colours) in 0.1 M $NaHCO_3/NaCO_3$ buffer solution; v = 50mV s^{-1}.

The resulting cyclic voltammogram in Ar-bubbled electrolyte (figure 4.15) shows distinct redox peak potentials at 0.68 and 0.44 V vs RHE, indicating the reversible oxidation and reduction of $Cu^{(II)}/Cu^{(I)}$.[208, 334, 335] Another reduction peak at 0.062 V vs RHE and corresponding oxidation peak at 0.49 V vs RHE indicate the redox couple of $Cu^{(0)}$ to $Cu^{(I)}$ and this is followed by a sharp current peak at -1.0 V vs RHE which is associated with the hydrogen evolution reaction. The large capacitance (hysteresis) can be linked to large resistance encountered during redox reaction in Ar-bubbled electrolyte. Furthermore, when the solution was saturated with CO_2, only one oxidation current wave was visible at 0.8 V vs RHE which corresponds to the oxidation of $Cu^{(0)}$ to $Cu^{(II)}$ while the reduction current waves at 0.46 V vs RHE and 0.25 V vs RHE represent the reduction of $Cu^{(II)/(I)}$ and $Cu^{(I)/(0)}$, respectively.[208] The increase in current between -0.50 V to -1.05 V is associated with the hydrogen evolution reaction. The difference in the current density between a glassy carbon electrode and the catalyst immobilized GCE electrode in Ar-bubbled electrolyte also supports the favourable activity of the catalyst toward HER. Additionally, there is difference in the current density of catalyst in Ar- and CO_2- bubbled electrolyte, however, this is not a sufficient proof of CO_2 reduction activities. Although CO_2 conversion may not have been achieved with this catalyst, its activity toward HER is interesting, as hydrogen fuel has been considered as clean fuel due to its high energy density and the fact that its combustion produces only water as "waste" product.[336, 337]

4.4. Hydrothermal synthesis of Cu framework

Several attempts have been made to use the hydrothermal synthesis protocol of BIRM-1[90] as a starting point, with the zinc nitrate substituted with Cu equivalent, aiming to synthesize MOFs that are isorecticular to BIRM-1. This effort did not yield any crystals; hence a new

synthesis strategy was adopted in this exploratory search for new MOF materials. We started this synthesis with copper as node, 3-phosphonopropionic acid as linker, NaOH as pH adjuster and water as solvent. The synthesis started by dissolving the quantities of reagents in Table 4.4 in 5mL of distilled water, adjusted to pH3 with 2M NaOH. The mixture was transferred into a Teflon-lined autoclave and placed in an oven at 80 °C for 24 h. After cooling to room temperature, there were no crystals obtained at this temperature. However, upon increasing the temperature to 100 °C, bluish yellow blocky crystals were obtained as a monophasic product (figure 4.16). The powder diffraction pattern of the material can be observed to have no significant peaks apart from those in the simulated pattern, confirming the monophasicity of the material (figure 4.19). The sample was submitted to the School of Chemistry's single crystal diffraction facility for structural characterisation. This material will now be referred to as BIRM-13.



Figure 4.16. Optical photography of BIRM-13 crystals.

4.4.1. Crystal structure of BIRM-13 [$Cu(O_3PC_2H_4COOH)$]

The crystallographic detail of the solved structure is presented in Table 4.7, with more extensive crystallographic information given in Chapter 9 Table A4.11. From the SCXRD data,

the BIRM-13 crystalized in monoclinic space group $P2_1/c$. The asymmetric unit of BIRM-13 comprises of a Cu (II) cation and $(O_3PCH_2CH_2COO)^{2-}$ anion (figure 4.17), with the Cu (II) cation exhibiting a trigonal bipyramidal geometry (figure 4.18a). As shown in figure 4.18a, the three phosphonic oxygens (O1, O2 and O3) are coordinated to Cu (II). The $[CuO_5]$ trigonal planes interconnect $[CPO_3]$ tetrahedra via corner sharing, forming a 1-dimensional chain along the y-axis (figure 4.18b). Two adjacent 1D chains are H-bonded via the carboxylic oxygen (O4 and O5) component of the 3-phosphonopropionic acid ligand, thereby giving rise to a layered compound (figure 4.18c). It is worth noting that the trigonal bipyramidal coordination geometry found in BIRM-13 represents an unusual property in its own right. Cu materials having tetrahedral, square planar and octahedra coordination geometry are prevalent in the literature[103, 338, 339], but trigonal bipyramidal coordination geometry is comparatively rare.[340, 341] The Cu-O bond distances range from 1.9097(16) to 2.1222(17) (chapter 9 Table A4.14) which are similar to those reported previously for Cu (II) carboxyphosphonates.[331]

Table 4.7 Crystallographic data for BIRM-13.

Sample	BIRM-13
Formula	$Cu(O_3PC_2H_4COOH)$
Formula weight	215.58
Space group	$P2_1/c$
a (Å)	14.4122(15)
b (Å)	5.6635(6)
c (Å)	7.5868(8)
Volume ($Å^3$)	610.06(11)
Goodness-of-fit on F2	1.140
wR2	0.0961
Largest diff. peak/hole / e $Å^{-3}$	0.66/-1.08

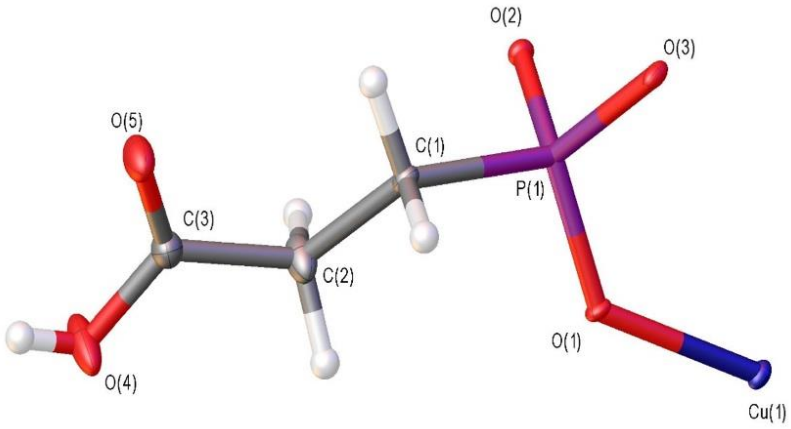


Figure 4.17. Asymmetric unit of BIRM-13. The thermal ellipsoids are drawn at the 50% probability level.

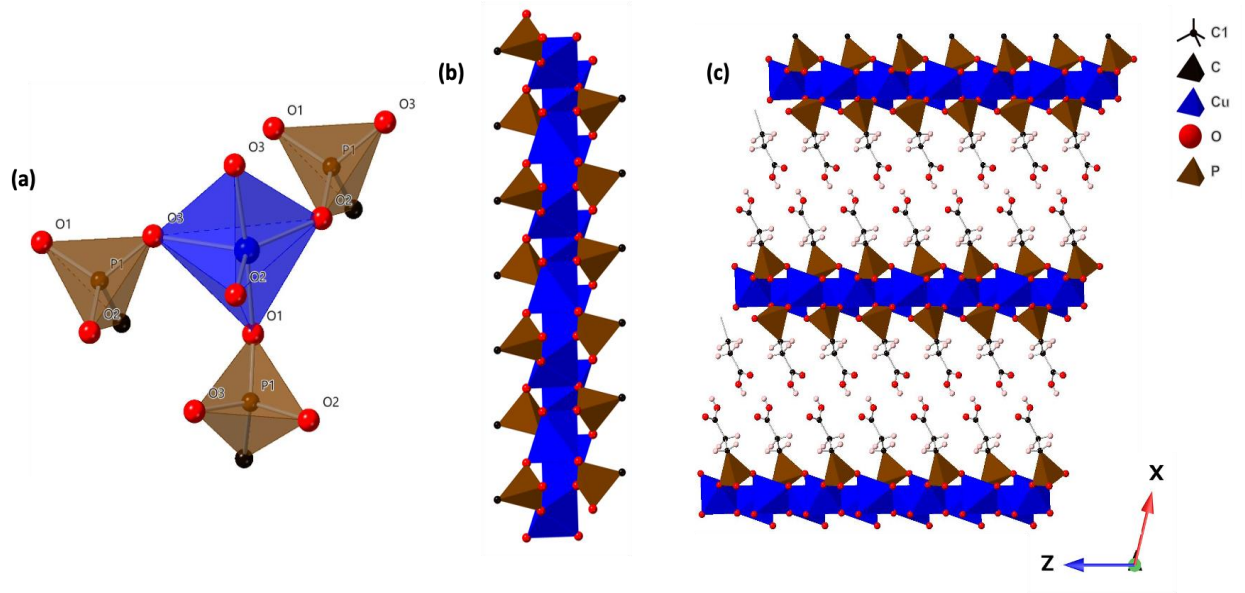


Figure 4.18. (a) Coordination geometry (b) one-dimensional chain of the inorganic building block (c) Layer structure of BIRM-13 viewed in xz-plane.

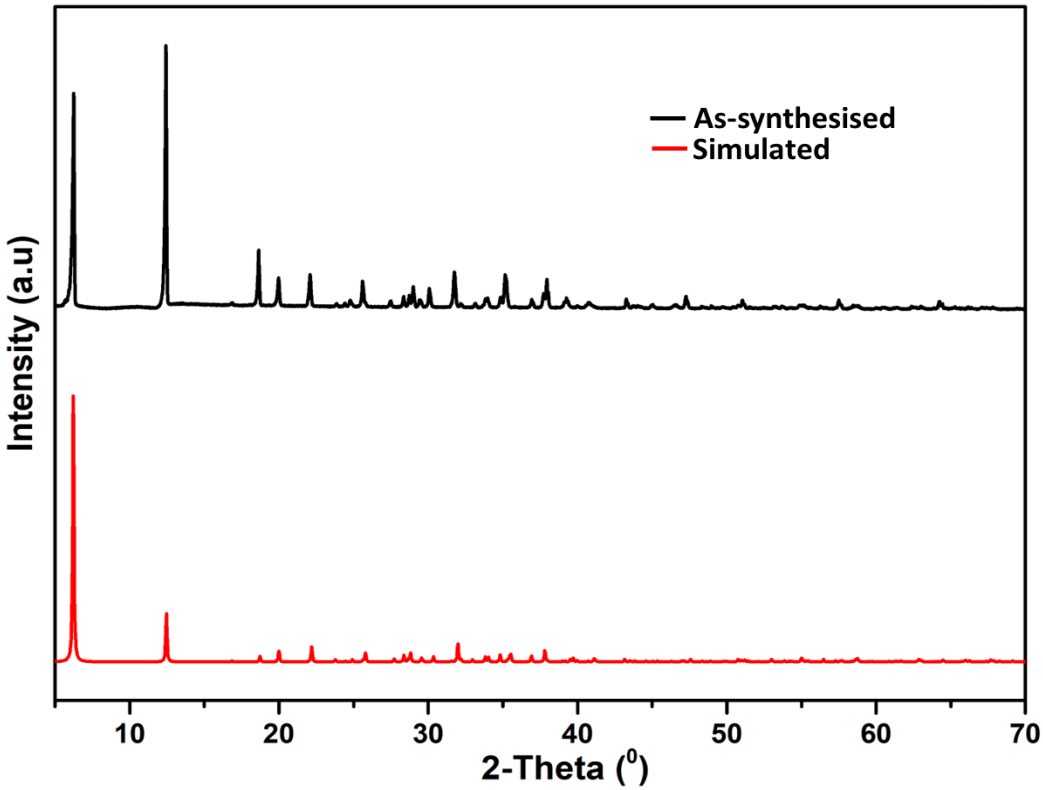


Figure 4.19. As-synthesised (black) and simulated (red) powder XRD pattern for BIRM-13.

4.4.2. Optimisation of the synthesis conditions

4.4.2.1. Adjusting the pH

Since an aim of this research work was to synthesise functional porous 3-dimensional MOFs, several attempts were made to optimize various reaction variables. Since the ligand in BIRM-13 does not completely deprotonate, this reduces the chance for the building blocks to self-assemble into a porous framework. Generally, pH plays a crucial role in the synthesis of metal carboxyphosphonate open frameworks.[342] For instance, synthesis at low pH results in deprotonation of only the phosphonic acid functional group while at higher pH, both carboxylic and phosphonic acid groups are deprotonated and bind to the metal.[343] Synthesis of BIRM-12 and BIRM-13 was only achieved at a low pH (≤3) as the solution precipitated upon attempt to adjust the pH higher than 3 with inorganic base. Under these conditions,

incomplete deprotonation of BIRM-12 and BIRM-13 resulted in formation of H-bonded layered structures.

4.4.2.2. Varying the temperature

Temperature can influence metal ligand orientation and induce crystal growth. So, the synthesis was attempted at a range of temperatures from 110-180°C to see if this would affect the growth of crystals (figure 4.20). The syntheses conducted at 110 and 120 °C yielded the same monophasic product as the initial synthesis. However, as the temperature increased further (130-160 °C), a mixture of bluish yellow blocky crystals and blue crystalline powder emerged, giving rise to different peaks in the corresponding powder diffraction patterns. A blue crystalline powder was obtained alone at temperatures above 160 °C, yielding mixture of unknown phases with different peak shape.

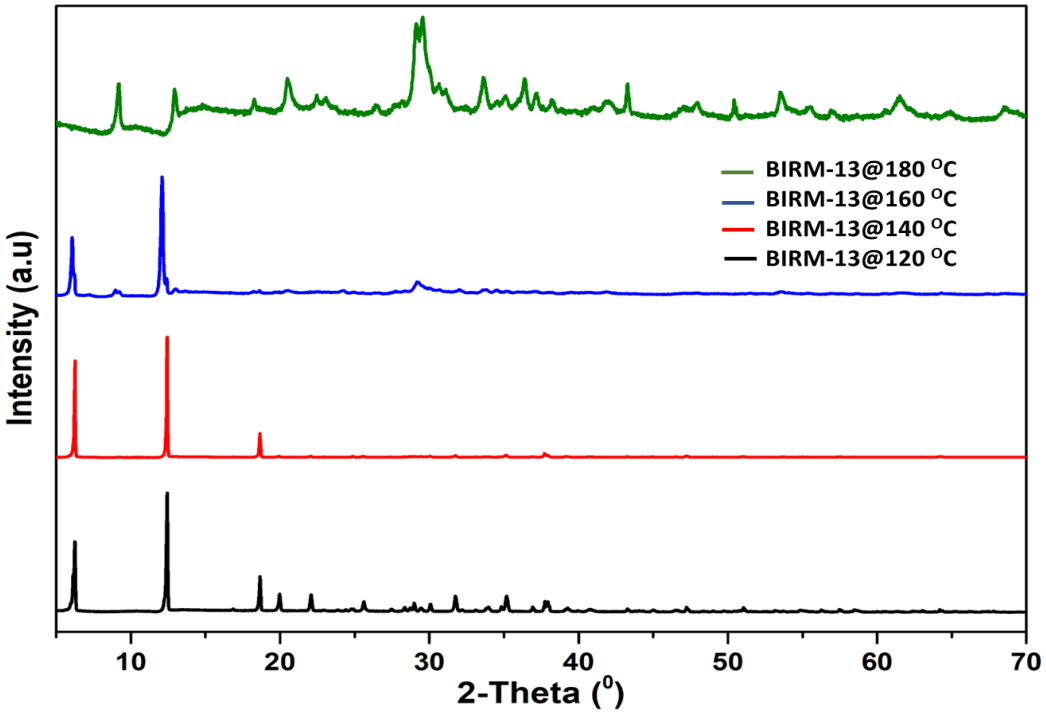


Figure 4.20. PXRD patterns of the products obtained from the attempted synthesis of a copper-based MOF at different temperatures.

4.4.2.3. Varying the mole ratio and use of solvent mixtures

Since synthesis of BIRM-13 at 100 ^{o}C yielded a good quality crystal, the reaction temperature was fixed at 100 ^{o}C while varying the molar ratio of the reactants. Modifying the stoichiometry ratio of the metal ions to the ligand has been proven to alter the topology and dimensionality of MOFs.[272] Therefore, different metal ion to ligand molar ratios of 1:1, 1.5:1, 2:1, 1:1.5 and 1:2 were attempted at 100 °C. However, all this modification did not have an effect on the crystallinity of BIRM-13.

Since it is practically impossible to adjust the pH of the reaction mixture of BIRM-13 beyond 3 and the general idea of working up the pH is to be able to achieve complete deprotonation of the ligand, the use of various solvents and solvent mixtures was attempted. It has been shown that the choice of solvent can influence the deprotonation of organic ligand and direct the coordination behaviour of metal and ligand[272]. Mixtures of water-DMF, and DMF-methanol in various volume ratios were tried to grow single crystals. All these trials yielded light blue crystalline powder, making structure solution extremely difficult.

4.4.3. FTIR studies of BIRM-13

The FTIR spectrum for BIRM-13 is given in figure 4.21 with notable peak assignments in Table 4.8. The most significant observation is the lack of a broad band between 3400 cm^{-1} and 3200 cm^{-1} attributable to stretching vibrations of O–H from the coordinated water molecules, which confirmed the absence of water in the crystal structure. The absorption bands typically at around 1704 cm^{-1} are attributed to O-H stretching from the uncoordinated carboxylic acid.[344] The C=O stretching mode is observed at 1462 cm^{-1}, while the strong bands between 1257 cm^{-1} and 953 cm^{-1} are due to the stretching vibration of the tetrahedral CPO_3 unit as expected. The peaks in the region of 900-450 cm^{-1} were consistent with the presence of Cu-

O bonds. All the expected peaks from the functional groups contained within the material were present.

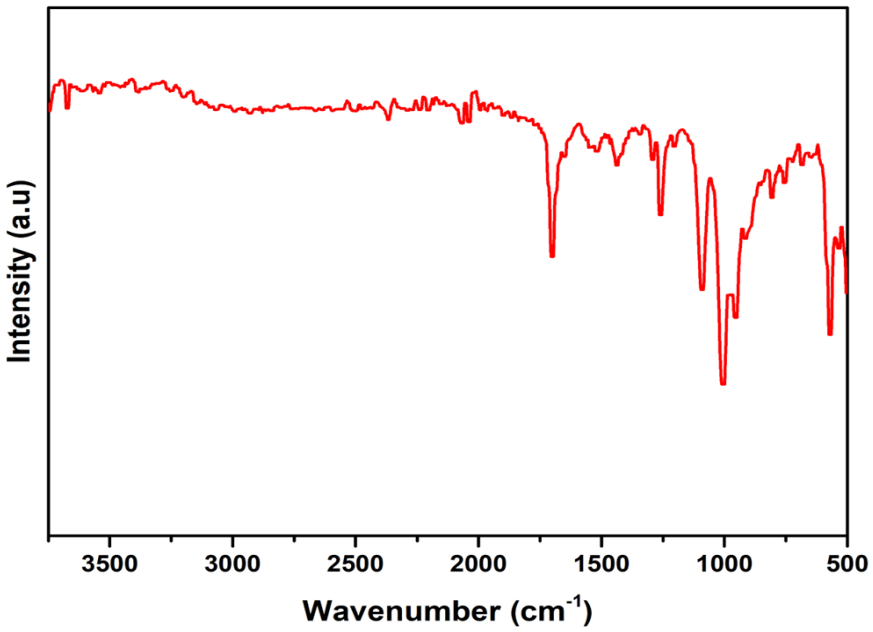


Figure 4.21. FTIR spectrum for BIRM-13.

Table 4.8. Observed FTIR shifts and assignments for BIRM-13.

Wavenumber (cm^{-1})	Peak Assignment
1704	Carboxylate O-H
1432	Phosphonate C=O
1257	Phosphonate P=O
1090	Phosphonate P–C
1000	Phosphonate P–O
953	Phosphonate P–O
<900	Cu-O

4.4.4. Morphological studies of BIRM-13

The plate shape morphology of BIRM-13 is obvious in the SEM images shown in figure 4.22. The absence of brighter or darker patches of material supports phase purity of the product. The EDX analysis of the same sample found an average Cu:P ratio of 1.03:1 across 6 sites which agrees with the value of 1:1 predicted by the solved structure.

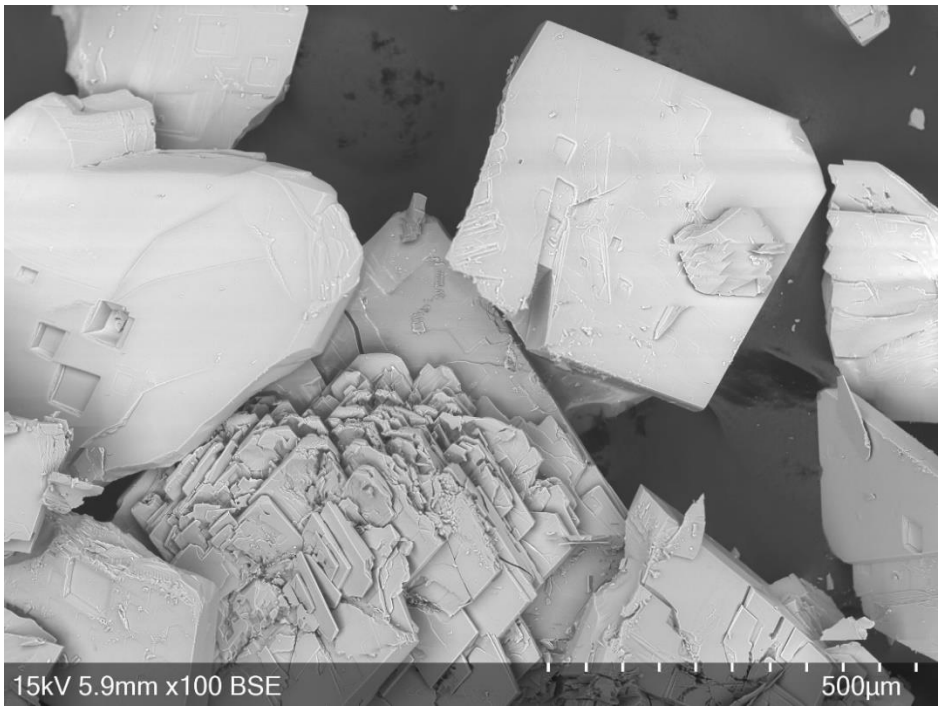


Figure 4.22. SEM image for BIRM-13 crystals.

4.4.5. Thermal stability of BIRM-13

As shown in figure 4.23, the thermogravimetric analysis indicates that the material contains no solvent water, as no mass loss was observed in the TGA until around 306 °C, indicating that BIRM-13 is stable up to this temperature. The most significant weight loss occurred in a sharp step of about 29% as evidenced by a sharp endothermic DTG peak with maximum temperature of 342 ^{o}C, followed by a slower but constant loss in mass until the transformation was complete at about 900°C, resulting in a total weight loss of 52.6%.

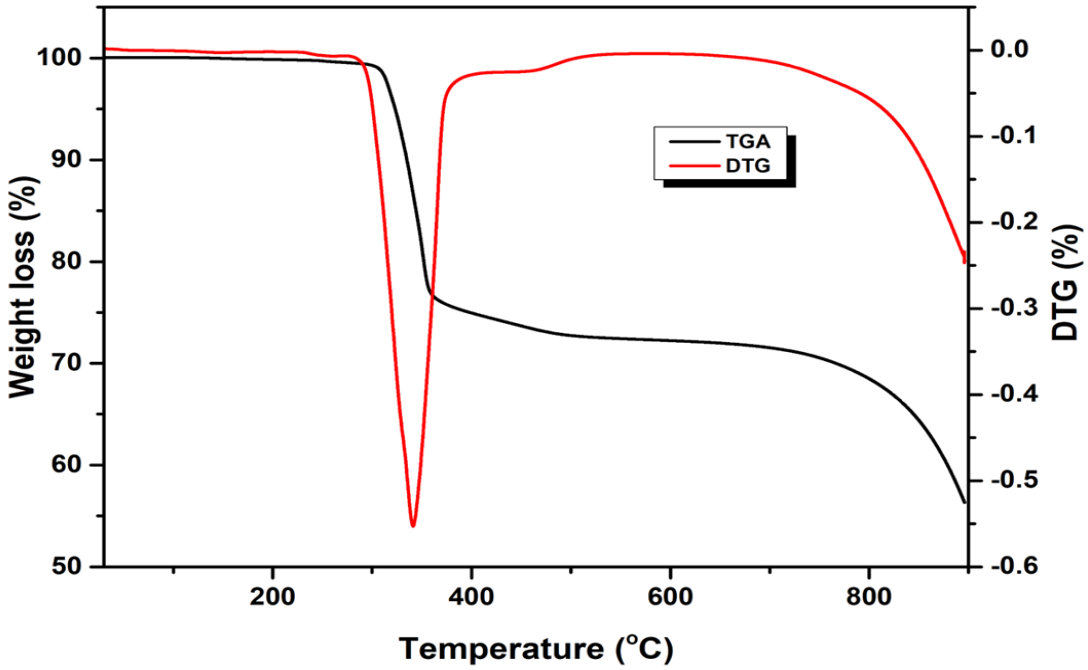


Figure 4.23. TGA (black trace) and DTG (red trace) of BIRM-13.

4.4.6. Electrochemical characterization of BIRM-13

The electrochemical performance of BIRM-13 was investigated by CV measurements in 0.1 M carbonate buffer saturated with Ar or CO_2. The procedure for catalyst preparation and cell set-up was similar to the process described for BIRM-12. Figure 4.24 shows the CV of the BIRM-13 catalyst in the absence and presence of a saturated atmosphere of CO_2; the current densities (*j*) shown have been normalized to current per mass (mg) loading of the copper active sites in the electrocatalyst.

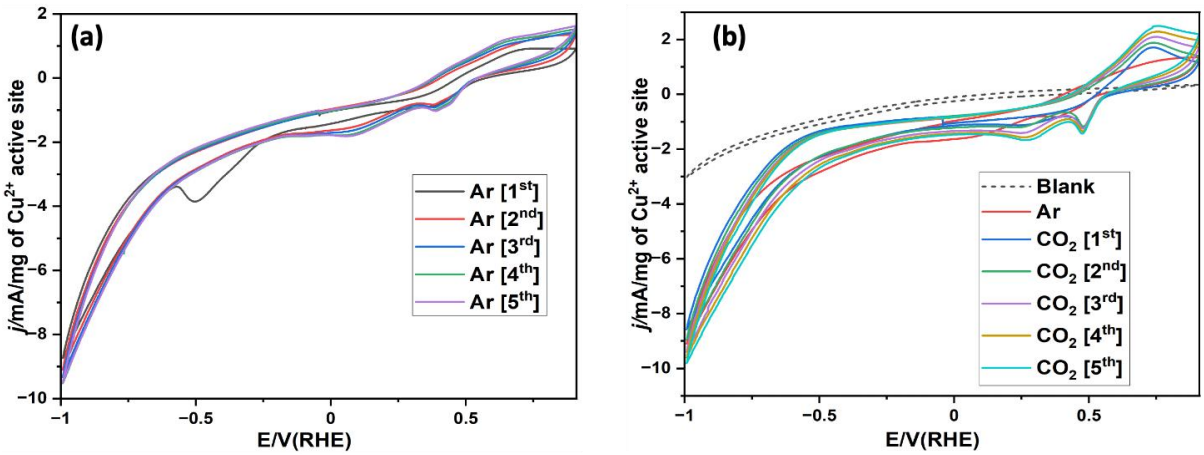


Figure 4.24. Cyclic voltammograms of: (a) the catalyst in Ar-saturated 0.1 M $NaHCO_3/NaCO_3$ buffer solution (b) blank (dotted line), catalyst in Ar -saturated (red line) and CO_2-saturated 0.1 M $NaHCO_3/NaCO_3$ buffer solution; v = 50mV s^{-1}.

For BIRM-13 in Ar-saturated electrolyte (figure 4.24a), the distinct weak redox peak potentials at 0.4 V and + 0.67 V vs RHE in the first CV scan are consistent with the well documented reversible oxidation and reduction of $Cu^{(II)}/Cu^{(I)}$ while the reduction current wave observed at 0.085 V vs RHE indicates further reduction of $Cu^{(I)}$ to $Cu^{(0)}$.[208] Furthermore, the distinct reduction current at - 0.5 V vs RHE corresponds to adsorption of OH^- onto $Cu^{(0)}$, with possible formation of Cu_2O,[345] and subsequent evolution of hydrogen gas at potential range of -0.57 to -1.0 V vs (RHE). In the subsequent scan, the disappearance of the current wave at - 0.5 V vs RHE suggested that BIRM-13 may have been transformed into Cu_2O which is now driving the redox reaction thereafter. In saturated CO_2 electrolyte (figure 4.24b), the CV profile of BIRM-13 is similar to its activity in Ar-saturated electrolyte, with reversible current at +0.47 V and +0.76 V vs RHE corresponding to redox couple of $Cu^{(II)}/Cu^{(I)}$ and reduction peak at 0.28 V vs RHE representing the reduction of $Cu^{(I)}$ to $Cu^{(0)}$. The increased current density at potential range of -0.5 to -1.0 V vs (RHE) indicates the hydrogen evolution reaction. The slight shift of

the redox peaks to a more positive potential might be due to increase in the pH of the electrochemical environment[346], which can lead to a change in local pH at the interface between electrode and electrolyte. Notably for HER, BIRM-13 catalyst did not show any significant change in current in Ar-and CO_2-bubbled electrolyte, indicating that the catalyst shows favourable activities for HER rather than CO_2RR. Also, CO_2RR might not have been achieved for this catalyst, however, its highest current density of 15 *j*/mA.cm^{-2} at -1.0 V vs RHE is an interesting one, indicating promising intrinsic activity.

4.4.7. Use of auxiliary ligand

After many unsuccessful attempts to influence the coordination behaviour of the building blocks of BIRM-13, it was decided to try introducing an auxiliary ligand into the reaction system. One strategy to disrupt dense layer formation in phosphonate MOFs is to incorporate auxiliary ligands which have the tendency of introducing porosity into the metal phosphonate material. The general idea is that, if the synthetic conditions can be fashioned in such a way that metal SBUs coordinate first to the auxiliary ligand before coordinating to the phosphonic acid ligand, this can have influence on the dimensionality of the materials with the possibility of producing MOFs with permanent porosity. [111] Using 4,4-bipyridine as an auxiliary ligand, the synthesis was carried out by dissolving the quantities of reagents in Table 4.9 in a solvent mixture of DMF and water (1:3 v/v). The mixture was transferred into a Teflon-lined autoclave and placed in an oven. After many trials (Chapter 9 Table A4.46-4.48), a mixture of needle-like yellow crystals and a dirty brown crystalline powder was obtained at a temperature of 120 ^{0}C after 24 hrs of reaction. The sample was submitted to the School of Chemistry's single crystal diffraction facility for structural characterisation. This material will now be named BIRM-14.

Table 4.9 Quantities of reagents used in the synthesis attempt of a framework material with auxiliary ligand.

	$Cu(CO_2CH_3)_2.H_2O$	3-phosphonopropionic acid	4,4-bipyridine
Mass (g)	0.7122	0.5015	0.25
Molar ratio	6.1	6.5	1

4.4.8. Crystal structure of BIRM-14 $[Cu_3(O_3PC_2H_4COO)(C_5H_4N)_2]$

The asymmetric unit of BIRM-14 is shown in Figure 4.25, while its expanded structure is presented in Figure 4.26, with some of the basic crystallographic details given in Table 4.10 and Chapter 9 Table A4.17. Single crystal X-ray diffraction analysis revealed that BIRM-14 crystallizes in monoclinic space group $P2_1/n$. The asymmetric unit of this crystal comprises three Cu (II) cations, one $(O_3PCH_2CH_2COO)^{2-}$ anion and one 4,4-bipyridine $(C_5H_4N)_2$ molecule. One 4,4-bipyridines is bonded to Cu(3) via carboxylic O(4), and another one bonded to Cu(1) via phosphonic O(1) forming a one dimensional chain (Figure 4.26a). This chain is then bridged by CPO_3 tetrahedra via Cu(2), forming a 2-dimensional metal organic framework structure, with some plausible channels and pores (Figure 4.26b and c). As can be observed in Figure 4.27, majority of the diffraction peaks in the simulated pattern were present in the powder pattern, indicating that BIRM-14 is the major phase present in the BIRM-14 crystal sample.

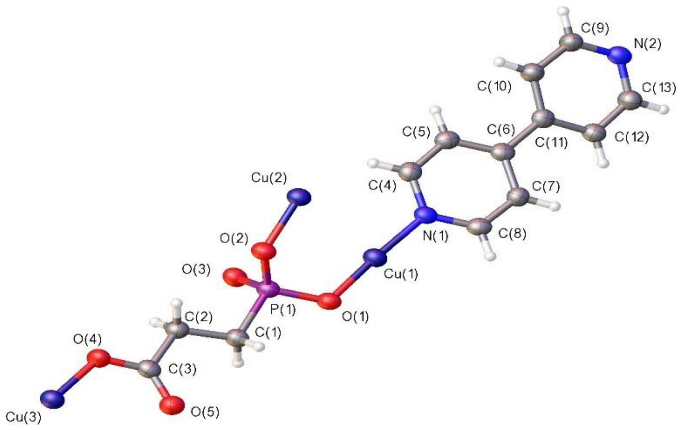
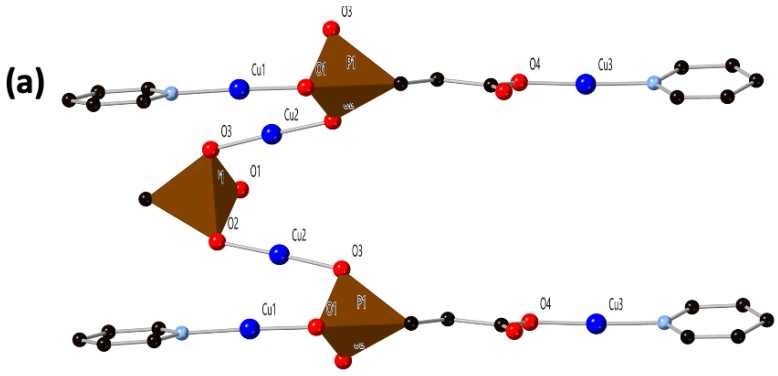


Figure 4.25. Asymmetric unit of BIRM-14. The thermal ellipsoids are drawn at the 50% probability level.

Table 4.10 Crystallographic data for BIRM-14.

Sample	BIRM-14
Formula	$Cu_3(O_3PC_2H_4COO)\ (C_5H_4N)_2$
Formula weight	497.84
Space group	$P2_1/n$
a (Å)	10.5235(8)
b (Å)	6.5966(5)
c (Å)	21.3034(17)
Volume($Å^3$)	1461.6(2)
Goodness-of-fit on F2	1.07
wR2	0.1808
Largest diff. peak/hole / e $Å^{-3}$	1.68/-0.76



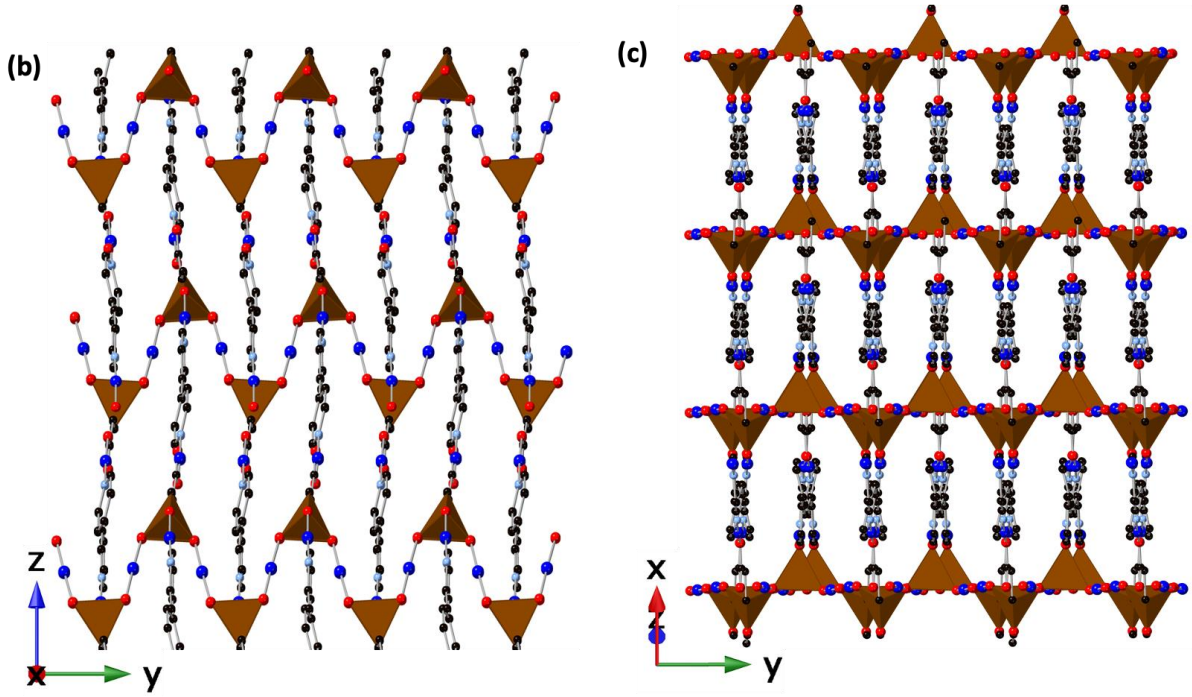


Figure 4.26. (a) Coordination geometry and the structure of BIRM-14 viewed along (b) x-axis (b) z-axis.

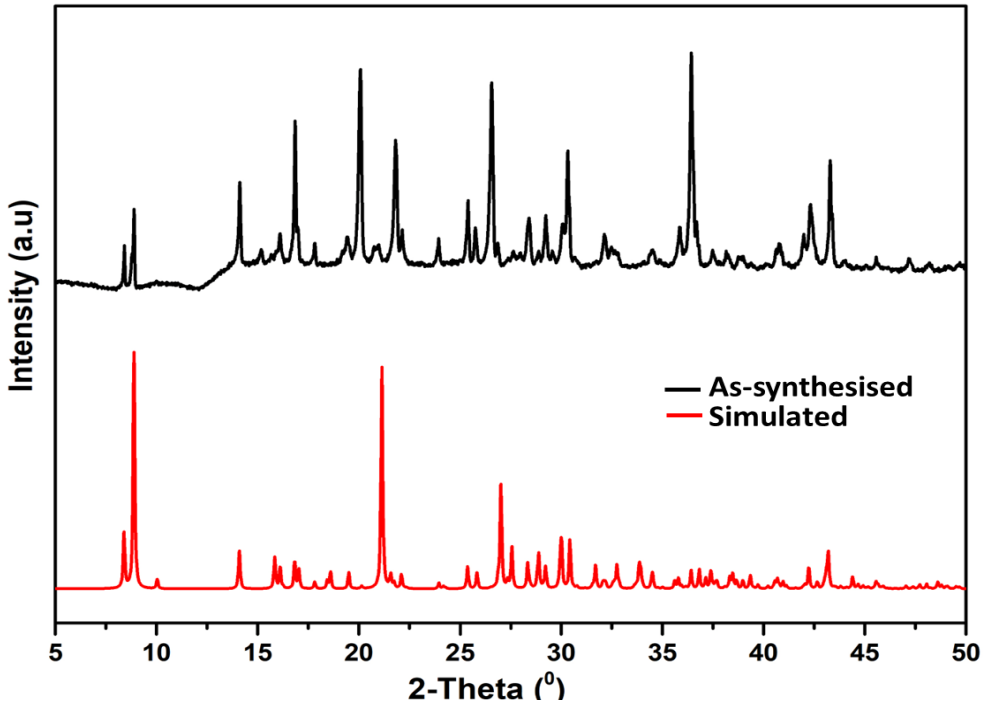


Figure 4.27. As-synthesised (black) and simulated (red) XRD pattern BIRM-14.

4.4.8.1. FTIR studies of BIRM-14

The FTIR spectrum showing the functional groups present in BIRM-14 structure is depicted in Figure 4.28 and Table 4.11. The weak and short peak at 3000 cm^{-1} and 2800 cm^{-1} can be attributed to =C-H and -C-H stretching vibrations, respectively while the sharp and highly intense peak at 1556 cm^{-1} can be assigned to the C=N stretch modes originating from 4,4-bipyridine auxiliary ligand. Highly intense sharp peaks at 1384 cm^{-1} are attributed to the C=O stretch mode from the uncoordinated carboxylic acid.[344] The P–C stretching mode is observed at 1343 cm^{-1}, while the P–O stretching modes of the phosphonate group are evidence as strong absorption bands at 1087 cm^{-1} and 1016 cm^{-1}, respectively. The peaks in the region less than 830 cm^{-1} are consistent with the presence of Cu-O bonds, therefore all the expected peaks from the functional groups contained within the material are present.

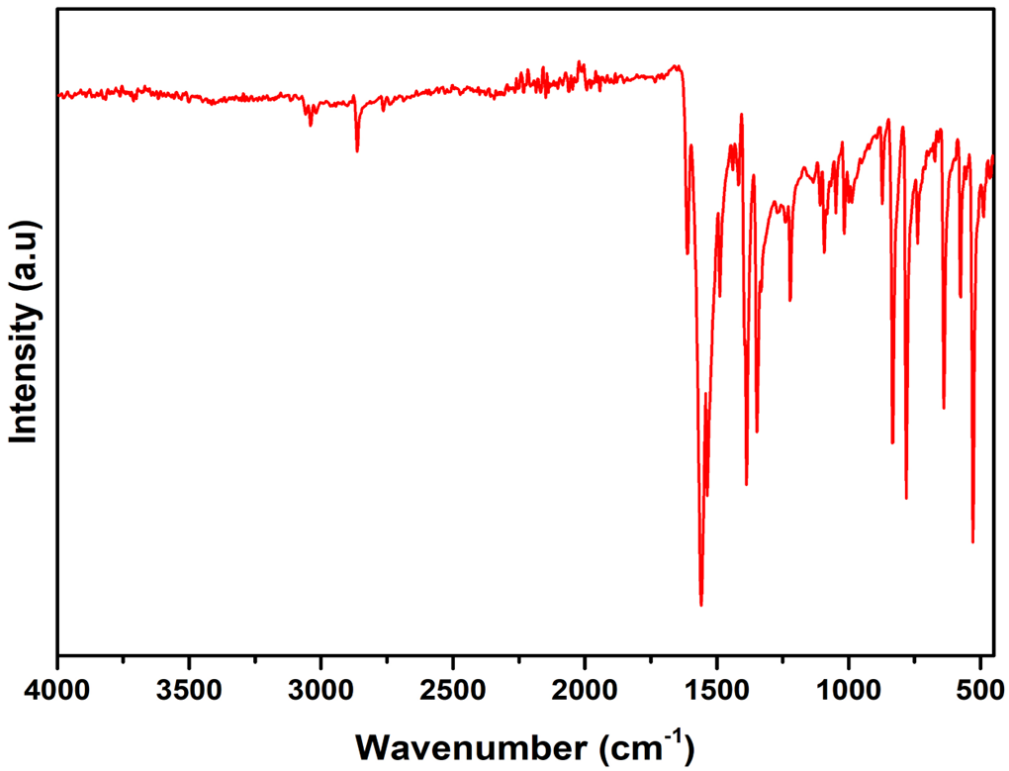


Figure 4.28. FTIR spectrum for BIRM-14.

Table 4.11. Observed FTIR shifts and assignments for BIRM-14.

Wavenumber (cm^{-1})	Peak Assignment
3000	=C-H
2800	-C-H
1556	C=N
1384	Carboxylate C=O
1343	Phosphonate P–C
1215	Phosphonate P=O
1087	Phosphonate P–O
1016	Phosphonate P–O
<830	Cu-O

4.4.8.2. Morphological studies of BIRM-14

An SEM image of the BIRM-14 crystals is presented in Figure 4.29. The image shows that BIRM-14 can be identified, among other crystals present, as rectangular prisms with flat faces. Also observed from the image, is the presence of other plate-shaped crystals, with each plate stacking over each other, indicating that the sample is heterogeneous mixture of phases, consistent with the observation that not all the peaks present in the powder pattern of BIRM-14 were present in the simulated pattern.



Figure 4.29. SEM image for BIRM-14 crystals.

4.4.8.3. Thermal stability of BIRM-14

TGA and DTG analysis (Figure 4.30) showed that BIRM-14 is thermally stable up to 266 °C. A fractional weight loss of 3.8 % was observed at 200 °C before complete collapse of the framework at 350 °C with equivalent weight loss of 45.57 %. As can be observed from the DTG curve, there is a corresponding sharp endothermic peak with a maximum temperature of 285 °C. The material thereafter continued to witness slower but constant weight loss until the transformation was complete at about 900°C, resulting in a total weight loss of 56.2%.

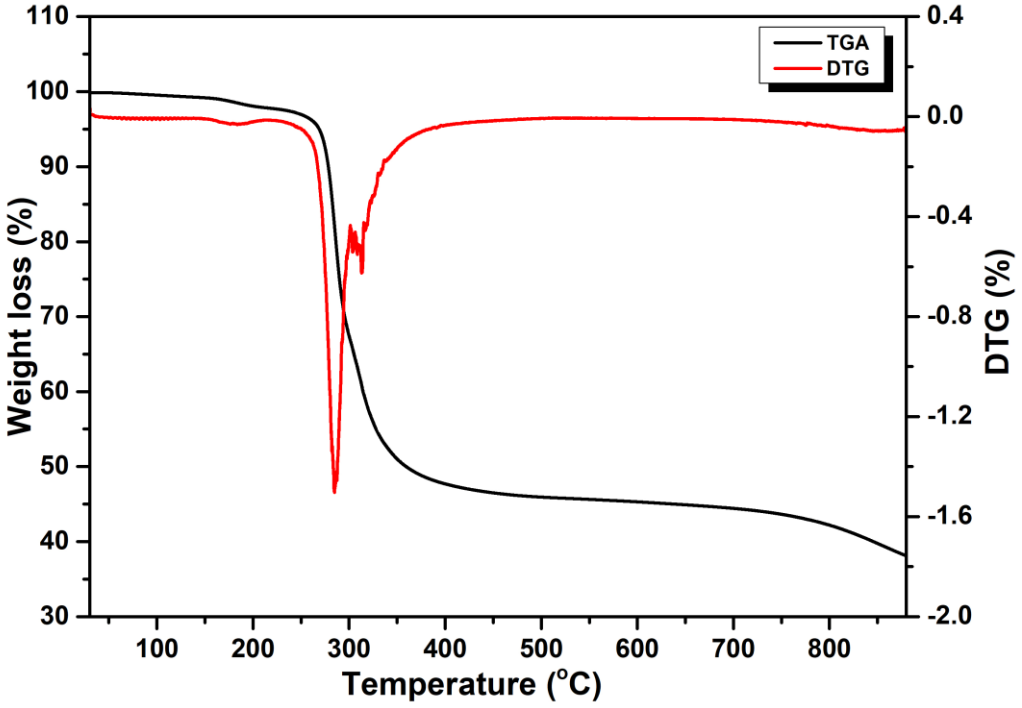


Figure 4.30. TGA (black trace) and DTG (red trace) of BIRM-14.

4.4.8.4. Electrochemical characterisation of BIRM-14

Electrochemical profiling of BIRM-14 was carried out by cyclic voltametric analysis to examine its electrocatalytic activity towards the CO_2 reduction reaction. The catalyst preparation and experimental set up followed the same procedure as described for BIRM-13. All potentials collected were subsequently calibrated to the reversible hydrogen electrode (RHE) according

to the equation: $E_{RHE} = E_{Hg/HgO} + 0.098 + 0.0591 \times pH$. The results showing the cyclic voltametric profile of BIRM-14 catalyst in the absence and presence of a saturated atmosphere of CO_2 are presented in Figure 4.31. The current densities (*j*) shown were normalized as current per mass (mg) loading of the copper active sites in the electrocatalyst.

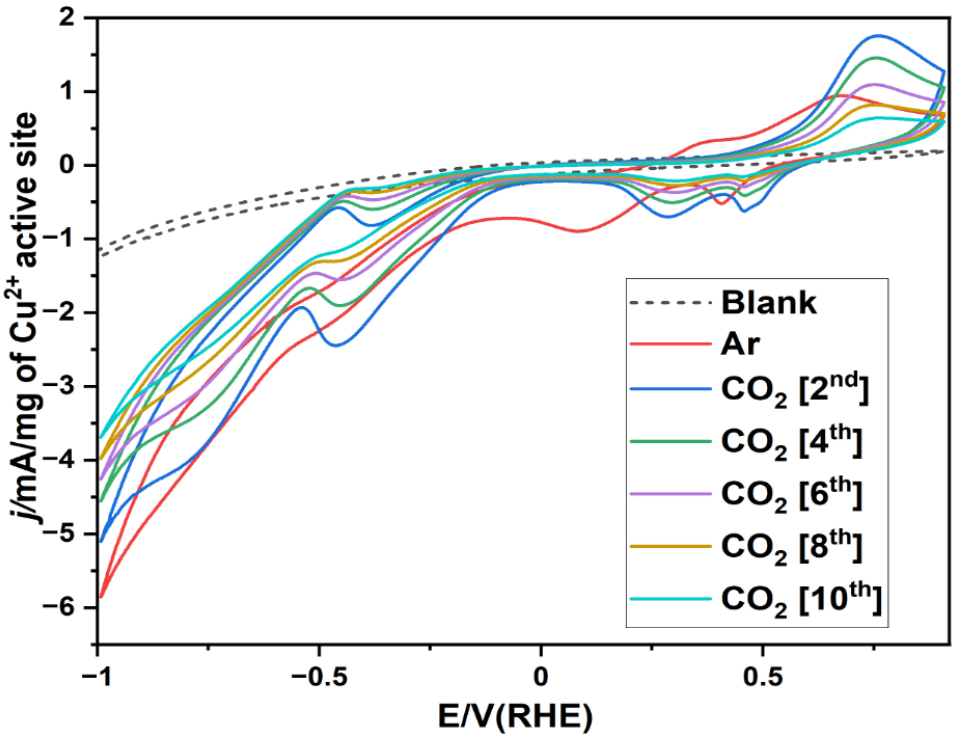


Figure 4.31. CV in 0.1 M carbonate buffer of BIRM-14 supported on a GC electrode in absence and presence of CO_2, recorded at 50mVs^{-1}.

From the voltametric profile of BIRM-14 catalyst in the absence of CO_2, the two distinct redox peak potentials at 0.67 V and 0.41 V vs RHE can be linked to the reversible oxidation and reduction of $Cu^{(II)}/Cu^{(I)}$ while the second set of current waves at 0.37 V and 0.086 V vs RHE correspond to the oxidation and reduction of $Cu^{(I)}/Cu^{(0)}$.[208, 334, 335] Subsequently, the reduction current wave in the potential range of -0.21 to -1.0 V vs (RHE) can be linked to the evolution of hydrogen gas. However, BIRM-14 in the presence of CO_2 saturated electrolyte gives a reversible current wave at 0.76 and 0.46 V vs RHE which is synonymous with the oxidation and reduction of $Cu^{(II)}/Cu^{(I)}$ while a second current wave at 0.28 V vs RHE represents the

reduction of $Cu^{(I)/(0)}$. Furthermore, the third reduction current at - 0.46 V vs RHE is associated with the adsorption of CO_2^- radical unto the surface of catalyst[251] while the oxidation peak at -0.45 V vs RHE can be associated with oxidation of $Cu^{(0)}$ to $Cu^{(II)}$. Lastly, the current wave ranging from -0.58 to -1.0 V vs RHE can be linked to both the CO_2 reduction reaction and hydrogen evolution reaction.[251, 347] The shift in the redox peaks of the catalyst in a CO_2-saturated solution to more positive potentials may be as a result of the increase in the pH of the electrochemical environment, leading to a change in local pH at the interface between electrode and electrolyte.[346] Notably from the CV profile, the CO_2 reduction current decreased as the number of scan increased which implies that the CO_2 reduction activity of the catalyst was continuously being inhibited due to the mass transport limitation of CO_2 and the competitive HER. The deactivation witnessed by the catalyst during subsequent CV scans may also be attributed to the blockage of the catalytic active site.[348, 349] While BIRM-14 demonstrated promising activity towards CO_2 reduction, controlled potential electrolysis experiments will need to be carried out to analyse the product, and determine product selectivity and catalyst stability. The CV scan and the CO_2 reduction activity of this catalyst resemble that of Cu nanoparticles[349], which may suggest that BIRM-14 might have been transformed to Cu nanoparticles that are driving the CO_2 reduction reaction. However, the argument will need to be proven right or otherwise by high resolution TEM, powder XRD before and after CO_2 reduction reaction.

4.5. MOF synthesis with cobalt metal

The initial attempt at synthesising a cobalt-based framework using 3-phosphonopropionic acid was conducted using the same method for the synthesis of BIRM-13 but replacing copper

(II) acetate dehydrated with cobalt (II) sulphate heptahydrate. The quantities of reagents used are shown in Table 4.12, below.

Table 4.12 Quantities of reagents used in the initial synthesis attempt of a framework material.

	$CoSO_4 \cdot 7H_2O$	3-phosphonopropionic acid
Mass (g)	0.0755	0.033
Molar ratio	2.28	1

The synthesis started by dissolving the quantities of reagents in Table 4.12 in 10mL of distilled water, adjusted to pH 5 with 2M NaOH. The mixture was transferred into a Teflon-lined autoclave and placed in an oven. After several efforts of varying the reaction between 80−160^{0}C and reaction time between 24 and 48 hrs (Chapter 9 Table A4.49), a wine-coloured needle-like crystals were obtained at a reaction temperature of 140^{0}C after 48hrs (Figure 4.32). The sample was submitted to the School of Chemistry's single crystal diffraction facility for structural characterisation. A good dataset was obtained, and the structure solved by Dr Louise Male. This material will now be named BIRM-15. All the main diffraction peaks in the experimental pattern were found in the simulated pattern, indicating that BIRM-15 has been formed as a relatively pure phase (Figure 4.33). However, peak splitting was observed at 10 degree which may indicate phase transformation upon exposure of the material to air.



Figure 4.32. Optical image of BIRM-15.

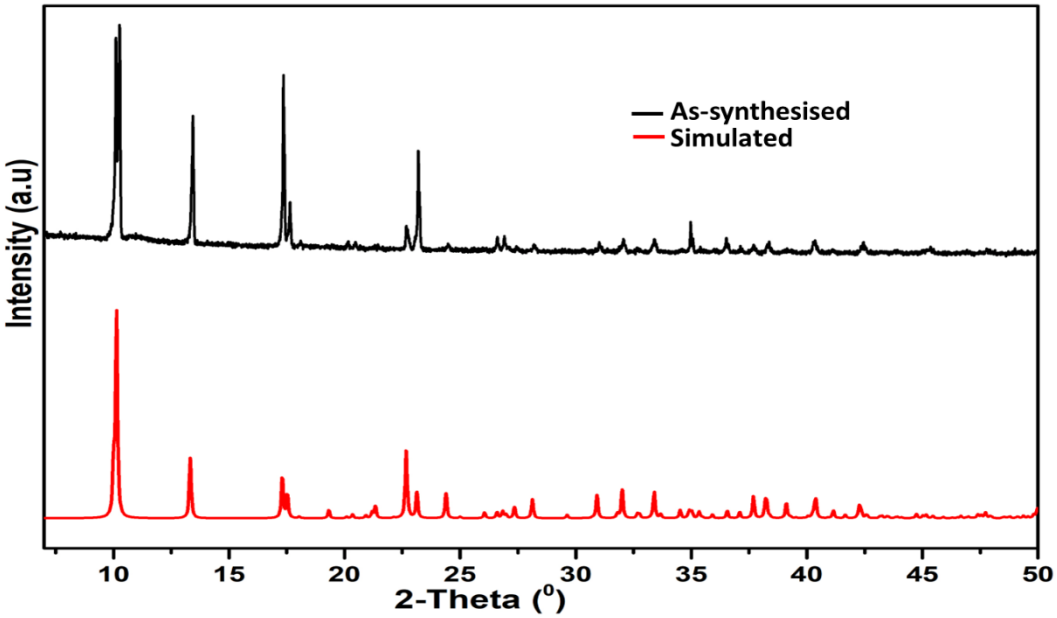


Figure 4.33. As-synthesised (black) and simulated (red) XRD pattern BIRM-15.

4.5.1. Crystal structure of BIRM-15 $[Co_3(O_3PCH_2CH_2COO)_2(H_2O)_3].3H_2O$

This material crystallised in the monoclinic space group $P2_1/c$, with the basic crystallographic details shown in Table 4.13 and detailed information given in Chapter 9 Table A 4.24. Each asymmetric unit comprises two crystallographically independent Co(II) cations, one $(O_3PCH_2CH_2COO)^{3-}$ anion, three coordinated water molecules and three lattice water molecules (Figure 4.34). The inorganic polymer in the structure can be best described as

cobalt octahedra which are cross linked by [CPO_3] tetrahedra and these building units are then bridged by the 3-phosphonopropionic acid ligand forming a 2D metal organic framework structure (Figure 4.35a, b and c). For Co1, the basal plane of the octahedra are filled by three oxygens from water molecules (O4, O5 and O6) and a coordinating oxygen (O3) while the two axial positions are occupied by phosphonate oxygen (O1) and carboxylic oxygen (O7). Similarly, the basal plane of the Co2 octahedra are occupied by two oxygens from water molecules (O6) and two phosphonate oxygens (O2), with the two axial positions occupied by phosphonate oxygens (O3). The Co–O bond distances are in the range of 2.044(3)–2.216(3) Å (chapter 9 Table A4.27), in agreement with those in other cobalt phosphonate compounds.[350, 351]

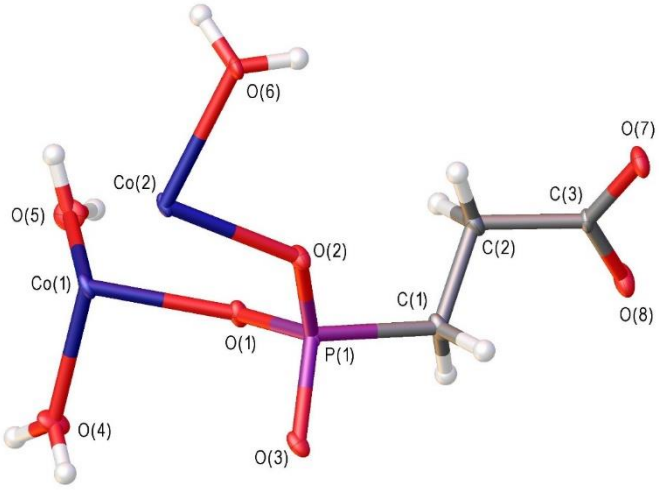
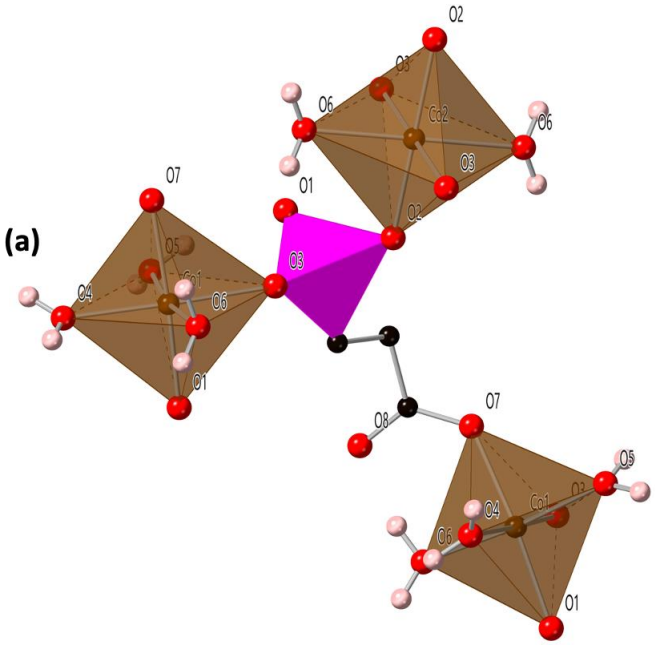


Figure 4.34 Asymmetric unit of BIRM-15. The thermal ellipsoids are drawn at the 50% probability level.

Table 4.13 Crystallographic data for BIRM-15.

Sample	BIRM-15
Formula	$Co_3(O_3PCH_2CH_2COO)_2(H_2O)_3].3H_2O$
Formula weight	586.95
Space group	$P2_1/c$
a (Å)	4.6133(2)
b (Å)	10.2387(5)
c (Å)	17.5296(8)
Volume ($Å^3$)	823.74(7)
Goodness-of-fit on F2	1.082
wR2	0.0951
Largest diff. peak/hole / e $Å^{-3}$	0.62/-0.52



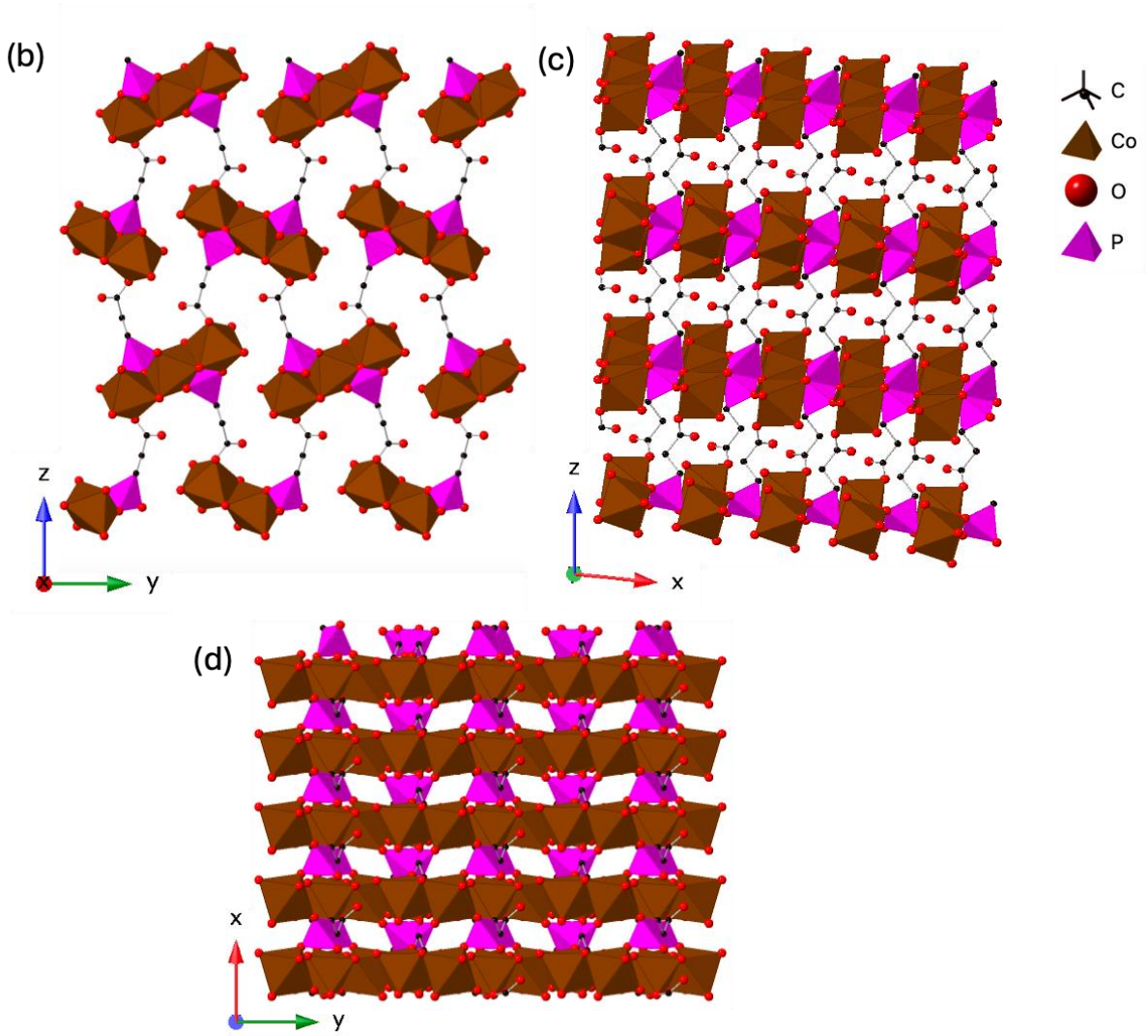


Figure 4.35. (a) Coordination geometry and the 2D framework structure of BIRM-15 viewed along (b) x-axis (c) y-axis and (d) z-axis.

4.5.2. FTIR studies of BIRM-15

Figure 4.36 gives the FTIR spectrum whilst Table 4.14 lists notable bands and assignments to functional groups. It is evident from the FTIR spectrum that all the expected peaks found in the solved structure of BIRM-15 are present. For instance, a broad peak found around 3223 cm^{-1} can be attributed to stretching vibrations from carboxylic O–H or O-H from the coordinated water molecules. Also, the strong bands observed at 1532 cm^{-1} and 1444 cm^{-1} arise from the symmetric and asymmetric stretching modes of the C-O bonds of the

carboxylate group. Lastly, the sharp absorption band observed at 1419 cm^{-1} and other sharp absorption bands seen in the range 1089–917 cm^{-1} are related to the P–C and P–O stretching modes of phosphonate group, respectively.

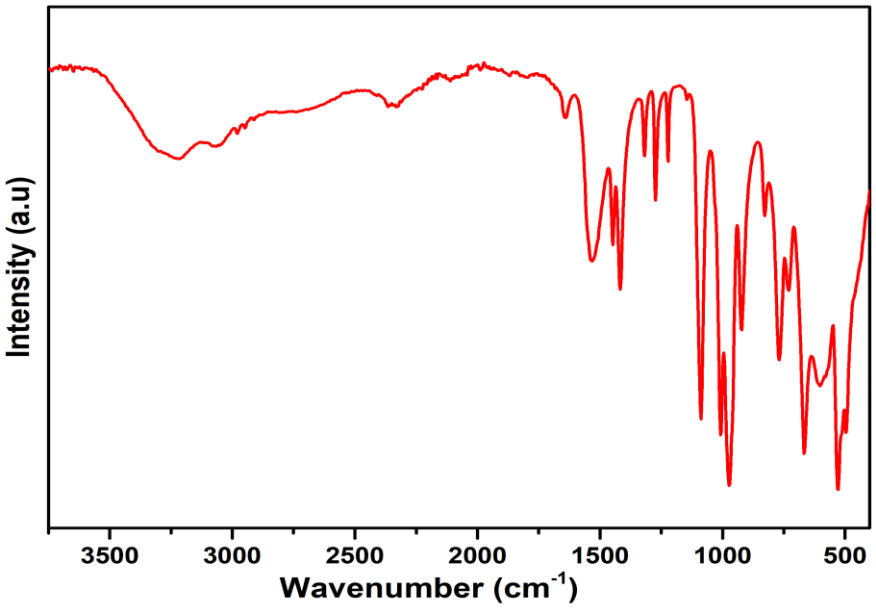


Figure 4.36 FTIR spectrum for BIRM-15.

Table 4.14. Observed FTIR shifts and assignments for BIRM-15.

Wavenumber (cm^{-1})	Peak Assignment
3223	Water O-H, carboxylic acid O–H
1532	Carboxylate C-O
1444	Carboxylate C-O
1419	Phosphonate P–C
1319	Phosphonate P=O
1273	Phosphonate P=O
1089-917	Phosphonate P–O
<900	Co-O

4.5.3. Morphology of BIRM-15

SEM images of the BIRM-15 crystals were taken, and an example is presented in Figure 4.37. The image shows that the crystals are rectangular prisms with flat faces. A few smaller crystals are visible in the image, which may be the result of other phases made up of lighter elements, such as excess organic material. EDX analysis was also performed on the sample, and it gave the average ratio of cobalt to phosphorus, taken across 5 crystal sites, to be 1:3.13, which is in good agreement with the structure solved through single crystal diffraction.



Figure 4.37. SEM image for BIRM-15 crystals.

4.5.4. Thermal stability of BIRM-15

Figure 4.38 illustrates the thermogravimetric behaviour of BIRM-15. There are five major regions of weight loss shown by the TGA curve. There was no significant weight loss up to 168 ^{0}C in the first region, but BIRM-15 witnessed a significant loss corresponding to 18.01 % in the second region (288 ^{0}C) and this can be attributed to the evaporation of both interstitial and

lattice water within the structure of BIRM-15. The percentage of all the 6 molecules of water present in the crystal structure of BIRM-15 was calculated to be 18.4 % which is very close to the percentage weight loss around 288°C, confirming the loss of all water molecules. The framework of BIRM-15 is stable up to 512 ^{0}C in the third region without any significant weight loss. In the fourth region, a significant weight loss of 12.8 % at 592 ^{0}C results in the decomposition of the organic component, causing the collapse of the framework. In the region which corresponds to temperatures > 592 ^{0}C, the material continued to exhibit gradual weight loss and the transformation was complete at about 900°C, resulting in a total weight loss of 36.01 %.

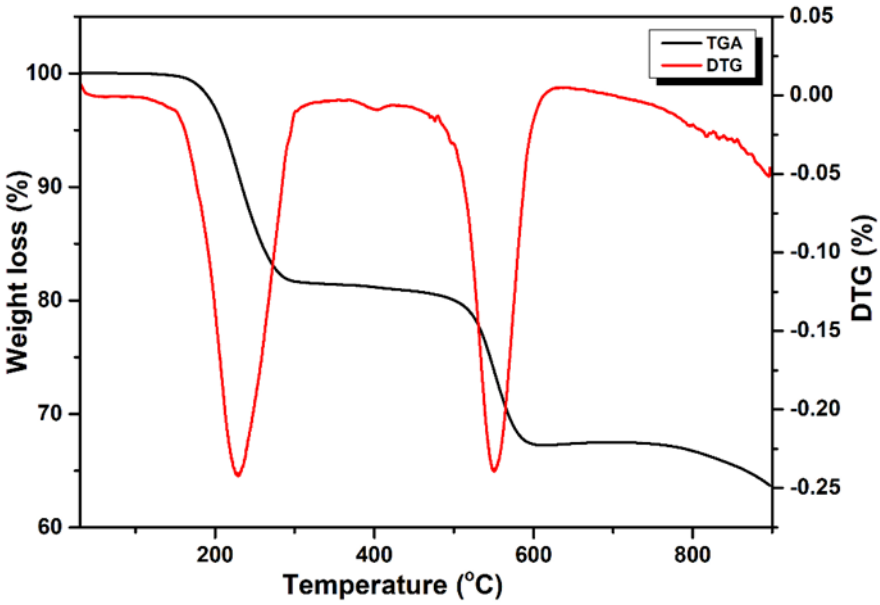


Figure 4.38 TGA (black trace) and DTG (red trace) of BIRM-15.

4.5.5. Electrochemical characterization of BIRM-15

The electrochemical performance of BIRM-15 was investigated by CV measurements in 0.1 M carbonate buffer saturated with Ar or CO_2. The procedure for catalyst preparation and cell set-up was similar to that described for BIRM-14 except that 15 mg of BIRM-15 was used in preparing the catalyst ink. Figure 4.39 shows the CV profile of the BIRM-15 catalyst in the

absence and presence of a saturated atmosphere of CO_2; the catalytic activity shown have been normalized to current per mass (mg) of the cobalt active site in the electrocatalyst. The voltametric profile of the catalyst in the absence of CO_2 shows a current peak at −0.43 V vs RHE during the scan towards negative potentials, which corresponds to the reduction of $Co^{(II)}$ to $Co^{(0)}$ [352] and this is followed by a sharp current peak at −1.0 V vs RHE which is associated with the hydrogen evolution reaction. Conversely, when the solution was saturated with CO_2, a current wave was observed in the cathodic scan at *ca.* −0.33 V (*vs*. RHE) during forward sweep and this peak can be attributed to oxidation of $Co^{(0)}$ atoms to $Co^{(II)}$. [352-354] This was followed by a rapid increase in current between −0.52 V to −1.0 V which is associated with the competitive CO_2 reduction and hydrogen evolution reactions. It can be observed from the cyclic voltammetry profile that there is little or negligible CO_2RR activity taking place. In other words, there is CO_2 reduction activities in the first cycle, after which the catalyst active site is blocked, resulting in negligible CO_2 reduction activities in the subsequent cycles. Another possibility is that BIRM-15 may have become degraded to a different cobalt compound during the potential sweep, driving only hydrogen evolution reaction.[166, 355] Although, BIRM-15 may not have demonstrated interesting activity toward CO_2RR, its activity toward HER is interesting and could be worth exploring in the future.

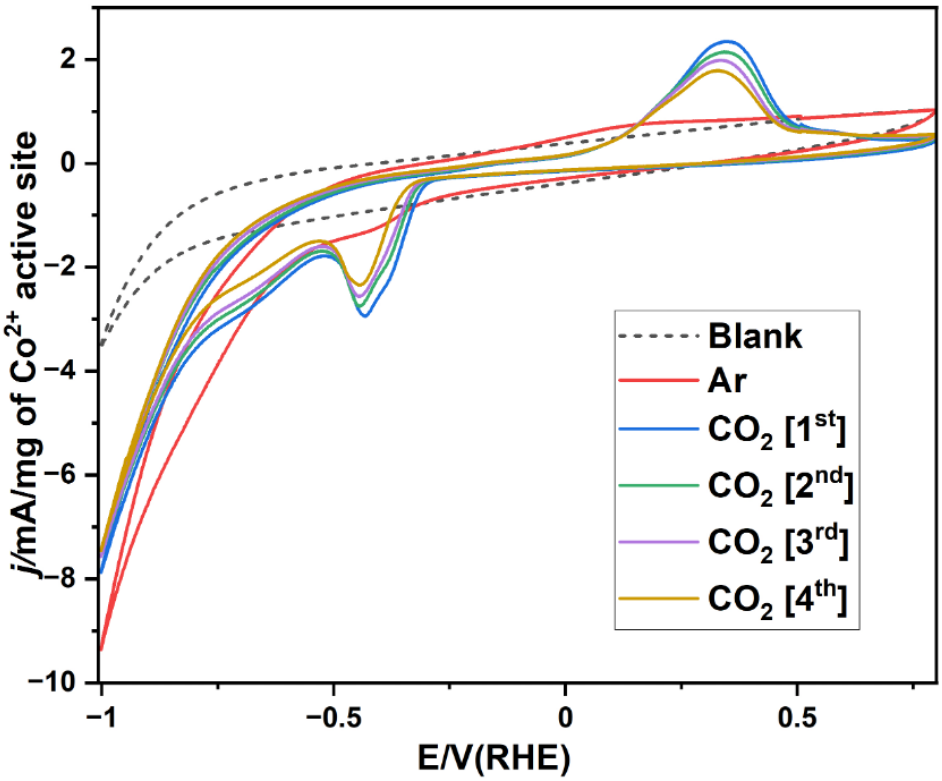


Figure 4.39 CV in 0.1 M carbonate buffer of BIRM-15 supported on a GC electrode in absence and presence of CO_2, recorded at 50mVs^{-1}.

4.5.6. Synthesis attempts with auxiliary ligand

After several experimental optimisation attempts to modify the coordinating mode of BIRM-15 did not produce a more open and porous framework, we tried to introduce 4,4-bipyridine as auxiliary ligand into the reaction system. It has been shown that auxiliary ligand can influence the coordination mode of MOF building blocks with the possibility of self-assembly into an open framework.[111] The quantity of reagents used are shown in Table 4.15, below.

Table 4.15 Quantities of reagents used in the initial synthesis attempt of a framework material.

	$CoSO_4 \cdot 7H_2O$	3-phosphonopropionic acid	4,4-bipyridine
Mass (g)	0.0755	0.033	0.025
Molar ratio	1.68	1.34	1

The synthesis was carried out by dissolving the quantities of reagents in Table 4.15 in a solvent mixture of DMF and water (1:3 v/v) and transferring the mixture into a Teflon-lined autoclave before placing in an oven. Using the same synthetic condition in BIRM-15, a blocky wine-coloured crystal suitable for SCXRD characterisation was obtained at a reaction temperature of 140^0C at 48hrs. The structural characterisation using single crystal XRD showed that this material is a non-porous coordination network built from cobalt cations, 4,4-bipyridine anions and formate ion which is a product obtained from the hydrolysis of DMF. During the solvothermal synthesis, DMF in the presence of NaOH undergo hydrolysis to formic acid and dimethylamine, shifting the solution pH to more basic region (equation i).[356] Under these pH conditions, formic acid undergo deprotonation over 3-phosphonopropionic acid ligand, forming formate ion (equation ii) . This formate ion and 4,4-bipyridine become coordinated to cobalt cation, forming a 3D coordination network. The coordination network obtained is named BIRM-16, and further crystal description and characterisation is given in subsequent sections.

$$(CH_3)_2NC(O)H \overset{OH^-/H_2O}{\Longleftrightarrow} (CH_3)_2NH + HCOOH \qquad (4.1)$$

$$HCOOH \overset{OH^-}{\longrightarrow} HCOO^- + H_2O \qquad (4.2)$$

4.5.7. Structure of BIRM-16 [$Co(C_5H_4N)_2(CHOO)$]

Single crystal X-ray diffraction analysis revealed that BIRM-16, crystallizes in tetragonal space group $P4_12_12$ (Table 4.16, Chapter 9 Table A 4.34). The asymmetric unit of this crystal comprises Co(II) cations, and 4,4-bipyridine and formate anions (Figure 4.40). In BIRM-16, the inorganic moieties can be described as cobalt octahedra where each cobalt octahedron is axially linked by 4,4-bipyridine auxiliary ligands and edge-linked by oxygen from the formate

anions, forming a 3D network (Figure 4.41). In other words, the basal plane of the Co1 octahedron is filled with carboxylic oxygens (O1 and O2) while the two axial positions are occupied by bipyridinic nitrogen (N1 and N2). A notable feature of this material is that it allows chirality which is an interesting property. Since homochiral coordination networks built from atropoisomeric 4,4'-bipyridine are very scarce[357], this homochiral coordination network material is a new addition to this list and its potential application can be explored in chiral separation and chiral synthesis.[358, 359] The chiral properties of this material can be explored to induce specific enantioselective interactions in a confined chiral environment, with potential of being able to recognise enantiomers in racemic mixtures, leading to enantiomeric separation.[360]

Table 4.16 Crystallographic data for BIRM-16.

Sample	BIRM-16
Formula	$Co(C_5H_4N)_2(CHOO)$
Formula weight	305.15
Space group	$P4_12_12$
a (Å)	7.9644(5)
b (Å)	7.9644(5)
c (Å)	17.3395(17)
Volume($Å^3$)	1099.87(18)
Goodness-of-fit on F2	1.101
wR2	0.0572
Largest diff. peak/hole / e $Å^{-3}$	0.35/-0.32

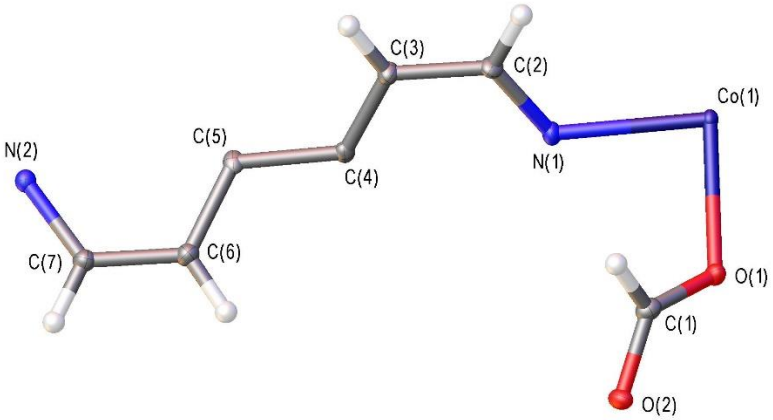


Figure 4.40. Asymmetric unit of BIRM-16. The thermal ellipsoids are drawn at the 50% probability level.

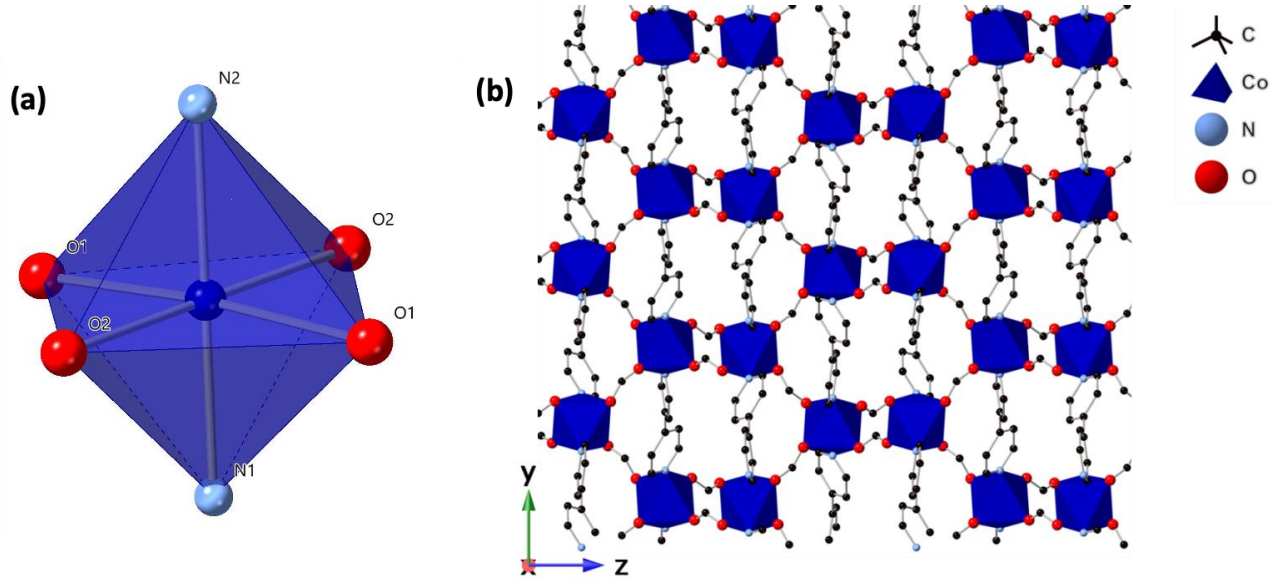


Figure 4.41. (a) Coordination geometry and (b) Structure of BIRM-16 viewed along x-axis.

4.5.7.1. FTIR studies of BIRM-16

Figure 4.42 and Table 4.17 shows the FTIR spectrum and assigned wavenumbers for BIRM-16. The absorption band around 1562 cm^{-1} is assignable to the C=N stretch mode originating from 4,4-bipyridine auxiliary ligand[361] while the peak at 1387 cm^{-1} originates from the C=O stretching mode arising from the carboxylic acid group coordinated to cobalt.[362] Further

information from the spectrum shows Co–O and Co–N characteristic peaks detected at 924-722 cm^{-1} and 623-450 cm^{-1}, respectively.[361]

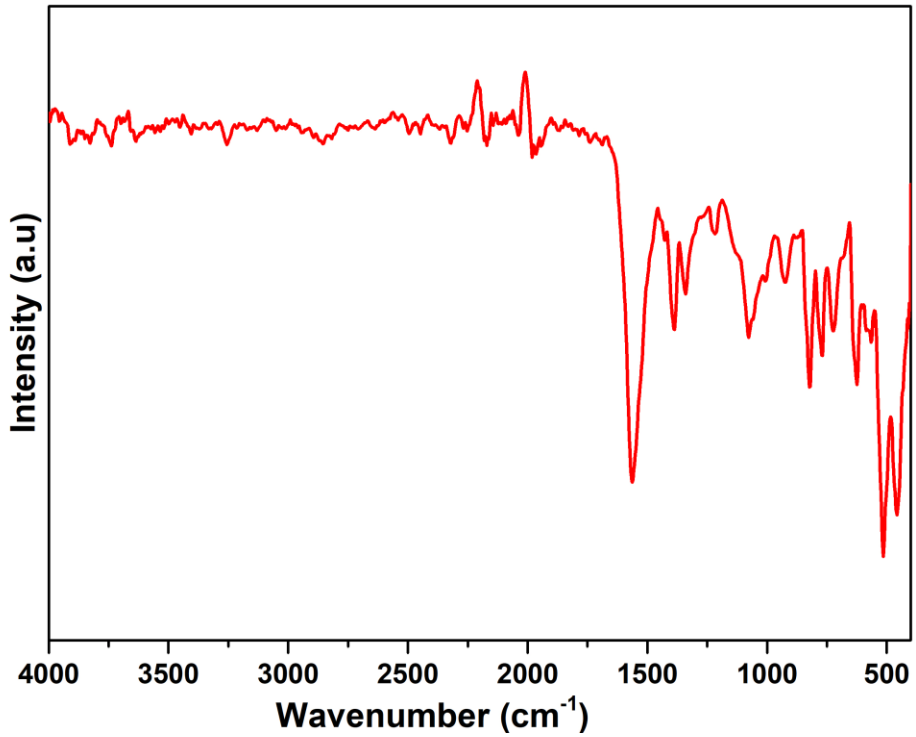


Figure 4.42. FTIR spectrum for BIRM-16.

Table 4.17 Observed FTIR shifts and assignments for BIRM-16.

Wavenumber (cm^{-1})	Peak Assignment
1562	C=N (stretching)
1387	Carboxylate C=O
1338	C=C
1073	C-N
924-722	Co-O
623-450	Co-N

4.5.7.2. Morphology of BIRM-16

SEM images of the crystals (Figure 4.43) were taken. The material appears as a monolith with no clear regular morphology. Additionally, some other smaller crystals are visible in the image, which may be suggest excess unreacted organic materials.

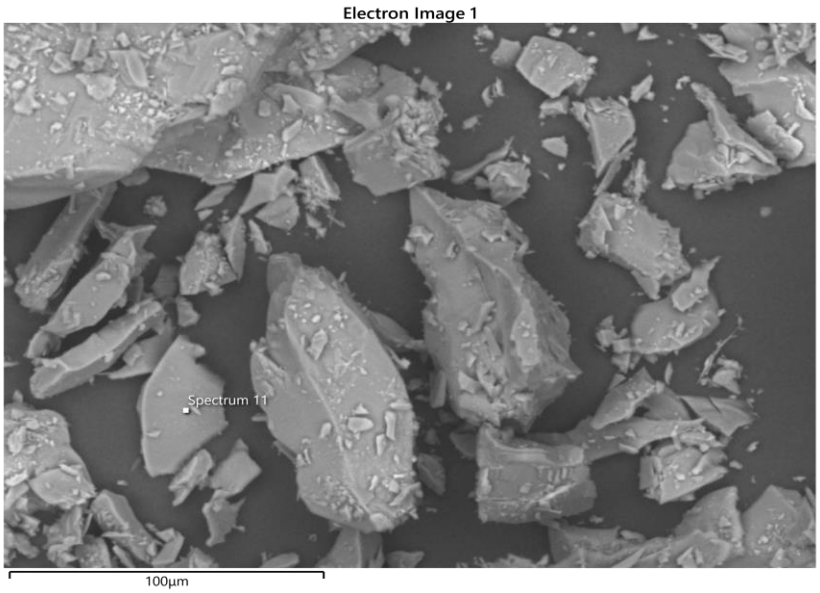


Figure 4.43 SEM image for BIRM-16 crystals.

4.5.7.3. Thermal stability studies of BIRM-16

The result of thermogravimetric analysis of BIRM-16 is presented in Figure 4.44 and shows that BIRM-16 is thermally stable up to 286 ^{0}C with no weight loss before the complete collapse of the framework at 395 ^{0}C, resulting in a significant weight loss of 57.1 %. The DTG curve confirms the complete decomposition of BIRM-16, showing an endothermic event with a sharp peak at temperature of 339 °C and this was followed by a slower but gradual weight loss until the transformation was complete at about 900°C, resulting in a total weight loss of 81.1 %.

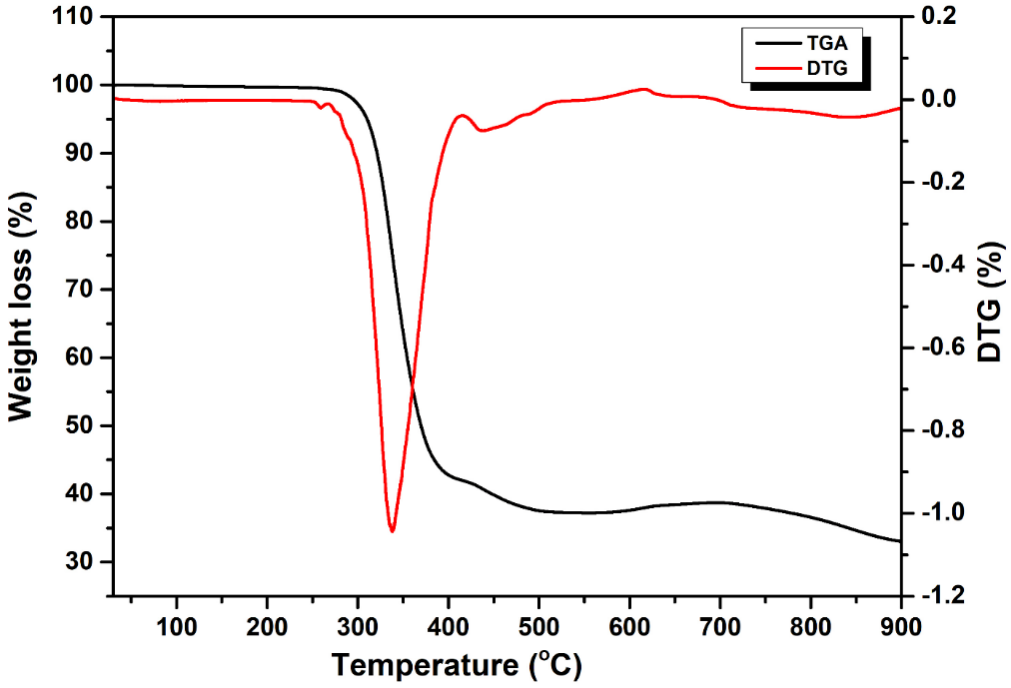


Figure 4.44. TGA (black trace) and DTG (red trace) of BIRM-16.

4.6. BIRM-16(Ni), an isoreticular version of BIRM-16

The same synthesis condition used in BIRM-16 was attempted by replacing cobalt metal with nickel node, yielding a blocky green and glassy crystal at reaction temperature of 140^0C at 48hrs (Figure 4.45). The single crystal XRD characterization reveals that this nickel material is a coordination network and is named BIRM-16 (Ni) as it is isoreticular to BIRM-16. As was the case for BIRM-16, BIRM-16(Ni) was also formed when the formate anion obtained from hydrolysis of DMF and 4,4-bipyridine become coordinated to the nickel cation, giving rise to 3D coordination network. The main ligand, 3-phosphonopropionic acid, did not participate in the reaction. The possible reason is that the basic pH of the reaction medium, favour the deprotonation of formic acid rather than the 3-phosphonopropionic acid. BIRM-16(Ni) has the same crystallographic properties as BIRM-16 and also exhibits chirality (Table 4.18, Figure 4.46 and 4.47).



Figure 4.45. Optical image of BIRM-16(Ni).

The inorganic cluster of BIRM-16 (Ni) can be described as nickel octahedra where each nickel octahedron is axially linked by 4,4-bipyridine auxiliary ligands and edge-linked by oxygens from the formate anions, giving rise to a 3D network (Figure 4.46). This material also possesses chiral properties which has potential of being able to recognise enantiomers in racemic mixture, leading to enantiomeric separation.

Table 4.18 Crystallographic data for BIRM-16(Ni).

Sample	BIRM-16(Ni)
Formula	$Ni(C_5H_4N)_2(CHOO)$
Formula weight	304.93
Space group	$P4_12_12$
a (Å)	7.8952(2)
b (Å)	7.8952(2)
c (Å)	17.3062(6)
Volume	1078.77(7)
Goodness-of-fit on F2	1.097
wR2	0.0572
Largest diff. peak/hole / e $Å^{-3}$	0.75/-0.24

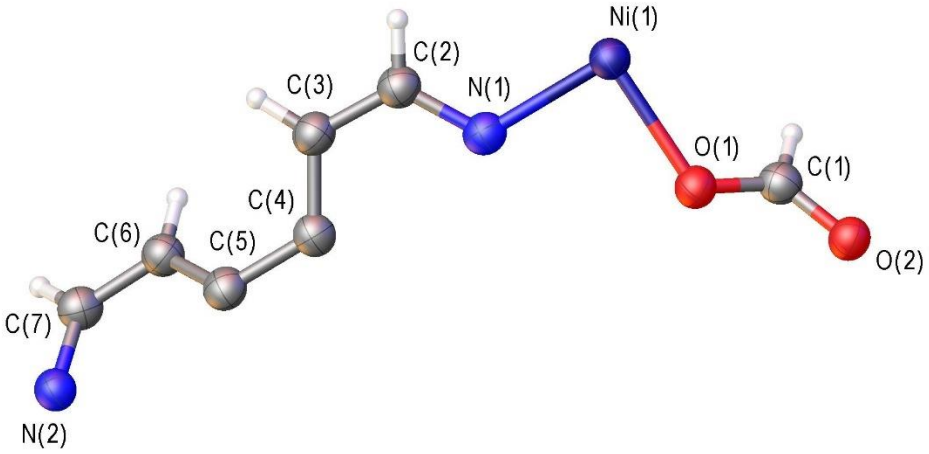


Figure 4.46. Asymmetric unit of BIRM-16(Ni). The thermal ellipsoids are drawn at the 50% probability level.

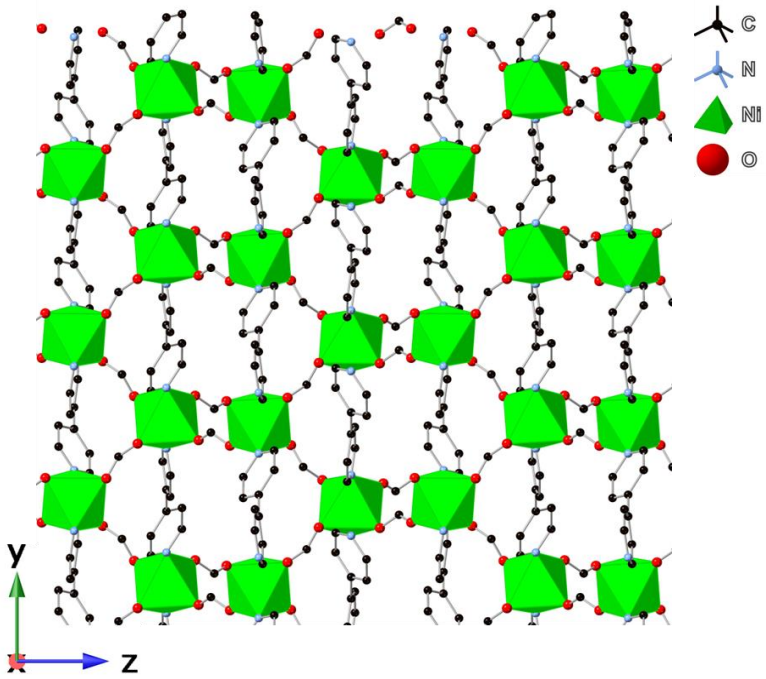


Figure 4.47 Structure of BIRM-16(Ni) viewed along x-axis.

4.6.1. Morphology studies of BIRM-16 (Ni)

From the SEM image (Figure 4.48), BIRM-16(Ni) appears as a block of crystals with no distinct regular morphology or shape, which is similar to BIRM-16. Additionally, some other smaller crystals are visible in the image which may correspond to the yellow crystalline powder visible

in the optical image BIRM-16(Ni) (Figure 4.48) and may be an excess unreacted organic material.

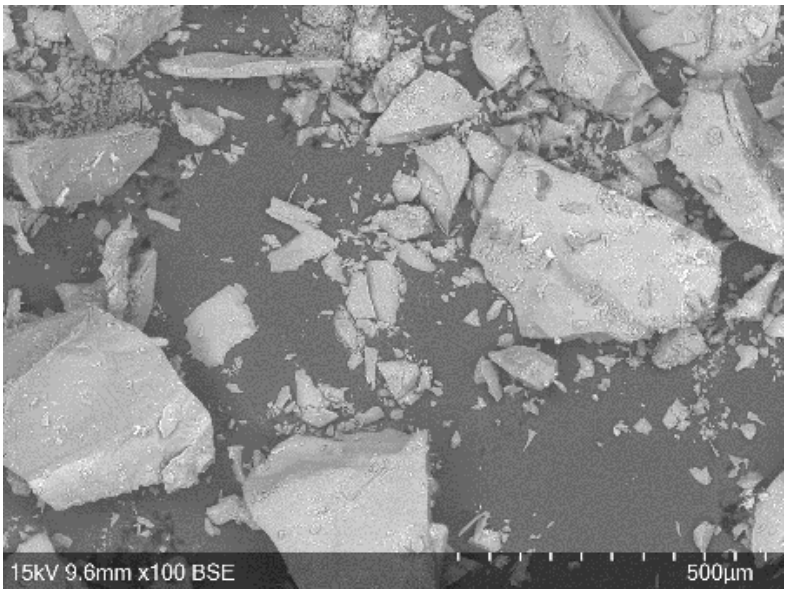


Figure 4.48. SEM image for BIRM-16(Ni) crystals.

4.6.2. Thermal stability of BIRM-16(Ni)

The thermal stability of BIRM-16(Ni) as revealed by TGA measurements shows a one-stage decomposition pattern which is similar to the degradation behaviour of BIRM-16 (Figure 4.49 and Figure 4.44). The results show that BIRM-16(Ni) is thermally stable up 271 ^{o}C before undergoing complete decomposition at 370 ^{o}C which is also in agreement with the thermal behaviour of BIRM-16. Additionally, the DTG curve confirmed this one stage decomposition behaviour and the material did not lose any significant weight up to the end of the reaction temperature of 900 ^{o}C, yielding a total weight loss of 77.1 %.

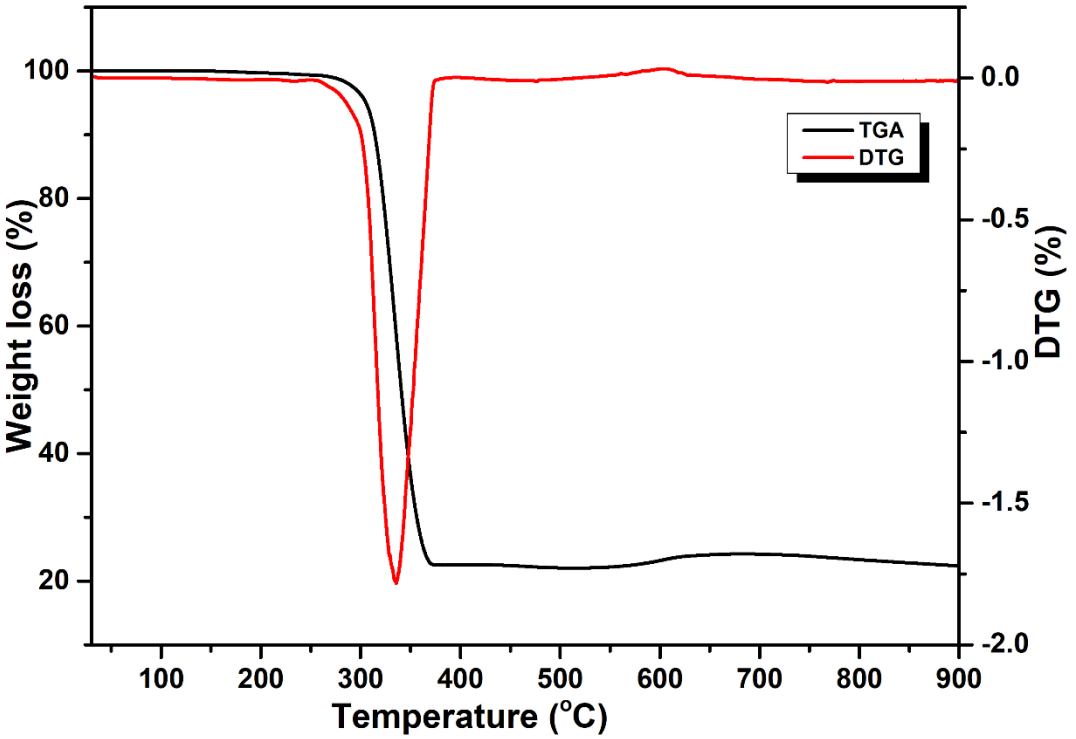


Figure 4.49 .TGA (black trace) and DTG (red trace) of BIRM-16(Ni).

4.7. Optimizing the reaction conditions for BIRM-16 and BIRM-16(Ni)

In the synthesis of BIRM-16 and BIRM-16(Ni), 3-phosphonopropionic acid was used as the main ligand and 4,4-bipyridine as auxiliary ligand. It was observed that under the reaction conditions used (Table 4.15), only 4,4-bipyridine was coordinated to the metal. On this note, we tried to modify the reaction conditions by changing the reaction solvent to water, keeping other reaction conditions the same. After some experimental trials, we found that changing the reaction solvent from DMF to water altered the coordination behaviour of BIRM-16 (Ni). That is, when a mixture of $Ni(CH_3COO)_2.4H_2O$ (1.89mol), 3-phosphonopropionic acid (1.34 mol), and 4,4-bipyridine (1 mol) were dissolved in 12 mL of distilled water and heated at 140 $^{\circ}$C for 48 h, light green crystals were obtained. Preliminary characterisation with powder XRD showed that this material matches well with a nickel carboxyphosphonate 2D material whose structure has already been established (Figure 4.50).[363] In this nickel carboxyphosphonate

material, both ligands were coordinated to the nickel metal. Chapter 6 of this thesis is dedicated to a fuller characterization and exploration of the CO_2 reduction potential of this nickel 2D material.

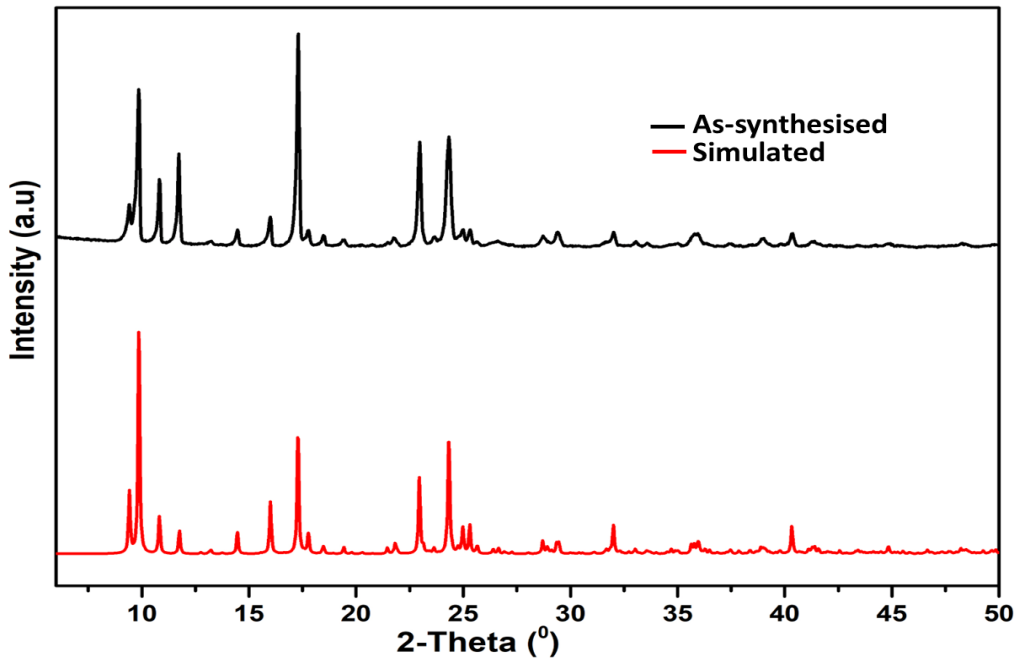


Figure 4.50 As-synthesised (black) and simulated (red) XRD pattern nickel carboxyphosphonate.[363]

4.8. Conclusion

This chapter has explored the possibility of synthesising new 3-dimensional metal carboxyphosphonate frameworks with potential as electrocatalysts for CO_2 reduction reaction. Previously, efforts have been made to achieve permanent porosity in BIRM-1 and its ion exchange products, and also attempt the synthesis of MOFs that are isostructural to BIRM-1. While previous attempts adopted almost the same protocol used for synthesis of BIRM-1, we decided first to modify the BIRM-1 protocol and thereafter attempt a new synthesis strategy with the goal of obtaining functional 3D MOFs. In this chapter, 5 new structures were established by single crystal XRD to be carboxylphosphonate materials: BIRM-11(Zn), BIRM-12(Cu), BIRM-13(Cu) and BIRM-14(Cu), BIRM-15(Co) are either layered

compound or 2D metal organic framework structures. Others, including BIRM-16(Co) and BIRM-16(Ni) were 3D coordination networks but not carboxylphosphonate materials. It is important note that pH plays a critical role in achieving complete deprotonation of the carboxylphosphonate ligand and metal–ligand coordination. Although complete deprotonation was achieved in BIRM-11(Zn), BIRM-14(Cu) and BIRM-15(Co), their crystal structures appeared as a 2D frameworks with covalent bonding. BIRM-12(Cu) and BIRM-13(Cu) were synthesized in acidic media because these reaction solutions were intolerant to pH > 3 and as such complete deprotonation of the ligand is not achieved. For this reason, their crystal structures appeared as hydrogen bonded layered structures. While the inorganic layers of BIRM-12(Cu) and BIRM-13(Cu) are linked by carboxylphosphonate via hydrogen bond, however, the inorganic layers of BIRM-11(Zn), BIRM-14(Cu) and BIRM-15(Co) were linked ligand(s) via covalent/coordination bonds. It can therefore be inferred that BIRM-12(Cu) and BIRM-13(Cu) are layered compounds while BIRM-11(Zn), BIRM-14(Cu) and BIRM-15(Co) are 2D metal organic frameworks (MOFs).

Attempts were made to modify the dimensionality of BIRM-13 into 3D structures using 4,4-bipyridine auxiliary ligand, producing BIRM-14, BIRM-16 and BIRM-16(Ni). For BIRM-14, coordination of 4,4-bipyridine auxiliary ligand to BIRM-13 was achieved, but structural reorientation of the coordination geometry of BIRM-13 to a 3D framework was not achieved as BIRM-14 crystallised as 2D structure. However, in BIRM-16 and BIRM-16(Ni), the coordination of 4,4-bipyridine auxiliary ligand to Co/Ni metals was influenced by the DMF reaction solvent used in the synthesis. The DMF solvent undergo hydrolysis to formic acid, shifting the solution pH to a high basic region, thereby favouring its deprotonation to formic acid over 3-phosphonopropionic acid ligand. For this reason, BIRM-16 and BIRM-16(Ni) are not carboxyphosphonate materials. Notably, one striking feature of BIRM-16 and BIRM-16(Ni)

is that they are isostructural and exhibit chirality which is an important feature in materials for enantiomeric separation. The future direction for this carboxylphosphonate material synthesis and discovery will be to explore various organic bases such as pyridine, amines, etc. as pH adjuster/deprotonator and can as well function as a structure directing agent. One of the potential drawbacks of 3-phosphonopropionic acid ligand is a lack of rigidity which makes the synthesis of porous 3D supramolecular structure difficult. Therefore, the use of more rigid phenylcarboxyphosphonate ligands is explored in chapter five with a view to preparing further novel porous carboxylphosphonate metal organic frameworks.

The electrocatalytic activities of BIRM-12(Cu), BIRM-13(Cu), BIRM-14(Cu) and BIRM-15(Co) were explored with respect to the CO_2 reduction reaction. Although CO_2 conversion may not have been achieved with BIRM-12, BIRM-13 and BIRM-15 catalysts, their activity toward HER is of interest, as hydrogen gas has been considered as a clean fuel of the future. Meanwhile, BIRM-14 demonstrated a promising activity towards CO_2 reduction, however, controlled potential electrolysis experiments are required to analyse the product and determine product selectivity and catalyst stability. The CV scan and the CO_2 reduction activity of this catalyst resemble that of Cu nanoparticles, which may suggest that BIRM-14 might have been transformed to Cu nanoparticles which might be what is driving the CO_2 reduction reaction. However, the argument will need to be proven right or otherwise by high resolution TEM, powder XRD before and after CO_2 reduction reaction.

CHAPTER FIVE

Synthesis, characterization, and crystal structure of novel metal- organic frameworks containing a rigid aromatic carboxyphosphonate linker

5.1. Introduction

The discovery of BIRM-1 by Zhao in 2012, opened up several possibilities for this three-dimensional and ion-exchangeable porous zinc carboxyethyl phosphonate MOF.[90] Zhao demonstrated the exchange of Li^+, K^+, Na^+, Co^{2+}, Mn^{2+} and Mg^{2+} with NH_4^+ in the pores of BIRM-1, and the structure of K^+-BIRM-1 and Mg^{2+}-BIRM-1 were fully resolved. The activation of BIRM-1, however, proved very challenging as attempts to dehydrate it caused the MOF framework to temporarily lose its long-range order, but upon rehydration, BIRM-1 was restored showing that it undergoes reversible amorphization, thereby proving its structural flexibility. The fact that BIRM-1 lost its porosity upon dehydration reduces the chance of exploring its potential application, as many of the applications of MOFs depend on the internal voids and channels they can provide. Attempts to synthesise other metal analogues of BIRM-1, as well some new porous MOFs with 3-phosphonopropionic acid ligand produced several two-dimensional layered or linked-layer structures which were presented in chapter four of this thesis. We therefore concluded that the 3-phosphonopropionic acid ligand might impart structural flexibility making formation of MOFs with predictable and rigid structures less likely.[364] Therefore the use of a more rigid linker might increase the chance of producing MOFs with permanent porosity. In this instance, the aromatic linker 4-phosphonobenzoic acid, whose chemical structure is depicted in Figure 5.1, was selected. Although some other rigid

carboxyphenylphosphonic acids such as 5-phosphonoisophthalic acid and 2,4,6-tri-(phenylene-4-phosphonic acid)-s-triazine were considered, these ligands are not commercially available, and several unsuccessful attempts were made to synthesize some of them. In this chapter, we explore the possibility of preparing novel porous carboxylphosphonate metal organic frameworks using 4-phosphonobenzoic acid ligand.

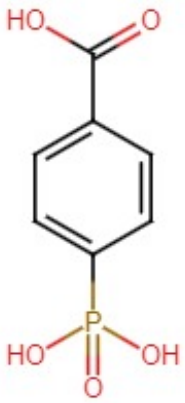


Figure 5.1. Chemical structure of 4-phosphonobenzoic acid, the linker used in this work.

5.2. Experimental

5.2.1. Solvothermal Synthesis

We started this exploratory synthesis with zinc as node, 4-phosphonobenzoic acid as linker, benzoic acid as a crystal modulator and a mixture of DMF and water (v/v 2:1) as solvent. Apart from 4-phosphonobenzoic acid which was purchased from abcr UK, all other reagents used for this work were sourced from Sigma-Aldrich. The synthesis started by dissolving the quantities of reagents in Table 5.1 in 4 mL of solvent mixture of dimethylformamide (DMF) and water (v/v 2:1). After sonication, the mixture was transferred into a 7 mL glass vial and placed in an oven at 65 °C for 12 hours. The product was recovered by vacuum filtration and washed with dimethylformamide (DMF) solvent. Further experiments started by varying the synthesis temperature and time.

Table 5.1 Quantities of reagents used in the initial synthesis attempt of a framework material.

	Zn $(NO_3).6H_2O$	4-phosphono benzoic acid	benzoic acid
Mass (g)	0.02	0.02	0.25
Molar ratio	1	0.15	30.5

5.3. Synthesis of BIRM-17 $[Zn_2 (O_3PC_6H_4CO_2)_3 (DMF)(DMA)]$

The initial synthesis attempt yielded a product composed of a mixture of white powder and some tiny needle-shaped crystals. The sample was submitted to the School of Chemistry's single crystal diffraction service run by Dr Louise Male. A suitable crystal was found and preliminary SCXRD data were collected. A preliminary check for crystallinity with PXRD obtained from CIF file showed that the material is highly crystalline with an intense early angle peak with large d-spacing (Figure 5.2). These preliminary data revealed that the material crystalised in a triclinic space group $P\bar{1}$. The asymmetric unit of this crystal comprises two Zn (II) cations, three $(O_3PC_6H_4CO_2)^{3-}$ anions, one DMF ($(CH_3)_2NCOH$) and one dimethylammonium ion ($(CH_3)_2N^+$) (Figure 5.3). The planes of $[ZnO_4]$ tetrahedra are interconnected with $[CPO_3]$ tetrahedra via corner sharing, forming a 1-Dimensional chains along the x-axis (Figure 5.4a). Two adjacent 1D chains are H-bonded via the carboxylate oxygens of the 4-phosphonobenzoic acid ligand, thereby giving rise to a 2-Dimensional layered structure in the xz plane (Figure 5.4b). Since the material was not a structure of interest, complete structural deduction and refinement was not prioritised and a full data set was not collected. This material will be named as BIRM-17 going forward.

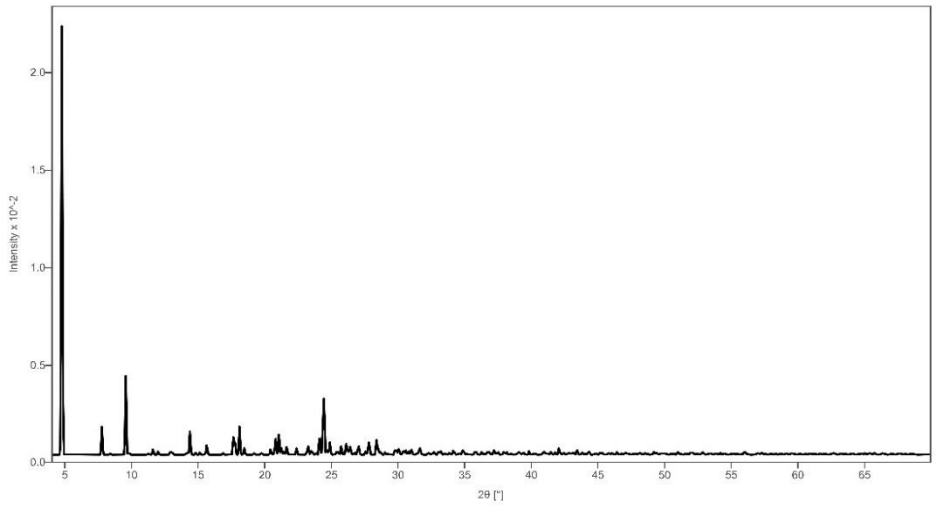


Figure 5.2. PXRD pattern obtained from the product of the BIRM-17 synthesis.

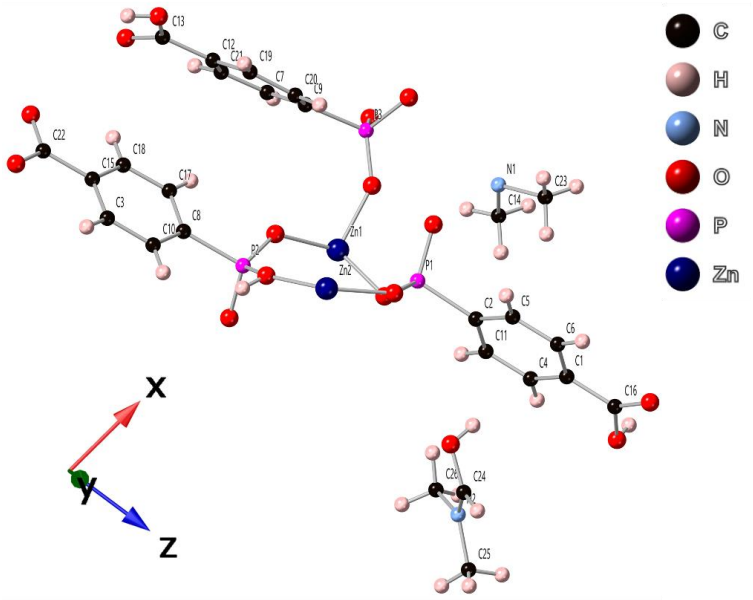


Figure 5.3. Asymmetric unit of BIRM-17 obtained from preliminary dataset.

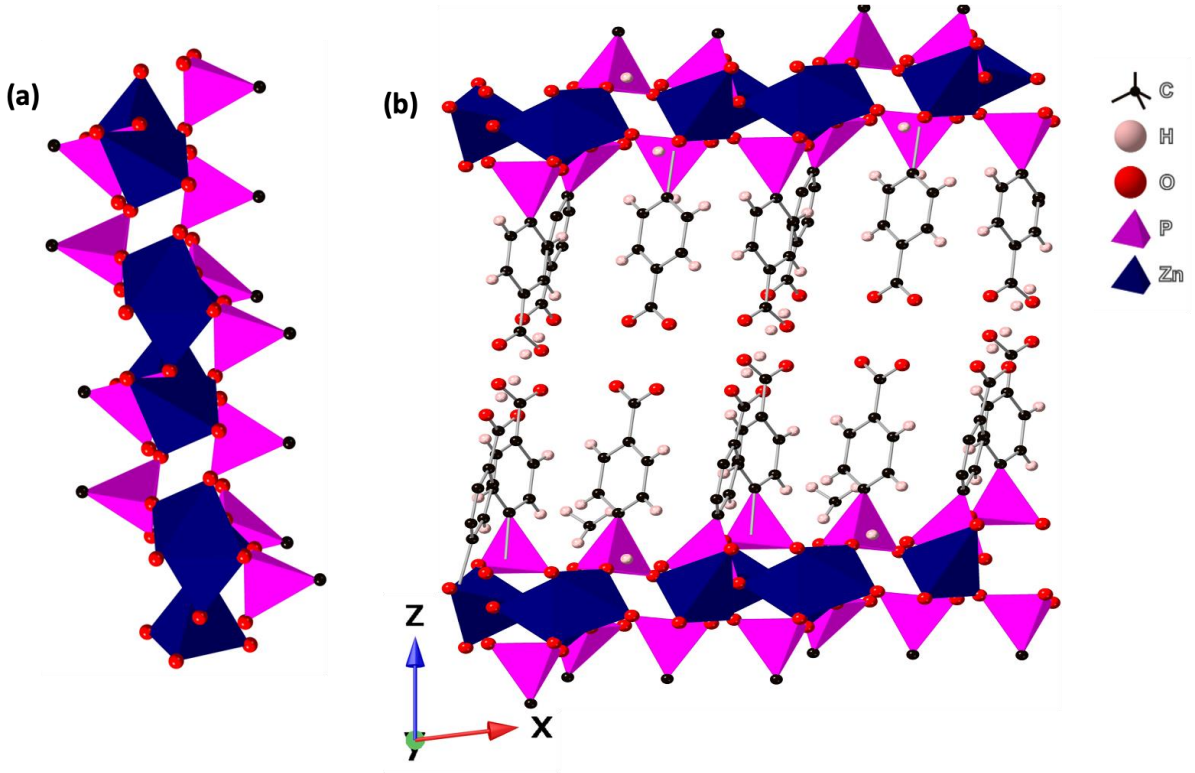


Figure 5.4. (a) one-dimensional chain of the inorganic building block (b) structure of BIRM-17 viewed along the y-axis.

5.4. Porous Framework: BIRM-18 $[Zn_2[(O_3PC_6H_4COO)_2].\ 4(H_2O)\ (DMF)\ 2(DMA)]$

Since the product obtained from the first attempt produced a mixture of powder and single crystals, it can be deduced that material is a mixture of phases, in which the single crystal component produces a layered structure described above. It can be inferred that the short reaction time may not have given the ligand sufficient time to undergo complete deprotonation[365] while the low reaction temperature prevented the optimum rate of ligand deprotonation and metal-ligand formation, resulting in the assemblage of structure with low dimensionality.[366] The synthesis time was increased to 24 hrs while the temperature was varied at an interval of 5°C between 65 and 140°C with the hope of obtaining a pure single and porous phase. However, at 80 °C, another white crystalline powder was obtained and a

preliminary check under microscope showed that the material was a mixture of powder and small shining prism-like crystals, indicating a mixture of phases. The sample was sent to the National Crystallography Service at the University of Southampton after unsuccessful attempts to collect data of sufficient quality for structure solution at Birmingham and Diamond Lightsource. A good and high-quality dataset was returned, and the structure was refined and solved with the assistance of Dr Louise Male. This material will be named as BIRM-18 going forward.

5.4.1. Crystal structure of BIRM-18

For single crystal diffraction analysis, a suitable single crystal was selected and mounted on the goniometer for characterization and a good dataset was collected. Single crystal X-ray diffraction analysis (Table 5.2 and chapter 9 Table A5.1-5.8 for structure details, selected bond lengths and angles) showed that BIRM-18 crystallizes in monoclinic space group *P* $2_1/c$. The asymmetric unit of this crystal comprises two Zn (II) cations, two $(O_3PC_6H_4CO_2)^{3-}$ anions, one dimethyl formamide ($(CH_3)_2NCOH$) and two dimethylammonium ion $[(CH_3)_2NH_2]^+$ (Figure 5.5a). The two Zn ions in the asymmetric unit have similar coordination environments and similar tetrahedral geometries, with each Zn atom coordinated to three phosphonate oxygen atoms from different 4-phosphonobenzoic acid ligands and one carboxylate oxygen atom from another 4-phosphonobenzoic ligand (Figure 5.5b). The corner-shared connection between the ZnO_4 and CPO_3 tetrahedra give rise to 1-dimensional polymeric chains along the z- axis (Figure 5.6a) and these chains are bridged by the ligand, giving rise to an extended 3-dimensional structure (Figure 5.6b). The resulting 3D framework contains two crystallographic channels along the x axis (Figure 5.6b). The large channels which are about 14.6 Å in diameter are filled with guest DMF molecules, Dma^+ cations, and water molecules that interact with the

framework through hydrogen bonds (Figure 5.6 and 5.7). The smaller channel is about 13.7 Å and is void. Calculations performed with MoloVol[367] showed that the solvent accessible volume is 810.61A^3 per unit cell, which is about 25.8% of the crystal volume. It can be observed from Figure 5.10 that the as-synthesised PXRD pattern did not match the simulated pattern obtained from the solved structure, indicating that BIRM-18 sample contained more than one phase.

Table 5.2 Crystallographic data for BIRM-18.

Sample	BIRM-18
Formula	$Zn_2[(O_3PC_6H_4COO)_2]$ $(CH_3)_2NCOH).2(CH_3)_2NH_2)^+.$ $4H_2O$
Formula Weight	766
Space group	P $2_1/c$
a (Å)	15.2833(7)
b (Å)	19.4779(11)
c (Å)	10.5400(5)
Volume (Å^3)	3137.6
Goodness-of-fit on F2	0.983
wR2	0.1737
Largest diff. peak/hole / e Å^{-3}	1.73/-0.77

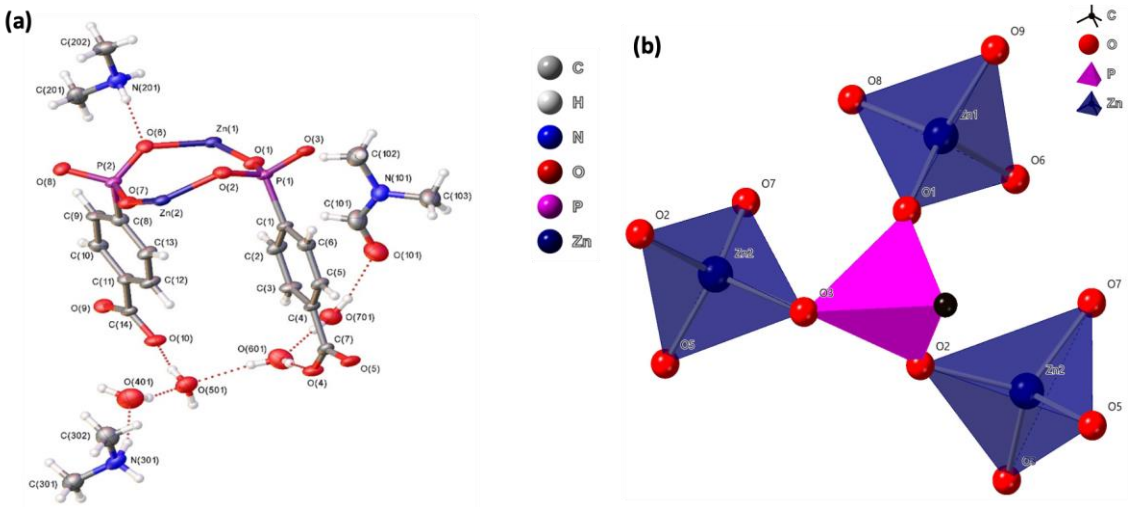


Figure 5.5. (a)Asymmetric unit of BIRM-18. The thermal ellipsoids are drawn at the 50% probability level. (b) coordination geometry of BIRM-18.

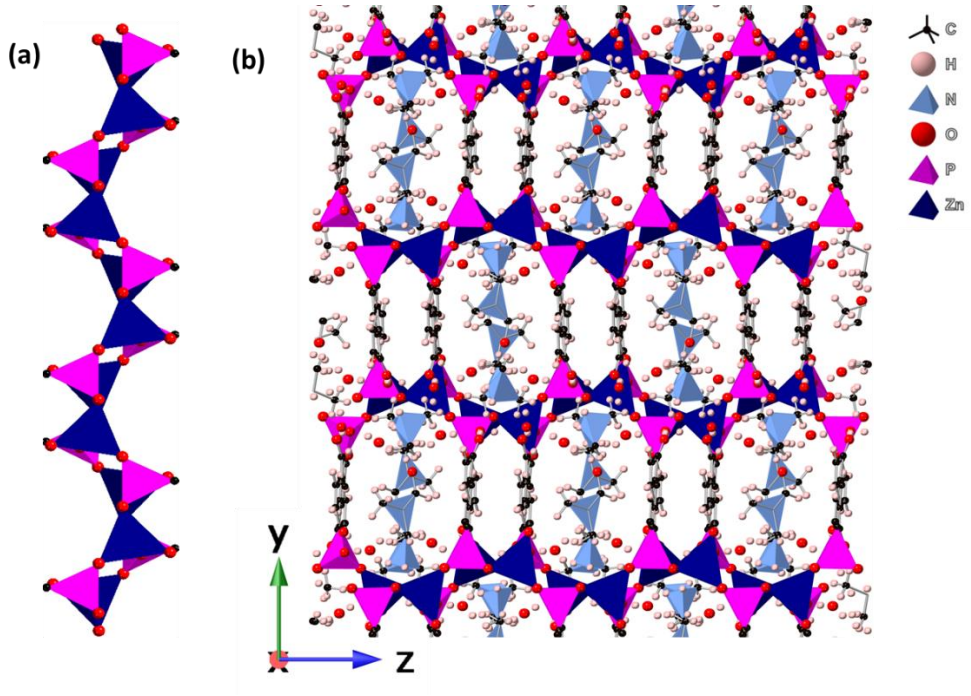


Figure 5.6. (a) Polymeric chain formed by ZnO_4 and CPO_3 tetrahedra in BIRM-18 (b) Polyhedral view of the structure of BIRM-18 along x axis showing a 3D framework filled with guest DMF molecules, Dma^+ cations, and water.

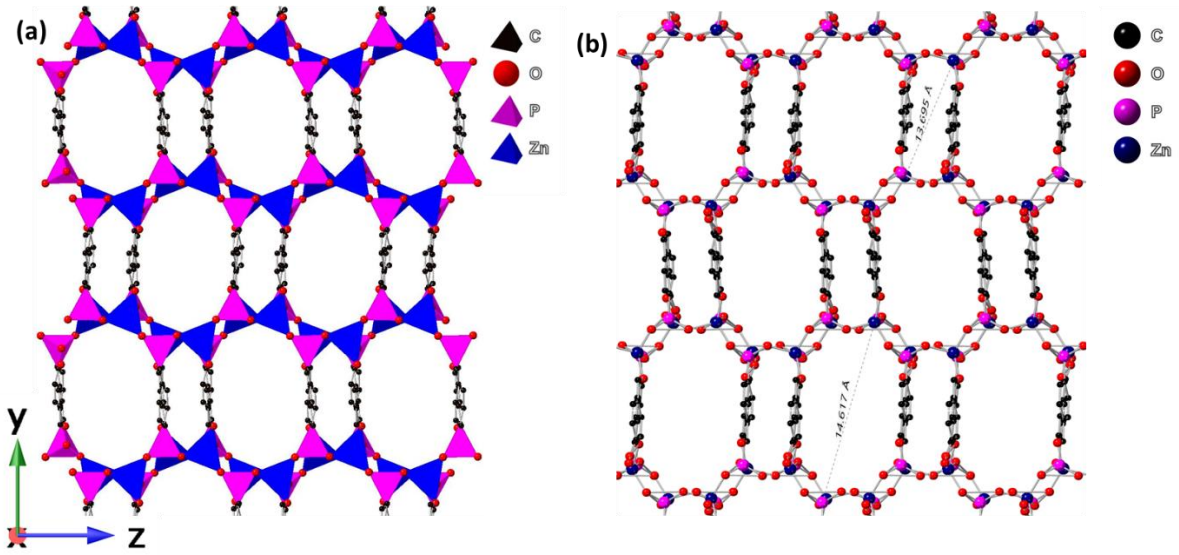


Figure 5.7 (a) Polyhedral view and (b) ball and stick view of BIRM-18 without channel contents, showing the two distinct crystallographic channels in the structure with the small channels having a diameter of ca 13.7 Å and the bigger channels having a diameter of ca 14.6 Å.

When the connectivity between the ZnO_4 and CPO_3 tetrahedra is viewed along the z-axis, double-crankshaft (dc) chains of inorganic clusters which are further cross-linked by the organic ligands can be observed, giving rise to a 3-dimensional structure with a visible large channel of diameter 16.7 Å along the z-axis (Figure 5.8). The topological analyses were performed using the Topospro program with Zn and P atoms considered as framework atoms. The framework of BIRM-18 is considered to exhibit a structure like the (4;2)-connected topology of zeolites.[368] As can be seen in Figure 5.9, this structure can also be described as stacking of parallel 2-D (4.8^2) sheets formed by 4-MRs and 8-MRs. Additionally, the 8-MRs in BIRM-18 have an arrangement where half of the vertices point upwards, while the other half point downward, which indicates the structure has the topology of GIS-type zeolites[101]. It is worthy of note that this GIS-type topology is not common for metal phosphonates as few have been reported for metal phosphonates framework[89, 369]

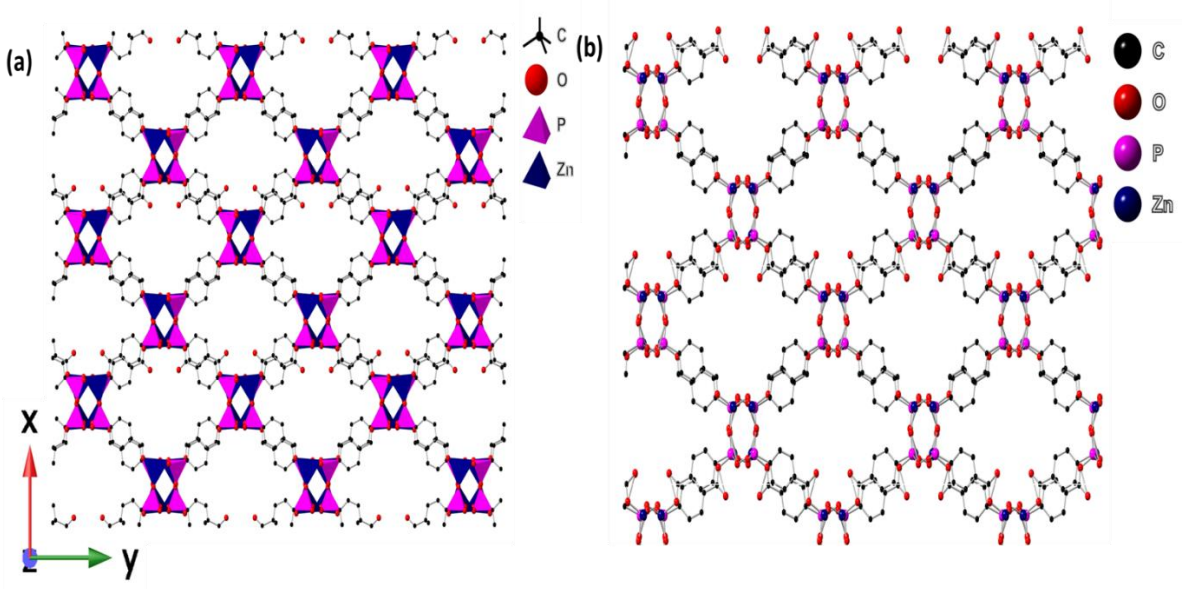


Figure 5.8. (a) Polyhedral (b) ball and stick representation of BIRM-18 framework without channel contents, viewed along the z-axis.

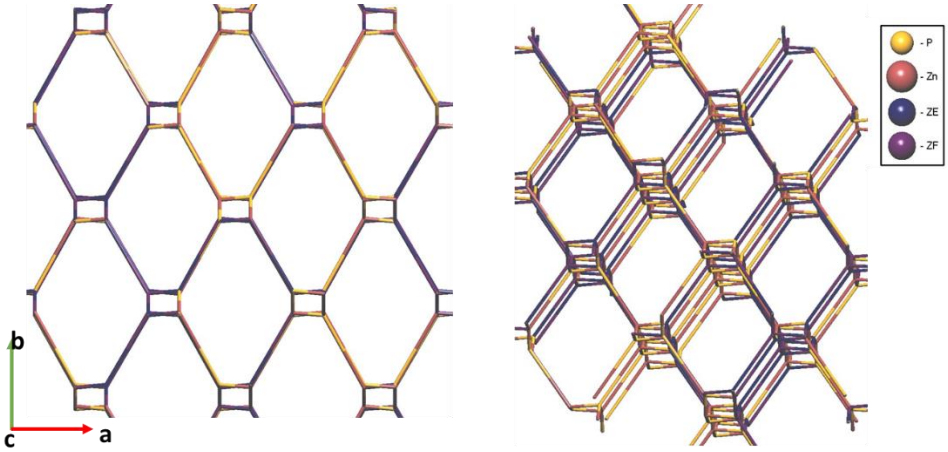


Figure 5.9. Stick representation of GIS topology of BIRM-18. Where ZE is a TopoSpro computation terminology for tetrahedral geometry of ZnO_4 and CPO_3 while ZF is standard simplification method used within the software program.

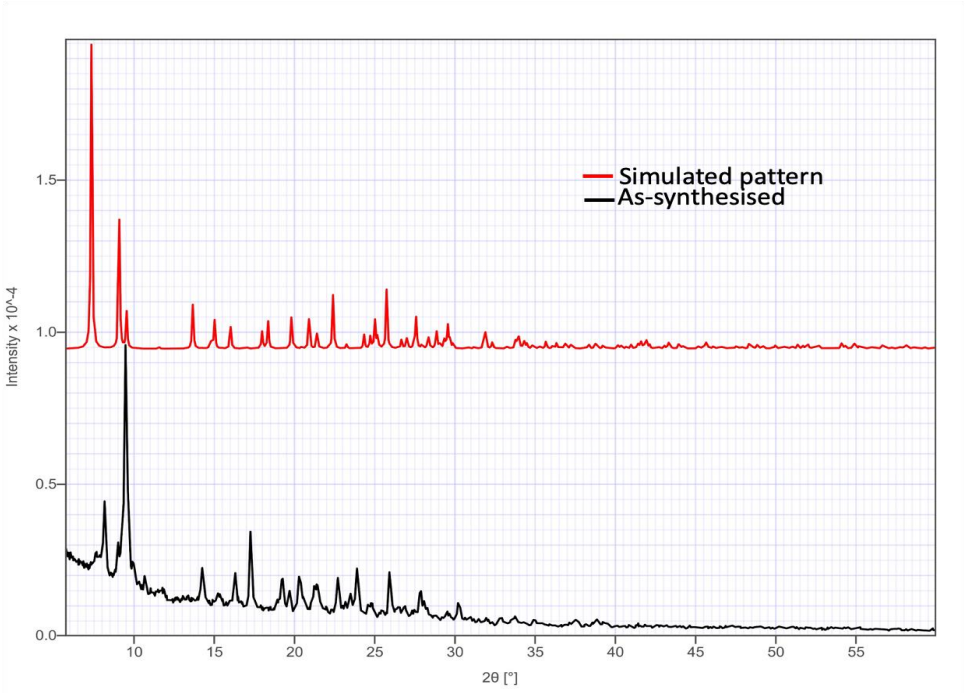


Figure 5.10. As-synthesised (black) and simulated (red) XRD pattern of BIRM-18.

5.4.2. FTIR studies of BIRM-18

The FTIR spectrum of BIRM-18 was recorded to obtain some additional crystallochemical information (Figure 5.11, Table 5.3). The FTIR spectra of some metal phosphonates from the previous work of Hix et al.,[95, 328] and Zhao[90] were used as a guide to assign various functional group in BIRM-16. A broad and weak peak found around 3457 cm^{-1} is due to stretching

vibrations of O–H the coordinated water molecules.[328] A sharp intense peak observed at 1683 cm^{-1} and short peak visible at 1550 cm^{-1} can be linked to C=O and N-H stretching vibration from the DMF solvent respectively.[370, 371] A broad peak at 2884 cm^{-1}, and two sharp ones at 2662 cm^{-1} and 2536 cm^{-1} are attributed to C–H stretching vibrations from the carboxylphosphonate groups.[90, 372] The symmetric and asymmetric stretching vibrations of -C=O in -COO-Zn^{2+} are evident as strong bands at 1419 cm^{-1} and 1268 cm^{-1}, respectively. The P–C stretching mode is observed at 1499 cm^{-1}, and the P–O stretching modes of the phosphonate groups are seen as a number of sharp peaks in the range 1143–955 cm^{-1}.[328] The peaks in the region of 900-450 cm^{-1} confirmed the presence of Zn-O bonds. It can therefore be inferred that all the peaks expected from the functional groups within the structure, such as those arising from deprotonated carboxylate and phosphonate groups are present in the FTIR spectra.

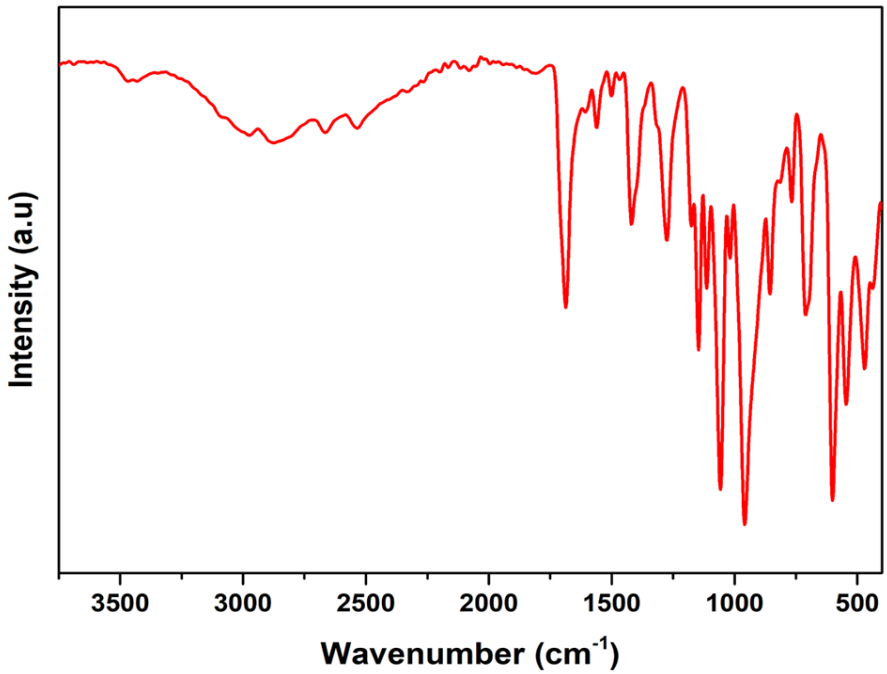


Figure 5.11. FTIR spectrum for BIRM-18.

Table 5.3. Observed FTIR shifts and assignments for BIRM-18.

Wavenumber (cm^{-1})	Peak Assignment
3457	Hydroxyl O–H
2884, 2662, 2536	Aromatic C-H
1683	C=O (from DMF)
1550	N-H (from DMF/DMA)
1499	P-C
1419	Carboxylate C-O (sym)
1268	Carboxylate C-O (asym)
1143	Phosphonate P-O
1055	Phosphonate P-O
955	Phosphonate P-O
<900	Zn-O

5.4.3. Morphological studies of BIRM-18

The SEM image shown in Figure 5.12 illustrates the crystal morphology of BIRM-18. Rectangular prisms-like crystals can be observed from the SEM image. Presents are also some other tiny crystals suggesting that BIRM-18 contain other phases. The EDX analysis showed an average Zn:P ratio of 1:1.02 which agrees well with the ratio found in the solved structure (1:1).

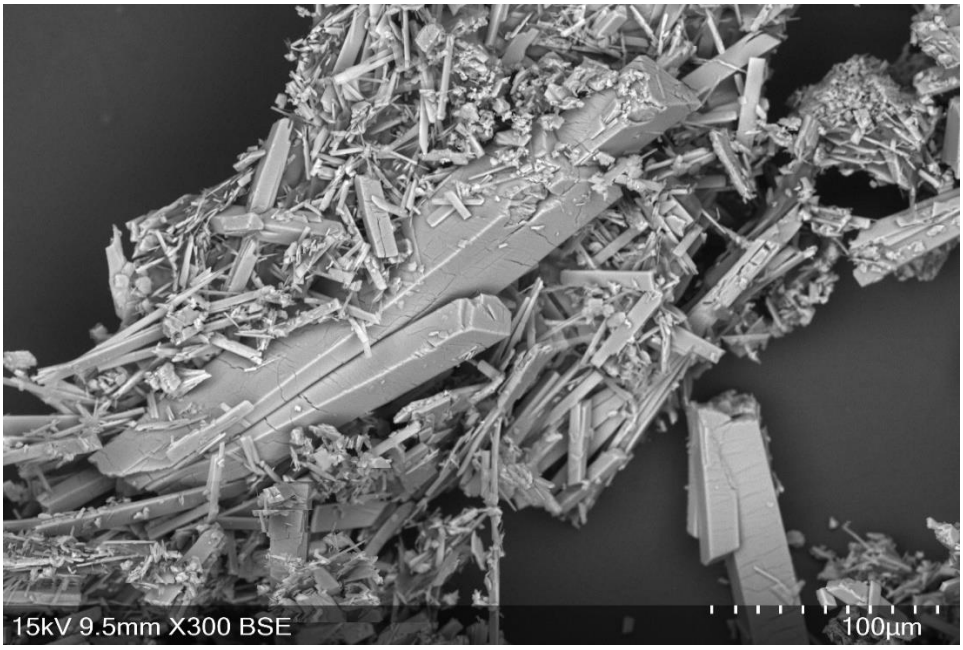


Figure 5.12. SEM image for BIRM-18 crystals at 100× magnification.

5.4.4. Thermal stability studies of BIRM-18

Figure 5.13 shows the thermogravimetric analysis (TGA) curve for the as-synthesised BIRM-18. As can be seen from the TGA curve, the thermal behaviour of BIRM-18 can be divided into three main regions. In the first region, the water trapped within the framework is evaporated as evidenced in the gradual and steady weight loss observed at the start of the TGA curve. The framework remained stable up to ca 480 ^{0}C. The weight loss witnessed in the region between 100-480 ^{0}C can be associated with the removal of DMF and DMA from the framework as the boiling point of DMF is 153 ^{0}C.[373] The most significant weight loss was observed at temperature > 480 ^{0}C (second region) which can be attributed to the decomposition of the coordination network and combustion of the organic components, demonstrating that the MOF is thermally stable up to 480 ^{0}C. At the third region which corresponds to the temperature > 600 ^{0}C, the material continued to exhibit gradual weight loss and the transformation was complete at about 900°C, resulting in a total weight loss of 45.5%. The final decomposition product is an amorphous material with some low intensity broad peaks around 20° and 30° 2θ (as shown by

the PXRD pattern in Figure 5.14), however, attempts to phase match it to known phases have been unsuccessful.

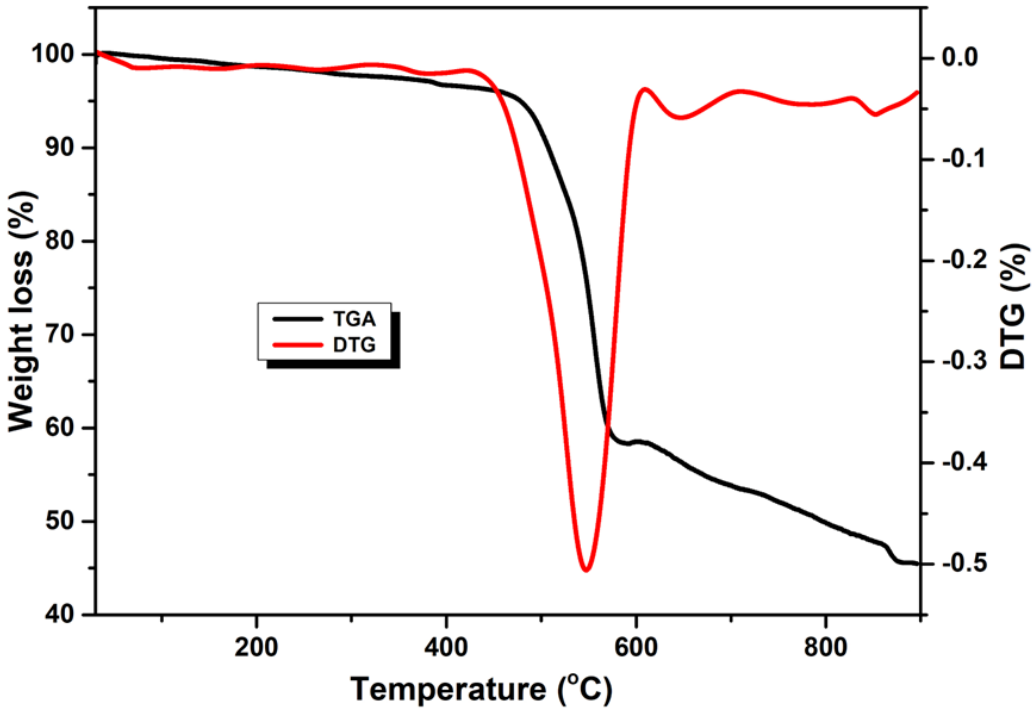


Figure 5.13. TGA (black trace) and DTG (red trace) of BIRM-18.

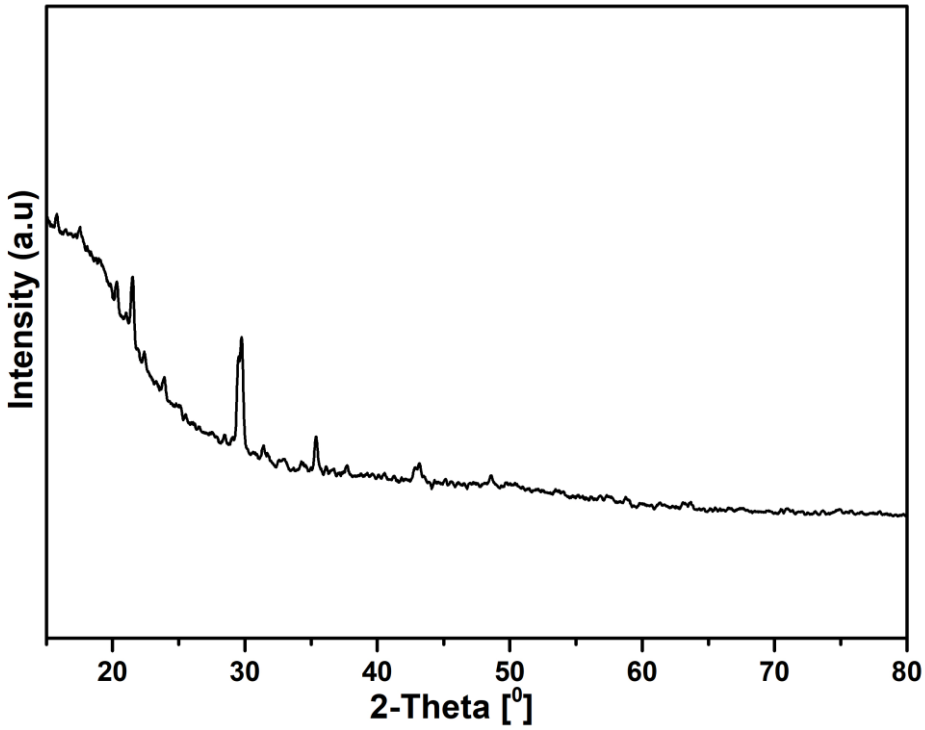


Figure 5.14. PXRD pattern of the TGA product from BIRM-18.

5.5. Synthesis Optimization

One of the difficulties with BIRM-18 is that its crystals are present in a mixture of other phases as the simulated pattern of the structure did not match the as-syntheses one (Figure 5.10). Optimization of the reaction system was attempted at a range of temperature 80 -170 ^{0}C at an interval of 10 ^{0}C. The PXRD patterns from the products of these syntheses are shown in Figure 5.15. It can be observed that the PXRD patterns at different temperatures were not consistent with that of BIRM-18 indicating the formation of a series of new phases. A preliminary view of these crystals under microscope showed that material synthesised at 100 ^{0}C and 120 ^{0}C contained a mixture of plate-like crystals and some other tiny crystals, indicating a mixture of phases. A plate-like crystal was picked out from these materials and its structure solved and presented as BIRM-19 in the next section. High intensity low angle peaks are noticed in the pattern of BIRM-18@ 130 ^{0}C and BIRM-18@ 140 ^{0}C, indicating large d-spacing. However, their structural solution could not be pursued because the crystals were too small for SXRD characterization. Varying the time of the synthesis did not produce pure phase of BIRM-18.

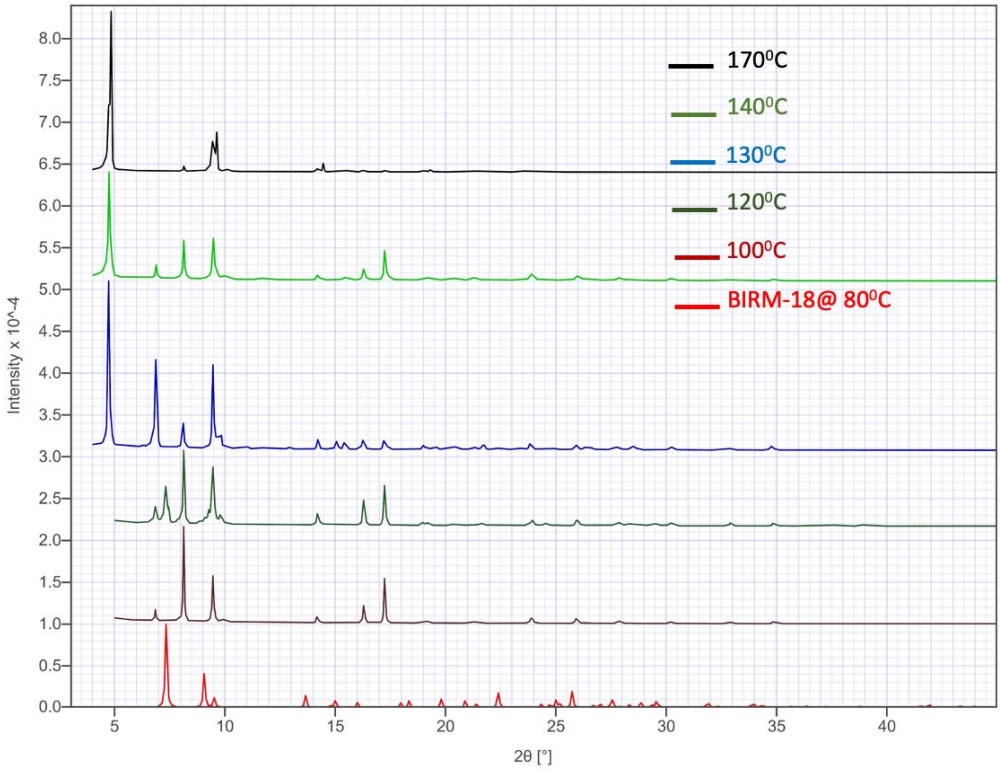


Figure 5.15. PXRD patterns from products of a range of syntheses across a temperature scale with a simulated pattern of BIRM-18 for comparison.

Since it is possible for the sample of BIRM-18 to contain some unreacted ligand and metal salt, it was hypothesized that washing with common solvent such as DMF, water, acetone etc might dissolve the uncoordinated ligand and metal salt and produce a pure phase of BIRM-18. Unfortunately washing had little or no effect on the XRD patterns. Modification of additional variables, including reaction ratio of ligand to zinc metal salt, concentration and solvent was also explored in optimizing the BIRM-18 synthesis. For instance, varying the reaction ratio and use of solvent mixtures did not result in growth of single crystals of BIRM-18. It is worthy of note that optimization of the reaction protocol could not be further explored due to time constraints as BIRM-18 was first synthesized towards the tail end of my time in the laboratory.

5.6. Second Porous Framework: BIRM-19 [$Zn_2[(O_3PC_6H_4COO)_2]$.2(DMA)]

An attempt to produce a pure phase of BIRM-18 by increasing the reaction temperature further, with all other reaction conditions remaining unchanged, produced a new porous phase at 120 ^{0}C. A preliminary check under microscope showed that the material was a mixture of powder and small plate-like shape crystals, indicating a mixture of phases. The sample was submitted to the School of Chemistry's single crystal diffraction service. A good dataset was obtained, and the structure was refined and solved by Dr Male. This phase will now be referred to as BIRM-19

5.6.1. Crystal structure of BIRM-19

Single crystal X-ray diffraction analysis (Table 5.4 and chapter 9 Table A5.9-5.17 for structure details, selected bond lengths and angles) revealed that the material, named BIRM-19, crystallizes in monoclinic space group C 2/c. The asymmetric unit of this crystal comprises of two Zn (II) cations, two $(O_3PC_2H_4CO_2)^{3-}$ anions, and two dimethylammonium ions $[(CH_3)_2NH_2]^+$ one of which is disordered over three positions at an occupancy ratio of 0.4 / 0.35 / 0.25, making refinement of the occupancy parameters more challenging (Figure 5.16a). Two crystallographically unique zinc atoms and two completely deprotonated carboxylphosphonate ions are visible from the framework. Zn1 is tetrahedrally bonded to four phosphonate oxygens (O1, O3, O6, O8) while Zn2 is coordinated to two phosphonate oxygens (O2, O7) and two carboxylate oxygens (O5, O9) (Figure 5.16b). On the other hand, the carboxylphosphonate ions occupy the same coordination environment with each coordinating to Zn atoms via three phosphonate oxygen atoms and one carboxylate oxygen atom, leaving the other carboxylate oxygen atom uncoordinated. The corner-sharing connection between the ZnO_4 and CPO_3 tetrahedra gives rise to 1-dimensional zig-zag chains

with each neighbouring chain linked by ligands along the x and z axes, giving rise to an extended 3-dimensional zeolite-like open framework (Figure 5.17). The zigzag chains in BIRM-19 are similar to those found in the large-pore aluminophosphate JDF-20[374] and some zinc phosphates.[375, 376] Two crystallographic channels measuring 9.47 Å and 15.71 Å are visible in the framework (measurement is taken as distance between the centers of opposite atoms). DMF, the solvent used in the synthesis, partially decomposed to DMA, which functions as structure-directing agent, and this protonated molecule occupies the pores and channels of the framework.

Table 5.4 Crystallographic data for BIRM-19.

Sample	BIRM-19
Formula	$Zn_2[(O_3PC_6H_4COO)_2].2(CH_3)_2NH_2)^+$
Formula Weight	621.11
Space group	C 2/c
a (Å)	25.9158(7)
b (Å)	8.4976(2)
c (Å)	25.6910(7)
Volume($Å^3$)	5657.6(3)
Goodness-of-fit on F2	1.051
wR2	0.1563
Largest diff. peak/hole / e $Å^{-3}$	0.81/-0.84

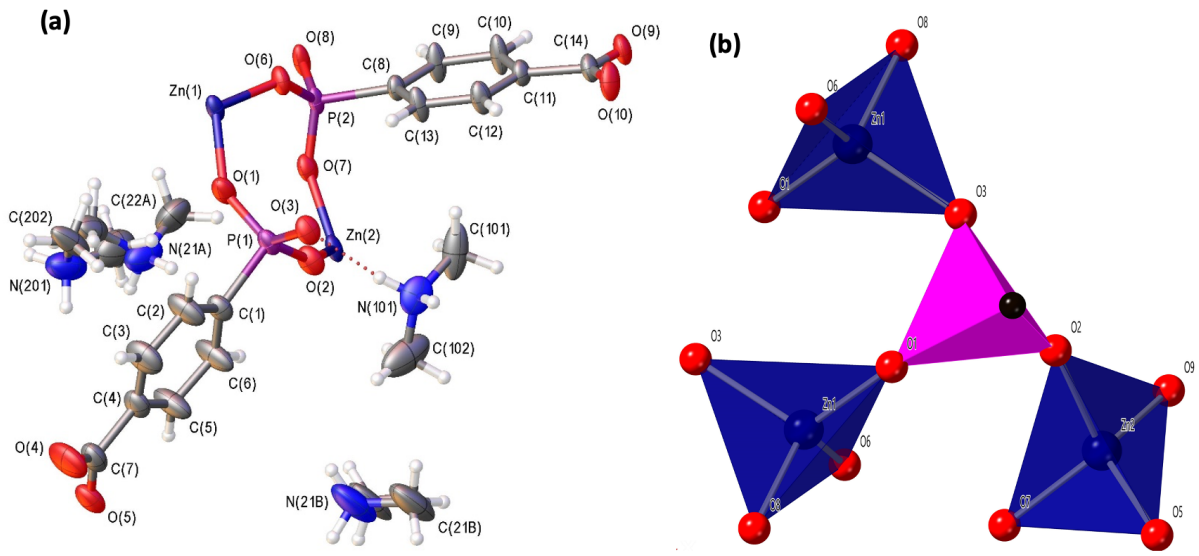


Figure 5.16. (a) Asymmetric unit of BIRM-19. The thermal ellipsoids are drawn at the 50% probability level. (b) coordination geometry of BIRM-19

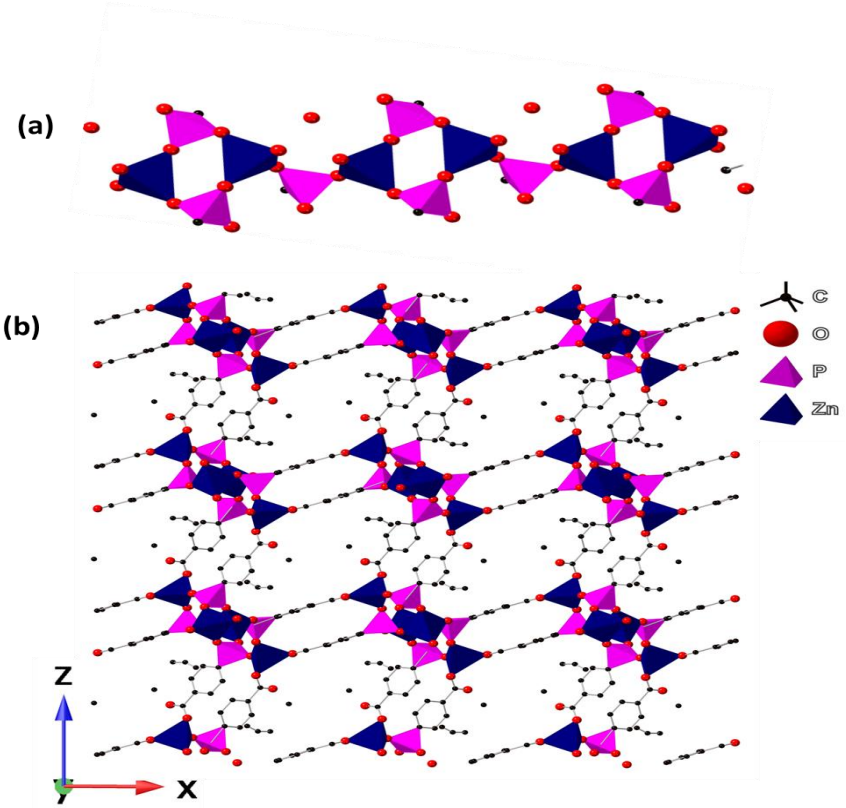


Figure 5.17. (a) Zig-zag chain formed by ZnO_4 and CPO_3 tetrahedra in BIRM-19 (b) Polyhedral view of the structure of BIRM-19 along the x axis showing a 3D framework. Hydrogen atoms and pore content have been omitted for clarity.

When the connectivity between the ZnO_4 and CPO_3 tetrahedra is viewed along the z-axis, 2-Dimensional polymeric chains along the y-axis, which are further cross-linked by the organic moieties of the ligands, give rise to a 3-dimensional porous structure with a visible large channel of diameter 9.12 Å along the z-axis (Figure 5.18). As described by Topospro analysis, the topology of BIRM-19 can be described as a (4;2)-connected zeolite-like framework with Zn and P occupying vertices of the network (Figure 5.19). Furthermore, the structure can either be projected as (4,8) sheet stacked along b-axis or a (4,6) sheet stacked along a-axis, both as ABAB sequences, and this topology arrangement is similar to those found in a similar Zn phosphonocarboxylate framework whose topology has not yet been observed in structures of molecular sieves.[375] BIRM-19 is also a 3-dimensional porous structure, however, its structure and topological net is similar to the structure obtained by Chen *et al*.[375] differing in the pore contents and synthetic route.

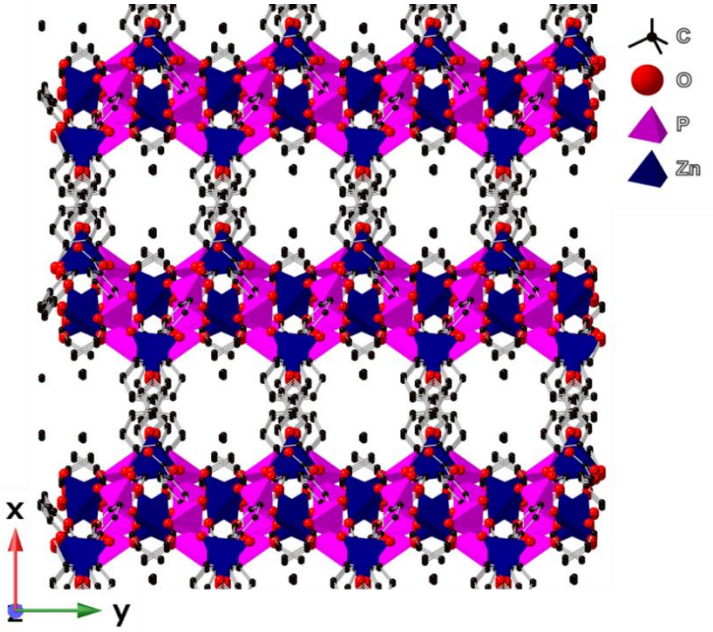


Figure 5.18. (a) Polyhedral view of BIRM-19 framework without channel contents, viewed along z-axis.

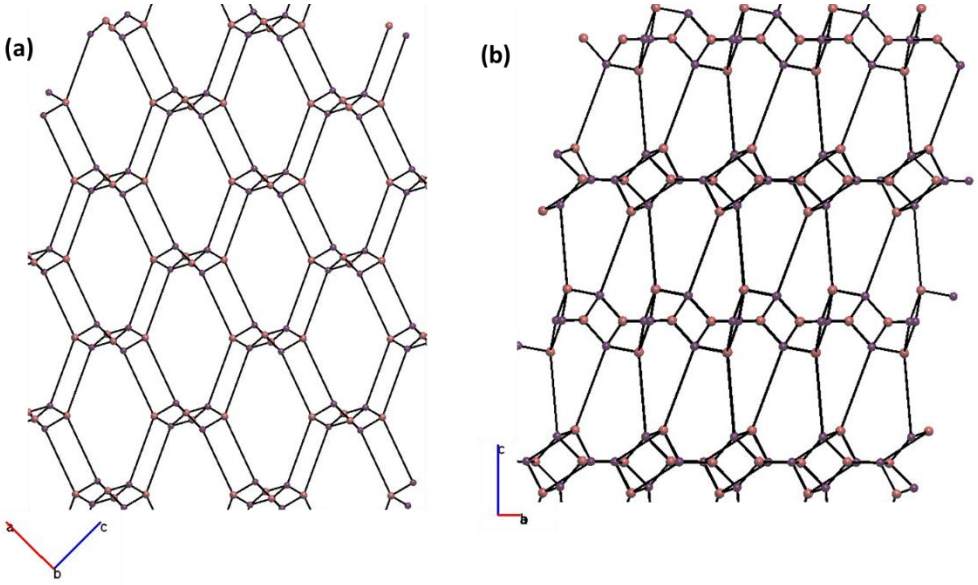


Figure 5.19. Schematic representation of the (a) (4,8) sheet and (b) (4,6) sheet in BIRM-19.

5.6.2. FTIR studies of BIRM-19

The FTIR spectrum for BIRM-19 is shown in Figure 5.20 with notable peak assignments in Table 5.5. The peak about 3050 cm^{-1} was attributed to the N–H stretches from dimethylammonium ion. The symmetric and asymmetric stretching vibrations of the carboxyl group are evident as strong bands at 1470 cm^{-1} and 1394 cm^{-1}, respectively. These wave numbers are lower than one might expect due to the coordination of the carboxylate group to the zinc atom. The P–C stretching mode is observed at 1262 cm^{-1}, and the P–O stretching modes of the phosphonate group are seen as symmetric and asymmetric stretching sharp peaks at 1064 cm^{-1} and 984 cm^{-1}, respectively. The peaks in the region of 900-450 cm^{-1} confirmed the presence of Zn-O bonds. All the expected peaks from the functional groups contained within the material were present.

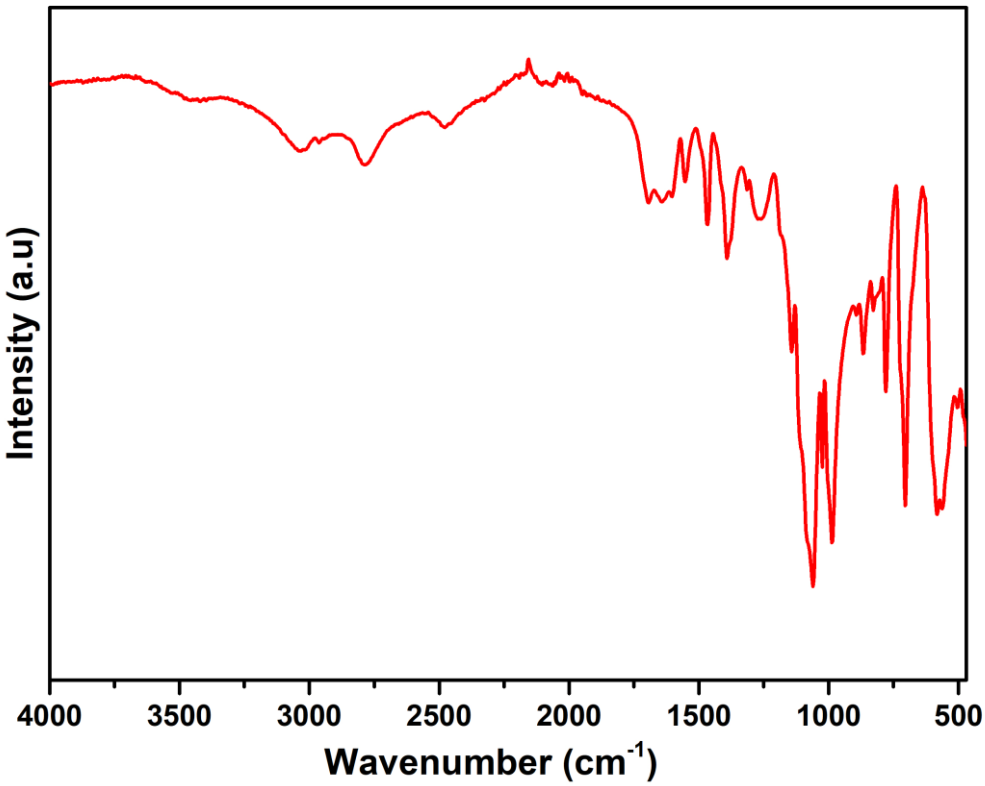


Figure 5.20 FTIR spectrum for BIRM-19.

Table 5.5. Observed FTIR shifts and assignments for BIRM-19.

Wavenumber (cm^{-1})	Peak Assignment
3050	N-H (DMA)
2787	Aromatic C-H
1645	Carboxylate C=O
1470	Carboxylate C-O (sym)
1394	Carboxylate C-O (asym)
1262	P-C
1064	P-O
984	P-O
<900	Zn-O

5.6.3. Morphological studies of BIRM-19

An SEM image of BIRM-19 at 1000x magnification is presented in Figure 5.21. The image shows that BIRM-19 can be identified, among other crystals present, as plate-shaped crystals, with each plate stacking over each other. The presence of brighter or darker areas of material indicates the sample is a heterogeneous mixture of phases. EDX analysis found an average Zn:P ratio of 1:1.33 which varies slightly from the Zn:P ratio found in the solved structure (1:1).

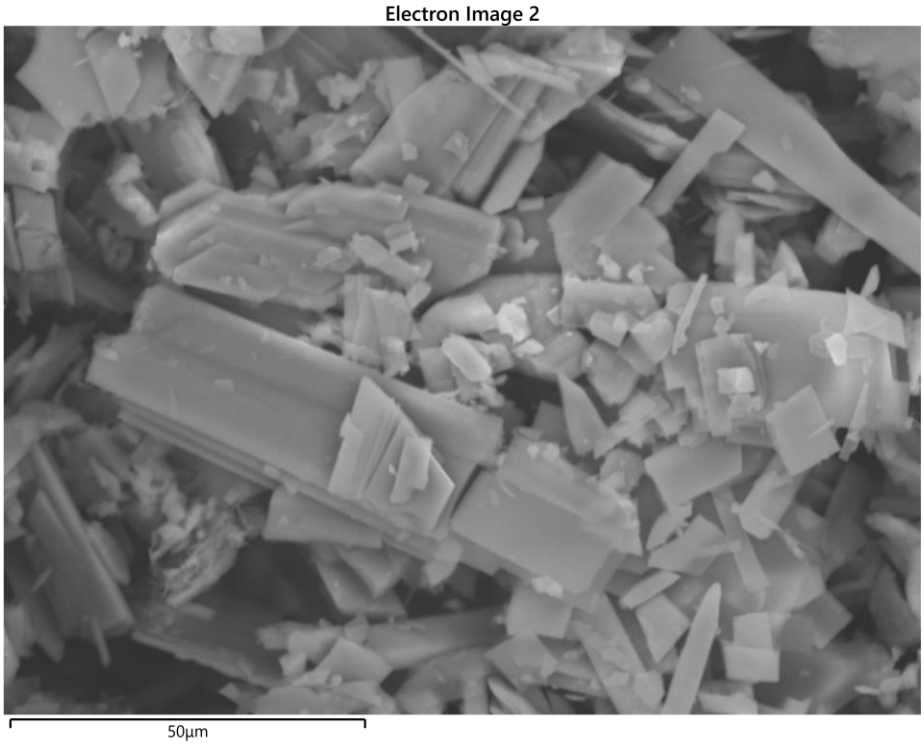


Figure 5.21. SEM image for BIRM-19 crystals at 1000× magnification

5.6.4. Thermal stability studies of BIRM-19

The thermogravimetric behaviour of BIRM-19 is presented in Figure 5.22. The TGA curve shows that the weight loss can be divided into five major regions. The weight loss at the first and second regions (292 ^{0}C) corresponds to 14.5 % and is due to the thermal decomposition of dimethylamine present in the channels of the structure. This weight loss agrees with percentage weight of $(CH_3)_2NH_2$ present in the solved structure which is calculated to be 14.7

%. The framework of BIRM-19 is stable up to 474 ^{0}C in the third region without any significant weight loss. At the fourth region, a significant weight loss of 28.93 % at 610 ^{0}C results in the decomposition of the organic component, causing the collapse of the framework. At the region which corresponds to the temperature > 610 ^{0}C, the material continued to exhibit gradual weight loss and the transformation was complete at about 900°C, resulting in a total weight loss of 62.2 %. Figure 5.23 shows the PXRD pattern for the final decomposition product of BIRM-19 compared to simulated patterns for zinc pyrophosphate. The peaks for the simulated patterns account for most peaks in the pattern from the decomposition product, suggesting that zinc pyrophosphate accounts for most of the compound in the decomposed product. There were also other minor peaks present suggesting that there are other crystalline phases still present.

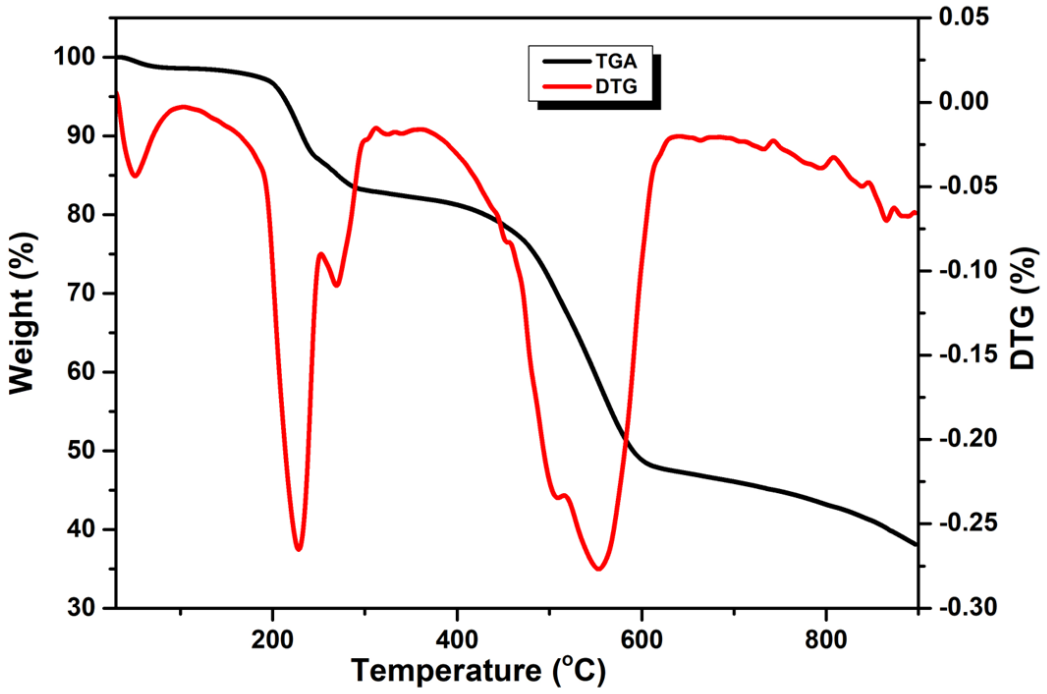


Figure 5.22. TGA (black trace) and DTG (red trace) of BIRM-19.

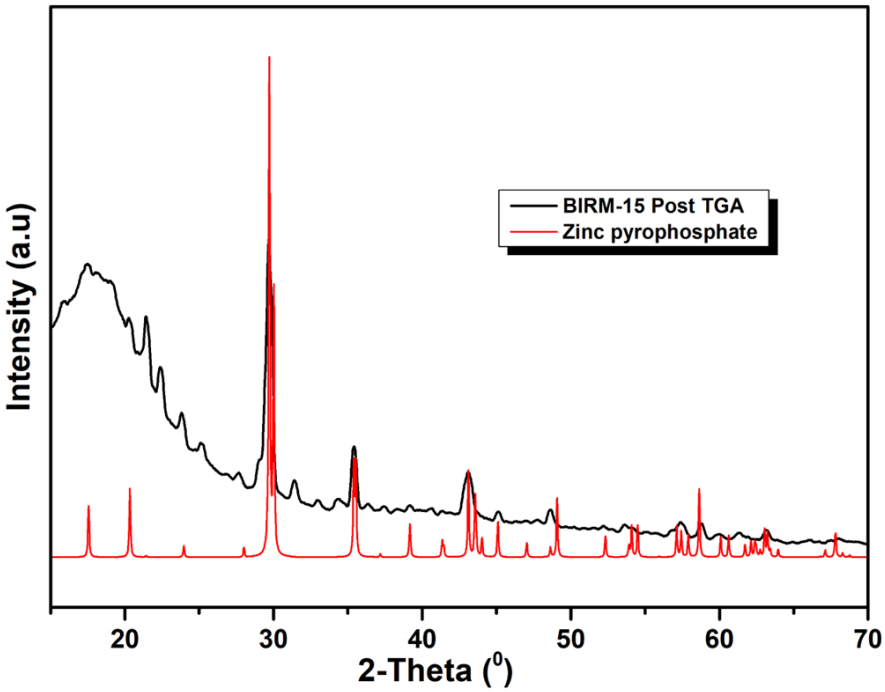


Figure 5.23. PXRD pattern of the TGA product from BIRM-19.

5.7. MOF synthesis attempt with Ni metal

With some level of success achieved with the use of Zn metal, it was attempted to use nickel in the synthesis of MOFs using 4-phosphonobenzoic acid as ligand. Similar synthetic conditions as that for Zn-MOF was used. The synthesis started by dissolving the quantities of reagents in Table 5.6 in 2 mL of dimethylformamide (DMF). Then, the mixture was transferred into a 7 mL glass vial and placed in an oven at 65 °C for 12 hours. No visible crystals were observed under these synthesis conditions. Several synthesis trials were made by varying some reaction conditions such as temperature, reaction time and reaction ratio, but unfortunately, none of the trials were successful.

Table 5.6 Quantities of reagents used in the initial synthesis attempt of a framework material.

	Zn $(NO_3).6H_2O$	4-phosphonobenzoic acid	4,4-bipyridine	benzoic acid
Mass (g)	0.02	0.02	0.02	0.25
Molar ratio	1	0.15	19.0	30.5

A new strategy involving introducing an auxiliary ligand into the reaction system was trialled. The general idea is that, if the synthetic conditions can be fashioned in such a way that metal SBUs coordinate first with the auxiliary ligand before coordinating to the phosphonic acid ligand, this can have influence on the dimensionality of the materials with the possibility of producing MOFs with permanent porosity. As a result, the synthetic conditions were modified by introducing 4,4-bipyridine as auxiliary ligand and the synthesis was carried out at temperatures and in the time range of 65-180 ^{0}C and 12-48 hrs, respectively. After many trials, findings reveal that using a solvent mixture of DMF and water at a temperature of 65 ^{0}C and time of 12 hrs, produced single crystals suitable for structural characterization. The powder diffraction pattern of the material is presented in Figure 5.24. The sample was submitted to the School of Chemistry's single crystal diffraction for structural characterization. This material will be known as BIRM-20.

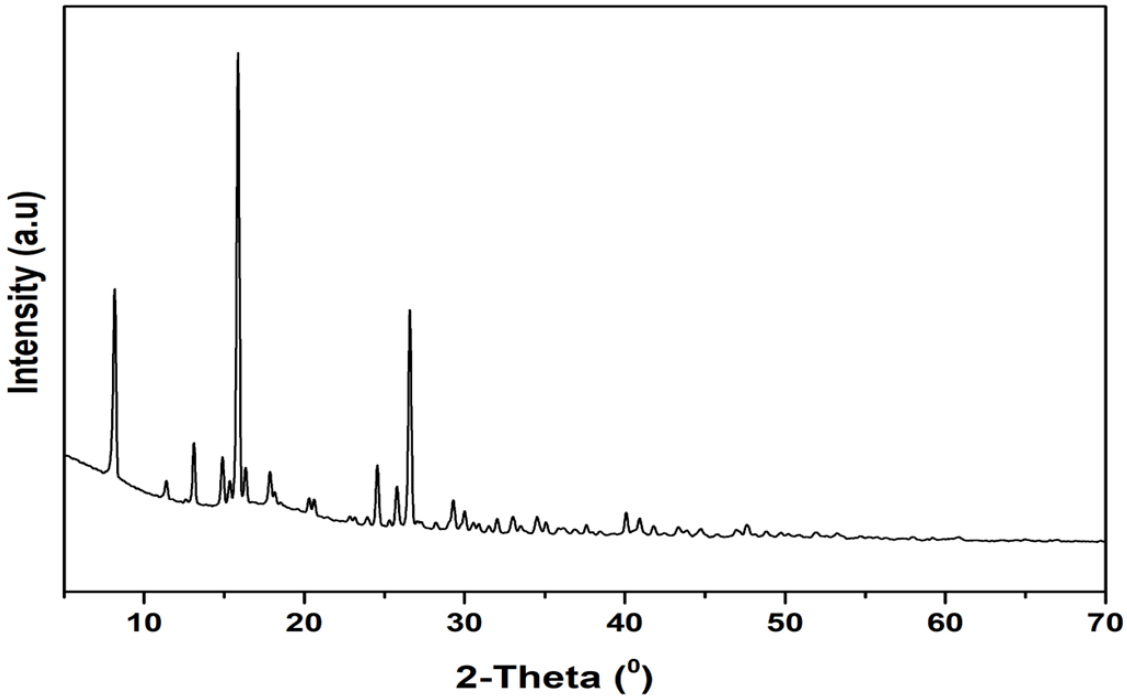


Figure 5.24. Powder XRD pattern of the BIRM-20.

5.8. Layered Structure of BIRM-20 [$Ni(O_3PC_6H_4COOH)(C_5H_4N)_2(H_2O)_3$]

A good dataset was obtained from the SCXRD characterization. A structure was solved from the data which is shown in Figure 5.25 with some of the basic crystallographic details in Table 5.7. More extensive crystallographic information is given in Chapter 9 Table A5.18-25. The expanded structure is shown in Figure 5.26.

Table 5.7 Crystallographic data for BIRM-20.

Sample	BIRM-20
Formula	$Ni(O_3PC_6H_4COOH)\ (C_5H_4N)_2\ (H_2O)_3$
Formula Weight	469
Space group	$P2_1$
a (Å)	7.2523(2)
b (Å)	11.1546(3)
c (Å)	11.2845(3)
Volume($Å^3$)	879.89(4)
Goodness-of-fit on F2	1.072
wR2	0.0904
Largest diff. peak/hole / e $Å^{-3}$	0.30/-0.55

Single crystal x-ray diffraction analysis revealed that BIRM-20 crystallizes in monoclinic space group $P2_1$. The asymmetric unit of this crystal comprises one Ni (II) cation, one $(O_3PC_2H_4CO_2)^{3-}$ anion, one 4,4-bipyridine $(C_5H_4N)_2$ and three coordinated water molecules (Figure 5.25). Nickel atoms can be observed to form octahedra with two axially bonded bipyridine nitrogen, one phosphonate oxygen from CPO_3 tetrahedra and three oxygens from coordinated water molecules. The NiO_6 octahedra and CPO_3 tetrahedra form a 1-Dimensional ladder-like chain, with two NiO_6 octahedra linked together via oxygen from coordinated water molecules. This ladder-like chain was then bridged by 4,4-bipyridine and partially deprotonated 4-phosphonobenzoic acid ligands, thereby giving rise to a 2-Dimensional layered structure in the xz plane (Figure 5.26). Rietveld refinement of the crystal structure against lab powder X-ray diffraction data confirmed the structure and verified the as-made sample contained only one crystalline phase (Figure 5.27). More information on Rietveld refinement including unit cell

parameters, occupancies and atomic positions are shown in the Chapter 9, table A5.26 and A5.27.

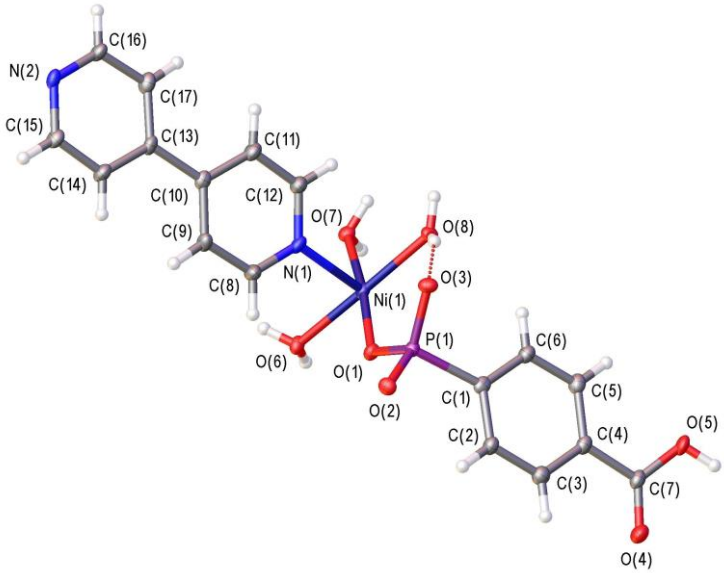


Figure 5.25. Asymmetric unit of BIRM-20. The thermal ellipsoids are drawn at the 50% probability level.

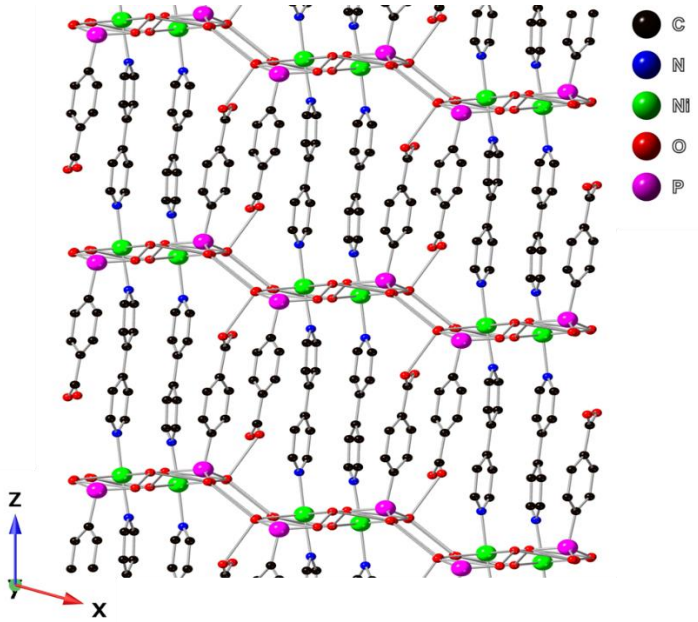


Figure 5.26. Structure of BIRM-20 viewed along the y-axis. Hydrogen atoms are omitted for clarity.

Since the main aim of this research work was to synthesize functional porous 3-dimensional MOFs, several attempts were made to optimize various reaction variables. Starting with varying the temperature at 5 ^{0}C intervals, synthesis attempts at a range of temperatures between 65 and 95 °C showed XRD patterns consistent with BIRM-18. However, as the temperature increased above 100 °C, the material began to lose its long-range ordering, eventually producing amorphous powder. Although the function of benzoic acid is not fully understood, the synthesis of BIRM-18 without it was not successful, with no crystalline material formed. Further optimization strategies were not fully explored before the end of my lab time.

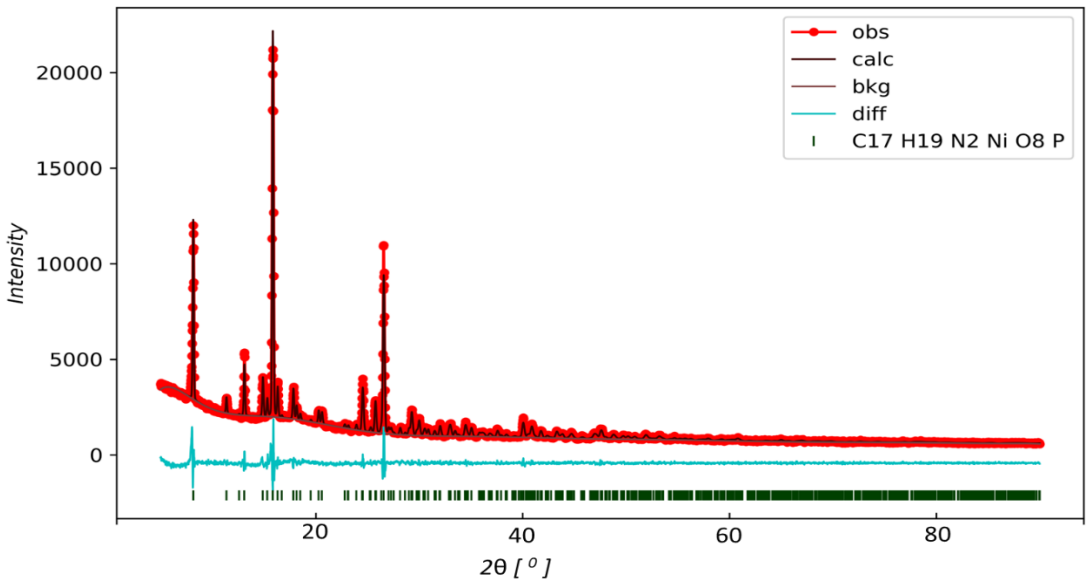


Figure 5.27. Final observed (red), calculated (black), difference (light blue) and reflection positions (green), for the final Rietveld refinement against powder XRD data for BIRM-20, R_P = 4.10 %, R_{wp} = 5.66 %, GOF = 2.05.

5.8.1. FTIR studies of BIRM-20

Figure 5.28 gives the FTIR spectrum of BIRM-20 whilst Table 5.8 lists notable bands and assignments to functional groups. A broad peak found around 3450 cm^{-1} and a sharp peak at

1700 cm^{-1} are due to stretching vibrations of O–H and bending vibrations of H-O-H from the coordinated water molecules.[328] The broad peaks that span between 2982 cm^{-1} and 2700 cm^{-1} can be attributed to C–H stretching vibration from the carboxylphosphonate groups[90, 372]. Additionally, the peak at 1610 cm^{-1} can be assigned to the C=N stretch mode originating from 4,4-bipyridine auxiliary ligand. The symmetric and asymmetric stretching vibrations of -C=O are evident as strong bands at 1420 cm^{-1} and 1281 cm^{-1}, respectively. The P–C stretching mode is observed at 1499 cm^{-1}, and the P–O stretching modes of the phosphonate group are seen as several sharp peaks in the range 1100–950 cm^{-1} [191, 328]. The peaks in the region of 900-450 cm^{-1} confirmed the presence of Ni-O bonds. It can therefore be inferred that FTIR spectrum displays all the peaks expected from the functional groups within the structure.

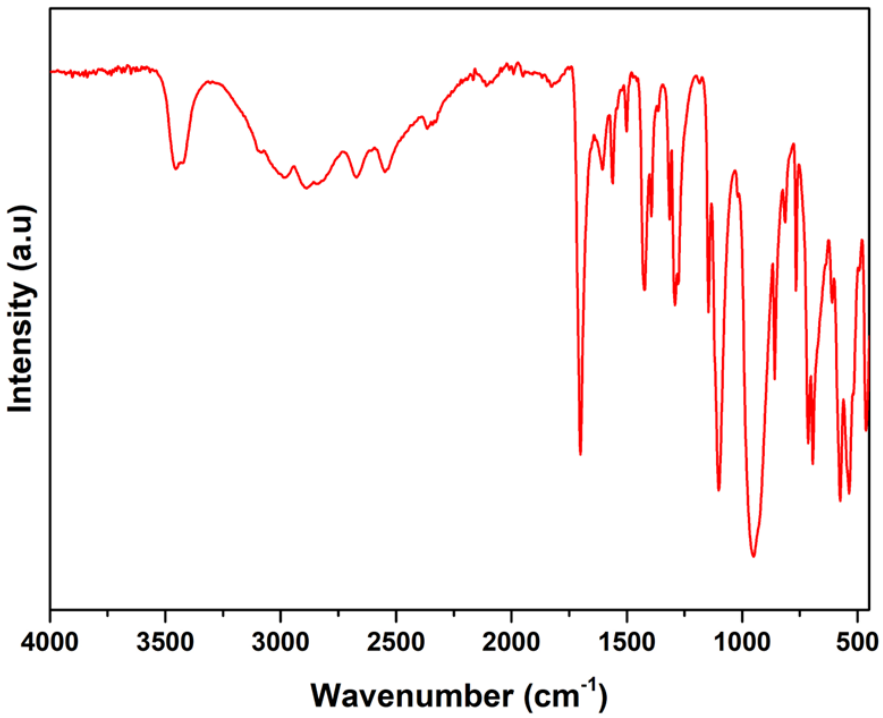


Figure 5.28. FTIR spectrum for BIRM-20.

Table 5.8. Observed FTIR shifts and assignments for BIRM-20.

Wavenumber (cm^{-1})	Peak Assignment
3450	Hydroxyl O-H
2982, 2890, 2700	Aromatic C-H
1700	Water H-O-H (bending vibration)
1610	C=N (stretching)
1499	P−C (stretching)
1420	Carboxylate C-O (sym)
1281	Carboxylate C-O (asym)
1100	P-O
950	P-O
<900	Ni-O

5.8.2. Morphological studies of BIRM-20

The SEM images (Figure 5.29) show the morphology of BIRM-20. A higher magnification is provided in the right of the Figure for a clearer view of the crystal geometry and shape. The crystals are rectangular prisms terminating with a truncated pyramid shape on the ends of the prism. EDX analysis found an average Ni:P ratio of 1.1:1 across 5 sites which agrees with the theoretical value of 1:1 found in the solved structure showing that BIRM-20 is a monophasic crystalline material.

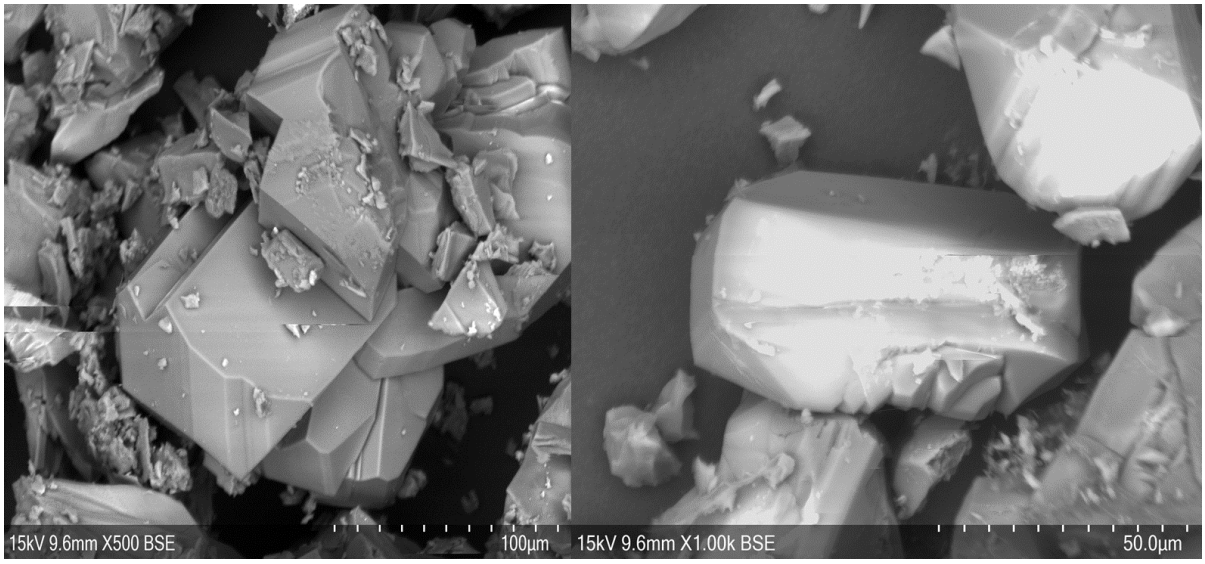


Figure 5.29. SEM image for BIRM-18 crystals at 500× magnification (left) and 1000× magnification (right).

5.8.3. Thermal stability studies of BIRM-20

The TGA decomposition profile of BIRM-20 is shown in Figure 5.30. The profile revealed five distinct thermal events, with the first and second events occurring at temperatures of 142°C and 186°C, resulting in a total weight loss of 6.7% which can be attributed to evaporation of coordinated water. This weight loss is less than the calculated percentage weight of H_2O (11.5 %) from the solved structure, indicating that not all coordinated water were loss at this temperature. The third degradation peak was observed at 467°C, demonstrating that the MOF is thermally stable up to 467 ^{0}C. The fourth event at 650°C was the most significant, with a TGA weight loss of approximately 40% which could be attributed to the combustion of organic components. At the fifth region which corresponds to the temperature > 650 ^{0}C, the material continued to witness gradual weight loss and the transformation was complete at about 900°C, resulting in a total weight loss of 45.5%. The powder diffraction pattern obtained from this product (Figure 5.31) did not contain many features but the most notable is a broad peak around 30° 2θ. This broad peak corresponds to two peaks found in the same region in

the diffraction pattern for dinickel diphosphate ($Ni_2O_7P_2$), therefore the product may contain this phase. The broad peaks may indicate very small crystallite size of the TGA product.

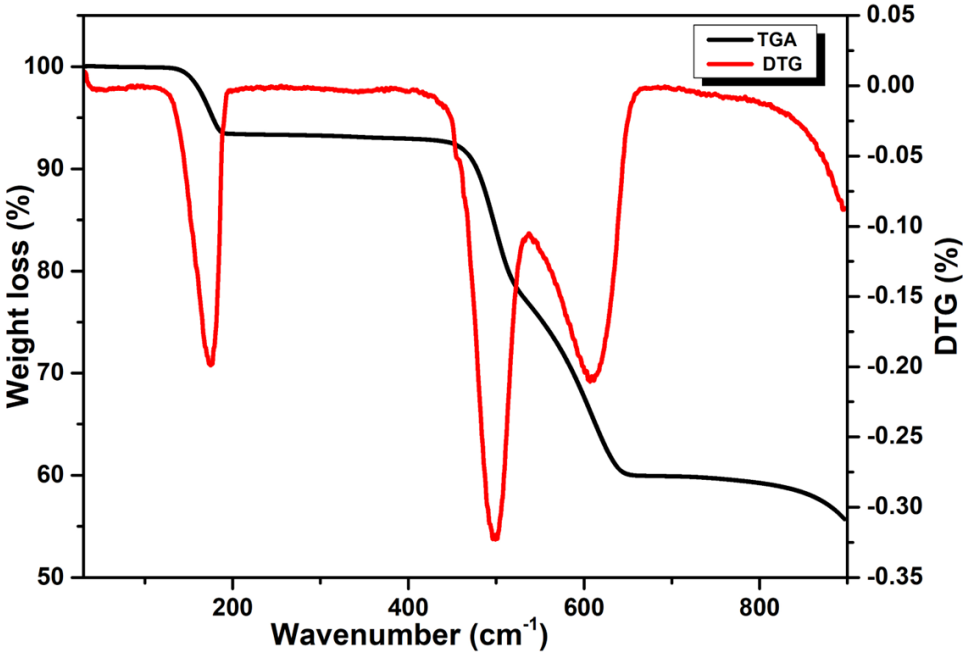


Figure 5.30. TGA (black trace) and DTG (red trace) of BIRM-20.

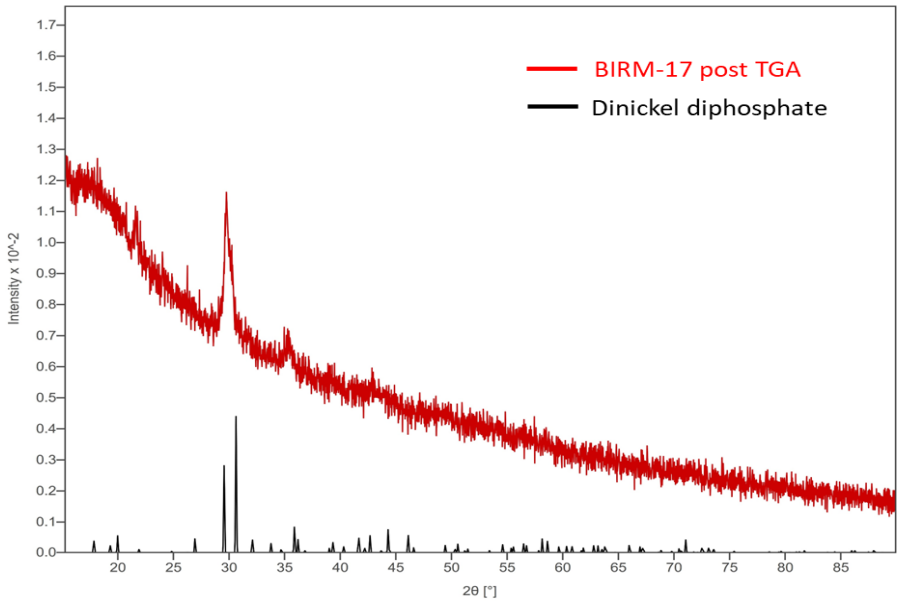


Figure 5.31. Powder diffraction pattern of the post-TGA product from BIRM-20 (red) compared to a simulated pattern of dinickel diphosphate (black).

5.9. MOF synthesis attempt with Co metal

A similar synthesis protocol to that used for BIRM-20 was attempted for a cobalt MOF synthesis. After many trials, a tiny crystal suitable for structural characterization was obtained by dissolving the quantities of reagents in Table 5.9 in 4 mL of a solvent mixture of dimethylformamide (DMF) and water (1:1, v/v) and the solution was heated hydrothermally at 80 °C for 24 hours in a 7 mL glass vial. The sample was submitted to the School of Chemistry's single crystal diffraction for structural characterization. This material will be referred to as BIRM-21.

Table 5.9 Quantities of reagents used in the synthesis of BIRM-19.

Compounds	Mass (mg)	Molar ratio
Co $(NO_3)_2.6H_2O$	12	1
4-phosphonobenzoic acid	10	1.2
4,4'-trimethylenedipyridine	16	1.9

5.9.1. Layered structure of BIRM-21 [$Co(O_3PC_6H_4COOH).H_2O$]

A suitable and well diffracting single crystal was picked for single crystal analysis. A structure was solved from the data in which the asymmetric unit is shown in Figure 5.32 with some of the basic crystallographic details presented in Table 5.10. More extensive crystallographic information is given in Chapter 9 Table A5.28-34. The expanded structure of BIRM-21 is shown in Figure 5.33. It is composed of sheets of CoO_6 octahedra and CPO_3 tetrahedra which are edge-sharing and extend out along two dimensions. The linker then extends outwards from this sheet along the y-axis and the layers are linked together by hydrogen bonding from the carboxylic acid group. The structure is similar to the layered phase of BIRM-2(Zn) found by Zhao[279] and isostructural to BIRM-8 (Zn) found by Barker[278]. The powder XRD pattern of the

as-synthesized material shows that it contained another phase as the simulated pattern for BIRM-21 did not match the as-synthesized pattern (Figure 5.34). Full optimization of this line of experiments could not be explored before the end of my laboratory time.

Table 5.10 Crystallographic data for BIRM-21.

Sample	BIRM-21
Formula	$Co(O_3PC_6H_4COOH).\ H_2O$
Formula Weight	277
Space group	Pnnm
a (Å)	4.7806(6)
b (Å)	38.077(5)
c (Å)	5.6017(8)
Volume ($Å^3$)	1019.7(2)
Goodness-of-fit on F^2	1.106
wR^2	0.1641
Largest diff. peak/hole / e $Å^{-3}$	0.82/-0.83

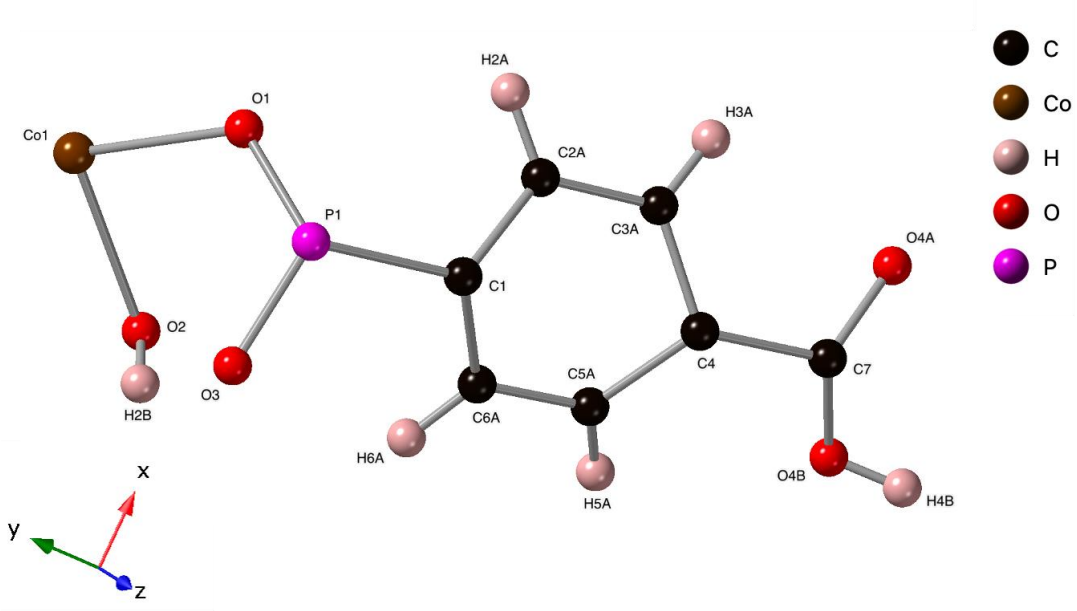


Figure 5.32. Asymmetric unit of BIRM-21. The thermal ellipsoids are drawn at the 50% probability level. The aromatic ring and carboxylate units are disordered over three positions and across a mirror plane that runs through C1, C4 and C7, O3, P1 and Co1. The water oxygen, O2, is also located on the mirror plane.

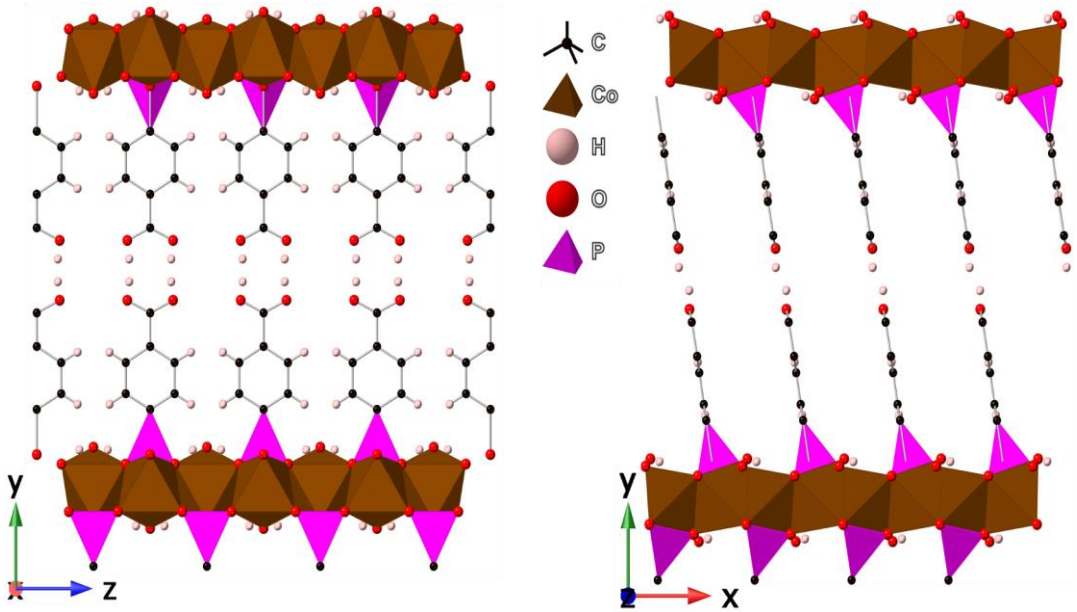


Figure 5.33 Structure of BIRM-21 viewed along the x-axis (left) and the z-axis (right).

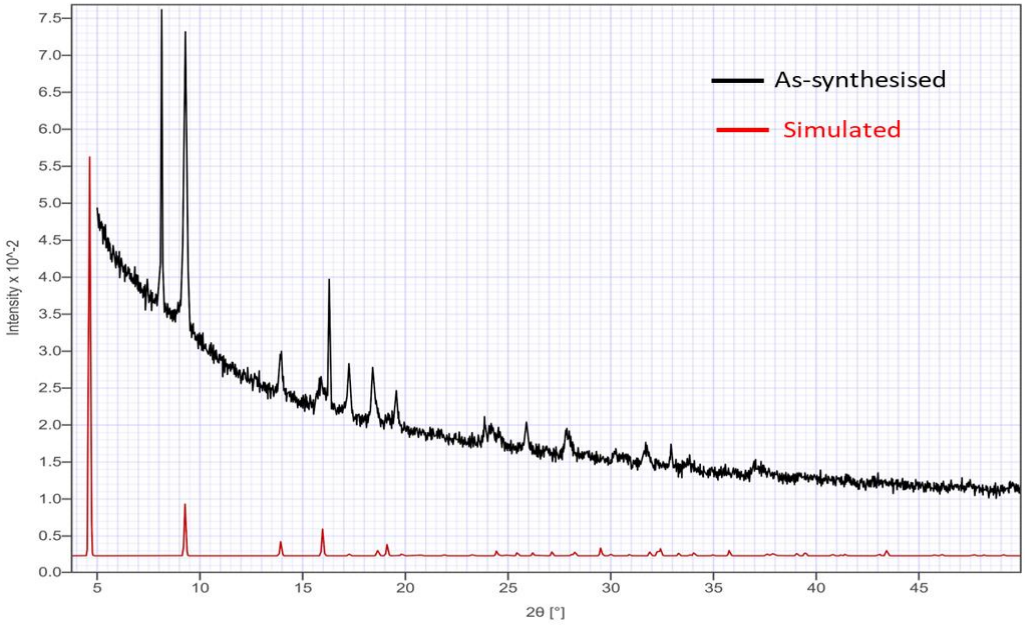


Figure 5.34. As-synthesised (black) and simulated (red) XRD pattern BIRM-21.

5.9.2. FTIR studies of BIRM-21

The FTIR spectrum of BIRM-21 is given in Figure 5.35 along with peak assignments in Table 5.11. The FTIR data confirm the structure solved from single crystal diffraction with evidence of the carboxylic acid being left protonated whilst the phosphonate group has been deprotonated. A broad peak found around 3398 cm^{-1} is due to stretching vibrations of O–H from the coordinated water molecules. The symmetric and asymmetric stretching vibrations of -C=O are evident as strong bands at 1674 cm^{-1} and 1603 cm^{-1}, respectively. The P–C stretching mode is observed at 1409 cm^{-1}, and the P–O stretching modes of the phosphonate group are seen as a number of sharp peaks in the range 1042–975 cm^{-1}.

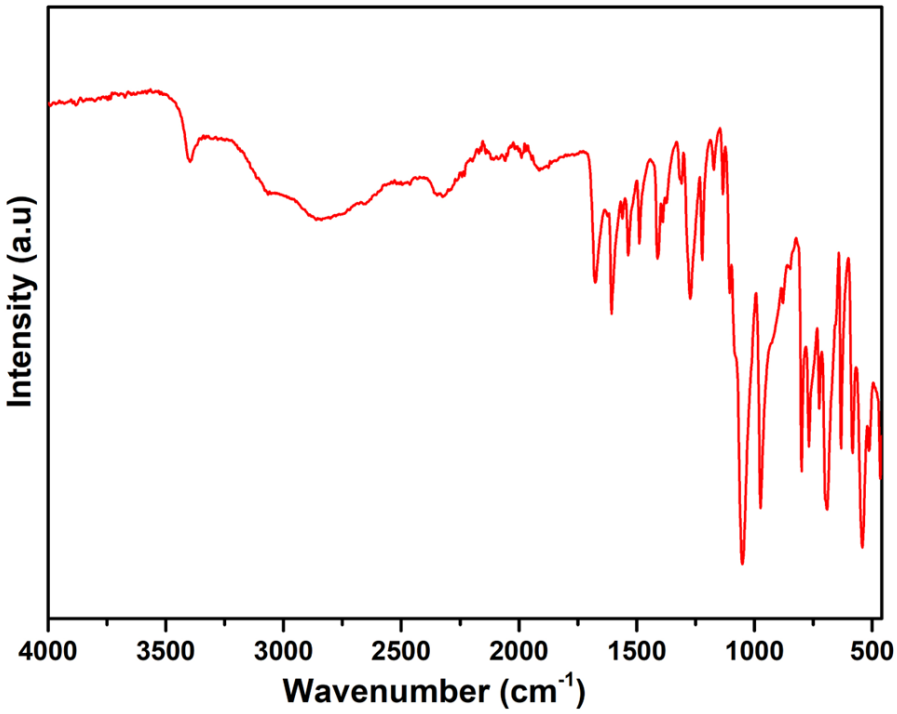


Figure 5.35 FTIR spectrum for BIRM-21.

Table 5.11. Observed FTIR shifts and assignments for BIRM-21.

Wavenumber (cm^{-1})	Peak Assignment
3398	Hydroxyl O-H
2800	Aromatic C-H
1674	Carboxylate C-O (sym)
1603	Carboxylate C-O (asym)
1488	Carboxylate O-H
1409	P-C
1042	P-O
975	P-O
<900	Co-O

5.9.3. Thermal stability studies of BIRM-21

The thermal decomposition profile of BIRM-21 is shown in Figure 5.36. The first weight loss occurring around 180 °C correspond to a loss of 18.02% which is above the weight of water from the BIRM-21 structure (6.5 %). This indicated that, in addition to loss of the water molecule, the decomposition of BIRM-21 structure started around this temperature. Above this temperature, the product showed a nearly continuous weight loss without a clear step. At a temperature range of 200–475 °C, BIRM-21 underwent another weight loss of 45 % which can be attributed to the combustion of the ligand and subsequent collapse of the framework. The final decomposition product is a crystalline material (as shown by the PXRD pattern in Figure 5.37), however, attempts to phase match it to known phases have been unsuccessful.

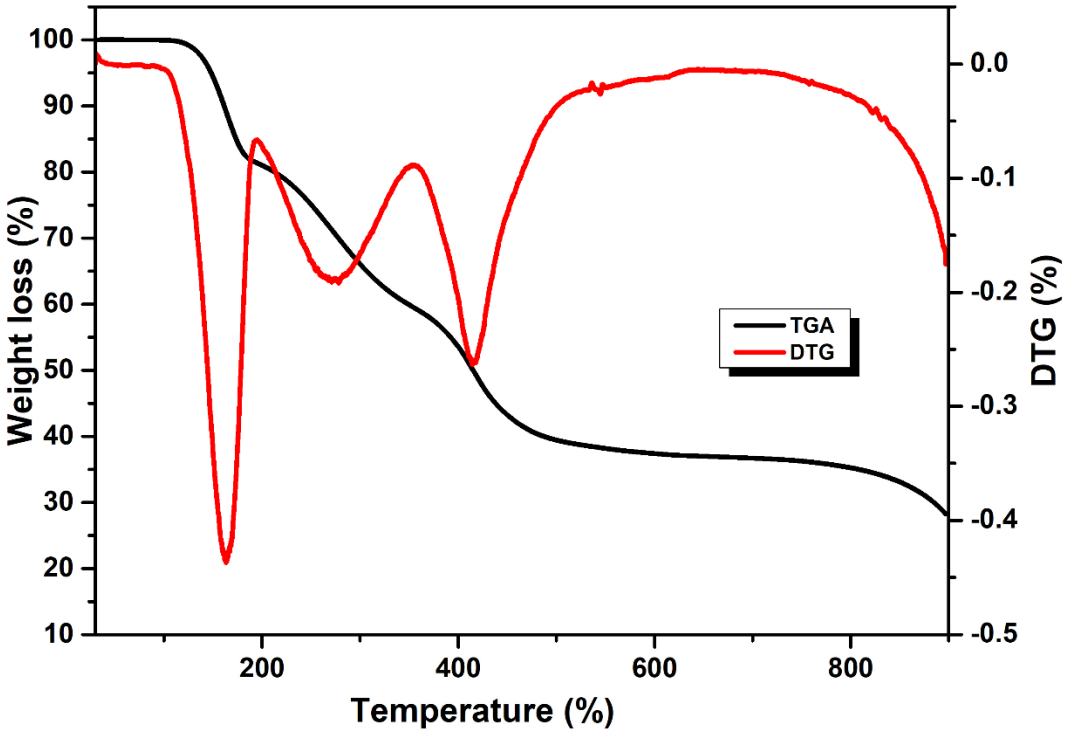


Figure 5.36 TGA (black trace) and DTG (red trace) of BIRM-21.

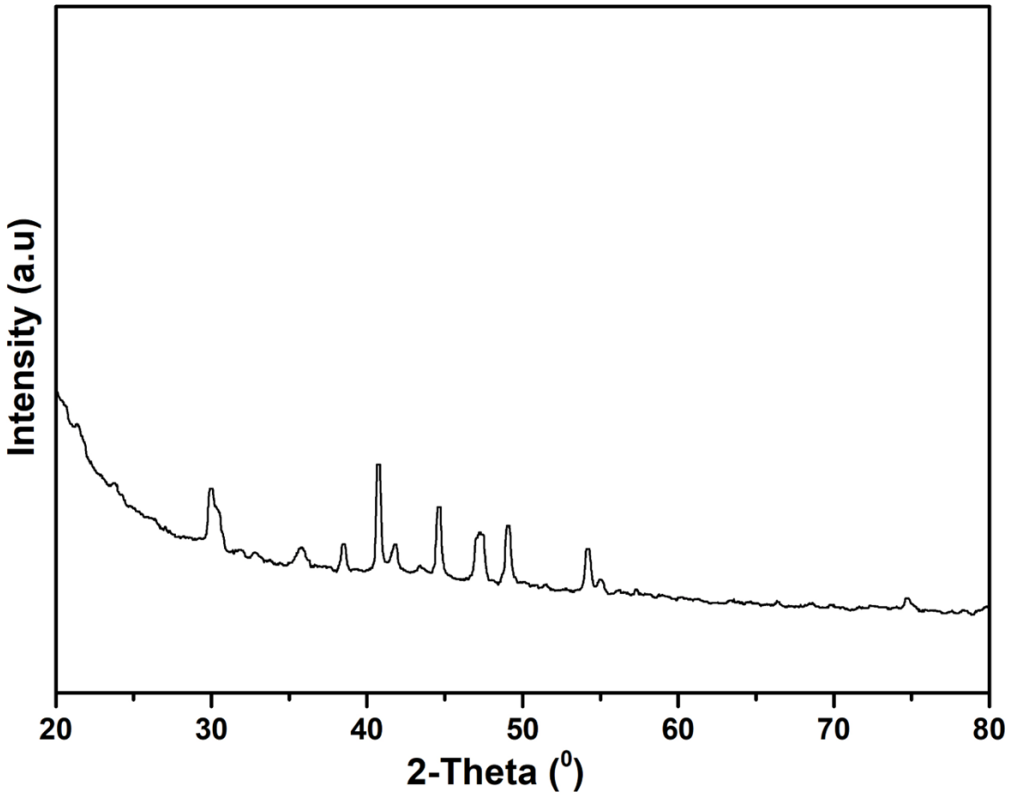


Figure 5.37 PXRD pattern of the TGA product from BIRM-21.

5.10. Conclusion

In this chapter, four novel framework materials (BIRM-17, 18, 19, 20 & 21) have been synthesised with BIRM-18 and 19 being of particular interest as porous MOFs. BIRM-17, 18, 19 and 21 were obtained from a mixture of phases while BIRM-20 was obtained as a single pure phase. BIRM-17 was obtained as a 2-dimensional layered structure, and upon modifying synthesis temperature and time, 3-dimensional and porous frameworks namely BIRM-18 and 19 were obtained. BIRM-18, as a novel MOF, possesses distinct crystallographic voids and channels which can be potentially accessible for gas adsorption and ion exchange reactions. Topological analysis shows that BIRM-18 exhibits a (4;2)-connected GIS-type topological structure seen in zeolites. However, obtaining a pure phase of BIRM-18 proved challenging, therefore fashioning an optimized strategy to obtain a pure phase of this material would be

a priority for future work. BIRM-19 is also a 3-dimensional porous structure with (4;2)-connected zeolite-like topology, however, its structure and topological net is similar to the structure obtained by Chen *et al*.[375] but differs in the pore contents and synthetic route. BIRM-20 and BIRM-21 are 2-dimensional layered structures obtained from trying to make nickel and cobalt-containing porous metal phosphonate MOFs. BIRM-21 is of interest because it is similar to the layered phase of BIRM-2 synthesised by Zhao[279] and isostructural to BIRM-8 found by Barker[278]. Since obtaining a 3-dimensional open framework is the goal, optimization of various synthetic parameters of BIRM-20 and BIRM-21 should be a priority for future work.

CHAPTER SIX

Probing the activity and selectivity of nickel carboxylethylphosphonate 2D-MOF for the electrochemical conversion of CO_2 to syngas

6.1. Introduction

As developed countries set various timelines to transition from fossil fuels to cleaner and more environmentally benign energy sources, it has become increasingly apposite to expedite research activities on CO_2 conversion technologies.[377, 378] This speedy energy transition is borne out of the fact that the burning of fossil fuels has been documented to account for increased concentrations of atmospheric CO_2 which have been linked to global climate change and other environmental disasters ravaging the world in recent times.[379] Among the numerous CO_2 capture and utilization techniques that have been proposed to tackle this problem, the electrochemical CO_2 reduction reaction (CO_2RR) is a promising technology to convert waste CO_2 streams into useful chemicals.[380] Unlike other chemical processes, electrochemical CO_2 reduction has the advantage of: proceeding under ambient conditions, enabling the adjustment of the electrolytic conditions (*e.g.* applied potential, electrode materials and electrolytes, *etc*.) to obtain diverse products, utilizing electrical energy from intermittent renewable sources to drive the reaction, with the protons needed to achieve CO_2 reduction coming from oxidation of water at the anode, making the overall operation a carbon neutral process.[10] Much effort has been devoted to tuning the operating conditions of the electrochemical CO_2 reduction reaction in order to obtain high added value products

(*e.g*. CO, HCOOH, C_2H_5OH *etc.*) while suppressing the competing hydrogen evolution reaction (HER).[203, 209, 381, 382] However, given the significance of syngas as a valuable building blocks for the synthesis of a range of chemicals and fuels through the industrially adopted Fischer–Tropsch (FT) process, the direct production of both CO and H_2 during CO_2RR is also attractive.[382, 383]

Previous extensive work on CO_2RR has been carried out on metal catalysts, including precious-metal catalysts, metal oxide catalysts, other metal-based catalysts of different types, *etc*.[384-390] However, the current scarcity of precious-metal resources, high negative potential requirement of metal catalysts coupled with the generation of variable products, hinder the deployment of metal-based catalysts in CO_2RR.[391] Homogeneous electrocatalysts based on metal complexes of phthalocyanine[384], porphyrin[385], phosphine[392], macrocyclic ligands[393] , carbon nanotubes[394] *etc.* have also been reported to be highly selective towards CO production, however, solubility of these catalysts in the reaction medium and recovery after use can be very difficult to achieve[395]. In recent years there has been a growing interest in the development of heterogeneous catalysts made of earth-abundant elements, containing highly active sites resembling those on molecular catalysts.[396-398]

Electrocatalytic porous functional materials such as carbon materials, including metal free heteroatom-doped (*i.e.,* N, P, O, B, halogens) porous carbon nanostructures (HA-PCs)[399, 400], metal and nitrogen-doped carbons (MNCs)[401, 402], metal-organic frameworks[403] *etc*., have been the subject of intense research in the literature. Among them, metal-organic frameworks have become very popular candidates and have shown tremendous catalytic activity for CO_2RR.[203, 209, 244] MOFs are a specific class of materials constructed through the coordination of metal-containing units, termed secondary building units (SBUs), with organic

linkers using strong bonds to create open crystalline frameworks with the potential for permanent porosity.[22] The growing interest in the application of MOFs as electrocatalysts in the CO_2 reduction reaction has been attributed to their catalytic properties including: high surface area which provides plentiful catalytic active sites for surface-related reactions and high and tunable porosity which facilitates mass transport of selected substrates to the active sites and as well providing a platform for loading guest species.[134] Nevertheless, a large number of active sites inside three-dimensional (3D) MOFs are not effectively utilized in catalysis because of the non-negligible diffusion barrier, resulting in low turnover efficiency.[404] Therefore, scaling down the dimensionality of the MOFs into 2D nanosheets destined for catalytic application can increase their surface area thereby exposing more metal active sites and improve electrical conductivity by decreasing the electron transfer distance from the ultrathin nanosheets to the current collector of the electrodes.[242] The use of 2D MOFs as electrocatalysts for CO_2RR was demonstrated by Yang *et al.*[243] where they attributed the significant catalytic activity and product affinity of their Cu-MOF nanosheets to the cathodized restructuring of the framework. Zhang *et al.*[244] proved further that using 2D porphyrin-based MOF (TCPP(Co)/Zr-BTB) to catalyse CO_2RR results in the production of CO with satisfactory results.

Herein, a 2D Ni-MOF electrocatalyst was hydrothermally synthesized for electrocatalytic CO_2RR in a basic aqueous carbonate electrolyte (pH 9.2). The catalyst was characterized with PXRD, HRTEM FT-IR and Raman spectroscopy, the CO_2 reduction activity of the catalyst was studied with cyclic voltammetry and density functional theory, and the product quantification determined by on-line electrochemical mass spectrometry (OLEMS). Additionally, the durability of the catalyst was monitored, and post-mortem analysis was also performed to track chemical changes that might occur during the course of the electrochemical reaction.

6.2. Experimental section

6.2.1. Material synthesis

$Ni_2(HO_3PC_2H_4COO)_2(4,4'\text{-bipy})_2(H_2O)$ was synthesized under hydrothermal conditions by mixing Ni $(CH_3COO)_2.4H_2O$ (1 mmol), 2-carboxyethylphosphonic acid (1 mmol), and 4,4-bipyridine (1 mmol) in 12 mL of distilled water. The reaction mixture was stirred at room temperature to homogeneity, and then placed in Teflon-lined stainless vessels (40 mL) which was heated to 140 °C for 48 h under autogenous pressure, and afterwards cooled to room temperature. The solid was filtered off, washed thoroughly with distilled water, and finally air-dried at room temperature. The resulting product was obtained as light green crystals.

6.2.2. Physical characterization

A Bruker D8 Powder X-ray diffraction (XRD) system with Cu Kα radiation (λ = 1.5418 Å) was used to characterize the crystal structure of the MOF powder. Thermogravimetric analysis (TGA) was conducted on a PerkinElmer thermogravimetric analyser under air atmosphere. Fourier transform infrared (FTIR) spectra were recorded on a Bruker Alpha II spectrometer while Raman spectra were obtained on Bruker Senterra II Raman microscope. The morphology of the catalyst was analysed using a benchtop Hitachi TM4000 Plus SEM coupled with an Oxford Instruments AztecOne EDX detector. High resolution transmission electron microscopy (HRTEM) images were recorded using a JEOL JEM-2100F instrument operating at 200 kV. The concentration of nickel in the catalyst was measured using Bruker S8 X-ray fluorescence spectrometer.

6.2.3. Electrochemical characterisation

The catalyst ink was prepared by dispersing 30 mg of the catalyst in 950 µL of Milli-Q water (PURELAB Ultra, 18.2 MΩ cm) containing 50 µL of Nafion solution (5 % isopropanol) and ultrasonically treated for 10 min. The electrode was then prepared by drop-casting the catalyst suspension onto a glassy carbon substrate (geometric surface area: 0.0314 cm^2) in volumes of 10 µL and drying in a fan oven at 60 °C to yield a total mass of the catalyst on the glassy carbon surface of 1.34 mg Ni cm^{-2}. Before drop-casting, the glassy carbon electrode was polished with alumina slurry, cleaned by repeated ultrasonication in ultrapure milli-Q water and dried in oven at 60 °C. To evaluate the influence of electrode loading, 10 µL, 15 µL, 20 µL and 25 µL of the ink were used for electrode preparation, yielding loadings of 42.06 µg, 57.06 µg, 85.56 µg, and 114.08 µg, respectively. A three-electrode cell configuration comprising a GCE with the drop-cast catalyst as a working electrode, a high-surface area gold flag as a counter electrode and Hg/HgO (1.0 M KOH) as reference electrode, was used. All potentials collected were subsequently calibrated to the reversible hydrogen electrode (RHE) according to the equation: $E_{RHE} = E_{Hg/HgO} + 0.098 + 0.0591 \times pH$. Cyclic voltammetry (CV) experiments were performed using a PGSTAT302N system (Metrohm Autolab B. V.,Utrecht, Netherlands). All CV measurements were conducted from 0.09 to -1.7 V (*vs* Hg/HgO) at a scan rate of 50 mV s^{-1} in 0.1 M carbonate buffer (pH ~9.2) electrolyte produced from $NaHCO_3$ (Acros Organics, >98%) and Na_2CO_3 (Sigma, ≥99%). The catalytic activity of the electrocatalyst were normalized to current per mass (mg) of the nickel active sites in the electrocatalyst. The concentration of nickel in the electrocatalyst was obtained from XRF analysis (Chapter 9 Table A6.1). Before measurement, the electrolyte was degassed by bubbling Ar for at least 30 min to purge-out the oxygen from the electrolyte. Subsequently the solution was saturated with CO_2 (BOC, N5).

6.2.4. Product characterisation

Gaseous products formed during the reaction were detected using OLEMS. A porous membrane tip was positioned close to the electrode to collect the gaseous products for onward analysis and detection by OLEMS. The tip was a 2 mm diameter porous Teflon cylinder (Porex with an average pore size of 5−10 µm and 45−55% porosity) in a home-made Kel-F holder. Before use, the tip was cleaned by soaking it overnight in a 2 M NaOH solution (VWR, EMSURE) after which it was rinsed five times with ultrapure warm water. The OLEMS experiment involves measuring multi-ion mass as a function of time. Before the experiment the profile parameters of the possible gaseous product to be detected were set up on six different detection channels, with each channel using a secondary electron multiplier (SEM) voltage of 1390 V for the analysis. Each measurement was conducted after 1 hour of pressure equilibration and a 50 ms of detection time was used on each channel. One of the channels was used to follow the changes in the total pressure, and the other five channels were used to measure the following fragments: m/z = 1, m/z = 15, m/z = 18, m/z = 26, and m/z = 28, corresponding to H_2, CH_4, H_2O, C_2H_4, and CO/N_2, respectively. To determine the quantitative proportion of CO (as a product), CO (as a fragment of CO_2), and N_2 during the reduction of CO_2, the calibration method described by Binninger *et al.* was implemented.[405]

6.2.5. Computational details

Density functional theory (DFT) calculations were conducted in accordance with the protocols outlined in our previous work.[406] To model the electronic structure, a cluster model (Figure 6.1) comprising four metal nodes was derived from the crystal structure of the 2D Ni-MOF. For computational efficiency, the 4,4-bypyridine linkers were truncated to pyridine linkers. To maintain charge balance, the Ni^{2+} sites at the ends of the cluster models were replaced with

Li^+ sites, and these sites were frozen at their crystallographic positions in order to capture the rigidity of the 2D Ni-MOF.

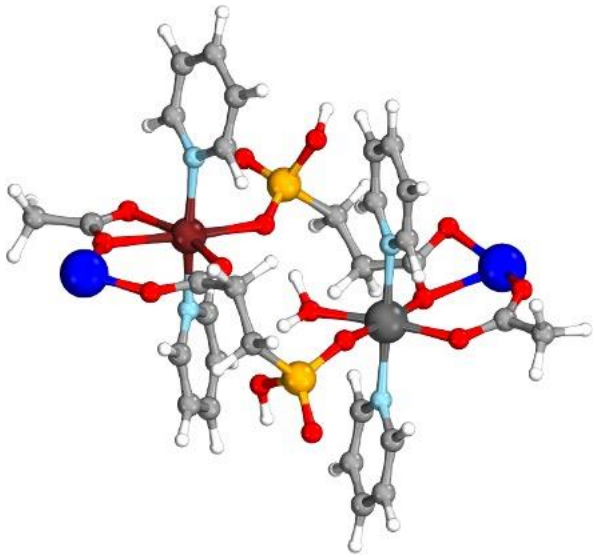


Figure 6.1. Cluster model used in this work. Color code: H (white), Li (dark blue), C (grey), N (light blue), P(yellow), O (red), inactive Ni (brown), and active Ni (black).

All calculations were performed using the M06L[407]density functional, known for accurately reproducing various aspects of MOF chemistry using cluster models[408], as implemented in the ORCA 5.0.3 software package.[409] The active Ni^{2+} site with the coordinated water molecule was assigned the def2-TZVPP basis set, and atoms in the first coordination sphere around that site were assigned the def2-TZVP basis set. All other atoms were assigned the def2-SV(P) basis set.[410] Four-index integrals were approximated using the resolution of identify (RI) method[411] with the def2/J auxiliary basis sets.[412] Unrestricted Kohn-Sham wavefunctions were assumed for all calculations, employing standard optimization and SCF criteria. Dispersion effects were considered using the D3zero method[413], as the M06L density functional already incorporates some dispersion. Implicit solvation effects were incorporated using the continuum-like

polarizable conductor model (CPCM), with water as the solvent.[414] Atomic charges are calculated using the CM5 method[415] as implemented in MultiWFN.[416]

The free energy (*G*) of the reactants, intermediates, and products was calculated according to Eq. 1, where *E* is the total electronic energy, *I* is the internal energy (zero-point energy and thermal effects), and *H* and *S* are the enthalpic and entropic effects, respectively, at *T* = 298K. Thermochemical values were determined using the Qausi-RRHO method of Grimme.[417] Each elementary step of the reaction was considered to proceed via a proton-coupled electron transfer (PCET) mechanism[418, 419] following the computational hydrogen electrode model (CHEM) of Peterson *et al.*[420] The limiting potential (U_L) was calculated based on the maximum energy difference (ΔG_{max}) between elementary reduction steps leading to the formation of either CO or H_2.

$$G = E + I + H - TS \qquad (6.1)$$

6.3. Results and discussion

6.3.1. Characterization of $Ni_2(HO_3PC_2H_4COO)_2(4,4'\text{-bipy})_2(H_2O)$

$Ni_2(HO_3PC_2H_4COO)_2(4,4'\text{-bipy})_2(H_2O)$ was hydrothermally synthesised, and the crystal structure comprises two independent nickel (II) ions linked through two phosphonate ligands ($HO_3PC_2H_4COO^{2-}$) forming a fourteen-membered ring, one water molecule coordinated to one of the metal atoms, and two non-equivalent coordinated 4,4′-bipyridine ligands (Figure 6.2a). The powder XRD pattern demonstrated that the as-prepared nickel 2D-MOF was highly crystalline and was well-matched with the typical crystalline structure reported by Fandaz *et al.*[363] To show that the powder pattern is consistent with the simulated pattern, refinement was carried out by the Rietveld method using the GSAS 2 program over the 2θ range from 5°

to 70°. More information on Rietveld refinement including unit cell parameters, occupancies and atomic positions are shown in the Chapter 9, table A6.3 and A6.4. The result shows that the experimental and simulated patterns match well with agreement factors of R_{wp} = 2.42 %, and GoF = 5.05 (Figure 6.2b). Further thermostability evaluation was carried out using thermogravimetric analysis (TGA) where the differential thermogravimetric (DTG) curve is obtained from the corresponding TGA curve by differential calculation (Figure 6.2c). The result of the analysis shows that the structure of the material remained stable until 200 °C. As the temperature increased to *ca* 240°C, a small weight loss which corresponds to loss of nickel-coordinated water was detected. After reaching T > 350 °C, the materials began decomposing, with a continuous loss of weight (endothermic branch between 350 °C and 500 °C), followed by the combustion of organic components at temperatures above 500 °C (exothermic band centred around 450 °C). Scanning electron microscopy (SEM) and transmission electron microscopy (TEM) were used to study the structure and elemental composition of the as prepared 2D MOF catalyst (Figure 6.3). The SEM and low-resolution TEM show that the crystals are rectangular prisms with flat faces and images are along [001] orientation. The high-resolution TEM and high angle annular dark field (HAADF) images of the as-prepared catalyst before CO_2RR confirmed the uniform distribution of Ni, P, C, N and O in the Ni-MOF sample. HRTEM imaging of the rectangular prisms also showed a distinct lattice spacing of 0.914 nm which corresponds to the $1\bar{1}0$ plane of the nickel 2D-MOF catalyst. The inset TEM image in Figure 6.3E shows the electron diffraction pattern, in which the bright circular dots at 9.30 Å, 8.00 Å and 5.43 Å correspond to the ($1\bar{1}0$), (110) and (201) lattice planes which show the highly crystalline nature of the catalyst and are also in good agreement with the XRD results. FTIR and Raman spectroscopy were performed to investigate the bonding characteristics of the organics in the Ni-MOF catalyst (Figure 6.4a). The FTIR peak

wave numbers at 1545 cm^{-1} and 1405 cm^{-1} represent the asymmetric and symmetric stretching modes of the coordinated (COO–) group from the main ligand while the peak at 1579 cm^{-1} can be assigned to the C=N stretch mode originating from 4,4-bipyridine auxiliary ligand. The P–C stretching mode is observed at 1353 cm^{-1}, while the P–O stretching modes of phosphonate group are evidence as strong absorption bands at 1050 cm^{-1} and 950 cm^{-1} respectively. The peaks in the region less than 950 cm^{-1} wavenumber confirmed the presence of Ni-O bonds. The Raman spectrum band at 1523 cm^{-1} can be attributed to the symmetric vibration $\nu_s(COO^-)$ while the peak at 1618 cm^{-1} corresponds to the bond stretching between sp^2 C and N atoms in the bipyridine ligand (Figure 6.4b).

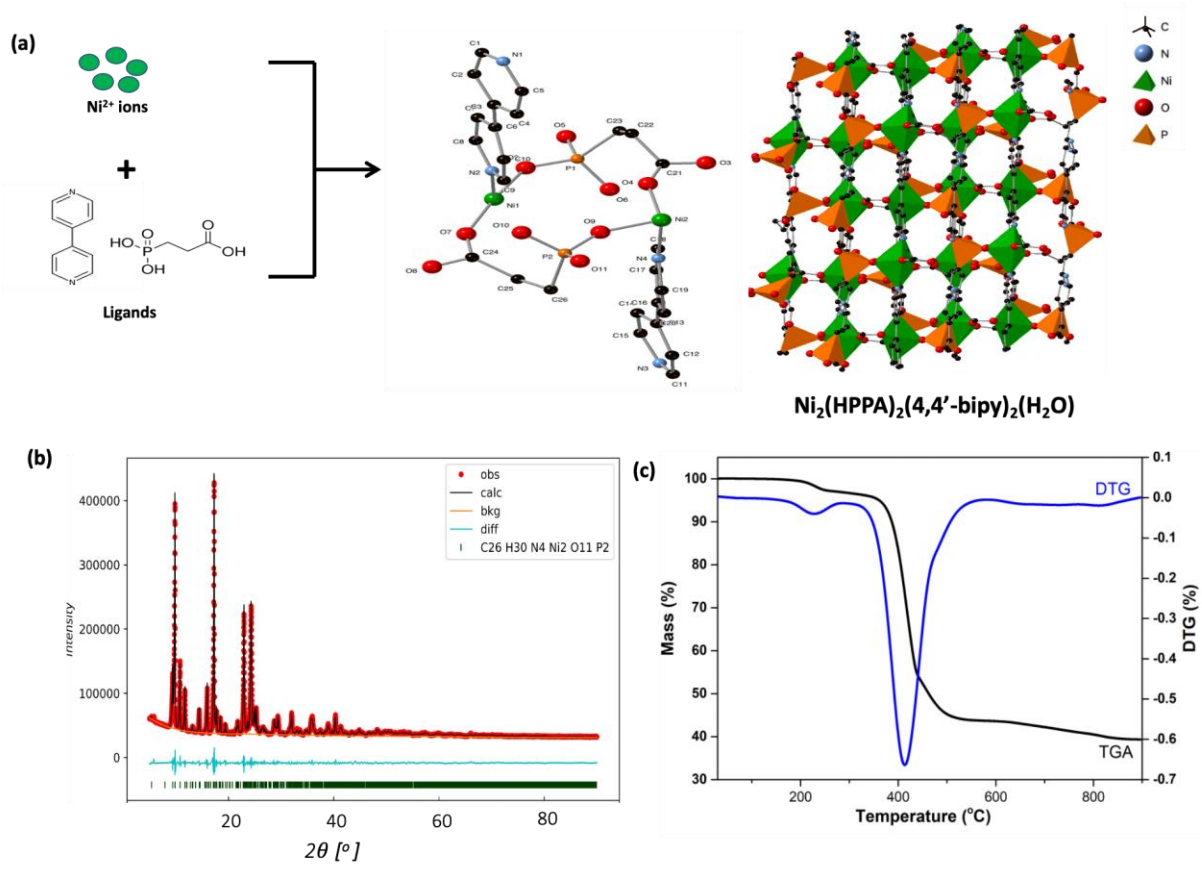


Figure 6.2. (a) Scheme showing the synthesis and crystal structure; (b) XRD and Rietveld refinement profile; and (c) TGA analysis revealing the temperature profile and the stability of the catalyst.

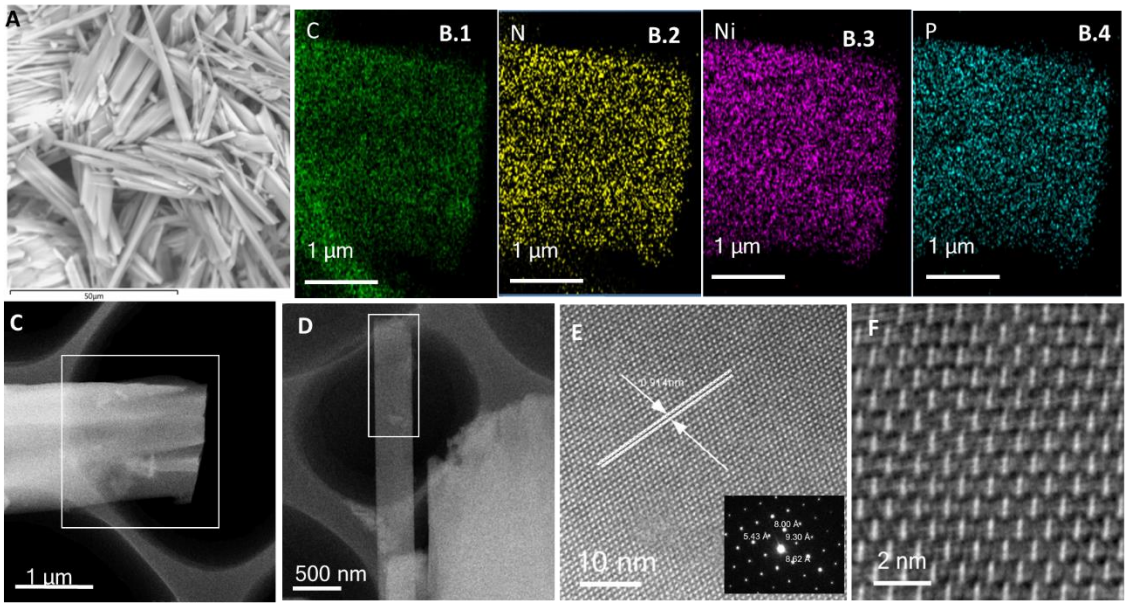


Figure 6.3. (a) Low-magnification SEM image; (b) HAADFSTEM and corresponding EDS elemental mapping images; (c) & (d) Low-magnification TEM image; and (e) & (f) HRTEM images of the catalyst after being dispersed by ultrasonication in water for 30 min.

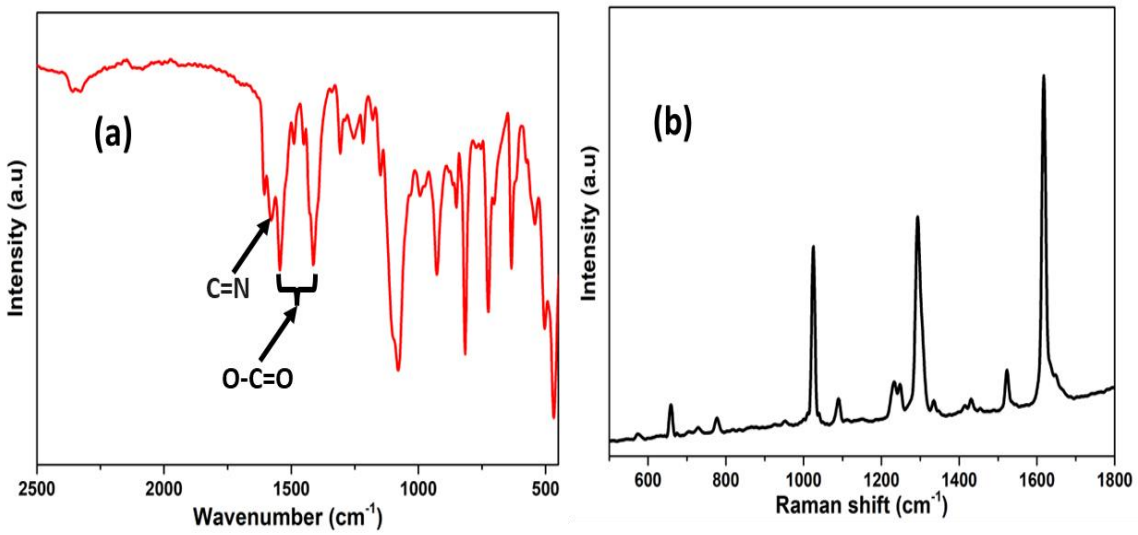


Figure 6.4. (a) FT-IR spectrum and (b) Raman spectrum of the as-prepared Ni-MOF catalyst.

6.3.2. Electrochemical characterization of the catalyst and assessment of its catalytic activity for the CO_2RR

To evaluate the electrocatalytic performance of the Ni-MOF, cyclic voltammetry of the supported catalyst was performed in 0.1 M carbonate buffer (pH 9.2) electrolyte. Figure 6.5a shows the CV of the Ni-MOF catalyst in the absence and presence of CO_2; the catalytic activity shown have been normalized to current per mass (mg) of the nickel active sites in the electrocatalyst. The voltametric profile of the catalyst in the absence of CO_2 shows an onset reduction potential at -0.4 V vs RHE, associated with the HER. When the solution was saturated with CO_2, a wave was observed in the cathodic scan at *ca.* −0.45 V (*vs*. RHE), possibly attributed to the reduction of Ni (II) to Ni (I)/Ni(0).[179] As the potential is swept between -0.60 V to -1.05 V, an increased current was observed associated with the competitive CO_2 reduction and hydrogen evolution reactions. As regard the Ni (II) reduction, it is presumed that either Ni (I) or Ni (0) sites are likely to be the electronic state that drives CO evolution rather than Ni (II) moieties.[179] However, monovalent Ni (I) site has been found to be more stable and as such most likely site responsible for the CO_2 reaction activities in our catalyst.[179, 421, 422] Electronic structure calculations of a twice-reduced Ni-MOF cluster show similar atomic charges on the two Ni sites, further indicating the presence of two Ni(I) sites and not a combination of Ni(II) and Ni(0) sites. The current density of the catalyst in Ar-saturated electrolyte was higher than in CO_2-saturated electrolyte. The lower current density of the catalyst in CO_2-saturated electrolyte is probably associated with the slow reaction rate of the CO_2RR in compare to the HER.[237] DFT calculations indicate that greater charge accumulation is found on the Ni(I) site following CO_2 adsorption which may further explain the change in charge density observed in the saturated CO_2 atmosphere due to less charge delocalization.

Notably, at 1.01 V (*vs* RHE), the CV profile shows a current density of 9.5 mA cm^2 in CO_2-saturated 0.1 M carbonate buffer solution, suggesting that the catalyst is active towards CO_2 reduction.

Additionally, the surface concentration of surface-active Ni on the working electrode (n) and the surface fraction of electrochemically active Ni sites (χ) in the catalyst material were calculated by integration of the Ni^{+}/Ni^{2+} cathodic wave of the CV curve in CO_2-saturated electrolyte (Figures A 6.2). The resulting value of the concentration of surface-active Ni site is given as 2.73×10^{-8} mol cm^{-2} while the fraction of electrochemically active Ni sites for CO_2 reduction is 17.9 % which is significantly higher than those reported for some MOFs and COFs[244, 423], and thereby reflecting the high accessibility of electrochemically active species in our Ni-MOF catalyst.

One important parameter on the electrochemical conversion of CO_2 is the accessibility of the active sites, and the mass transport through the catalyst layer. To investigate the influence of catalyst mass loading on the measurement of CO_2 activity, four loadings of Ni-MOF catalyst on GCE were used, *i.e*. 42.76 µg, 57.06 µg, 85.56 µg, and 114.08 µg yielding loadings of 1360 µg/cm^2, 1816 µg/cm^2, 2723 µg/cm^2 and 3630 µg/cm^2, respectively. As can be seen in Figure 6.5b and Figure A6.3 (Chapter 9), as the loading of the catalyst increases, the charges also increase but the activities of the catalyst for CO_2RR decreases. This indicates that increasing the electrode loading does affect the kinetics of the CO_2 reduction reactions. This is understandable, as discussed above, because the distance for electron transport is increased and more parts of the catalyst will not get wetted by the electrolyte with the increase of the electrode loading, and simultaneously a higher rate for ion diffusion is required for a higher current.[148, 424]

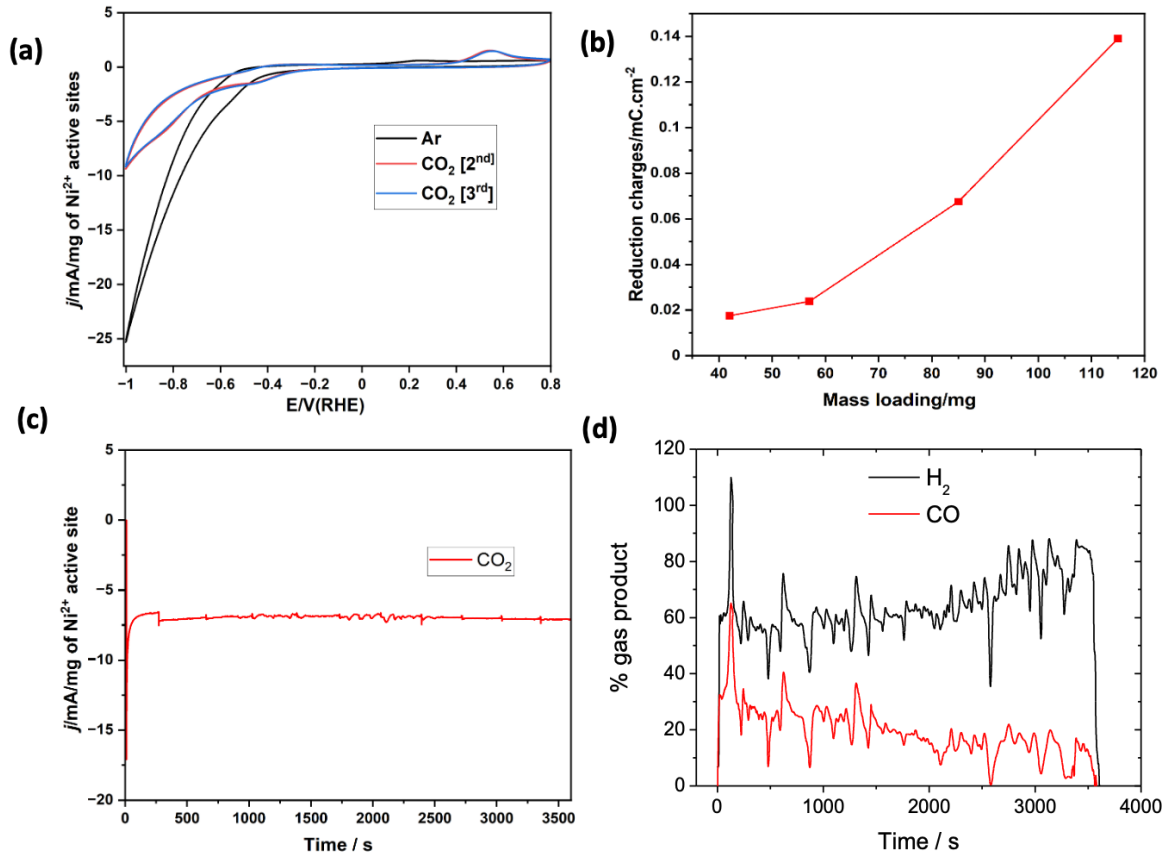


Figure 6.5. (a) Cyclic voltammograms of the catalyst in Ar-saturated 0.1 M $NaHCO_3/NaCO_3$ buffer solution [black lines] and selected successive cyclic voltammograms in CO_2-saturated 0.1 M $NaHCO_3/NaCO_3$ buffer solution, v = 50mV s^{-1}. (b) The Integrated reduction charges as a function of catalyst mass loading (c) 1h-chronoamperometry of the Ni-MOF supported catalyst in CO_2-saturated 0.1 M $NaHCO_3/NaCO_3$ at −0.8 V *vs*. RHE, and (d) gas products analysis generated during the CO_2RR.

To gain insights regarding the selectivity of this Ni-MOF catalyst during the CO_2RR, potential-controlled electrolysis experiments were performed following the gas products via OLEMS. The current stability of the chronoamperometric experiment at −0.8 V *vs* RHE is shown in Figure 6.5c while Figure 6.5d shows the relative distribution of gaseous products during the CO_2RR on Ni-MOF catalyst during 1h electrolysis at −0.8 V *vs* RHE. As can be seen, only CO (m/z = 28) and H_2 (m/z = 2) were detected during the electrolysis. Interestingly, the selectivity

changed during the long-term electrolysis. At early stages of the electrolysis, a CO and H_2 mixture was produced at an efficiency ratio of 40:60 %, respectively. However, as the reaction progressed with time, the efficiency ratio of production of the CO and H_2 mixture decreased to 20:80 %. These products constitute a potential feedstock for Fischer–Tropsch synthesis of hydrocarbons.[381, 425] The promising performance of this catalyst toward CO_2 reduction can be attributed to the abundance of Ni-nitrogen sites within the Ni-MOF which act as electrocatalytic centres and redox-hopping-based conduit that facilitates the charge transfer for Ni-MOF in electrochemical CO_2RR.[426-428] Additionally, the TOF of the catalyst per active nickel was calculated to assess the specific activity of CO_2 reduction, producing a TOF value of 5,046 hr^{-1} at potential of -0.8 V (*vs* RHE), and suggesting an impressive intrinsic activity and a faster reaction rate for electrocatalytic CO_2RR.

Since the change of product distribution as a function of time can indicates changes in the structure and composition of the catalyst during operation, CVs were recorded before and after the chronoamperometry. As can be seen in Figure 6.6, small changes were observed between the CV before and after the 1h-chronoamperometry. The overall currents increased, and the onset potential was statistically slightly shifted towards less negative potentials. These changes are in agreement with an increased production of H_2 over CO as indicated earlier when comparing the CVs in the absence and presence of CO_2.

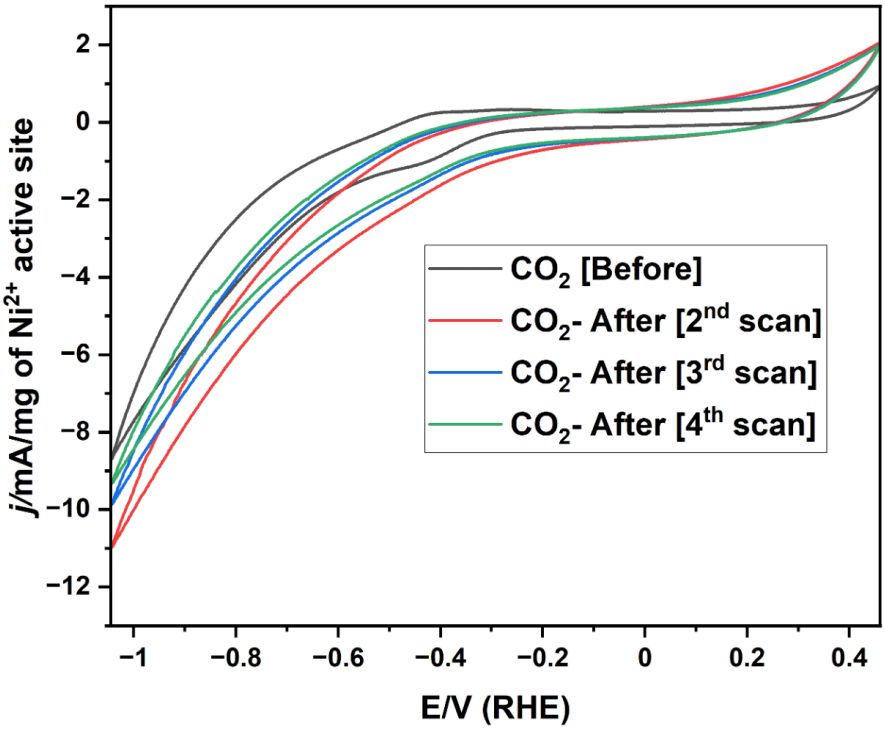


Figure 6.6. (a) Cyclic voltammograms of the catalyst before and after 1 h of electrolysis at −0.8 V *vs*. RHE in CO_2-saturated 0.1M $NaHCO_3$/$NaCO_3$ buffer solution (pH=9.2).

To gain further information regarding the changes in the durability and selectivity of the catalyst, SEM, high-resolution TEM, XRD and Raman were performed on the catalyst, post-mortem. The images in Figure 6.7, show no obvious changes in the morphology of the catalyst after the long-term CO_2RR testing. Moreover, the long-range ordering and crystallinity of the Ni-MOF was retained, also confirmed by the powder XRD patterns of the catalyst after the long-term CO_2RR testing (Figure 6.8).

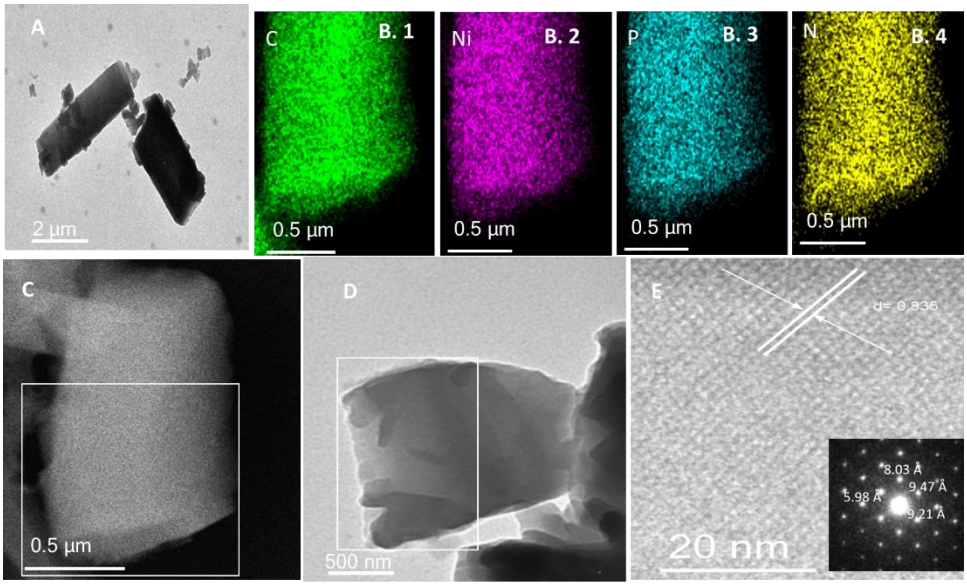


Figure 6.7 (a) Low-magnification SEM image (b) HAADFSTEM and corresponding EDS elemental mapping images (c)&(d) Low-magnification TEM image (e) HRTEM image of the catalyst ink after 1h of electrolysis at −0.8 V *vs*. RHE in CO_2-saturated 0.1 M $NaHCO_3$/$NaCO_3$ buffer solution(pH=9.2).

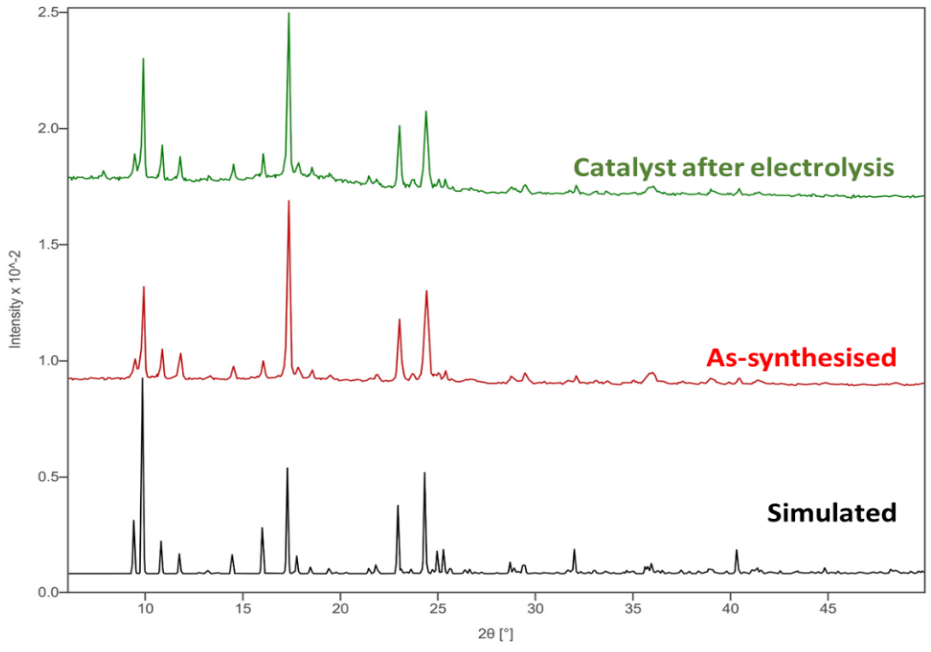


Figure 6.8. XRD data of Ni-MOF samples for simulated (black), as synthesised (red) and after one hour of electrolysis (in green).

The absence of changes in the Raman spectra before and after CO_2RR testing also indicate to the stability of the catalyst as no obvious shift in the bands at 1523 and 1618 cm^{-1} was observed in the Raman spectra (Figure 6.9). Additionally, FT-IR analysis of the Ni-MOF catalyst before and after the long-term CO_2RR testing was also carried out to monitor changes that might occur in the catalyst during the electrochemical reaction (Figure 6.10). Two strong bands at ~1545 and~1405 cm^{-1}, which were assigned to the asymmetric and symmetric stretching modes of the coordinated (COO–) group from the ligand remain unchanged after electrolysis, indicating that the ligands remain coordinated to the Ni metal, and this further demonstrated the integrity of the coordination networks and the stability of the Ni-MOF. Since no significant changes in crystallinity, morphology and composition were observed in the post-mortem analysis, we might attribute the changes in selectivity to the changes in the local pH during the electrolysis. [429-431]

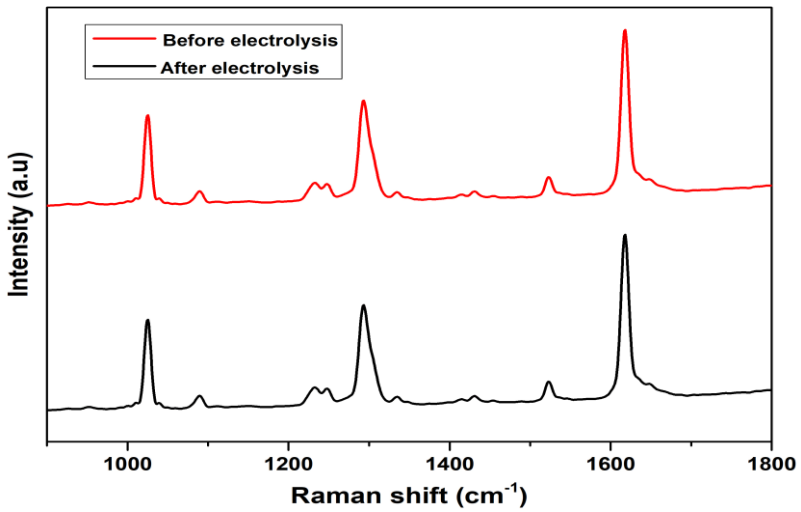


Figure 6.9. Raman spectra of the catalyst before and after 1hr of electrolysis at −0.8 V *vs*. RHE in CO_2-saturated 0.1M $NaHCO_3$/$NaCO_3$ buffer solution (pH=9.2).

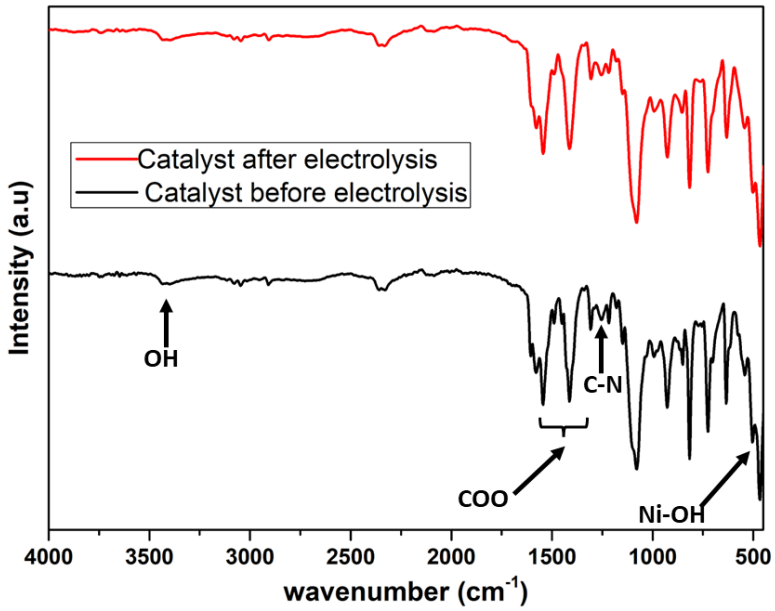


Figure 6.10. FT-IR spectra of the catalyst before and after 1h of electrolysis at −0.8 V *vs*. RHE in CO_2-saturated 0.1 M $NaHCO_3$/$NaCO_3$ buffer solution (pH=9.2).

6.3.3. Mechanistic insights

To further understand the processes of CO_2 and hydrogen reduction on the 2D Ni-MOF, we conducted DFT calculations using a cluster model of the MOF. The enhanced catalytic activity of the 2D Ni-MOF is attributed specifically to the Ni(II) site with an adsorbed H_2O molecule, as this site can transition into an open-metal site upon H_2O removal. The weak binding of the adsorbed H_2O to the Ni site (4.4 kcal mol^{-1} or 0.19 eV) facilitates the formation of the active catalyst from the precatalyst.

Figure 6.11 illustrates the reaction mechanism for both CO_2 reduction (left) and hydrogen reduction (right). The reaction begins with the formation of the active catalyst (**2**) following the decoordination of H_2O from the precatalyst **(1)**. Hydrogen reduction involves the formation of a Ni-H bond (**3**), accompanied by a limiting potential of 1.22 eV. This intermediate can then undergo a subsequent reduction to yield H_2 which is weakly physiosorbed to the Ni site, allowing for facile desorption. Similarly, the formation of CO

involves two reduction steps following CO_2 adsorption (**4**). The intermediate leading to CO formation involves the reduction of one of the O atoms of CO_2, yielding intermediate **5**. This step determines the limiting potential for CO_2 reduction at a value of 1.74 eV, significantly higher (0.52 eV) than that of hydrogen reduction. This energy difference underscores the thermodynamic driving forces that partly explain the experimentally observed 30:70% ratio for CO and H_2 formation. Following the first reduction step to form **5**, the OH group is further reduced, producing one equivalent each of CO and H_2O. The binding of CO to the Ni(II) site is less energetically favourable compared to the binding of H_2O. Thus, the formation of CO and H_2O following a second reduction step results in a free CO molecule and an adsorbed H_2O, closing the reaction mechanism cycle and allowing for further reduction of CO_2 or hydrogen.

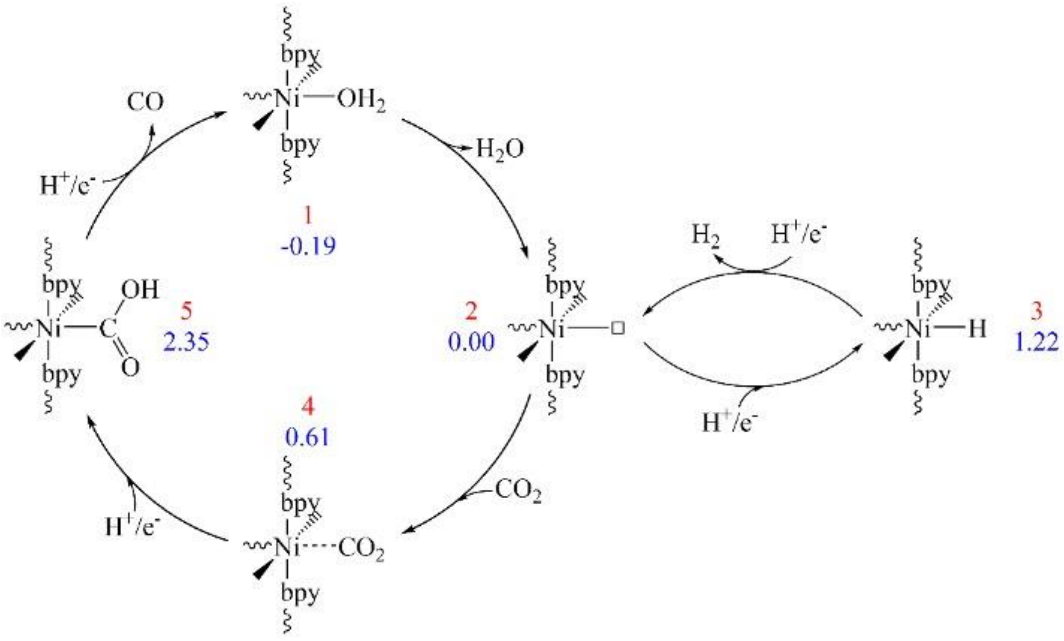


Figure 6.11. Reaction mechanism for CO_2RR (left) and HER (right) on the 2D Ni-MOF. Numbers in red indicate the structure number referenced in the text and reaction energetics in eV are given in blue. Dashed, wedged, and squiggly lines indicate the coordination between Ni sites through either the phosphonic acid or 4,4-bipyridine ligands.

6.4. Conclusion

In this study, we have demonstrated the significant potential of a 2D Ni-MOF as a promising electrocatalyst for the reduction of CO_2 to produce syngas. This electrocatalyst was hydrothermally synthesized by the reaction of 2-carboxyethylphosphonic acid and 4,4-bipyridine with Ni $(CH_3COO)_2.4H_2O$. This Ni-MOF catalyst demonstrated a considerably good electrocatalytic CO_2RR performance, giving an onset potential of -0.51 V *vs* RHE and a current-mass activity of 9.5 mA/mg. Long term electrolysis at a CO_2/CO potential of -0.8 V (vs RHE) yielded a gaseous mixture to of CO and H_2 at an average production ratio of 30:70%, respectively. These products constitute a potential feedstock for Fischer–Tropsch synthesis of hydrocarbons. DFT calculations were performed to assess the high catalytic activity of the Ni-MOF, revealing a difference of 0.52 eV in the limiting potentials for HER and CO_2RR, favouring HER, highlighting the thermodynamic driving forces behind the predominant production of H_2 over CO. The Ni-MOF catalyst retained its crystallinity and morphology after electrolysis as confirmed by powder XRD, HRTEM FT-IR and Raman spectroscopy, indicating a promising durability of the Ni-MOF for CO_2RR. Changes observed in the selectivity of the H_2 over CO during the electrolysis can therefore most likely be linked to a change in the local pH of the electrolyte. Our findings demonstrate the potential of 2D MOFs as heterogeneous electrocatalysts for CO_2 reduction.

CHAPTER SEVEN

Conclusions and future work

7.0. Conclusions and future work

In this research work, several new carboxyphosphonate metal-organic frameworks (MOFs) materials were synthesised and characterised, and their structure established. Electrochemical studies of some of these new materials were also carried out to evaluate their potential as electrocatalysts for the CO_2 reduction reaction.

This research work started by first by studying the ion exchange capability of BIRM-1 with nickel metal. We were able to demonstrate for the first time, the successful incorporation of nickel (II) cations into BIRM-1. The structure of Ni^{2+}-BIRM-1 was established by single crystal XRD, showing that its crystallographic properties tally with those of BIRM-1, with no ammonium cations present in the pores and channels of Ni^{2+}-BIRM-1, indicating structure preservation and full ion exchange. However, the porosimetry measurements showed that the BET surface area of Ni^{2+}-BIRM-1 was estimated to be 75 m^2/g suggesting that the material showed little or no porosity. The electrochemical studies showed that Ni^{2+}-BIRM-1 catalyst did not show activity toward CO_2 reduction. Therefore, some other experimental methods could be explored in the future to dehydrate the water present in the framework of Ni^{2+}-BIRM-1 in order to achieve a structure with permanent porosity which is the key feature for most MOF applications. Methods such as supercritical fluid or freeze drying would be worth trying.

The research then focused on synthesis of new carboxyphosphonate materials. Initially we explored the possibility of making new MOFs by modifying the BIRM-1 synthesis protocol and thereafter employed a new synthesis strategy with the goal of obtaining new functional 3D carboxylphosphonate framework materials. With 3-phosphonopropionic acid as ligand, we explored the possibility of synthesising new MOF materials with Zn, Cu, Co and Ni metals. Over hundred reactions were carried out where changes to the solvent mixture, modulator, reactant ratios, reaction temperature and reaction time were made to try and produce a single crystal which are characterised by single crystal XRD, powder XRD, FTIR and SEM. Five new carboxyphosphonate compounds, namely: BIRM-11(Zn), BIRM-12(Cu), BIRM-13(Cu) and BIRM-14(Cu), BIRM-15(Co) were synthesised, characterised and crystallographically established as either hydrogen-bonded or covalent 2D layered materials. Other new materials, including BIRM-16(Co) and BIRM-16(Ni) were 3D coordination networks but not carboxylphosphonate materials.

It has been noted that pH plays a critical role in achieving complete deprotonation of the carboxylphosphonate ligand and metal–ligand coordination. Although complete ligand deprotonation was achieved in BIRM-11(Zn), BIRM-14(Cu) and BIRM-15(Co), their crystal structures appeared as 2D metal organic frameworks (MOFs) with inorganic layers directly linked via ligand through covalent/coordination bonds. BIRM-12(Cu) and BIRM-13(Cu) were synthesized in acidic media because these reaction solutions were intolerant of pH > 3 and as such complete deprotonation of the ligand was not achieved. For this reason, their crystal structures appeared as hydrogen-bonded layered structures.

Attempts were made to tune the dimensionality of BIRM-13 into 3D structures using 4,4-bipyridine auxiliary ligand, producing BIRM-14(Cu), BIRM-16(Co) and BIRM-16(Ni).

Coordination of 4,4-bipyridine auxiliary ligand to BIRM-13 was achieved, but structural reorientation of the coordination geometry of BIRM-13 to a 3D framework was not achieved as BIRM-14 crystallised as 2D structure. However, in BIRM-16(Co) and BIRM-16(Ni), the coordination of 4,4-bipyridine auxiliary ligand to Co/Ni metals was influenced by the DMF solvent used in the synthesis. The DMF solvent underwent hydrolysis to formic acid, shifting the solution pH into the high basic region, thereby favouring the deprotonation of formic acid over 3-phosphonopropionic acid ligand. For this reason, BIRM-16(Co) and BIRM-16(Ni) are not carboxyphosphonate materials. One striking feature of these isostructural materials is that they exhibit chirality which is an important prerequisite in materials for enantiomeric separation. The future direction for this carboxylphosphonate material synthesis and discovery will be to explore various organic bases such as pyridine, amines, etc. as pH adjusters/deprotonators which can also function as a structure directing agent. Studying the properties of BIRM-11(Zn), BIRM-12(Cu), BIRM-13(Cu) and BIRM-14(Cu), BIRM-15(Co) in detail to establish their viability as proton conductors is also a priority in the future.

The electrocatalytic activity of BIRM-12(Cu), BIRM-13(Cu), BIRM-14(Cu) and BIRM-15(Co) was explored with respect to the CO_2 reduction reaction. Although CO_2 conversion may not have been achieved with BIRM-12, BIRM-13 and BIRM-15 catalysts, their activity toward the HER is of interest, as hydrogen gas has been considered as a clean fuel of the future. Further electrochemical studies on BIRM-12, BIRM-13 and BIRM-15 to fully explore their potential as electrocatalysts for hydrogen evolution reaction should be a priority for future work. Meanwhile, BIRM-14 demonstrated a promising activity towards CO_2 reduction, however, controlled potential electrolysis experiments are required to analyse the products and determine product selectivity and catalyst stability.

One of the potential drawbacks of the 3-phosphonopropionic acid ligand is a lack of rigidity which makes the synthesis of porous 3D supramolecular structures difficult. Therefore, the use of a different and more rigid ligand was explored to synthesise novel frameworks. 4-phosphonobenzoic acid was chosen for this synthesis as the longer, more rigid linker should be able to produce structures with larger internal voids. Four novel framework materials [BIRM-17(Zn), BIRM-18(Zn), BIRM-19(Zn), BIRM-20(Ni) & BIRM-21(Co)] have been synthesised with BIRM-18 (Zn) and BIRM-19(Zn) being of particular interest as porous MOFs. BIRM-17(Zn), BIRM-18(Zn), BIRM-19(Zn) and BIRM-21(Co) were obtained from a mixture of phases while BIRM-20(Ni) was obtained as a single pure phase. BIRM-17(Zn) was obtained as a hydrogen-bonded 2-dimensional layered structure, and upon modifying synthesis temperature and time, 3-dimensional and porous frameworks namely BIRM-18(Zn) and BIRM-19(Zn) were obtained. BIRM-18, as a novel MOF, possesses distinct crystallographic voids and channels which are potentially accessible for gas adsorption and ion-exchange reactions. Topological analysis shows that BIRM-18 exhibits a (4;2)-connected GIS-type topological structure seen in zeolites. However, obtaining a pure phase of BIRM-18 proved challenging, therefore fashioning an optimized strategy to obtain a pure phase of this material would be a priority for future work. Once a synthesis protocol for BIRM -18 has been established, a method for structure evacuation, porosimetry studies and ion-exchange attempts with different metal cations are possible future work. BIRM-19 is also a 3-dimensional porous structure with (4;2)-connected zeolite-like topology, its structure and topological net is similar to the structure obtained by Chen *et al*.[375] but differs in both the pore contents and synthetic route. BIRM-20 and BIRM-21 are 2-dimensional layered structures obtained from trying to make nickel and cobalt-containing porous metal phosphonate MOFs. BIRM-21 is of interest because it is similar to the layered phase of BIRM-

2 synthesised by Zhao[279] and isostructural to BIRM-8 found by Barker[278]. Since obtaining a 3-dimensional open framework was the goal, optimization of various synthetic parameters of BIRM-20 and BIRM-21 should be a priority for future work.

Finally, an interesting 2D nickel carboxyethylphosphonate material was also obtained while optimizing the synthetic conditions for BIRM-16(Ni). The structure of this material matches a previously synthesised material and as such it was not named as new material. However, this 2D Ni-MOF demonstrated significant potential as an electrocatalyst for the reduction of CO_2 to syngas, giving an onset potential of -0.51 V *vs* RHE and a current-mass activity of 9.5 mA/mg. Long term electrolysis at a CO_2/CO potential of -0.8 V (vs RHE) yielded a mixture CO and H_2, at an average production ratio of 30:70%, respectively. These products constitute a potential feedstock for Fischer–Tropsch synthesis of hydrocarbons. DFT calculations were performed to assess the high catalytic activity of the Ni-MOF, revealing a difference of 0.52 eV in the limiting potentials for HER and CO_2RR, favouring HER, highlighting the thermodynamic driving forces behind the predominant production of H_2 over CO. The Ni-MOF catalyst retained its crystallinity and morphology after electrolysis as confirmed by powder XRD, HRTEM FT-IR and Raman spectroscopy, indicating a promising durability of the Ni-MOF for CO_2RR. Changes observed in the selectivity of the H_2 over CO during the electrolysis can therefore most likely be linked to a change in the local pH of the electrolyte. Further studies to ascertain which oxidation state of nickel in the catalyst is driving the CO_2 reduction activities might prove interesting. For instant in-situ x-ray absorption spectroscopy (XAS) can be employed in monitoring the change in oxidation state of the Ni active site during the CO_2 reduction reaction.

8.0. References

1. Intergovernmental Panel on Climate, *Climate Change 2021 – The Physical Science Basis: Working Group I Contribution to the Sixth Assessment Report of the Intergovernmental Panel on Climate Change*, Cambridge University Press, Cambridge, 2023.

2. D. J. Easterbrook, in *Evidence-Based Climate Science (Second Edition)*, ed. D. J. Easterbrook, Elsevier, 2016, DOI: https://doi.org/10.1016/B978-0-12-804588-6.00009-4, pp. 163-173.

3. L. J. R. Nunes, *Env.*, 2023, **10**, 66

4. K. Hashimoto, in *Global Carbon Dioxide Recycling: For Global Sustainable Development by Renewable Energy*, ed. K. Hashimoto, Springer Singapore, Singapore, 2019, DOI: 10.1007/978-981-13-8584-1_3, pp. 5-17.

5. M. Scibioh and B. Viswanathan, in *Carbon Dioxide to Chemicals and Fuels,* Elsevier, 2018, DOI: 10.1016/B978-0-444-63996-7.00001-8, pp. 1-22.

6. V. Masson-Delmotte, P. Zhai, H.O. Pörtner, D. Roberts, J. Skea, P. R. Shukla, A. Pirani, W. Moufouma-Okia, C. Péan and R. Pidcock, *An IPCC Special Report on the impacts of global warming*, 2019, **1**, 93-174.

7. A. Averchenkova, S. Fankhauser and J. J. Finnegan, *Climate Policy*, 2021, **21**, 251-263.

8. J. Delbeke, A. Runge-Metzger, Y. Slingenberg and J. Werksman, in *Towards a climate-neutral Europe*, Routledge, 2019, pp. 24-45.

9. S. Dröge and V. Rattani, *After the Katowice Climate Summit: Building Blocks for the EU Climate Agenda*, SWP, 2019, DOI:10.18449/2019C09.

10. D. Narváez-Celada and A. S. Varela, *J. Mater. Chem. A,* 2022, **10**, 5899-5917.

11. K. Wiranarongkorn, K. Eamsiri, Y.-S. Chen and A. Arpornwichanop, *J. CO_2 Util.*, 2023, **71**, 102477.

12. R. Kortlever, J. Shen, K. J. Schouten, F. Calle-Vallejo and M. T. Koper, *J. Phys Chem Lett*, 2015, **6**, 4073-4082.

13. J. T. Feaster, C. Shi, E. R. Cave, T. Hatsukade, D. N. Abram, K. P. Kuhl, C. Hahn, J. K. Nørskov and T. F. Jaramillo, *ACS Catal.*, 2017, **7**, 4822-4827.

14. E. E. Benson, C. P. Kubiak, A. J. Sathrum and J. M. Smieja, *Chem. So. Rev.*, 2009, **38**, 89-99.

15. Y. Wang, D. He, H. Chen and D. Wang, *J. Photochem. Photobiol. C: Photochem. Rev.*, 2019, **40**, 117-149.

16. D. Ren, J. Fong and B. S. Yeo, *Nat. Commun.*, 2018, **9**, 925.

17. L. Zhang, Z.J. Zhao and J. Gong, *Angew. Chem. Int. Ed.*, 2017, **56**, 11326-11353.

18. Y. Zheng, A. Vasileff, X. Zhou, Y. Jiao, M. Jaroniec and S.-Z. Qiao, *J. Am. Chem.*, 2019, **141**, 7646-7659.

19. J. C. Bui, C. Kim, A. J. King, O. Romiluyi, A. Kusoglu, A. Z. Weber and A. T. Bell, *Acc. Chem. Res*., 2022, **55**, 484-494.

20. C. Sun, R. Gobetto and C. Nervi, *New J. Chem.*, 2016, **40**, 5656-5661.

21. H. Zhong, M. Ghorbani-Asl, K. H. Ly, J. Zhang, J. Ge, M. Wang, Z. Liao, D. Makarov, E. Zschech, E. Brunner, I. M. Weidinger, J. Zhang, A. V. Krasheninnikov, S. Kaskel, R. Dong and X. Feng, *Nat. Commun.*, 2020, **11**, 1409.

22. K. Naka, in *Encyclopedia of Polymeric Nanomaterials*, eds. S. Kobayashi and K. Müllen, Springer Berlin Heidelberg, Berlin, Heidelberg, 2015, DOI: 10.1007/978-3-642-29648-2_148, pp. 1233-1238.

23. H. Furukawa, K. E. Cordova, M. O'Keeffe and O. M. Yaghi, *Sci.*, 2013, **341**, 974.

24. M. S. Alhumaimess, *J. Saudi Chem. Soc.*, 2020, **24**, 461-473.

25. B. F. Hoskins and R. Robson, *J. Am. Chem.*, 1989, **111**, 5962-5964.

26. D. J. Tranchemontagne, J. L. Mendoza-Cortés, M. O'Keeffe and O. M. Yaghi, *Chem. So. Rev.*, 2009, **38**, 1257-1283.

27. A. U. Czaja, N. Trukhan and U. Müller, *Chem. So. Rev.*, 2009, **38**, 1284-1293.

28. R. J. Kuppler, D. J. Timmons, Q.-R. Fang, J.R. Li, T. A. Makal, M. D. Young, D. Yuan, D. Zhao, W. Zhuang and H.C. Zhou, *Coord. Chem. Rev.*, 2009, **253**, 3042-3066.

29. S. Dou, X. G. Li and X. Wang, *ACS Mater. Lett.*, 2020, **2**, 1251-1267.

30. C. Jiang, X. Wang, Y. Ouyang, K. Lu, W. Jiang, H. Xu, X. Wei, Z. Wang, F. Dai and D. Sun, *Nanoscale Adv.*, 2022, **4**, 2077-2089.

31. O. M. Yaghi, G. Li and H. Li, *Nat.*, 1995, **378**, 703-706.

32. M. Kondo, T. Yoshitomi, H. Matsuzaka, S. Kitagawa and K. Seki, *Angew. Chem., Int. Ed. Engl.*, 1997, **36**, 1725-1727.

33. H. Li, M. Eddaoudi, M. O'Keeffe and O. M. Yaghi, *Nat.*, 1999, **402**, 276-279.

34. J. L. C. Rowsell and O. M. Yaghi, *Micropor. Mesopor. Mater.*, 2004, **73**, 3-14.

35. M. Eddaoudi, J. Kim, N. Rosi, D. Vodak, J. Wachter, M. O'Keeffe and O. M. Yaghi, *Sci.*, 2002, **295**, 469-472.

36. S. M. F. Stephen S.Y Chui, Jonathan P.H Charmant, A. Guy Orpen, Ian D. Williams, *Sci.*, 1999, **283**, 1148-1150.

37. K. Barthelet, J. Marrot, D. Riou and G. Férey, *Angew. Chem., Int. Ed.*, 2002, **41**, 281-284.

38. F. Millange, C. Serre and G. Férey, *Chem Commun*, 2002, DOI: 10.1039/B201381A, 822-823.

39. S. Surblé, C. Serre, C. Mellot-Draznieks, F. Millange and G. Férey, *Chem Commun*, 2006, DOI: 10.1039/B512169H, 284-286.

40. G. Ferey, C. Mellot-Draznieks, C. Serre, F. Millange, J. Dutour, S. Surble and I. Margiolaki, *Sci.*, 2005, **309**, 2040-2042.

41. O. M. Yaghi, M. O'Keeffe, N. W. Ockwig, H. K. Chae, M. Eddaoudi and J. Kim, *Nat.*, 2003, **423**, 705-714.

42. J. R. Long and O. M. Yaghi, *Chem. So. Rev.*, 2009, **38**, 1213-1214.

43. G. K. H. Shimizu, R. Vaidhyanathan and J. M. Taylor, *Chem. So. Rev.*, 2009, **38**, 1430-1449.

44. S. J. I. Shearan, N. Stock, F. Emmerling, J. Demel, P. A. Wright, K. D. Demadis, M. Vassaki, F. Costantino, R. Vivani, S. Sallard, I. R. Salcedo, A. Cabeza and M. Taddei, *Cryst.*, 2019, **9**.

45. G. Alberti, *Solid-State Supramolecular Chemistry: Two- and Three-Dimensional Inorganic Networks 7*, Pergamon, Oxford, UK, 1996.

46. J. Szejtli, J. L. Atwood, and J.M. Lehn, *Comprehensive Supramolecular Chemistry*, Pargamon Press, New York, 1996.

47. G. Alberti, U. Costantino, S. Allulli and N. Tomassini, *J. Inorg. Nucl. Chem.*, 1978, **40**, 1113-1117.

48. M. Poojary, H.-L. Hu, F. Campbell and A. Clearfield, *Acta Crystallogr. B Struct. Sci.*, 1993, **49**, 996-1001.

49. A. Clearfield and K. Demadis, *Metal phosphonate chemistry: From synthesis to applications*, Royal Society of Chemistry, 2011.

50. G. Alberti, M. Casciola, U. Costantino and R. Vivani, *Adv Mater*, 1996, **8**, 291-303.

51. K. Rathore and R. Jangir, *Inorg. Chim. Acta*, 2024, **559**, 121804.

52. J. Svoboda, V. Zima, K. Melánová, L. Beneš and M. Trchová, *J. Solid State Chem.*, 2013, **208**, 58-64.

53. S.-S. Bao, G. K. H. Shimizu and L.-M. Zheng, *Coord. Chem. Rev.*, 2019, **378**, 577-594.

54. G. Alberti, R. Vivani, F. Marmottini and P. Zappelli, *J. Por. Mater.*, 1998, **5**, 205-220.

55. G. Alberti, U. Costantino, F. Marmottini, R. Vivani and P. Zappelli, *Angew. Chem., Int. Ed. Engl.*, 1993, **32**, 1357-1359.

56. J. Le Bideau, C. Payen, P. Palvadeau and B. Bujoli, *Inorg. Chem.*, 1994, **33**, 4885-4890.

57. K. Maeda, Y. Kiyozumi and F. Mizukami, *Angew. Chem., Int. Ed. Engl.*, 1994, **33**, 2335-2337.

58. K. Maeda, J. Akimoto, Y. Kiyozumi and F. Mizukami, *Angew. Chem., Int. Ed. Engl.*, 1995, **34**, 1199-1201.

59. K. Maeda, *Micropor. Mesopor. Mater.*, 2004, **73**, 47-55.

60. D. L. Lohse and S. C. Sevov, *Angew. Chem., Int. Ed. Engl.*, 1997, **36**, 1619-1621.

61. K. Barthelet, C. Merlier, C. Serre, M. Riou-Cavellec, D. Riou and G. Férey, *J. Mater. Chem.*, 2002, **12**, 1132-1137.

62. Q. Gao, N. Guillou, M. Nogues, A. K. Cheetham and G. Férey, *Chem. Mater.*, 1999, **11**, 2937-2947.

63. C. A. Merrill and A. K. Cheetham, *Inorg. Chem.*, 2005, **44**, 5273-5277.

64. W. Ouellette, M. H. Yu, C. J. O'Connor and J. Zubieta, *Inorg. Chem.*, 2006, **45**, 3224-3239.

65. M. P. Attfield, Z. Yuan, H. G. Harvey and W. Clegg, *Inorg. Chem.*, 2010, **49**, 2656-2666.

66. K. J. Gagnon, H. P. Perry and A. Clearfield, *Chem. Rev.*, 2012, **112**, 1034-1054.

67. M. T. Wharmby and P. A. Wright, in *Metal Phosphonate Chemistry: From Synthesis to Applications*, eds. A. Clearfield and K. Demadis, The Royal Society of Chemistry, 2011, DOI: 10.1039/9781849733571-00317, p. 0.

68. J. A. Groves, S. R. Miller, S. J. Warrender, C. Mellot-Draznieks, P. Lightfoot and P. A. Wright, *Chem. Commun*, 2006, DOI: 10.1039/B605400E, 3305-3307.

69. M. T. Wharmby, J. P. S. Mowat, S. P. Thompson and P. A. Wright, *J. Am.Chem.*, 2011, **133**, 1266-1269.

70. C. Serre, J. A. Groves, P. Lightfoot, A. M. Z. Slawin, P. A. Wright, N. Stock, T. Bein, M. Haouas, F. Taulelle and G. Férey, *Chem. Mater.*, 2006, **18**, 1451-1457.

71. S. R. Miller, G. M. Pearce, P. A. Wright, F. Bonino, S. Chavan, S. Bordiga, I. Margiolaki, N. Guillou, G. Férey, S. Bourrelly and P. L. Llewellyn, *J. Am.Chem.*, 2008, **130**, 15967-15981.

72. B. M. Ramesha and V. Meynen, *Mater.*, 2020, **13**.

73. G. Yücesan, Y. Zorlu, M. Stricker and J. Beckmann, *Coord. Chem. Rev.*, 2018, **369**, 105-122.

74. T. Rhauderwiek, H. Zhao, P. Hirschle, M. Döblinger, B. Bueken, H. Reinsch, D. De Vos, S. Wuttke, U. Kolb and N. Stock, *Chem. Sci.*, 2018, **9**, 5467-5478.

75. T. Rhauderwiek, K. Wolkersdörfer, S. Øien-Ødegaard, K.-P. Lillerud, M. Wark and N. Stock, *Chem. Commun*, 2018, **54**, 389-392.

76. B. Wang, T. Rhauderwiek, A. K. Inge, H. Xu, T. Yang, Z. Huang, N. Stock and X. Zou, *Chem. Eur. J.*, 2018, **24**, 17429-17433.

77. Y.-P. Zhu, T.Y. Ma, Y.L. Liu, T.Z. Ren and Z.Y. Yuan, *Inorg. Chem. Front.*, 2014, **1**, 360-383.

78. S. Drumel, P. Janvier, P. Barboux, M. Bujoli-Doeuff and B. Bujoli, *Inorg. Chem.*, 1995, **34**, 148-156.

79. M. Riou-Cavellec, M. Sanselme, N. Guillou and G. Férey, *Inorg. Chem.*, 2001, **40**, 723-725.

80. N. Stock, S. A. Frey, G. D. Stucky and A. K. Cheetham, *J. Chem. Soc., Dalton Trans.*, 2000, DOI: 10.1039/B006411O, 4292-4296.

81. F. Serpaggi and G. Férey, *Inorg.Chem.*, 1999, **38**, 4741-4744.

82. E. M. Sabbar, M. E. de Roy and J. P. Besse, *Mater. Res. Bull.*, 2000, **35**, 93-107.

83. S. F. Tang, J. L. Song and J. G. Mao, *J. Inorg.Chem.*, 2006, 2011-2019

84. S.F. Tang, J.L. Song, X.L. Li and J.G. Mao, *Cryst. Growth Des.*, 2006, **6**, 2322-2326.

85. T.H. Zhou, F.Y. Yi, P.X. Li and J.G. Mao, *Inorg. Chem*, 2010, **49**, 905-915.

86. S.F. Tang, X.B. Pan, X. X. Lv and X.B. Zhao, *J Solid State Chem.*, 2013, **197**, 139-146.

87. J. Zhu, X. Bu, P. Feng and G. D. Stucky, *J. Am.Chem.*, 2000, **122**, 11563-11564.

88. C. Serre, N. Stock, T. Bein and G. Férey, *Inorganic Chemistry*, 2004, **43**, 3159-3163.

89. Z. Chen, Y. Zhou, L. Weng and D. Zhao, *Cryst Growth Des*, 2008, **8**, 4045-4053.

90. C. Zhao, L. Male, T.Y. Chen, J. A. Barker, I. J. Shannon and P. A. Anderson, *Chem. Eur. J.*, 2019, **25**, 13865-13868.

91. M. Tuikka, M. Haukka and M. Ahlgrén, *Solid State Sci.*, 2007, **9**, 535-541.

92. R. N. Devi, P. Wormald, P. A. Cox and P. A. Wright, *Chem. Mater.*, 2004, **16**, 2229-2237.

93. H. G. Harvey, J. Hu and M. P. Attfield, *Chem. Mater.*, 2003, **15**, 179-188.

94. K. O. Kongshaug and D. Riou, *J. Chem. Soc., Dalton Trans.*, 2002, DOI: 10.1039/B205469H, 4152-4155.

95. G. B. Hix, A. Turner, B. M. Kariuki, M. Tremayne and E. J. MacLean, *J. Mater. Chem.*, 2002, **12**, 3220-3227.

96. S. Lodhia, A. Turner, M. Papadaki, K. D. Demadis and G. B. Hix, *Cryst. Growth Des.*, 2009, **9**, 1811-1822.

97. S. Ayyappan, G. Diaz de Delgado, A. K. Cheetham, G. Férey and C. N. R. Rao, *J. Chem. Soc., Dalton Trans.*, 1999, DOI: 10.1039/A905326C, 2905-2907.

98. J.T. Li, D.K. Cao, T. Akutagawa and L.M. Zheng, *Dalton Trans.*, 2010, **39**, 8606-8608.

99. J.T. Li, L.R. Guo, Y. Shen and L.M. Zheng, *Crystengcomm.*, 2009, **11**, 1674-1678.

100. J.T. Li, D.K. Cao, B. Liu, Y.Z. Li and L.M. Zheng, *Cryst. Growth Des.*, 2008, **8**, 2950-2953.

101. C. Baerlocher and W. M. Meier, *Helvetica Chimica Acta*, 1970, **53**, 1285-1293.

102. C. Heering, B. Nateghi and C. Janiak, *Cryst.*, 2016, **6**., 22

103. P. Garczarek, J. K. Zaręba, M. Duczmal, J. Janczak, J. Zoń, M. Samoć and M. Nyk, *Cryst. Growth Des.*, 2017, **17**, 1373-1383.

104. C. Liu, W. Yang, N. Qu, L.-J. Li, Q.J. Pan and Z.M. Sun, *Inorg. Chem.*, 2017, **56**, 1669-1678.

105. C. Zhao, PhD Thesis, University of Birmingham, 2013.

106. H. B. Wu and X. W. Lou, *Sci. Adv.*, 2017, **3**, 9252.

107. T. G. Glover and B. Mu, *Gas adsorption in metal-organic frameworks: Fundamentals and applications*, CRC Press, 2018.

108. L. Huang, H. Wang, J. Chen, Z. Wang, J. Sun, D. Zhao and Y. Yan, *Micropor. mesopor.mater.*, 2003, **58**, 105-114.

109. D. J. Tranchemontagne, J. R. Hunt and O. M. Yaghi, *Tetrahedron*, 2008, **64**, 8553-8557.

110. N. Stock and S. Biswas, *Chem. Rev.*, 2012, **112**, 933-969.

111. K. O. Kirlikovali, S. L. Hanna, F. A. Son and O. K. Farha, *ACS Nanoscience Au.*, 2023, **3**, 37-45.

112. J. Cravillon, S. Münzer, S.-J. Lohmeier, A. Feldhoff, K. Huber and M. Wiebcke, *Chem. Mater.*, 2009, **21**, 1410-1412.

113. H. Li, M. Eddaoudi, T. L. Groy and O. M. Yaghi, *J. Am. Chem.*, 1998, **120**, 8571-8572.

114. X.C. Huang, Y.Y. Lin, J.P. Zhang and X.M. Chen, *Angew. Chem., Int. Ed.*, 2006, **45**, 1557-1559.

115. M. Schlesinger, S. Schulze, M. Hietschold and M. Mehring, *Micropor. Mesopor. Mater.*, 2010, **132**, 121-127.

116. K. M. Taylor-Pashow, J. Della Rocca, Z. Xie, S. Tran and W. Lin, *J. Am. Chem.*, 2009, **131**, 14261-14263.

117. Z. Ni and R. I. Masel, *J. Am. Chem.*, 2006, **128**, 12394-12395.

118. Y.K. Seo, G. Hundal, I. T. Jang, Y. K. Hwang, C.-H. Jun and J.-S. Chang, *Micropor. Mesopor. Mater.*, 2009, **119**, 331-337.

119. J.H. Park, S.H. Park and S.H. Jhung, *J. Korean Chem. Soc.*, 2009, **53**, 553-559.

120. Y.R. Lee, J. Kim and W.S. Ahn, *Korean J. Chem. Eng.*, 2013, **30**, 1667-1680.

121. W.J. Son, J. Kim, J. Kim and W.S. Ahn, *Chem Commun*, 2008, DOI: 10.1039/B814740J, 6336-6338.

122. Z.Q. Li, L.G. Qiu, T. Xu, Y. Wu, W. Wang, Z.Y. Wu and X. Jiang, *Mater. Lett.*, 2009, **63**, 78-80.

123. H.Y. Cho, J. Kim, S.N. Kim and W.S. Ahn, *Micropor. Mesopor. Mater.s*, 2013, **169**, 180-184.

124. D.A. Yang, H.Y. Cho, J. Kim, S.T. Yang and W.S. Ahn, *Energy Environ. Sci.*, 2012, **5**, 6465-6473.

125. A. Pichon, A. Lazuen-Garay and S. L. James, *Crystengcomm.*, 2006, **8**, 211-214.

126. T. Friščić, D. G. Reid, I. Halasz, R. S. Stein, R. E. Dinnebier and M. J. Duer, *Angew. Chem., Int. Ed.*, 2010, **4**, 712-715.

127. P. J. Beldon, L. Fábián, R. S. Stein, A. Thirumurugan, A. K. Cheetham and T. Friščić, *Angew. Chem.*, 2010, **50**, 9834-9837.

128. A. Pichon and S. L. James, *Crystengcomm*, 2008, **10**, 1839-1847.

129. U. Mueller, M. Schubert, F. Teich, H. Puetter, K. Schierle-Arndt and J. Pastré, *J. Mater. Chem.*, 2006, **16**, 626-636.

130. A. Martinez Joaristi, J. Juan-Alcañiz, P. Serra-Crespo, F. Kapteijn and J. Gascon, *Cryst Growth Des.*, 2012, **12**, 3489-3498.

131. Y. Yang, Y. Yang, Y. Liu, S. Zhao and Z. Tang, *Small Sci.*, 2021, **1**, 2100015.

132. Z. Di, Y. Qi, X. Yu and F. Hu, *Catal*, 2022, **12**, 1582

133. C. Li, H. Zhang, M. Liu, F.-F. Lang, J. Pang and X.-H. Bu, *Ind. Chem. Mater.*, 2023, **1**, 9-38.

134. B. Y. Guan, X. Y. Yu, H. B. Wu and X. W. Lou, *Adv Mater*, 2017, **29**, 1703614.

135. D. Li, H.Q. Xu, L. Jiao and H.L. Jiang, *Energy Chem.*, 2019, **1**, 100005.

136. R. Li, F. Liu, Y. Zhang, M. Guo and D. Liu, *ACS Appl. Mater. Interfaces*, 2020, **12**, 44578-44587.

137. H. Yang, Y. Wu, Q. Lin, L. Fan, X. Chai, Q. Zhang, J. Liu, C. He and Z. Lin, *Angew. Chem., Int. Ed.*, 2018, **57**, 15476-15480.

138. S. Bhattacharyya, C. Das and T. K. Maji, *RSC Adv.*, 2018, **8**, 26728-26754.

139. M.X. Yang, L.J. Chen, Y.Z. Ye, X.Y. Lin and S. Lin, *Dalton Trans.*, 2021, **50**, 4904-4913.

140. Y. Li, M. Cui, Z. Yin, S. Chen and T. Ma, *Chem. Sci.*, 2020, **11**, 11646-11671.

141. Y. Zhu, K. Yue, C. Xia, S. Zaman, H. Yang, X. Wang, Y. Yan and B. Y. Xia, *Nano-Micro Lett.*, 2021, **13**, 137.

142. G. Dey, Shadab and A. Aijaz, *ChemElectroChem*, 2021, **8**, 3782-3803.

143. L. Chen and Q. Xu, *Matt.*, 2019, **1**, 57-89.

144. X. Huang, P. Sheng, Z. Tu, F. Zhang, J. Wang, H. Geng, Y. Zou, C.-a. Di, Y. Yi, Y. Sun, W. Xu and D. Zhu, *Nat. Commun.*, 2015, **6**, 7408.

145. L. Sun, M. G. Campbell and M. Dincă, *Angew. Chem., Int. Ed.*, 2016, **55**, 3566-3579.

146. E. M. Johnson, S. Ilic and A. J. Morris, *ACS Central Sci.*, 2021, **7**, 445-453.

147. J.H. Li, Y.S. Wang, Y.C. Chen and C.W. Kung, *Appl. Sci.*, 2019, **9**.

148. B. A. Johnson, A. M. Beiler, B. D. McCarthy and S. Ott, *J. Am. Chem.*, 2020, **142**, 11941-11956.

149. T. Yue, C. Xia, X. Liu, Z. Wang, K. Qi and B. Y. Xia, *ChemElectroChem*, 2021, **8**, 1021-1034.

150. P. Li and B. Wang, *Israel J. Chem.*, 2018, **58**, 1010-1018.

151. Y. Kobayashi, B. Jacobs, M. D. Allendorf and J. R. Long, *Chem. Mater.* 2010, **22**, 4120-4122.

152. A. A. Talin, A. Centrone, A. C. Ford, M. E. Foster, V. Stavila, P. Haney, R. A. Kinney, V. Szalai, F. El Gabaly, H. P. Yoon, F. Léonard and M. D. Allendorf, *Sci.*, 2014, **343**, 66-69.

153. C.-W. Kung, K. Otake, C. T. Buru, S. Goswami, Y. Cui, J. T. Hupp, A. M. Spokoyny and O. K. Farha, *J. Am. Chem.*, 2018, **140**, 3871-3875.

154. Z. Xin, Y.-R. Wang, Y. Chen, W.L. Li, L.Z. Dong and Y.Q. Lan, *Nano Energy*, 2020, **67**, 104233.

155. J. J. Calvo, S. M. Angel and M. C. So, *APL Mater.*, 2020, **8**.

156. S. Lin, P. M. Usov and A. J. Morris, *Chem. Commun.*, 2018, **54**, 6965-6974.

157. L. Sun, T. Miyakai, S. Seki and M. Dincă, *J. Am. Chem.*, 2013, **135**, 8185-8188.

158. S. Lin, P. M. Usov and A. J. Morris, *Chem Commun*, 2018, **54**, 6965-6974.

159. T. C. Narayan, T. Miyakai, S. Seki and M. Dincă, *J. Am. Chem.*, 2012, **134**, 12932-12935.

160. S. S. Park, E. R. Hontz, L. Sun, C. H. Hendon, A. Walsh, T. Van Voorhis and M. Dincă, *J. Am. Chem.*, 2015, **137**, 1774-1777.

161. L. Sun, S. S. Park, D. Sheberla and M. Dincă, *J. Am. Chem.*, 2016, **138**, 14772-14782.

162. D. Sheberla, L. Sun, M. A. Blood-Forsythe, S. Er, C. R. Wade, C. K. Brozek, A. Aspuru-Guzik and M. Dincă, *J. Am. Chem.*, 2014, **136**, 8859-8862.

163. M. G. Campbell, D. Sheberla, S. F. Liu, T. M. Swager and M. Dincă, *Angew. Chem., Int. Ed.*, 2015, **54**, 4349-4352.

164. A. J. Clough, J. M. Skelton, C. A. Downes, A. A. de la Rosa, J. W. Yoo, A. Walsh, B. C. Melot and S. C. Marinescu, *J. Am. Chem.*, 2017, **139**, 10863-10867.

165. C. F. Leong, P. M. Usov and D. M. D'Alessandro, *MRS Bull.*, 2016, **41**, 858-864.

166. D. Bohra, J. H. Chaudhry, T. Burdyny, E. A. Pidko and W. A. Smith, *Energy Environ. Sci.*, 2019, **12**, 3380.

167. W. Zheng, M. Liu and L. Y. S. Lee, *ACS Catal.*, 2020, **10**, 81-92.

168. P. M. Usov, C. McDonnell-Worth, F. Zhou, D. R. MacFarlane and D. M. D'Alessandro, *Electrochim. Acta*, 2015, **153**, 433-438.

169. D. O. Miles, D. Jiang, A. D. Burrows, J. E. Halls and F. Marken, *Electrochem. Commun.* 2013, **27**, 9-13.

170. W. Zheng and L. Y. S. Lee, *ACS Energy Lett.*, 2021, **6**, 2838-2843.

171. M. Ding, X. Cai and H. L. Jiang, *Chem. Sci.*, 2019, **10**, 10209.

172. B. Cui, C. Wang, S. Huang, L. He, S. Zhang, Z. Zhang and M. Du, *J. Colloid Interface Sci.*, 2020, **578**, 10-23.

173. N. C. Burtch, H. Jasuja and K. S. Walton, *Chem. Rev.*, 2014, **114**, 10575-10612.

174. D. Bůžek, S. Adamec, K. Lang and J. Demel, *Inorg. Chem. Front.*, 2021, **8**, 720-734.

175. W. Wang, H. Yan, U. Anand and U. Mirsaidov, *J. Am. Chem.*, 2021, **143**, 1854-1862.

176. B. Han, K. A. Stoerzinger, V. Tileli, A. D. Gamalski, E. A. Stach and Y. Shao-Horn, *Nat. Mater.*, 2017, **16**, 121.

177. X. Zhao, H. Ren and L. Luo, *Langmuir*, 2019, **35**, 5392.

178. S. Dou, X. Li and X. Wang, *ACS Mater. Lett.*, 2020, **2**, 1251.

179. H. Kim, D. Shin, W. Yang, D. H. Won, H.S. Oh, M. W. Chung, D. Jeong, S. H. Kim, K. H. Chae, J. Y. Ryu, J. Lee, S. J. Cho, J. Seo, H. Kim and C. H. Choi, *J. Am. Chem.*, 2021, **143**, 925-933.

180. A. Moysiadou, S. Lee, C.S. Hsu, H. M. Chen and X. Hu, *J. Am. Chem.*, 2020, **142**, 11901-11914.

181. S. Yuan, J.S. Qin, C. T. Lollar and H.C. Zhou, *ACS Central Sci.*, 2018, **4**, 440-450.

182. W. Lu, Z. Wei, Z.Y. Gu, T.F. Liu, J. Park, J. Park, J. Tian, M. Zhang, Q. Zhang, T. Gentle Iii, M. Bosch and H.C. Zhou, *Chem.So. Rev.*, 2014, **43**, 5561-5593.

183. J. H. Cavka, S. Jakobsen, U. Olsbye, N. Guillou, C. Lamberti, S. Bordiga and K. P. Lillerud, *J. Am. Chem.*, 2008, **130**, 13850-13851.

184. D. Feng, Z.Y. Gu, Y.P. Chen, J. Park, Z. Wei, Y. Sun, M. Bosch, S. Yuan and H.C. Zhou, *J. Am. Chem.*, 2014, **136**, 17714-17717.

185. D. Feng, W.C. Chung, Z. Wei, Z.Y. Gu, H.L. Jiang, Y.P. Chen, D. J. Darensbourg and H.C. Zhou, *J. Am. Chem*, 2013, **135**, 17105-17110.

186. K. S. Park, Z. Ni, A. P. Côté, J. Y. Choi, R. Huang, F. J. Uribe-Romo, H. K. Chae, M. O'Keeffe and O. M. Yaghi, *Proc. Natl. Acad. Sci.*, 2006, **103**, 10186-10191.

187. R. Banerjee, A. Phan, B. Wang, C. Knobler, H. Furukawa, M. O'Keeffe and O. M. Yaghi, *Sci.*, 2008, **319**, 939-943.

188. V. Colombo, S. Galli, H. J. Choi, G. D. Han, A. Maspero, G. Palmisano, N. Masciocchi and J. R. Long, *Chem. Sci.*, 2011, **2**, 1311-1319.

189. B. D. McCarthy, A. M. Beiler, B. A. Johnson, T. Liseev, A. T. Castner and S. Ott, *Coord. Chem. Rev.*, 2020, **406**, 213137.

190. N. Zaman, N. Iqbal and T. Noor, *Arabian J. Chem.*, 2022, **15**, 103906.

191. P. Salcedo-Abraira, S. M. F. Vilela, A. A. Babaryk, M. Cabrero-Antonino, P. Gregorio, F. Salles, S. Navalón, H. García and P. Horcajada, *Nano Res.*, 2021, **14**, 450-457.

192. M. Moura de Salles Pupo and R. Kortlever, *ChemPhysChem*, 2019, **20**, 2926-2935.

193. X.H. Yang, M. Papasizza, A. Cuesta and J. Cheng, *ACS Catal.*, 2022, **12**, 6770-6780.

194. P. Anastas and N. Eghbali, *Chem. So. Rev.*, 2010, **39**, 301-312.

195. S. Dou, J. Song, S. Xi, Y. Du, J. Wang, Z.F. Huang, Z. J. Xu and X. Wang, *Angew. Chem.Intl. Ed.*, 2019, **58**, 4041-4045.

196. Y. Wang, P. Hou, Z. Wang and P. Kang, *ChemPhysChem*, 2017, **18**, 3142-3147.

197. K. AlKaabi, Casey R. Wade and M. Dincă, *Chem*, 2016, **1**, 264-272.

198. C. R. Wade, M. Li and M. Dincă, *Angew. Chem.Intl. Ed.*, 2013, **52**, 13377-13381.

199. B. A. Johnson, A. Bhunia, H. Fei, S. M. Cohen and S. Ott, *J. Am. Chem.*, 2018, **140**, 2985-2994.

200. W. Liu and X.B. Yin, *TrAC*, 2016, **75**, 86-96.

201. O. Shekhah, J. Liu, R. A. Fischer and C. Wöll, *Chem. So. Rev.*, 2011, **40**, 1081-1106.

202. L. Wang, Y. Wu, R. Cao, L. Ren, M. Chen, X. Feng, J. Zhou and B. Wang, *ACS Appl. Mater. Interfaces.*, 2016, **8**, 16736-16743.

203. B.X. Dong, S.L. Qian, F.Y. Bu, Y.C. Wu, L.G. Feng, Y.L. Teng, W.L. Liu and Z.W. Li, *ACS Appl. Energy Mater.*, 2018, **1**, 4662-4669.

204. W. Ju, A. Bagger, G.P. Hao, A. S. Varela, I. Sinev, V. Bon, B. Roldan Cuenya, S. Kaskel, J. Rossmeisl and P. Strasser, *Nat. Commun.*, 2017, **8**, 944.

205. J. Duan, S. Chen and C. Zhao, *Nat. Commun.*, 2017, **8**, 15341.

206. J. Li, P. Pršlja, T. Shinagawa, A. J. Martín Fernández, F. Krumeich, K. Artyushkova, P. Atanassov, A. Zitolo, Y. Zhou, R. García-Muelas, N. López, J. Pérez-Ramírez and F. Jaouen, *ACS Catal.*, 2019, **9**, 10426-10439.

207. H. Sun, Z. Yan, F. Liu, W. Xu, F. Cheng and J. Chen, *Adv Mater*, 2020, **32**, 1806326.

208. R. Senthil Kumar, S. Senthil Kumar and M. Anbu Kulandainathan, *Electrochem. Commun.*, 2012, **25**, 70-73.

209. J.X. Wu, S.Z. Hou, X.D. Zhang, M. Xu, H.F. Yang, P.S. Cao and Z.Y. Gu, *Chem. Sci.*, 2019, **10**, 2199-2205.

210. A. M. Szczepkowska, M. Janeta, M. Siczek, W. Tylus, A. M. Trzeciak and W. Bury, *Dalton Trans.*, 2021, **50**, 9051-9058.

211. R. Matheu, E. Gutierrez-Puebla, M. Á. Monge, C. S. Diercks, J. Kang, M. S. Prévot, X. Pei, N. Hanikel, B. Zhang, P. Yang and O. M. Yaghi, *J. Am. Chem.*, 2019, **141**, 17081-17085.

212. N. Sikdar, J. R. C. Junqueira, S. Dieckhöfer, T. Quast, M. Braun, Y. Song, H. B. Aiyappa, S. Seisel, J. Weidner, D. Öhl, C. Andronescu and W. Schuhmann, *Angew. Chem. Intl. Ed.*, 2021, **60**, 23427-23434.

213. D. Frederichi, M. H. N. O. Scaliante and R. Bergamasco, *Environ. Sci. Pollut. Res. Int.*, 2021, **28**, 23610-23633.

214. J. Albo, D. Vallejo, G. Beobide, O. Castillo, P. Castaño and A. Irabien, *ChemSusChem*, 2017, **10**, 1100-1109.

215. G. Genesio, J. Maynadié, M. Carboni and D. Meyer, *New J. Chem.*, 2018, **42**, 2351-2363.

216. B. A. Johnson, A. Bhunia and S. Ott, *Dalton Trans.*, 2017, **46**, 1382-1388.

217. Z. Dou, J. Yu, H. Xu, Y. Cui, Y. Yang and G. Qian, *Thin Solid Films*, 2013, **544**, 296-300.

218. O. Shekhah, H. Wang, S. Kowarik, F. Schreiber, M. Paulus, M. Tolan, C. Sternemann, F. Evers, D. Zacher, R. A. Fischer and C. Wöll, *J. Am. Chem.*, 2007, **129**, 15118-15119.

219. B. Liu and R. A. Fischer, *Science China Chem.*, 2011, **54**, 1851-1866.

220. D.J. Li, Q.H. Li, Z.G. Gu and J. Zhang, *J. Mater. Chem. A*, 2019, **7**, 18519-18528.

221. L. Ye, J. Liu, Y. Gao, C. Gong, M. Addicoat, T. Heine, C. Wöll and L. Sun, *J. Mater. Chem. A*, 2016, **4**, 15320-15326.

222. I. Hod, M. D. Sampson, P. Deria, C. P. Kubiak, O. K. Farha and J. T. Hupp, *ACS Catal.*, 2015, **5**, 6302-6309.

223. A. Bétard and R. A. Fischer, *Chem. Rev.*, 2012, **112**, 1055-1083.

224. J.-L. Zhuang, A. Terfort and C. Wöll, *Coord. Chem. Rev.*, 2016, **307**, 391-424.

225. V. M. V and G. Nageswaran, *J. Electrochem. So.*, 2020, **167**, 155527.

226. M. Hartmann, S. Kunz, D. Himsl, O. Tangermann, S. Ernst and A. Wagener, *Langmuir*, 2008, **24**, 8634-8642.

227. W.-J. Li, J. Lü, S.-Y. Gao, Q.-H. Li and R. Cao, *J. Mater. Chem. A*, 2014, **2**, 19473-19478.

228. S. Khazalpour, V. Safarifard, A. Morsali and D. Nematollahi, *RSC Adv.*, 2015, **5**, 36547-36551.

229. N. Campagnol, T. R. C. Van Assche, M. Li, L. Stappers, M. Dincă, J. F. M. Denayer, K. Binnemans, D. E. De Vos and J. Fransaer, *J. Mater. Chem. A*, 2016, **4**, 3914-3925.

230. L.L. Jiang, X. Zeng, M. Li, M.Q. Wang, T.Y. Su, X.C. Tian and J. Tang, *RSC Adv.*, 2017, **7**, 9316-9320.

231. M. Li and M. Dincă, *J. Am. Chem.*, 2011, **133**, 12926-12929.

232. M. Li and M. Dincă, *Chem. Sci.*, 2014, **5**, 107-111.

233. S. Dutt, A. Kumar and S. Singh, *Clean techno.*, 2023, **5**, 140-166.

234. I. Hod, W. Bury, D. M. Karlin, P. Deria, C.W. Kung, M. J. Katz, M. So, B. Klahr, D. Jin, Y.-W. Chung, T. W. Odom, O. K. Farha and J. T. Hupp, *Adv Mater*, 2014, **26**, 6295-6300.

235. H. Al-Kutubi, J. Gascon, E. J. R. Sudhölter and L. Rassaei, *ChemElectroChem*, 2015, **2**, 462-474.

236. X. Kang, B. Wang, K. Hu, K. Lyu, X. Han, B. F. Spencer, M. D. Frogley, F. Tuna, E. J. L. McInnes, R. A. W. Dryfe, B. Han, S. Yang and M. Schröder, *J. Am. Chem.*, 2020, **142**, 17384-17392.

237. R. Hinogami, S. Yotsuhashi, M. Deguchi, Y. Zenitani, H. Hashiba and Y. Yamada, *ECS Electrochem. Lett.*, 2012, **1**, H17-H19.

238. N. Kornienko, Y. Zhao, C. S. Kley, C. Zhu, D. Kim, S. Lin, C. J. Chang, O. M. Yaghi and P. Yang, *J. Am. Chem.*, 2015, **137**, 14129-14135.

239. X. Kang, Q. Zhu, X. Sun, J. Hu, J. Zhang, Z. Liu and B. Han, *Chem. Sci.*, 2016, **7**, 266-273.

240. C. Cadena, J. L. Anthony, J. K. Shah, T. I. Morrow, J. F. Brennecke and E. J. Maginn, *J. Am. Chem.*, 2004, **126**, 5300-5308.

241. D. R. MacFarlane, M. Forsyth, P. C. Howlett, J. M. Pringle, J. Sun, G. Annat, W. Neil and E. I. Izgorodina, *Acc. Chem. Res.*, 2007, **40**, 1165-1173.

242. Q. Cui, G. Qin, W. Wang, K. R. Geethalakshmi, A. Du and Q. Sun, *Appl. Surf. Sci.*, 2020, **500**, 143993.

243. F. Yang, A. Chen, P. L. Deng, Y. Zhou, Z. Shahid, H. Liu and B. Y. Xia, *Chem. Sci.*, 2019, **10**, 7975-7981.

244. X. D. Zhang, S. Z. Hou, J. X. Wu and Z. Y. Gu, *Chem.*, 2019, DOI: 10.1002/chem.201904072.

245. J. Albo, D. Vallejo, G. Beobide, O. Castillo, P. Castano and A. Irabien, *ChemSusChem*, 2017, **10**, 1100-1109.

246. Y. Wang, P. Hou, Z. Wang and P. Kang, *Chemphyschem*, 2017, **18**, 3142-3147.

247. S. Dou, J. Song, S. Xi, Y. Du, J. Wang, Z. F. Huang, Z. J. Xu and X. Wang, *Angew. Chem. Intl. Ed. Engl.*, 2019, **58**, 4041-4045.

248. Y. R. Wang, Q. Huang, C. T. He, Y. Chen, J. Liu, F. C. Shen and Y. Q. Lan, *Nat. Commun.*, 2018, **9**, 4466.

249. F. Mao, Y.-H. Jin, P. F. Liu, P. Yang, L. Zhang, L. Chen, X.-M. Cao, J. Gu and H. G. Yang, *J. Mater. Chem. A*, 2019, **7**, 23055-23063.

250. X. Tan, C. Yu, C. Zhao, H. Huang, X. Yao, X. Han, W. Guo, S. Cui, H. Huang and J. Qiu, *ACS Appl. Mater. Interfaces*, 2019, **11**, 9904-9910.

251. C.-W. Kung, C. O. Audu, A. W. Peters, H. Noh, O. K. Farha and J. T. Hupp, *ACS Energy Lett.*, 2017, **2**, 2394-2401.

252. X. L. Jiang, H. H. Wu, S. J. Chang, R. Si, S. Miao, W. X. Huang, Y. H. Li, G. X. Wang and X. H. Bao, *J. Mater. Chem. A*, 2017, **5**, 19371-19377.

253. D. H. Nam, O. S. Bushuyev, J. Li, P. De Luna, A. Seifitokaldani, C. T. Dinh, F. P. Garcia de Arquer, Y. Wang, Z. Liang, A. H. Proppe, C. S. Tan, P. Todorovic, O. Shekhah, C. M. Gabardo, J. W. Jo, J. Choi, M. J. Choi, S. W. Baek, J. Kim, D. Sinton, S. O. Kelley, M. Eddaoudi and E. H. Sargent, *J. Am. Chem.*, 2018, **140**, 11378-11386.

254. K. Zhao, Y. Liu, X. Quan, S. Chen and H. Yu, *ACS Appl. Mater. Interfaces*, 2017, **9**, 5302-5311.

255. Y. Guo, H. Yang, X. Zhou, K. Liu, C. Zhang, Z. Zhou, C. Wang and W. Lin, *J. Mater. Chem. A*, 2017, **5**, 24867-24873.

256. C. Zhao, X. Dai, T. Yao, W. Chen, X. Wang, J. Wang, J. Yang, S. Wei, Y. Wu and Y. Li, *J. Am. Chem.,* 2017, **139**, 8078-8081.

257. X. Q. Wang, Z. Chen, X. Y. Zhao, T. Yao, W. X. Chen, R. You, C. M. Zhao, G. Wu, J. Wang, W. X. Huang, J. L. Yang, X. Hong, S. Q. Wei, Y. Wu and Y. D. Li, *Angew. Chem. Intl. Ed.*, 2018, **57**, 1944-1948.

258. Y. F. Ye, F. Cai, H. B. Li, H. H. Wu, G. X. Wang, Y. S. Li, S. Miao, S. H. Xie, R. Si, J. Wang and X. H. Bao, *Nano Energy*, 2017, **38**, 281-289.

259. P. L. Lu, Y. J. Yang, J. N. Yao, M. Wang, S. Dipazir, M. L. Yuan, J. X. Zhang, X. Wang, Z. J. Xie and G. J. Zhang, *Appl. Catal. B-Environ.*, 2019, **241**, 113-119.

260. Y. Zheng, P. Cheng, J. Xu, J. Han, D. Wang, C. Hao, H. R. Alanagh, C. Long, X. Shi and Z. Tang, *Nanoscale*, 2019, **11**, 4911-4917.

261. S. An, G. Zhang, T. Wang, W. Zhang, K. Li, C. Song, J. T. Miller, S. Miao, J. Wang and X. Guo, *ACS Nano.*, 2018, **12**, 9441.

262. C. C. Yan, Y. F. Ye, L. Lin, H. H. Wu, Q. K. Jiang, G. X. Wang and X. H. Bao, *Catal.Today*, 2019, **330**, 252-258.

263. T. N. Huan, N. Ranjbar, G. Rousse, M. Sougrati, A. Zitolo, V. Mougel, F. Jaouen and M. Fontecave, *ACS Catal.*, 2017, **7**, 1520-1525.

264. S. S. A. Shah, T. Najam, M. Wen, S.-Q. Zang, A. Waseem and H.-L. Jiang, *Small Structures*, 2022, **3**, 2100090.

265. A. A. Al-Omari, Z. H. Yamani and H. L. Nguyen, *Mol.*, 2018, **23**.

266. F. Schüth, M. D. Ward and J. M. Buriak, *Chem. Mater*, 2018, **30**, 3599-3600.

267. W. Chaikittisilp, K. Ariga and Y. Yamauchi, *J. Mater. Chem. A*, 2013, **1**, 14-19.

268. B. Qiao, A. Wang, X. Yang, L. F. Allard, Z. Jiang, Y. Cui, J. Liu, J. Li and T. Zhang, *Nat. Chem.*, 2011, **3**, 634.

269. S. Ji, Y. Chen, X. Wang, Z. Zhang, D. Wang and Y. Li, *Chem Rev*, 2020, **120**, 11900-11955.

270. S. Back, J. Lim, N.-Y. Kim, Y.-H. Kim and Y. Jung, *Chem. Sci.*, 2017, **8**, 1090-1096.

271. H. Yitong, Y. Hong and G. Xinwen, in *Synthesis Methods and Crystallization*, ed. M. Riadh, IntechOpen, Rijeka, 2020, DOI: 10.5772/intechopen.90435.

272. R. Seetharaj, P. V. Vandana, P. Arya and S. Mathew, *Arabian J. Chem.*, 2019, **12**, 295-315.

273. O. V. Dolomanov, L. J. Bourhis, R. J. Gildea, J. A. K. Howard and H. Puschmann, *J. Appl. Crystallogr.*, 2009, **42**, 339-341.

274. D. B. Sirdeshmukh, L. Sirdeshmukh and K. G. Subhadra, in *Atomistic Properties of Solids*, eds. D. B. Sirdeshmukh, L. Sirdeshmukh and K. G. Subhadra, Springer Berlin Heidelberg, Berlin, Heidelberg, 2011, DOI: 10.1007/978-3-642-19971-4_4, pp. 115-164.

275. E. S. Ameh, *Int. J. Adv. Manuf. Tech.*, 2019, **105**, 3289-3302.

276. V. K. Pecharsky and Y. Z. Peter. *Fundamentals of diffraction*. Springer US, 2003.

277. A. A. Coelho, *J. Appl. Crystallogr.*, 2003, **36**, 86-95.

278. J. A. Barker, PhD Thesis, University of Birmingham, 2022.

279. C. Zhao, PhD, PhD Thesis, University of Birmingham, 2012.

280. D. B. Sirdeshmukh, L. Sirdeshmukh and K. G. Subhadra, in *Atomistic Properties of Solids*, eds. D. B. Sirdeshmukh, L. Sirdeshmukh and K. G. Subhadra, Springer Berlin Heidelberg, Berlin, Heidelberg, 2011, DOI: 10.1007/978-3-642-19971-4_3, pp. 65-114.

281. A. Putnis, *An introduction to mineral sciences*, Cambridge University Press, 1992.

282. N. Raval, R. Maheshwari, D. Kalyane, S. R. Youngren-Ortiz, M. B. Chougule and R. K. Tekade, in *Basic Fundamentals of Drug Delivery*, ed. R. K. Tekade, Academic Press, 2019, DOI: https://doi.org/10.1016/B978-0-12-817909-3.00010-8, pp. 369-400.

283. N. K. Singh, PhD Thesis, Chhattisgarh Swami Vivekanand Technical University, 2014.

284. M. Omidi, A. Fatehinya, M. Farahani, Z. Akbari, S. Shahmoradi, F. Yazdian, M. Tahriri, K. Moharamzadeh, L. Tayebi and D. Vashaee, in *Biomaterials for Oral and Dental Tissue Engineering*, eds. L. Tayebi and K. Moharamzadeh, Woodhead Publishing, 2017, DOI: https://doi.org/10.1016/B978-0-08-100961-1.00007-4, pp. 97-115.

285. A. W. Coats and J. P. Redfern, *Analyst*, 1963, **88**, 906-924.

286. M. A. Mohamed, J. Jaafar, A. F. Ismail, M. H. D. Othman and M. A. Rahman, in *Membrane Characterization*, eds. N. Hilal, A. F. Ismail, T. Matsuura and D. Oatley-Radcliffe, Elsevier, 2017, DOI: https://doi.org/10.1016/B978-0-444-63776-5.00001-2, pp. 3-29.

287. V. K. Undavalli, C. Ling and B. Khandelwal, in *Aviation Fuels*, ed. B. Khandelwal, Academic Press, 2021, DOI: https://doi.org/10.1016/B978-0-12-818314-4.00001-7, pp. 113-132.

288. Spectroscopy: CVD diamond attenuated-total-reflection prisms benefit FTIR spectroscopy,https://www.laserfocusworld.com/test-measurement/test measurement/article /16547028 spectroscopy-cvd-diamond-attenuated-total-reflection-prisms-benefit-ftir-spectroscopy (accessed February 2024).

289. R. R. Jones, D. C. Hooper, L. Zhang, D. Wolverson and V. K. Valev, *Nanoscale Res. Lett.*, 2019, **14**, 231.

290. T. Chen, PhD Thesis, *University of Birmingham,* 2013.

291. K. S. Sing, *Pure Appl. Chem.*, 1982, **54**, 2201-2218.

292. G. Leofanti, M. Padovan, G. Tozzola and B. Venturelli, *Catal. today*, 1998, **41**, 207-219.

293. M. C. Henstridge and R. G. Compton, *Chem. Rec.*, 2012, **12**, 63-71.

294. R. G. Compton and C. E. Banks, *Understanding Voltammetry*, World Scientific Publishing Europe Ltd. London, 3rd edn., 2018.

295. T. J. Davies and R. G. Compton, *J. Electroanal. Chem.,* 2005, **585**, 63-82.

296. A. J. Bard, L. R. Faulkner and H. S. White, *Electrochemical methods: fundamentals and applications*, John Wiley & Sons, 2022.

297. N. Elgrishi, K. J. Rountree, B. D. McCarthy, E. S. Rountree, T. T. Eisenhart and J. L. Dempsey, *J. Chem. Edu.*, 2018, **95**, 197-206.

298. B. Rezaei and N. Irannejad, in *Electrochemical Biosensors*, ed. A. A. Ensafi, Elsevier, 2019, DOI: https://doi.org/10.1016/B978-0-12-816491-4.00002-4, pp. 11-43.

299. B. Setterfield-Price, PhD, University of Manchester, 2013.

300. A.M. Bond, D.A. Fiedler, G. Inzelt, H. Kahlert, Š. Komorsky-Lovri´c, H. Lohse, M. Lovri´c, F. Marken, A. Neudeck, U. Retter, F. Scholz, Z. Stojek, *Electroanalytical Methods: Guide to Experiments and Applications*, Springer-Verlag Berlin Heidelberg, 2nd edn., 2010

301. O. J. Guy and K.A. D. Walker, in *Silicon Carbide Biotechnology (Second Edition)*, ed. S. E. Saddow, Elsevier, 2016, DOI: https://doi.org/10.1016/B978-0-12-802993-0.00004-6, pp. 85-141.

302. E. S. Rountree, B. D. McCarthy, T. T. Eisenhart and J. L. Dempsey, *Inorg. Chem.*, 2014, **53**, 9983-10002.

303. C. Gong, W. Li, Y. Lei, X. He, H. Chen, X. Du, W. Fang, D. Wang and L. Zhao, *Compos. B Eng.*, 2022, **236**, 109823.

304. H. Baltruschat, *J. Am. Soc. Mass Spectrom.*, 2004, **15**, 1693-1706.

305. Y. Gao, H. Tsuji, H. Hattori and H. Kita, *J. Electroanal. Chem.*, 1994, **372**, 195-200.

306. N. Todoroki, H. Tsurumaki, H. Tei, T. Mochizuki and T. Wadayama, *J. Electrochem. So.*, 2020, **167**, 106503.

307. P. Cui, J. Wu, X. Zhao, D. Sun, L. Zhang, J. Guo and D. Sun, *Cryst Growth Des*, 2011, **11**, 5182-5187.

308. L. J. Murray, M. Dincă and J. R. Long, *Chem. So. Rev.*, 2009, **38**, 1294-1314.

309. S. S. Kaye and J. R. Long, *J. Am.Chem.*, 2005, **127**, 6506-6507.

310. L. Zhu, X. Q. Liu, H. L. Jiang and L. B. Sun, *Chem Rev*, 2017, **117**, 8129-8176.

311. H. D. Lawson, S. P. Walton and C. Chan, *ACS Appl. Mater. Interfaces*, 2021, **13**, 7004-7020.

312. Y. Cui, Y. Yue, G. Qian and B. Chen, *Chem. Rev.*, 2012, **112**, 1126-1162.

313. L. S. Xie, G. Skorupskii and M. Dincă, *Chem. Rev.*, 2020, **120**, 8536-8580.

314. J. J. Oppenheim, G. Skorupskii and M. Dincă, *Chem.Sci.*, 2020, **11**, 11094-11103.

315. J. Li, Y.N. Wu, Z. Li, B. Zhang, M. Zhu, X. Hu, Y. Zhang and F. Li, *The J.Phy. Chem. C*, 2014, **118**, 27382-27387.

316. S. Rapti, A. Pournara, D. Sarma, I. T. Papadas, G. S. Armatas, Y. S. Hassan, M. H. Alkordi, M. G. Kanatzidis and M. J. Manos, *Inorg. Chem. Front.*, 2016, **3**, 635-644.

317. H.R. Fu, Z.X. Xu and J. Zhang, *Chem. Mater.*, 2015, **27**, 205-210.

318. K. L. Mulfort, O. K. Farha, C. L. Stern, A. A. Sarjeant and J. T. Hupp, *J. Am. Chem.*, 2009, **131**, 3866-3868.

319. H. Fei, D. L. Rogow and S. R. J. Oliver, *J. Am. Chem.*, 2010, **132**, 7202-7209.

320. Z. Yao, PhD Thesis, University of Birmingham, 2013.

321. S. V. Priya, J. H. Mabel, S. Gopalakrishnan, M. Palanichamy and V. Murugesan, *J. Por Mater.*, 2009, **16**, 419-427.

322. P. Castaldi, L. Santona, S. Enzo and P. Melis, *J. Hazard. Mater.*, 2008, **156**, 428-434.

323. M. A. Petrova, V. I. Shitova, G. A. Mikirticheva, V. F. Popova and A. E. Malshikov, *J. Solid State Chem.*, 1995, **119**, 219-223.

324. P. Villars, *Ni_2P phase (Ni_2P) Crystal Structure: Datasheet from "PAULING FILE Multinaries Edition – 2022" in Springer Materials (https://materials.springer.com/isp/crystallographic/docs/sd_1930239)*, Springer-Verlag Berlin Heidelberg & Material Phases Data System (MPDS), Switzerland & National Institute for Materials Science (NIMS), Japan, 2022.

325. A. C. Larson and R. B. Von-Dreele, *General Structure Analysis System (GSAS)*, Alamos National Laboratory, Los, 2004.

326. K. C. Ng, M. Burhan, M. W. Shahzad and A. B. Ismail, *Sci. Rep*, 2017, **7**, 10634.

327. L. Li, S. Wang, T. Chen, Z. Sun, J. Luo and M. Hong, *Cryst. Growth Des.*, 2012, **12**, 4109-4115.

328. G. B. Hix, B. M. Kariuki, S. Kitchin and M. Tremayne, *Inorg. Chem.*, 2001, **40**, 1477-1481.

329. A. K. Paul, R. Kanagaraj, A. K. Jana and P. K. Maji, *Crystengcomm*, 2017, **19**, 6425-6435.

330. J. P. Metherall, R. C. Carroll, S. J. Coles, M. J. Hall and M. R. Probert, *Chem. So. Rev.*, 2023, **52**, 1995-2010.

331. C. Q. Jiao, Z. Zhao, C. Ma, Z. G. Sun, D. P. Dong, Y. Y. Zhu and J. Li, *Cryst. Growth Des.*, 2016, **16**, 5624-5635.

332. K. Yao, Y. Xia, J. Li, N. Wang, J. Han, C. Gao, M. Han, G. Shen, Y. Liu, A. Seifitokaldani, X. Sun and H. Liang, *J. Mater. Chem. A*, 2020, **8**, 11117-11123.

333. S.-M. Hwang, S. Y. Choi, M. H. Youn, W. Lee, K. T. Park, K. Gothandapani, A. N. Grace and S. K. Jeong, *ACS Omega*, 2020, **5**, 23919-23930.

334. Y.G. Kim, J. H. Baricuatro and M. P. Soriaga, *Electrocatal.*, 2018, **9**, 526-530.

335. A. Doménech, H. García, M. T. Doménech-Carbó and F. Llabrés-i-Xamena, *J. Phys. Chem. C*, 2007, **111**, 13701-13711.

336. S. Roy, Z. Huang, A. Bhunia, A. Castner, A. K. Gupta, X. Zou and S. Ott, *J. Am. Chem.*, 2019, **141**, 15942-15950.

337. B. L. Salvi and K. A. Subramanian, *Renew. Sustain. Energy Rev.*, 2015, **51**, 1132-1155.

338. M.M. Gu, C.X. Han, K. Zhou, C.H. Xue, J.Y. Ji and Y.F. Bi, *Inorg. Chim. Acta*, 2021, **525**, 120462.

339. J.Y. Wu, S.H. Jhan, Y.J. Lin, D.L. Cai, Z.J. Hu and H.L. Sung, *J. Solid State Chem.*, 2020, **291**, 121638.

340. C. C. Cody, H. R. Kelly, B. Q. Mercado, V. S. Batista, R. H. Crabtree and G. W. Brudvig, *Inorg. Chem.*, 2021, **60**, 14759-14764.

341. O. Carugo and C. B. Castellani, *J. Chem. So. Dalton Trans.*, 1990, DOI: 10.1039/DT9900002895, 2895-2902.

342. L. Y. Zhao, X. C. Deng, G. Liang, X. B. Zheng and X. Y. Li, *J. Chem. Sci.*, 2020, **132**, 27.

343. A. Cabeza and M. A. G. Aranda, in *Metal Phosphonate Chemistry: From Synthesis to Applications,* ed. A. Clearfield and K. Demadis, The Royal Society of Chemistry, 2011, ch. 4, pp. 107-132.

344. C. N. Wang, P. J. Feng, J. T. Li and X. T. Luo, *J. Solid State Chem.*, 2017, **249**, 136-140.

345. A. H. M. da Silva, S. J. Raaijman, C. S. Santana, J. M. Assaf, J. F. Gomes and M. T. M. Koper, *J. Electroanal. Chem.*, 2021, **880**, 114750.

346. X. Ding, B. Garlyyev, S. A. Watzele, T. Kobina Sarpey and A. S. Bandarenka, *Chem.– A Euro. J.*, 2021, **27**, 10016-10020.

347. H. De Jesús-Cardona, C. del Moral and C. R. Cabrera, *J. Electroanal. Chem.*, 2001, **513**, 45-51.

348. Y. Hori, H. Konishi, T. Futamura, A. Murata, O. Koga, H. Sakurai and K. Oguma, *Electrochim. Acta*, 2005, **50**, 5354-5369.

349. C. S. Chen, A. D. Handoko, J. H. Wan, L. Ma, D. Ren and B. S. Yeo, *Catal. Sci. Tech.*, 2015, **5**, 161-168.

350. E. Fernández-Zapico, J. M. Montejo-Bernardo, R. D'Vries, J. R. García, S. García-Granda, J. Rodríguez Fernández, I. de Pedro and J. A. Blanco, *J. Solid State Chem.*, 2011, **184**, 3289-3298.

351. P. Yin, X.C. Wang, S. Gao and L.M. Zheng, *J. Solid State Chem.*, 2005, **178**, 1049-1053.

352. Q. Song, Y. Zhao, C. Wang, H. Xie, H. Yin and Z. Ning, *Hydrometallurgy*, 2019, **189**, 105111.

353. C. Cometto, L. Chen, P.K. Lo, Z. Guo, K.C. Lau, E. Anxolabéhère-Mallart, C. Fave, T.C. Lau and M. Robert, *ACS Catal.*, 2018, **8**, 3411-3417.

354. C. Cometto, L. Chen, E. Anxolabéhère-Mallart, C. Fave, T.C. Lau and M. Robert, *Organomet.*, 2019, **38**, 1280-1285.

355. J. Liu, R.-Z. Liao, F. W. Heinemann, K. Meyer, R. P. Thummel, Y. Zhang and L. Tong, *Inorg. Chem.*, 2021, **60**, 17976-17985.

356. N. K. Noel, M. Congiu, A. J. Ramadan, S. Fearn, D. P. McMeekin, J. B. Patel, M. B. Johnston, B. Wenger and H. J. Snaith, *Joule*, 2017, **1**, 328-343.

357. E. Aubert, M. Abboud, A. Doudouh, P. Durand, P. Peluso, A. Ligresti, B. Vigolo, S. Cossu, P. Pale and V. Mamane, *RSC Adv.*, 2017, **7**, 7358-7367.

358. P. Larpent, A. Jouaiti, N. Kyritsakas and M. W. Hosseini, *Crystengcomm*, 2019, **21**, 2534-2540.

359. A. Tahli, A.C. Chamayou, Ü. Köc, R. Brückner, R. F. M. Elshaarawy, C. Heering and C. Janiak, *Inorg. Chim. Acta*, 2016, **450**, 190-201.

360. C. S. Ong, J. Z. Oor, S. J. Tan and J. W. Chew, *ACS Appl. Mater. Interfaces*, 2022, **14**, 10875-10885.

361. H. Wang, H. Qiao, J. Guo, J. Sun, H. Li, S. Zhang and X. Gu, *Compos. B Eng.*, 2020, **182**, 107498.

362. E. Rahmati and Z. Rafiee, *J. Por. Mater.*, 2021, **28**, 19-27.

363. E. Fernández-Zapico, I. da Silva, R. Mendoza-Meroño, J. Montejo-Bernardo, D. Martínez-Blanco, S. García-Granda and J. R. García, *Inorg. Chim. Acta*, 2016, **448**, 78-85.

364. N. Aljammal, C. Jabbour, S. Chaemchuen, T. Juzsakova and F. Verpoort, *Catal.*, 2019, **9**.

365. H. Guo, Y. Zhu, S. Wang, S. Su, L. Zhou and H. Zhang, *Chem. Mater.*, 2012, **24**, 444-450.

366. P. Mahata, M. Prabu and S. Natarajan, *Inorg. Chem.*, 2008, **47**, 8451-8463.

367. J. B. Maglic and R. Lavendomme, *J. Appl. Crystallogr.*, 2022, **55**, 1033-1044.

368. J. V. Smith, *Chem. Rev.*, 1988, **88**, 149-182.

369. Z. Chen, Y. Ling, H. Yang, Y. Guo, L. Weng and Y. Zhou, *Crystengcomm*, 2011, **13**, 3378-3382.

370. M. Malathi, R. Sabesan and S. Krishnan, *Curr. Sci.*, 2004, 838-842.

371. Y.K. Ren, S.D. Liu, B. Duan, Y.F. Xu, Z.Q. Li, Y. Huang, L.H. Hu, J. Zhu and S.Y. Dai, *J. Alloys Compd.*, 2017, **705**, 205-210.

372. X.Z. Lin and Z.-Y. Yuan, *RSC Adv.*, 2014, **4**, 32443-32450.

373. N. Basma, P. L. Cullen, A. J. Clancy, M. S. P. Shaffer, N. T. Skipper, T. F. Headen and C. A. Howard, *Mole. Phys.*, 2019, **117**, 3353-3363.

374. Q. Huo, R. Xu, S. Li, Z. Ma, J. M. Thomas, R. H. Jones and A. M. Chippindale, *J. Chem. Soc., Chem. Commun.*, 1992, DOI: 10.1039/C39920000875, 875-876.

375. Z. Chen, Y. Zhou, L. Weng, C. Yuan and D. Zhao, *Chem. Asian J.,* 2007, **2**, 1549-1554.

376. A. Choudhury, S. Natarajan and C. N. R. Rao, *Inorg. Chem.*, 2000, **39**, 4295-4304.

377. M. J. B. Kabeyi and O. A. Olanrewaju, *Front. energy res.*, 2022, **9**.

378. D. Pierre, *Euro. Energy Clim. J.,* 2023, **11**, 100-103.

379. O. Omoregbe, A. N. Mustapha, R. Steinberger-Wilckens, A. El-Kharouf and H. Onyeaka, *Energy Rep.*, 2020, **6**, 1200-1212.

380. P. Shao, L. Yi, S. Chen, T. Zhou and J. Zhang, *J. Energy Chem.*, 2020, **40**, 156-170.

381. K. Chen, J. Deng, J. Zhao, X. Liu, S. Imhanria and W. Wang, *Ind. Eng. Chem. Res.*, 2021, **60**, 7739-7745.

382. R. Daiyan, R. Chen, P. Kumar, N. M. Bedford, J. Qu, J. M. Cairney, X. Lu and R. Amal, *ACS Appl. Mater. Interfaces*, 2020, **12**, 9307-9315.

383. J. Leverett, R. Daiyan, L. Gong, K. Iputera, Z. Tong, J. Qu, Z. Ma, Q. Zhang, S. Cheong, J. Cairney, R.S. Liu, X. Lu, Z. Xia, L. Dai and R. Amal, *ACS Nano*, 2021, **15**, 12006-12018.

384. M. Wang, K. Torbensen, D. Salvatore, S. Ren, D. Joulié, F. Dumoulin, D. Mendoza, B. Lassalle-Kaiser, U. Işci, C. P. Berlinguette and M. Robert, *Nat. Commun.*, 2019, **10**, 3602.

385. B. Mondal, P. Sen, A. Rana, D. Saha, P. Das and A. Dey, *ACS Catal.*, 2019, **9**, 3895-3899.

386. F. Franco, C. Rettenmaier, H. S. Jeon and B. Roldan Cuenya, *Chem. So. Rev.*, 2020, **49**, 6884-6946.

387. J. Monzó, Y. Malewski, R. Kortlever, F. J. Vidal-Iglesias, J. Solla-Gullón, M. T. M. Koper and P. Rodriguez, *J. Mater. Chem. A*, 2015, **3**, 23690-23698.

388. C. S. Le Duff, M. J. Lawrence and P. Rodriguez, *Angew. Chem. Intl. Edn.*, 2017, **56**, 12919-12924.

389. J. J. L. Humphrey, D. Plana, V. Celorrio, S. Sadasivan, R. P. Tooze, P. Rodríguez and D. J. Fermín, *ChemCatChem*, 2016, **8**, 952-960.

390. E. Sargeant, A. Kolodziej, C. S. Le Duff and P. Rodriguez, *ACS Catal.*, 2020, **10**, 7464-7474.

391. Z.-L. Wang, C. Li and Y. Yamauchi, *Nano Today*, 2016, **11**, 373-391.

392. S. K. Lee, M. Kondo, G. Nakamura, M. Okamura and S. Masaoka, *Chem. Commun.*, 2018, **54**, 6915-6918.

393. J. J. Liu, A. Chapovetsky, R. Haiges and S. C. Marinescu, *Inorg. Chem.*, 2021, **60**, 17517-17528.

394. M. Abdinejad, C. Dao, B. Deng, M. E. Sweeney, F. Dielmann, X.A. Zhang and H. B. Kraatz, *Chem. Select*, 2020, **5**, 979-984.

395. D. J. Cole-Hamilton and R. P. Tooze, in *Catalyst Separation, Recovery and Recycling: Chemistry and Process Design*, eds. D. J. Cole-Hamilton and R. P. Tooze, Springer Netherlands, Dordrecht, 2006, DOI: 10.1007/1-4020-4087-3_1, pp. 1-8.

396. F. Zaera, *Coord. Chem. Rev.*, 2021, **448**, 214179.

397. L. Liu and A. Corma, *Chem. Rev.*, 2018, **118**, 4981.

398. F. Poovan, V. G. Chandrashekhar, K. Natte and R. V. Jagadeesh, *Catal. Sci. Technol.*, 2022, **12**, 6623-6649.

399. S. Lu, Y. Shi, N. Meng, Y. Yu and B. Zhang, *Cell Rep. Phys. Sci.,* 2020, **11**. 100237

400. Z. Zhang, L. Yu, Y. Tu, R. Chen, L. Wu, J. Zhu and D. Deng, *Cell Rep. Phys Sci.*, 2020, **1**, 100145.

401. A. S. Varela, W. Ju, A. Bagger, P. Franco, J. Rossmeisl and P. Strasser, *ACS Catal.*, 2019, **9**, 7270-7284.

402. W. Ju, A. Bagger, X. Wang, Y. Tsai, F. Luo, T. Möller, H. Wang, J. Rossmeisl, A. S. Varela and P. Strasser, *ACS Energy Lett.*, 2019, **4**, 1663-1671.

403. H. He, J. A. Perman, G. Zhu and S. Ma, *Small*, 2016, **12**, 6309-6324.

404. A. Dhakshinamoorthy, A. M. Asiri and H. Garcia, *Adv. Mater.*, 2019, **31**, 1900617.

405. T. Binninger, B. Pribyl, A. Pătru, P. Ruettimann, S. Bjelić and T. J. Schmidt, *J. Mass Spec.*, 2018, **53**, 1214-1221.

406. G. A. McCarver, T. Yildirim and W. Zhou, *ChemPhysChem*, 2023, **24**, e202300645.

407. Y. Zhao and D. G. Truhlar, *J.Chem. Phys.*, 2006, **125**.

408. G. A. McCarver, T. Rajeshkumar and K. D. Vogiatzis, *Coord. Chem. Rev.*, 2021, **436**, 213777.

409. F. Neese, F. Wennmohs, U. Becker and C. Riplinger, *J. Chem. Phys.*, 2020, **152**.

410. F. Weigend, *Phys. Chem. Chem. Phys.*, 2006, **8**, 1057-1065.

411. J. Kalinowski, F. Wennmohs and F. Neese, *J. Chem. Theory Comput.*, 2017, **13**, 3160-3170.

412. F. Weigend and R. Ahlrichs, *Phys. Chem. Chem. Phys.*, 2005, **7**, 3297-3305.

413. S. Grimme, J. Antony, S. Ehrlich and H. Krieg, *J. Chem. Phys.*, 2010, **132**.

414. V. Barone and M. Cossi, *The J.Phys. Chem. A*, 1998, **102**, 1995-2001.

415. A. V. Marenich, S. V. Jerome, C. J. Cramer and D. G. Truhlar, *J. Chem. Theory Comput*, 2012, **8**, 527-541.

416. T. Lu and F. Chen, *J. Comput.Chem.*, 2012, **33**, 580-592.

417. S. Grimme, *Chem. – A Euro. J.*, 2012, **18**, 9955-9964.

418. D. R. Weinberg, C. J. Gagliardi, J. F. Hull, C. F. Murphy, C. A. Kent, B. C. Westlake, A. Paul, D. H. Ess, D. G. McCafferty and T. J. Meyer, *Chem. Rev.*, 2012, **112**, 4016-4093.

419. N. Elgrishi, B. D. McCarthy, E. S. Rountree and J. L. Dempsey, *ACS Catal.*, 2016, **6**, 3644.

420. A. A. Peterson, F. Abild-Pedersen, F. Studt, J. Rossmeisl and J. K. Nørskov, *Energy Environ. Sci.*, 2010, **3**, 1311-1315.

421. D. Shin, H. Choi, J. An, C. H. Sohn, C. H. Choi, H. Shin and H. Kim, *J. Mater. Chem. A*, 2022, **10**, 22523-22530.

422. W. Hua, H. Sun, L. Lin, Q. Mu, B. Yang, Y. Su, H. Wu, F. Lyu, J. Zhong, Z. Deng and Y. Peng, *Chem. Eng. J.*, 2022, **446**, 137296.

423. N. Han, Y. Wang, L. Ma, J. Wen, J. Li, H. Zheng, K. Nie, X. Wang, F. Zhao, Y. Li, J. Fan, J. Zhong, T. Wu, D. J. Miller, J. Lu, S.-T. Lee and Y. Li, *Chem*, 2017, **3**, 652-664.

424. L. Yu, S. Sun, H. Li and Z. J. Xu, *Fundam. Res.*, 2021, **1**, 448-452.

425. Q. Zhang, K. Cheng, J. Kang, W. Deng and Y. Wang, *ChemSusChem*, 2014, **7**, 1251-1264.

426. H. Wang, G. Liu, C. Chen, W. Tu, Y. Lu, S. Wu, D. O'Hare and R. Xu, *ACS Sustain. Chem. Eng.*, 2021, **9**, 3792-3801.

427. Q. Hao, H.X. Zhong, J.Z. Wang, K.H. Liu, J.M. Yan, Z.H. Ren, N. Zhou, X. Zhao, H. Zhang, D.X. Liu, X. Liu, L.W. Chen, J. Luo and X.B. Zhang, *Nat. Synth.*, 2022, **1**, 719-728.

428. X. Li, W. Bi, M. Chen, Y. Sun, H. Ju, W. Yan, J. Zhu, X. Wu, W. Chu, C. Wu and Y. Xie, *J. Am. Chem.*, 2017, **139**, 14889-14892.

429. M. C. O. Monteiro, A. Mirabal, L. Jacobse, K. Doblhoff-Dier, S. C. Barton and M. T. M. Koper, *JACS Au*, 2021, **1**, 1915-1924.

430. X. Liu, M. C. O. Monteiro and M. T. M. Koper, *Phys. Chem. Chem. Phys.*, 2023, **25**, 2897-2906.

431. D. Raciti, M. Mao, J. H. Park and C. Wang, *J. Electrochem. So.*, 2018, **165**, F799.

9.0. Appendix

Crystallographic Details

Ni-BIRM-1

Table A3.1 Crystal data and structure refinement for Ni-BIRM-1

Identification code	Ni-BIRM-1
Empirical formula	$C_6H_{26}NiO_{18}P_2Zn_2$
Formula weight	637.66
Temperature/K	100.01(10)
Crystal system	tetragonal
Space group	$I4_1/acd$
a/Å	22.1734(4)
b/Å	22.1734(4)
c/Å	17.8103(5)
α/°	90
β/°	90
γ/°	90
Volume/Å^3	8756.6(4)
Z	16
ρ_{calc}g/cm^3	1.935
μ/mm^{-1}	5.688
F(000)	5184
Crystal size/mm^3	0.23 × 0.057 × 0.038
Radiation	CuKα (λ = 1.54184)
2Θ range for data collection/°	7.974 to 145.998
Index ranges	-27 ≤ h ≤ 24, -20 ≤ k ≤ 26, -21 ≤ l ≤ 19
Reflections collected	14897
Independent reflections	2186 [R_{int} = 0.0292, R_{sigma} = 0.0148]
Data/restraints/parameters	2185/114/182
Goodness-of-fit on F^2	1.070
Final R indexes [I>=2σ (I)]	R_1 = 0.0894, wR_2 = 0.2702
Final R indexes [all data]	R_1 = 0.0927, wR_2 = 0.2750
Largest diff. peak/hole / e Å^{-3}	1.82/-1.81

Table A3.2 Fractional Atomic Coordinates (×10^4) and Equivalent Isotropic Displacement Parameters (Å^2×10^3) for Ni-BIRM-1

Atom	*x*	*y*	*z*	U(eq)
C1	5788(3)	3993(3)	5230(4)	39.8(15)
C2	5525(3)	4467(4)	5743(4)	42.5(15)
C3	4852(3)	4441(3)	5840(4)	40.2(15)
O1	6900(2)	4245(2)	5747(3)	39.3(11)
O2	6581(2)	4767(2)	4578(3)	39.0(10)
O3	6796(2)	3641(2)	4546(3)	43.0(12)
O4	4647(2)	4840(3)	6276(4)	61.9(17)
O5	4530(2)	4073(3)	5513(4)	59.9(16)
P1	6557.0(7)	4169.1(7)	5006.9(9)	34.3(5)
Zn1	7510.5(4)	3712.6(4)	6131.7(5)	35.5(4)
Ni11	5603(4)	3694(4)	8094(4)	184(4)
O101	5370(13)	3291(17)	7097(14)	190(12)
O102	5917(19)	3970(20)	9117(16)	230(14)
O103	5255(9)	4490(11)	7695(10)	193(11)
O104	5944(16)	2890(11)	8439(16)	185(12)
O105	4770(7)	3354(13)	8163(16)	184(11)
O106	6340(7)	4122(10)	7671(11)	162(11)
O11A	4705(8)	2235(9)	6947(10)	90(5)
O201	7050(20)	5370(30)	6390(40)	74(14)
O21A	6994(12)	5140(15)	7050(30)	85(12

Table A3.3 Anisotropic Displacement Parameters ($Å^2×10^3$) for Ni-BIRM-1

Atom	U_{11}	U_{22}	U_{33}	U_{23}	U_{13}	U_{12}
C1	32(3)	37(3)	51(4)	-8(3)	9(3)	-2(3)
C2	26(3)	51(4)	51(4)	-5(3)	9(3)	6(3)
C3	29(3)	48(4)	43(3)	2(3)	9(3)	9(3)
O1	33(2)	35(2)	50(3)	-4.8(19)	3.7(19)	4.9(18)
O2	40(2)	31(2)	46(2)	-4.8(19)	10.3(19)	-3.5(18)
O3	38(2)	30(2)	61(3)	-9(2)	23(2)	-5.9(18)
O4	30(3)	82(4)	74(4)	-33(3)	12(2)	6(3)
O5	32(3)	57(3)	91(4)	-20(3)	13(3)	-2(2)
P1	25.0(8)	30.0(8)	48.0(10)	-6.3(6)	12.7(6)	-1.8(6)
Zn1	30.4(6)	25.3(5)	50.7(7)	6.6(3)	13.1(3)	-0.8(3)
Ni11	165(7)	226(9)	160(7)	-68(6)	-38(6)	100(6)
O101	124(18)	280(30)	170(20)	-20(20)	-13(17)	100(20)
O102	210(30)	290(30)	190(20)	-50(30)	20(20)	30(30)
O103	89(12)	410(30)	80(11)	-73(17)	-17(9)	136(16)
O104	150(20)	250(30)	151(19)	-10(20)	-47(17)	70(20)
O105	92(14)	270(30)	190(20)	30(20)	-38(14)	92(16)
O106	86(12)	230(20)	166(17)	-142(17)	-56(12)	85(14)
O11A	72(10)	103(13)	94(10)	31(10)	1(8)	-7(8)
O201	25(12)	60(20)	140(40)	-40(20)	-20(20)	8(13)
O21A	34(12)	63(18)	160(30)	-60(20)	-13(16)	7(11)

Table A3.4 Bond Lengths for Ni-BIRM-1

Atom	Atom	Length/Å	Atom	Atom	Length/Å
C1	C2	1.509(9)	O3	P1	1.526(5)
C1	P1	1.795(7)	O3	$Zn1^2$	1.961(4)
C2	C3	1.503(9)	O4	$Zn1^3$	1.950(5)
C3	O4	1.262(9)	Ni11	O101	2.054(18)
C3	O5	1.230(9)	Ni11	O102	2.041(19)
O1	P1	1.531(5)	Ni11	O103	2.054(17)
O1	Zn1	1.922(5)	Ni11	O104	2.032(18)
O2	P1	1.532(5)	Ni11	O105	1.998(18)
O2	$Zn1^1$	1.936(5)	Ni11	O106	2.034(18)

Table A3.5 Bond Angles for Ni-BIRM-1

Atom	Atom	Atom	Angle/˚	Atom	Atom	Atom	Angle/˚
C2	C1	P1	110.5(5)	O2[4]	Zn1	O3[2]	111.7(2)
C3	C2	C1	115.2(6)	O2[4]	Zn1	O4[5]	112.8(2)
O4	C3	C2	113.6(6)	O4[5]	Zn1	O3[2]	97.2(2)
O5	C3	C2	123.1(6)	O102	Ni11	O101	170.3(17)
O5	C3	O4	123.2(6)	O102	Ni11	O103	100.6(16)
P1	O1	Zn1	126.1(3)	O103	Ni11	O101	88.9(12)
P1	O2	Zn1[1]	129.8(3)	O104	Ni11	O101	88.5(13)
P1	O3	Zn1[2]	122.8(3)	O104	Ni11	O102	82.0(17)
C3	O4	Zn1[3]	122.7(5)	O104	Ni11	O103	177.3(11)
O1	P1	C1	107.8(3)	O104	Ni11	O106	102.8(13)
O1	P1	O2	108.5(3)	O105	Ni11	O101	69.9(14)
O2	P1	C1	109.4(3)	O105	Ni11	O102	111.8(17)
O3	P1	C1	106.4(3)	O105	Ni11	O103	89.9(11)
O3	P1	O1	112.0(3)	O105	Ni11	O104	89.7(13)
O3	P1	O2	112.6(3)	O105	Ni11	O106	160.3(10)
O1	Zn1	O2[4]	103.32(19)	O106	Ni11	O101	94.8(13)
O1	Zn1	O3[2]	112.5(2)	O106	Ni11	O102	85.3(16)
O1	Zn1	O4[5]	119.6(3)	O106	Ni11	O103	76.9(9)

[1]1/4+Y,5/4-X,-1/4+Z; [2]3/2-X,+Y,1-Z; [3]3/4-Y,-1/4+X,5/4-Z; [4]5/4-Y,-1/4+X,1/4+Z; [5]1/4+Y,3/4-X,5/4-Z

Table A3.6 Hydrogen Atom Coordinates (Å×10^4) and Isotropic Displacement Parameters (Å^2×10^3) for Ni-BIRM-1

Atom	*x*	*y*	*z*	U(eq)
H1A	5547.52	3971.71	4762.42	48
H1B	5768.18	3594.28	5479.14	48
H2A	5715.34	4427.08	6242.78	51
H2B	5632.63	4869.36	5542.86	51
H10A	4985.41	3107.78	7042.31	285
H10B	5647.37	3287.92	6690.09	285
H10C	5671.21	3921.87	9550.36	346
H10D	6308.5	4135.82	9159.08	346
H10E	4831.86	4534.14	7630.88	289
H10F	5517.21	4814.96	7573.47	289
H10G	5680.65	2564.19	8548.01	277
H10H	6367.81	2840.8	8492.48	277
H10I	4712.28	2948.73	8319.36	276
H10J	4432.15	3598.21	8039.88	276
H10K	6328.2	4288.62	7180.19	244
H10L	6696.41	4154.12	7964.65	244

Table A3.7 Atomic Occupancy for Ni-BIRM-1

Atom	*Occupancy*	Atom	*Occupancy*	Atom	*Occupancy*
Ni11	0.5	O101	0.5	H10A	0.5
H10B	0.5	O102	0.5	H10C	0.5
H10D	0.5	O103	0.5	H10E	0.5
H10F	0.5	O104	0.5	H10G	0.5
H10H	0.5	O105	0.5	H10I	0.5
H10J	0.5	O106	0.5	H10K	0.5
H10L	0.5	O11A	0.5	O201	0.26(2)
O21A	0.24(2)				

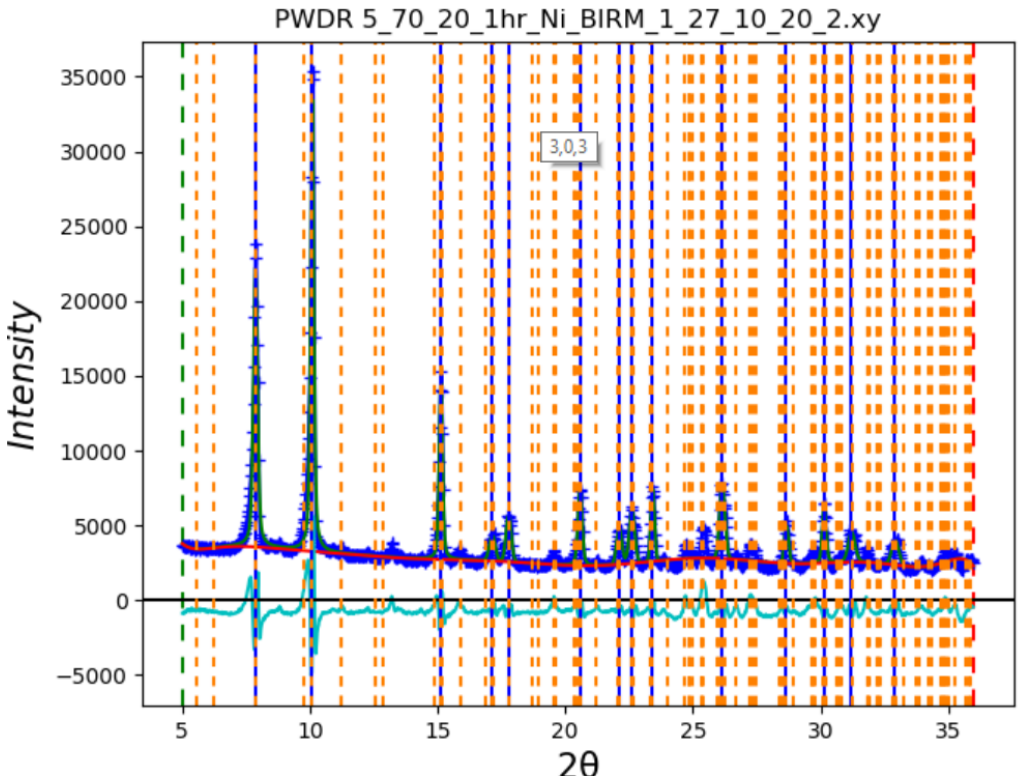


Figure A3.1 Diffraction pattern of Ni-BIRM-1 (blue) used for indexing. Peak positions used are indicated by blue lines and calculated positions based of the indexed cell are shown by the dotted orange lines. The difference line is shown in teal.

Appendix table A3.8-A3.10. Refinement parameters, unit cell parameters, refined atom positions, multiplicities, occupancies and isotropic displacement parameters from the refinement of powder X-ray diffraction for pyrolyzed Ni-BIRM-1

Table A3.8. Refinement and lattice parameters

Refinement parameters			**Lattice parameters**	
R_{wp}	3.94 %		**Phase 1**	**Phase 2**
R_P	3.10 %	**Formular**	Ni_2P	$Zn_2P_2O_7$
X^2	1.40	**Space group**	P -6 2 m	I 1 2/c 1
		a(Å)	5.8634(3)	20.062(8)
		b(Å)	5.8634(3)	8.2824(7)
		c(Å)	3.3871(1)	9.102(2)
		V(Å^3)	100.844(8)	1451.3(2)

Table A3.9. Refined atom positions, multiplicities, occupancies and isotropic displacement parameters for Ni_2P phase

Atom label	Element	x	y	z	Occup	Mult	U_{iso}
P	P1	0.333	0.667	0	1	2	0.022(1)
Ni	Ni1	0.256(7)	0	0	1	3	0.022(1)
Ni	Ni2	0.597(6)	0	0.5	1	3	0.022(1)
P	P2	0	0	0.5	1	1	0.022(1)

Table A3.10. Refined atom positions, multiplicities, occupancies and isotropic displacement parameters for $Zn_2 P_2 O_7$ phase

Atom label	Element	x	y	z	Occup	Mult	U_{iso}
O-2	O6	0.040(5)	0.57(1)	0.18(1)	1	8	0.022(1)
Zn+2	Zn1	0.001(1)	0.308(4)	-0.026(3)	1	8	0.022(1)
O-2	O9	0.275(5)	0.67(1)	0.05(1)	1	8	0.022(1)
O-2	O3	-0.100(6)	0.14(1)	0.38(1)	1	8	0.022(1)
P	P3	0.239(4)	0.524(9)	0.190(6)	1	8	0.022(1)
O-2	O7	0.315(4)	0.53(2)	0.400(9)	1	8	0.022(1)
O-2	O8	0.067(5)	0.68(1)	0.34(1)	1	8	0.022(1)
O-2	O4	0.051(5)	-0.18(2)	0.17(1)	1	8	0.022(1)
P	P1	0.067(3)	0.036(8)	0.181(7)	1	8	0.022(1)
O-2	O11	0.229(6)	0.30(1)	0.09(1)	1	8	0.022(1)
P	P2	0.081(3)	0.510(8)	0.226(7)	1	8	0.022(1)
O-2	O10	0.131(5)	0.37(1)	0.39(1)	1	8	0.022(1)
O-2	O2	-0.100(5)	-0.08(1)	0.15(1)	1	8	0.022(1)
O-2	O5	0.167(6)	0.49(2)	0.19(1)	1	8	0.022(1)
Zn+2	Zn2	0.152(2)	0.203(4)	0.005(3)	1	8	0.022(1)
Zn+2	Zn3	0.196(2)	0.801(4)	-0.002(3)	1	8	0.022(1)
O-2	O1	0	0.09(2)	0.25	1	4	0.022(1)

BIRM-11

Table A4.1 Crystal data and structure refinement for BIRM-11.

Identification code	BIRM-11
Empirical formula	$C_6H_8O_{10}P_2Zn_3$
Formula weight	498.17
Temperature/K	100.00(10)
Crystal system	monoclinic
Space group	$P2_1/c$
a/Å	8.0779(8)
b/Å	9.1238(7)
c/Å	8.8421(9)
α/°	90
β/°	104.142(10)
γ/°	90
Volume/Å^3	631.92(11)
Z	2
ρ_{calc}g/cm^3	2.618
μ/mm^{-1}	9.563
F(000)	488
Crystal size/mm^3	0.149 × 0.079 × 0.045
Radiation	Cu Kα (λ = 1.54184)
2Θ range for data collection/°	11.296 to 145.012
Index ranges	-9 ≤ h ≤ 9, -10 ≤ k ≤ 10, -10 ≤ l ≤ 10
Reflections collected	2395
Independent reflections	2395 [R_{int} =?, R_{sigma} = 0.0434]
Data/restraints/parameters	2395/0/98
Goodness-of-fit on F^2	0.913
Final R indexes [I>=2σ (I)]	R_1 = 0.0439, wR_2 = 0.1058
Final R indexes [all data]	R_1 = 0.0592, wR_2 = 0.1110
Largest diff. peak/hole / e Å^{-3}	1.07/-0.61

Table A4.2 Fractional Atomic Coordinates (×10^4) and Equivalent Isotropic Displacement Parameters (Å^2×10^3) for BIRM-11

Atom	x	y	z	U(eq)
C1	6549(7)	2385(6)	7408(7)	12.3(11)
C2	5370(7)	3656(6)	6750(8)	16.3(12)
C3	3466(7)	3311(7)	6319(7)	14.3(12)
O1	9077(5)	3320(4)	6117(5)	11.5(8)
O2	9848(5)	1459(4)	8123(5)	10.4(8)
O3	9249(5)	4050(4)	8936(5)	10.8(8)
O4	3021(5)	1970(4)	6399(5)	15.0(8)
O5	2494(5)	4362(4)	5908(5)	17.3(9)
P1	8754.1(16)	2853.8(14)	7673.4(16)	8.7(3)
Zn1	10000	5000	5000	9.0(3)
Zn2	696.6(9)	1298.8(8)	6128.4(9)	10.9(2)

Table A4.3 Anisotropic Displacement Parameters (Å^2×10^3) for BIRM-11

Atom	U_{11}	U_{22}	U_{33}	U_{23}	U_{13}	U_{12}
C1	11(2)	6(2)	20(3)	3(2)	4(2)	0(2)
C2	15(3)	10(3)	24(3)	1(2)	3(2)	-1(2)
C3	16(3)	11(3)	15(3)	-2(2)	4(2)	-2(2)
O1	16.3(18)	8.1(18)	10(2)	-1.4(15)	3.4(15)	-1.7(15)
O2	13.4(17)	4.4(18)	13(2)	1.2(14)	3.2(15)	1.9(14)
O3	13.9(18)	6.2(17)	11.5(19)	-0.8(15)	1.5(14)	0.2(14)
O4	10.9(17)	7.5(19)	26(2)	2.2(16)	4.3(16)	-2.5(14)
O5	15.3(19)	8.9(19)	26(2)	1.7(17)	1.7(17)	0.3(16)
P1	9.6(6)	5.3(6)	10.7(7)	0.2(5)	1.6(5)	0.6(5)
Zn1	11.0(5)	4.3(5)	11.8(5)	0.2(4)	2.7(4)	-0.6(4)
Zn2	12.6(4)	6.5(4)	13.1(4)	-0.6(3)	2.5(3)	-0.7(3)

Table A4.4 Bond Lengths for BIRM-11

Atom	Atom	Length/Å	Atom	Atom	Length/Å
C1	C2	1.523(7)	O2	Zn1[2]	2.107(4)
C1	P1	1.791(6)	O2	Zn2[1]	2.048(4)
C2	C3	1.524(8)	O3	P1	1.542(4)
C3	O4	1.283(7)	O3	Zn2[3]	2.030(4)
C3	O5	1.236(8)	O3	Zn2[4]	2.054(4)
O1	P1	1.523(4)	O4	Zn2	1.933(4)
O1	Zn1	2.059(4)	O5	Zn1[5]	2.062(4)
O1	Zn2[1]	2.260(4)	P1	Zn2[1]	2.7182(15)
O2	P1	1.545(4)	Zn2	Zn2[6]	3.1254(15)

[1]1+X,+Y,+Z; [2]2-X,-1/2+Y,3/2-Z; [3]1+X,1/2-Y,1/2+Z; [4]1-X,1/2+Y,3/2-Z; [5]-1+X,+Y,+Z; [6]-X,-Y,1-Z

Table A4.5 Bond Angles for BIRM-11

Atom	Atom	Atom	Angle/˚	Atom	Atom	Atom	Angle/˚
C2	C1	P1	112.2(4)	O1	Zn1	O5[1]	92.12(16)
C1	C2	C3	115.9(5)	O1[6]	Zn1	O5[1]	87.88(16)
O4	C3	C2	117.5(5)	O1[6]	Zn1	O5[9]	92.12(16)
O5	C3	C2	116.3(5)	O1	Zn1	O5[9]	87.88(16)
O5	C3	O4	126.1(5)	O2[8]	Zn1	O2[7]	180
P1	O1	Zn1	143.5(2)	O5[9]	Zn1	O2[8]	89.55(16)
P1	O1	Zn2[1]	89.69(19)	O5[1]	Zn1	O2[7]	89.55(16)
Zn1	O1	Zn2[1]	109.45(16)	O5[1]	Zn1	O2[8]	90.45(16)
P1	O2	Zn1[2]	130.0(2)	O5[9]	Zn1	O2[7]	90.45(16)
P1	O2	Zn2[1]	97.3(2)	O5[9]	Zn1	O5[1]	180
Zn2[1]	O2	Zn1[2]	131.76(18)	O1[5]	Zn2	P1[5]	34.08(10)
P1	O3	Zn2[3]	133.7(2)	O1[5]	Zn2	Zn2[10]	119.89(11)
P1	O3	Zn2[4]	124.6(2)	O2[5]	Zn2	O1[5]	68.32(14)
Zn2[4]	O3	Zn2[3]	99.89(17)	O2[5]	Zn2	O3[11]	96.26(15)
C3	O4	Zn2	124.9(4)	O2[5]	Zn2	P1[5]	34.31(11)
C3	O5	Zn1[5]	145.4(4)	O2[5]	Zn2	Zn2[10]	117.37(11)
C1	P1	Zn2[1]	119.15(19)	O3[11]	Zn2	O1[5]	146.29(15)
O1	P1	C1	109.4(3)	O3[12]	Zn2	O1[5]	85.73(15)
O1	P1	O2	104.4(2)	O3[12]	Zn2	O2[5]	126.70(15)
O1	P1	O3	112.7(2)	O3[12]	Zn2	O3[11]	80.11(17)
O1	P1	Zn2[1]	56.23(15)	O3[12]	Zn2	P1[5]	107.04(11)
O2	P1	C1	108.9(2)	O3[11]	Zn2	P1[5]	123.67(11)
O2	P1	Zn2[1]	48.35(15)	O3[11]	Zn2	Zn2[10]	39.77(11)
O3	P1	C1	109.7(2)	O3[12]	Zn2	Zn2[10]	40.34(11)
O3	P1	O2	111.5(2)	O4	Zn2	O1[5]	106.60(16)
O3	P1	Zn2[1]	130.83(16)	O4	Zn2	O2[5]	112.97(18)
O1[6]	Zn1	O1	180	O4	Zn2	O3[12]	118.92(17)
O1	Zn1	O2[7]	87.09(15)	O4	Zn2	O3[11]	107.04(16)
O1	Zn1	O2[8]	92.91(15)	O4	Zn2	P1[5]	115.78(13)
O1[6]	Zn1	O2[8]	87.09(15)	O4	Zn2	Zn2[10]	120.43(13)
O1[6]	Zn1	O2[7]	92.91(15)	P1[5]	Zn2	Zn2[10]	123.69(5)

[1]1+X,+Y,+Z; [2]2-X,-1/2+Y,3/2-Z; [3]1-X,1/2+Y,3/2-Z; [4]1+X,1/2-Y,1/2+Z; [5]-1+X,+Y,+Z; [6]2-X,1-Y,1-Z; [7]+X,1/2-Y,-1/2+Z; [8]2-X,1/2+Y,3/2-Z; [9]1-X,1-Y,1-Z; [10]-X,-Y,1-Z; [11]1-X,-1/2+Y,3/2-Z; [12]-1+X,1/2-Y,-1/2+Z

BIRM-12

Table A4.6 Crystal data and structure refinement for BIRM-12

Identification code	Cu-Mat-1-RT-SC
Empirical formula	$C_3H_9CuO_7P$
Formula weight	251.61
Temperature/K	100.01(10)
Crystal system	orthorhombic
Space group	Pbca
a/Å	20.9797(17)
b/Å	8.0859(7)
c/Å	9.1604(8)
α/°	90
β/°	90
γ/°	90
Volume/Å^3	1554.0(2)
Z	8
ρ_{calc}g/cm^3	2.151
μ/mm^{-1}	6.051
F(000)	1016
Crystal size/mm^3	0.159 × 0.063 × 0.032
Radiation	Cu Kα (λ = 1.54184)
2Θ range for data collection/°	8.43 to 146.088
Index ranges	-25 ≤ h ≤ 22, -8 ≤ k ≤ 9, -11 ≤ l ≤ 10
Reflections collected	3914
Independent reflections	1511 [R_{int} = 0.0291, R_{sigma} = 0.0315]
Data/restraints/parameters	1511/1/129
Goodness-of-fit on F^2	1.046
Final R indexes [I>=2σ (I)]	R_1 = 0.0286, wR_2 = 0.0740
Final R indexes [all data]	R_1 = 0.0337, wR_2 = 0.0784
Largest diff. peak/hole / e Å^{-3}	0.59/-0.45

Table A4.7 Fractional Atomic Coordinates (×10^4) and Equivalent Isotropic Displacement Parameters (Å^2×10^3) for BIRM-12.

Atom	*x*	*y*	*z*	U(eq)
C1	6489.7(11)	3556(3)	3377(3)	9.8(5)
C2	6953.8(11)	3796(3)	4640(3)	13.3(5)
C3	7646.0(11)	3704(3)	4185(3)	12.2(5)
Cu1	4782.0(2)	2509.2(4)	1403.0(4)	6.19(14)
O1	5267.3(8)	4092(2)	2544.7(18)	9.1(3)
O2	5484.5(8)	2710(2)	5015.0(19)	9.4(3)
O3	5694.2(7)	5773(2)	4599.3(17)	7.4(3)
O4	7842.3(8)	2950(3)	3128(2)	19.3(4)
O5	8012.0(9)	4516(3)	5098(2)	20.2(4)
O6	4078.4(8)	2683(2)	2855(2)	9.4(3)
O7	4255.8(8)	4535(2)	139(2)	9.3(3)
P1	5682.1(3)	4039.9(7)	3911.5(6)	6.23(16)

Table A4.8 Anisotropic Displacement Parameters (Å^2×10^3) for BIRM-12

Atom	U_{11}	U_{22}	U_{33}	U_{23}	U_{13}	U_{12}
C1	7.6(11)	12.0(12)	9.9(11)	-0.7(9)	2.3(8)	0.8(9)
C2	6.9(11)	19.1(13)	13.8(12)	-0.3(9)	0.5(9)	1.1(9)
C3	8.7(11)	13.6(12)	14.3(12)	3.5(10)	-0.1(9)	1.8(9)
Cu1	4.4(2)	7.2(2)	7.0(2)	-1.13(12)	0.33(11)	-0.80(11)
O1	7.8(7)	10.8(8)	8.7(8)	-0.6(6)	-0.2(6)	-0.7(6)
O2	9.0(8)	8.5(8)	10.8(8)	2.2(6)	2.5(6)	0.5(6)
O3	7.0(8)	7.9(8)	7.4(8)	-1.1(6)	0.0(6)	-0.3(6)
O4	9.5(8)	30.1(10)	18.3(10)	-8.5(8)	1.0(7)	1.8(8)
O5	5.1(8)	30.9(11)	24.6(10)	-11.2(8)	-0.5(7)	-2.8(8)
O6	6.9(9)	11.9(8)	9.4(8)	-2.1(7)	-1.5(7)	0.5(6)
O7	9.6(8)	9.7(9)	8.5(9)	0.3(7)	0.9(6)	-0.5(6)
P1	4.7(3)	6.9(3)	7.1(3)	-0.2(2)	0.36(19)	-0.2(2)

Table A4.9 Bond Lengths for BIRM-12

Atom	Atom	Length/Å	Atom	Atom	Length/Å
C1	C2	1.525(3)	Cu1	O3[2]	1.9528(16)
C1	P1	1.806(2)	Cu1	O6	1.9921(18)
C2	C3	1.513(3)	Cu1	O7	2.2896(17)
C3	O4	1.216(3)	O1	P1	1.5255(17)
C3	O5	1.312(3)	O2	P1	1.5330(17)
Cu1	O1	1.9410(17)	O3	P1	1.5363(17)
Cu1	O2[1]	1.9544(17)			

[1]+X,1/2-Y,-1/2+Z; [2]1-X,-1/2+Y,1/2-Z

Table A4.10 Hydrogen Bonds for BIRM-12

D	H	A	d(D-H)/Å	d(H-A)/Å	d(D-A)/Å	D-H-A/°
O5	H5	O7[1]	0.731(18)	1.91(2)	2.619(3)	165(4)
O6	H6A	O4[2]	0.84(3)	1.91(3)	2.754(3)	177(3)
O6	H6B	O3[3]	0.73(4)	1.96(4)	2.688(2)	171(5)
O7	H7A	O2[4]	0.93(3)	1.71(3)	2.628(2)	167(3)
O7	H7B	O1[5]	0.73(5)	2.34(5)	2.877(2)	131(4)
O7	H7B	O6[6]	0.73(5)	2.19(5)	2.781(3)	138(5)

[1]1/2+X,+Y,1/2-Z; [2]-1/2+X,+Y,1/2-Z; [3]1-X,1-Y,1-Z; [4]1-X,1/2+Y,1/2-Z; [5]1-X,1-Y,-Z; [6]+X,1/2-Y,-1/2+Z

BIRM-13

Table A4.11 Crystal data and structure refinement for BIRM-13

Identification code	BIRM-13
Empirical formula	$C_3H_5CuO_5P$
Formula weight	215.58
Temperature/K	100.00(10)
Crystal system	monoclinic
Space group	$P2_1/c$
a/Å	14.4122(15)
b/Å	5.6635(6)
c/Å	7.5868(8)
α/°	90
β/°	99.887(10)
γ/°	90
Volume/Å^3	610.06(11)
Z	4
ρ_{calc}g/cm^3	2.347
μ/mm^{-1}	7.306
F(000)	428
Crystal size/mm^3	0.286 × 0.15 × 0.071
Radiation	CuKα (λ = 1.54184)
2Θ range for data collection/°	16.854 to 145.462
Index ranges	$-16 \le h \le 17$, $-6 \le k \le 5$, $-7 \le l \le 9$
Reflections collected	2074
Independent reflections	1177 [R_{int} = 0.0178, R_{sigma} = 0.0202]
Data/restraints/parameters	1177/0/95
Goodness-of-fit on F^2	1.14
Final R indexes [I>=2σ (I)]	R_1 = 0.0341, wR_2 = 0.0954
Final R indexes [all data]	R_1 = 0.0352, wR_2 = 0.0961
Largest diff. peak/hole / e Å^{-3}	0.66/-1.08

Table A4.12 Fractional Atomic Coordinates (×10^4) and Equivalent Isotropic Displacement Parameters (Å^2×10^3) for BIRM-13

Atom	*x*	*y*	*z*	U(eq)
C1	2635.1(16)	6547(4)	3312(3)	8.4(5)
C2	2062.3(19)	4283(5)	2939(4)	17.5(6)
C3	1153.1(17)	4650(5)	1657(3)	14.7(5)
Cu1	4687.0(2)	3870.4(6)	8135.4(4)	7.03(19)
O1	3741.2(11)	4633(3)	6130(2)	7.4(3)
O2	4288.6(12)	4466(3)	3104(2)	7.2(3)
O3	4351.7(12)	8302(3)	4751(2)	7.6(3)
O4	565.7(15)	2888(4)	1658(3)	29.2(5)
O5	1002.4(14)	6368(3)	684(3)	19.8(4)
P1	3812.6(4)	5936.9(10)	4406.5(8)	5.3(2)

Table A4.13 Anisotropic Displacement Parameters (Å^2×10^3) for BIRM-13

Atom	U_{11}	U_{22}	U_{33}	U_{23}	U_{13}	U_{12}
C1	8.9(10)	10.3(11)	6.0(11)	0.2(8)	1.5(9)	0.9(9)
C2	13.5(12)	14.9(12)	21.4(13)	6.1(11)	-4.7(10)	-2.4(10)
C3	13.3(12)	17.6(13)	12.8(12)	0.8(10)	1.0(9)	-3.1(10)
Cu1	9.8(3)	5.8(3)	4.9(3)	0.92(11)	-0.65(17)	-0.15(11)
O1	9.5(7)	8.3(8)	4.3(7)	1.8(6)	1.2(6)	-0.7(6)
O2	8.8(8)	6.9(8)	6.0(8)	-1.2(6)	2.0(6)	-0.4(7)
O3	12.6(8)	5.4(7)	4.3(7)	0.0(6)	0.2(6)	-1.7(6)
O4	17.7(10)	26.9(13)	36.8(12)	15.9(10)	-12.6(9)	-11.4(9)
O5	14.7(9)	22.7(10)	19.3(10)	7.3(8)	-4.8(7)	-5.1(7)
P1	7.0(3)	5.2(3)	3.8(3)	0.05(19)	1.1(2)	-0.22(19)

Table A4.14 Bond Lengths for BIRM-13

Atom	Atom	Length/Å	Atom	Atom	Length/Å
C1	C2	1.525(3)	Cu1	O2[2]	1.9737(17)
C1	P1	1.790(2)	Cu1	O3[3]	1.9574(17)
C2	C3	1.506(3)	Cu1	O3[4]	2.1222(17)
C3	O4	1.309(3)	O1	P1	1.5206(16)
C3	O5	1.218(3)	O2	P1	1.5410(17)
Cu1	O1	1.9097(16)	O3	P1	1.5480(17)
Cu1	O2[1]	2.1043(17)			

[1]1-X,1-Y,1-Z; [2]+X,1/2-Y,1/2+Z; [3]1-X,-1/2+Y,3/2-Z; [4]+X,3/2-Y,1/2+Z

Table A4.15 Bond Angles for BIRM-13

Atom	Atom	Atom	Angle/˚	Atom	Atom	Atom	Angle/˚
C2	C1	P1	111.31(17)	O3[4]	Cu1	O3[3]	81.39(7)
C3	C2	C1	112.8(2)	P1	O1	Cu1	130.58(10)
O4	C3	C2	112.7(2)	Cu1[5]	O2	Cu1[1]	102.07(7)
O5	C3	C2	123.1(2)	P1	O2	Cu1[1]	117.92(9)
O5	C3	O4	124.2(2)	P1	O2	Cu1[5]	132.10(10)
O1	Cu1	O2[1]	90.14(7)	Cu1[6]	O3	Cu1[7]	98.61(7)
O1	Cu1	O2[2]	92.32(7)	P1	O3	Cu1[7]	135.47(10)
O1	Cu1	O3[3]	95.01(7)	P1	O3	Cu1[6]	123.01(10)
O1	Cu1	O3[4]	176.20(7)	O1	P1	C1	107.10(10)
O2[2]	Cu1	O2[1]	130.40(6)	O1	P1	O2	113.10(9)
O2[2]	Cu1	O3[3]	129.41(6)	O1	P1	O3	112.40(9)
O2[1]	Cu1	O3[3]	99.61(6)	O2	P1	C1	107.32(10)
O3[4]	Cu1	O2[2]	90.92(7)	O2	P1	O3	108.07(9)
O3[4]	Cu1	O2[1]	89.28(7)	O3	P1	C1	108.64(10)

[1]1-X,1-Y,1-Z; [2]+X,1/2-Y,1/2+Z; [3]+X,3/2-Y,1/2+Z; [4]1-X,-1/2+Y,3/2-Z; [5]+X,1/2-Y,-1/2+Z; [6]1-X,1/2+Y,3/2-Z; [7]+X,3/2-Y,-1/2+Z

Table A4.16 Torsion Angles for BIRM-13

A	B	C	D	Angle/˚	A	B	C	D	Angle/˚
C1	C2	C3	O4	-164.9(2)	Cu1[1]	O2	P1	O1	7.97(17)
C1	C2	C3	O5	17.6(4)	Cu1[1]	O2	P1	O3	133.08(12)
C2	C1	P1	O1	-58.1(2)	Cu1[2]	O2	P1	O3	-9.85(12)
C2	C1	P1	O2	63.6(2)	Cu1[3]	O3	P1	C1	-58.24(16)
C2	C1	P1	O3	-179.77(17)	Cu1[4]	O3	P1	C1	145.57(11)
Cu1	O1	P1	C1	-168.78(13)	Cu1[3]	O3	P1	O1	-176.57(12)
Cu1	O1	P1	O2	73.19(15)	Cu1[4]	O3	P1	O1	27.23(14)
Cu1	O1	P1	O3	-49.54(15)	Cu1[4]	O3	P1	O2	-98.29(12)
Cu1[1]	O2	P1	C1	-109.93(14)	Cu1[3]	O3	P1	O2	57.91(16)
Cu1[2]	O2	P1	C1	107.15(11)	P1	C1	C2	C3	-166.67(18)
Cu1[2]	O2	P1	O1	-134.95(10)					

[1]+X,1/2-Y,-1/2+Z; [2]1-X,1-Y,1-Z; [3]+X,3/2-Y,-1/2+Z; [4]1-X,1/2+Y,3/2-Z

BIRM-14

Table A4.17 Crystal data and structure refinement for BIRM-14

Identification code	BIRM-14
Empirical formula	$C_{13}H_{12}Cu_3N_2O_5P$
Formula weight	497.84
Temperature/K	100.01(10)
Crystal system	monoclinic
Space group	$P2_1/n$
a/Å	10.5235(8)
b/Å	6.5966(5)
c/Å	21.3034(17)
α/°	90
β/°	98.757(7)
γ/°	90
Volume/Å^3	1461.6(2)
Z	4
ρ_{calc}g/cm^3	2.262
μ/mm^{-1}	6.385
F(000)	984
Crystal size/mm^3	0.123 × 0.088 × 0.053
Radiation	CuKα (λ = 1.54184)
2Θ range for data collection/°	8.398 to 145.494
Index ranges	-12 ≤ h ≤ 9, -7 ≤ k ≤ 5, -20 ≤ l ≤ 25
Reflections collected	5014
Independent reflections	2801 [R_{int} = 0.0427, R_{sigma} = 0.0443]
Data/restraints/parameters	2801/0/217
Goodness-of-fit on F^2	1.078
Final R indexes [I>=2σ (I)]	R_1 = 0.0634, wR_2 = 0.1632
Final R indexes [all data]	R_1 = 0.0716, wR_2 = 0.1808
Largest diff. peak/hole / e Å^{-3}	1.68/-0.76

Table A4.18 Fractional Atomic Coordinates (×10^4) and Equivalent Isotropic Displacement Parameters (Å^2×10^3) for BIRM-14

Atom	*x*	*y*	*z*	U(eq)
C(1)	1389(5)	7075(7)	4267(2)	33.1(10)
C(2)	-66(5)	7148(7)	4096(2)	33.1(10)
C(3)	-800(5)	7422(7)	4659(2)	33.1(10)
C(4)	5583(5)	6984(7)	2028(3)	34.6(10)
C(5)	6467(5)	7049(7)	1610(2)	33.3(10)
C(6)	7786(5)	7136(7)	1841(2)	31.7(10)
C(7)	8146(5)	7174(7)	2502(2)	32.9(10)
C(8)	7216(5)	7118(7)	2892(2)	32.8(10)
C(9)	9337(5)	7674(8)	363(3)	36.4(10)
C(10)	8401(5)	7674(8)	763(3)	35.7(10)
C(11)	8749(5)	7197(7)	1399(2)	32.0(10)
C(12)	10057(5)	6752(7)	1619(2)	33.0(10)
C(13)	10914(5)	6796(8)	1185(3)	37.5(11)
Cu(1)	4742.7(7)	6947.4(11)	3230.1(4)	33.8(3)
Cu(2)	2468.4(6)	9289.7(12)	2459.2(3)	34.2(3)
Cu(3)	-3180.7(7)	7689.3(12)	5027.1(4)	36.0(3)
N(1)	5950(4)	7021(6)	2668(2)	31.5(8)
N(2)	10576(4)	7250(6)	566(2)	33.6(8)
O(1)	3625(3)	6958(5)	3814.2(17)	34.4(7)
O(2)	1719(3)	8744(6)	3164.3(16)	35.6(7)
O(3)	1756(3)	4914(6)	3232.6(17)	37.6(7)
O(4)	-2030(3)	7522(6)	4465.1(18)	39.1(8)
O(5)	-265(3)	7514(6)	5208.8(18)	38.9(8)
P(1)	2173.0(11)	6900.6(18)	3578.7(6)	31.3(3)

Table A4.19 Anisotropic Displacement Parameters ($Å^2×10^3$) for BIRM-14

Atom	U_{11}	U_{22}	U_{33}	U_{23}	U_{13}	U_{12}
C(1)	36(2)	33(3)	32(2)	1.0(17)	8.3(18)	1.3(16)
C(2)	36(2)	31(2)	32(2)	2.3(17)	5.6(18)	0.8(17)
C(3)	37(2)	29(2)	34(3)	1.3(19)	10.1(19)	-0.3(18)
C(4)	36(2)	28(2)	39(3)	2.1(18)	4.6(19)	-0.1(16)
C(5)	41(2)	27(2)	32(2)	-0.4(17)	3.8(19)	0.3(16)
C(6)	40(2)	22(2)	33(2)	2.1(17)	6.2(19)	-0.5(15)
C(7)	34(2)	29(2)	35(3)	-1.7(18)	4.2(18)	-0.3(16)
C(8)	41(2)	26(2)	31(2)	2.5(17)	5.9(19)	2.5(16)
C(9)	36(2)	41(3)	32(3)	-1(2)	5.1(19)	-0.2(18)
C(10)	36(2)	38(3)	33(2)	0.3(19)	6.6(19)	1.3(18)
C(11)	36(2)	25(2)	35(3)	-2.5(17)	5.3(19)	-1.4(16)
C(12)	37(2)	28(2)	34(2)	1.2(18)	7.6(19)	2.4(17)
C(13)	38(2)	38(3)	38(3)	1(2)	7(2)	1.7(18)
Cu(1)	36.3(4)	33.4(5)	33.0(4)	0.4(3)	9.2(3)	0.4(2)
Cu(2)	38.4(4)	33.7(5)	31.1(4)	2.4(3)	7.6(3)	-0.5(3)
Cu(3)	36.9(4)	38.7(5)	34.0(4)	0.0(3)	10.2(3)	0.6(3)
N(1)	36.9(19)	28(2)	30(2)	2.3(15)	7.6(16)	-2.0(14)
N(2)	40(2)	30(2)	32(2)	-1.5(16)	9.4(16)	-0.9(15)
O(1)	37.6(17)	38(2)	28.1(17)	2.6(13)	7.9(13)	1.2(12)
O(2)	39.4(17)	36.0(19)	32.3(17)	4.2(14)	8.5(13)	0.4(14)
O(3)	40.7(17)	39(2)	34.4(16)	-1.6(15)	10.8(13)	-4.7(14)
O(4)	33.6(17)	54(2)	30.7(18)	-0.8(15)	8.9(14)	0.3(14)
O(5)	40.7(18)	42(2)	33.8(19)	0.2(15)	6.1(15)	-0.8(14)
P(1)	34.1(6)	30.8(7)	29.5(6)	0.9(4)	6.7(5)	0.9(4)

Table A4.20 Bond Lengths for BIRM-14

Atom	Atom	Length/Å	Atom	Atom	Length/Å
C(1)	C(2)	1.519(7)	C(10)	C(11)	1.384(8)
C(1)	P(1)	1.792(5)	C(11)	C(12)	1.416(7)
C(2)	C(3)	1.533(7)	C(12)	C(13)	1.386(7)
C(3)	O(4)	1.299(6)	C(13)	N(2)	1.346(7)
C(3)	O(5)	1.222(7)	Cu(1)	N(1)	1.874(4)
C(4)	C(5)	1.383(7)	Cu(1)	O(1)	1.838(3)
C(4)	N(1)	1.360(7)	Cu(2)	O(2)	1.835(3)
C(5)	C(6)	1.402(7)	Cu(2)	O(3)[1]	1.837(3)
C(6)	C(7)	1.400(7)	Cu(2)	P(1)[1]	2.8726(14)
C(6)	C(11)	1.485(7)	Cu(3)	N(2)[2]	1.868(4)
C(7)	C(8)	1.378(7)	Cu(3)	O(4)	1.831(4)
C(8)	N(1)	1.347(7)	O(1)	P(1)	1.534(4)
C(9)	C(10)	1.398(7)	O(2)	P(1)	1.535(4)
C(9)	N(2)	1.340(7)	O(3)	P(1)	1.535(4)

[1]1/2-X,1/2+Y,1/2-Z; [2]-3/2+X,3/2-Y,1/2+Z

Table A4.21 Bond Angles for BIRM-14

Atom	Atom	Atom	Angle/˚	Atom	Atom	Atom	Angle/˚
C(2)	C(1)	P(1)	112.3(4)	O(3)[1]	Cu(2)	P(1)[1]	28.55(12)
C(1)	C(2)	C(3)	115.2(4)	O(4)	Cu(3)	N(2)[2]	176.32(18)
O(4)	C(3)	C(2)	110.7(4)	C(4)	N(1)	Cu(1)	121.6(3)
O(5)	C(3)	C(2)	122.8(4)	C(8)	N(1)	C(4)	118.1(4)
O(5)	C(3)	O(4)	126.4(5)	C(8)	N(1)	Cu(1)	120.4(3)
N(1)	C(4)	C(5)	122.0(4)	C(9)	N(2)	C(13)	117.5(4)
C(4)	C(5)	C(6)	120.1(5)	C(9)	N(2)	Cu(3)[3]	122.3(4)
C(5)	C(6)	C(11)	120.9(5)	C(13)	N(2)	Cu(3)[3]	120.1(4)
C(7)	C(6)	C(5)	117.1(4)	P(1)	O(1)	Cu(1)	119.1(2)
C(7)	C(6)	C(11)	122.1(4)	P(1)	O(2)	Cu(2)	119.4(2)
C(8)	C(7)	C(6)	119.9(4)	P(1)	O(3)	Cu(2)[4]	116.6(2)
N(1)	C(8)	C(7)	122.9(5)	C(3)	O(4)	Cu(3)	121.4(3)
N(2)	C(9)	C(10)	122.9(5)	C(1)	P(1)	Cu(2)[4]	143.03(17)
C(11)	C(10)	C(9)	119.4(5)	O(1)	P(1)	C(1)	106.9(2)
C(10)	C(11)	C(6)	121.5(4)	O(1)	P(1)	Cu(2)[4]	91.46(14)
C(10)	C(11)	C(12)	118.0(4)	O(1)	P(1)	O(2)	112.1(2)
C(12)	C(11)	C(6)	120.5(5)	O(1)	P(1)	O(3)	112.1(2)
C(13)	C(12)	C(11)	118.2(5)	O(2)	P(1)	C(1)	106.1(2)
N(2)	C(13)	C(12)	123.8(5)	O(2)	P(1)	Cu(2)[4]	95.62(15)
O(1)	Cu(1)	N(1)	176.69(18)	O(3)	P(1)	C(1)	108.3(2)
O(2)	Cu(2)	O(3)[1]	178.03(17)	O(3)	P(1)	Cu(2)[4]	34.88(12)
O(2)	Cu(2)	P(1)[1]	150.56(12)	O(3)	P(1)	O(2)	111.0(2)

[1]1/2-X,1/2+Y,1/2-Z; [2]-3/2+X,3/2-Y,1/2+Z; [3]3/2+X,3/2-Y,-1/2+Z; [4]1/2-X,-1/2+Y,1/2-Z

Table A4.22 Torsion Angles for BIRM-14

A	B	C	D	Angle/˚	A	B	C	D	Angle/˚
C(1)	C(2)	C(3)	O(4)	178.2(4)	C(10)	C(9)	N(2)	Cu(3)[2]	-178.7(4)
C(1)	C(2)	C(3)	O(5)	-2.2(7)	C(10)	C(11)	C(12)	C(13)	-0.7(7)
C(2)	C(1)	P(1)	Cu(2)[1]	-66.4(5)	C(11)	C(6)	C(7)	C(8)	179.8(4)
C(2)	C(1)	P(1)	O(1)	177.0(3)	C(11)	C(12)	C(13)	N(2)	0.4(8)
C(2)	C(1)	P(1)	O(2)	57.2(4)	C(12)	C(13)	N(2)	C(9)	-0.2(8)
C(2)	C(1)	P(1)	O(3)	-62.1(4)	C(12)	C(13)	N(2)	Cu(3)[2]	178.8(4)
C(2)	C(3)	O(4)	Cu(3)	176.1(3)	Cu(1)	O(1)	P(1)	C(1)	-176.7(2)
C(4)	C(5)	C(6)	C(7)	-0.7(7)	Cu(1)	O(1)	P(1)	Cu(2)[1]	35.8(2)
C(4)	C(5)	C(6)	C(11)	179.7(4)	Cu(1)	O(1)	P(1)	O(2)	-60.9(3)
C(5)	C(4)	N(1)	C(8)	-0.2(7)	Cu(1)	O(1)	P(1)	O(3)	64.7(3)
C(5)	C(4)	N(1)	Cu(1)	179.6(4)	Cu(2)	O(2)	P(1)	C(1)	172.3(2)
C(5)	C(6)	C(7)	C(8)	0.2(7)	Cu(2)	O(2)	P(1)	Cu(2)[1]	-37.9(2)
C(5)	C(6)	C(11)	C(10)	16.2(7)	Cu(2)	O(2)	P(1)	O(1)	55.9(3)
C(5)	C(6)	C(11)	C(12)	-163.3(5)	Cu(2)	O(2)	P(1)	O(3)	-70.2(3)
C(6)	C(7)	C(8)	N(1)	0.2(7)	Cu(2)[1]	O(3)	P(1)	C(1)	-175.4(2)
C(6)	C(11)	C(12)	C(13)	178.9(4)	Cu(2)[1]	O(3)	P(1)	O(1)	-57.8(3)
C(7)	C(6)	C(11)	C(10)	-163.4(5)	Cu(2)[1]	O(3)	P(1)	O(2)	68.4(3)
C(7)	C(6)	C(11)	C(12)	17.1(7)	N(1)	C(4)	C(5)	C(6)	0.6(7)
C(7)	C(8)	N(1)	C(4)	-0.3(7)	N(2)	C(9)	C(10)	C(11)	-0.7(8)
C(7)	C(8)	N(1)	Cu(1)	179.9(3)	O(5)	C(3)	O(4)	Cu(3)	-3.4(8)
C(9)	C(10)	C(11)	C(6)	-178.8(4)	P(1)	C(1)	C(2)	C(3)	-176.6(3)
C(9)	C(10)	C(11)	C(12)	0.8(7)	P(1)[3]	Cu(2)	O(2)	P(1)	-171.74(8)
C(10)	C(9)	N(2)	C(13)	0.4(8)					

[1]1/2-X,-1/2+Y,1/2-Z; [2]3/2+X,3/2-Y,-1/2+Z; [3]1/2-X,1/2+Y,1/2-Z

Table A4.23 Hydrogen Atom Coordinates (Å×10^4) and Isotropic Displacement Parameters (Å^2×10^3) for BIRM-14

Atom	*x*	*y*	*z*	U(eq)
H(1A)	1627.78	5914.65	4538.6	40
H(1B)	1682.18	8286.9	4503.13	40
H(2A)	-352.88	5899.76	3878.58	40
H(2B)	-291.2	8254.14	3800.27	40
H(4)	4712.05	6913.2	1866.67	42
H(5)	6185.04	7035.48	1174.46	40
H(7)	9010.51	7236.01	2676.22	39
H(8)	7474.47	7149.95	3329.48	39
H(9)	9087.92	7982.5	-64.3	44
H(10)	7552.13	7991.23	604.26	43
H(12)	10334.46	6438.13	2043.31	40
H(13)	11771.51	6494.56	1329.94	45

BIRM-15

Table A4.24 Crystal data and structure refinement for BIRM-15

Identification code	BIRM-15
Empirical formula	$C_6H_{20}Co_3O_{16}P_2$
Formula weight	586.95
Temperature/K	100.01(10)
Crystal system	monoclinic
Space group	$P2_1/c$
a/Å	4.6133(2)
b/Å	10.2387(5)
c/Å	17.5296(8)
α/°	90
β/°	95.809(4)
γ/°	90
Volume/Å^3	823.74(7)
Z	2
ρ_{calc}g/cm^3	2.366
μ/mm^{-1}	26.07
F(000)	590
Crystal size/mm^3	0.194 × 0.053 × 0.031
Radiation	Cu Kα (λ = 1.54184)
2Θ range for data collection/°	10.018 to 145.646
Index ranges	-5 ≤ h ≤ 3, -12 ≤ k ≤ 12, -16 ≤ l ≤ 21
Reflections collected	2948
Independent reflections	1596 [R_{int} = 0.0330, R_{sigma} = 0.0450]
Data/restraints/parameters	1596/6/142
Goodness-of-fit on F^2	1.082
Final R indexes [I>=2σ (I)]	R_1 = 0.0353, wR_2 = 0.0916
Final R indexes [all data]	R_1 = 0.0397, wR_2 = 0.0951
Largest diff. peak/hole / e Å^{-3}	0.62/-0.52

Table A4.25 Fractional Atomic Coordinates (×10^4) and Equivalent Isotropic Displacement Parameters (Å^2×10^3) for BIRM-15

Atom	*x*	*y*	*z*	U(eq)
C1	7036(8)	7760(3)	6270(2)	10.2(7)
C2	5173(8)	8111(4)	6915(2)	12.7(7)
C3	7065(7)	8430(3)	7647.3(19)	7.9(6)
Co1	-146.2(12)	7743.3(5)	4169.2(3)	7.64(18)
Co2	0	5000	5000	6.6(2)
O1	3087(5)	8141(2)	5035.1(14)	9.6(5)
O2	3401(5)	5902(2)	5654.5(13)	9.5(5)
O3	7453(5)	6693(2)	4898.3(14)	9.5(5)
O4	2168(6)	8702(3)	3406.8(15)	14.7(5)
O5	-2467(6)	9464(2)	4341.6(16)	14.2(5)
O6	-1722(5)	4215(2)	6005.7(14)	9.0(5)
O7	6826(6)	7700(2)	8226.4(14)	12.8(5)
O8	8871(6)	9350(3)	7648.4(14)	13.9(5)
P1	5088.5(18)	7085.6(8)	5423.2(5)	7.4(2)

Table A4.26 Anisotropic Displacement Parameters (Å^2×10^3) for BIRM-15

Atom	U_{11}	U_{22}	U_{33}	U_{23}	U_{13}	U_{12}
C1	16.6(17)	7.0(16)	6.7(15)	-1.0(12)	-0.2(13)	1.3(13)
C2	16.8(17)	14.6(17)	6.6(16)	0.3(13)	0.8(14)	-0.2(15)
C3	9.6(15)	8.4(15)	5.1(15)	-0.3(12)	-2.3(12)	0.5(13)
Co1	14.3(3)	4.3(3)	4.1(3)	0.20(19)	-0.3(2)	-0.4(2)
Co2	12.1(4)	3.0(4)	4.4(4)	-0.1(3)	-0.9(3)	-0.3(3)
O1	13.2(11)	8.0(11)	7.2(11)	-0.1(9)	-1.2(9)	2.5(9)
O2	15.0(11)	6.2(11)	7.2(11)	0.3(9)	0.5(9)	-1.3(10)
O3	17.0(12)	5.4(11)	6.3(11)	1.1(9)	1.5(9)	-0.6(10)
O4	19.4(12)	12.2(13)	13.6(12)	7.0(10)	6.4(10)	4.6(11)
O5	19.5(13)	4.3(11)	18.9(13)	-3.3(10)	2.2(11)	-0.3(10)
O6	12.7(11)	9.2(11)	4.7(10)	-0.5(9)	-0.8(9)	-1.9(10)
O7	19.5(13)	11.5(13)	6.6(12)	1.1(9)	-3.0(10)	-3.8(10)
O8	22.3(13)	9.7(12)	8.6(12)	0.8(9)	-3.3(10)	-2.3(11)
P1	13.3(4)	4.4(4)	4.1(4)	-0.7(3)	-0.7(3)	-0.6(3)

Table A4.27 Bond Lengths for BIRM-15

Atom	Atom	Length/Å	Atom	Atom	Length/Å
C1	C2	1.532(5)	Co1	O7[3]	2.103(3)
C1	P1	1.793(4)	Co2	O2[2]	2.066(2)
C2	C3	1.513(5)	Co2	O2	2.066(2)
C3	O7	1.275(4)	Co2	O3[4]	2.091(2)
C3	O8	1.257(4)	Co2	O3[1]	2.091(2)
Co1	O1	2.058(2)	Co2	O6[2]	2.161(2)
Co1	O3[1]	2.074(2)	Co2	O6	2.161(2)
Co1	O4	2.044(3)	O1	P1	1.535(3)
Co1	O5	2.100(3)	O2	P1	1.517(3)
Co1	O6[2]	2.216(3)	O3	P1	1.550(2)

[1]-1+X,+Y,+Z; [2]-X,1-Y,1-Z; [3]-1+X,3/2-Y,-1/2+Z; [4]1-X,1-Y,1-Z

Table A4.28 Bond Angles for BIRM-15

Atom	Atom	Atom	Angle/˚	Atom	Atom	Atom	Angle/˚
C2	C1	P1	115.5(3)	O2	Co2	O3[1]	93.74(9)
C3	C2	C1	111.0(3)	O2[2]	Co2	O6	88.02(9)
O7	C3	C2	117.4(3)	O2[2]	Co2	O6[2]	91.98(9)
O8	C3	C2	119.3(3)	O2	Co2	O6[2]	88.02(9)
O8	C3	O7	123.3(3)	O2	Co2	O6	91.98(9)
O1	Co1	O3[1]	92.32(10)	O3[4]	Co2	O3[1]	180
O1	Co1	O5	94.01(10)	O3[1]	Co2	O6[2]	82.63(9)
O1	Co1	O6[2]	91.04(9)	O3[4]	Co2	O6[2]	97.37(9)
O1	Co1	O7[3]	175.24(10)	O3[1]	Co2	O6	97.37(9)
O3[1]	Co1	O5	91.98(10)	O3[4]	Co2	O6	82.63(9)
O3[1]	Co1	O6[2]	81.70(9)	O6	Co2	O6[2]	180
O3[1]	Co1	O7[3]	91.08(10)	P1	O1	Co1	123.10(15)
O4	Co1	O1	89.98(11)	P1	O2	Co2	126.17(14)
O4	Co1	O3[1]	176.90(11)	Co1[5]	O3	Co2[5]	98.74(10)
O4	Co1	O5	89.93(11)	P1	O3	Co1[5]	133.08(15)
O4	Co1	O6[2]	96.18(10)	P1	O3	Co2[5]	125.98(14)
O4	Co1	O7[3]	86.50(11)	Co2	O6	Co1[2]	92.49(9)
O5	Co1	O6[2]	172.08(10)	C3	O7	Co1[6]	130.4(2)
O5	Co1	O7[3]	89.21(10)	O1	P1	C1	108.92(15)
O7[3]	Co1	O6[2]	86.15(9)	O1	P1	O3	110.34(14)
O2[2]	Co2	O2	180	O2	P1	C1	108.29(15)
O2[2]	Co2	O3[1]	86.26(9)	O2	P1	O1	112.24(14)
O2	Co2	O3[4]	86.26(9)	O2	P1	O3	111.26(14)
O2[2]	Co2	O3[4]	93.74(9)	O3	P1	C1	105.51(16)

[1]-1+X,+Y,+Z; [2]-X,1-Y,1-Z; [3]-1+X,3/2-Y,-1/2+Z; [4]1-X,1-Y,1-Z; [5]1+X,+Y,+Z; [6]1+X,3/2-Y,1/2+Z

Table A4.29 Hydrogen Bonds for BIRM-15

D	H	A	d(D-H)/Å	d(H-A)/Å	d(D-A)/Å	D-H-A/°
O4	H4A	O7[1]	0.84(2)	1.80(2)	2.630(4)	168(5)
O4	H4B	O8[2]	0.85(2)	1.89(2)	2.730(4)	172(5)
O5	H5A	O1[3]	0.85(2)	1.88(2)	2.711(4)	165(5)
O5	H5B	O1[4]	0.83(2)	2.05(3)	2.833(4)	158(5)
O5	H5B	O4[4]	0.83(2)	2.48(5)	2.932(4)	115(4)
O6	H6A	O2[4]	0.847(19)	2.18(4)	2.854(4)	137(4)
O6	H6A	O3[5]	0.847(19)	2.49(4)	3.085(3)	128(4)
O6	H6B	O8[6]	0.85(2)	1.76(2)	2.586(3)	162(5)

[1]+X,3/2-Y,-1/2+Z; [2]1-X,2-Y,1-Z; [3]-X,2-Y,1-Z; [4]-1+X,+Y,+Z; [5]-X,1-Y,1-Z; [6]1-X,-1/2+Y,3/2-Z

Table A4.30 Torsion Angles for BIRM-15

A	B	C	D	Angle/˚	A	B	C	D	Angle/˚
C1	C2	C3	O7	-117.8(3)	Co1[2]	O3	P1	O1	37.8(2)
C1	C2	C3	O8	59.0(4)	Co1[2]	O3	P1	O2	163.12(17)
C2	C1	P1	O1	66.9(3)	Co2	O2	P1	C1	163.59(17)
C2	C1	P1	O2	-55.4(3)	Co2	O2	P1	O1	43.3(2)
C2	C1	P1	O3	-174.6(2)	Co2	O2	P1	O3	-80.89(19)
C2	C3	O7	Co1[1]	153.0(2)	Co2[2]	O3	P1	C1	79.8(2)
Co1	O1	P1	C1	-167.71(17)	Co2[2]	O3	P1	O1	-162.74(15)
Co1	O1	P1	O2	-47.8(2)	Co2[2]	O3	P1	O2	-37.5(2)
Co1	O1	P1	O3	76.91(19)	O8	C3	O7	Co1[1]	-23.6(5)
Co1[2]	O3	P1	C1	-79.7(2)	P1	C1	C2	C3	169.5(2)

[1]1+X,3/2-Y,1/2+Z; [2]1+X,+Y,+Z

Table A4.31 Hydrogen Atom Coordinates (Å×10^4) and Isotropic Displacement Parameters (Å^2×10^3) for BIRM-15

Atom	*x*	*y*	*z*	U(eq)
H1A	8507.59	7136.1	6466.98	12
H1B	8038.97	8541.2	6126.56	12
H2A	3955.44	8857.01	6762.36	15
H2B	3906.9	7382.41	7006	15
H4A	3630(80)	8290(50)	3280(30)	22
H4B	1690(100)	9320(40)	3100(20)	22
H5A	-2330(100)	10240(30)	4520(30)	21
H5B	-4060(70)	9230(50)	4480(30)	21
H6A	-3550(50)	4330(50)	5990(30)	13
H6B	-870(90)	4430(50)	6440(16)	13

BIRM-16

Table A4.32 Crystal data and structure refinement for BIRM-16

Identification code	BIRM-16
Empirical formula	$C_{12}H_{10}CoN_2O_4$
Formula weight	305.15
Temperature/K	100.00(10)
Crystal system	tetragonal
Space group	$P4_12_12$
a/Å	7.9644(5)
b/Å	7.9644(5)
c/Å	17.3395(17)
α/°	90
β/°	90
γ/°	90
Volume/Å^3	1099.87(18)
Z	4
ρ_{calc}g/cm^3	1.843
μ/mm^{-1}	1.572
F(000)	620
Crystal size/mm^3	0.233 × 0.16 × 0.094
Radiation	Mo Kα (λ = 0.71073)
2Θ range for data collection/°	6.948 to 59.08
Index ranges	-9 ≤ h ≤ 10, -10 ≤ k ≤ 10, -23 ≤ l ≤ 23
Reflections collected	6358
Independent reflections	1419 [R_{int} = 0.0348, R_{sigma} = 0.0320]
Data/restraints/parameters	1419/0/89
Goodness-of-fit on F^2	1.101
Final R indexes [I>=2σ (I)]	R_1 = 0.0250, wR_2 = 0.0560
Final R indexes [all data]	R_1 = 0.0269, wR_2 = 0.0572
Largest diff. peak/hole / e Å^{-3}	0.35/-0.32
Flack parameter	-0.004(12)

Table A4.33 Fractional Atomic Coordinates (×10^4) and Equivalent Isotropic Displacement Parameters (Å^2×10^3) for BIRM-16

Atom	*x*	*y*	*z*	U(eq)
C1	4699(3)	8227(3)	3796.2(10)	11.2(5)
C2	3834(3)	4148(3)	2608.6(11)	10.4(4)
C3	5019(3)	2879(3)	2607.2(11)	10.6(4)
C4	6690(3)	3310(3)	2500	8.8(6)
C5	8008(2)	1992(2)	2500	9.2(6)
C6	9493(3)	2212(3)	2908.6(11)	11.5(5)
C7	10671(3)	942(3)	2907.0(12)	10.8(4)
Co1	2349.3(3)	7650.7(3)	2500	6.47(12)
N1	4230(2)	5770(2)	2500	9.8(5)
N2	10478(2)	-478(2)	2500	8.6(5)
O1	3889.9(19)	9015.9(19)	3290.8(7)	10.5(3)
O2	6013(2)	8702.7(19)	4126.6(8)	11.3(3)

Table A4.34 Anisotropic Displacement Parameters (Å^2×10^3) for BIRM-16

Atom	U_{11}	U_{22}	U_{33}	U_{23}	U_{13}	U_{12}
C1	12.8(11)	10.3(11)	10.5(9)	-0.4(8)	1.2(9)	-1.8(9)
C2	7.2(10)	10.4(10)	13.7(9)	-0.2(9)	2.2(9)	-1.3(8)
C3	9.9(10)	8.4(10)	13.5(9)	0.3(9)	0.8(9)	0.0(8)
C4	9.5(8)	9.5(8)	7.5(12)	-1.3(9)	-1.3(9)	1.4(11)
C5	8.3(8)	8.3(8)	11.2(13)	2.7(9)	2.7(9)	-0.6(10)
C6	11.9(10)	10.2(11)	12.4(9)	-1.3(9)	-0.8(8)	0.3(9)
C7	10.6(11)	10.2(10)	11.5(9)	-0.5(9)	-1.5(8)	0.0(9)
Co1	5.93(14)	5.93(14)	7.56(19)	0.3(1)	0.3(1)	0.68(15)
N1	9.2(7)	9.2(7)	11.1(11)	-0.1(8)	-0.1(8)	2.3(9)
N2	8.9(7)	8.9(7)	8.0(10)	1.0(7)	1.0(7)	0.4(9)
O1	11.8(8)	8.7(7)	10.9(7)	-0.5(6)	-2.9(6)	1.3(7)
O2	10.9(8)	10.6(8)	12.5(6)	0.7(6)	-3.6(7)	-1.1(6)

Table A4.35 Bond Lengths for BIRM-16

Atom	Atom	Length/Å	Atom	Atom	Length/Å
C1	O1	1.256(2)	C6	C7	1.380(3)
C1	O2	1.251(2)	C7	N2	1.342(2)
C2	C3	1.383(3)	Co1	N1	2.119(2)
C2	N1	1.343(2)	Co1	N2[2]	2.107(2)
C3	C4	1.387(2)	Co1	O1[1]	2.1373(14)
C4	C5	1.485(4)	Co1	O1	2.1373(14)
C5	C6	1.389(2)	Co1	O2[3]	2.1421(14)
C5	C6[1]	1.389(2)	Co1	O2[4]	2.1421(14)

[1]1-Y,1-X,1/2-Z; [2]-1+X,1+Y,+Z; [3]-1/2+X,3/2-Y,3/4-Z; [4]-1/2+Y,3/2-X,-1/4+Z

Table A4.36 Bond Angles for BIRM-16

Atom	Atom	Atom	Angle/˚	Atom	Atom	Atom	Angle/˚
O2	C1	O1	126.7(2)	N2[4]	Co1	O1[1]	92.65(4)
N1	C2	C3	122.9(2)	N2[4]	Co1	O2[2]	90.25(4)
C2	C3	C4	118.3(2)	N2[4]	Co1	O2[3]	90.25(4)
C3	C4	C3[1]	119.6(3)	O1[1]	Co1	O1	174.70(8)
C3[1]	C4	C5	120.22(13)	O1	Co1	O2[3]	84.95(6)
C3	C4	C5	120.22(13)	O1	Co1	O2[2]	95.03(6)
C6	C5	C4	120.83(14)	O1[1]	Co1	O2[2]	84.94(6)
C6[1]	C5	C4	120.83(14)	O1[1]	Co1	O2[3]	95.03(6)
C6	C5	C6[1]	118.3(3)	O2[2]	Co1	O2[3]	179.49(9)
C7	C6	C5	119.0(2)	C2[1]	N1	C2	118.1(2)
N2	C7	C6	122.8(2)	C2[1]	N1	Co1	120.94(12)
N1	Co1	O1[1]	87.35(4)	C2	N1	Co1	120.94(12)
N1	Co1	O1	87.35(4)	C7	N2	C7[1]	118.0(3)
N1	Co1	O2[2]	89.75(4)	C7	N2	Co1[5]	121.00(13)
N1	Co1	O2[3]	89.75(4)	C7[1]	N2	Co1[5]	121.00(13)
N2[4]	Co1	N1	180	C1	O1	Co1	119.20(14)
N2[4]	Co1	O1	92.65(4)	C1	O2	Co1[6]	125.94(15)

[1]1-Y,1-X,1/2-Z; [2]-1/2+X,3/2-Y,3/4-Z; [3]-1/2+Y,3/2-X,-1/4+Z; [4]-1+X,1+Y,+Z; [5]1+X,-1+Y,+Z; [6]3/2-Y,1/2+X,1/4+Z

Table A4.37 Torsion Angles for BIRM-16

A	B	C	D	Angle/˚	A	B	C	D	Angle/˚
C2	C3	C4	C3[1]	-0.45(13)	C4	C5	C6	C7	178.65(13)
C2	C3	C4	C5	179.55(13)	C5	C6	C7	N2	2.9(3)
C3	C2	N1	C2[1]	-0.50(14)	C6[1]	C5	C6	C7	-1.35(13)
C3	C2	N1	Co1	179.50(14)	C6	C7	N2	C7[1]	-1.45(14)
C3	C4	C5	C6	-134.64(13)	C6	C7	N2	Co1[2]	178.55(14)
C3[1]	C4	C5	C6[1]	-134.64(13)	N1	C2	C3	C4	1.0(3)
C3[1]	C4	C5	C6	45.36(13)	O1	C1	O2	Co1[3]	178.99(15)
C3	C4	C5	C6[1]	45.36(13)	O2	C1	O1	Co1	155.33(17)

[1]1-Y,1-X,1/2-Z; [2]1+X,-1+Y,+Z; [3]3/2-Y,1/2+X,1/4+Z

Table A4.38 Hydrogen Atom Coordinates (Å×10^4) and Isotropic Displacement Parameters (Å^2×10^3) for BIRM-16

Atom	*x*	*y*	*z*	U(eq)
H1	4279.59	7183.43	3939.38	13
H2	2714.5	3865.72	2688.08	13
H3	4703.85	1764.5	2676.42	13
H6	9689.29	3200.26	3179.3	14
H7	11639.43	1075.53	3200.27	13

BIRM-16(Ni)

Table A4.39 Crystal data and structure refinement for BIRM-16(Ni)

Identification code	BIRM-16(Ni)
Empirical formula	$C_{12}H_{10}N_2NiO_4$
Formula weight	304.93
Temperature/K	100.01(10)
Crystal system	tetragonal
Space group	$P4_12_12$
a/Å	7.8952(2)
b/Å	7.8952(2)
c/Å	17.3062(6)
α/°	90
β/°	90
γ/°	90
Volume/Å^3	1078.77(7)
Z	4
ρ_{calc}g/cm^3	1.878
μ/mm^{-1}	2.747
F(000)	624
Crystal size/mm^3	0.153 × 0.105 × 0.084
Radiation	CuKα (λ = 1.54184)
2Θ range for data collection/°	12.322 to 145.824
Index ranges	-9 ≤ h ≤ 8, -9 ≤ k ≤ 9, -21 ≤ l ≤ 21
Reflections collected	9885
Independent reflections	1075 [R_{int} = 0.0755, R_{sigma} = 0.0247]
Data/restraints/parameters	1075/0/89
Goodness-of-fit on F^2	1.097
Final R indexes [I>=2σ (I)]	R_1 = 0.0365, wR_2 = 0.0902
Final R indexes [all data]	R_1 = 0.0372, wR_2 = 0.0917
Largest diff. peak/hole / e Å^{-3}	0.75/-0.24
Flack parameter	-0.05(3)

Table A4.40 Fractional Atomic Coordinates (×10^4) and Equivalent Isotropic Displacement Parameters (Å^2×10^3) for BIRM-16(Ni)

Atom	*x*	*y*	*z*	U(eq)
C(1)	6782(4)	313(4)	6203.3(14)	37.8(6)
C(2)	5684(3)	5921(3)	7917.8(15)	37.5(6)
C(3)	4500(4)	7200(4)	7921.8(15)	39.0(6)
C(4)	3003(4)	6997(4)	7500	35.8(8)
C(5)	1688(4)	8312(4)	7500	38.1(8)
C(6)	2117(3)	10014(4)	7399.2(16)	38.1(6)
C(7)	836(4)	11205(4)	7394.3(15)	38.7(6)
N(1)	5506(3)	4494(3)	7500	35.7(7)
N(2)	-805(3)	10805(3)	7500	36.2(7)
Ni(1)	7345.4(6)	2654.6(6)	7500	34.6(3)
O(1)	5978(3)	1105(2)	6721.3(10)	37.4(4)
O(2)	6311(3)	-1013(3)	5873.0(10)	38.3(5)

Table A4.41 Anisotropic Displacement Parameters (Å^2×10^3) for BIRM-16(Ni)

Atom	U_{11}	U_{22}	U_{33}	U_{23}	U_{13}	U_{12}
C(1)	37.0(13)	41.4(15)	35.0(12)	1.1(11)	-0.3(10)	0.2(12)
C(2)	38.6(14)	39.6(14)	34.4(13)	-0.5(11)	0.0(10)	-1.6(12)
C(3)	41.6(15)	39.4(14)	36.1(12)	-2.4(11)	-0.9(10)	-0.5(13)
C(4)	36.3(12)	36.3(12)	34.8(18)	2.4(10)	2.4(10)	-0.7(15)
C(5)	41.4(13)	41.4(13)	31.4(16)	-0.2(11)	-0.2(11)	0.2(17)
C(6)	37.0(13)	39.0(14)	38.3(12)	-1.4(12)	0.8(11)	-0.8(11)
C(7)	40.2(14)	38.2(13)	37.8(13)	3.0(10)	-0.4(11)	-2.7(12)
N(1)	38.2(10)	38.2(10)	30.8(14)	1.9(8)	1.9(8)	-2.8(13)
N(2)	36.9(10)	36.9(10)	34.7(15)	0.2(10)	0.2(10)	1.3(13)
Ni(1)	35.5(3)	35.5(3)	32.8(4)	0.14(17)	0.14(17)	0.9(3)
O(1)	38.6(10)	38.2(10)	35.2(9)	-2.1(8)	-0.7(8)	1.5(9)
O(2)	38.9(10)	38.8(10)	37.3(9)	-3.8(8)	1.6(8)	-1.3(8)

Table A4.42 Bond Lengths for BIRM-16(Ni)

Atom	Atom	Length/Å	Atom	Atom	Length/Å
C(1)	O(1)	1.264(3)	C(6)	C(7)	1.381(4)
C(1)	O(2)	1.249(3)	C(7)	N(2)	1.346(3)
C(2)	C(3)	1.376(4)	N(1)	Ni(1)	2.053(3)
C(2)	N(1)	1.346(3)	N(2)	Ni(1)[2]	2.065(3)
C(3)	C(4)	1.398(3)	Ni(1)	O(1)[1]	2.1162(19)
C(4)	C(5)	1.469(6)	Ni(1)	O(1)	2.1162(19)
C(5)	C(6)	1.396(3)	Ni(1)	O(2)[3]	2.1249(19)
C(5)	C(6)[1]	1.396(3)	Ni(1)	O(2)[4]	2.1249(19)

[1]1-Y,1-X,3/2-Z; [2]-1+X,1+Y,+Z; [3]3/2-X,1/2+Y,5/4-Z; [4]1/2-Y,-1/2+X,1/4+Z

Table A4.43 Bond Angles for BIRM-16 (Ni)

Atom	Atom	Atom	Angle/˚	Atom	Atom	Atom	Angle/˚
O(2)	C(1)	O(1)	126.1(3)	N(1)	Ni(1)	N(2)[3]	180
N(1)	C(2)	C(3)	123.1(3)	N(1)	Ni(1)	O(1)	92.76(5)
C(2)	C(3)	C(4)	119.2(3)	N(1)	Ni(1)	O(1)[1]	92.76(5)
C(3)	C(4)	C(3)[1]	117.8(4)	N(1)	Ni(1)	O(2)[4]	90.18(6)
C(3)	C(4)	C(5)	121.10(19)	N(1)	Ni(1)	O(2)[5]	90.18(6)
C(3)[1]	C(4)	C(5)	121.10(19)	N(2)[3]	Ni(1)	O(1)	87.24(5)
C(6)	C(5)	C(4)	120.59(19)	N(2)[3]	Ni(1)	O(1)[1]	87.24(5)
C(6)[1]	C(5)	C(4)	120.59(19)	N(2)[3]	Ni(1)	O(2)[5]	89.82(6)
C(6)	C(5)	C(6)[1]	118.8(4)	N(2)[3]	Ni(1)	O(2)[4]	89.82(6)
C(7)	C(6)	C(5)	118.6(3)	O(1)[1]	Ni(1)	O(1)	174.47(11)
N(2)	C(7)	C(6)	123.0(3)	O(1)[1]	Ni(1)	O(2)[4]	84.92(7)
C(2)[1]	N(1)	C(2)	117.6(4)	O(1)	Ni(1)	O(2)[5]	84.92(7)
C(2)[1]	N(1)	Ni(1)	121.22(18)	O(1)[1]	Ni(1)	O(2)[5]	95.06(7)
C(2)	N(1)	Ni(1)	121.22(18)	O(1)	Ni(1)	O(2)[4]	95.06(7)
C(7)[1]	N(2)	C(7)	118.0(3)	O(2)[4]	Ni(1)	O(2)[5]	179.65(11)
C(7)	N(2)	Ni(1)[2]	120.98(17)	C(1)	O(1)	Ni(1)	118.80(19)
C(7)[1]	N(2)	Ni(1)[2]	120.98(17)	C(1)	O(2)	Ni(1)[6]	126.25(19)

[1]1-Y,1-X,3/2-Z; [2]-1+X,1+Y,+Z; [3]1+X,-1+Y,+Z; [4]3/2-X,1/2+Y,5/4-Z; [5]1/2-Y,-1/2+X,1/4+Z; [6]1/2+Y,1/2-X,-1/4+Z

Table A4.44 Torsion Angles for BIRM-16(Ni)

A	B	C	D	Angle/˚	A	B	C	D	Angle/˚
C(2)	C(3)	C(4)	C(3)[1]	-1.28(17)	C(4)	C(5)	C(6)	C(7)	179.26(17)
C(2)	C(3)	C(4)	C(5)	178.72(17)	C(5)	C(6)	C(7)	N(2)	1.6(4)
C(3)	C(2)	N(1)	C(2)[1]	-1.38(18)	C(6)[1]	C(5)	C(6)	C(7)	-0.74(17)
C(3)	C(2)	N(1)	Ni(1)	178.62(18)	C(6)	C(7)	N(2)	C(7)[1]	-0.81(19)
C(3)	C(4)	C(5)	C(6)	45.92(18)	C(6)	C(7)	N(2)	Ni(1)[2]	179.19(19)
C(3)[1]	C(4)	C(5)	C(6)	-134.07(18)	N(1)	C(2)	C(3)	C(4)	2.7(4)
C(3)[1]	C(4)	C(5)	C(6)[1]	45.93(18)	O(1)	C(1)	O(2)	Ni(1)[3]	179.85(19)
C(3)	C(4)	C(5)	C(6)[1]	-134.08(18)	O(2)	C(1)	O(1)	Ni(1)	155.4(2)

[1]1-Y,1-X,3/2-Z; [2]-1+X,1+Y,+Z; [3]1/2+Y,1/2-X,-1/4+Z

Table A4.45 Hydrogen Atom Coordinates (Å×10^4) and Isotropic Displacement Parameters (Å^2×10^3) for BIRM-16 (Ni)

Atom	*x*	*y*	*z*	U(eq)
H(1)	7821.7	758.85	6053.89	45
H(2)	6652.32	6048.85	8217.98	45
H(3)	4692.24	8186.68	8201.6	47
H(6)	3240.62	10337.91	7336.65	46
H(7)	1119.64	12334.8	7314.28	46

BIRM-18

Table A5.1 Crystal data and structure refinement for BIRM-18.

Identification code	BIRM-18
Empirical formula	$C_{21}H_{39}N_3O_{15}P_2Zn_2$
Formula weight	766.23
Temperature/K	100.15
Crystal system	monoclinic
Space group	$P2_1/c$
a/Å	15.2833(7)
b/Å	19.4779(11)
c/Å	10.5400(5)
α/°	90
β/°	90.113(4)
γ/°	90
Volume/Å^3	3137.6(3)
Z	4
ρ_{calc}g/cm^3	1.622
μ/mm^{-1}	3.484
F(000)	1584
Crystal size/mm^3	0.08 × 0.015 × 0.015
Radiation	Cu Kα (λ = 1.54178)
2Θ range for data collection/°	5.782 to 140.094
Index ranges	-18 ≤ h ≤ 18, -23 ≤ k ≤ 23, -8 ≤ l ≤ 12
Reflections collected	28203
Independent reflections	5890 [R_{int} = 0.1277, R_{sigma} = 0.0980]
Data/restraints/parameters	5890/4/430
Goodness-of-fit on F^2	0.983
Final R indexes [I>=2σ (I)]	R_1 = 0.0638, wR_2 = 0.1462
Final R indexes [all data]	R_1 = 0.1188, wR_2 = 0.1737
Largest diff. peak/hole / e Å^{-3}	1.73/-0.77

Table A5.2 Fractional Atomic Coordinates (×10^4) and Equivalent Isotropic Displacement Parameters (Å^2×10^3) for BIRM-18

Atom	*x*	*y*	*z*	U(eq)
C1	9016(4)	4017(3)	6720(5)	20.2(12)
C2	8429(4)	4557(3)	6553(6)	28.0(14)
C3	8740(4)	5224(3)	6460(6)	28.5(14)
C4	9636(4)	5363(3)	6518(5)	21.4(12)
C5	10206(4)	4815(3)	6692(5)	22.6(12)
C6	9904(4)	4152(3)	6787(5)	24.2(13)
C7	9973(4)	6080(3)	6385(5)	22.1(12)
C8	6004(4)	4007(3)	3541(5)	23.1(13)
C9	5115(4)	4109(3)	3283(5)	23.6(13)
C10	4773(4)	4776(3)	3246(5)	24.8(13)
C11	5310(4)	5330(3)	3468(5)	21.0(12)
C12	6178(4)	5227(3)	3753(6)	27.1(13)
C13	6530(4)	4567(3)	3780(6)	26.6(13)
C14	4931(4)	6050(3)	3437(5)	21.5(12)
O1	7627(3)	3215(2)	6983(4)	25.4(9)
O2	8840(3)	2772(2)	5568(4)	24.6(9)
O3	9052(3)	2798(2)	7904(4)	22.7(9)
O4	9482(3)	6560(2)	6057(4)	25.6(9)
O5	10789(3)	6150(2)	6618(4)	25.6(9)
O6	6235(3)	2783(2)	4748(4)	23.3(9)
O7	7431(3)	3252(2)	3322(4)	24.3(9)
O8	6009(3)	2779(2)	2413(3)	22.3(9)
O9	4126(3)	6096(2)	3111(4)	23.6(9)
O10	5396(3)	6558(2)	3705(4)	26.9(9)
P1	8596.8(9)	3141.2(8)	6782.5(13)	19.3(3)
P2	6461.3(9)	3148.1(8)	3506.3(13)	18.5(3)
Zn1	6449.5(5)	3022.2(4)	6520.7(6)	20.3(2)
Zn2	8599.4(5)	2997.6(4)	3803.8(7)	19.3(2)
C101	7166(5)	4979(4)	9459(7)	40.0(17)
C102	7414(6)	3768(4)	9902(7)	41.7(17)
C103	8081(6)	4690(4)	11227(7)	45.2(19)
N101	7521(4)	4505(3)	10165(5)	33.2(12)
O101	7243(4)	5611(3)	9660(5)	50.2(14)
C201	4160(4)	2229(4)	4199(6)	35.6(16)
C202	5023(5)	1246(4)	4987(7)	36.1(16)
N201	4775(4)	1971(3)	5156(5)	33.3(13)
C301	9068(5)	7286(4)	-1182(6)	37.9(16)

C302	9953(5)	6375(5)	-222(7)	42.4(18)
N301	9490(4)	7024(4)	-30(6)	38.3(14)
O401	8148(4)	6469(4)	1438(6)	49.0(14)
O601	7711(3)	6794(3)	5992(5)	42.5(13)
O501	7102(3)	6918(3)	3484(4)	35.0(11)
O701	6717(3)	6685(3)	8096(4)	35.0(11)

Table A5.3 Anisotropic Displacement Parameters ($Å^2 \times 10^3$) for BIRM-18

Atom	U_{11}	U_{22}	U_{33}	U_{23}	U_{13}	U_{12}
C1	21(3)	13(3)	26(3)	0(2)	1(2)	-4(2)
C2	20(3)	20(3)	44(3)	-4(3)	0(2)	-1(3)
C3	24(3)	14(3)	47(4)	3(3)	2(3)	1(3)
C4	24(3)	15(3)	25(3)	-1(2)	3(2)	-6(3)
C5	18(3)	18(3)	32(3)	-2(2)	2(2)	-4(3)
C6	19(3)	22(3)	31(3)	2(2)	2(2)	2(3)
C7	20(3)	21(3)	25(3)	-3(2)	5(2)	-7(3)
C8	19(3)	20(3)	30(3)	2(2)	2(2)	4(3)
C9	26(3)	10(3)	35(3)	2(2)	0(2)	2(3)
C10	18(3)	23(4)	33(3)	4(2)	3(2)	2(3)
C11	24(3)	12(3)	26(3)	0(2)	0(2)	4(2)
C12	23(3)	15(3)	44(3)	-3(3)	2(2)	-3(3)
C13	24(3)	16(3)	40(3)	-4(3)	-1(2)	2(3)
C14	28(3)	14(3)	23(3)	-1(2)	6(2)	-5(3)
O1	13.7(19)	19(2)	43(2)	0.5(18)	0.2(16)	1.2(17)
O2	26(2)	17(2)	32(2)	2.5(17)	2.7(16)	1.9(18)
O3	21(2)	16(2)	32(2)	2.5(16)	0.7(15)	-5.4(17)
O4	23(2)	15(2)	39(2)	2.5(17)	4.6(17)	-0.9(18)
O5	21(2)	17(2)	39(2)	3.2(17)	-0.3(16)	-6.3(18)
O6	23(2)	16(2)	30(2)	-1.6(16)	-0.2(15)	4.4(17)
O7	20(2)	17(2)	37(2)	1.2(17)	0.7(16)	1.7(18)
O8	21(2)	16(2)	30(2)	-3.6(16)	-0.3(15)	3.0(17)
O9	21(2)	17(2)	33(2)	-2.7(17)	3.6(16)	8.1(18)
O10	23(2)	15(2)	42(2)	2.9(18)	4.2(17)	0.8(18)
P1	17.6(7)	13.1(8)	27.3(7)	0.7(5)	1.8(5)	-2.5(6)
P2	16.0(7)	12.0(8)	27.5(7)	-1.6(5)	1.6(5)	1.4(6)
Zn1	17.3(4)	14.0(4)	29.6(4)	1.5(3)	2.6(3)	-0.1(3)
Zn2	16.5(4)	12.3(4)	29.3(4)	-1.0(3)	2.9(3)	-0.5(3)
C101	34(4)	46(5)	40(4)	-2(3)	-8(3)	10(3)
C102	42(4)	39(4)	44(4)	-8(3)	2(3)	3(4)

C103	49(5)	41(5)	45(4)	1(3)	-10(3)	6(4)
N101	35(3)	30(3)	35(3)	-4(2)	-3(2)	4(3)
O101	54(4)	47(4)	50(3)	8(3)	-3(2)	10(3)
C201	24(3)	44(5)	39(3)	2(3)	3(3)	-6(3)
C202	38(4)	25(4)	45(4)	-2(3)	11(3)	-5(3)
N201	29(3)	33(4)	38(3)	-1(3)	1(2)	-4(3)
C301	34(4)	37(5)	43(4)	-6(3)	5(3)	-3(3)
C302	30(4)	51(5)	46(4)	0(3)	6(3)	4(4)
N301	40(3)	32(4)	43(3)	-9(3)	4(3)	-13(3)
O401	38(3)	52(4)	57(3)	-4(3)	17(2)	0(3)
O601	27(2)	51(4)	49(3)	5(2)	8(2)	14(3)
O501	26(2)	33(3)	46(3)	-3(2)	4.0(19)	-3(2)
O701	29(2)	36(3)	40(3)	5(2)	4.9(19)	2(2)

Table A5.4 Bond Lengths for BIRM-18

Atom	Atom	Length/Å	Atom	Atom	Length/Å
C1	C2	1.394(9)	O1	Zn1	1.902(4)
C1	C6	1.384(8)	O2	P1	1.516(4)
C1	P1	1.823(6)	O2	Zn2	1.945(4)
C2	C3	1.386(9)	O3	P1	1.525(4)
C3	C4	1.399(9)	O3	Zn2[1]	1.945(4)
C4	C5	1.390(9)	O5	Zn2[2]	1.956(4)
C4	C7	1.494(9)	O6	P2	1.530(4)
C5	C6	1.376(9)	O6	Zn1	1.953(4)
C7	O4	1.248(8)	O7	P2	1.508(4)
C7	O5	1.277(7)	O7	Zn2	1.921(4)
C8	C9	1.400(8)	O8	P2	1.522(4)
C8	C13	1.376(9)	O8	Zn1[3]	1.944(4)
C8	P2	1.814(6)	O9	Zn1[4]	1.969(4)
C9	C10	1.400(9)	C101	N101	1.302(10)
C10	C11	1.374(9)	C101	O101	1.255(10)
C11	C12	1.375(9)	C102	N101	1.471(10)
C11	C14	1.518(8)	C103	N101	1.454(9)
C12	C13	1.393(9)	C201	N201	1.466(9)
C14	O9	1.279(7)	C202	N201	1.473(10)
C14	O10	1.251(8)	C301	N301	1.465(10)
O1	P1	1.504(4)	C302	N301	1.461(11)

[1]+X,1/2-Y,1/2+Z; [2]2-X,1-Y,1-Z; [3]+X,1/2-Y,-1/2+Z; [4]1-X,1-Y,1-Z

Table A5.5 Bond Angles for BIRM-18

Atom	Atom	Atom	Angle/˚	Atom	Atom	Atom	Angle/˚
C2	C1	P1	119.0(5)	P2	O8	Zn1[3]	126.0(2)
C6	C1	C2	119.6(6)	C14	O9	Zn1[4]	116.0(4)
C6	C1	P1	121.4(5)	O1	P1	C1	105.2(3)
C3	C2	C1	119.7(6)	O1	P1	O2	114.0(2)
C2	C3	C4	121.0(6)	O1	P1	O3	112.4(2)
C3	C4	C7	121.0(6)	O2	P1	C1	109.1(3)
C5	C4	C3	118.1(6)	O2	P1	O3	109.5(2)
C5	C4	C7	120.9(5)	O3	P1	C1	106.2(2)
C6	C5	C4	121.3(5)	O6	P2	C8	108.9(3)
C5	C6	C1	120.3(6)	O7	P2	C8	104.9(3)
O4	C7	C4	121.2(5)	O7	P2	O6	113.4(2)
O4	C7	O5	124.0(6)	O7	P2	O8	114.2(2)
O5	C7	C4	114.8(5)	O8	P2	C8	106.1(2)
C9	C8	P2	120.0(5)	O8	P2	O6	108.9(2)
C13	C8	C9	119.3(6)	O1	Zn1	O6	116.73(18)
C13	C8	P2	120.7(5)	O1	Zn1	O8[1]	111.29(18)
C8	C9	C10	119.9(6)	O1	Zn1	O9[4]	101.55(18)
C11	C10	C9	120.0(6)	O6	Zn1	O9[4]	108.83(17)
C10	C11	C12	119.9(6)	O8[1]	Zn1	O6	102.34(17)
C10	C11	C14	119.6(5)	O8[1]	Zn1	O9[4]	116.74(18)
C12	C11	C14	120.5(6)	O2	Zn2	O3[3]	102.68(17)
C11	C12	C13	120.7(6)	O2	Zn2	O5[2]	108.65(18)
C8	C13	C12	120.2(6)	O3[3]	Zn2	O5[2]	113.21(18)
O9	C14	C11	115.9(5)	O7	Zn2	O2	119.01(17)
O10	C14	C11	120.6(6)	O7	Zn2	O3[3]	114.06(17)
O10	C14	O9	123.4(6)	O7	Zn2	O5[2]	99.54(18)
P1	O1	Zn1	151.3(3)	O101	C101	N101	124.1(7)
P1	O2	Zn2	130.9(3)	C101	N101	C102	122.6(6)
P1	O3	Zn2[1]	124.4(2)	C101	N101	C103	120.5(7)
C7	O5	Zn2[2]	120.9(4)	C103	N101	C102	116.9(6)
P2	O6	Zn1	132.0(3)	C201	N201	C202	114.2(6)
P2	O7	Zn2	147.6(3)	C302	N301	C301	113.5(6)

[1]+X,1/2-Y,1/2+Z; [2]2-X,1-Y,1-Z; [3]+X,1/2-Y,-1/2+Z; [4]1-X,1-Y,1-Z

Table A5.6 Hydrogen Bonds for BIRM-18

D	H	A	d(D-H)/Å	d(H-A)/Å	d(D-A)/Å	D-H-A/°
N201	H20G	O6	0.83(10)	1.94(10)	2.769(8)	175(9)
N201	H20H	O701[1]	0.88(9)	2.32(9)	2.986(8)	132(7)
N301	H30G	O401	0.96(9)	1.86(9)	2.789(9)	161(7)
N301	H30H	O2[2]	0.86(2)	2.46(7)	2.995(8)	121(7)
N301	H30H	O3[3]	0.86(2)	2.60(7)	3.176(7)	125(7)
N301	H30H	O4[4]	0.86(2)	2.30(6)	2.987(8)	137(8)
O401	H40A	O501	0.81(10)	2.03(11)	2.826(8)	168(10)
O401	H40B	O101[5]	0.87(10)	2.00(10)	2.865(9)	172(9)
O601	H60A	O4	0.78(10)	1.97(11)	2.746(7)	176(10)
O601	H60B	O501	0.856(19)	1.97(2)	2.811(7)	169(9)
O501	H50A	O701[4]	0.83(11)	2.01(11)	2.815(8)	163(8)
O501	H50B	O10	0.84(10)	1.89(10)	2.709(7)	162(9)
O701	H70A	O601	0.85(2)	1.85(2)	2.699(7)	177(10)
O701	H70B	O101	0.82(10)	1.97(10)	2.781(8)	168(9)

[1]1-X,-1/2+Y,3/2-Z; [2]2-X,1/2+Y,1/2-Z; [3]2-X,1-Y,1-Z; [4]+X,3/2-Y,-1/2+Z; [5]+X,+Y,-1+Z

Table A5.7 Torsion Angles for BIRM-18

A	B	C	D	Angle/˚	A	B	C	D	Angle/˚
C1	C2	C3	C4	0.6(9)	C12	C11	C14	O10	-2.0(8)
C2	C1	C6	C5	0.1(8)	C13	C8	C9	C10	1.1(8)
C2	C1	P1	O1	-14.9(5)	C13	C8	P2	O6	102.8(5)
C2	C1	P1	O2	107.8(5)	C13	C8	P2	O7	-18.9(6)
C2	C1	P1	O3	-134.3(5)	C13	C8	P2	O8	-140.1(5)
C2	C3	C4	C5	-1.0(9)	C14	C11	C12	C13	-179.8(5)
C2	C3	C4	C7	178.4(5)	O4	C7	O5	Zn2[1]	-10.8(7)
C3	C4	C5	C6	0.9(8)	O10	C14	O9	Zn1[2]	-15.8(7)
C3	C4	C7	O4	-9.3(8)	P1	C1	C2	C3	-177.8(5)
C3	C4	C7	O5	171.3(5)	P1	C1	C6	C5	177.7(4)
C4	C5	C6	C1	-0.5(9)	P2	C8	C9	C10	-176.7(5)
C4	C7	O5	Zn2[1]	168.5(3)	P2	C8	C13	C12	177.4(5)
C5	C4	C7	O4	170.1(5)	Zn1	O1	P1	C1	127.0(6)
C5	C4	C7	O5	-9.3(8)	Zn1	O1	P1	O2	7.5(7)
C6	C1	C2	C3	-0.2(9)	Zn1	O1	P1	O3	-117.9(6)
C6	C1	P1	O1	167.5(4)	Zn1	O6	P2	C8	-56.0(4)
C6	C1	P1	O2	-69.8(5)	Zn1	O6	P2	O7	60.4(4)
C6	C1	P1	O3	48.2(5)	Zn1	O6	P2	O8	-171.3(3)

C7	C4	C5	C6	-178.5(5)	Zn1[3]	O8	P2	C8	158.3(3)
C8	C9	C10	C11	-0.2(9)	Zn1[3]	O8	P2	O6	-84.6(3)
C9	C8	C13	C12	-0.5(9)	Zn1[3]	O8	P2	O7	43.3(4)
C9	C8	P2	O6	-79.4(5)	Zn2	O2	P1	C1	-56.5(4)
C9	C8	P2	O7	158.9(4)	Zn2	O2	P1	O1	60.7(4)
C9	C8	P2	O8	37.7(5)	Zn2	O2	P1	O3	-172.3(3)
C9	C10	C11	C12	-1.5(9)	Zn2[4]	O3	P1	C1	157.3(3)
C9	C10	C11	C14	-179.5(5)	Zn2[4]	O3	P1	O1	42.8(4)
C10	C11	C12	C13	2.2(9)	Zn2[4]	O3	P1	O2	-85.1(3)
C10	C11	C14	O9	-4.8(7)	Zn2	O7	P2	C8	136.1(5)
C10	C11	C14	O10	176.0(5)	Zn2	O7	P2	O6	17.4(6)
C11	C12	C13	C8	-1.2(9)	Zn2	O7	P2	O8	-108.2(5)
C11	C14	O9	Zn1[2]	165.0(4)	O101	C101	N101	C102	179.8(7)
C12	C11	C14	O9	177.2(5)	O101	C101	N101	C103	-3.2(12)

[1]2-X,1-Y,1-Z; [2]1-X,1-Y,1-Z; [3]+X,1/2-Y,-1/2+Z; [4]+X,1/2-Y,1/2+Z

Table A5.8 Hydrogen Atom Coordinates (Å×10^4) and Isotropic Displacement Parameters (Å^2×10^3) for BIRM-18

Atom	*x*	*y*	*z*	U(eq)
H2	7831.1	4470.92	6505.23	34
H3	8345.73	5583.37	6357.79	34
H5	10804.56	4898.81	6744.58	27
H6	10297.85	3792.85	6896.04	29
H9	4751.28	3734.52	3135.51	28
H10	4182.79	4844.31	3072.33	30
H12	6534.74	5601.72	3931.25	33
H13	7120.35	4504.31	3958.24	32
H101	6836.18	4839.88	8763.06	48
H10A	7124	3552.37	10603.76	62
H10B	7979.14	3562.01	9785	62
H10C	7070.9	3708.91	9146.69	62
H10D	8652.39	4807.67	10919.27	68
H10E	8125.42	4308.91	11800.25	68
H10F	7834.64	5077.25	11663.92	68
H20A	4406.97	2169.8	3369.56	53
H20B	4050.15	2707.44	4347	53
H20C	3620.8	1978.16	4254.59	53
H20D	5300.83	1188.83	4177.95	54

H20E	4508.82	963.79	5024.44	54
H20F	5420.98	1113.2	5648.78	54
H30A	9500.56	7349.18	-1831.01	57
H30B	8791.94	7717.35	-1000.25	57
H30C	8636.48	6963.11	-1468.27	57
H30D	10384.99	6432.07	-873.06	64
H30E	9542.92	6027.13	-473.8	64
H30F	10233.59	6240.82	554.48	64
H20G	5230(60)	2190(50)	5050(70)	42
H20H	4550(60)	2060(50)	5910(80)	42
H30G	9070(60)	6910(50)	610(70)	42
H30H	9780(50)	7350(30)	330(70)	42
H40A	7900(70)	6650(50)	2030(90)	52
H40B	7830(70)	6240(50)	900(80)	52
H60A	8210(70)	6740(50)	5990(80)	52
H60B	7550(60)	6780(50)	5210(30)	52
H50A	7000(70)	7340(60)	3530(80)	52
H50B	6600(70)	6750(50)	3430(80)	52
H70A	7020(50)	6710(50)	7420(50)	52
H70B	6890(60)	6410(50)	8630(80)	52

BIRM-19

Table A5.9 Crystal data and structure refinement for BIRM-19

Identification code	BIRM-19
Empirical formula	$C_{18}H_{24}N_2O_{10}P_2Zn_2$
Formula weight	621.07
Temperature/K	100.01(10)
Crystal system	monoclinic
Space group	C2/c
a/Å	25.9158(7)
b/Å	8.4976(2)
c/Å	25.6910(7)
α/°	90
β/°	90.368(3)
γ/°	90
Volume/Å^3	5657.6(3)
Z	8
ρ_{calc}g/cm^3	1.458
μ/mm^{-1}	3.586
F(000)	2528
Crystal size/mm^3	0.252 × 0.079 × 0.029
Radiation	Cu Kα (λ = 1.54184)
2Θ range for data collection/°	9.726 to 146.41
Index ranges	-31 ≤ h ≤ 28, -8 ≤ k ≤ 10, -27 ≤ l ≤ 31
Reflections collected	12303
Independent reflections	5381 [R_{int} = 0.0373, R_{sigma} = 0.0487]
Data/restraints/parameters	5381/93/369
Goodness-of-fit on F^2	1.051
Final R indexes [I>=2σ (I)]	R_1 = 0.0526, wR_2 = 0.1437
Final R indexes [all data]	R_1 = 0.0672, wR_2 = 0.1563
Largest diff. peak/hole / e Å^{-3}	0.81/-0.84

Table A5.10 Fractional Atomic Coordinates (×10^4) and Equivalent Isotropic Displacement Parameters (Å^2×10^3) for BIRM-19

Atom	*x*	*y*	*z*	U(eq)
C1	2421.4(18)	2025(6)	3520.5(17)	33.1(10)
C2	2028(3)	904(8)	3561(2)	55.4(16)
C3	1727(3)	556(8)	3126(2)	57.3(16)
C4	1820.1(19)	1276(6)	2650.7(19)	38.8(11)
C5	2220(3)	2307(8)	2610(2)	57.1(17)
C6	2525(2)	2668(8)	3046(2)	58.6(18)
C7	1507(2)	800(7)	2176(2)	44.3(13)
C8	3915.7(16)	6164(5)	5284.7(16)	24.9(8)
C9	4305.0(19)	7108(6)	5471(2)	42.3(13)
C10	4757.9(19)	6456(6)	5677(2)	43.2(13)
C11	4826.0(16)	4858(5)	5687.8(17)	27.8(9)
C12	4437.3(18)	3909(6)	5506(2)	37.5(11)
C13	3981.7(19)	4546(6)	5311(2)	37.5(11)
C14	5335.1(17)	4184(6)	5877.6(17)	30.3(9)
O1	2385.3(13)	3560(4)	4402.9(12)	38.5(8)
O2	3246.2(13)	3469(4)	3920.7(13)	37.1(8)
O3	2936.3(12)	1117(4)	4383.9(12)	33.7(7)
O4	1184.6(19)	-295(6)	2214.1(17)	70.4(14)
O5	1617.9(15)	1492(4)	1754.7(13)	44.6(9)
O6	2902.3(11)	6001(4)	5212.4(12)	30.1(7)
O7	3382.6(12)	6920(4)	4411.7(12)	31.7(7)
O8	3303.2(11)	8696(4)	5177.6(13)	33.9(7)
O9	5678.1(12)	5203(4)	5990.7(13)	35.8(7)
O10	5390.9(13)	2732(4)	5915.4(15)	42.8(9)
P1	2771.9(4)	2609.3(13)	4099.7(4)	28.3(3)
P2	3335.3(4)	6986.1(12)	4999.8(4)	24.7(2)
Zn1	2290.3(2)	4935.1(6)	4983.8(2)	25.29(17)
Zn2	3614.7(2)	5435.9(7)	3883.7(2)	26.08(17)
C101	4195(2)	737(7)	4424(4)	80(3)
C102	3909(4)	161(10)	3511(3)	98(3)
N101	3859(2)	-146(5)	4071(2)	53.1(12)
C201	1843(8)	6460(30)	3511(11)	83(4)
C202	1251(7)	4406(16)	3695(5)	65(4)
N201	1383(7)	5641(19)	3366(5)	79(4)
C21A	1568(6)	6010(20)	3693(6)	57(3)
C22A	2369(7)	7390(30)	3786(9)	79(5)
N21A	2084(7)	6280(20)	3504(7)	69(4)
C21B	4227(14)	60(40)	2262(13)	108(9)
C22B	4105(14)	2480(30)	2006(11)	105(8)
N21B	3828(10)	1050(30)	2095(10)	109(8)

Table A5.11 Anisotropic Displacement Parameters ($Å^2×10^3$) for BIRM-19

Atom	U_{11}	U_{22}	U_{33}	U_{23}	U_{13}	U_{12}
C1	38(2)	26(2)	35(2)	-4.8(18)	-11.3(18)	-3(2)
C2	69(4)	55(4)	42(3)	3(3)	-21(3)	-28(3)
C3	63(4)	57(4)	52(3)	-3(3)	-18(3)	-28(3)
C4	39(3)	36(3)	42(2)	-12(2)	-15(2)	-2(2)
C5	69(4)	68(4)	34(2)	6(3)	-18(2)	-31(3)
C6	64(4)	75(5)	36(3)	7(3)	-18(2)	-42(4)
C7	44(3)	43(3)	46(3)	-13(2)	-19(2)	5(3)
C8	22.2(19)	19(2)	33.3(19)	1.2(16)	-7.8(15)	4.6(17)
C9	29(2)	15(2)	82(4)	2(2)	-24(2)	3(2)
C10	27(2)	19(2)	83(4)	-2(2)	-27(2)	1(2)
C11	24(2)	25(2)	34(2)	3.3(17)	-7.8(16)	6.3(18)
C12	33(2)	22(2)	57(3)	0(2)	-18(2)	5(2)
C13	31(2)	20(2)	62(3)	0(2)	-24(2)	2(2)
C14	24(2)	31(2)	36(2)	6.7(18)	-10.3(16)	5.0(19)
O1	40.8(18)	32.9(18)	41.4(17)	-15.1(14)	-16.8(14)	9.5(16)
O2	42.1(19)	25.8(17)	43.1(17)	-2.3(14)	-13.1(14)	-5.2(15)
O3	38.4(17)	20.9(16)	41.7(16)	3.9(13)	-9.9(13)	2.4(14)
O4	70(3)	84(4)	56(2)	-8(2)	-25(2)	-33(3)
O5	56(2)	37(2)	40.3(18)	-8.3(15)	-23.0(16)	0.3(18)
O6	21.5(14)	28.1(17)	40.5(16)	2.5(13)	-10.9(12)	-2.3(13)
O7	31.1(16)	24.7(16)	39.2(16)	2.5(13)	-13.1(12)	6.6(14)
O8	26.7(15)	19.2(16)	55.6(19)	-8.5(14)	-21.6(13)	6.8(13)
O9	25.3(15)	35.2(19)	46.5(18)	-1.8(14)	-16.9(13)	5.0(14)
O10	28.1(17)	26.8(18)	73(2)	13.0(17)	-13.1(15)	5.6(15)
P1	31.9(6)	20.6(5)	32.1(5)	-3.0(4)	-13.3(4)	-1.4(5)
P2	20.8(5)	15.4(5)	37.7(5)	-3.0(4)	-13.8(4)	3.8(4)
Zn1	24.5(3)	16.2(3)	35.0(3)	-2.8(2)	-13.6(2)	2.8(2)
Zn2	23.3(3)	20.9(3)	33.8(3)	3.1(2)	-13.8(2)	2.1(2)
C101	37(3)	27(3)	177(9)	2(4)	-17(4)	1(3)
C102	130(8)	71(5)	95(6)	33(5)	50(6)	57(6)
N101	57(3)	24(2)	78(3)	12(2)	6(2)	3(2)
C201	102(11)	70(9)	78(8)	2(8)	11(9)	38(8)
C202	110(10)	37(7)	46(6)	-15(5)	-42(7)	28(7)
N201	109(9)	81(8)	47(6)	-16(5)	-8(6)	35(7)
C21A	76(8)	60(8)	34(6)	-3(6)	-16(6)	30(7)
C22A	68(9)	91(11)	79(10)	-21(9)	13(8)	31(8)
N21A	88(9)	63(8)	57(7)	9(6)	14(7)	36(8)
C21B	150(20)	105(16)	72(11)	-36(12)	-69(13)	37(14)

C22B	140(20)	101(16)	71(11)	-40(12)	-80(12)	36(14)
N21B	148(19)	106(15)	74(10)	-36(12)	-71(12)	36(14)

Table A5.12 Bond Lengths for BIRM-19

Atom	Atom	Length/Å	Atom	Atom	Length/Å
C1	C2	1.399(8)	O1	Zn1	1.913(3)
C1	C6	1.366(7)	O2	P1	1.504(4)
C1	P1	1.808(4)	O2	Zn2	1.928(3)
C2	C3	1.390(7)	O3	P1	1.522(3)
C3	C4	1.389(8)	O3	Zn1[1]	1.948(3)
C4	C5	1.362(8)	O5	Zn2[2]	1.961(3)
C4	C7	1.515(6)	O6	P2	1.505(3)
C5	C6	1.400(7)	O6	Zn1	1.915(3)
C7	O4	1.255(7)	O7	P2	1.518(3)
C7	O5	1.267(7)	O7	Zn2	1.950(3)
C8	C9	1.373(6)	O8	P2	1.525(3)
C8	C13	1.387(6)	O8	Zn1[3]	1.970(3)
C8	P2	1.809(4)	O9	Zn2[4]	1.937(3)
C9	C10	1.398(6)	C101	N101	1.460(9)
C10	C11	1.370(6)	C102	N101	1.468(10)
C11	C12	1.370(6)	C201	N201	1.427(15)
C11	C14	1.516(5)	C202	N201	1.391(15)
C12	C13	1.390(6)	C21A	N21A	1.444(14)
C14	O9	1.273(6)	C22A	N21A	1.399(14)
C14	O10	1.246(6)	C21B	N21B	1.398(16)
O1	P1	1.508(4)	C22B	N21B	1.435(16)

[1]1/2-X,1/2-Y,1-Z; [2]1/2-X,-1/2+Y,1/2-Z; [3]1/2-X,3/2-Y,1-Z; [4]1-X,1-Y,1-Z

Table A5.13 Bond Angles for BIRM-19

Atom	Atom	Atom	Angle/˚	Atom	Atom	Atom	Angle/˚
C2	C1	P1	119.2(4)	P2	O7	Zn2	138.02(19)
C6	C1	C2	119.1(4)	P2	O8	Zn1[3]	122.91(16)
C6	C1	P1	121.6(4)	C14	O9	Zn2[4]	120.4(3)
C3	C2	C1	119.4(5)	O1	P1	C1	103.9(2)
C4	C3	C2	120.9(6)	O1	P1	O3	112.5(2)
C3	C4	C7	119.7(5)	O2	P1	C1	106.8(2)
C5	C4	C3	119.2(4)	O2	P1	O1	116.4(2)
C5	C4	C7	120.9(5)	O2	P1	O3	108.91(19)
C4	C5	C6	120.4(5)	O3	P1	C1	107.7(2)
C1	C6	C5	120.8(5)	O6	P2	C8	104.97(18)
O4	C7	C4	119.3(5)	O6	P2	O7	113.95(18)
O4	C7	O5	124.4(4)	O6	P2	O8	112.26(19)
O5	C7	C4	116.1(5)	O7	P2	C8	108.44(19)
C9	C8	C13	118.2(4)	O7	P2	O8	109.76(19)
C9	C8	P2	121.5(3)	O8	P2	C8	107.07(18)
C13	C8	P2	120.3(3)	O1	Zn1	O3[1]	114.28(15)
C8	C9	C10	120.9(4)	O1	Zn1	O6	114.68(15)
C11	C10	C9	120.6(4)	O1	Zn1	O8[3]	107.50(13)
C10	C11	C14	119.5(4)	O3[1]	Zn1	O8[3]	101.98(14)
C12	C11	C10	118.8(4)	O6	Zn1	O3[1]	102.41(13)
C12	C11	C14	121.6(4)	O6	Zn1	O8[3]	115.41(13)
C11	C12	C13	121.0(4)	O2	Zn2	O5[5]	106.77(14)
C8	C13	C12	120.5(4)	O2	Zn2	O7	111.81(15)
O9	C14	C11	114.9(4)	O2	Zn2	O9[4]	102.54(15)
O10	C14	C11	120.0(4)	O7	Zn2	O5[5]	101.01(15)
O10	C14	O9	125.1(4)	O9[4]	Zn2	O5[5]	123.59(16)
P1	O1	Zn1	145.1(2)	O9[4]	Zn2	O7	111.18(13)
P1	O2	Zn2	147.4(2)	C101	N101	C102	117.4(7)
P1	O3	Zn1[1]	134.2(2)	C202	N201	C201	114.7(16)
C7	O5	Zn2[2]	115.6(3)	C22A	N21A	C21A	114.9(15)
P2	O6	Zn1	140.31(19)	C21B	N21B	C22B	101(2)

[1]1/2-X,1/2-Y,1-Z; [2]1/2-X,-1/2+Y,1/2-Z; [3]1/2-X,3/2-Y,1-Z; [4]1-X,1-Y,1-Z; [5]1/2-X,1/2+Y,1/2-Z

Table A5.14 Hydrogen Bonds for BIRM-19

D	H	A	d(D-H)/Å	d(H-A)/Å	d(D-A)/Å	D-H-A/°
N101	H10G	O3	0.89	1.89	2.747(6)	161.2
N101	H10H	O7[1]	0.89	2.26	2.919(6)	130.6
N101	H10H	O10[2]	0.89	2.24	2.934(6)	134.7

[1]+X,-1+Y,+Z; [2]1-X,-Y,1-Z

Table A5.15 Torsion Angles for BIRM-19

A	B	C	D	Angle/˚	A	B	C	D	Angle/˚
C1	C2	C3	C4	1.7(11)	C12	C11	C14	O9	173.9(4)
C2	C1	C6	C5	4.7(10)	C12	C11	C14	O10	-6.5(7)
C2	C1	P1	O1	-70.8(5)	C13	C8	C9	C10	0.6(8)
C2	C1	P1	O2	165.6(5)	C13	C8	P2	O6	43.3(4)
C2	C1	P1	O3	48.7(5)	C13	C8	P2	O7	-78.8(4)
C2	C3	C4	C5	1.5(10)	C13	C8	P2	O8	162.8(4)
C2	C3	C4	C7	176.2(6)	C14	C11	C12	C13	-176.9(5)
C3	C4	C5	C6	-1.6(10)	O4	C7	O5	Zn2[1]	-14.6(8)
C3	C4	C7	O4	-3.4(9)	O10	C14	O9	Zn2[2]	11.7(7)
C3	C4	C7	O5	-179.2(5)	P1	C1	C2	C3	174.2(5)
C4	C5	C6	C1	-1.5(11)	P1	C1	C6	C5	-174.2(6)
C4	C7	O5	Zn2[1]	160.9(4)	P2	C8	C9	C10	-178.1(5)
C5	C4	C7	O4	171.2(6)	P2	C8	C13	C12	176.9(4)
C5	C4	C7	O5	-4.6(8)	Zn1	O1	P1	C1	-169.5(4)
C6	C1	C2	C3	-4.7(10)	Zn1	O1	P1	O2	-52.4(5)
C6	C1	P1	O1	108.1(5)	Zn1	O1	P1	O3	74.3(5)
C6	C1	P1	O2	-15.5(6)	Zn1[3]	O3	P1	C1	-106.7(3)
C6	C1	P1	O3	-132.4(5)	Zn1[3]	O3	P1	O1	7.2(3)
C7	C4	C5	C6	-176.3(6)	Zn1[3]	O3	P1	O2	137.9(3)
C8	C9	C10	C11	1.1(9)	Zn1	O6	P2	C8	-133.8(3)
C9	C8	C13	C12	-1.9(8)	Zn1	O6	P2	O7	-15.4(4)
C9	C8	P2	O6	-137.9(4)	Zn1	O6	P2	O8	110.2(3)
C9	C8	P2	O7	99.9(4)	Zn1[4]	O8	P2	C8	-175.1(2)
C9	C8	P2	O8	-18.4(5)	Zn1[4]	O8	P2	O6	-60.4(3)
C9	C10	C11	C12	-1.6(8)	Zn1[4]	O8	P2	O7	67.4(3)
C9	C10	C11	C14	175.7(5)	Zn2	O2	P1	C1	112.9(4)
C10	C11	C12	C13	0.4(8)	Zn2	O2	P1	O1	-2.6(4)
C10	C11	C14	O9	-3.4(7)	Zn2	O2	P1	O3	-131.1(4)

C10	C11	C14	O10	176.2(5)	Zn2	O7	P2	C8	43.1(3)
C11	C12	C13	C8	1.4(8)	Zn2	O7	P2	O6	-73.3(3)
C11	C14	O9	Zn2[2]	-168.7(3)	Zn2	O7	P2	O8	159.8(3)

[1]1/2-X,-1/2+Y,1/2-Z; [2]1-X,1-Y,1-Z; [3]1/2-X,1/2-Y,1-Z; [4]1/2-X,3/2-Y,1-Z

Table A5.16 Hydrogen Atom Coordinates (Å×10^4) and Isotropic Displacement Parameters (Å^2×10^3) for BIRM-19

Atom	*x*	*y*	*z*	U(eq)
H2	1968.75	397.08	3875.58	66
H3	1459.31	-167.65	3154.37	69
H5	2290.93	2773.8	2290.98	69
H6	2802.34	3355.67	3010.9	70
H9	4267	8195.89	5460.55	51
H10	5015.01	7113.1	5806.97	52
H12	4478.74	2822.15	5514.13	45
H13	3719.2	3882.88	5196.1	45
H10A	4156.06	1843.34	4358.42	121
H10B	4547.43	436.75	4367.02	121
H10C	4102.79	512.2	4777.12	121
H10D	3654.85	-437.99	3323.46	148
H10E	4247.65	-140.97	3398.9	148
H10F	3857.67	1261.65	3444.99	148
H10G	3533.92	47.16	4159.88	64
H10H	3915.93	-1166.46	4124.34	64
H20A	2006.31	6865.26	3204.62	125
H20B	2073.65	5753.43	3687.24	125
H20C	1757.2	7317.4	3738.59	125
H20D	1439.48	3479.09	3597.6	97
H20E	887.87	4203.8	3666.72	97
H20F	1336	4681.26	4047.87	97
H20G	1123.1	6324.31	3357.64	95
H20H	1421.88	5263.07	3045.94	95
H21A	1324.88	6560.93	3477.32	85
H21B	1542.98	6380.7	4044.76	85
H21C	1494.4	4901.6	3683.06	85
H22A	2404.07	8334.75	3584.03	119
H22B	2705.32	6972.96	3863.69	119
H22C	2194.49	7627.81	4105.14	119
H21D	2254.93	5372.39	3507.65	83

H21E	2063.16	6598.7	3174.14	83
H21F	4159.39	-293.77	2609.66	162
H21G	4547.53	626.18	2256.55	162
H21H	4248.81	-832.29	2033.62	162
H22D	3945.81	3322.19	2197.54	158
H22E	4097.37	2728.18	1641.41	158
H22F	4455.86	2360.89	2119.99	158
H21I	3589.07	1164.69	2339.76	131
H21J	3679.6	692.5	1804.67	131

Table A5.17 Atomic Occupancy for BIRM-19

Atom	Occupancy	Atom	Occupancy	Atom	Occupancy
C201	0.4	H20A	0.4	H20B	0.4
H20C	0.4	C202	0.4	H20D	0.4
H20E	0.4	H20F	0.4	N201	0.4
H20G	0.4	H20H	0.4	C21A	0.35
H21A	0.35	H21B	0.35	H21C	0.35
C22A	0.35	H22A	0.35	H22B	0.35
H22C	0.35	N21A	0.35	H21D	0.35
H21E	0.35	C21B	0.25	H21F	0.25
H21G	0.25	H21H	0.25	C22B	0.25
H22D	0.25	H22E	0.25	H22F	0.25
N21B	0.25	H21I	0.25	H21J	0.25

BIRM-20

Table A5.18 Crystal data and structure refinement for BIRM-20

Identification code	BIRM-20
Empirical formula	$C_{17}H_{19}N_2NiO_8P$
Formula weight	469.02
Temperature/K	100.01(10)
Crystal system	monoclinic
Space group	$P2_1$
a/Å	7.2523(2)
b/Å	11.1546(3)
c/Å	11.2845(3)
α/°	90
β/°	105.450(2)
γ/°	90
Volume/Å^3	879.89(4)
Z	2
ρ_{calc}g/cm^3	1.77
μ/mm^{-1}	2.946
F(000)	484
Crystal size/mm^3	0.151 × 0.068 × 0.038
Radiation	Cu Kα (λ = 1.54184)
2Θ range for data collection/°	8.128 to 164.346
Index ranges	-9 ≤ h ≤ 9, -13 ≤ k ≤ 14, -14 ≤ l ≤ 10
Reflections collected	16437
Independent reflections	3565 [R_{int} = 0.0466, R_{sigma} = 0.0369]
Data/restraints/parameters	3565/8/284
Goodness-of-fit on F^2	1.072
Final R indexes [I>=2σ (I)]	R_1 = 0.0356, wR_2 = 0.0888
Final R indexes [all data]	R_1 = 0.0374, wR_2 = 0.0904
Largest diff. peak/hole / e Å^{-3}	0.30/-0.55
Flack parameter	0.05(4)

Table A5.19 Fractional Atomic Coordinates (×10^4) and Equivalent Isotropic Displacement Parameters (Å^2×10^3) for BIRM-20

Atom	*x*	*y*	*z*	U(eq)
C1	8370(6)	5482(5)	7627(4)	15.0(9)
C2	9123(6)	6442(5)	8393(4)	16.8(9)
C3	9324(7)	6378(5)	9650(4)	19.0(9)
C4	8824(6)	5337(4)	10166(4)	15.7(9)
C5	8135(7)	4356(5)	9412(4)	17.9(9)
C6	7908(6)	4427(5)	8157(4)	16.8(9)
C7	9128(7)	5317(4)	11528(4)	17.0(10)
C8	4117(8)	5939(4)	2577(4)	19.1(10)
C9	4077(7)	5981(4)	1334(4)	18.1(10)
C10	3716(6)	4946(5)	630(4)	15.6(8)
C11	3535(7)	3891(5)	1249(4)	19.5(10)
C12	3600(7)	3921(5)	2486(4)	18.0(10)
C13	3497(6)	4954(5)	-729(4)	15.0(8)
C14	3785(7)	5985(5)	-1340(4)	17.7(10)
C15	3617(7)	5945(5)	-2597(4)	17.6(10)
C16	2823(7)	3958(5)	-2687(4)	17.3(9)
C17	2945(7)	3923(5)	-1440(4)	18.9(10)
N1	3824(5)	4932(4)	3144(3)	16.2(7)
N2	3185(5)	4945(4)	-3262(3)	15.5(7)
Ni1	3454.6(10)	4924.8(7)	4933.7(6)	13.14(19)
O1	5817(4)	6014(3)	5501(3)	14.2(6)
O2	9224(4)	6653(3)	5763(3)	15.3(6)
O3	8329(5)	4448(3)	5466(3)	16.0(7)
O4	9515(5)	6226(3)	12144(3)	23.1(8)
O5	8998(5)	4229(3)	11981(3)	19.5(7)
O6	1820(4)	6461(3)	4537(3)	15.3(6)
O7	841(5)	3973(3)	4303(3)	14.4(6)
O8	5008(4)	3334(3)	5323(3)	14.5(6)
P1	7920.4(15)	5650.5(10)	5960.8(10)	12.3(2)

Table A5.20 Anisotropic Displacement Parameters ($Å^2 \times 10^3$) for BIRM-20.

Atom	U_{11}	U_{22}	U_{33}	U_{23}	U_{13}	U_{12}
C1	9.9(19)	20(3)	15(2)	-1.1(18)	4.0(16)	2.3(18)
C2	17(2)	20(2)	13(2)	0.7(17)	3.6(16)	-0.8(18)
C3	17(2)	21(3)	18(2)	0.0(19)	4.2(17)	0.0(19)
C4	12.6(19)	22(3)	13(2)	0.6(16)	3.2(16)	1.2(17)
C5	17(2)	23(3)	16(2)	2.2(18)	7.5(17)	3(2)
C6	16(2)	21(2)	13(2)	-1.0(17)	4.6(17)	0.0(19)
C7	16(2)	23(3)	12(2)	0.7(17)	3.8(16)	2.9(17)
C8	27(3)	16(3)	14(2)	-0.7(17)	5.6(18)	-1(2)
C9	21(2)	18(3)	14(2)	2.7(17)	3.5(18)	-4.1(19)
C10	10.7(17)	22(2)	14(2)	1(2)	3.7(14)	0(2)
C11	23(2)	23(3)	13(2)	-1.4(19)	5.3(18)	0(2)
C12	21(2)	19(3)	14(2)	-0.7(18)	4.9(17)	0.3(19)
C13	10.9(17)	23(2)	10.6(19)	2(2)	1.6(14)	0(2)
C14	18(2)	23(3)	12(2)	-2.3(17)	4.1(17)	-2.2(19)
C15	18(2)	24(3)	13(2)	-1.2(17)	7.2(17)	-1.5(19)
C16	19(2)	22(3)	11(2)	-1.4(18)	4.0(17)	-3.9(19)
C17	17(2)	27(3)	15(2)	3.0(19)	6.8(18)	1(2)
N1	15.9(16)	22(2)	9.7(16)	-2.1(17)	2.1(13)	-0.7(19)
N2	12.1(16)	23(2)	10.6(16)	3.3(18)	2.1(12)	0.5(19)
Ni1	12.6(3)	18.0(4)	9.0(3)	0.3(3)	3.0(2)	0.7(3)
O1	12.6(14)	17.8(17)	11.7(14)	-0.2(11)	2.6(11)	-1.2(12)
O2	15.0(15)	15.8(17)	17.4(15)	1.1(12)	8.4(12)	-1.6(13)
O3	16.8(15)	15.1(17)	18.0(16)	-3.7(12)	7.8(12)	-1.7(13)
O4	29.2(19)	24(2)	14.1(16)	-1.6(14)	2.7(14)	0.8(15)
O5	23.3(17)	24.4(19)	9.1(15)	2.2(13)	1.7(13)	0.4(15)
O6	13.6(15)	20.6(18)	11.8(15)	1.7(13)	3.9(12)	3.4(13)
O7	14.9(15)	16.5(17)	12.6(14)	-1.8(12)	5.1(12)	-0.6(13)
O8	14.0(14)	12.1(17)	17.6(16)	-0.8(12)	4.3(13)	2.0(13)
P1	11.4(5)	15.3(5)	11.0(5)	0.7(4)	4.1(4)	0.0(4)

Table A5.21 Bond Lengths for BIRM-20

Atom	Atom	Length/Å	Atom	Atom	Length/Å
C1	C2	1.392(7)	C12	N1	1.336(7)
C1	C6	1.401(7)	C13	C14	1.384(7)
C1	P1	1.831(5)	C13	C17	1.398(7)
C2	C3	1.389(6)	C14	C15	1.391(6)
C3	C4	1.390(7)	C15	N2	1.334(7)
C4	C5	1.394(7)	C16	C17	1.387(6)
C4	C7	1.494(6)	C16	N2	1.339(6)
C5	C6	1.384(6)	N1	Ni1	2.107(3)
C7	O4	1.219(6)	N2	Ni1[1]	2.097(3)
C7	O5	1.330(6)	Ni1	O1	2.059(3)
C8	C9	1.396(7)	Ni1	O6	2.064(3)
C8	N1	1.338(7)	Ni1	O7	2.123(3)
C9	C10	1.386(7)	Ni1	O8	2.085(3)
C10	C11	1.393(7)	O1	P1	1.529(3)
C10	C13	1.499(5)	O2	P1	1.519(3)
C11	C12	1.384(7)	O3	P1	1.512(3)

[1]+X,+Y,-1+Z

Table A5.22 Bond Angles for BIRM-20

Atom	Atom	Atom	Angle/˚	Atom	Atom	Atom	Angle/˚
C2	C1	C6	118.7(4)	C12	N1	C8	117.0(4)
C2	C1	P1	119.5(4)	C12	N1	Ni1	120.1(4)
C6	C1	P1	121.8(3)	C15	N2	C16	117.5(4)
C3	C2	C1	120.8(5)	C15	N2	Ni1[1]	119.1(3)
C2	C3	C4	120.1(5)	C16	N2	Ni1[1]	122.9(3)
C3	C4	C5	119.5(4)	N1	Ni1	O7	90.62(14)
C3	C4	C7	117.4(4)	N2[2]	Ni1	N1	177.94(16)
C5	C4	C7	123.1(4)	N2[2]	Ni1	O7	91.43(13)
C6	C5	C4	120.3(5)	O1	Ni1	N1	89.31(14)
C5	C6	C1	120.6(5)	O1	Ni1	N2[2]	88.68(14)
O4	C7	C4	121.5(4)	O1	Ni1	O6	87.71(13)
O4	C7	O5	124.7(4)	O1	Ni1	O7	173.83(14)
O5	C7	C4	113.8(4)	O1	Ni1	O8	94.50(14)
N1	C8	C9	123.1(5)	O6	Ni1	N1	90.08(15)
C10	C9	C8	119.9(5)	O6	Ni1	N2[2]	90.28(15)

C9	C10	C11	116.4(4)	O6	Ni1	O7	86.13(14)
C9	C10	C13	122.3(5)	O6	Ni1	O8	177.75(14)
C11	C10	C13	121.3(5)	O8	Ni1	N1	90.33(15)
C12	C11	C10	120.2(5)	O8	Ni1	N2[2]	89.39(15)
N1	C12	C11	123.2(5)	O8	Ni1	O7	91.66(13)
C14	C13	C10	121.7(4)	P1	O1	Ni1	128.4(2)
C14	C13	C17	117.1(4)	O1	P1	C1	105.33(19)
C17	C13	C10	121.2(4)	O2	P1	C1	106.21(19)
C13	C14	C15	119.8(5)	O2	P1	O1	111.02(19)
N2	C15	C14	122.9(5)	O3	P1	C1	106.8(2)
N2	C16	C17	123.2(5)	O3	P1	O1	112.69(18)
C16	C17	C13	119.3(5)	O3	P1	O2	114.05(18)
C8	N1	Ni1	122.6(3)				

[1]+X,+Y,-1+Z; [2]+X,+Y,1+Z

Table A5.23 Hydrogen Bonds for BIRM-20

D	H	A	d(D-H)/Å	d(H-A)/Å	d(D-A)/Å	D-H-A/°
O5	H5A	O7[1]	0.85(3)	1.80(3)	2.621(4)	164(7)
O6	H6A	O2[2]	0.85(3)	1.79(3)	2.625(4)	169(6)
O6	H6B	O4[3]	0.83(3)	1.97(3)	2.784(4)	165(6)
O7	H7A	O2[4]	0.86(3)	1.73(3)	2.589(5)	177(6)
O7	H7B	O3[2]	0.85(3)	1.76(4)	2.568(4)	157(6)
O8	H8A	O1[4]	0.84(3)	1.92(3)	2.761(5)	173(6)
O8	H8B	O3	0.86(3)	1.87(4)	2.677(5)	157(6)

[1]1+X,+Y,1+Z; [2]-1+X,+Y,+Z; [3]-1+X,+Y,-1+Z; [4]1-X,-1/2+Y,1-Z

Table A5.24 Torsion Angles for BIRM-20

A	B	C	D	Angle/˚	A	B	C	D	Angle/˚
C1	C2	C3	C4	1.8(7)	C9	C10	C13	C17	-173.5(5)
C2	C1	C6	C5	2.2(7)	C10	C11	C12	N1	0.4(8)
C2	C1	P1	O1	-94.6(4)	C10	C13	C14	C15	178.3(4)
C2	C1	P1	O2	23.2(4)	C10	C13	C17	C16	-177.8(4)
C2	C1	P1	O3	145.3(4)	C11	C10	C13	C14	-176.2(4)
C2	C3	C4	C5	0.6(7)	C11	C10	C13	C17	5.5(6)
C2	C3	C4	C7	178.3(4)	C11	C12	N1	C8	-4.4(7)
C3	C4	C5	C6	-1.5(7)	C11	C12	N1	Ni1	170.0(4)
C3	C4	C7	O4	11.1(7)	C13	C10	C11	C12	-175.2(4)
C3	C4	C7	O5	-166.8(4)	C13	C14	C15	N2	-0.1(7)
C4	C5	C6	C1	0.2(7)	C14	C13	C17	C16	3.8(7)
C5	C4	C7	O4	-171.3(4)	C14	C15	N2	C16	2.9(7)
C5	C4	C7	O5	10.9(6)	C14	C15	N2	Ni1[1]	-169.1(4)
C6	C1	C2	C3	-3.2(7)	C17	C13	C14	C15	-3.3(7)
C6	C1	P1	O1	82.8(4)	C17	C16	N2	C15	-2.4(7)
C6	C1	P1	O2	-159.3(4)	C17	C16	N2	Ni1[1]	169.3(3)
C6	C1	P1	O3	-37.2(4)	N1	C8	C9	C10	0.1(8)
C7	C4	C5	C6	-179.2(4)	N2	C16	C17	C13	-1.0(7)
C8	C9	C10	C11	-4.1(7)	Ni1	O1	P1	C1	-90.0(3)
C8	C9	C10	C13	174.9(4)	Ni1	O1	P1	O2	155.4(2)
C9	C8	N1	C12	4.1(7)	Ni1	O1	P1	O3	26.1(3)
C9	C8	N1	Ni1	-170.1(4)	P1	C1	C2	C3	174.4(4)
C9	C10	C11	C12	3.9(7)	P1	C1	C6	C5	-175.3(4)
C9	C10	C13	C14	4.8(6)					

[1]+X,+Y,-1+Z

Table A5.25 Hydrogen Atom Coordinates (Å×10^4) and Isotropic Displacement Parameters (Å^2×10^3) for BIRM-20

Atom	*x*	*y*	*z*	U(eq)
H2	9494.68	7133.53	8058.25	20
H3	9795.78	7033.84	10148.28	23
H5	7826.63	3650.57	9755.04	21
H6	7443.98	3769.11	7661.41	20
H8	4359.44	6644.08	3031.37	23
H9	4292.27	6701.41	978.62	22
H11	3369.47	3164.42	830.51	23
H12	3482.57	3202.45	2877.37	22
H14	4089.62	6701.3	-911.58	21
H15	3813.42	6647.23	-2990.95	21
H16	2473.52	3262.72	-3145.91	21
H17	2660.96	3221.41	-1079.87	23
H5A	9430(90)	4230(60)	12760(30)	29
H6A	1070(70)	6590(60)	4990(50)	23
H6B	1170(70)	6520(60)	3810(30)	23
H7A	830(90)	3200(20)	4310(60)	22
H7B	220(80)	4030(60)	4840(40)	22
H8A	4760(90)	2650(30)	5010(50)	22
H8B	6170(50)	3490(60)	5350(60)	22

Appendix A5.26 and A5.27. Refinement parameters, unit cell parameters, refined atom positions, multiplicities, occupancies and isotropic displacement parameters from the refinement of powder X-ray diffraction for BIRM-20

Table A5.26. Refinement and lattice parameters

Refinement parameters		**Lattice parameters**	
R_{wp}	5.66 %	**Formular**	$C_{17}H_{19}N_2NiO_8P$
R_P	4.10 %	**Space group**	$P2_1$
X^2	2.05	**a(Å)**	7.296(1)
		b(Å)	11.2031(7)
		c(Å)	11.277(4)
		V(Å³)	889.7(1)

Table A5.27. Refined atom positions, multiplicities, occupancies and isotropic displacement parameters

Atom label	**Element**	**x**	**y**	**z**	**Occup**	**Mult**	**Uiso**
C1	C	0.93(1)	0.57(2)	0.763(9)	1	2	0.069(5)
C2	C	0.82(2)	0.65(2)	0.79(1)	1	2	0.069(5)
H2	H	0.9495	0.7134	0.8058	1	2	0.02
C3	C	0.86(3)	0.62(2)	0.97(2)	1	2	0.069(5)
H3	H	0.9796	0.7034	1.0148	1	2	0.02
C4	C	0.88(3)	0.55(2)	1.00(2)	1	2	0.069(5)
C5	C	0.88(2)	0.48(2)	0.92(1)	1	2	0.069(5)
H5	H	0.7825	0.3651	0.9755	1	2	0.02
C6	C	0.76(2)	0.48(2)	0.80(1)	1	2	0.069(5)
H6	H	0.7444	0.3769	0.7661	1	2	0.02
C7	C	0.90(2)	0.63(2)	1.10(1)	1	2	0.069(5)
C8	C	0.35(2)	0.66(2)	0.24(1)	1	2	0.069(5)
H8	H	0.4359	0.6644	0.3031	1	2	0.02
C9	C	0.31(2)	0.65(2)	0.13(1)	1	2	0.069(5)
H9	H	0.4292	0.6701	0.0977	1	2	0.02
C10	C	0.36(2)	0.55(2)	0.07(1)	1	2	0.069(5)
C11	C	0.39(2)	0.42(2)	0.11(1)	1	2	0.069(5)
H11	H	0.3370	0.3164	0.0831	1	2	0.02
C12	C	0.42(2)	0.47(2)	0.31(1)	1	2	0.069(5)
H12	H	0.3483	0.3203	0.2877	1	2	0.02
C13	C	0.35(2)	0.56(2)	-0.09(1)	1	2	0.069(5)
C14	C	0.31(2)	0.65(2)	-0.17(1)	1	2	0.069(5)
H14	H	0.4090	0.6701	-0.0912	1	2	0.02
C15	C	0.28(2)	0.65(2)	-0.28(2)	1	2	0.069(5)
H15	H	0.3813	0.6647	-0.2991	1	2	0.02

C16	C	0.35(2)	0.45(2)	-0.26(1)	1	2	0.069(5)
H16	H	0.2474	0.3263	-0.3146	1	2	0.02
C17	C	0.42(2)	0.41(2)	-0.083(8)	1	2	0.069(5)
H17	H	0.2661	0.3221	-0.1080	1	2	0.02
N1	N	0.35(1)	0.58(2)	0.290(8)	1	2	0.069(5)
N2	N	0.28(1)	0.58(2)	-0.316(9)	1	2	0.069(5)
Ni1	Ni	0.338(3)	0.55(2)	0.489(2)	1	2	0.069(5)
O1	O	0.57(1)	0.66(2)	0.561(5)	1	2	0.069(5)
O2	O	0.90(1)	0.71(1)	0.552(7)	1	2	0.069(5)
O3	O	0.87(1)	0.52(2)	0.571(7)	1	2	0.069(5)
O4	O	0.96(1)	0.65(2)	1.228(6)	1	2	0.069(5)
O5	O	0.92(1)	0.49(2)	1.187(7)	1	2	0.069(5)
H5A	H	0.943	0.423	1.276	1	2	0.02
O6	O	0.15(1)	0.69(2)	0.435(7)	1	2	0.069(5)
H6A	H	0.1768	0.6882	0.4884	1	2	0.02
H6B	H	0.0654	0.6457	0.3447	1	2	0.02
O7	O	0.051(9)	0.50(2)	0.441(7)	1	2	0.069(5)
H7A	H	0.083	0.32	0.431	1	2	0.02
H7B	H	0.022	0.403	0.484	1	2	0.02
O8	O	0.50(1)	0.37(2)	0.511(9)	1	2	0.069(5)
H8A	H	0.4089	0.3261	0.4790	1	2	0.02
H8B	H	0.617	0.349	0.535	1	2	0.02
P1	P	0.792(5)	0.63(2)	0.585(4)	1	2	0.069(5)

BIRM-21

Table A5.28 Crystal data and structure refinement for BIRM-21

Identification code	BIRM-21
Empirical formula	$C_7H_7CoO_6P$
Formula weight	277.03
Temperature/K	100.01(10)
Crystal system	orthorhombic
Space group	Pnnm
a/Å	4.7806(6)
b/Å	38.077(5)
c/Å	5.6017(8)
α/°	90
β/°	90
γ/°	90
Volume/Å^3	1019.7(2)
Z	4
ρ_{calc}g/cm^3	1.805
μ/mm^{-1}	14.804
F(000)	556
Crystal size/mm^3	0.157 × 0.075 × 0.022
Radiation	Cu Kα (λ = 1.54184)
2Θ range for data collection/°	9.29 to 144.924
Index ranges	-5 ≤ h ≤ 4, -46 ≤ k ≤ 35, -6 ≤ l ≤ 5
Reflections collected	2158
Independent reflections	1084 [R_{int} = 0.0459, R_{sigma} = 0.0623]
Data/restraints/parameters	1084/1/130
Goodness-of-fit on F^2	1.106
Final R indexes [I>=2σ (I)]	R_1 = 0.0603, wR_2 = 0.1515
Final R indexes [all data]	R_1 = 0.0732, wR_2 = 0.1641
Largest diff. peak/hole / e Å^{-3}	0.82/-0.83

Table A5.29 Fractional Atomic Coordinates (×10^4) and Equivalent Isotropic Displacement Parameters (Å^2×10^3) for BIRM-21

Atom	*x*	*y*	*z*	U(eq)
C1	7712(14)	6598.1(19)	10000	17.5(14)
C2	7970(20)	6418(3)	7846(19)	26(2)
C2A	10260(40)	6449(5)	9170(40)	21(4)
C3	8430(30)	6060(3)	7850(20)	32(3)
C3A	10720(50)	6093(6)	9250(40)	32(6)
C4	8649(17)	5875(2)	10000	32(2)
C5A	6140(50)	6007(5)	9030(50)	29(3)
C6A	5630(50)	6351(5)	9090(40)	29(3)
C7	9200(20)	5489(2)	10000	46(2)
Co1	6423(2)	7446.4(3)	5000	12.9(4)
O1	8585(6)	7226.3(9)	7827(6)	15.9(7)
O2	3472(9)	7032.8(13)	5000	15.8(10)
O3	3979(10)	7117.4(12)	10000	16.1(10)
O4	9440(30)	5344(2)	7982(19)	55(3)
O4A	11530(40)	5379(4)	9330(40)	48(9)
O4B	7190(40)	5292(4)	9140(50)	64(11)
P1	7105(3)	7061.6(4)	10000	12.9(4)

Table A5.30 Anisotropic Displacement Parameters (Å²×10³) for BIRM-21

Atom	U_{11}	U_{22}	U_{33}	U_{23}	U_{13}	U_{12}
C1	14(3)	21(3)	18(3)	0	0	2(3)
C2	38(6)	24(5)	16(5)	-3(4)	-1(4)	3(5)
C2A	15(9)	25(9)	22(9)	-2(7)	4(7)	8(8)
C3	50(7)	16(5)	29(6)	-5(5)	-6(5)	7(5)
C3A	22(9)	21(9)	54(19)	-13(9)	19(9)	6(8)
C4	33(5)	20(4)	44(5)	0	0	3(3)
C5A	30(8)	14(6)	43(8)	-3(6)	-13(6)	-10(6)
C6A	30(8)	14(6)	43(8)	-3(6)	-13(6)	-10(6)
C7	43(5)	23(4)	73(7)	0	0	3(4)
Co1	10.1(6)	16.2(6)	12.3(6)	0	0	0.1(4)
O1	9.2(15)	20.0(17)	18.4(17)	1.1(14)	-4.1(12)	1.7(11)
O2	12(2)	22(2)	13(2)	0	0	-1.5(17)
O3	13(2)	16(2)	19(2)	0	0	1.6(17)
O4	93(9)	25(5)	46(6)	-5(4)	2(6)	15(6)
O4A	44(9)	25(8)	80(30)	-6(8)	34(11)	3(6)
O4B	32(8)	15(7)	150(30)	-19(11)	-32(12)	5(6)
P1	12.4(8)	15.8(8)	10.6(8)	0	0	0.6(6)

Table A5.31 Bond Lengths for BIRM-21

Atom	Atom	Length/Å	Atom	Atom	Length/Å
C1	C2	1.394(11)	C7	O4A	1.247(19)
C1	C2A	1.421(19)	C7	O4B	1.310(19)
C1	C6A	1.46(2)	Co1	$O1^1$	2.208(3)
C1	P1	1.789(7)	Co1	O1	2.069(3)
C2	C3	1.378(15)	Co1	$O1^2$	2.208(3)
C2A	C3A	1.37(3)	Co1	$O1^3$	2.068(3)
C3	C4	1.401(13)	Co1	O2	2.115(5)
C3A	C4	1.36(2)	Co1	$O3^4$	2.062(5)
C4	C5A	1.41(2)	Co1	$P1^1$	2.787(2)
C4	C7	1.494(12)	O1	P1	1.541(3)
C5A	C6A	1.33(3)	O3	P1	1.509(5)
C7	O4	1.263(11)			

[1]-1/2+X,3/2-Y,-1/2+Z; [2]-1/2+X,3/2-Y,3/2-Z; [3]+X,+Y,1-Z; [4]1/2+X,3/2-Y,-1/2+Z

Table A5.32 Bond Angles for BIRM-21

Atom	Atom	Atom	Angle/˚	Atom	Atom	Atom	Angle/˚
C2	C1	P1	120.0(5)	O1^{2}	Co1	P1^{3}	129.97(9)
C2A	C1	C6A	102.2(14)	O1^{3}	Co1	P1^{3}	33.46(9)
C2A	C1	P1	122.2(10)	O1	Co1	P1^{3}	129.97(9)
C6A	C1	P1	121.7(10)	O2	Co1	O1^{3}	90.60(14)
C3	C2	C1	120.0(10)	O2	Co1	O1^{1}	90.60(14)
C3A	C2A	C1	121.3(18)	O2	Co1	P1^{3}	90.37(14)
C2	C3	C4	120.7(10)	O3^{4}	Co1	O1	91.74(13)
C4	C3A	C2A	119.8(17)	O3^{4}	Co1	O1^{1}	84.81(14)
C3	C4	C7	120.6(5)	O3^{4}	Co1	O1^{2}	91.74(13)
C3A	C4	C5A	106.4(14)	O3^{4}	Co1	O1^{3}	84.81(14)
C3A	C4	C7	118.3(11)	O3^{4}	Co1	O2	174.5(2)
C5A	C4	C7	120.1(11)	O3^{4}	Co1	P1^{3}	84.12(14)
C6A	C5A	C4	119.8(18)	Co1	O1	Co1^{5}	120.02(16)
C5A	C6A	C1	121.2(19)	P1	O1	Co1	122.69(18)
O4	C7	C4	116.4(6)	P1	O1	Co1^{5}	94.37(16)
O4A	C7	C4	119.1(11)	P1	O3	Co1^{6}	134.4(3)
O4A	C7	O4B	110.7(14)	C1	P1	Co1^{5}	122.9(2)
O4B	C7	C4	115.7(10)	O1	P1	C1	109.08(19)
O1	Co1	O1^{1}	96.53(8)	O1^{7}	P1	C1	109.08(19)
O1^{2}	Co1	O1	99.91(19)	O1^{7}	P1	Co1^{5}	52.17(13)
O1	Co1	O1^{3}	163.30(16)	O1	P1	Co1^{5}	52.17(13)
O1^{2}	Co1	O1^{3}	96.53(8)	O1	P1	O1^{7}	104.3(3)
O1^{2}	Co1	O1^{1}	163.30(16)	O3	P1	C1	107.4(3)
O1^{3}	Co1	O1^{1}	66.92(18)	O3	P1	Co1^{5}	129.7(2)
O1	Co1	O2	91.80(13)	O3	P1	O1	113.41(16)
O1^{2}	Co1	O2	91.80(13)	O3	P1	O1^{7}	113.41(16)
O1^{1}	Co1	P1^{3}	33.46(9)				

^{1}-1/2+X,3/2-Y,3/2-Z; ^{2}+X,+Y,1-Z; ^{3}-1/2+X,3/2-Y,-1/2+Z; ^{4}1/2+X,3/2-Y,-1/2+Z; ^{5}1/2+X,3/2-Y,1/2+Z; ^{6}-1/2+X,3/2-Y,1/2+Z; ^{7}+X,+Y,2-Z

Table A5.33 Hydrogen Bonds for BIRM-21

D	H	A	d(D-H)/Å	d(H-A)/Å	d(D-A)/Å	D-H-A/°
O2	H2B	O1[1]	0.838(11)	2.18(3)	2.917(5)	148(6)
O2	H2B	O3	0.838(11)	2.22(5)	2.8297(10)	129(5)

[1]-1+X,+Y,+Z

Table A5.34 Torsion Angles for BIRM-21

A	B	C	D	Angle/˚	A	B	C	D	Angle/˚
C1	C2	C3	C4	-0.3(18)	C6A	C1	C2A	C3A	-42(2)
C1	C2A	C3A	C4	4(3)	C6A	C1	P1	Co1[1]	-155.8(12)
C2	C1	P1	Co1[1]	-89.5(7)	C6A	C1	P1	O1	-99.1(12)
C2	C1	P1	O1[2]	-146.1(7)	C6A	C1	P1	O1[2]	147.5(12)
C2	C1	P1	O1	-32.8(8)	C6A	C1	P1	O3	24.2(12)
C2	C1	P1	O3	90.5(7)	C7	C4	C5A	C6A	178.2(19)
C2	C3	C4	C7	-178.8(10)	Co1[1]	O1	P1	C1	-117.3(2)
C2A	C1	C6A	C5A	37(3)	Co1	O1	P1	C1	112.5(3)
C2A	C1	P1	Co1[1]	-22.9(10)	Co1	O1	P1	Co1[1]	-130.2(3)
C2A	C1	P1	O1[2]	-79.6(10)	Co1	O1	P1	O1[2]	-131.04(15)
C2A	C1	P1	O1	33.8(10)	Co1[1]	O1	P1	O1[2]	-0.9(3)
C2A	C1	P1	O3	157.1(10)	Co1	O1	P1	O3	-7.2(3)
C2A	C3A	C4	C5A	39(3)	Co1[1]	O1	P1	O3	123.0(2)
C2A	C3A	C4	C7	178.2(17)	Co1[3]	O3	P1	C1	180
C3	C4	C7	O4	0.0(16)	Co1[3]	O3	P1	Co1[1]	0
C3A	C4	C5A	C6A	-44(3)	Co1[3]	O3	P1	O1	-59.39(17)
C3A	C4	C7	O4A	0.5(18)	Co1[3]	O3	P1	O1[2]	59.39(17)
C3A	C4	C7	O4B	-135.4(19)	P1	C1	C2	C3	-179.7(9)
C4	C5A	C6A	C1	4(4)	P1	C1	C2A	C3A	177.8(17)
C5A	C4	C7	O4A	133.5(18)	P1	C1	C6A	C5A	177.8(19)
C5A	C4	C7	O4B	-2.4(19)					

[1]1/2+X,3/2-Y,1/2+Z; [2]+X,+Y,2-Z; [3]-1/2+X,3/2-Y,1/2+Z

Table A5.35 Hydrogen Atom Coordinates (Å×10^4) and Isotropic Displacement Parameters (Å^2×10^3) for BIRM-21

Atom	*x*	*y*	*z*	U(eq)
H2	7839.19	6538.56	6407.5	31
H2A	11636.27	6595.23	8548.91	25
H3	8591.09	5941.15	6406.32	38
H3A	12443.46	6001.81	8801.25	39
H5A	4844.72	5855.26	8343.49	35
H6A	3917.62	6435	8546.18	35
H2B	2530(110)	7063(16)	6250(60)	24
H4	9463.16	5130.47	8145.86	82
H4B	7259.63	5097.01	9750.27	97

Table A5.36 Atomic Occupancy for BIRM-21

Atom	*Occupancy*	Atom	*Occupancy*	Atom	*Occupancy*
C2	0.5	H2	0.5	C2A	0.25
H2A	0.25	C3	0.5	H3	0.5
C3A	0.25	H3A	0.25	C5A	0.25
H5A	0.25	C6A	0.25	H6A	0.25
O4	0.5	H4	0.25	O4A	0.25
O4B	0.25	H4B	0.25		

Experimental tables

Table AE4.1: List of experimental conditions used in search for new Cu-MOF

Sample code	$Cu(NO_3)_2.2.5H_20$ (mg)	3-PPN acid (mg)	Pyridine (mL)	Solv. (H_2O) (mL)	Temp. (^oC)	Time (hr)	Single crystal	Remark
CuA01	80	50	2	8	70	12	No	
CuA02	80	50	2	8	80	12	No	
CuA03	80	50	2	8	90	12	No	
CuA04	80	50	2	8	100	12	No	
CuA05	80	50	2	8	110	12	No	
CuA06	80	50	2	8	120	12	No	
CuA07	80	50	2	8	130	12	No	
CuA08	80	50	2	8	140	12	No	
CuA09	80	50	2	8	150	12	No	
CuA10	80	50	2	8	160	12	No	
CuA11	80	50	2	8	70	24	No	
CuA12	80	50	2	8	80	24	No	
CuA13	80	50	2	8	90	24	No	
CuA14	80	50	2	8	100	24	No	
CuA15	80	50	2	8	110	24	No	
CuA16	80	50	2	8	120	24	No	
CuA17	80	50	2	8	130	24	No	
CuA18	80	50	2	8	140	24	No	
CuA19	80	50	2	8	150	24	No	
CuA20	80	50	2	8	160	24	No	

Table AE4.2: List of experimental conditions used in search for new Cu-MOF

Sample code	$Cu(NO_3)_2.2.5H_20$ (mg)	3-PPN acid (mg)	4,4-trimethylenepyridine (mg)	Solv. (H_2O) (mL)	Temp. (^oC)	Time (hr)	Single crystal	Remark
CuA21	80	50	25	8	70	12	No	
CuA22	80	50	25	8	80	12	No	
CuA23	80	50	25	8	90	12	No	
CuA24	80	50	25	8	100	12	No	
CuA25	80	50	25	8	110	12	No	
CuA26	80	50	25	8	120	12	No	
CuA27	80	50	25	8	130	12	No	
CuA28	80	50	25	8	140	12	No	
CuA29	80	50	25	8	150	12	No	
CuA30	80	50	25	8	160	12	No	
CuA31	80	50	25	8	70	24	No	
CuA32	80	50	25	8	80	24	No	
CuA33	80	50	25	8	90	24	No	
CuA34	80	50	25	8	100	24	No	
CuA35	80	50	25	8	110	24	No	
CuA36	80	50	25	8	120	24	No	
CuA37	80	50	25	8	130	24	No	
CuA38	80	50	25	8	140	24	No	
CuA39	80	50	25	8	150	24	No	
CuA40	80	50	25	8	160	24	No	

Table AE4.3: List of experimental conditions used in search for new Cu-MOF

Sample code	$Cu(NO_3)_2.2.5H_20$ (mg)	3-PPN acid (mg)	4,4-Bipyridine (mg)	Solv. (H_2O) (mL)	Temp. (^oC)	Time (hr)	Single crystal	Remarks
CuA41	80	50	25	8	70	12	No	
CuA42	80	50	25	8	80	12	No	
CuA43	80	50	25	8	90	12	No	
CuA44	80	50	25	8	100	12	No	
CuA45	80	50	25	8	110	12	No	
CuA46	80	50	25	8	120	12	No	
CuA47	80	50	25	8	130	12	No	
CuA48	80	50	25	8	140	12	No	
CuA49	80	50	25	8	150	12	No	
CuA50	80	50	25	8	160	12	No	
CuA51	80	50	25	8	70	24	No	
CuA52	80	50	25	8	80	24	No	
CuA53	80	50	25	8	90	24	No	
CuA54	80	50	25	8	100	24	No	
CuA55	80	50	25	8	110	24	No	
CuA56	80	50	25	8	120	24	No	
CuA57	80	50	25	8	130	24	No	
CuA58	80	50	25	8	140	24	Yes	Mixture of single crystal and brown powder
CuA59	80	50	25	8	150	24	Yes	dirty green powder
CuA60	80	50	25	8	160	24	Yes	dirty green powder

Table AE4.4: List of experimental conditions used in search for new Co-MOF

Sample code	$CoSO_4$.$7H_20$ (mg)	3-PPN acid (mg)	Solv. (H_2O) (mL)	Temp. (^oC)	Time (hr)	Single crystal	Remark
Co01	75.5	33	10	80	24	No	
Co02	75.5	33	10	85	24	No	
Co03	75.5	33	10	90	24	No	
Co04	75.5	33	10	95	24	No	
Co05	75.5	33	10	100	24	No	
Co06	75.5	33	10	105	24	No	
Co07	75.5	33	10	110	24	No	
Co08	75.5	33	10	115	24	No	
Co09	75.5	33	10	120	24	Powder	Crystalline powder
Co10	75.5	33	10	125	24	Powder	Crystalline powder
Co11	75.5	33	10	130	24	Powder	Crystalline powder
Co12	75.5	33	10	135	24	Powder	Crystalline powder
Co13	75.5	33	10	140	24	Powder	Crystalline powder
Co14	75.5	33	10	145	24	Powder	Crystalline powder
Co15	75.5	33	10	150	24	Powder	Crystalline powder
Co16	75.5	33	10	155	24	Powder	Crystalline powder
Co17	75.5	33	10	160	24	Powder	Crystalline powder
Co18	75.5	33	10	80	48	Powder	Crystalline powder
Co19	75.5	33	10	85	48	Powder	Crystalline powder
Co20	75.5	33	10	90	48	Powder	Crystalline powder
Co21	75.5	33	10	95	48	Powder	Crystalline powder
Co22	80	33	10	100	48	Yes	Powder+single crystal
Co23	80	33	10	105	48	Yes	Powder+single crystal
Co24	80	50	10	110	48	Yes	Powder+single crystal
Co25	80	50	10	115	48	Yes	Powder+single crystal
Co26	80	50	10	120	48	Yes	Powder+single crystal
Co27	80	50	10	125	48	Yes	Powder+single crystal
Co28	80	50	10	130	48	Yes	Powder+single crystal
Co29	80	50	10	135	48	Yes	Pure single crystal
Co30	80	50	10	140	48	Yes	Same as Co29
Co31	80	50	10	145	48	Yes	Same as Co29
Co32	80	50	10	150	48	Yes	Same as Co29
Co33	80	50	10	155	48	Yes	Powder+single crystal
Co34	80	50	10	160	48	Yes	Powder+single crystal

Table AE5.1 Table showing the synthesis conditions for some zinc MOFs								
Sample	**$Zn(NO_3).6H_2O$ (mg)**	**4-cppH (mg)**	**Benzoic Acid (mg)**	**Solv. (DMF) (mL)**	**Temp. (^oC)**	**Time (Hrs)**	**Single crystal**	**Remarks**
ZnOO1 BIRM-17	20 mg	20 mg	250	2	65	12	Yes	PXRD shows that it contains more than one phases
ZnOO2	20 mg	20 mg	250	2	70	12	Yes	Same as 1
ZnOO3 BIRM-18	20 mg	20 mg	250	2	80	24	Yes	SCXRD *3D PXRD shows that it contains more than one phases
ZnOO4	20 mg	20 mg	250	2	85	24	Yes	Mixtures of phase
ZnOO5	20 mg	20 mg	250	2	90	24	Yes	Same as 4
ZnOO6	20 mg	20 mg	250	2	100	24	Yes	Same as 4
ZnOO7	20 mg	20 mg	250	2	110	24	Yes	Same as 4
ZnOO8	20 mg	20 mg	250	2	120	24	Yes	7and 8 are possibly the same but 8 is a better crystal and well diffracted
ZnOO9	20 mg	20 mg	250	2	130	24	Yes	Crystal not well diffracted
ZnOO10	20 mg	20 mg	250	2	130	24	Yes	Mixture of powder and single crystal. Crystal not well diffracted
ZnOO3 optimization								
ZnOO31	20 mg	20 mg	125	2	80	24	Yes	PXRD is not consistent with SCXRD
ZnOO32	40 mg	20 mg	125	2	80	24	Yes	PXRD is not consistent with SCXRD
ZnOO33	60 mg	20 mg	125	2	80	24	Yes	PXRD is not consistent with SCXRD
Phase purification attempt (50ul of water is added)								
ZnOO34	20mg	20mg	250mg	2	80	24	yes	PXRD is not consistent with SCXRD

ZnOO35	40mg	20mg	250mg	2	80	24	Chunks of crystals	PXRD is not consistent with SCXRD
ZnOO36	60mg	20mg	250mg	2	80	24	Chunks of crystals	PXRD is not consistent with SCXRD
ZnOO37	80mg	20mg	250mg	2	80	24	Chunks of crystals	PXRD is not consistent with SCXRD
ZnOO38	20mg	40mg	250mg	2	80	24	Chunks of crystals	PXRD is not consistent with SCXRD
ZnOO39	20mg	60mg	250mg	2	80	24	Chunks of crystals	PXRD is not consistent with SCXRD
ZnOO321	20mg	80mg	250mg	2	80	24	Chunks of crystals	PXRD is not consistent with SCXRD
ZnOO322	20mg	20mg	250mg	2	80	24	Chunks of crystals	PXRD is not consistent with SCXRD
ZnOO323	20mg	20mg	250mg	2	80	48	Chunks of crystals	PXRD is not consistent with SCXRD
ZnOO324	20mg	60mg	250mg	2	80	48	Chunks of crystals	PXRD is not consistent with SCXRD
Oxalic acid as deprotonator								
ZnOO325	10 mg	10 mg	125	2	120	24	Yes	SCXRD is not interesting
ZnOO326	10 mg	10 mg	125	2	120	24	Yes	SCXRD is not interesting

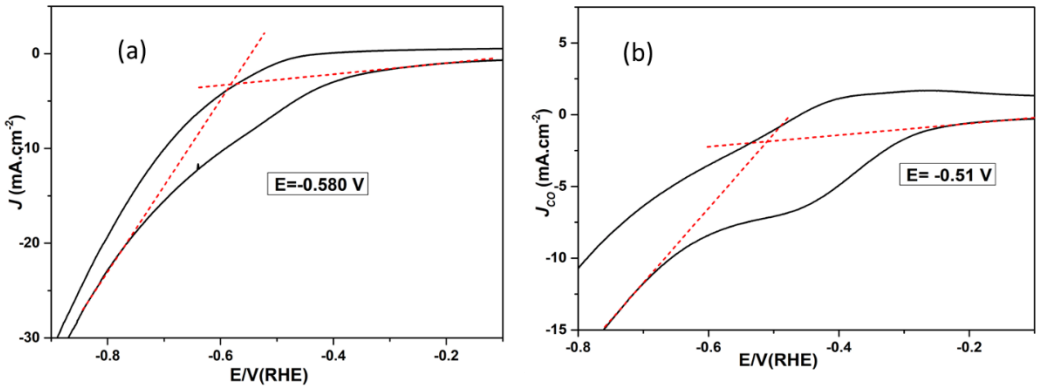


Figure A6.1. Determination of catalyst onset potentials in Ar-saturated 0.1 M $NaHCO_3/NaCO_3$ buffer solution (pH = 8) and CO_2-saturated 0.1 M $NaHCO_3/NaCO_3$ buffer solution (pH=9.2)

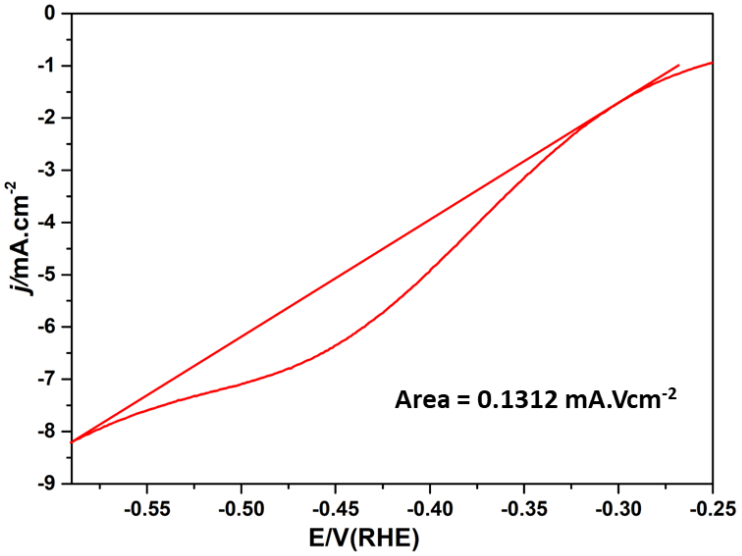


Figure A6.2. Total charge integrated from the Ni^{1+} / Ni^{2+} cathodic wave of the 2D MOF catalyst. Using CV value at 50 mV s^{-1}, which was in CO_2 - saturated $NaHCO_3/NaCO_3$ buffer solution (pH=9.2). The amount of surface-active Ni available for CO_2RR = [0.1312($mA{\cdot}Vcm^{-2}$) / 50 (mVs^{-1})] / 96485 $Cmol^{-1}$ = 2.720×10^{-8} mol cm^{-2}.

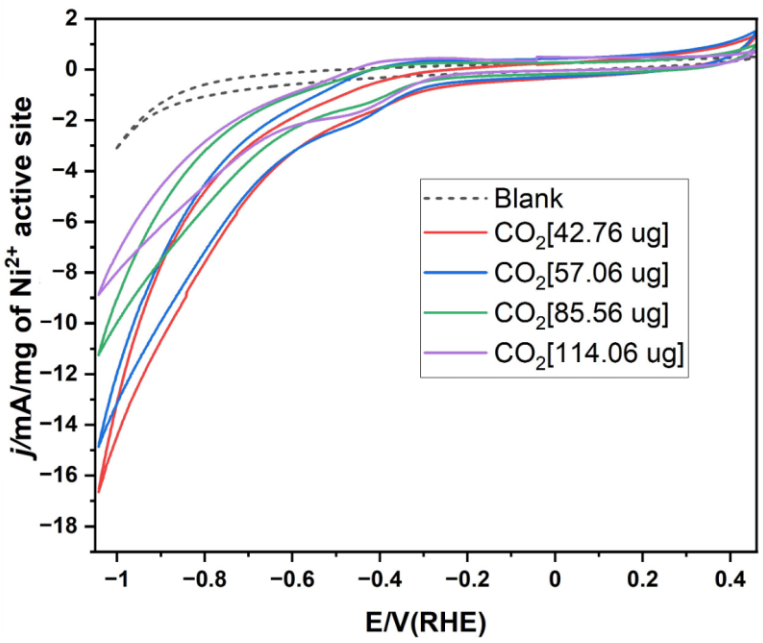


Figure A6.3. CV curves collected at 50 mV s^{-1} 0.1 M $NaHCO_3/NaCO_3$ buffer solution for the electrodes with different catalyst loadings.

Table A6.1. Analysis of Ni concentration before and after electrolysis.

XRF-pre-CO_2RR		
Element	**Ni**	**P**
%	21.10	12.00
XRF-post-CO_2RR		
%	19.20	11.23

Section S2 Calculation method

Calculation of the surface concentration of electrochemically active Ni-MOF sites

We integrated the cathodic wave in CV curve of electrocatalyst at the CO_2-saturated electrolytes. Then we calculated the integrated charge of the cathodic wave (Q):

$$Q = \frac{S}{v} \qquad Eq1$$

Where S is the area under the reduction peak of the cyclic voltammetry curve and *v* is the scan rate. Assuming a one-electron redox process, then we calculated the amount of surface-active Ni by:

$$n = \frac{Q}{F} \qquad Eq\ 2$$

where n is the amount of surface-active Ni on the working electrode (mole), Q is the integrated charge of the cathodic wave (Culumb), and F=96485 C/mol.

The total amount of Ni-MOF is calculated as follows:

$$n_{total} = \frac{m}{M} \qquad Eq\ 3$$

Where m is the mass of the Ni-MOF catalyst loaded on the electrode while M is the molecular mass of the catalyst. Then, the surface fraction of electrochemically active Ni sites was calculated as follows:

$$x = \frac{n}{n_{total}} \qquad Eq\ 4$$

Turnover Frequency (TOF, h^{-1})

The TOF for CO was calculated as follow:

$$TOF = \frac{I_{product/NF}}{m_{cat} \times \omega / M_{Ni}} \times 3600$$

$Iproduct$: partial current for certain product, CO;

N: the number of electrons transferred for product formation, which is 2 for CO;

F: Faradaic constant, 96485 C mol^{-1};

m_{cat}: mass of catalyst (g),

ω: % of Ni in the catalyst (obtained from EDX, XRF or ICP-OES);

M_{Ni}: atomic mass of Ni, 58.69 g mol^{-1}.

Table A6.2. CO_2 electroreduction performances of Ni-2D-MOF and other electrocatalysts

Catalyst	Electrolyte	Electrode potential	FE (%)	Main Product	Reference
Ni-2D-MOF	**0.1 M $NaHCO_3/NaCO_3$**	**-1.0 vs RHE**	**-**	**$CO+H_2$**	**This work**
CR-MOF	0.5 M $KHCO_3$	-0.78 V	98	HCOOH	[237]
$Al_2(OH)_2$TCPP-Co	0.5 M $KHCO_3$	−0.7 V *vs*. RHE	76	CO	[238]
Fe_MOF-525	1 M $TBATF_6$ in DMF	-1.3 *vs* NHE	50	CO	[222]
Cu_2(CuTCPP)	CH_3CN with 1 M H_2O and 0.5 M $EMIMBF_4$	−1.55 V *vs* Ag/Ag^+	68.4	Acetate	[209]
HKUST-1	0.5m $KHCO_3$	-0.9 *vs* Ag/Ag^+	15.9	CH_3OH and C_2H_5OH	[245]
M-PMOF	0.5 M $KHCO_3$	−0.8 V *vs*. RHE	98.7	CO	[248]
Cu-SIM NU-1000	0.1 M $NaClO_4$	-0.82	28	$HCOO^-$	[251]
TCPP(Co)/Zr-BTB	0.5 M $KHCO_3$	-0.769 *vs*. RHE)	85.1	CO	[244]
PCN-222(Fe)	0.5 M $KHCO_3$	1.2	91	CO	[203]
HKUST-1 mediate Cu	1 M KOH	−1.07 V *vs*. RHE	45	C_2H_4	[253]
OD Cu/C-1000 (Cu-based HKUST-1)	0.1 M $KHCO_3$	−0.1 V *vs*. RHE	45.2-71.2	CH_3OH and C_2H_5OH	[254]
ZIF-8 to Ni SAs/N-C	0.5 M $KHCO_3$	−1.0 V *vs*. RHE	71.9	CO	[256]
Ni SAs/NCNTs	0.5 M $KHCO_3$	-1.0 V *vs*. RHE	95	CO	[259]
ZIF-8 derived Fe-N	0.5 M $NaHCO_3$	-0.4 *vs*. RHE	90	CO	[263]

Appendix A6.3 and A6.4. Refinement parameters, unit cell parameters, refined atom positions, multiplicities, occupancies and isotropic displacement parameters from the refinement of powder X-ray diffraction for 2D-Ni-MOF

Table A6.3. Refinement and lattice parameters

Refinement parameters		**Lattice parameters**	
R_{wp}	2.43 %	**Formular**	$Ni_2(HO_3PC_2H_4COO)_2(4,4'\text{-bipy})_2(H_2O)$
R_P	1.61 %	**Space group**	P-1
X^2	5.05	**a(Å)**	16.5626(9)
		b(Å)	11.3212(6)
		c(Å)	7.7869(4)
		V(Å^3)	1409.3(1)

Table A6.4. Refined atom positions, multiplicities, occupancies and isotropic displacement parameters

Atom label	**element**	**x**	**y**	**z**	**Occup**	**mult**	**U_{iso}**
N1	N	0.690(3)	-0.041(4)	0.158(6)	1	2	0.021(2)
C1	C	0.650(4)	0.011(5)	0.085(8)	1	2	0.021(2)
H1	H	0.576	-0.0417	0.021	1	2	0.019
C2	C	0.628(3)	0.117(5)	0.098(8)	1	2	0.021(2)
H2	H	0.5778	0.1565	-0.016	1	2	0.019
C3	C	0.686(4)	0.120(5)	0.005(7)	1	2	0.021(2)
C4	C	0.746(3)	0.107(5)	0.260(8)	1	2	0.021(2)
H4	H	0.7941	0.2165	0.315	1	2	0.019
C5	C	0.784(3)	0.170(4)	0.167(7)	1	2	0.021(2)
H5	H	0.7844	0.019	0.352	1	2	0.019
C6	C	0.638(4)	0.388(5)	0.103(7)	1	2	0.021(2)
C7	C	0.578(3)	0.305(4)	0.082(6)	1	2	0.021(2)
H7	H	0.5692	0.3456	0.026	1	2	0.019
C8	C	0.636(3)	0.577(7)	0.14(1)	1	2	0.021(2)
H8	H	0.5779	0.5483	0.012	1	2	0.019
N2	N	0.669(2)	0.574(6)	0.169(8)	1	2	0.021(2)
C9	C	0.697(3)	0.427(5)	0.245(6)	1	2	0.021(2)
H9	H	0.802	0.5862	0.276	1	2	0.019
C10	C	0.749(3)	0.370(4)	0.188(8)	1	2	0.021(2)
H10	H	0.804	0.3809	0.275	1	2	0.019
Ni1	Ni	0.6729(7)	0.781(1)	0.174(2)	1	2	0.021(2)
N3	N	0.889(3)	1.495(6)	0.930(9)	1	2	0.021(2)
C11	C	0.843(3)	1.301(6)	0.798(7)	1	2	0.021(2)

H11	H	0.9397	1.5455	0.99	1	2	0.019
C12	C	0.860(4)	1.486(5)	1.005(7)	1	2	0.021(2)
H12	H	0.9517	1.3408	0.985	1	2	0.019
C13	C	0.779(3)	1.351(5)	0.723(6)	1	2	0.021(2)
C14	C	0.774(3)	1.502(5)	0.766(7)	1	2	0.021(2)
H14	H	0.7306	1.2779	0.671	1	2	0.019
C15	C	0.854(5)	1.506(7)	0.87(1)	1	2	0.021(2)
H15	H	0.7251	1.4842	0.684	1	2	0.019
C16	C	0.799(3)	1.120(4)	0.585(7)	1	2	0.021(2)
C17	C	0.847(4)	1.14(1)	0.84(1)	1	2	0.021(2)
H17	H	0.7214	1.1266	0.765	1	2	0.019
C18	C	0.762(4)	1.070(4)	0.825(8)	1	2	0.021(2)
H18	H	0.7201	0.9223	0.769	1	2	0.019
N4	N	0.768(2)	0.896(3)	0.712(6)	1	2	0.021(2)
C19	C	0.827(3)	0.985(4)	0.879(6)	1	2	0.021(2)
H19	H	0.9582	0.9385	0.92	1	2	0.019
C20	C	0.872(5)	1.152(9)	0.89(1)	1	2	0.021(2)
H20	H	0.9624	1.1477	0.954	1	2	0.019
Ni2	Ni	0.8230(7)	0.728(1)	0.842(2)	1	2	0.021(2)
O1	O	0.711(2)	0.730(3)	0.346(4)	1	2	0.021(2)
HO1a	H	0.7228	1.0334	0.6111	1	2	0.019
HO1b	H	0.6652	1.4777	0.6833	1	2	0.019
O2	O	0.596(2)	0.764(3)	0.218(4)	1	2	0.021(2)
C21	C	0.632(3)	0.709(4)	0.720(7)	1	2	0.021(2)
C22	C	0.573(3)	0.615(4)	0.636(6)	1	2	0.021(2)
H22a	H	0.5334	0.5849	0.669	1	2	0.019
H22b	H	0.5849	0.5881	0.525	1	2	0.019
C23	C	0.506(2)	0.703(4)	0.484(6)	1	2	0.021(2)
H23a	H	0.4732	0.758	0.634	1	2	0.019
H23b	H	0.4621	0.663	0.462	1	2	0.019
O3	O	0.660(2)	0.727(3)	0.899(4)	1	2	0.021(2)
O4	O	0.740(2)	0.715(3)	0.772(5)	1	2	0.021(2)
P1	P	0.532(1)	0.842(2)	0.397(2)	1	2	0.021(2)
O5	O	0.417(2)	0.854(2)	0.287(4)	1	2	0.021(2)
O6	O	0.523(2)	0.881(3)	0.588(4)	1	2	0.021(2)
HO6	H	0.2878	1.1039	-0.2108	1	2	0.019
C24	C	0.925(3)	0.827(4)	0.242(7)	1	2	0.021(2)
C25	C	0.944(3)	0.808(4)	0.442(7)	1	2	0.021(2)
H25a	H	0.87	0.84	0.417	1	2	0.019
H25b	H	0.92	0.934	0.358	1	2	0.019
C26	C	1.040(3)	0.934(4)	0.717(5)	1	2	0.021(2)
H26a	H	0.9885	0.877	0.613	1	2	0.019
H26b	H	1.0228	0.814	0.451	1	2	0.019
O7	O	0.799(2)	0.764(3)	0.046(4)	1	2	0.021(2)
O8	O	0.899(2)	0.761(3)	0.090(5)	1	2	0.021(2)
P2	P	0.9484(9)	0.664(1)	0.540(2)	1	2	0.021(2)

O9	O	0.893(2)	0.850(3)	0.673(4)	1	2	0.021(2)
O10	O	0.901(2)	0.525(3)	0.427(5)	1	2	0.021(2)
O11	O	1.003(2)	0.531(3)	0.644(4)	1	2	0.021(2)

Table A6.5. Cartesian Coordinates of DFT-optimized Structures

Intermediate 1 (S = 5, Charge = 0)

Ni	9.77939062	7.11470203	8.88727047
Ni	11.0441511	5.48807384	14.0228742
Li	8.36149006	5.27638002	16.2995399
Li	12.3789099	6.82602998	6.28305014
P	6.93335171	7.33900787	10.7274465
P	13.6229347	5.28478215	11.9298626
O	7.84433024	6.69875316	9.66690377
O	9.04896112	7.17028792	6.95010841
O	7.72413263	5.42990972	14.5357858
O	10.7215871	6.58612105	5.55254011
O	9.3080167	5.49118968	12.9424165
O	5.87553663	8.32424014	10.2955772
O	7.92964125	8.05844721	11.8681577
O	11.7706552	7.44907833	8.21897536
O	10.2125713	5.34559235	16.0662748
O	13.6554145	6.38464822	7.80778216
O	12.3685082	5.51521138	15.722902
O	12.1573531	5.68016445	12.249521
O	13.4399583	3.89841364	11.0424302
O	14.5766771	5.0650004	13.0743036
N	9.47235779	9.17768037	9.05351003
N	9.93998163	5.02487595	8.72644386
N	11.2598978	3.39017134	13.8312269
N	11.0451018	7.57702269	14.0942045
H	9.99424793	1.14982144	8.54280914
C	9.9815107	2.24437322	8.5910741
C	8.91304533	2.96635259	8.06095709
C	8.93034618	4.35295938	8.1526675
C	10.9667166	4.33142776	9.22664427
C	11.0297838	2.94164275	9.18569273
C	12.249654	2.74037653	14.4623453
C	12.5416866	1.40133513	14.2220415
C	11.7834955	0.70532098	13.2832669
C	10.7594847	1.38034975	12.6217196
C	10.535899	2.7197767	12.923478
H	11.9904437	-0.348781	13.0676065
C	9.90253291	8.26309277	14.1922341
C	12.1788953	8.23635858	13.8163281
C	9.51909687	6.83252855	5.82088287
C	8.11880135	5.31650766	13.347415
C	8.49608562	6.67709523	4.7167622

C	7.11349764	4.91120117	12.2784473
C	6.20631032	6.02729078	11.7637293
C	12.9138714	7.01287073	8.6003599
C	11.40384	5.42500194	16.5218657
C	13.4043181	7.42359133	9.97735401
C	14.3369839	6.50021722	10.7529691
C	8.32320164	9.72100424	8.63493243
C	10.3604886	9.94917598	9.6938619
C	9.83995922	9.63944596	13.9897796
C	12.2086077	9.60882714	13.600396
C	8.00605189	11.0572429	8.85896413
C	10.1235564	11.2919894	9.96417892
C	11.0126198	10.3236503	13.6793236
C	8.91933927	11.8559646	9.54340423
H	10.9975648	11.4047611	13.5016128
H	8.69762301	12.9097566	9.74532865
C	11.6257989	5.39295471	18.0008534
H	7.63914981	9.04321528	8.11500877
H	8.06859411	2.46257051	7.5801935
H	8.11025947	4.96573504	7.76660868
H	11.7694872	4.90684894	9.6981173
H	11.8891857	2.43156528	9.62943709
H	12.8303059	3.32744103	15.1818921
H	13.3596815	0.91542086	14.7630421
H	10.1394959	0.88104103	11.8704789
H	9.74936465	3.29040033	12.4173045
H	9.00655892	7.6762593	14.4288392
H	13.0901053	7.62809579	13.7650712
H	6.47031122	4.12635494	12.7160599
H	7.65716593	4.45553779	11.4313179
H	5.69168498	6.53259088	12.602442
H	5.40663247	5.57864284	11.1459347
H	7.96467884	9.02484655	11.7424719
H	12.5455165	7.72887395	10.5927985
H	13.9505576	8.36664767	9.77222438
H	15.0015001	7.11579629	11.3856092
H	15.0060717	5.95145495	10.0644966
H	11.2874672	9.44998582	9.99600778
H	8.87923433	10.1585294	14.0678709
H	13.1560519	10.1074532	13.3728134
H	7.05152217	11.4572799	8.50272166
H	10.8753144	11.8819156	10.4978346
H	8.9498746	6.76696245	3.71725607

H	7.67608577	7.40551276	4.82209065
H	8.0466423	5.66990331	4.79562096
H	14.3013757	3.47375437	10.8731758
H	12.6931673	5.47505854	18.2512277
H	11.228984	4.4502724	18.4148722
H	11.072774	6.21284197	18.489235
O	10.4010769	7.19390412	10.9078575
H	11.0030182	6.54315093	11.3357333
H	9.60632271	7.2255534	11.4684389

Intermediate 1 (S = 3, Charge = 0)

Ni	9.77107111	7.07784901	8.83456753
Ni	10.861705	5.43970429	14.0184062
Li	8.36149009	5.27638003	16.2995398
Li	12.3789099	6.82602997	6.2830502
P	6.922363	7.24064212	10.6643516
P	13.6555299	5.37605232	11.8511266
O	7.84467972	6.59978232	9.61454176
O	9.04226689	7.11022208	6.89625203
O	7.9041191	5.25796101	14.4748979
O	10.7413148	6.55382758	5.52111929
O	9.33210677	5.44385371	12.7661215
O	5.84420844	8.19717203	10.219616
O	7.90700364	7.99861965	11.7883423
O	11.7613039	7.46168866	8.18354969
O	10.1297139	5.53829377	16.6704921
O	13.7053037	6.50299589	7.79579657
O	12.0722591	5.43573815	15.5922561
O	12.1560186	5.63018774	12.1053669
O	13.652529	4.00644233	10.9110664
O	14.5591616	5.19322869	13.0468958
N	9.40349951	9.13459826	8.99534115
N	10.0191711	5.00165043	8.65742514
N	10.8343375	3.44559215	13.9379502
N	10.9339368	7.4264236	14.0594939
H	10.3999368	1.16585613	8.21926402
C	10.2932305	2.24923404	8.34269578
C	9.15154989	2.90730083	7.8859868
C	9.05429554	4.28197232	8.06565926
C	11.110716	4.36892244	9.09699465
C	11.2915217	2.99578277	8.96273976
C	10.7899409	2.65818999	15.0233894
C	10.7798708	1.27113278	14.936303

C	10.8162102	0.67587117	13.6771473
C	10.8588591	1.49547096	12.5509259
C	10.8645023	2.87441908	12.7221985
H	10.8123702	-0.414624	13.5747712
C	9.83985597	8.19695424	14.0677336
C	12.1415116	7.9975509	13.9178737
C	9.53029944	6.77154898	5.77494702
C	8.17984627	5.21028685	13.2518843
C	8.52228899	6.57765133	4.66364108
C	7.11742742	4.8176098	12.2413109
C	6.21527137	5.94044811	11.7320148
C	12.9255013	7.09841822	8.57756135
C	11.3863237	5.56368948	16.65491
C	13.3871265	7.54851874	9.95287206
C	14.3495538	6.67202025	10.7459259
C	8.25243435	9.65074851	8.54651918
C	10.2511776	9.92734828	9.66471182
C	9.90717089	9.5777413	13.9063129
C	12.2926007	9.36698367	13.7449875
C	7.89531448	10.9780139	8.76259297
C	9.97226725	11.2633209	9.92963619
C	11.1537226	10.1731596	13.7307298
C	8.76801909	11.7986088	9.47337893
H	11.238878	11.2560065	13.5869339
H	8.51488036	12.8460704	9.67109856
C	12.1280201	5.73185795	17.9491977
H	7.59883608	8.95930781	8.00559174
H	8.33892348	2.36481909	7.39274031
H	8.17604969	4.84663881	7.73746681
H	11.8704861	4.98184792	9.59094507
H	12.2027469	2.53714803	9.35717443
H	10.7531874	3.15956645	15.995354
H	10.7497453	0.67070645	15.8505262
H	10.8948262	1.07537623	11.5412579
H	10.9149523	3.56298313	11.8728733
H	8.88038585	7.68385586	14.1881749
H	13.0043584	7.32221337	13.9306797
H	6.47853948	4.05442732	12.7198303
H	7.62147636	4.33537697	11.3846399
H	5.71927229	6.45952075	12.5734252
H	5.40009853	5.48592988	11.1395475
H	7.89835728	8.96588837	11.6645464
H	12.5117462	7.82061275	10.5611873

H	13.8954886	8.51169362	9.74315935
H	14.9416019	7.31605717	11.4212643
H	15.0843832	6.19388816	10.0717022
H	11.1779779	9.45364498	10.0054513
H	8.98641718	10.1697438	13.9055505
H	13.2937387	9.7912972	13.6193026
H	6.94042374	11.3552197	8.38293937
H	10.6891633	11.8694082	10.4923282
H	8.98385558	6.66461668	3.66745364
H	7.68465542	7.28820785	4.7504838
H	8.09408947	5.56194483	4.7512332
H	14.5570506	3.66470062	10.7872474
H	13.2174051	5.76818706	17.803004
H	11.8800314	4.89579197	18.6243349
H	11.7935805	6.65504472	18.4514507
O	10.4073249	7.1763191	10.8329246
H	11.0180784	6.5194531	11.2486862
H	9.60948055	7.18124092	11.38793

Intermediate 1 (S = 1, Charge = 0)

Ni	9.65595489	7.12675574	8.69079635
Ni	10.7558314	5.46420451	13.8729597
Li	8.36149007	5.27638003	16.2995398
Li	12.3789099	6.82602997	6.28305018
P	6.7697115	7.23280976	10.6806758
P	13.5517016	5.42864679	11.7014712
O	7.61212784	6.51568285	9.62101074
O	8.95393822	7.20031113	6.82602301
O	7.96654267	5.2653475	14.4609181
O	10.7114558	6.51840507	5.58829711
O	9.21555993	5.45583219	12.6240225
O	5.70009553	8.21683665	10.2684425
O	7.85391907	8.01534505	11.6970376
O	11.8412181	7.71905434	8.08954525
O	10.1342318	5.48393167	16.6718563
O	13.6543014	6.47694557	7.83751601
O	11.9837324	5.43641659	15.4269215
O	12.0520718	5.69887962	11.9483753
O	13.5333227	4.16315874	10.6254443
O	14.4235352	5.10324366	12.8895818
N	9.24596272	9.09996886	8.90087674
N	9.90170156	5.13157894	8.49798573
N	10.7650357	3.47501786	13.7543736

N	10.8090452	7.4488264	13.9512757
H	10.2470797	1.29427548	8.06193521
C	10.1492562	2.37830185	8.18647384
C	9.00574481	3.04403209	7.74607012
C	8.92013045	4.4189958	7.92159768
C	10.9938897	4.49299243	8.93018276
C	11.160439	3.11861674	8.79181657
C	10.6850564	2.6762752	14.8286287
C	10.7007933	1.29015604	14.725986
C	10.8011232	0.71050198	13.4627929
C	10.8761435	1.54336902	12.3478123
C	10.85342	2.92043688	12.5341478
H	10.8197911	-0.3787301	13.3486859
C	9.7139749	8.21751262	13.9745859
C	12.0143291	8.02446593	13.8017508
C	9.51241226	6.84337231	5.73622521
C	8.11193748	5.2242296	13.2140534
C	8.59427532	6.77443317	4.54017596
C	6.94239133	4.85463723	12.3220765
C	6.0698527	6.01904036	11.8568609
C	12.9300462	7.22918551	8.54015529
C	11.382079	5.52933448	16.5433036
C	13.374378	7.6885191	9.92026635
C	14.2981204	6.80306168	10.7435578
C	8.06413267	9.5802813	8.49272983
C	10.0900292	9.9109251	9.55523577
C	9.77726865	9.59929508	13.8193005
C	12.1611099	9.39473918	13.6356506
C	7.67308609	10.892839	8.73456746
C	9.77366536	11.2336373	9.84079923
C	11.020287	10.1985621	13.6353375
C	8.54025594	11.7344174	9.42624849
H	11.1018892	11.2823858	13.4970004
H	8.2605128	12.7714547	9.64172221
C	12.2317097	5.68752002	17.7717218
H	7.41410928	8.8734694	7.9694638
H	8.18174352	2.50782233	7.26535796
H	8.04242939	4.98712725	7.60257702
H	11.7646099	5.09747013	9.41418938
H	12.0752901	2.65441162	9.16989978
H	10.5955009	3.16889293	15.8025645
H	10.6421244	0.67896568	15.6314321
H	10.9600331	1.13476714	11.3360166

H	10.9301614	3.6236417	11.6986021
H	8.75698175	7.70310473	14.1026533
H	12.8795455	7.35249765	13.8069683
H	6.31000952	4.14819722	12.8876844
H	7.33484783	4.31785001	11.4400991
H	5.69677947	6.59699653	12.7230478
H	5.17251224	5.60510858	11.3616163
H	7.75211534	8.98208315	11.6286514
H	12.4824696	7.96613201	10.5060489
H	13.8938281	8.64887486	9.72533991
H	14.8104572	7.42555089	11.4999816
H	15.0991346	6.37584945	10.1117706
H	11.0404745	9.462867	9.85896756
H	8.85514051	10.1890686	13.8290838
H	13.1604074	9.82135843	13.5038319
H	6.69468591	11.2405888	8.3889949
H	10.4879952	11.8565304	10.3877336
H	9.14071983	6.97637244	3.60546019
H	7.74138698	7.46451507	4.63278328
H	8.18609511	5.74946335	4.46853553
H	14.4336982	3.82592757	10.464276
H	13.3054275	5.70973486	17.5355884
H	12.029974	4.85969206	18.4722059
H	11.9554191	6.61761279	18.2965707
O	10.3087494	7.20416504	10.6316771
H	10.9235939	6.54866866	11.049997
H	9.51575158	7.22833188	11.1982422

Intermediate 1 (S = 4, Charge = -4)

Ni	9.72129842	7.21426012	8.81982204
Ni	10.9116928	5.56281259	13.9714735
Li	8.36149005	5.27638002	16.2995399
Li	12.37891	6.82602998	6.28305012
P	6.82492155	7.42558917	10.6861936
P	13.5858987	5.45169274	11.9106062
O	7.71936206	6.73206928	9.64969813
O	9.01872095	7.21488476	6.84676986
O	7.70281345	5.44039727	14.566945
O	10.7358908	6.52460763	5.56025139
O	9.1341229	5.68735905	12.8600992
O	5.76780077	8.40126118	10.2208524
O	7.82676176	8.19942286	11.7840359
O	11.8073126	7.66865553	8.17613287

O	10.0755283	5.40244553	16.8036009
O	13.5987971	6.42086244	7.82019775
O	12.049664	5.50219152	15.7566086
O	12.0970836	5.78723684	12.1216521
O	13.5419697	4.01388316	11.0769148
O	14.4750801	5.30925372	13.1237868
N	9.35851877	9.26330166	8.94671687
N	9.956266	5.1389743	8.69620606
N	10.9005169	3.5269364	13.8142671
N	10.9385139	7.6143353	14.132149
H	10.2993924	1.290346	8.3087735
C	10.2031124	2.37636104	8.41852436
C	9.07005695	3.04122841	7.94865261
C	8.9867027	4.41901726	8.11003455
C	11.0365384	4.49696739	9.15336679
C	11.2040201	3.12042629	9.03828293
C	11.6681526	2.73151196	14.5948018
C	11.9238416	1.39809886	14.3101147
C	11.3721724	0.8240174	13.1590788
C	10.5846739	1.64079433	12.3411189
C	10.3826008	2.96705538	12.6950151
H	11.5564677	-0.2256777	12.9063682
C	9.85640656	8.40499396	14.0734506
C	12.1479481	8.18186339	13.9667013
C	9.52107456	6.77680967	5.76944874
C	7.99982836	5.42283467	13.3389967
C	8.54327963	6.49361396	4.64984109
C	6.92502736	5.03378609	12.3306393
C	6.07157155	6.18045763	11.7912864
C	12.9038187	7.15076129	8.57493356
C	11.3357372	5.482463	16.79394
C	13.4061952	7.56984579	9.94721532
C	14.3343581	6.64759452	10.728674
C	8.20057942	9.77440116	8.50943937
C	10.2143659	10.0658754	9.59474253
C	9.93318937	9.77384274	13.836011
C	12.3168164	9.53834656	13.7183974
C	7.84347256	11.1032724	8.71654871
C	9.93656238	11.4041568	9.84996741
C	11.186773	10.3568637	13.6465175
C	8.72450046	11.9332189	9.40608946
H	11.2830664	11.4301961	13.4474307
H	8.47223844	12.9823244	9.59643769

C	12.0301124	5.54832973	18.1335179
H	7.54006927	9.07570407	7.98607002
H	8.25388616	2.50071806	7.45863928
H	8.11614331	4.98815036	7.7690616
H	11.7941917	5.11156306	9.6484096
H	12.1075755	2.65738494	9.44494073
H	12.0977984	3.21040725	15.4811792
H	12.5540695	0.81164762	14.9874966
H	10.1329765	1.25267677	11.4215609
H	9.78315016	3.63560751	12.066018
H	8.88908104	7.90855025	14.2068764
H	13.0071703	7.50107613	14.0173952
H	6.25073998	4.30143752	12.810122
H	7.41747262	4.5214116	11.4824525
H	5.59504441	6.73806964	12.6197891
H	5.23746797	5.75069942	11.2055392
H	7.84766441	9.15854782	11.6116667
H	12.5421194	7.87486669	10.5581358
H	13.950228	8.51397295	9.73979237
H	15.0024059	7.26303339	11.3582892
H	14.9985337	6.08999313	10.0428515
H	11.1480115	9.59549998	9.92195774
H	9.0154386	10.3709086	13.7955147
H	13.32335	9.94861733	13.5827886
H	6.88247398	11.4747611	8.34635096
H	10.6610949	12.0178343	10.394648
H	9.01813345	6.58231044	3.6595137
H	7.65816254	7.14799024	4.6971363
H	8.18416837	5.45241721	4.75094431
H	14.4226818	3.59656283	11.0635445
H	13.1254221	5.59313267	18.0342361
H	11.758584	4.66688311	18.740173
H	11.6855297	6.43302435	18.696497
O	10.3410783	7.33475808	10.8544682
H	10.9547199	6.68806076	11.2760186
H	9.54067929	7.33317999	11.4083636

Intermediate 1 (S = 6, Charge = -1)

Ni	9.73179721	7.08694685	8.85982033
Ni	11.0393401	5.49244292	14.0194866
Li	8.36149007	5.27638003	16.2995398
Li	12.3789099	6.82602997	6.28305015
P	6.86100868	7.29798751	10.6671093

P	13.6301943	5.26087884	11.9171268
O	7.77845249	6.64081122	9.62055805
O	9.02845553	7.15409702	6.88869787
O	7.70347429	5.41944876	14.5440692
O	10.7339336	6.58681353	5.52312894
O	9.28667696	5.46920417	12.95079
O	5.74679621	8.19667611	10.1869171
O	7.82315378	8.08177912	11.7816419
O	11.7643455	7.43502843	8.21213264
O	10.2101057	5.33314528	16.0773699
O	13.6640743	6.39295727	7.80384229
O	12.3673872	5.4954397	15.724387
O	12.1622165	5.63976734	12.235226
O	13.4690161	3.88097947	11.0140296
O	14.582782	5.03706157	13.0628157
N	9.44246788	9.12668286	9.07795698
N	9.92693704	5.01685677	8.66797059
N	11.2327325	3.37761119	13.8482637
N	11.0473582	7.55241827	14.0848565
H	10.1278899	1.13799202	8.33083055
C	10.0726722	2.22786097	8.42536214
C	8.97139082	2.93874211	7.93045002
C	8.93905416	4.31731176	8.07035144
C	10.9826984	4.33116868	9.14326302
C	11.0981758	2.95153741	9.04174611
C	12.1748919	2.70448457	14.526241
C	12.4549085	1.36121801	14.2940786
C	11.7330853	0.68297595	13.3144531
C	10.7568457	1.38073098	12.6056871
C	10.5443394	2.72328645	12.9012487
H	11.9335068	-0.3728874	13.1013432
C	9.89817671	8.26345166	14.1453256
C	12.1905092	8.22322182	13.8019037
C	9.52190815	6.81304884	5.77260364
C	8.09500856	5.30682481	13.3548768
C	8.52157354	6.62393274	4.65177116
C	7.08559182	4.90997649	12.2875019
C	6.17276013	6.0252125	11.7798855
C	12.9068001	7.0062024	8.59575309
C	11.404012	5.4087019	16.5247743
C	13.3813028	7.40801192	9.98219798
C	14.3304788	6.49663576	10.7523453
C	8.2998295	9.73712036	8.65590183

C	10.3702703	9.90312103	9.69651838
C	9.84053337	9.62326815	13.8923606
C	12.2210324	9.58050442	13.5386546
C	8.04782434	11.0813855	8.85526104
C	10.1928468	11.2542373	9.93306352
C	11.0179771	10.312315	13.5532079
C	9.0021862	11.8808698	9.51303579
H	11.0063353	11.3870708	13.3437023
H	8.82797293	12.9475867	9.68754145
C	11.6325881	5.37161422	18.0039017
H	7.5763545	9.08484018	8.15727045
H	8.13967112	2.42528023	7.43621968
H	8.09346886	4.91121829	7.70952831
H	11.7656657	4.91652292	9.63671536
H	11.9848513	2.46159316	9.4545333
H	12.7284339	3.27543699	15.2792027
H	13.237179	0.85973848	14.8722918
H	10.1701558	0.89664323	11.818406
H	9.79830933	3.31278443	12.3562935
H	8.9951216	7.68873294	14.3849615
H	13.1050081	7.61671535	13.7777555
H	6.44719834	4.12086654	12.7249138
H	7.62621596	4.45884047	11.4355001
H	5.69246854	6.55578513	12.6237183
H	5.34364033	5.56919589	11.2082232
H	8.36032437	8.78424429	11.3669191
H	12.5125044	7.68863688	10.5961805
H	13.9045476	8.36775386	9.79485575
H	14.9824415	7.11912879	11.3916205
H	15.0104554	5.96722091	10.0594591
H	11.2840424	9.37843357	9.99715663
H	8.87456265	10.1385877	13.9367226
H	13.1770056	10.0658677	13.3118523
H	7.1037794	11.5066742	8.49542559
H	10.9858515	11.8175132	10.4381439
H	8.9887713	6.72280001	3.65904106
H	7.67848619	7.32815027	4.73853283
H	8.1000175	5.60433756	4.7259695
H	14.3368098	3.46440157	10.8582846
H	12.7012362	5.44977945	18.2506624
H	11.2349501	4.42867786	18.4168225
H	11.0839712	6.19137502	18.4975886
O	10.3470276	7.08329105	10.9114314

H	11.0477866	6.49480043	11.2770406
H	9.58393687	6.88516319	11.4799143

Intermediate 2 (S = 5, Charge = 0)

Ni	9.60337543	7.41512006	8.49146194
Ni	10.9804772	5.56316994	14.0843188
Li	8.36149007	5.27638002	16.2995398
Li	12.3789099	6.82602997	6.28305015
P	7.80014227	8.05919824	10.6380782
P	13.5124164	5.4838311	11.9338763
O	7.57564845	7.41027546	9.25886425
O	9.00271545	7.22687087	6.56700836
O	7.66509735	5.4947818	14.5655008
O	10.7943313	6.51007752	5.39998852
O	9.26872306	5.40247967	12.9967689
O	7.62113665	9.53940928	10.8514638
O	9.4398124	7.65997683	10.8095997
O	11.6322355	7.46556237	8.07804993
O	10.1907861	5.49229813	16.1328635
O	13.6303611	6.56724755	7.93798383
O	12.3315947	5.78141677	15.7667745
O	12.0593759	5.7610294	12.3579251
O	13.3580415	4.21363235	10.875884
O	14.563641	5.19262018	12.9757315
N	9.56536226	9.4923246	8.40408298
N	9.59218861	5.36593105	8.78404762
N	11.3538062	3.48905519	13.9937891
N	10.8155378	7.67120867	14.0636448
H	9.39147145	1.56776713	9.53256096
C	9.4481331	2.6413482	9.31986654
C	8.506391	3.2537136	8.492983
C	8.61585292	4.6178034	8.25048979
C	10.4941951	4.77889795	9.57840996
C	10.4640083	3.41928083	9.86872757
C	12.5119879	3.00079644	14.4630775
C	12.9310198	1.69811204	14.2134795
C	12.1206489	0.86754682	13.4411546
C	10.9160978	1.3732625	12.956508
C	10.5734326	2.68838459	13.2551217
H	12.4234745	-0.1614708	13.218004
C	9.63363496	8.29657278	14.1072771
C	11.9069919	8.37452289	13.7326724
C	9.57303675	6.76317684	5.52770553

C	8.06771046	5.5061264	13.3711614
C	8.65633137	6.45907491	4.36688028
C	7.04626551	5.70785333	12.260182
C	6.83591071	7.1888947	11.9226729
C	12.7483903	7.13003873	8.62005229
C	11.3756902	5.68518348	16.5738395
C	12.9820119	7.5765168	10.0479046
C	14.0480566	6.8810708	10.8823117
C	8.57202974	10.1188362	7.76182832
C	10.4401809	10.2191692	9.10835293
C	9.4836645	9.64261101	13.7850987
C	11.85097	9.72320828	13.3930751
C	8.41803542	11.4998758	7.79488981
C	10.3578217	11.6030735	9.20386502
C	10.6139351	10.3670854	13.4079565
C	9.32499678	12.2567704	8.53378446
H	10.5339473	11.426111	13.1383894
H	9.2285016	13.3466955	8.58615329
C	11.5903836	5.78482153	18.0507852
H	7.88307166	9.47512499	7.20488352
H	7.6924007	2.68472825	8.03352137
H	7.90272784	5.14942851	7.61192042
H	11.2536503	5.43153388	10.0198647
H	11.233572	2.99948869	10.5219252
H	13.1209645	3.69390664	15.0523351
H	13.8862895	1.3450416	14.6146799
H	10.2493374	0.76283402	12.3382879
H	9.64478502	3.13287002	12.8799405
H	8.77339237	7.68677819	14.4108451
H	12.8530875	7.82138556	13.7345306
H	6.08395278	5.29083446	12.6021483
H	7.35255227	5.14240169	11.3612324
H	6.88592922	7.81129103	12.8354818
H	5.80236833	7.33069815	11.5523977
H	9.91781464	8.32897889	11.3315395
H	12.0154469	7.59083926	10.5813944
H	13.2592309	8.64492228	9.93948049
H	14.4820902	7.60734521	11.5945262
H	14.8884521	6.54842118	10.2455275
H	11.2322239	9.65872976	9.61931304
H	8.49268672	10.1051466	13.8166603
H	12.7655977	10.2574881	13.1166419
H	7.59319536	11.9738051	7.25384323

H	11.0957399	12.1551317	9.79359527
H	9.17883163	6.55946721	3.40250481
H	7.75577643	7.09288439	4.37302605
H	8.32022541	5.40902553	4.45018513
H	14.2298759	3.83984282	10.6515856
H	12.6215625	6.08086346	18.2918669
H	11.3831061	4.80782458	18.5205027
H	10.8831106	6.50764297	18.4898117

Intermediate 2 (S = 4, Charge = -1)

Ni	9.52423995	7.32033254	8.45764936
Ni	10.9501723	5.56262236	14.0933278
Li	8.36149009	5.27638004	16.2995398
Li	12.3789099	6.82602996	6.28305022
P	7.72148275	8.03390265	10.5664144
P	13.5009766	5.67208448	11.8844409
O	7.48595116	7.30728515	9.22839033
O	9.00397587	6.9520151	6.49910351
O	7.61551169	5.46934844	14.586344
O	10.8636051	6.38500604	5.35383325
O	9.22202366	5.49690275	13.0185411
O	7.4839208	9.51583996	10.6986162
O	9.37224661	7.69210091	10.7213851
O	11.5589044	7.35767794	8.049211
O	10.1861157	5.31476325	16.22041
O	13.6719297	6.77492489	7.95589053
O	12.3411903	5.50136612	15.7940612
O	12.0341435	5.76484091	12.3250501
O	13.4728613	4.47309618	10.7313886
O	14.579253	5.40897009	12.9126562
N	9.45752697	9.39044499	8.19029011
N	9.53959662	5.26322226	8.83176313
N	11.1018176	3.43170405	13.9759597
N	10.8745679	7.67321789	14.2942489
H	9.26256321	1.57736782	10.0096521
C	9.34510776	2.61744513	9.67385952
C	8.45248494	3.13316461	8.73131048
C	8.58315824	4.46056189	8.34182366
C	10.4015493	4.76447599	9.72440481
C	10.3401306	3.45027985	10.1774197
C	12.2549425	2.88411677	13.5553864
C	12.3412325	1.58206311	13.0754459
C	11.1846773	0.79942219	13.0295857

C	9.98571489	1.36327863	13.4745397
C	9.99206979	2.67445611	13.935365
H	11.2167641	-0.2302933	12.6564422
C	9.66230845	8.28220782	14.1628513
C	11.9307224	8.32175167	13.728932
C	9.6189788	6.48331021	5.49184466
C	8.02248366	5.53865291	13.3916734
C	8.73864194	5.96397761	4.37706183
C	7.00005894	5.73702865	12.2796499
C	6.82124803	7.22099022	11.933264
C	12.7034487	7.21683279	8.61195471
C	11.4010408	5.37251582	16.6113097
C	12.8486737	7.73250915	10.0277848
C	13.9414444	7.15426812	10.9114943
C	8.46858539	9.95424204	7.47904729
C	10.2416015	10.1870015	8.93713386
C	9.4583558	9.45281025	13.4557407
C	11.819182	9.48865064	12.9967154
C	8.23357749	11.3219894	7.47309401
C	10.0733163	11.5644927	8.99695781
C	10.5482224	10.0755589	12.8114033
C	9.04999482	12.1496657	8.25093636
H	10.4228666	11.0056439	12.245962
H	8.89106538	13.2331774	8.27124525
C	11.6759034	5.27967778	18.0852636
H	7.85340772	9.26427145	6.89015539
H	7.65754451	2.51417532	8.30407613
H	7.90090121	4.91411697	7.6142893
H	11.147139	5.45737767	10.1276091
H	11.0688179	3.105328	10.9195523
H	13.1395563	3.53512981	13.5886525
H	13.3064238	1.19048825	12.7363866
H	9.0534428	0.78863319	13.4684713
H	9.07013009	3.15316652	14.290723
H	8.8226272	7.77582132	14.6595999
H	12.9111295	7.84754033	13.8778388
H	6.03114566	5.33113205	12.6164253
H	7.31099495	5.16102089	11.387616
H	6.98703914	7.85012384	12.8279656
H	5.76762719	7.41411216	11.6546624
H	9.83366524	8.36343712	11.2679231
H	11.8685046	7.66851777	10.5306155
H	13.0333586	8.81797386	9.89465487

H	14.2618026	7.91094099	11.650787
H	14.8401155	6.91506027	10.3124705
H	11.0393011	9.68346662	9.49504236
H	8.44975705	9.87423174	13.3817992
H	12.7214443	9.94495783	12.5708437
H	7.42317906	11.7338882	6.86360753
H	10.7398732	12.1700158	9.61995414
H	9.2611318	5.97435747	3.40770537
H	7.79573568	6.52885102	4.30446692
H	8.47311401	4.91422352	4.60166315
H	14.3752765	4.27230645	10.4221738
H	12.7526725	5.33469745	18.304282
H	11.274137	4.33298703	18.4856173
H	11.1560299	6.09444596	18.6180845

Intermediate 2 (S = 6, Charge = -1)

Ni	9.59925659	7.43384587	8.47960182
Ni	10.9758917	5.57027211	14.0910669
Li	8.36149008	5.27638003	16.2995398
Li	12.3789099	6.82602997	6.28305019
P	7.76560871	8.07540619	10.6471543
P	13.5060837	5.53439638	11.9608572
O	7.54792362	7.42462842	9.26999822
O	9.02684776	7.25691336	6.52202746
O	7.65050955	5.48536991	14.5723646
O	10.8120367	6.47630192	5.38494192
O	9.25844574	5.44299931	13.0060173
O	7.54264039	9.54862263	10.8758401
O	9.40659083	7.70938051	10.8379852
O	11.6428353	7.48950924	8.05314878
O	10.1828258	5.52668978	16.153054
O	13.6336687	6.56913025	7.93995095
O	12.3238198	5.81878432	15.7823431
O	12.0397813	5.79110611	12.3460462
O	13.4195862	4.22765738	10.9398473
O	14.5404734	5.29954468	13.0348488
N	9.56765163	9.48920102	8.38980938
N	9.59472697	5.40284392	8.73157209
N	11.3090883	3.51473827	13.9936111
N	10.8052767	7.68670723	14.0765371
H	9.47168812	1.51275473	9.1410926
C	9.49970956	2.60243107	9.03341325
C	8.51889499	3.28884771	8.29896115

C	8.59941044	4.66331651	8.1679624
C	10.5248154	4.74199424	9.45762579
C	10.5237764	3.36679712	9.62279167
C	12.3171459	2.90310977	14.6580343
C	12.7086097	1.5986301	14.4084232
C	12.0460209	0.85956042	13.4113036
C	11.0092946	1.49330701	12.7156322
C	10.6742597	2.80167812	13.0291088
H	12.3330216	-0.1726226	13.1839167
C	9.62154908	8.30714791	14.1415494
C	11.8880086	8.39794691	13.7332994
C	9.58983421	6.73609575	5.50883976
C	8.05627161	5.51553824	13.3781182
C	8.66704015	6.3656655	4.37049402
C	7.03563337	5.70698821	12.2651
C	6.81210195	7.18713075	11.9320105
C	12.7470066	7.14373896	8.60871989
C	11.3667648	5.7338772	16.5883629
C	12.9627482	7.59171758	10.0390347
C	14.0344692	6.91538536	10.8818399
C	8.61832337	10.1505145	7.69022812
C	10.4257528	10.2241178	9.13357599
C	9.46141832	9.655691	13.8351817
C	11.8213272	9.74887495	13.4049575
C	8.48803843	11.5285827	7.71398757
C	10.3605866	11.6041748	9.2180557
C	10.5824341	10.3889254	13.4475587
C	9.36900424	12.2883121	8.49957779
H	10.4940192	11.4503252	13.1906486
H	9.28827983	13.3793099	8.54530827
C	11.5801591	5.86033806	18.0644673
H	7.94586971	9.52261629	7.09519181
H	7.69257329	2.75405151	7.81684359
H	7.85407687	5.22958991	7.60033754
H	11.2960873	5.35809282	9.93431288
H	11.3230482	2.90580187	10.2104099
H	12.8300567	3.51156038	15.412116
H	13.531925	1.16189308	14.9838492
H	10.4639045	0.97640968	11.9171299
H	9.88022847	3.32961205	12.4902682
H	8.7674902	7.69116914	14.4502699
H	12.8370914	7.84991973	13.7184076
H	6.07703883	5.27555173	12.6001354

H	7.35471853	5.14935701	11.3652344
H	6.86189861	7.80578704	12.8476735
H	5.77554146	7.32266489	11.567814
H	9.86509872	8.38903453	11.3633879
H	11.9902302	7.58505778	10.5624405
H	13.217108	8.66615247	9.93461241
H	14.4679016	7.65423168	11.5813993
H	14.8746422	6.57587207	10.2481811
H	11.1883052	9.65729741	9.68023336
H	8.46897201	10.1136578	13.8888461
H	12.7294351	10.2892096	13.1184772
H	7.69713481	12.0079266	7.12715178
H	11.0837674	12.14243	9.84000287
H	9.19053911	6.38468383	3.40171511
H	7.77845746	7.01545049	4.33340458
H	8.30874995	5.33227654	4.53325603
H	14.3095824	3.87837375	10.7514793
H	12.6100558	6.16405147	18.3018147
H	11.3758946	4.8906741	18.5506085
H	10.8700445	6.58765349	18.4916145

Intermediate H2 (S = 5, Charge = 0)

92

Coordinates from ORCA-job orca

Ni	9.64499507	7.05627866	8.7920941
Ni	11.0351169	5.48565751	13.9843743
Li	8.36149005	5.27638002	16.2995399
Li	12.3789099	6.82602998	6.28305012
P	6.9415321	7.2804266	10.7193306
P	13.6318371	5.21541528	11.9166569
O	7.80013422	6.58990447	9.63741501
O	8.95141266	7.24428839	6.90143039
O	7.71929146	5.39895816	14.5328447
O	10.6941633	6.6374596	5.60484163
O	9.29359929	5.4028345	12.92775
O	5.87723611	8.26344434	10.2939106
O	7.99467274	8.01867492	11.7707435
O	11.6507287	7.45912381	8.33694152
O	10.2121317	5.38177575	16.0572012
O	13.547798	6.44180397	7.85030758
O	12.3629504	5.56282367	15.6765346
O	12.1955857	5.62508741	12.2886021
O	13.406748	3.88240783	10.9510013

O	14.6375273	4.91480656	12.9996344
N	9.38335422	9.08539966	9.1821599
N	9.86732022	5.00096989	8.61533632
N	11.255193	3.36561531	13.8718897
N	10.9517047	7.57853845	14.0336479
H	9.94971374	1.12597951	8.53141885
C	9.9293428	2.22117703	8.55148606
C	8.90358482	2.92396713	7.91978086
C	8.90939034	4.31199145	7.97749821
C	10.8537326	4.32700546	9.2174094
C	10.9246514	2.937564	9.21107587
C	12.2341588	2.72938313	14.5323622
C	12.5448722	1.39102521	14.310927
C	11.8171969	0.68014432	13.3588476
C	10.8018225	1.33946945	12.6692652
C	10.5573508	2.67868035	12.9557144
H	12.040678	-0.3728038	13.1541993
C	9.7973406	8.2143205	14.2599025
C	12.047986	8.30022399	13.7619928
C	9.49531702	6.95368396	5.78665488
C	8.10819078	5.25745055	13.3427533
C	8.56662539	6.95864251	4.59609484
C	7.09030992	4.85477198	12.2854873
C	6.20349593	5.98529801	11.7701939
C	12.8060475	7.02358955	8.67688866
C	11.4095014	5.47491754	16.4904152
C	13.3002145	7.38722701	10.0648946
C	14.3035043	6.48725534	10.7738736
C	8.28267238	9.70510357	8.7404224
C	10.2481708	9.76454538	9.94705925
C	9.68803996	9.60167454	14.2163959
C	12.0293487	9.68900766	13.6967308
C	7.99845093	11.0303214	9.05425595
C	10.04132	11.0888546	10.3120877
C	10.8240446	10.3531782	13.9262781
C	8.89132531	11.7345001	9.85818808
H	10.7723042	11.4466036	13.8751772
H	8.69437533	12.7784992	10.1252719
C	11.6564383	5.45875392	17.9664378
H	7.61288777	9.1015553	8.11994552
H	8.09876823	2.40437087	7.39055165
H	8.12126414	4.90886289	7.50701611
H	11.6079819	4.91696495	9.75098827

H	11.7501741	2.441664	9.72882748
H	12.7944252	3.3272432	15.2594086
H	13.3545429	0.91764367	14.8750146
H	10.2070035	0.82893156	11.9048661
H	9.77544385	3.23661684	12.4286865
H	8.92997522	7.57768109	14.4710926
H	12.9683682	7.73058686	13.5843091
H	6.43492207	4.08468764	12.7316629
H	7.62255902	4.38287284	11.4387849
H	5.70636629	6.50520588	12.610913
H	5.38783074	5.55132124	11.1626005
H	7.80234942	8.97193234	11.8287541
H	12.4350756	7.5747901	10.7220167
H	13.7589391	8.38579778	9.91416642
H	14.956138	7.10951923	11.4125976
H	14.9761415	5.99502883	10.0476592
H	11.1382038	9.21111553	10.2678295
H	8.71807246	10.0778194	14.393064
H	12.9468935	10.2389243	13.4641689
H	7.08417377	11.494637	8.67236125
H	10.7754178	11.603309	10.9396018
H	9.11121231	7.17098828	3.66270998
H	7.74331392	7.67905134	4.72233137
H	8.11451249	5.9548502	4.49499626
H	14.2564317	3.44420531	10.7609375
H	12.7268114	5.5523551	18.1995529
H	11.2735151	4.51624128	18.3939295
H	11.1036118	6.27774095	18.4566139
H	10.6296854	6.8531855	10.6856138
H	9.95001059	6.86200995	11.015887

Intermediate 3 (S = 4, Charge = 0)

Ni	9.74417253	7.04731357	8.86154923
Ni	11.0385851	5.4369106	14.0374745
Li	8.36149003	5.27638001	16.2995399
Li	12.37891	6.82602999	6.28305007
P	7.00849299	7.34166675	10.7263025
P	13.6091988	5.27706544	11.9690235
O	7.8207203	6.63741494	9.615747
O	9.01619371	7.17657271	7.00210177
O	7.73098434	5.42517797	14.5345428
O	10.6856041	6.58064824	5.59823211
O	9.32134416	5.38976919	12.9453884

O	5.96353763	8.35449977	10.3192139
O	8.09558076	8.05289633	11.7583651
O	11.6916692	7.42719819	8.18465057
O	10.208584	5.32296749	16.0924961
O	13.6710202	6.53104741	7.8622674
O	12.3650522	5.48484742	15.7411647
O	12.1412814	5.59917562	12.3060197
O	13.4894806	3.91215099	11.0298637
O	14.6103437	5.06594511	13.0773897
N	9.48572719	9.02029977	9.14940107
N	9.95747835	5.05715388	8.70353708
N	11.2707538	3.32692115	13.880609
N	11.024903	7.53078894	14.1103667
H	10.1872428	1.20755885	8.35720991
C	10.1240456	2.29692398	8.45320624
C	9.02686019	2.99112562	7.94616478
C	8.97750224	4.37115082	8.09375247
C	11.0109761	4.39451246	9.19486942
C	11.1335859	3.01355812	9.08993738
C	12.2445837	2.68075203	14.5387987
C	12.5686606	1.35100166	14.2863037
C	11.8593744	0.66075369	13.3055248
C	10.8511617	1.33202784	12.6165748
C	10.5937333	2.66201683	12.9329819
H	12.0920018	-0.3856352	13.0784106
C	9.89021395	8.22629052	14.2289695
C	12.1664962	8.18619469	13.8556895
C	9.49771223	6.87421121	5.85884664
C	8.12768993	5.27691379	13.3479997
C	8.48033276	6.83335862	4.74390751
C	7.10682978	4.9081384	12.2825749
C	6.24651603	6.06417711	11.7811836
C	12.8348025	7.04897955	8.63469537
C	11.4013725	5.40672771	16.5423426
C	13.1565693	7.37936162	10.0775725
C	14.2161664	6.56799495	10.8127237
C	8.35237435	9.58112646	8.71056734
C	10.3736587	9.76641275	9.82036609
C	9.8451231	9.61028987	14.0780051
C	12.212777	9.56471557	13.6853057
C	8.05968651	10.9217635	8.93703135
C	10.1514029	11.1085962	10.096653
C	11.0257822	10.2912473	13.7926979

C	8.96957805	11.6984635	9.64849528
H	11.023378	11.3781475	13.6534456
H	8.76158189	12.7542145	9.85307072
C	11.6268031	5.39196662	18.0217252
H	7.66736468	8.91913507	8.17574713
H	8.20759647	2.47272597	7.43874279
H	8.13478991	4.96267989	7.72701475
H	11.7690851	4.98621826	9.71445234
H	12.010619	2.52572978	9.52260551
H	12.7887832	3.26305767	15.2903896
H	13.3736154	0.86862275	14.8495399
H	10.2719351	0.83686079	11.830334
H	9.81823751	3.231113	12.4077733
H	8.98615249	7.64154685	14.4372134
H	13.0715056	7.56972873	13.7923506
H	6.43399213	4.14735162	12.7187414
H	7.62948495	4.43439595	11.4319059
H	5.77012571	6.59302593	12.6281684
H	5.4146013	5.65736797	11.1768669
H	7.93050114	9.01193893	11.8040476
H	12.2155271	7.3899694	10.6564683
H	13.4743046	8.44097135	10.0345217
H	14.8257265	7.23809042	11.4448641
H	14.9239603	6.10711585	10.0992969
H	11.2841176	9.25189922	10.1391699
H	8.88987356	10.1371829	14.1714186
H	13.1666299	10.0586533	13.4744018
H	7.1199633	11.3384828	8.56201609
H	10.8998915	11.6774264	10.6563975
H	8.95308465	6.95394447	3.75686061
H	7.6954041	7.5939884	4.88086844
H	7.98240652	5.84653271	4.76257912
H	14.3690108	3.52870128	10.8581934
H	12.6941867	5.48252019	18.2693289
H	11.2359372	4.45102354	18.4454551
H	11.0697206	6.21306492	18.5033768
H	10.1811359	6.94481932	10.2410849

Intermediate 3 (S = 6, Charge = 0)

Ni	9.54662246	7.05981756	8.87245646
Ni	11.0215585	5.41183353	14.0450569
Li	8.36149005	5.27638002	16.2995399
Li	12.3789099	6.82602998	6.28305012

P	6.88132927	7.30765475	10.7673501
P	13.5596594	5.24035296	11.9176118
O	7.86162591	6.61864262	9.75853925
O	9.09059493	7.26666111	6.92434687
O	7.6881084	5.4306515	14.5567453
O	10.7186695	6.61677024	5.51536317
O	9.2860823	5.39214871	12.9775382
O	5.8149528	8.18194793	10.1637184
O	7.77810869	8.12451001	11.8797721
O	11.5629614	7.38720856	8.26802454
O	10.2071623	5.30707561	16.1015484
O	13.5554187	6.55182848	7.88221637
O	12.3623441	5.44710779	15.7332039
O	12.1145394	5.58045076	12.3206448
O	13.3663456	3.92920199	10.9160235
O	14.5848743	4.94598958	12.9847909
N	9.27333105	9.14401074	9.10668811
N	9.75981053	4.98206529	8.59359679
N	11.2335919	3.30014807	13.8857584
N	11.0309116	7.50647447	14.110882
H	9.90335031	1.11687688	8.43359714
C	9.86591334	2.21103041	8.47552474
C	8.84886326	2.91035574	7.82563014
C	8.83479772	4.29787901	7.90937832
C	10.73359	4.31443345	9.22035148
C	10.8289242	2.92705648	9.18257114
C	12.2271046	2.6556563	14.5162128
C	12.548418	1.32766329	14.2520964
C	11.8155051	0.63692268	13.2895108
C	10.7847515	1.30521284	12.631515
C	10.5309804	2.63334658	12.9587487
H	12.0463562	-0.4079124	13.0536221
C	9.90178434	8.21554453	14.1980615
C	12.1836278	8.14501202	13.8667127
C	9.52843578	6.88285343	5.78811161
C	8.09185528	5.27294367	13.3745295
C	8.47684209	6.7233352	4.71829662
C	7.08235977	4.87410375	12.3070869
C	6.17396384	5.99177476	11.8014127
C	12.7293505	7.05147814	8.68278383
C	11.404286	5.37918858	16.5422858
C	13.1226856	7.41911023	10.0974025
C	14.1685287	6.57645134	10.8172751

C	8.18638659	9.73788175	8.60064596
C	10.1342177	9.86511668	9.83587053
C	9.87397772	9.59729516	14.024931
C	12.2482785	9.52064565	13.6782233
C	7.90381284	11.0816125	8.82470351
C	9.93220502	11.2139237	10.1032513
C	11.0676818	10.2613134	13.7520911
C	8.79062959	11.8319336	9.59336363
H	11.0799295	11.3462753	13.5996987
H	8.59520093	12.8911445	9.7928188
C	11.6408024	5.36255238	18.019613
H	7.52710503	9.10163127	8.00115886
H	8.06687921	2.38910312	7.26502294
H	8.05586588	4.89451166	7.42068888
H	11.4455894	4.91426766	9.79992733
H	11.6460416	2.43046205	9.71366164
H	12.7896396	3.23826865	15.2537202
H	13.3692439	0.84640159	14.7930789
H	10.1843994	0.80961239	11.8616359
H	9.73877569	3.19969365	12.4560262
H	8.98848998	7.64474441	14.4052148
H	13.0819566	7.5172483	13.8224217
H	6.43538618	4.09187106	12.7437686
H	7.62082795	4.41689211	11.4569368
H	5.65829518	6.49362153	12.6414292
H	5.37538203	5.54913216	11.1786429
H	7.86653132	9.06908235	11.6539495
H	12.2082887	7.50458591	10.7086548
H	13.5012918	8.45681371	9.99663131
H	14.7664596	7.22539758	11.4827011
H	14.8896895	6.14446988	10.0987173
H	11.0085217	9.32294678	10.2151579
H	8.92335985	10.1364873	14.0909778
H	13.2117472	10.000799	13.4793284
H	6.99769225	11.5258197	8.40160502
H	10.6612349	11.768275	10.7020377
H	8.91206771	6.8051377	3.71031671
H	7.66329597	7.45604155	4.83853103
H	8.02837072	5.71765182	4.81489063
H	14.226376	3.52352255	10.7020299
H	12.7102706	5.44972558	18.2591531
H	11.2507727	4.42184471	18.4446745
H	11.0890774	6.1841865	18.5063998

H	10.3091132	7.0138028	10.3743916

Intermediate 4 (S = 5, Charge = 0)

Ni	9.69067758	7.33360181	8.51191989
Ni	11.1227066	5.8843468	14.3095015
Li	8.36149005	5.27638002	16.2995399
Li	12.3789099	6.82602998	6.28305012
P	6.99379139	7.55442012	10.5852485
P	13.5190475	5.70867121	12.0575751
O	7.84925964	6.98773243	9.4367904
O	9.01597989	7.55648449	6.61974338
O	7.73678815	5.51252239	14.5223329
O	10.7618163	6.77208023	5.43156991
O	9.4696868	5.86710708	13.142458
O	5.8091371	8.42948088	10.2518755
O	8.06167143	8.38753899	11.5465239
O	11.7836457	7.54794808	8.16763344
O	10.2080247	5.33748066	16.2451345
O	13.6128299	6.35914403	7.86139307
O	12.3586341	5.72724596	16.0808403
O	12.4075601	6.50722825	12.7760292
O	12.7664569	4.57405966	11.1063856
O	14.5857656	5.03630303	12.8873884
N	9.56720689	9.40992257	8.83149957
N	9.74867128	5.26577874	8.28634978
N	11.4858414	3.82781923	13.8643212
N	10.8299184	7.88340412	14.8519286
H	9.60305282	1.39811796	8.0635765
C	9.64619697	2.49101066	8.12506871
C	8.62838683	3.27304549	7.57954091
C	8.71663083	4.65549162	7.68430207
C	10.7261756	4.51744408	8.80656395
C	10.7152269	3.12690677	8.75068176
C	12.4720839	3.16259464	14.4844361
C	12.7815799	1.83602937	14.2006394
C	12.0383511	1.16447986	13.2330719
C	11.0190506	1.85507486	12.5800321
C	10.7861192	3.18395293	12.9187551
H	12.253775	0.11831215	12.9884672
C	9.61094333	8.427827	14.9459129
C	11.9023359	8.65890173	15.0475663
C	9.58094532	7.17634512	5.54222101
C	8.26905606	5.55179892	13.3799075

C	8.70133882	7.19250867	4.31597321
C	7.43562565	5.15411624	12.1642088
C	6.42629377	6.18827887	11.6605815
C	12.9152817	7.10583419	8.5843338
C	11.362444	5.43449557	16.7867057
C	13.4763318	7.66807094	9.88332914
C	14.3097456	6.77939788	10.8024862
C	8.36381053	9.9954522	8.73445636
C	10.6241898	10.1708062	9.14785822
C	9.41544745	9.77323972	15.2413399
C	11.8000661	10.0133305	15.3469099
C	8.17134798	11.3521976	8.96431197
C	10.5200429	11.5334489	9.40313206
C	10.5314141	10.5823512	15.4445342
C	9.2685486	12.1378302	9.31265145
H	10.4137971	11.6468228	15.6752788
H	9.14911598	13.2091554	9.50691951
C	11.5014596	5.17369661	18.2527515
H	7.5263626	9.34054546	8.47623656
H	7.76822377	2.81652534	7.08040028
H	7.94053217	5.31392806	7.28097646
H	11.539896	5.04772847	9.30654496
H	11.5366486	2.56198487	9.20261315
H	13.0326818	3.72276078	15.2390763
H	13.5979035	1.34030688	14.7354026
H	10.4132755	1.37724723	11.8036245
H	10.020179	3.77035458	12.4011078
H	8.76330076	7.75471846	14.7640325
H	12.8768135	8.16908224	14.9411272
H	6.87573675	4.24458954	12.449141
H	8.11591373	4.87229338	11.3385424
H	5.89505505	6.66208174	12.5082829
H	5.64130318	5.6721765	11.0772446
H	7.59724494	9.05819125	12.0795658
H	12.6865709	8.18290882	10.4488598
H	14.1324019	8.48860557	9.52960841
H	14.9921732	7.42226253	11.3883687
H	14.9641574	6.12080438	10.2018897
H	11.5861572	9.65107325	9.18985331
H	8.40006264	10.1759085	15.3101411
H	12.7052207	10.6090844	15.4993517
H	7.16880434	11.7810709	8.87075127
H	11.4127507	12.1078799	9.66855924

H	9.29722325	7.17884746	3.39051863
H	8.02810624	8.06460728	4.31522202
H	8.06264462	6.29032063	4.32451703
H	13.1552025	3.69460229	11.2621955
H	12.5203334	5.38719056	18.6062767
H	11.2653167	4.11595616	18.4618538
H	10.7775971	5.77960587	18.8221842
C	10.6211561	7.93858129	11.4291203
O	10.8116345	8.87149132	12.083851
O	10.4577998	7.04739376	10.6989792

Intermediate 4 (S = 4, Charge = -1)

Ni	9.29979863	6.91727249	6.62506483
Ni	10.4255773	5.30846353	13.6712162
Li	8.36149006	5.27638002	16.2995399
Li	12.3789099	6.82602998	6.28305013
P	6.13877878	6.89356229	10.7327475
P	12.4882046	4.65292084	11.2347151
O	6.55997527	5.76906656	9.79859277
O	9.48060118	7.55634397	4.70883182
O	7.3076046	5.33631075	14.8439034
O	11.6672494	7.08532879	4.63562142
O	8.50251506	5.28651613	12.949837
O	5.19334012	7.98649087	10.2687384
O	7.56110122	7.62421528	11.2202385
O	12.7433519	8.01340788	7.83588584
O	10.1297625	5.29645932	15.8569092
O	12.7013481	5.80893983	7.97733848
O	12.1504138	5.30937063	15.0142259
O	11.3389124	5.49925371	11.8477861
O	11.9467505	3.99023175	9.82964145
O	13.097702	3.55879418	12.0764343
N	8.85669778	8.67226118	7.36029761
N	9.52184622	5.00203864	6.3701601
N	10.3684822	3.21995087	13.5102304
N	10.4714403	7.40707387	13.8064369
H	9.81515985	1.14545081	5.90355442
C	9.73159214	2.22923971	6.03596915
C	9.45929164	3.06244531	4.95115582
C	9.36518929	4.43173676	5.15638944
C	9.78194678	4.18942066	7.41654763
C	9.89665775	2.81196205	7.29122774
C	10.8663627	2.36275639	14.4071547

C	10.9550744	0.99462855	14.1686955
C	10.5095	0.49852565	12.9450204
C	9.9862766	1.39153079	12.011061
C	9.93583812	2.74229465	12.3347267
H	10.5674263	-0.572687	12.7227277
C	9.40048046	8.12873603	14.156907
C	11.618656	8.04070944	13.5343208
C	10.5882152	7.43780263	4.09726478
C	7.4228462	5.19532058	13.5952475
C	10.5651399	7.70475162	2.61366188
C	6.16061477	4.90603758	12.8045669
C	5.46046369	6.15456094	12.2658519
C	12.9037218	6.95180108	8.49969613
C	11.3978014	5.35430278	16.0143582
C	13.3801302	7.07677093	9.93615066
C	13.7859998	5.80654366	10.6652298
C	7.83289254	8.81996119	8.22338493
C	9.60001037	9.75695238	7.06452185
C	9.43038785	9.51774791	14.2398818
C	11.7432605	9.42392333	13.6061298
C	7.5258457	10.0318859	8.82786839
C	9.36227737	11.0021431	7.63103295
C	10.6259924	10.1779453	13.9614243
C	8.30794609	11.1468739	8.5335989
H	10.685833	11.2704312	14.0205874
H	8.10299999	12.1174808	8.99795261
C	11.9463297	5.46692167	17.4021079
H	7.24313766	7.92259976	8.44075641
H	9.32230977	2.65718964	3.94390819
H	9.15313234	5.11783337	4.33042777
H	9.91471814	4.67346833	8.38659752
H	10.1252602	2.21238454	8.17820681
H	11.2189779	2.78881529	15.3538508
H	11.3708467	0.33063885	14.9328416
H	9.62320529	1.04907541	11.0365051
H	9.53992839	3.48473171	11.6323773
H	8.48672704	7.56081581	14.3763516
H	12.459804	7.40278211	13.238895
H	5.46798627	4.36149142	13.4696852
H	6.40603631	4.24175283	11.9566108
H	5.37931632	6.93685001	13.0456483
H	4.41704271	5.89236521	12.007207
H	7.3875006	8.5174971	11.5661743

H	12.6041677	7.61912148	10.5087113
H	14.2330098	7.78011344	9.9113349
H	14.3413337	6.08259679	11.5808709
H	14.4950255	5.21550161	10.0554362
H	10.4095824	9.59887716	6.3436101
H	8.52903639	10.0706855	14.5223791
H	12.7028831	9.89989925	13.3814132
H	6.67836514	10.0672536	9.52014039
H	9.99902401	11.8504604	7.36159422
H	11.5781782	7.82345936	2.20014792
H	9.96119395	8.59571911	2.37620608
H	10.0827727	6.8510158	2.10384111
H	12.1683718	4.58990747	9.06128972
H	13.039135	5.58790448	17.3987457
H	11.6849494	4.56391209	17.9802851
H	11.4805443	6.32062842	17.9223051
C	10.0373135	7.62354086	10.1315798
O	10.2565977	8.58480604	10.7411348
O	9.85902513	6.68836711	9.46893277

Intermediate 4 (S = 6, Charge = -1)

Ni	9.70401196	7.07160886	8.50129204
Ni	10.9976787	5.87919941	14.2643596
Li	8.36149004	5.27638001	16.2995399
Li	12.37891	6.82602999	6.28305009
P	6.87796402	7.55148901	10.3217767
P	13.6654247	5.99711489	12.4169422
O	7.78657562	6.7869619	9.34305257
O	9.01155706	6.95716615	6.59442892
O	7.6374531	5.48559953	14.6037471
O	10.8431051	6.40392886	5.40865857
O	9.21163998	6.40809392	13.3154059
O	5.65940741	8.27186245	9.79319122
O	7.85662238	8.65099815	11.095241
O	11.7953686	7.55885256	8.1091832
O	10.1978276	5.37932135	16.2717289
O	13.7163415	6.55254879	7.70038628
O	12.3557202	5.32956176	15.8779381
O	12.175931	6.35298886	12.6346377
O	13.8131326	4.35995855	12.6336343
O	14.7083083	6.64455281	13.2926575
N	9.37702321	9.13227621	8.50074225
N	10.1752608	5.08383816	8.62568015

N	10.7770678	3.92826221	13.637972
N	11.1728927	7.83662486	14.9938194
H	11.7233966	1.49320494	8.25821415
C	11.2842369	2.48960107	8.37166713
C	10.1436938	2.88080855	7.63442273
C	9.63037642	4.15233754	7.78472038
C	11.229766	4.67758854	9.38503036
C	11.8036465	3.42329376	9.28595053
C	11.0293609	2.80708068	14.3580477
C	10.7734601	1.53246405	13.8900756
C	10.2131864	1.36422661	12.603202
C	9.98177625	2.5177985	11.8467049
C	10.2879405	3.76082915	12.377981
H	9.98381057	0.36825515	12.2104387
C	10.1045611	8.48276679	15.4708172
C	12.350976	8.46960589	14.9465342
C	9.6085902	6.58453119	5.53535616
C	8.11231032	5.80397259	13.4795354
C	8.71885388	6.30100368	4.34931332
C	7.32673432	5.39807001	12.2333099
C	6.3358347	6.41572335	11.6541466
C	12.9374368	7.12406701	8.50090444
C	11.398057	5.21045262	16.6789562
C	13.3656435	7.38068967	9.93506668
C	14.0492611	6.19929184	10.630162
C	8.20388115	9.60734589	8.0558824
C	10.2304167	9.98266916	9.09055491
C	10.1653577	9.7967567	15.9237374
C	12.5016519	9.78547734	15.3757348
C	7.83493387	10.9390869	8.19417613
C	9.93620316	11.3261696	9.28478742
C	11.3894268	10.4621092	15.8731709
C	8.71171455	11.8176173	8.83103744
H	11.4739775	11.4987079	16.2180784
H	8.44721929	12.8713831	8.96953461
C	11.6268345	4.87603237	18.1200483
H	7.53640486	8.87215644	7.59594011
H	9.66209754	2.189259	6.93373658
H	8.75212603	4.47995521	7.21684229
H	11.5920361	5.41067699	10.113564
H	12.6520315	3.17240222	9.93488911
H	11.465401	2.95673311	15.3533641
H	11.0093095	0.67015544	14.5232219

H	9.56829366	2.45945391	10.8334336
H	10.1327351	4.68163061	11.8095198
H	9.16302558	7.91974829	15.4673707
H	13.1907327	7.89719475	14.5266046
H	6.76729993	4.48496171	12.5016258
H	8.03986692	5.11869723	11.436972
H	5.87307032	7.03675033	12.4443372
H	5.49486976	5.86603004	11.1924764
H	7.33522396	9.43087145	11.3568446
H	12.4837915	7.70632542	10.5039255
H	14.0415884	8.25690995	9.91201044
H	15.148887	6.2579732	10.5455884
H	13.7741648	5.25541108	10.1278189
H	11.1857073	9.55415626	9.4146156
H	9.26440786	10.2862272	16.3062978
H	13.4807654	10.2707151	15.3120179
H	6.86452421	11.2785753	7.81801978
H	10.6615591	11.976847	9.78282717
H	9.25111356	6.45496784	3.39748774
H	7.80112022	6.90960957	4.36707095
H	8.41128194	5.23957564	4.38626569
H	13.0143489	3.89857042	12.3162547
H	12.6853772	4.65887529	18.3243808
H	11.0093648	4.01038182	18.4126742
H	11.3082952	5.72440404	18.7499653
C	10.3287091	8.03357371	11.553957
O	10.4992363	8.90136271	12.2986464
O	10.2151763	7.20723514	10.7448769

Intermediate 5 (S = 4, Charge = 0)

94

Coordinate from ORCA-job orca

Ni	9.55270815	7.54177047	8.5870233
Ni	11.051057	5.30910494	14.0678711
Li	8.36149004	5.27638001	16.2995399
Li	12.37891	6.82602999	6.2830501
P	6.47627334	7.78265286	10.3286274
P	13.666549	5.35553685	11.8363802
O	7.5645882	7.53040394	9.2684973
O	8.92971193	7.03117468	6.73220092
O	7.60374722	5.58996281	14.6018606
O	10.7591372	6.52045616	5.51974214
O	9.247752	5.20668399	13.1236904

O	5.11975472	7.18028061	10.0601659
O	6.40883999	9.43635826	10.4138553
O	11.5970754	7.52595641	8.17856523
O	10.2215303	5.18080606	16.1169278
O	13.5557987	6.56774439	7.94614786
O	12.3844115	5.26319226	15.7516853
O	12.2363295	5.49680333	12.3748887
O	13.5099218	4.18725468	10.6649905
O	14.7875161	5.02103629	12.7950323
N	9.44479583	9.46215903	7.91121465
N	9.5390053	5.50778893	9.00651133
N	11.1949126	3.21123271	13.9417933
N	11.0658517	7.40098567	14.1950932
H	9.26029045	1.72483898	9.80691421
C	9.3428939	2.79238766	9.57406438
C	8.34507934	3.44131612	8.84667423
C	8.47991991	4.79867635	8.58379054
C	10.5002606	4.88473429	9.69353388
C	10.4432417	3.52853789	10.0018379
C	12.3844682	2.6542099	13.6772707
C	12.5376572	1.28695723	13.4687181
C	11.4125501	0.46683956	13.534666
C	10.1779205	1.04601443	13.822162
C	10.116088	2.42173698	14.0208576
H	11.4965582	-0.6124574	13.366301
C	9.94541402	8.12220257	14.2906932
C	12.2238668	8.03463679	13.9674979
C	9.52204915	6.62678378	5.68175679
C	8.06220484	5.5050645	13.4273732
C	8.60773816	6.20675981	4.55555414
C	7.1602952	5.82261433	12.2401909
C	7.02396897	7.33267239	12.0168496
C	12.7222915	7.14792856	8.67563072
C	11.423171	5.19251304	16.5560475
C	13.0402947	7.55918896	10.0988459
C	14.136906	6.8406322	10.8709127
C	8.26032698	9.89104519	7.45561413
C	10.508111	10.2727349	7.84486967
C	9.92868662	9.50702449	14.1378464
C	12.3028518	9.4128476	13.7981705
C	8.09588694	11.1601935	6.91209281
C	10.4275622	11.5539787	7.31333395
C	11.1304274	10.1651366	13.8772609

C	9.19870486	12.0081158	6.83830822
H	11.1540838	11.2523775	13.7436736
H	9.09959383	13.0139672	6.41596253
C	11.6573714	5.113965	18.0322839
H	7.43360344	9.18168584	7.55132568
H	7.45931121	2.90586853	8.49201659
H	7.71934156	5.3570634	8.03264692
H	11.3281207	5.49702731	10.0562524
H	11.2577594	3.08152943	10.5800589
H	13.2427321	3.33699566	13.6217975
H	13.5292629	0.87572673	13.2557453
H	9.2667279	0.44286015	13.8820428
H	9.16591289	2.92107424	14.2425597
H	9.02453173	7.56532945	14.5028442
H	13.1197279	7.40411367	13.9236166
H	6.15786045	5.38099865	12.3833997
H	7.61109148	5.35167795	11.347629
H	7.97430623	7.85276329	12.2280347
H	6.27960571	7.75987928	12.7151753
H	5.63747142	9.72711271	10.9339325
H	12.1175107	7.54814984	10.695876
H	13.299261	8.63431331	10.0079412
H	14.5652955	7.53783919	11.6146361
H	14.9766457	6.55541359	10.210224
H	11.4444891	9.86712524	8.23902619
H	8.98382921	10.0538393	14.2206843
H	13.2725605	9.88557449	13.6127986
H	7.11082743	11.4758921	6.55575469
H	11.3214161	12.1841576	7.28375587
H	9.10561913	6.29736566	3.57752425
H	7.67043903	6.7849302	4.55397559
H	8.33941054	5.14395294	4.6976116
H	14.3790975	3.94854648	10.2938176
H	12.728481	5.16578036	18.2755998
H	11.2445603	4.16955371	18.4262461
H	11.1257464	5.93243803	18.5463153
C	9.84381075	8.10578097	10.4080533
O	10.0062375	7.32187562	11.2941948
O	9.82313129	9.4316617	10.5685977
H	9.94025842	9.60776039	11.5237685

Intermediate 5 (S = 6, Charge = 0)

94

Coordinate from ORCA-job orca

Ni	9.8270156	7.51652337	8.46780928
Ni	10.9066762	5.64921367	14.151764
Li	8.36149006	5.27638001	16.2995399
Li	12.3789099	6.82602999	6.28305014
P	6.89659656	7.91886323	10.2245588
P	13.4780301	6.16906677	12.0971301
O	8.36824062	7.9209825	9.78013736
O	9.01334509	6.86840724	6.74017549
O	7.60496739	5.59280799	14.6676907
O	10.8038606	6.42026913	5.44785256
O	9.17712717	6.00984572	13.1243184
O	5.92630941	7.00675055	9.51115688
O	6.43957959	9.50069003	10.0728594
O	11.7810457	7.44730185	7.95498326
O	10.1772073	5.18495859	16.1756306
O	13.934671	7.11236187	8.28237759
O	12.3234151	5.15088575	15.7346655
O	11.9913183	6.03496561	12.4699873
O	13.6937116	4.99527987	10.9432071
O	14.5349652	6.05782979	13.1709213
N	9.67750664	9.49194948	7.79483772
N	9.83432028	5.53006756	9.19480436
N	10.8704269	3.61525205	13.6924378
N	11.0420592	7.64383433	14.7622182
H	9.53291989	1.8649365	10.4460016
C	9.61764274	2.89997065	10.0968974
C	8.48120565	3.63135994	9.75283275
C	8.63248963	4.93856974	9.30669528
C	10.9228743	4.82468641	9.52270599
C	10.8618291	3.51232518	9.9818847
C	12.0221671	3.01192063	13.3733719
C	12.093205	1.65535473	13.0740719
C	10.9224519	0.89902542	13.1127443
C	9.72594869	1.52781299	13.4534619
C	9.74644534	2.89035031	13.7339882
H	10.9425216	-0.1718034	12.881713
C	9.9603252	8.34956358	15.1105889
C	12.2395221	8.24313129	14.7731411
C	9.5708753	6.45525747	5.67247903
C	7.97641061	5.89666154	13.5031526
C	8.63575708	5.93327465	4.60882373
C	6.93449089	6.17183354	12.4358203

C	6.88214443	7.65514795	12.0294606
C	12.8322742	7.45792324	8.71962991
C	11.3877855	5.01374525	16.5555852
C	12.6007001	7.98172888	10.1171664
C	13.6617491	7.7276397	11.1728579
C	8.45203785	9.89247771	7.43148117
C	10.687906	10.3664169	7.73132253
C	10.0284705	9.68767909	15.4847817
C	12.3992503	9.57886945	15.1278785
C	8.18878186	11.184356	6.99190259
C	10.5151779	11.6789865	7.30557905
C	11.2722467	10.3154891	15.4900318
C	9.24059071	12.0967723	6.92829406
H	11.3618503	11.3698937	15.7736461
H	9.0684762	13.1235429	6.5880518
C	11.6468414	4.66312034	17.9867718
H	7.65995124	9.14157921	7.51889793
H	7.47934669	3.19752087	9.83260619
H	7.76201184	5.54800084	9.03646577
H	11.8928022	5.31777014	9.42302171
H	11.7877304	2.98926868	10.2387863
H	12.9148119	3.6498166	13.3640054
H	13.0557501	1.20220648	12.8178256
H	8.78407794	0.97235476	13.495679
H	8.8315556	3.43158148	14.0068555
H	9.00216994	7.81474213	15.0803055
H	13.0966443	7.6198715	14.4813726
H	5.94558615	5.83215567	12.7827197
H	7.19425702	5.54540774	11.5611787
H	7.73773214	8.22045652	12.4447986
H	5.97259141	8.13320862	12.434507
H	5.46865335	9.58220012	10.1047556
H	11.617339	7.61946939	10.4758138
H	12.4524714	9.0727677	9.98873176
H	13.6176156	8.52681971	11.9366064
H	14.6756102	7.77229407	10.7352221
H	11.6706406	9.99409197	8.04009858
H	9.11774856	10.2282751	15.7602832
H	13.3960845	10.0304933	15.1196156
H	7.17038653	11.467171	6.7080479
H	11.3729679	12.3574996	7.27596613
H	9.03615266	6.12252419	3.60049949
H	7.62515557	6.3600876	4.70118354

H	8.54684963	4.83759128	4.72201382
H	14.6327766	4.92696736	10.6898525
H	12.7106944	4.45118932	18.1667831
H	11.0406675	3.79029177	18.2810677
H	11.3353743	5.50210707	18.6324623
C	10.0549893	9.88897236	11.0353976
O	10.2776591	9.2688703	12.0256393
O	9.25044998	10.8918942	10.7990582
H	8.70839843	11.0879464	11.5906449

Intermediate CO (S = 5, Charge = 0)

Ni	9.79530534	7.17739704	8.99712705
Ni	11.0922409	5.53078569	14.079697
Li	8.36149007	5.27638003	16.2995398
Li	12.3789099	6.82602997	6.28305017
P	6.85582266	7.40442155	10.7356755
P	13.6581854	5.35922439	12.0811101
O	7.88221906	6.80656613	9.7502595
O	9.05053593	7.14898267	7.07846228
O	7.75206495	5.52279449	14.5445035
O	10.6949306	6.57864182	5.64246469
O	9.36741219	5.58675998	12.9816969
O	5.71971287	8.20397385	10.1424056
O	7.65026025	8.30407729	11.8855779
O	11.7722599	7.52196197	8.31181547
O	10.2065118	5.25336126	16.1091122
O	13.5802337	6.37874338	7.77763314
O	12.3762761	5.39336798	15.8361322
O	12.2325065	5.87478642	12.3725189
O	13.423212	3.84348933	11.4436221
O	14.6635456	5.28378143	13.2048236
N	9.45146392	9.27880429	8.90552581
N	10.008581	5.09232093	8.88940622
N	11.313279	3.44102339	13.7818856
N	11.0829155	7.56840277	14.472731
H	10.217853	1.22878511	8.64098973
C	10.1600727	2.32080097	8.70967516
C	9.05524736	3.00595347	8.20671384
C	9.01766054	4.39054843	8.31959738
C	11.0662683	4.43351352	9.37371456
C	11.1846851	3.04892294	9.30877866
C	12.3755695	2.80809427	14.3014697
C	12.6586574	1.47214207	14.0370063

C	11.8145685	0.76192742	13.1863774
C	10.7186861	1.42119082	12.6343346
C	10.5074378	2.75781883	12.9581043
H	12.0114052	-0.2907088	12.9541954
C	9.95321247	8.22742353	14.7493565
C	12.2322524	8.24711344	14.3821009
C	9.49885466	6.8169834	5.93742217
C	8.17221875	5.41133239	13.3623045
C	8.44984535	6.66114884	4.85933015
C	7.18226933	4.99448783	12.2842942
C	6.21669372	6.07815557	11.8104524
C	12.9107327	7.02172447	8.62114735
C	11.3866354	5.27779693	16.598342
C	13.5101023	7.36025264	9.97490746
C	14.3756235	6.31564848	10.6745417
C	8.24438283	9.69951322	8.50110655
C	10.4109517	10.185544	9.13300122
C	9.92472924	9.60474018	14.9458207
C	12.2967134	9.62397192	14.5671903
C	7.95219409	11.0457858	8.31218458
C	10.204797	11.5500039	8.96353439
C	11.1198982	10.3161395	14.8525883
C	8.95056353	11.9895853	8.54410286
H	11.1341185	11.401921	14.9986166
H	8.75303231	13.0572807	8.40002728
C	11.5633798	5.16941077	18.0808387
H	7.49257721	8.92067303	8.34244927
H	8.22485059	2.47729005	7.728549
H	8.16862881	4.97684033	7.95572464
H	11.8377384	5.04198717	9.85733913
H	12.0665009	2.56629142	9.73758384
H	13.0194472	3.40805549	14.9527146
H	13.5354825	1.00165034	14.4929082
H	10.0302347	0.91208909	11.9526055
H	9.67010777	3.31771875	12.5274337
H	9.04076677	7.61718463	14.7876069
H	13.1224174	7.65444755	14.1349973
H	6.58547108	4.16342631	12.7026264
H	7.73808603	4.59469876	11.4182362
H	5.7156974	6.5662128	12.6671843
H	5.40937209	5.60300756	11.2238759
H	7.91058755	9.17699988	11.5367031
H	12.7285086	7.74195216	10.6468423

H	14.1364905	8.24616828	9.74793511
H	15.2592073	6.80729107	11.1165208
H	14.7770454	5.59517662	9.93849717
H	11.3798056	9.79252209	9.46170748
H	8.97709191	10.1082904	15.1606643
H	13.2563519	10.1429869	14.4815591
H	6.95120085	11.3453276	7.98692869
H	11.0191798	12.2542924	9.15749755
H	8.88256279	6.74348612	3.85009005
H	7.63732388	7.39554294	4.97974422
H	7.99598264	5.65745397	4.95444803
H	14.2285027	3.30345484	11.5379664
H	12.6252797	5.20401467	18.3645088
H	11.122729	4.22658782	18.4466563
H	11.0261497	5.98950011	18.5869601
C	10.3828071	7.56858398	10.9485007
O	10.6015383	8.31011083	11.7709587